## 4.8.   FLECHT SEASET Forced Reflood Test 31504

The Full-Length Emergency Core Heat Transfer (FLECHT) Separate Effects and System-Effects Test (SEASET) facility was designed, built, and operated by the Westinghouse Electric Corporation. The objective of the test program was to obtain test data on reflooding heat transfer under simulated LOCA conditions for use in evaluating the heat-transfer capabilities of a PWR ECCS. The test program investigated the effects of parameters such as initial clad temperature, flooding rate, power, inlet subcooling, and system pressure on core heat transfer.

### 4.8.1.   Facility Description

The FLECHT SEASET facility[4.8-1,4.8-2] was operated as a once-through system. It consisted of a low-mass-flow housing for the test bundle and upper and lower plenums, an external pipe downcomer, the test rod bundle, a coolant injection system, a coolant carryover tank, a steam boiler for back-pressure regulation, a gas supply for coolant injection, an entrainment separator, and the associated piping and valves. The low-mass-flow housing used in the test was designed to minimize the wall effects so that the rods one row or more away from the housing in the bundle are representative of any region in a PWR core. To preserve proper thermal scaling of the facility with respect to a PWR, the power-to-flow-area ratio is nearly the same as that of a PWR fuel assembly. An external downcomer (pipe) was connected to the flow housing lower plenum for the gravity reflood tests. The downcomer was not used for forced reflood tests.

The rod bundle was composed of 161 heater rods (93 uninstrumented and 68 instrumented), 4 instrumented thimbles, 12 steam probes, 8 solid triangular fillers, and 8 grids. A plan view of the test bundle is shown in Fig. 4.8-1. The test bundle rod geometry is typical of a Westinghouse 17 x 17 fuel rod design and was deemed to be representative of the Westinghouse, Babcock & Wilcox, and Combustion Engineering fuel assemblies of that period (1980). Each rod has a cosine axial power profile. The fillers were welded to the grids to maintain the proper grid location; they also reduced the amount of excess flow area near the low-mass-flow housing.

The coolant injection system provided reflood water to quench the rod bundle during testing. Coolant injection water was supplied by a gas-charged accumulator, which then passed through a series of valves and flowmeters before entering the flow housing. The desired injection characteristic was accomplished by sequencing the valves to attain the specified injection flow characteristics. Coolant injection water was supplied to lower plenum for the forced reflood tests.

The design of the upper-plenum extension prevented the entrained liquid collected in the upper plenum from falling back into the bundle. The housing for the rod bundle extended upward about 0.15 m into the upper-plenum extension. The two-phase flow exiting the bundle was forced to move radially outward, downward, and then upward into an exhaust pipe that subsequently led to the separator. Much of the liquid in the two-phase flow exiting the core was separated from the vapor as it followed the tortuous path to the exhaust inlet. The liquid collected at the bottom of the upper-plenum extension housing where it drained through a tube to the carryover tank.

Located in the exhaust line, the separator was designed to remove any remaining water droplets exiting the test section so that a meaningful single-phase flow measurement could be obtained by an orifice section positioned downstream of the separator. The separator operated by utilizing centrifugal action to force the heavier moisture against the wall, where it drained to the bottom and through an outlet to a drain tank. A resistance orifice plate was installed before the inlet flange of the entrainment separator for the gravity reflood tests to simulate the hot-leg resistances.

The instrumentation of the FLECHT SEASET facility was extensive and included housing differential pressure cells every 0.3 m to obtain void fraction measurements along the heated length of the bundle, steam probes in each of the 11 thimble tubes to measure steam superheat radially and axially across the bundle, and 177 heat-rod thermocouples. In addition, flow was measured at several locations as previously described. Additional instrumentation details are found in Ref. 4.9-1.

## 4.8.2. Test Procedure and Description

The following general procedure was used to establish initial test conditions and perform a typical FLECHT SEASET unblocked bundle reflood test. The accumulator was filled with water and heated to the desired temperature. The carryover vessel, entrainment separator, separator drain tank, test section upper plenum, and test section outlet piping were heated while empty to slightly above the saturation temperature corresponding to the test-run pressure. The test section lower plenum was heated to the temperature of the coolant in the accumulator. The test section, carryover vessel, and exhaust-line components were pressurized to the desired system pressure. The coolant in the accumulator was pressurized to 2.76 MPa. Water was injected into the test section lower plenum until it reached the beginning of the heated length of the bundle heater rods. Coolant was circulated and drained to ensure that the water in the lower plenum and injection line was at the specified temperature before the run.

Power was then applied to the test bundle, and the rods were allowed to heat up. When the temperatures in any two designated bundle thermocouples reached their preset value, coolant injection was automatically initiated, as was the power decay for the heater rods. The injected coolant flow rate was controlled by valves. The system pressure was controlled to a preset value by releasing steam to the atmosphere through an exhaust control valve. The test was terminated when all the designated heater rods were quenched, as indicated by the rod thermocouples.

The initial conditions set for FLECHT SEASET forced reflood test 31504 are tabulated in Table 4.8-1, as well as a summary of key bundle reflood test data.

## 4.8.3. TRAC Model

The FLECHT SEASET facility configured for forced reflood tests was modeled as shown in the input model schematic (Fig. 4.8-2). The test vessel was modeled as a 1D Vessel in Cartesian coordinates. The rod bundle occupied cells 3 through 17. The fine axial noding used in the FLECHT SEASET test 31504 input model is not consistent width the noding used in standard full-plant models. For example, core nodes in the AP600 plant model are ~0.6 m high. The lower plenum was modeled with cells 1 and 2. The upper plenum was modeled with cell 18. pressure boundary condition is specified to be a constant 0.28 MPa.

Coolant injection was to the lower plenum through a Pipe component supplied by a Fill providing the coolant injection flow measured in the test. Figure 4.8-3 shows the core inlet mass flow and Fig. 4.8-4 shows the time-averaged core flooding rate, defined as the time-averaged core inlet mass flow divided by the core inlet flow area and the density of the core inlet flow.

The 161-heater rods were modeled as a single Rod component. We prepared models with and without the 8 spacer grids in the facility.

A listing of the input model used for this developmental assessment calculation is found in Appendix K. Archival storage information for this input model is provided in Section 4.8.8.

### 4.8.4. Comparison of Predicted and Measured Results

The calculation was performed with TRAC-M/F77, Version 5.5. These results are for newrfd=3, which activates the reflood model with explicit top-down reflood modeling. An identical set of graphical code-data comparisons for Version 5.5 with newrfd=1 is presented, without analysis, in Appendix L. Setting newrfd=1 activates the reflood model as it existed in the 1993 developmental assessment calculation.[4.10-4] We have run FLECHT SEASET 31504 calculations both with and without the grid-spacer model. We have determined that the grid-spacer model should not be used because it results in excessive and nonphysical heat-transfer processes in the upper portions of the core. Therefore, the base-case assessment results for FLECHT SEASET 31504 do not use the TRAC grid-spacer model (see Section 4.4-5 for details). We also report the calculation results with the grid spacer to illustrate the impact of a grid-spacer model (Section 4.8-5).

FLECHT SEASET Test 31504 was one of a series of forced reflood tests conducted in the facility. Test conditions are summarized in Table 4.8-1. All initial conditions were established via input. The initial heater-rod axial temperature distribution input at the start of the test is compared with the measured heater-rod axial temperature distribution in Fig. 4.8-5. The input and measured initial cladding profiles are in reasonable agreement, although the temperatures of a number of the rods at the core midplane were higher than specified. The initial axial vapor-temperature distribution input at the start of the test is compared with the measured axial vapor temperature in Fig. 4.8-6. The input and measured axial vapor temperature profiles are in reasonable agreement.

The test was initiated when power was applied to the core and the ECCS injection flow rate was initiated.

A comparison of predicted and measured cladding quench times at various levels in the core is presented in Fig. 4.8-7. The predicted and measured quench times are in reasonable agreement to an elevation of 1.5 m. Between 1.5 and 2.75 m, the predicted quench times are earlier than measured by as much as ~130 s. For elevations higher than 2.75 m, the predicted quench time is later than measured. Overall, the agreement between predicted and measured quench times is judged to range between minimal and reasonable.

In other assessments in this report, we have shown that the code predicts too much entrainment and carryover of liquid, resulting in a deficiency of liquid ahead of the quench front. We have also shown that the code underpredicts the amount of heat transfer ahead of the quench front. These are general deficiencies in the reflood model. However, with FLECHT SEASET 31504, we observe a second, significant effect. In FLECHT SEASET 31504, the grid spacer is a key component and has a major impact on cladding thermal response.

*The following observations apply to the test.* For all but the highest elevations of the core, the quench front advances coherently throughout the test bundle (Fig. 4.8-7). At an elevations above 3.25 m, radial variations in quenching behavior are seen in the test data. During the test, the quench front advances from the bottom of the core upward. There appears to be no top-down quenching, even at the highest elevations in the core.

*The following observations apply to the predicted quench behavior without grid spacers modeled.* The predicted quench front advances from the bottom of the core upward. The calculated quench front advances slightly slower than observed in the test to an elevation of 1 m. The measured quench front advances to the core midplane at a rate of ~7.2 mm/s. The predicted quench front advances at ~9.6 mm/s. At the core midplane, the predicted quench occurs ~65 s earlier than in the test.

The predicted cladding temperature responses at a number of levels through the core are shown in Fig. 4.8-8 (lower half of core) and Fig. 4.8-9 (upper half of core). Quenching is seen to progress upward from the bottom of the core as was the case in the test.

The predicted and measured cladding thermal responses at 7 axial locations are compared in Figs. 4.8-10 through 4.8-16. The trends discussed previously are evident in these figures. At the 0.3048-m level above the bottom of the heated core (Fig. 4.8-10), the predicted quench time is slightly late, as is the peak temperature PCT time. The predicted PCT is in reasonable agreement with that measured. The predicted and measured thermal performance are also in agreement at the 0.9906-m level (Fig. 4.8-11), although the predicted cooling rate following the peak temperature turnaround is too high. The cooling rate slightly above the core midplane at the 1.9812-m level (Fig. 4.8-12) is also too large, and the turnaround time is early. However, the PCT is in reasonable agreement with that measured. At the 2.8194-m level (Fig. 4.8-13), the predicted PCT is again in reasonable agreement with the measured value. The agreement with the measured peak temperature turnaround time and the quench time is also reasonable. At this level, the onset of cooling/reheat cycles is predicted, which are not observed in the data. These are related to variations in liquid content of the two-phase flow as will be described in the next paragraph. Similar behavior is predicted at the 3.0480-m level (Fig. 4.8-14). In the upper elevations of the core (3.3528 and 3.5052 m as shown in Figs. 4.8-15 and 4.8-16, respectively), too little cooling is predicted, resulting in significantly higher PCTs and delayed quench times.

The predicted and measured differential pressures across 12, 1-ft segments through the core are presented in Figs. 4.8-17 through 4.8-28. The pressure differentials are interpreted as a direct measurement of liquid present between each set of pressure taps. The predicted and measured differential pressure results are consistent with the cladding thermal discussions presented above.

The differential pressure trace corresponding to the heater-rod cladding temperature history at the 0.3048-m level (Fig. 4.8-10) is Fig. 4.8-17. A slightly slower initial accumulation of liquid at this level results in the slightly delayed PCT time. The predicted post-turnaround cooling mirrors the measured rate until the predicted accumulation of liquid stalls at 15 s, and the cooling rate is slowed until ~35 s when the coolant again begins to increase to fill this level with liquid.

The differential pressure trace corresponding to the heater-rod cladding temperature history at the 0.9906-m level (Fig. 4.8-11) is Fig. 4.8-18. At this level, the code predicts a too-rapid filling with liquid and the predicted cooling rate is too high.

The differential pressure trace corresponding to the heater-rod cladding temperature history at the 1.9812-m level (Fig. 4.8-12) is Fig. 4.8-21. At this level, the code again predicts a too-rapid filling with liquid, and the predicted cooling rate is too high. In addition, the ΔP oscillations beginning at ~150 s causes the corresponding small reheat and cooling cycle observed in the cladding response. The cause of these oscillations has not been thoroughly investigated but they are clearly nonphysical.

The differential pressure trace corresponding to the heater-rod cladding temperature histories at the 2.8194 and 3.0480-m levels (Figs. 4.8-13 and 4.8-14) is Fig. 4.8-24. At this level, the code again underpredicts the liquid inventory. However, the ΔP oscillations beginning at ~150 s appear to provide sufficient cooling so that the predicted and measured thermal response are in reasonable agreement. Thus, it appears that reasonable thermal performance is predicted but with the wrong physics.

The differential pressure trace corresponding to the heater-rod cladding temperature histories at the 3.328 and 3.5052-m levels (Figs. 4.8-15 and 4.8-16) is Fig. 4.8-28. At this level, the code again underpredicts the liquid inventory. The ΔP oscillations are still present but they are not sufficiently strong to compensate for the diminished liquid content. Therefore, too little cooling is predicted, the PCTs are higher than measured, and the quench times are late.

The total core-predicted and measured ΔPs are shown in Fig. 4.8-29. TRAC overpredicts the core liquid content and distribution in that too much liquid resides in the core except at the highest elevations where there is too little liquid.

Figures 4.8-30 and 4.8-31 show the predicted and measured vapor temperatures at two levels in the core (Cells 7 and 14, respectively, in Fig. 4.8-2). In general, the predicted vapor temperatures are in reasonable agreement with the measured vapor temperatures.

### 4.8.5. Comparison of Predicted and Measured Results (with Grid Spacers)
In this section we provide a comparison of the predicted and measured results for FLECHT SEASET 31504 with the TRAC grid-spacer model activated. We present the figures in the same order as in Section 4.4. The following tabulation is provided to facilitate the comparison of figures.

| Without Grid Spacers | With Grid Spacers |
| --- | --- |
| 4.8-7 | 4.8-32 |
| 4.8-8 | 4.8-33 |
| 4.8-9 | 4.8-34 |
| 4.8-10 | 4.8-35 |
| 4.8-11 | 4.8-36 |
| 4.8-12 | 4.8-37 |
| 4.8-13 | 4.8-38 |
| 4.8-14 | 4.8-39 |
| 4.8-15 | 4.8-40 |
| 4.8-16 | 4.8-41 |
| 4.8-17 | 4.8-42 |
| 4.8-18 | 4.8-43 |
| 4.8-19 | 4.8-44 |
| 4.8-20 | 4.8-45 |
| 4.8-21 | 4.8-46 |
| 4.8-22 | 4.8-47 |
| 4.8-23 | 4.8-48 |
| 4.8-24 | 4.8-49 |
| 4.8-25 | 4.8-50 |
| 4.8-26 | 4.8-51 |
| 4.8-27 | 4.8-52 |
| 4.8-28 | 4.8.53 |
| 4.8-29 | 4.8-54 |
| 4.8-30 | 4.8-55 |
| 4.8-31 | 4.8-56 |

A comparison of predicted and measured cladding quench times at various levels in the core is presented in Fig. 4.8-32. The grid-spacer model acts to delay the quench times (compare with Fig. 4.8-7).

*The following observations apply to the predicted quench behavior with grid spacers modeled.* The calculated quench front advances from the bottom of the core upward. The calculated quench front advances slower than observed in the test. The measured quench front advances to the core midplane at a rate of ~7.2 mm/s. The predicted quench front advances at ~4.4 mm/s. At the core midplane, the predicted quench occurs ~160 s later than in the test. The presence of grid spacers continues downstream of the cell in which the grid spacer is modeled, particularly in the higher elevations of the core.

The predicted cladding temperature responses at a number of levels through the core are shown in Fig. 4.8-33 (lower half of core) and Fig. 4.8-34 (upper half of core). Quenching progresses upward from the bottom of the core to an elevation of 2.4 m. However, the existence or nonexistence of a modeled grid spacer within a given hydro cell has a significant impact upon the thermal behavior in the upper portions of the core.

The predicted and measured cladding thermal responses at 7 axial locations are compared in Figs. 4.8-35 through 4.8-41. At the 0.3048-m level (Fig. 4.8-10), the

predicted quench time is slightly late, as is the peak temperature turnaround time. The PCT is in reasonable agreement with that measured. The only impact of the grid spacer is to slightly delay the quench time. The impact of the grid spacers is much more pronounced at the 0.9906-m level. The initial cooling rate is well predicted to 83 s, at which time the predicted cooling rate slows. The quench is predicted to occur at a much later time than for the no-grid-spacer case. At the 1.9812-m level, the predicted PCT is much greater than measured temperatures and is also much greater than the predicted PCT without the grid spacer. The PCT time and the quench time are also much later. In the upper portions of the core, the impact of the grid-spacer model is ever more evident. At the 2.8194-m level (compare Fig. 4.8-13 with no grid-spacer modeling and Fig. 4.8-37 with grid-spacer modeling), the effect of the grid spacers is pronounced and nonphysical. Excessive cooling is predicted. This trend continues at the 3.0480-, 3.3528-, and 3.5052-m levels (Figs. 4.8-39 through 4.8-41, respectively).

The predicted and measured differential pressures across 12, 1-ft segments through the core are presented in Figs. 4.8-42 through 4.8-53. The predicted and measured differential pressure results are consistent with the cladding thermal discussions presented above. The differential pressure trace corresponding to the heater-rod cladding temperature history at the 0.3048-m level (Fig. 4.8-35) is Fig. 4.8-42. Compared with the no-grid-spacer calculation, the accumulation of liquid at this level is slowed, and this results in a relatively later quenching of the heater rod.

The differential pressure trace corresponding to the heater-rod cladding temperature history at the 0.9906-m level (Fig. 4.8-36) is Fig. 4.8-45. Compared with the no-grid-spacer calculation, the accumulation of liquid at this level is also slowed and this delays the quenching of the heater rod by ~75 s.

The differential pressure trace corresponding to the heater-rod cladding temperature history at the 1.9812-m level (Fig. 4.8-37) is Fig. 4.8-44. Compared with the no-grid-spacer calculation, the accumulation of liquid at this level is also slowed and this delays the quenching of the heater rod by ~275 s and ~150 s relative to the data. However, the additional cooling predicted at this level in the no-grid-spacer calculation is promoted by nonphysical chugging.

The differential pressure trace corresponding to the heater-rod cladding temperature history at the 2.8194-m level (Fig. 4.8-38) is Fig. 4.8-51. Compared with the no-grid-spacer calculation, the accumulation of liquid at this level and quenching is not predicted to occur during the 700 s of transient time evaluated. For the non-grid-spacer calculation, the average liquid content at this level is also underpredicted. However, additional cooling is once again predicted at this level in the no-grid-spacer calculation by significant liquid-level oscillations. Even though the liquid content at this level is severely underpredicted with the grid-spacer model activated, the predicted thermal response shows excess cooling beginning at ~25 s (Fig. 4.8-38). This trend becomes more pronounced at higher levels where the amount of liquid is underpredicted but excessive cooling is predicted. The differential pressure traces corresponding to the heat-rod cladding temperature histories at the 3.0480-, 3.3528-, and 3.5052-m levels (Figs. 4.8-39 through 4.8-41) are Figs 4.4-52 and 4.4-53. The 3.048-m level is in a cell in which a grid spacer is modeled and liquid far in excess of that measured accumulates in this cell (Fig. 4.8-52). This causes the overcooling shown in Fig. 4.8-39. Overcooling is also

overpredicted at the 3.353- and 3.505-m levels, even though the amount of liquid at this level is underpredicted. A grid spacer is also modeled in the hydro cell containing these levels.

The total predicted and measured differential pressure across the heated core is presented in Fig. 4.8-54. As with the no-grid-spacer case, the amount of liquid in the core at any instant is overpredicted.

Figures 4.8-55 and 4.8-56 show the predicted and measured vapor temperatures at two levels in the core (Cells 7 and 14, respectively, in Fig. 4.8-2). In general, the predicted vapor temperatures are in reasonable agreement with the measured vapor temperatures. Cell 7 is immediately downstream of a cell in which a grid spacer is modeled. A grid spacer is modeled in cell 14. The respective figures with no-grid-spacer model are 4.8-30 and 4.8-31. The impact of the grid-spacer model on the vapor superheat, both downstream and within the cell in which the grid spacer is modeled, is significant. Particularly evident is the on-off nature of the grid-spacer model, which acts to drive the vapor temperature to saturation when it is activated. Given this behavior, we have concluded that the current TRAC grid-spacer model is seriously flawed and should not be used.

### 4.8.6. Conclusions

A developmental assessment of TRAC-M, Version 5.5 has been completed using data from FLECHT SEASET test 31504, a forced reflood case. The base-case calculation was performed using an input model that contained no model of the FLECHT SEASET grid spacers. With respect to key parameters, such as cladding temperatures and coolant distribution, the agreement between code-predicted and measured values is judged to vary between minimal and reasonable.

We performed a parametric calculation in which the FLECHT SEASET grid spacers were modeled with the TRAC grid-spacer model. When applied to other facilities and tests, we have found that the grid-spacer model produces excessive and nonphysical cooling rates. The same effect was observed in the present calculations. The TRAC grid-spacer model lacks an appropriate physical basis and its use is, therefore, discouraged.

In other tests that included in the present assessment activity, several behaviors were consistently observed. These behaviors are as follows: (1) the prediction of too little liquid inventory in the test vessel, particularly in advance of the quench front, (2) the prediction of too-little heat transfer in advance of the quench front, and (3) the prediction of a too-large liquid-transport rate through the test vessel. For this test, however, we found that too much liquid was present in the vessel and this implies that there was not an excess of liquid transported out of the vessel. We also found a significant amount of precursory cooling for the non-grid-spacer case caused by chugging in the core.

### 4.8.7. Code Performance

FLECHT SEASET TEST 31504 was run with code Versions 5.5 and 5.4.29r9+; the run performance information plus other pertinent comments follow.

Code Version 5.5

| Platform | Sun Enterprise 3000 |
|---|---|
| Total CPU time (s) | 8690.3 |
| Archive location of input model | CFS    /tida/f77da_decks/infs31504 |
| Archive location of calculation | CFS    /trac-da/F77DA/1.11Rrfd3nogs/ FLECHT.tar.gz |

Code Version 5.4.29R9+

| Platform | Sun Enterprise 3000 |
|---|---|
| Total CPU time (s) | 7859.0 |
| Archive location of input model | CFS    /tida/f77da_decks/ infs31504 |
| Archive location of calculation | CFS    /trac-da/F77DA/5429R9rfd3/ FLECHT.tar.gz |

## REFERENCES

4.8-1.  M. J. Loftus, L. E. Hochreiter, C. E. Conway, C. E. Dodge, A. Tong, E. R. Rosal, M. M. Valkovic, and S. Wong, "PWR FLECHT SEASET Unblocked Bundle, Forced and Gravity Reflood Task Data Report," US Nuclear Regulatory Commission document NUREG/CR-1532, Electric Power Research Institute document EPRI NP-1459, Westinghouse Electric Corporation document WCAP 9699 (June 1980).

4.8-2.  "Compendium of ECCS Research for Realistic LOCA Analysis," US Nuclear Regulatory Commission document NUREG-1230 (December 1988).

4.8-3.  N. Lee, S. Wong, H. C. Yeh, and L. E. Hochreiter, "PWR FLECHT SEASET Unblocked Bundle, Forced and Gravity Reflood Task Data Evaluation and Analysis Report," US Nuclear Regulatory Commission document NUREG/CR-2256, Electric Power Research Institute document EPRI NP-2013, Westinghouse Electric Corporation document WCAP 9891 (September 1981).

4.8-4.  C. Unal, K. Tuzla, and J. C. Chen, "Comparison of TRAC-PF1/MOD1 Post-Test Calculation to Data Obtained From Lehigh University 3 x 3 Rod Bundle Bottom-Reflood Test," Institute of Thermo-Fluid Engineering and Science, Lehigh University document TS-862 (February 1989).

# TABLE 4.8-1

## CONDITIONS AND KEY RESULTS FOR TEST 31504

| Parameter | Test Condition Value |
|---|---|
| Upper-plenum pressure | 0.28 MPa |
| Rod initial clad temperature at the 1.83-m level | 1136 K |
| Rod peak power | 2.3 kW/m |
| ECCS injection rate | ~0.37 kg/s |
| Coolant temperature | 324 K |
| Radial power distribution | Uniform |
| Initial temperature of hottest rod | 1093 K |
| Elevation of maximum temperature of hottest rod | 1.98 m |
| Maximum temperature of hottest rod | 1423 K |
| Temperature rise | 330 K |
| Turnaround time of hottest rod | 130 s |
| Quench time of hottest rod | 325 s |
| Bundle quench time | 594 s |
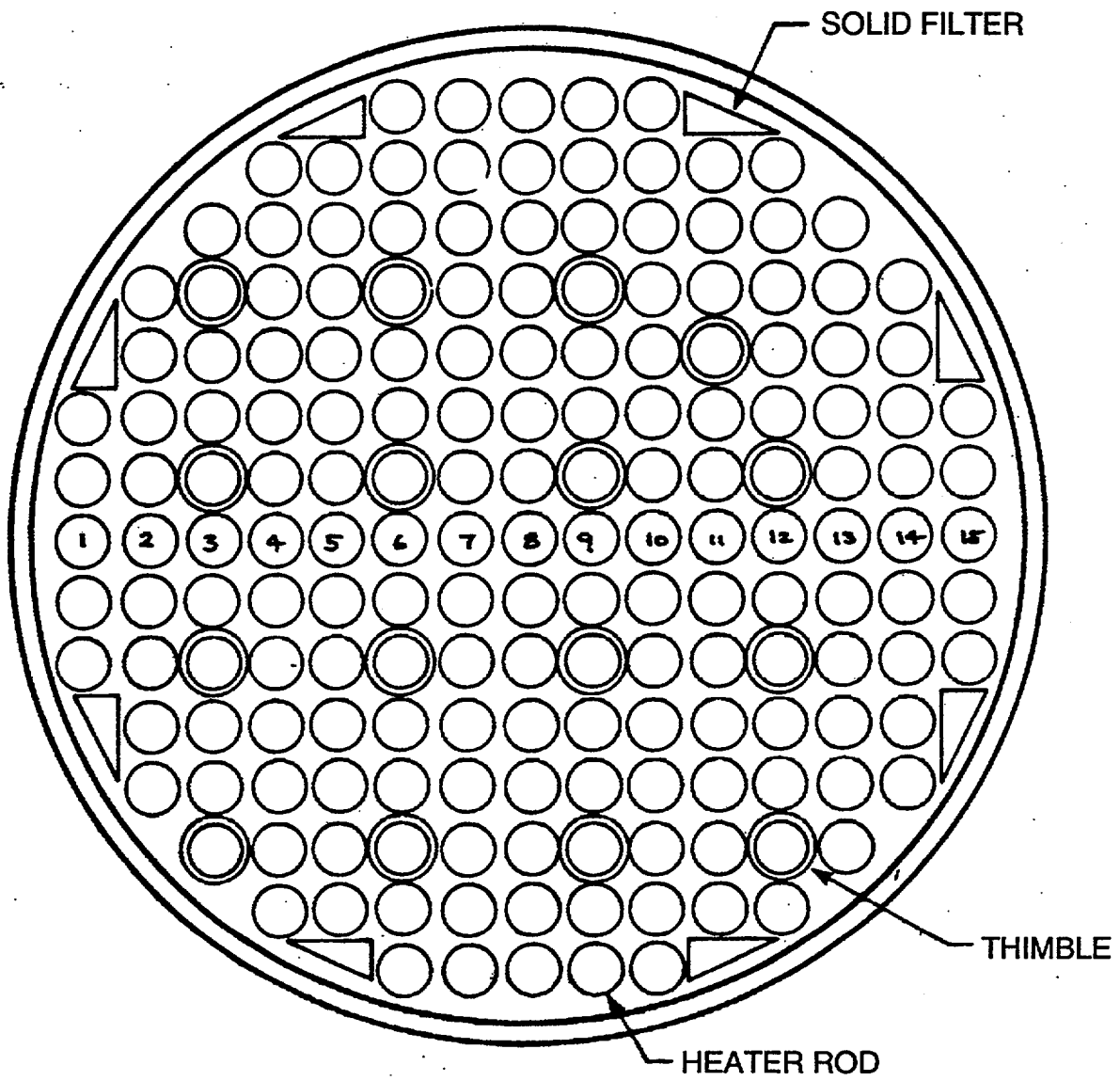
Fig. 4.8-1. Plan view of FLECHT SEASET test bundle.

Core Section
of Vessel Wall   Fuel Rods
ROD               ROD

⑦               ⑥

End
of Heating   3.6578

· VESSEL
Cartesian Geometry
(x=1, y=1, z=18)

⑤

Height (m)

Start
of Heating   0.0

④   BREAK
4

③   PIPE
3

Grid Spacer Locations

| | | |
|---|---|---|
| 18 | 4.2926 | ← 4.2926 |
| | 4.0640 | |
| 17 | | |
| 16 | 3.5154 | ← 3.5568 |
| 15 | 3.3325 | |
| 14 | 3.1496 | |
| 13 | 2.9667 | ← 3.0226 |
| 12 | 2.7838 | |
| 11 | 2.6010 | |
| 10 | 2.4181 | ← 2.5146 |
| 9 | 2.0523 | ← 1.9812 |
| 8 | 1.8694 | |
| 7 | 1.6866 | |
| 6 | 1.5037 | ← 1.4478 |
| 5 | 1.3208 | |
| 4 | 1.1379 | |
| 3 | 0.9550 | ← 0.9398 |
| 2 | 0.4064 | ← 0.4064 |
| 1 | 0.1778 | |
| | 0.0 | |

3.1090
2.9261
2.7432
2.5603
2.3774
2.1946
2.0117
1.6459
1.4630
1.2802
1.0973
0.9114
0.7315
0.5486

2

②   PIPE
1

①   FILL

Fig. 4.8-2. FLECHT SEASET Test 31504 input model diagram.
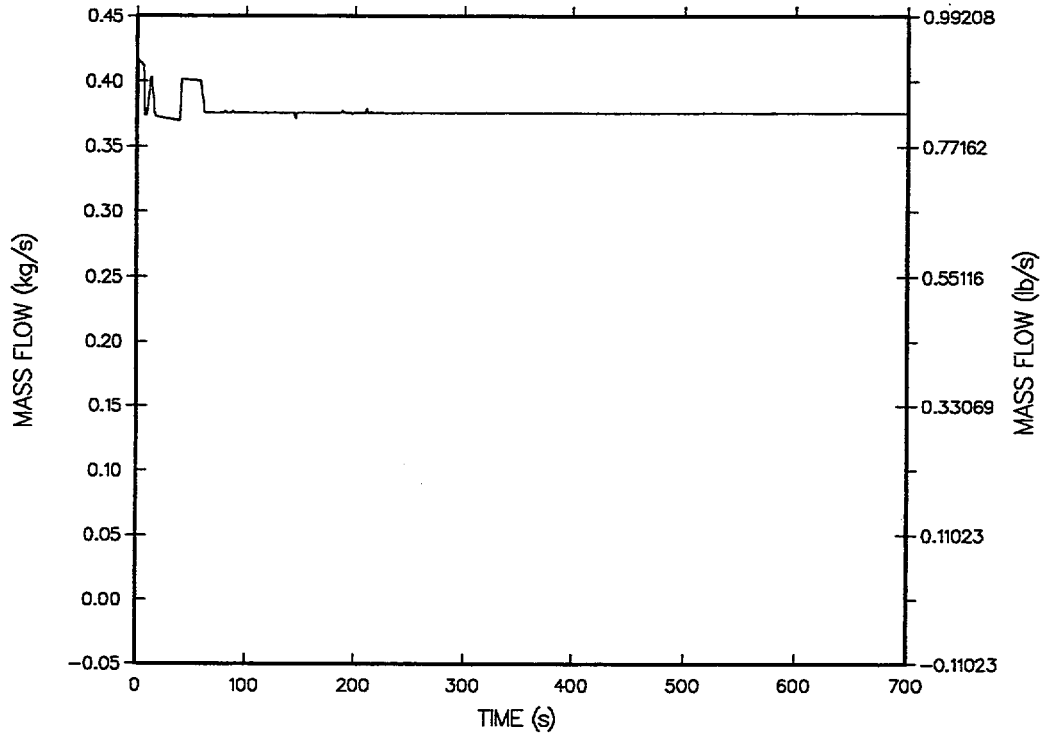
Fig. 4.8-3. Core inlet mass flow.
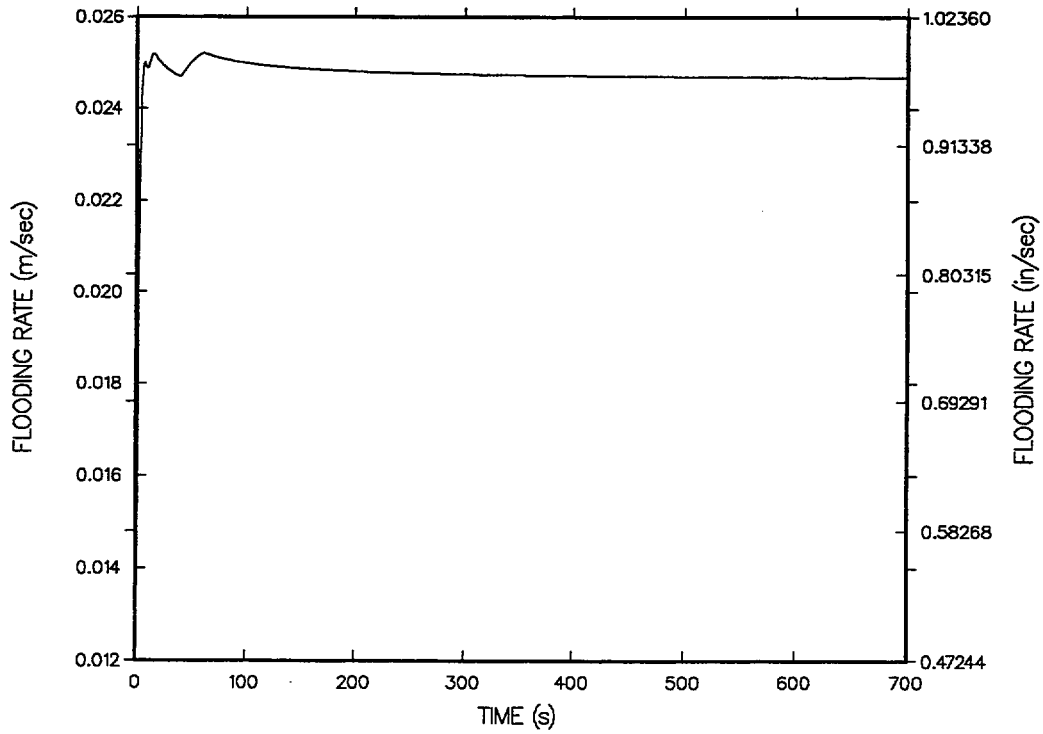


Fig. 4.8-4. Time-averaged core flooding rate.
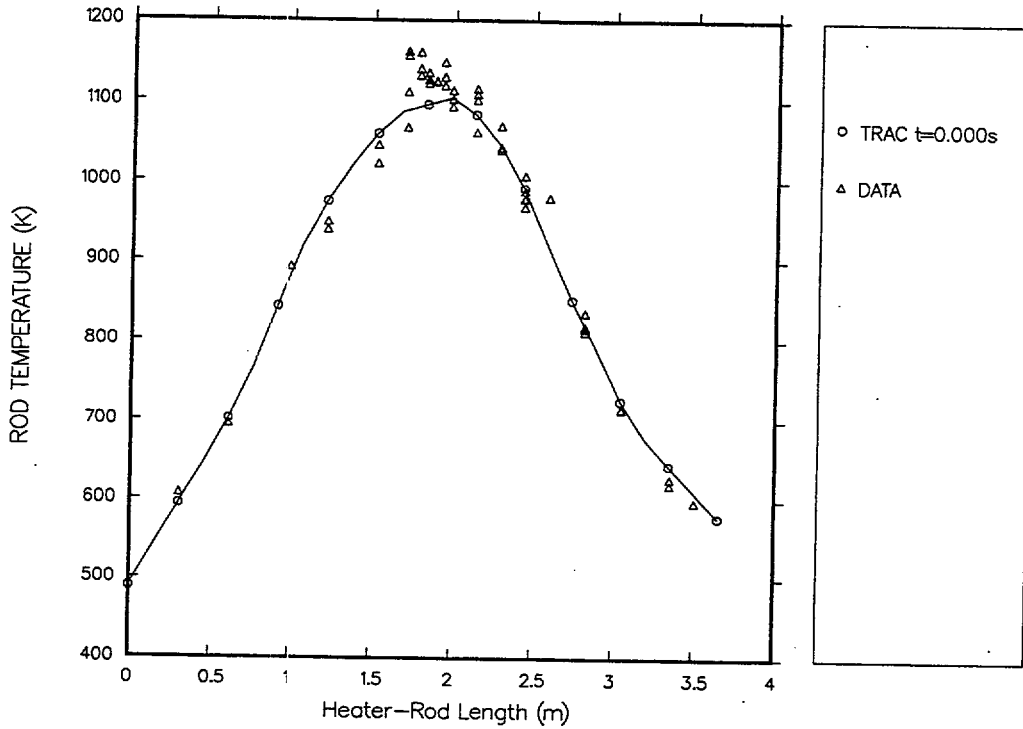
Fig. 4.8-5. Comparison of initial predicted and measured axial heater-rod cladding temperatures (0.0 s).
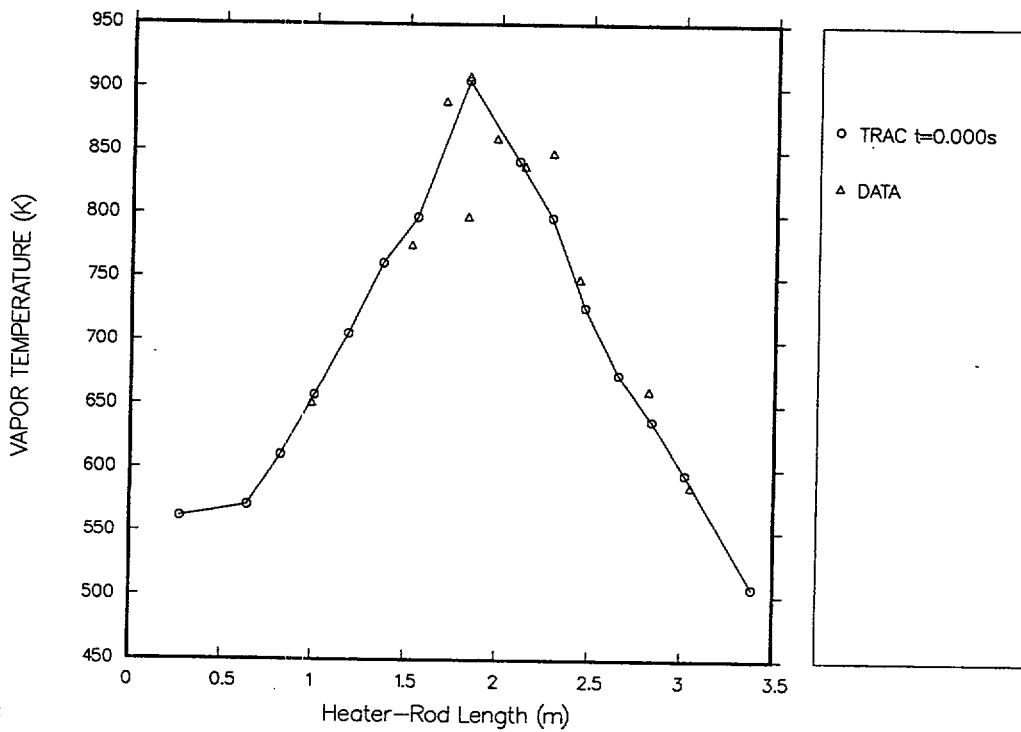


Fig. 4.8-6. Comparison of initial predicted and measured axial vapor temperatures (0.0 s).
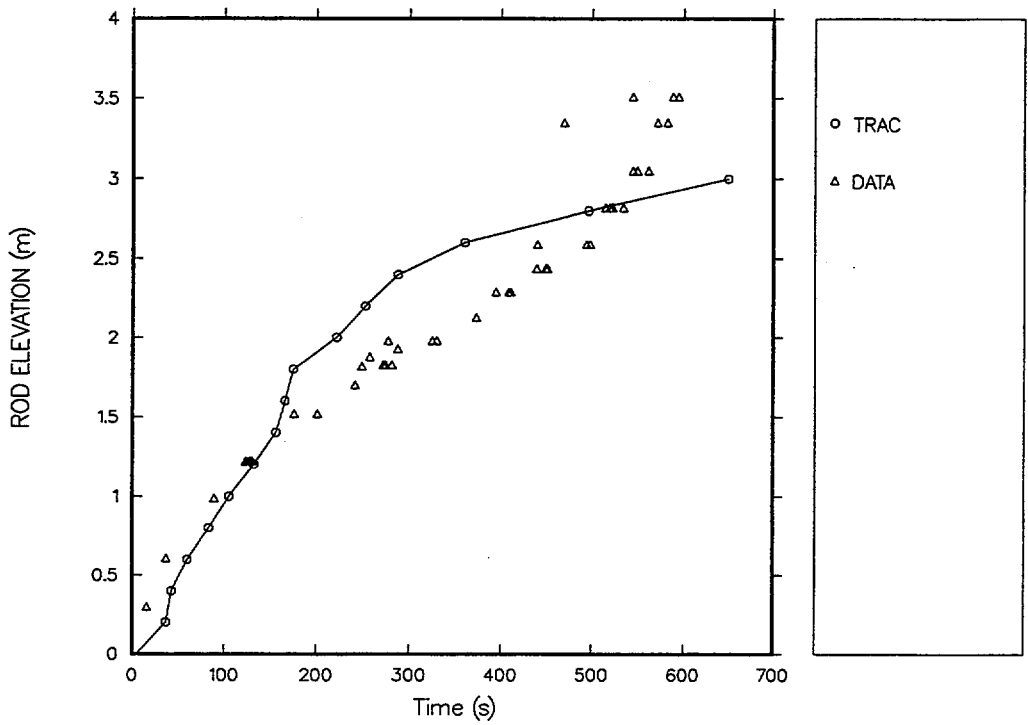
Fig. 4.8-7. Comparison of predicted and measured cladding quench times.
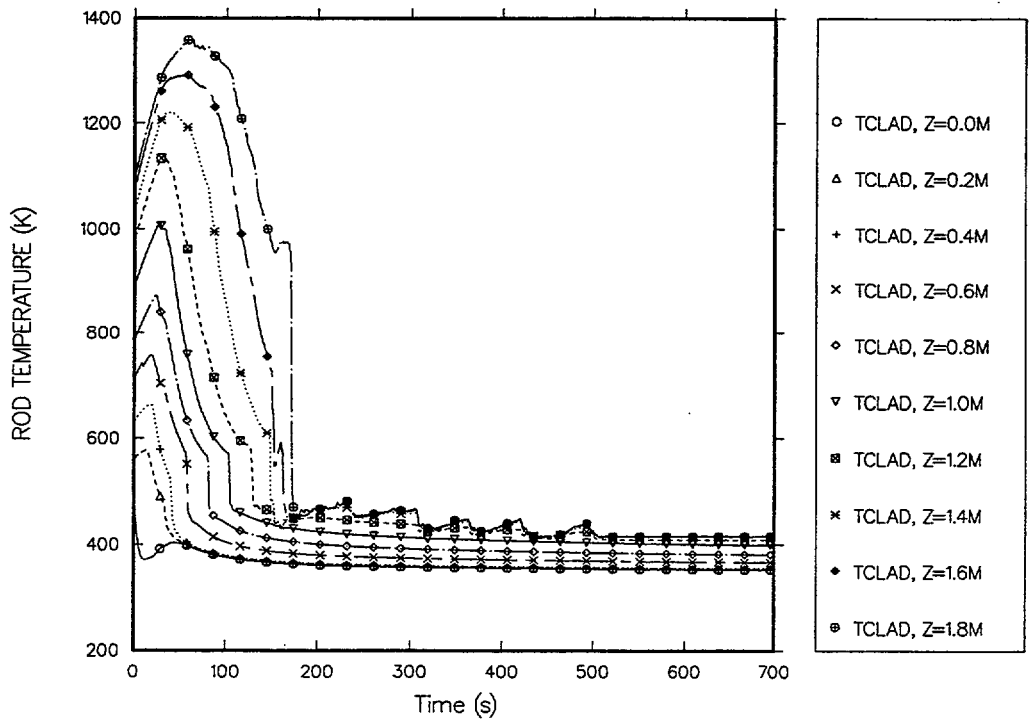


Fig. 4.8-8. Predicted cladding temperature responses in lower half of core.
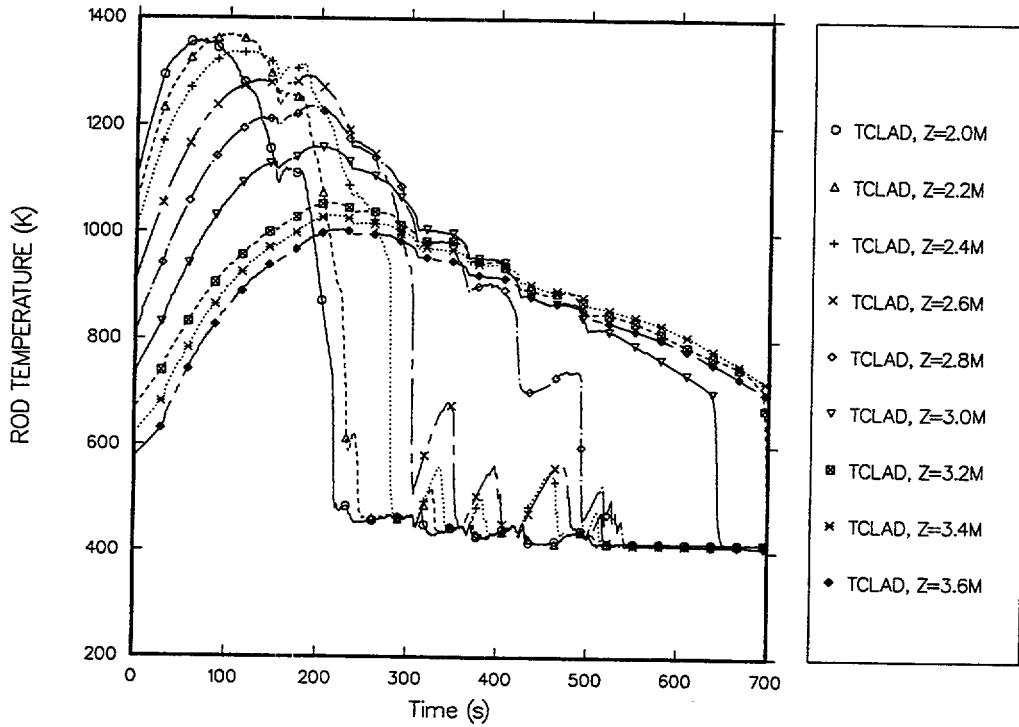
Fig. 4.8-9. Predicted cladding temperature responses in upper half of core.
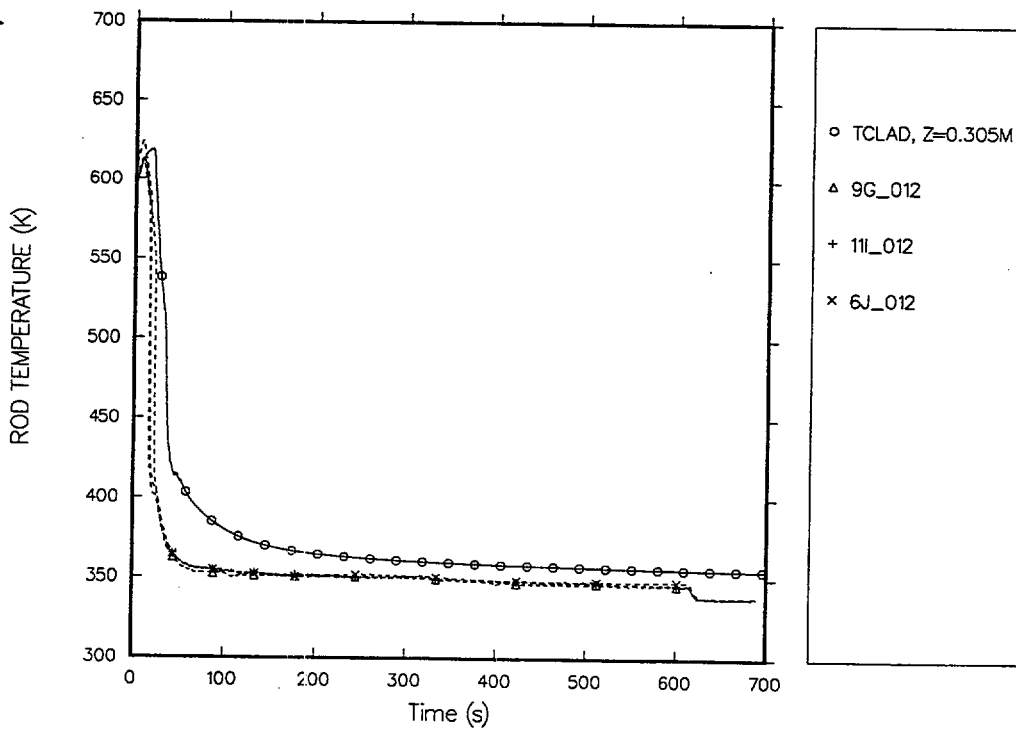


Fig. 4.8-10. Comparison of predicted and measured heater-rod cladding temperatures at 0.3048-m elevation.

2
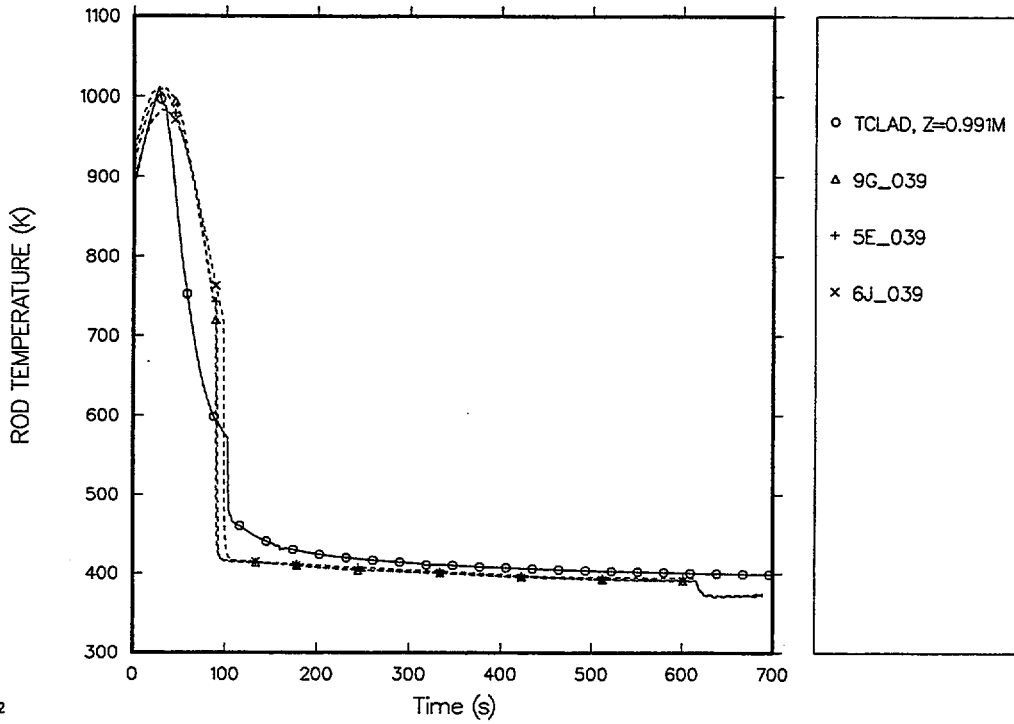
Fig. 4.8-11.  Comparison of predicted and measured heater-rod cladding temperatures at 0.9906-m elevation.



3
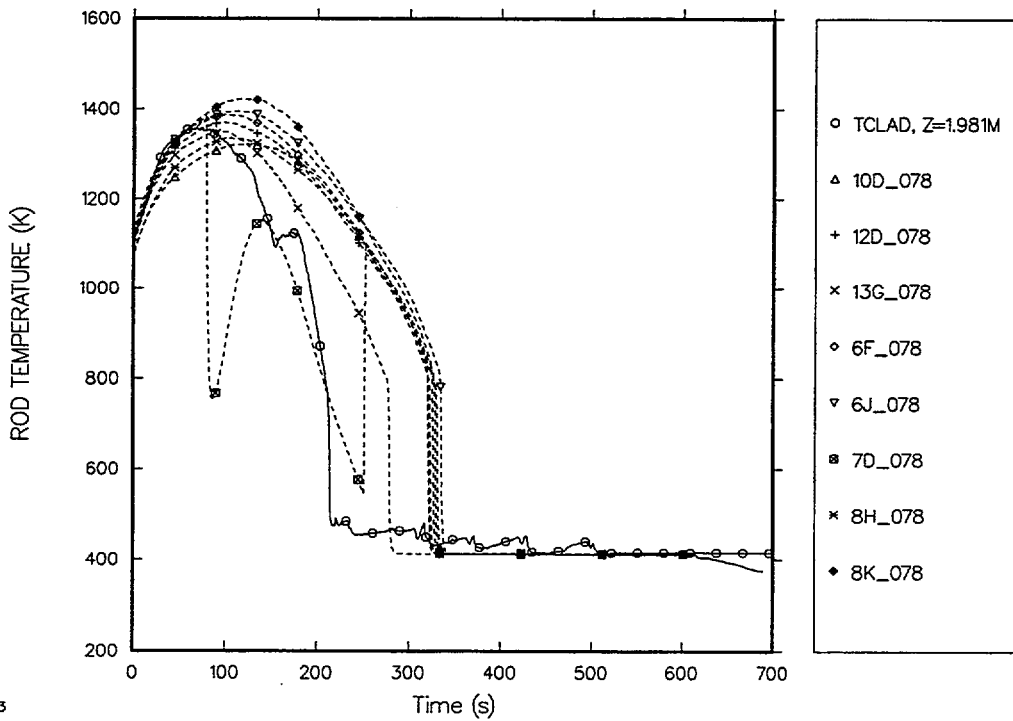
Fig. 4.8-12.  Comparison of predicted and measured heater-rod cladding temperatures at 1.9812-m elevation.
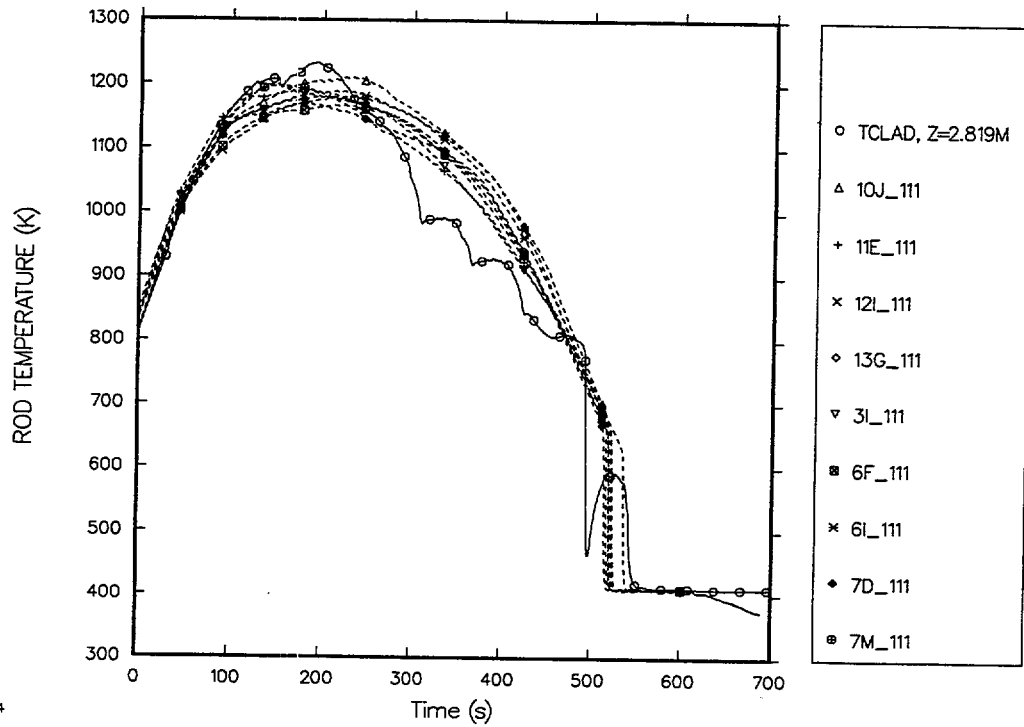
**Fig. 4.8-13.** Comparison of predicted and measured heater-rod cladding temperatures at 2.8194-m elevation.
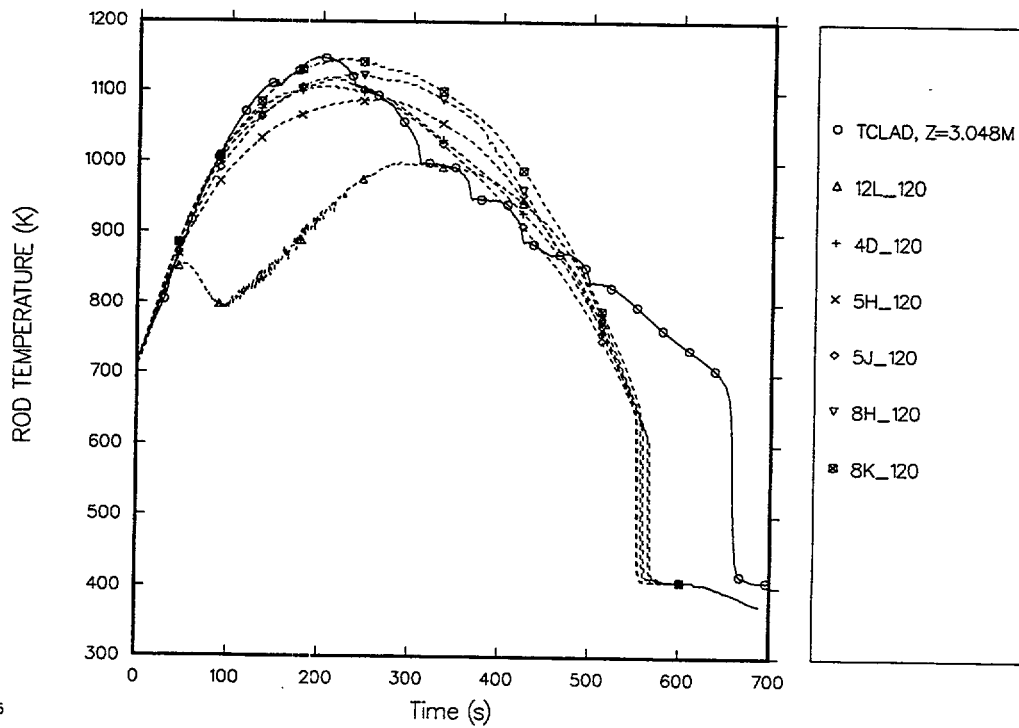


**Fig. 4.8-14.** Comparison of predicted and measured heater-rod cladding temperatures at 3.0480-m elevation.
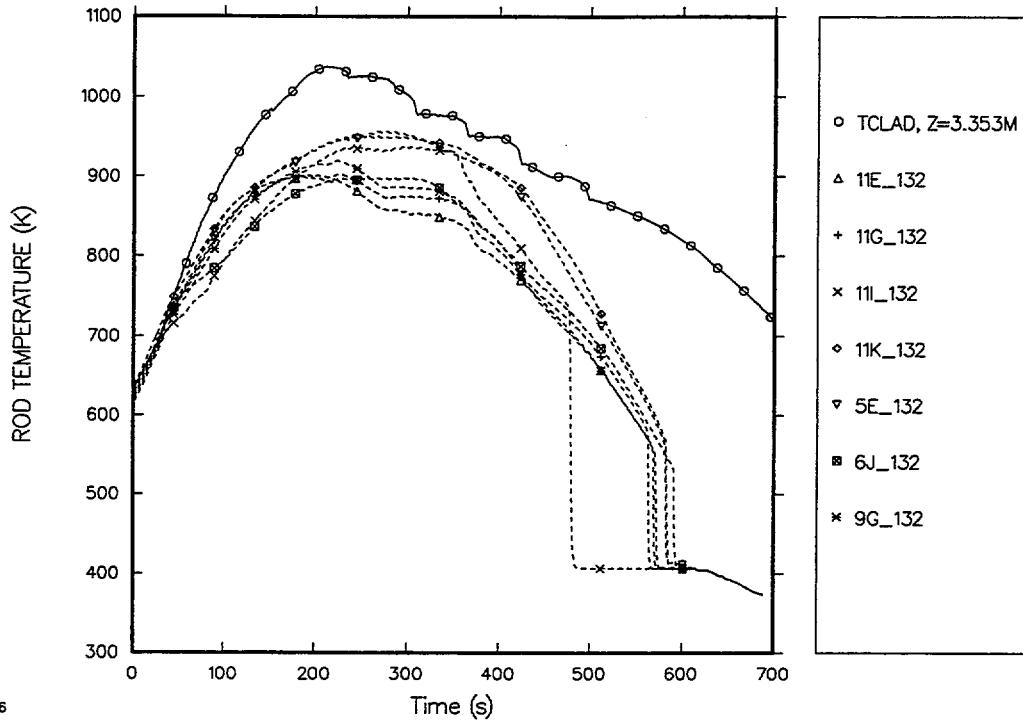
Fig. 4.8-15. Comparison of predicted and measured heater-rod cladding temperatures at 3.3528-m elevation.
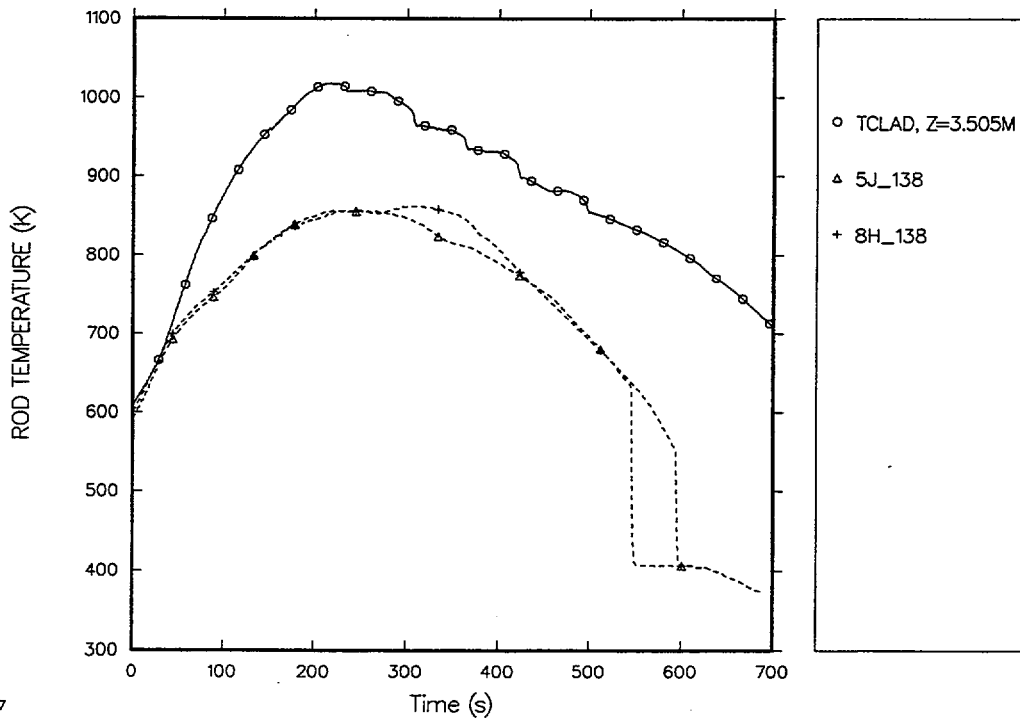


Fig. 4.8-16. Comparison of predicted and measured heater-rod cladding temperatures at 3.5052-m elevation.
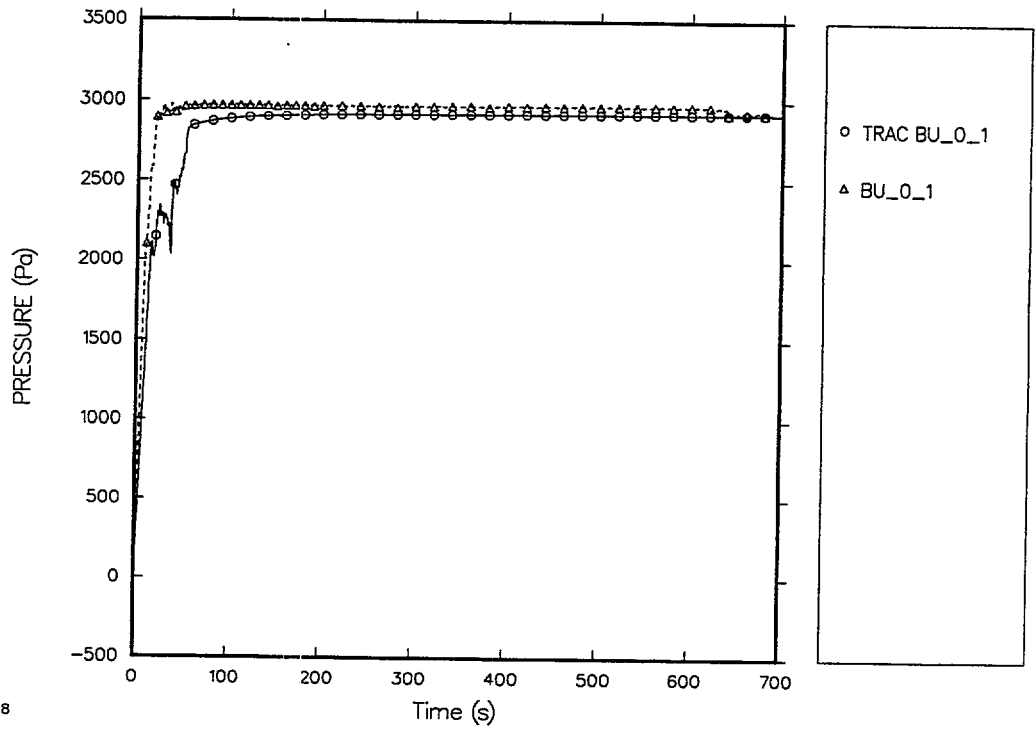
Fig. 4.8-17. Comparison of predicted and measured differential pressures (0–1 ft).
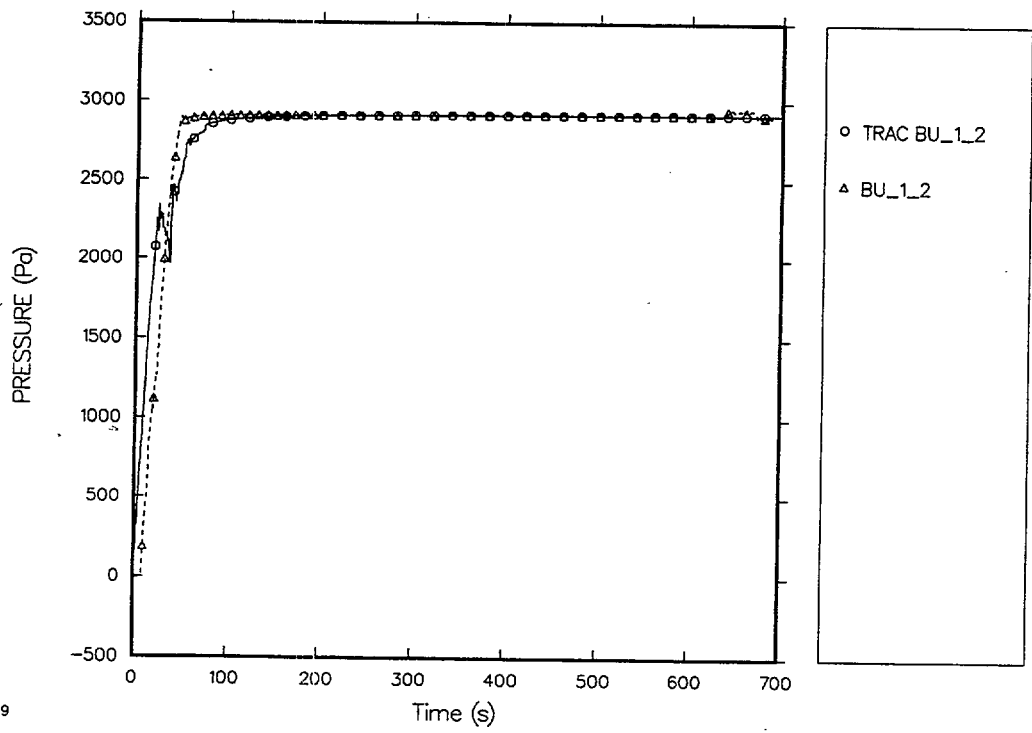


Fig. 4.8-18. Comparison of predicted and measured differential pressures (1–2 ft).
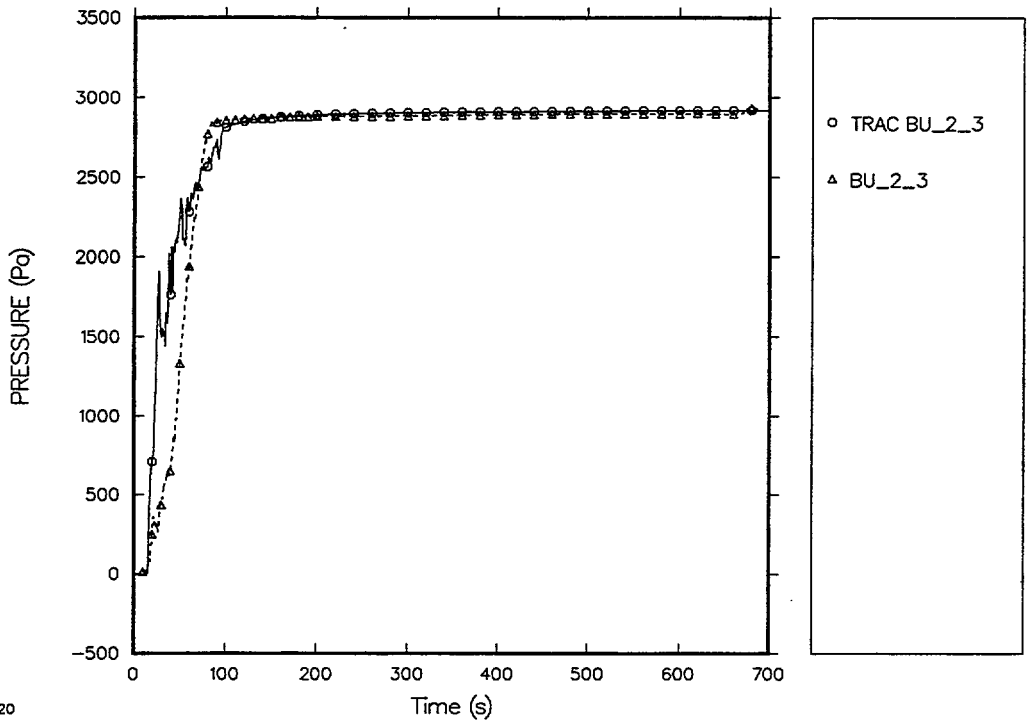
**Fig. 4.8-19.** Comparison of predicted and measured differential pressures (2–3 ft).
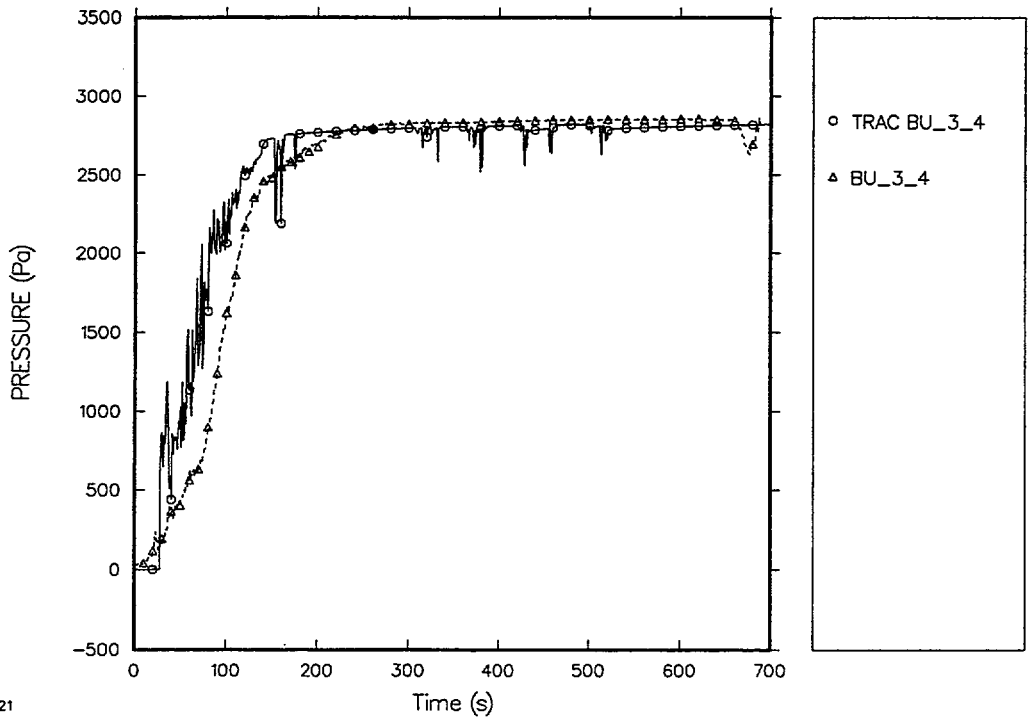


**Fig. 4.8-20.** Comparison of predicted and measured differential pressures (3–4 ft).
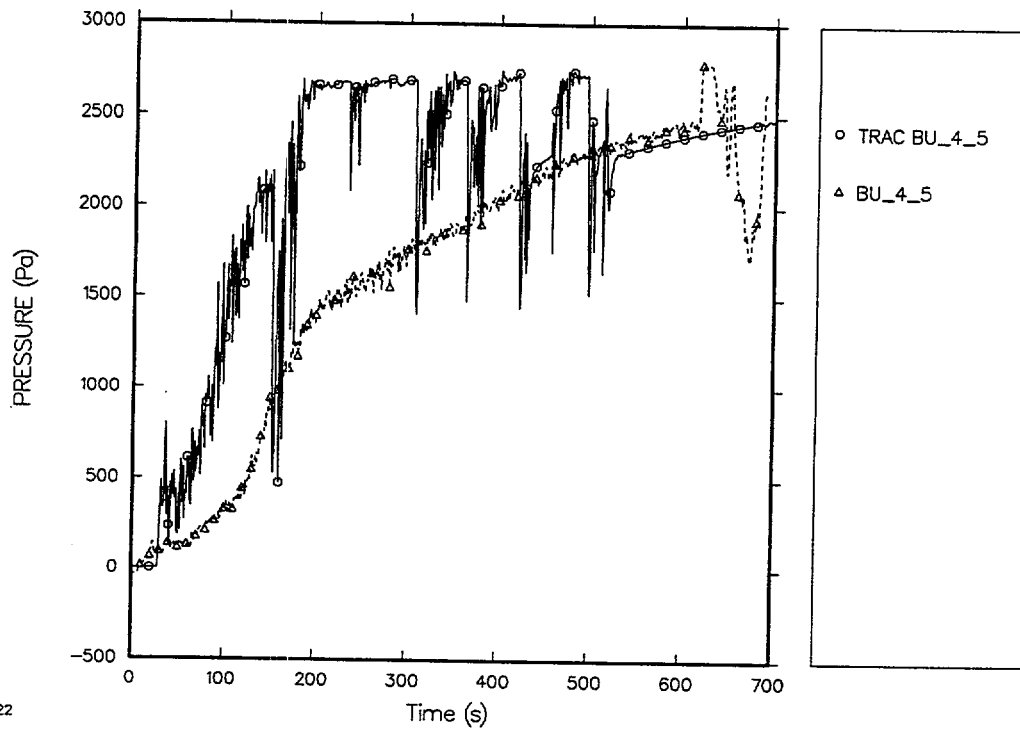
Fig. 4.8-21. Comparison of predicted and measured differential pressures (4–5 ft).
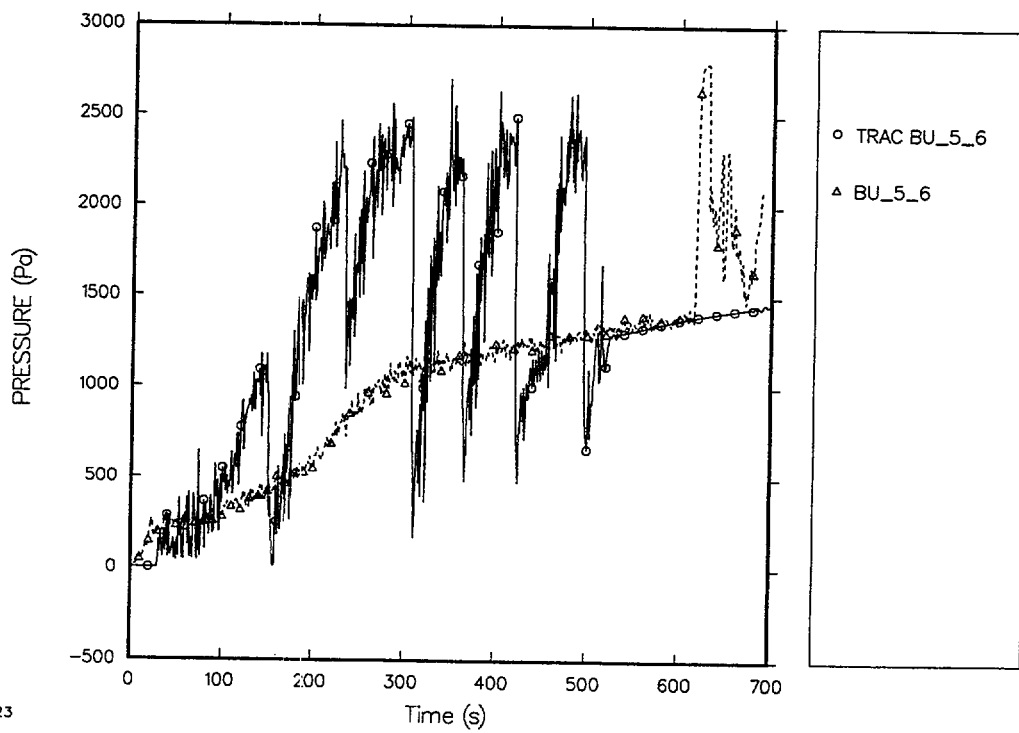


Fig. 4.8-22.   Comparison of predicted and measured differential pressures (5–6 ft).
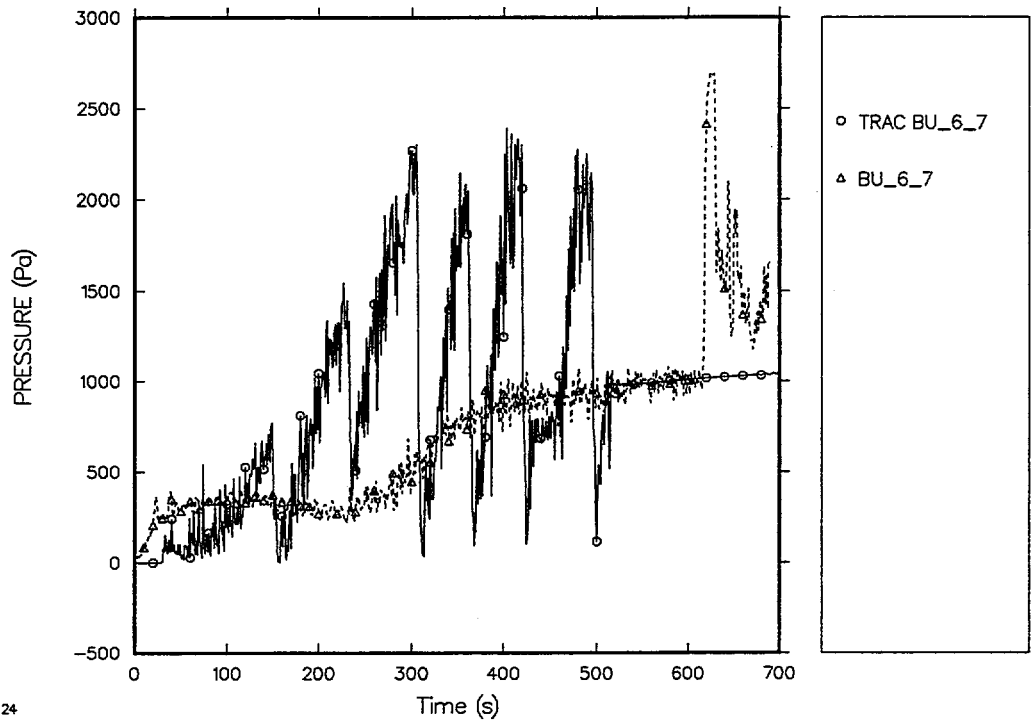
Fig. 4.8-23. Comparison of predicted and measured differential pressures (6–7 ft).
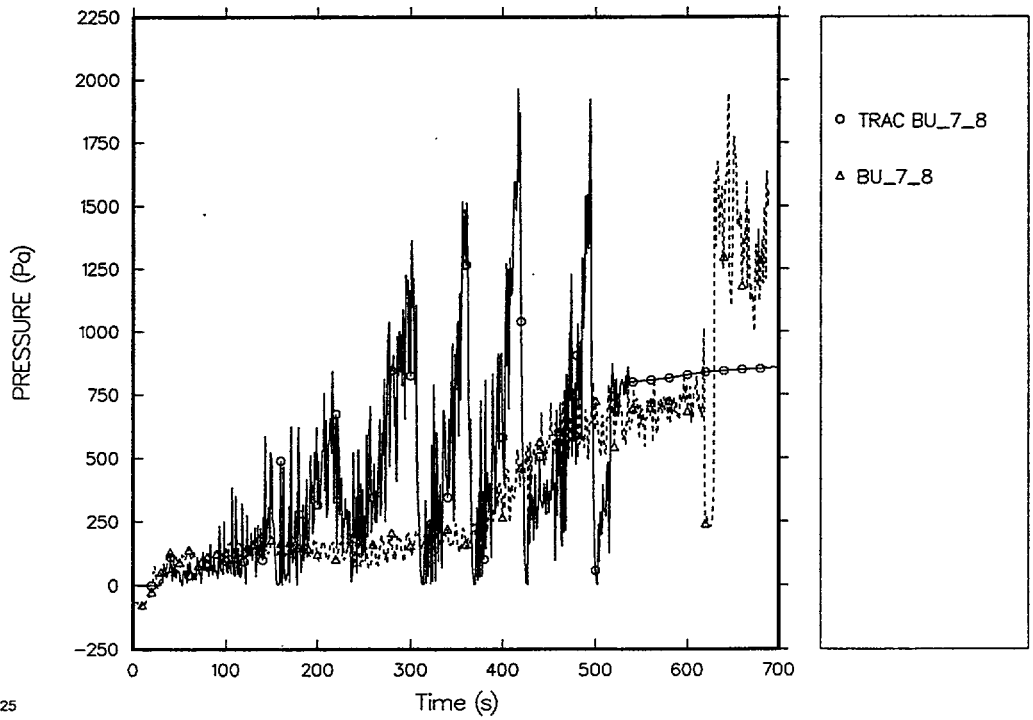


Fig. 4.8-24. Comparison of predicted and measured differential pressures (7–8 ft).
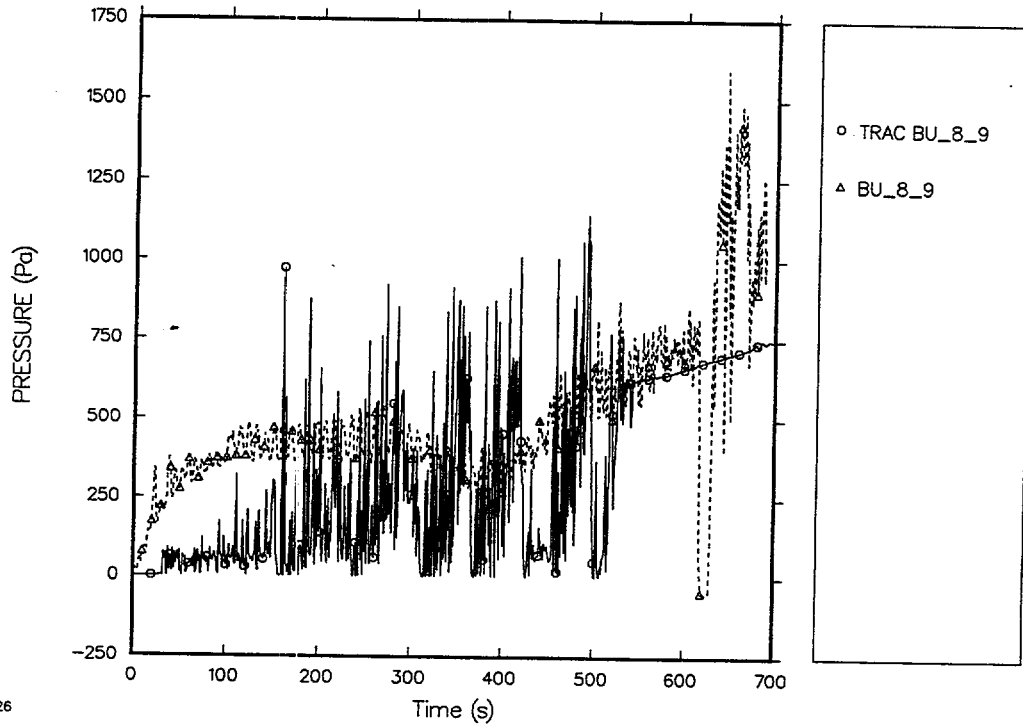
Fig. 4.8-25. Comparison of predicted and measured differential pressures (8–9ft).
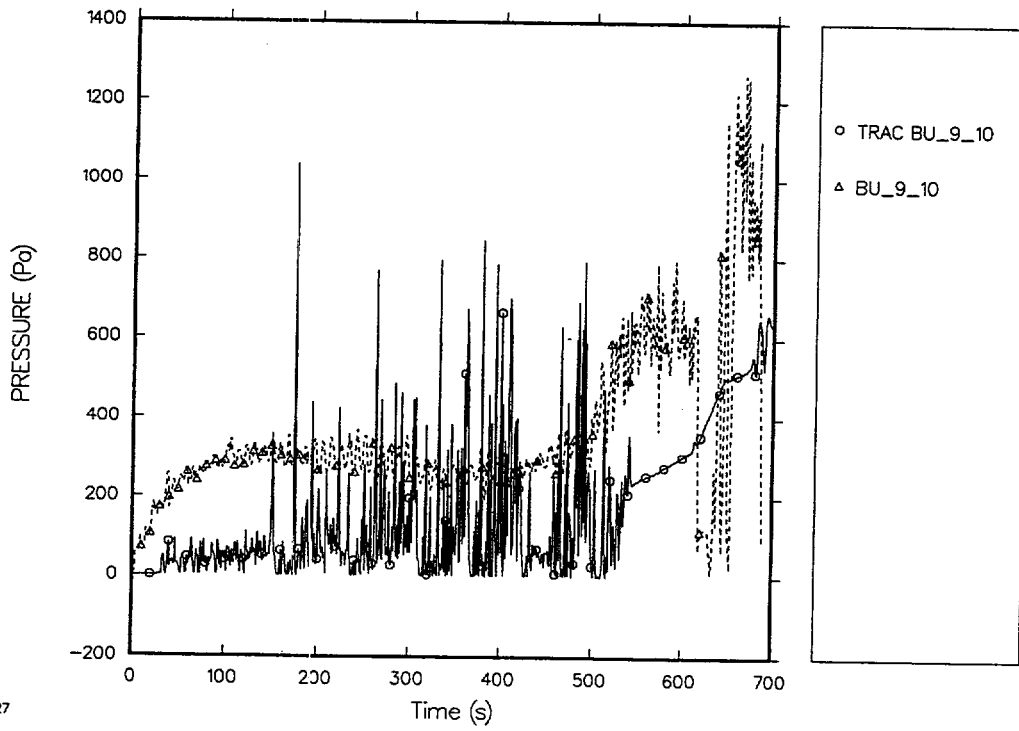


Fig. 4.8-26. Comparison of predicted and measured differential pressures (9-10 ft).
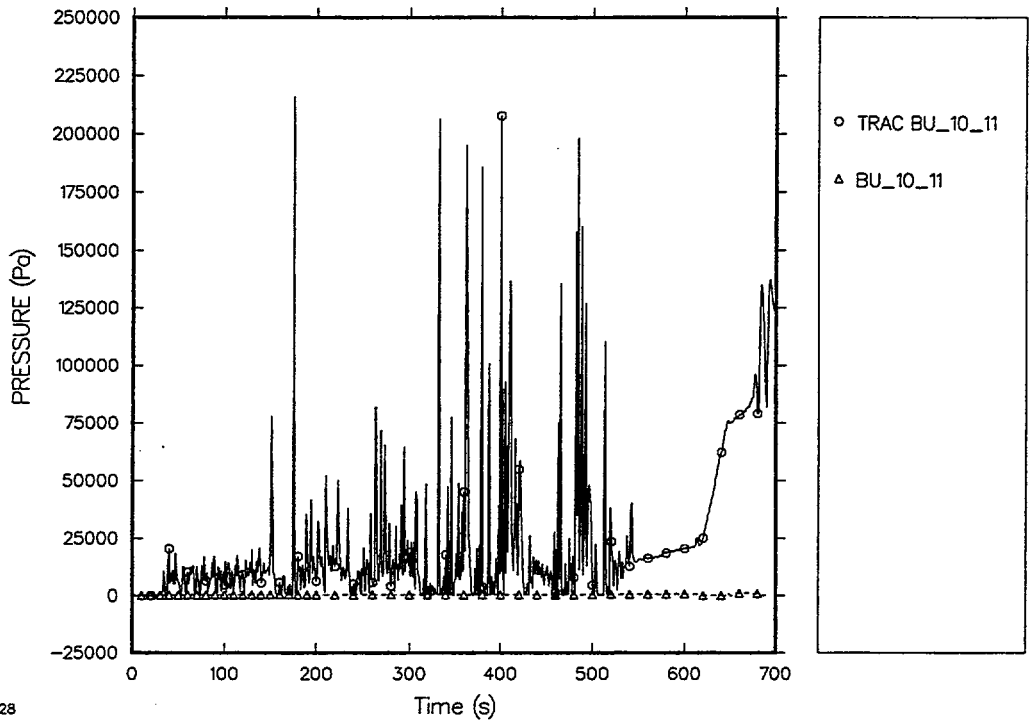
Fig. 4.8-27. Comparison of predicted and measured differential pressures (10–11 ft).
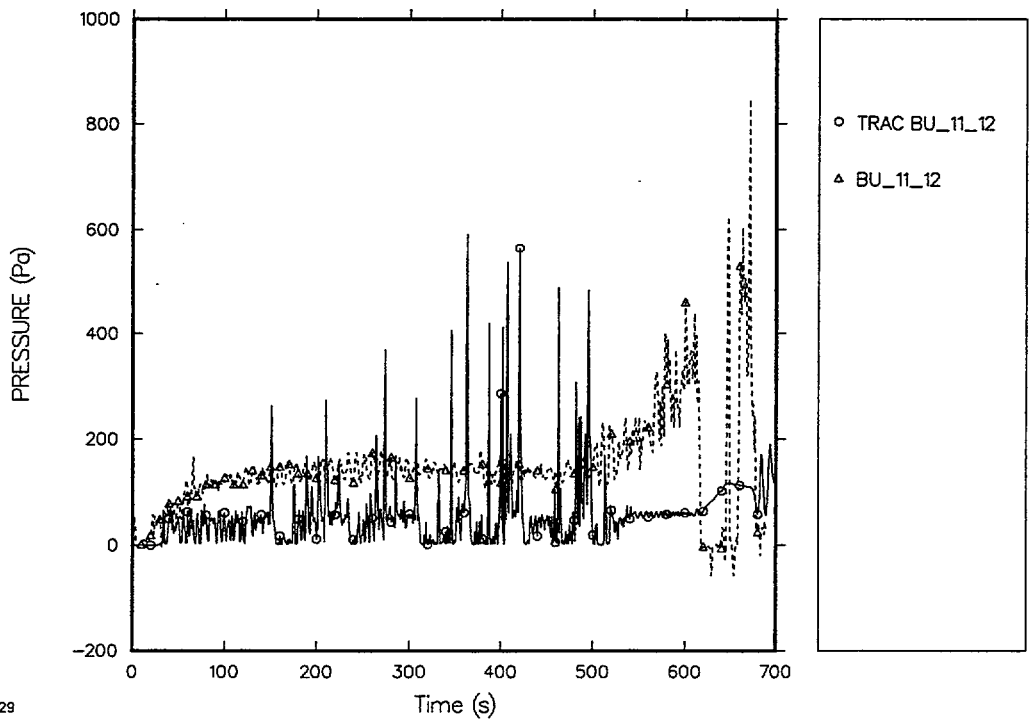


Fig. 4.8-28. Comparison of predicted and measured differential pressures (11–12 ft).

**Fig. 4.8-29.** Comparison of predicted and measured total core differential pressures (0-12 ft).



**Fig. 4.8-30.** Comparison of predicted and measured vapor temperatures in cell 7.

4.8-26
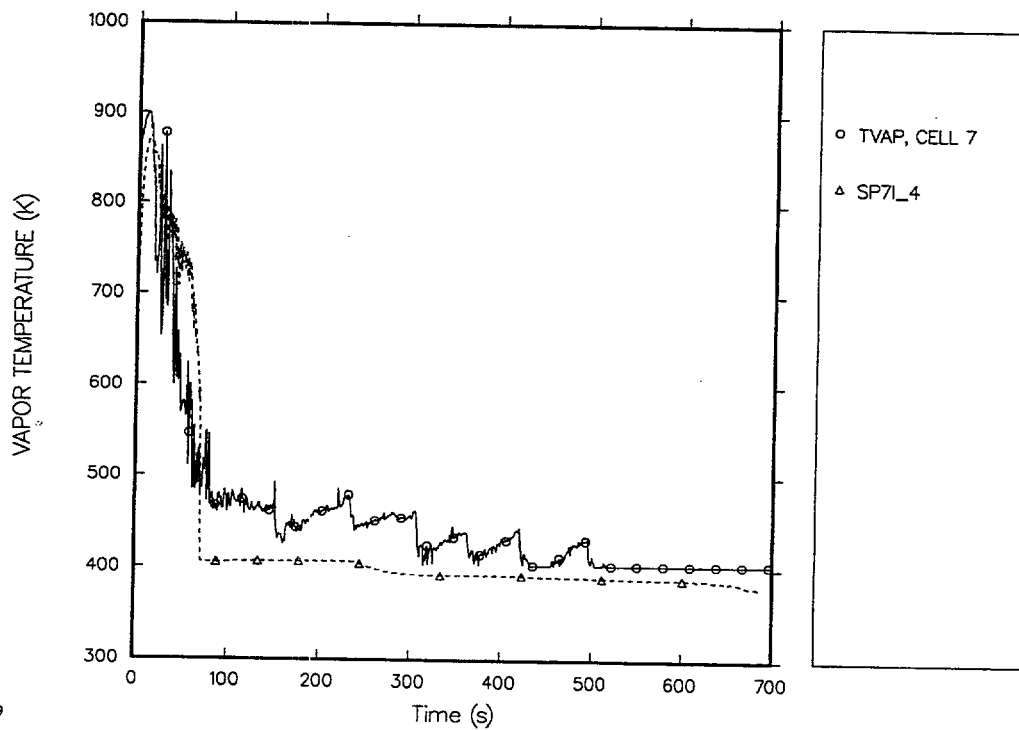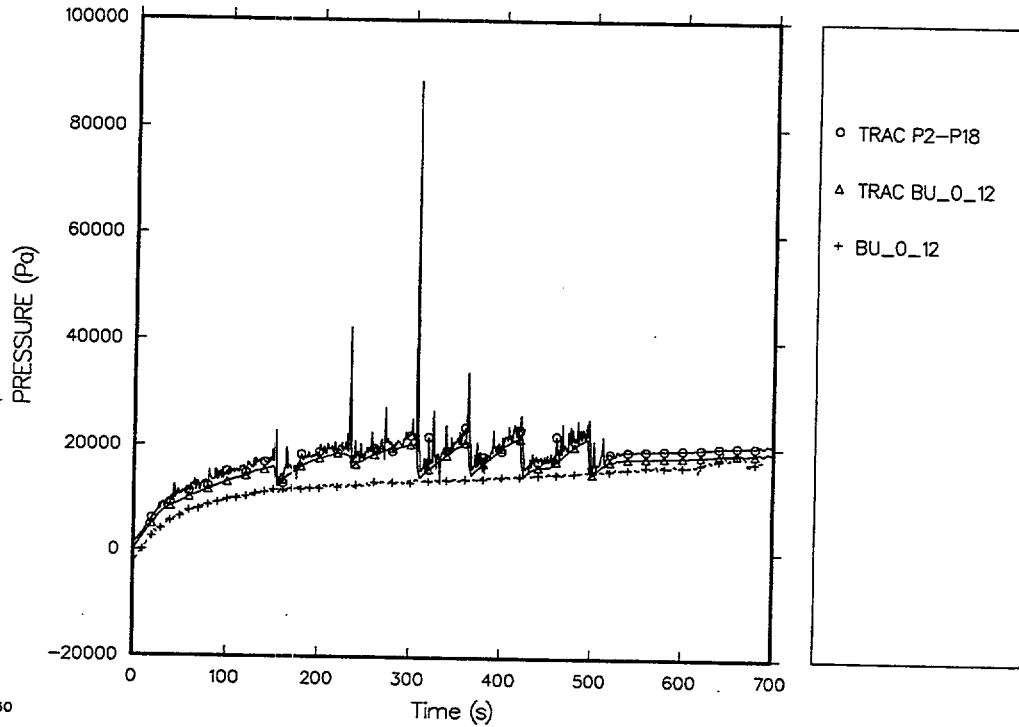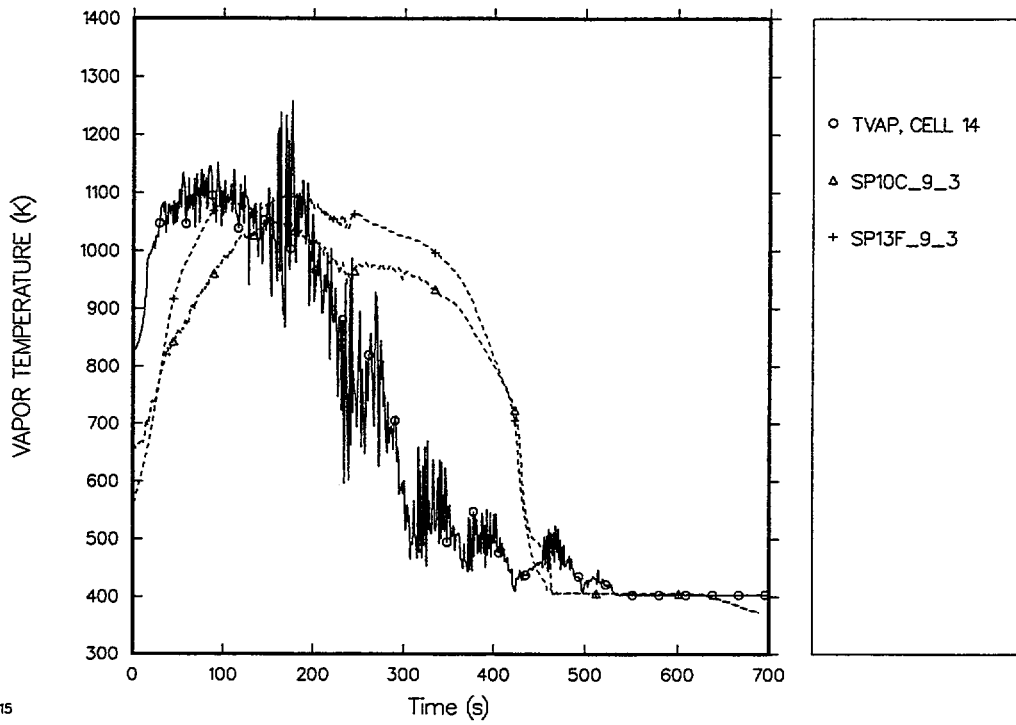
Fig. 4.8-31.   Comparison of predicted and measured vapor temperatures in cell 14.

This space is intentionally left blank.
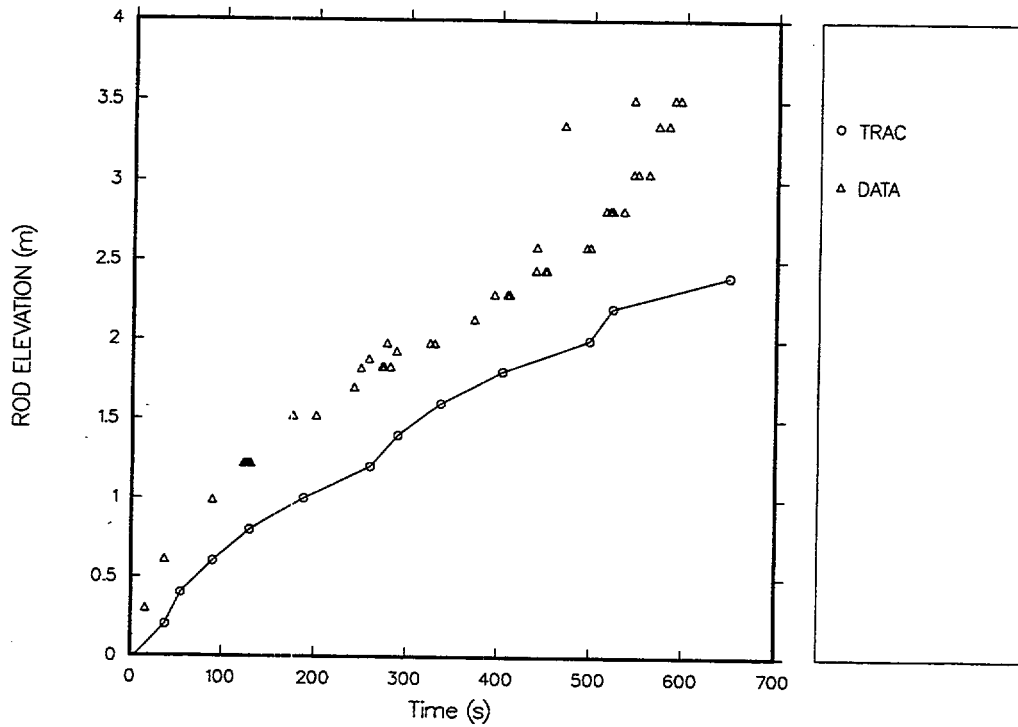
Fig. 4.8-32. Comparison of predicted and measured cladding quench times (with grid-spacer model).
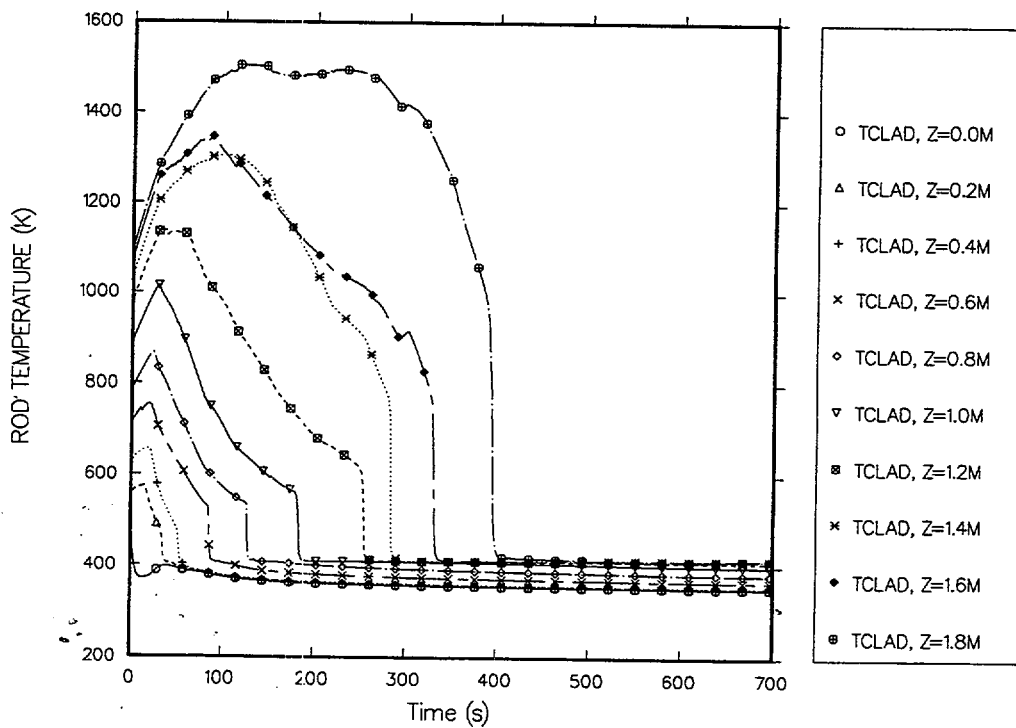


Fig. 4.8-33. Predicted cladding temperature responses in lower half of core (with grid-spacer model).
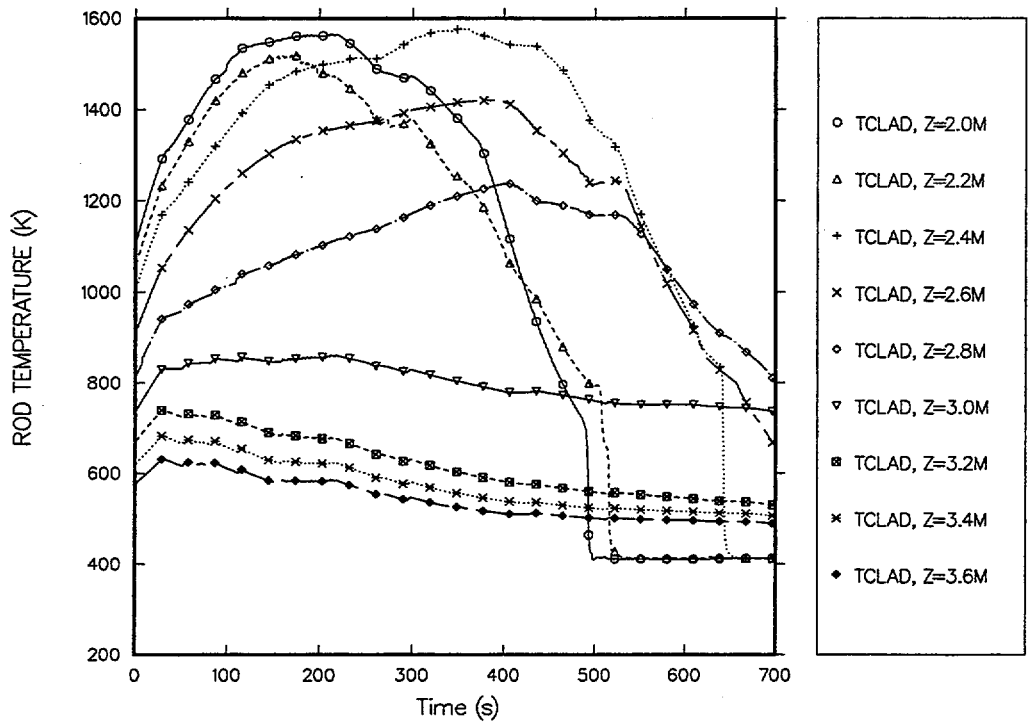
Fig. 4.8-34. Predicted cladding temperature responses in upper half of core (with grid-spacer model).
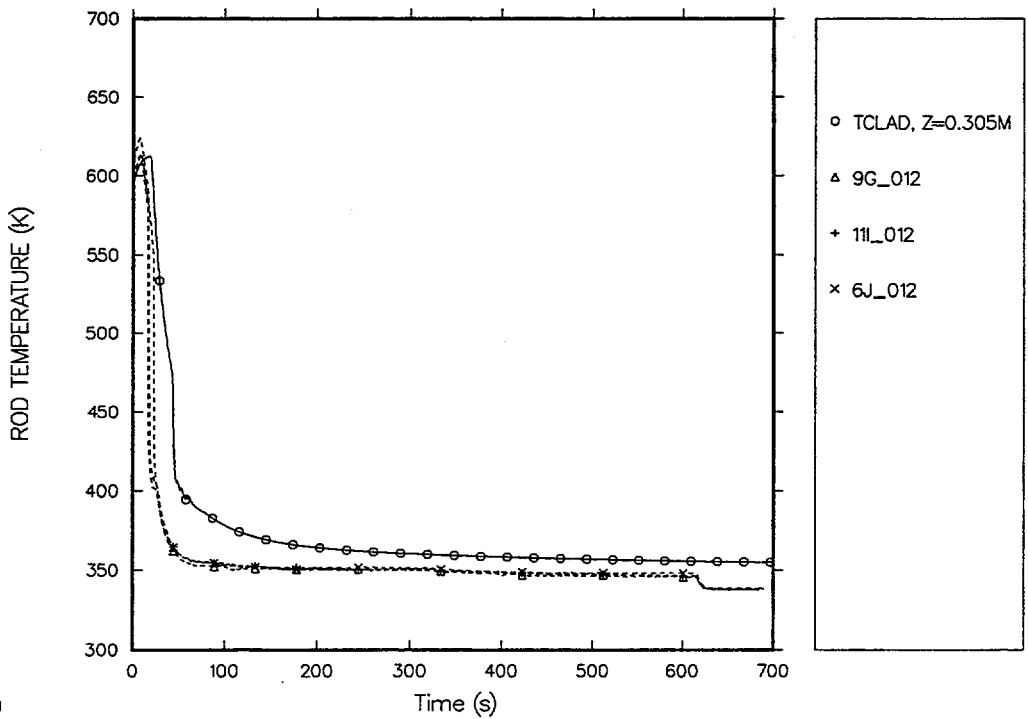


Fig. 4.8-35. Comparison of predicted and measured heater-rod cladding temperatures at 0.3048-m elevation (with grid-spacer model).
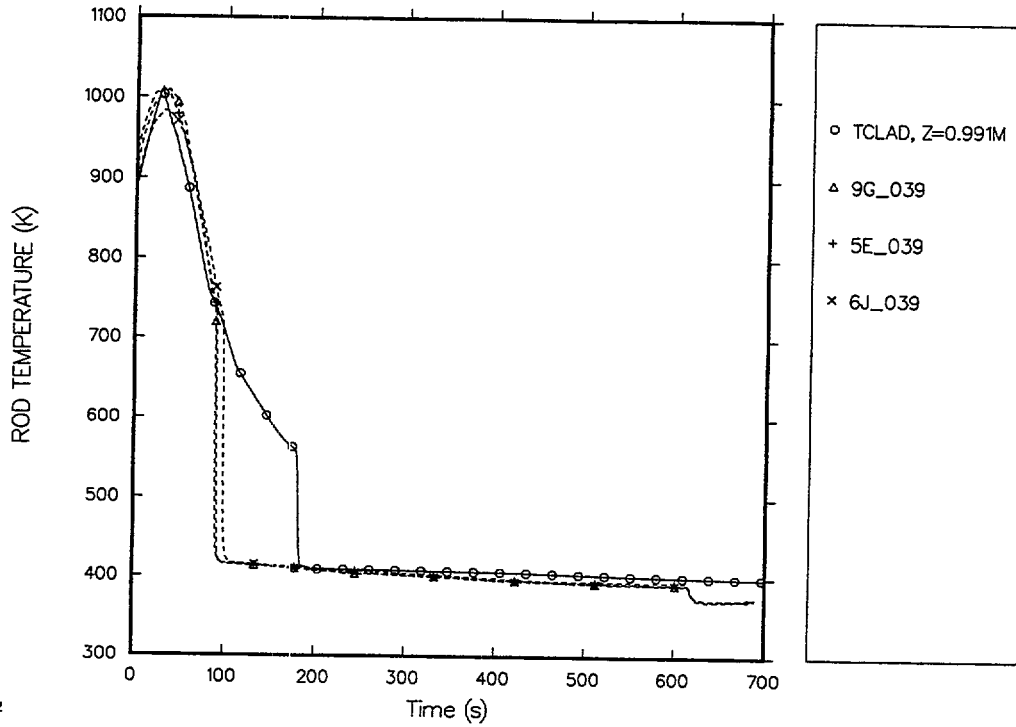
Fig. 4.8-36. Comparison of predicted and measured heater-rod cladding temperatures at 0.9906-m elevation (with grid-spacer model).
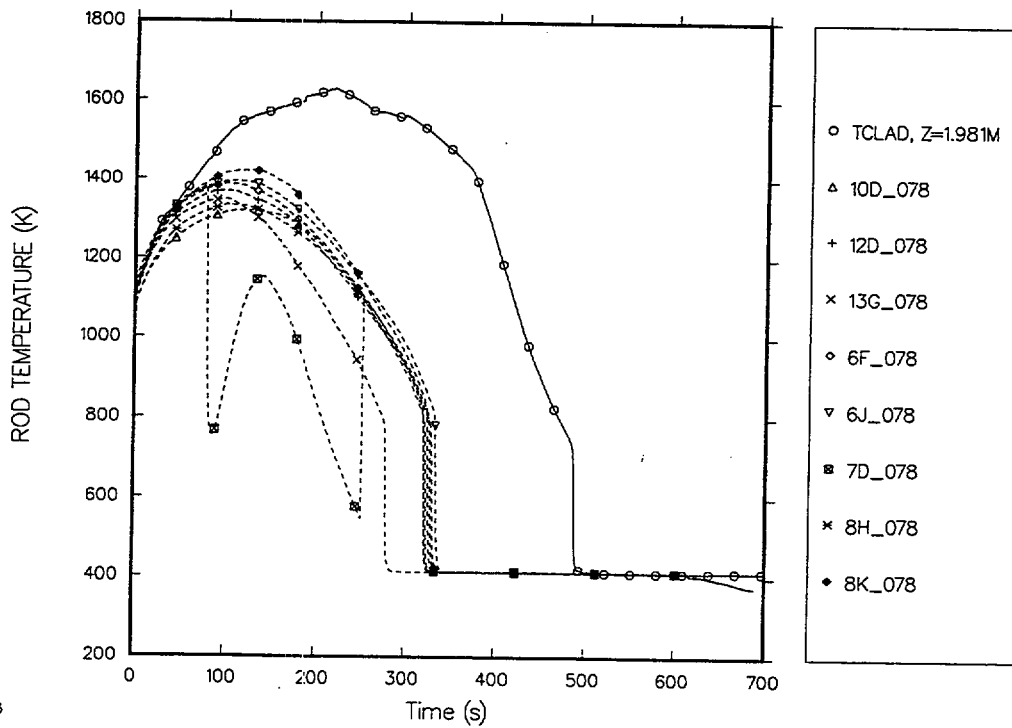


Fig. 4.8-37. Comparison of predicted and measured heater-rod cladding temperatures at 1.9812-m elevation (with grid-spacer model).

4.8-30
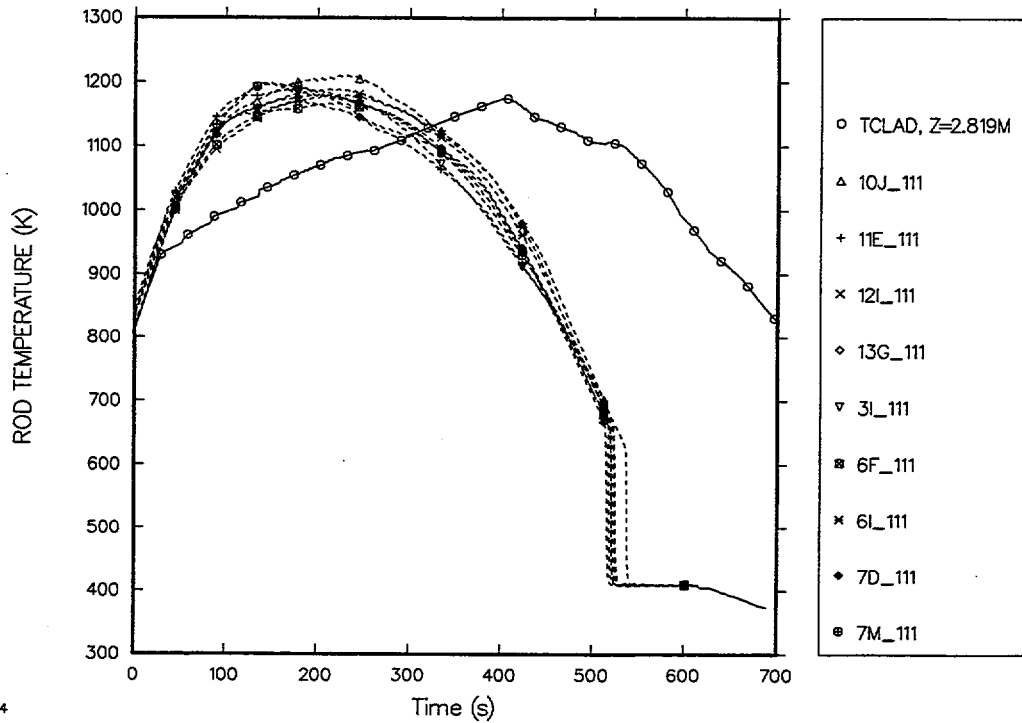
Fig. 4.8-38.  Comparison of predicted and measured heater-rod cladding temperatures at 2.8194-m elevation (with grid-spacer model).
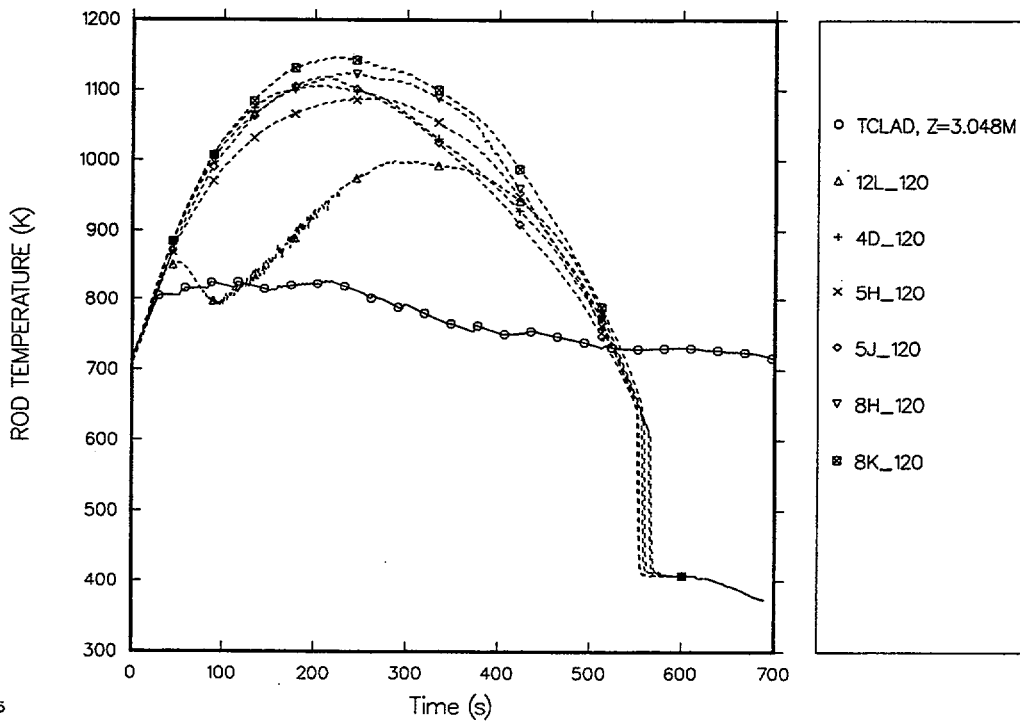


Fig. 4.8-39. Comparison of predicted and measured heater-rod cladding temperatures at 3.0480-m elevation (with grid-spacer model).
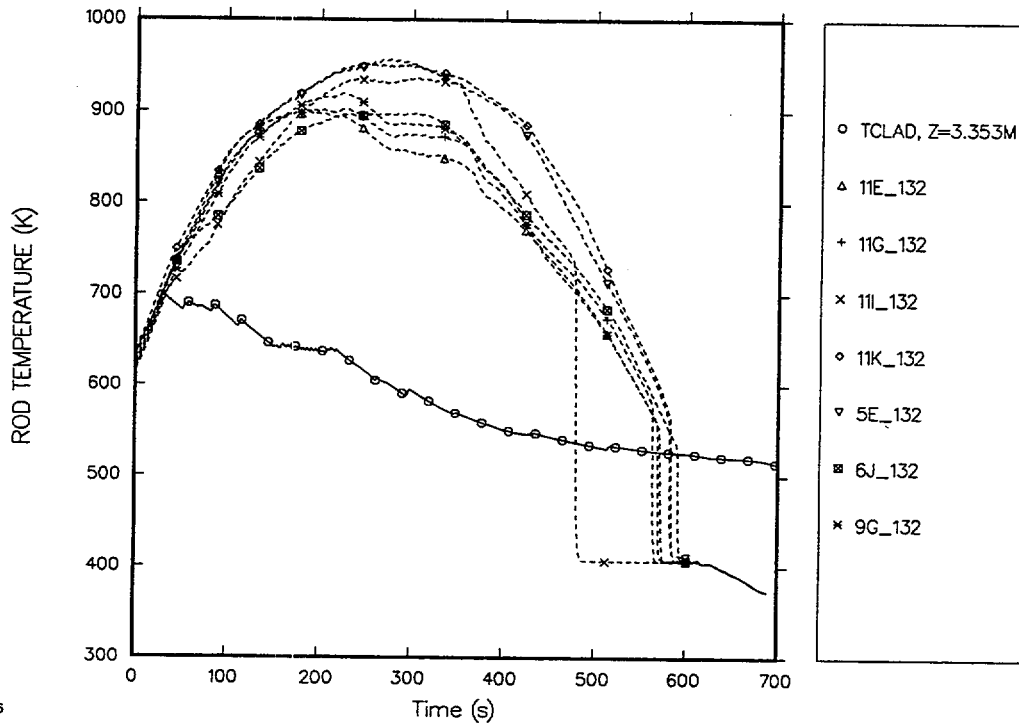
Fig. 4.8-40.   Comparison of predicted and measured heater-rod cladding temperatures at 3.3528-m elevation (with grid-spacer model).
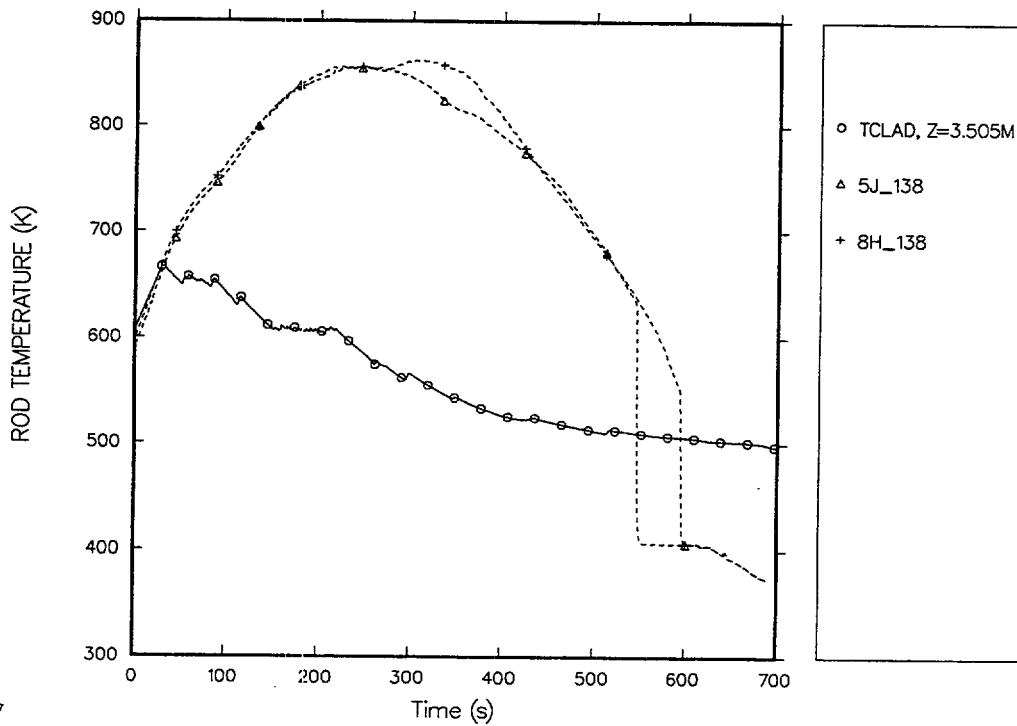


Fig. 4.8-41.   Comparison of predicted and measured heater-rod cladding temperatures at 3.5052-m elevation (with grid-spacer model).
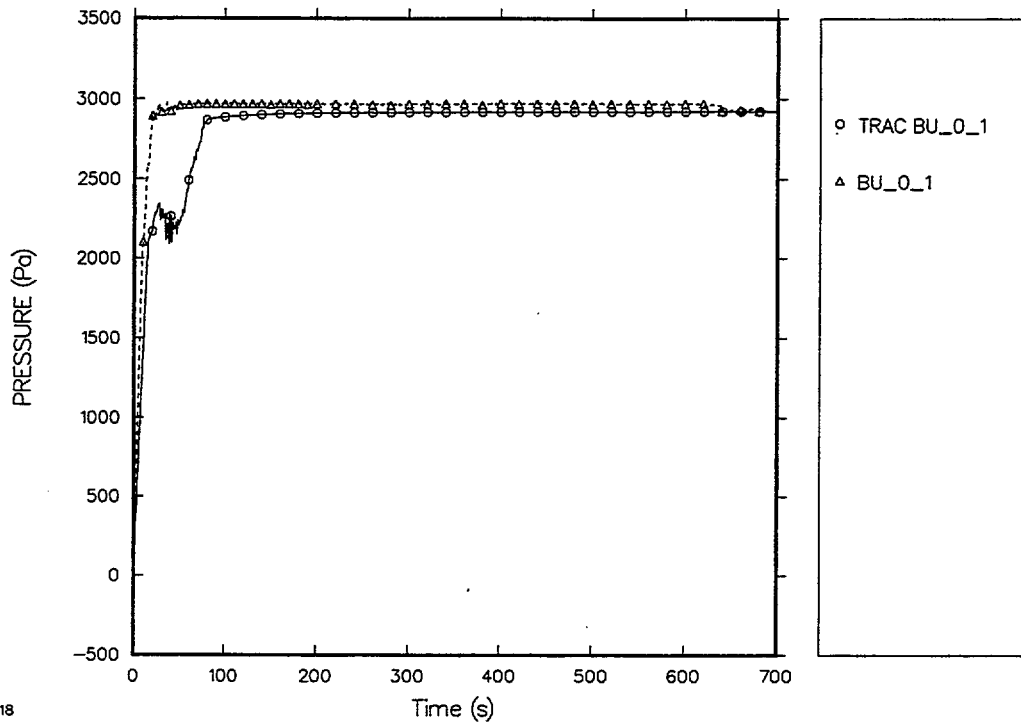
Fig. 4.8-42. Comparison of predicted and measured differential pressures (0–1 ft, with grid-spacer model).
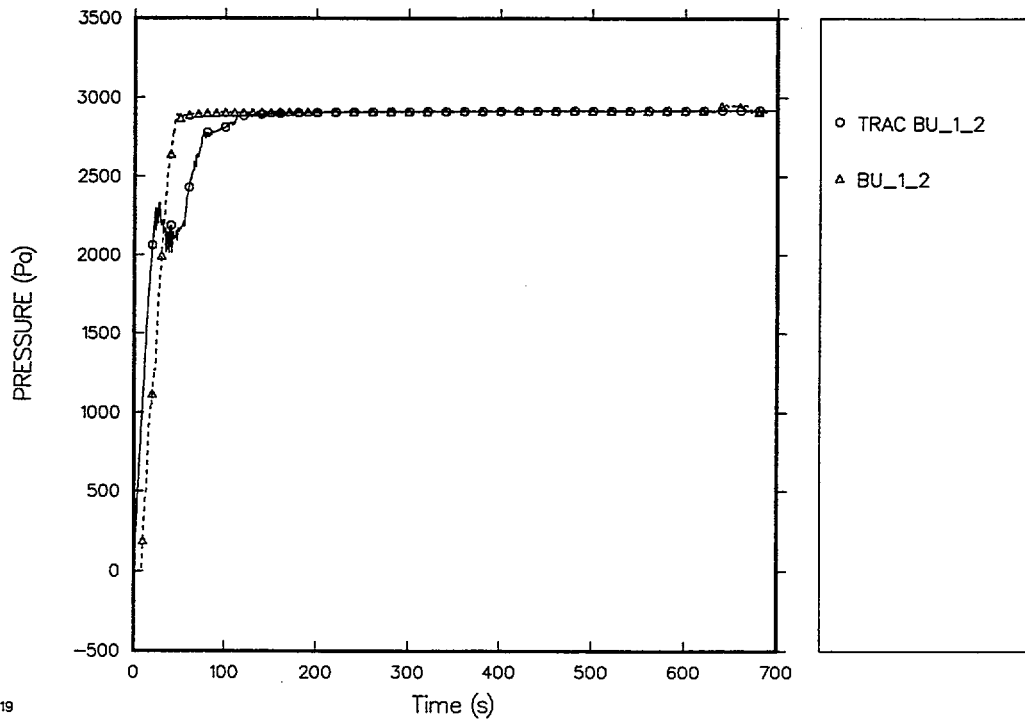


Fig. 4.8-43. Comparison of predicted and measured differential pressures (1–2 ft, with grid-spacer model).
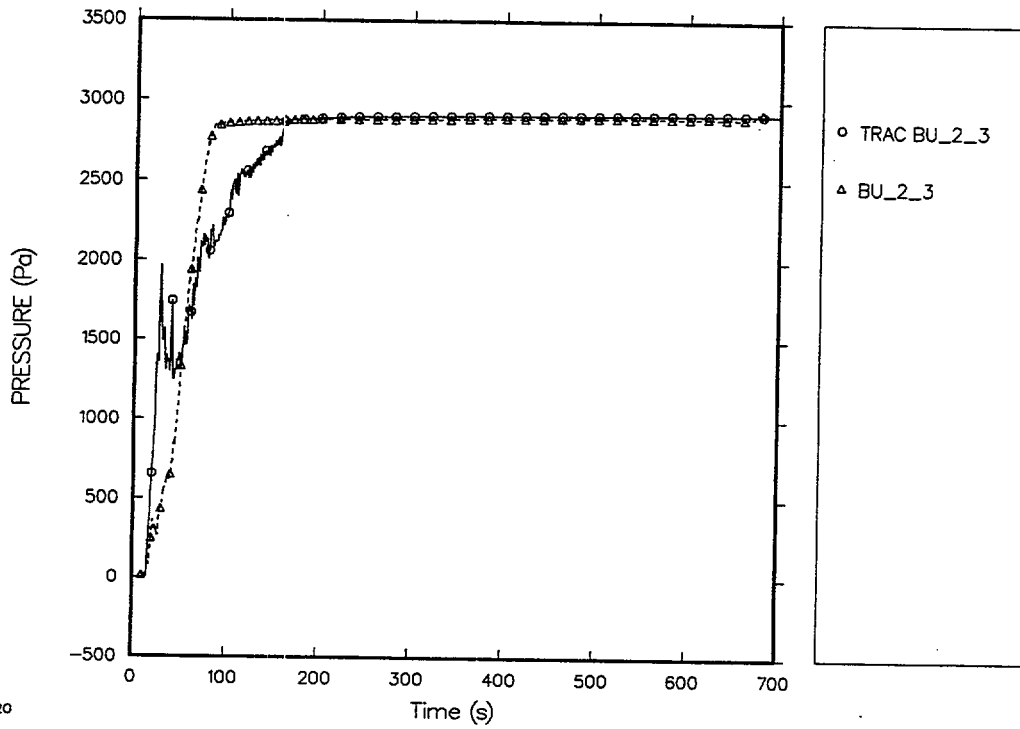
Fig. 4.8-44. Comparison of predicted and measured differential pressures (2–3 ft, with grid-spacer model).
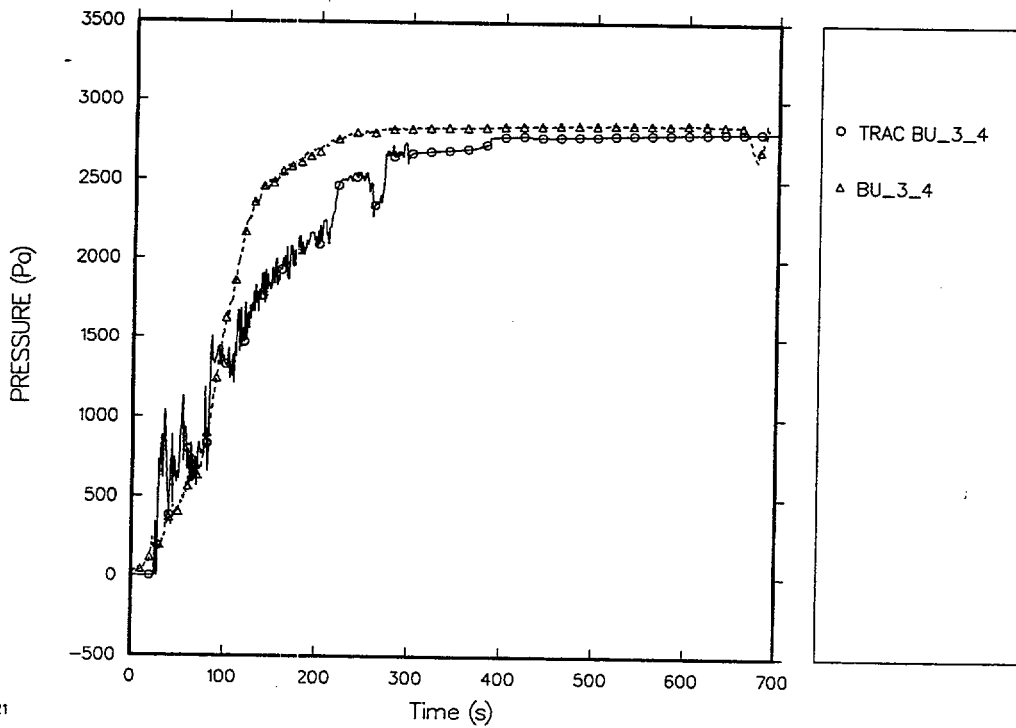


Fig. 4.8-45. Comparison of predicted and measured differential pressures (3–4 ft, with grid-spacer model).
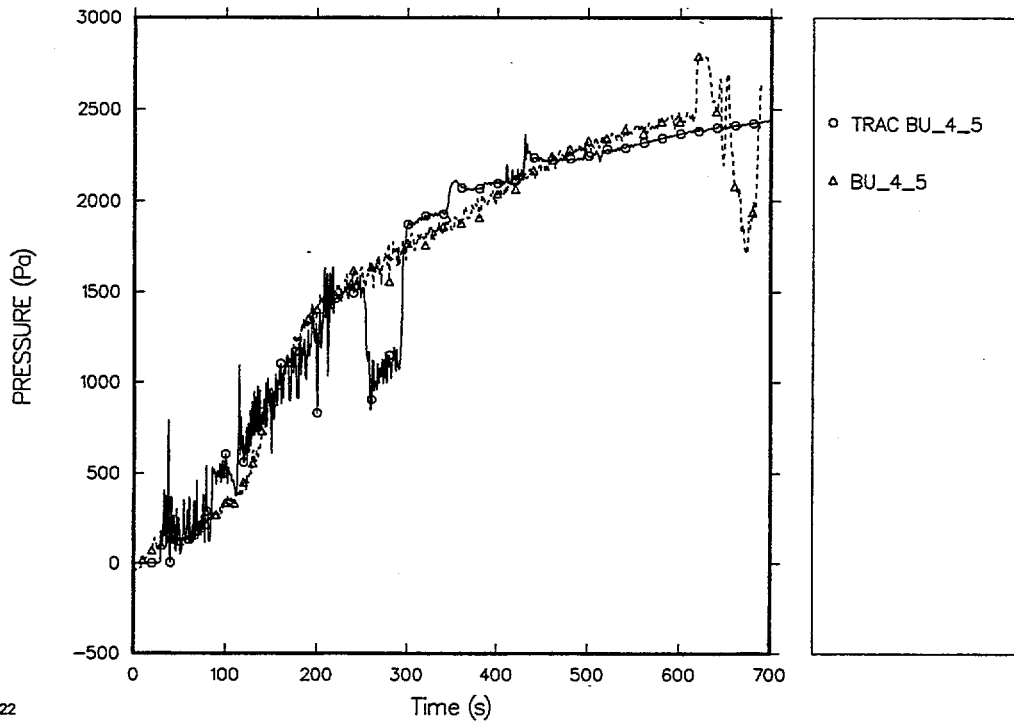
Fig. 4.8-46. Comparison of predicted and measured differential pressures (4–5 ft, with grid-spacer model).
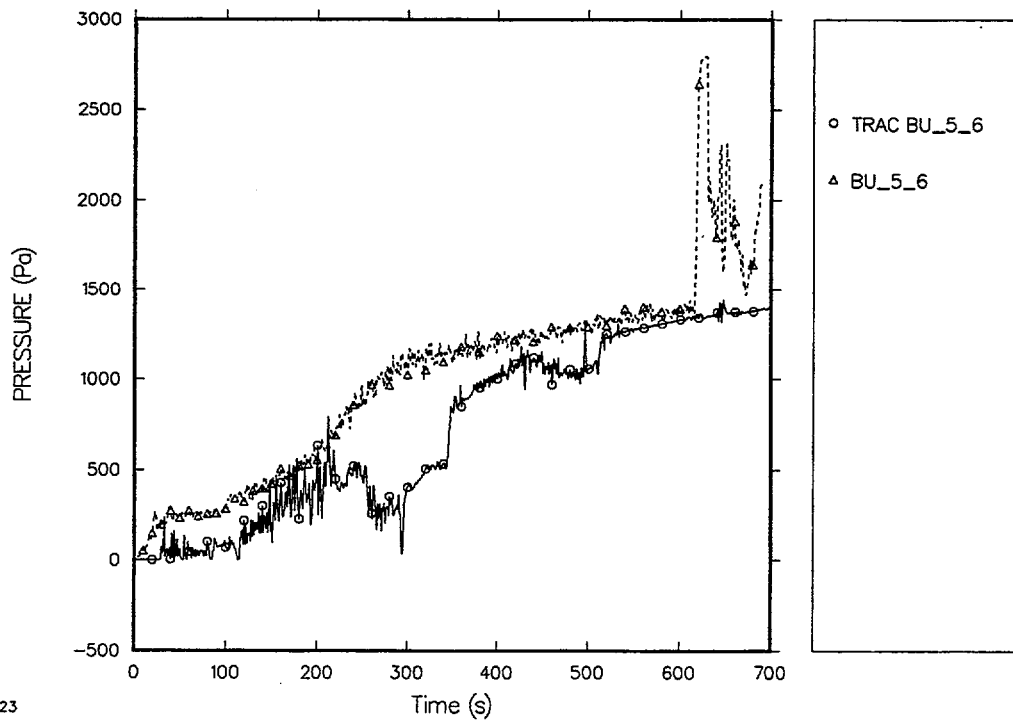


Fig. 4.8-47. Comparison of predicted and measured differential pressures (5–6 ft, with grid-spacer model).
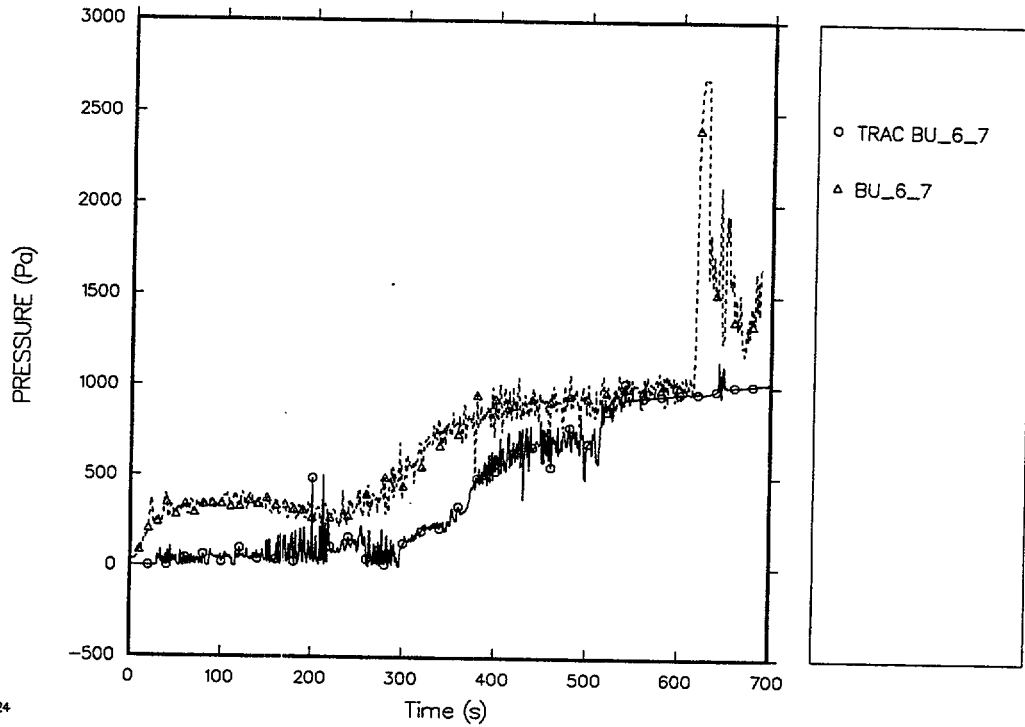
Fig. 4.8-48. Comparison of predicted and measured differential pressures (6–7 ft, with grid-spacer model).
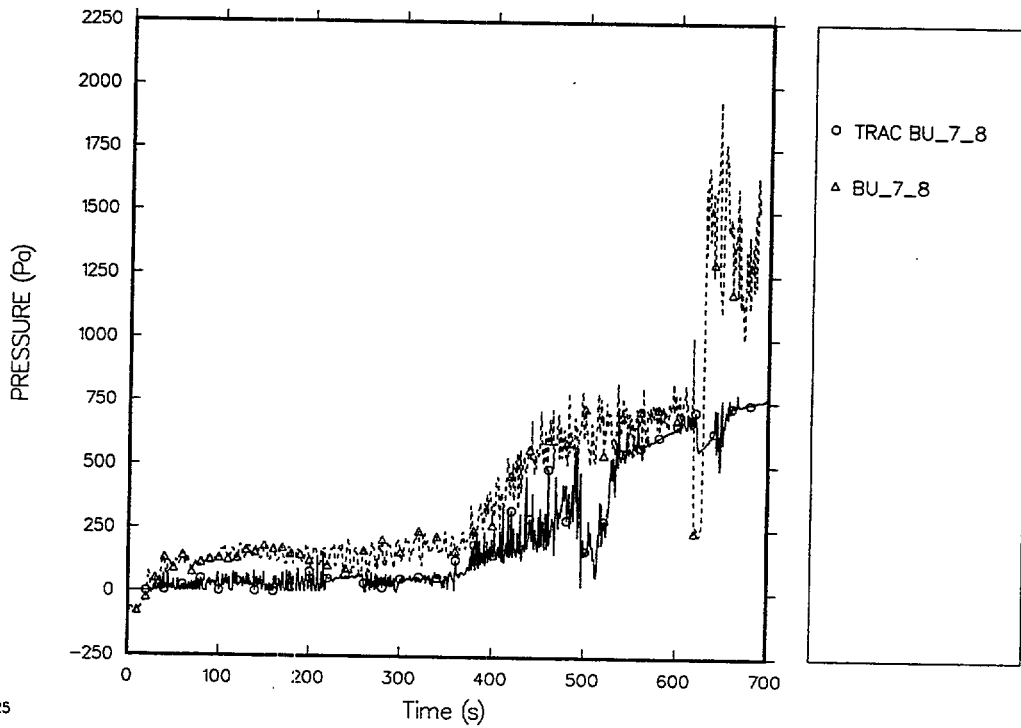


Fig. 4.8-49. Comparison of predicted and measured differential pressures (7–8 ft, with grid-spacer model).
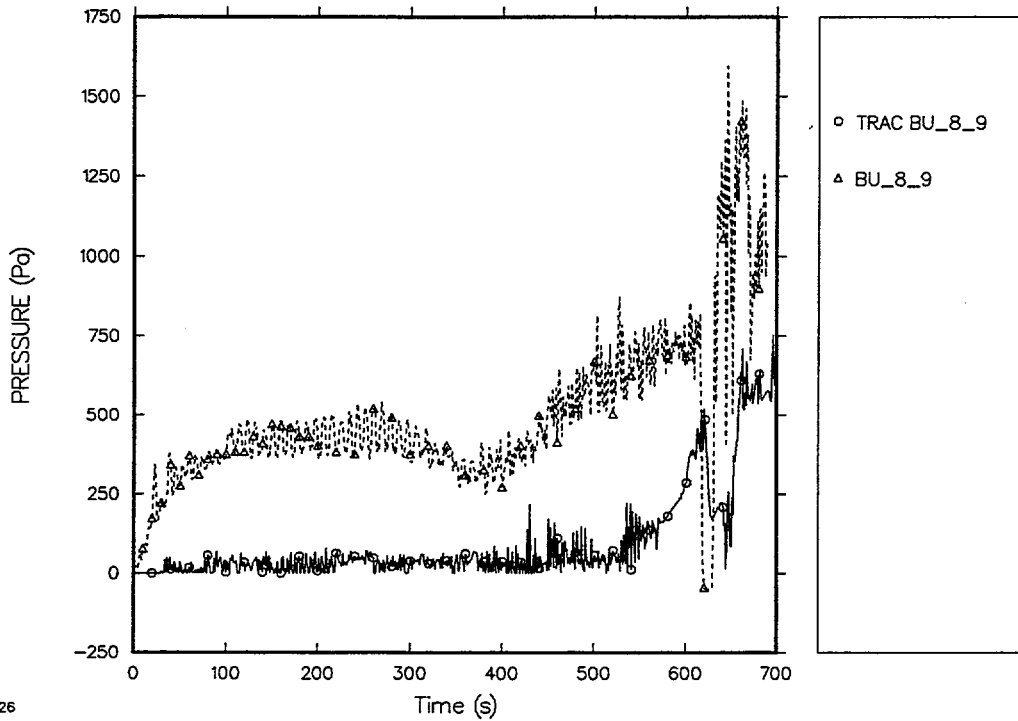
4.8-36

Fig. 4.8-50. Comparison of predicted and measured differential pressures (8–9ft, with grid-spacer model).
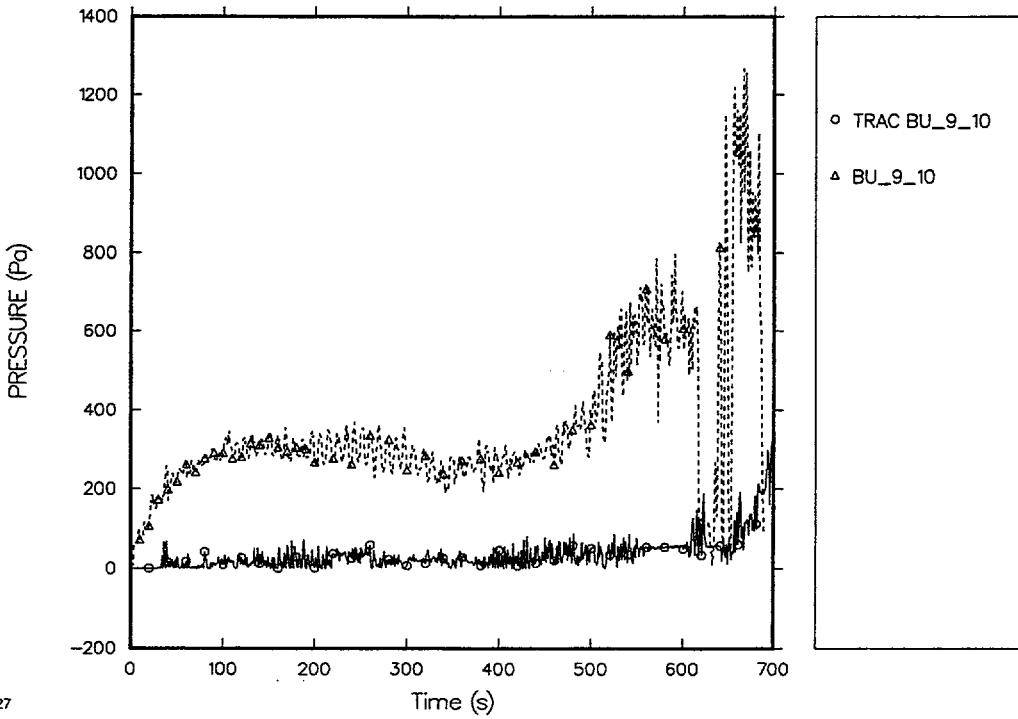


Fig. 4.8-51. Comparison of predicted and measured differential pressures (9–10 ft, with grid-spacer model).
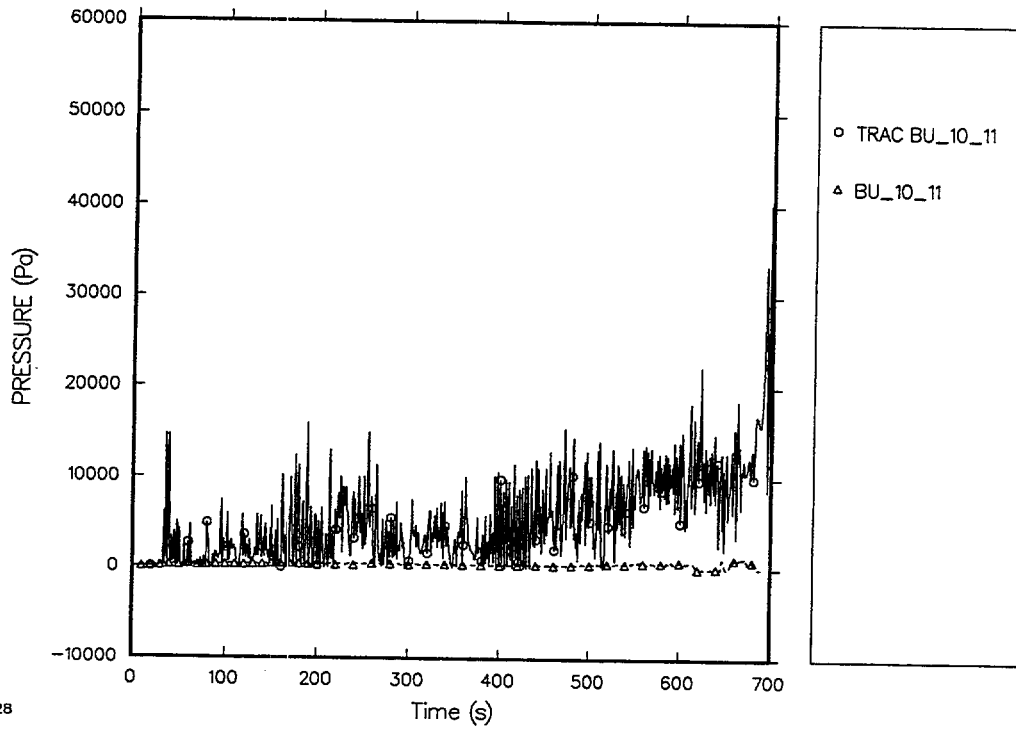
Fig. 4.8-52. Comparison of predicted and measured differential pressures (10–11 ft, with grid-spacer model).
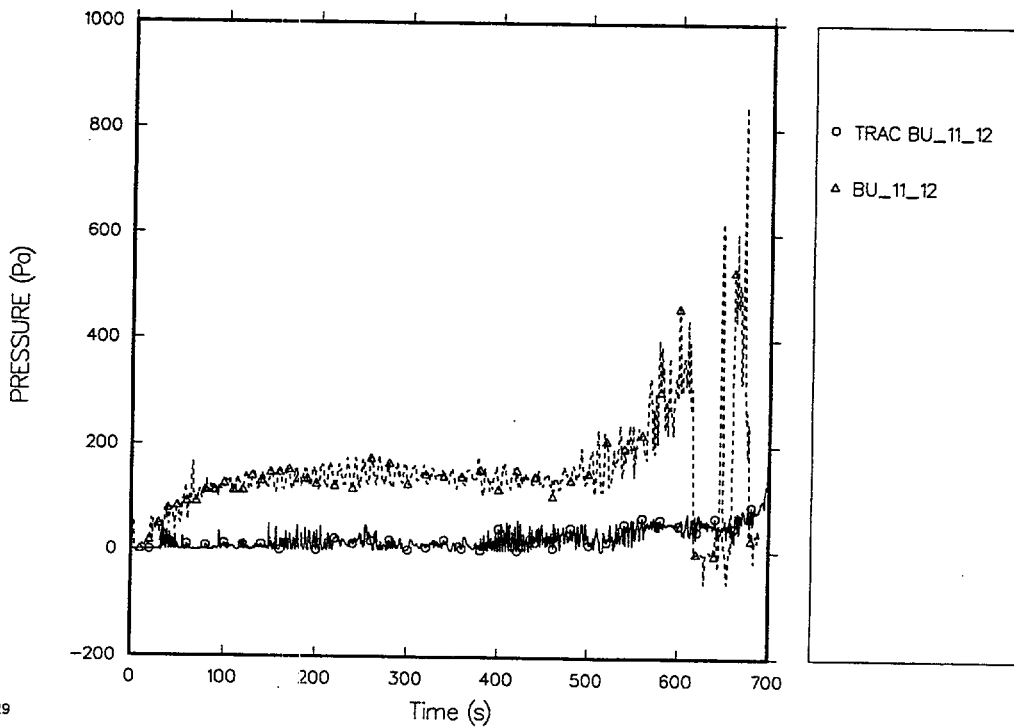


Fig. 4.8-53. Comparison of predicted and measured differential pressures (11–12 ft, with grid-spacer model).
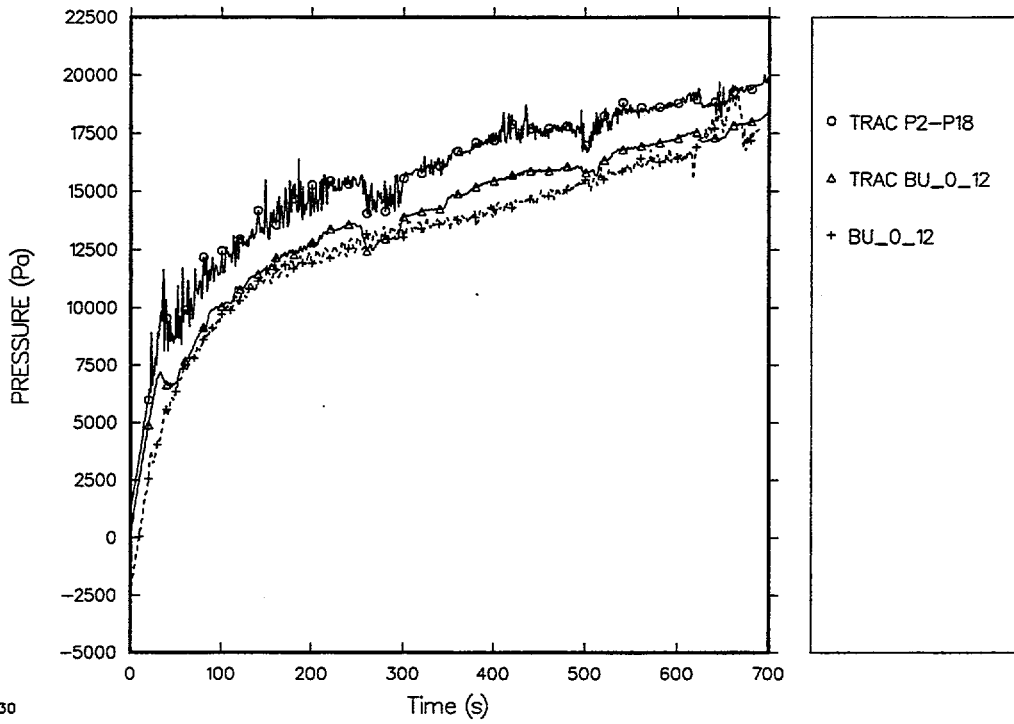
Fig. 4.8-54. Comparison of predicted and measured total core differential pressures (0–12 ft, with grid-spacer model).
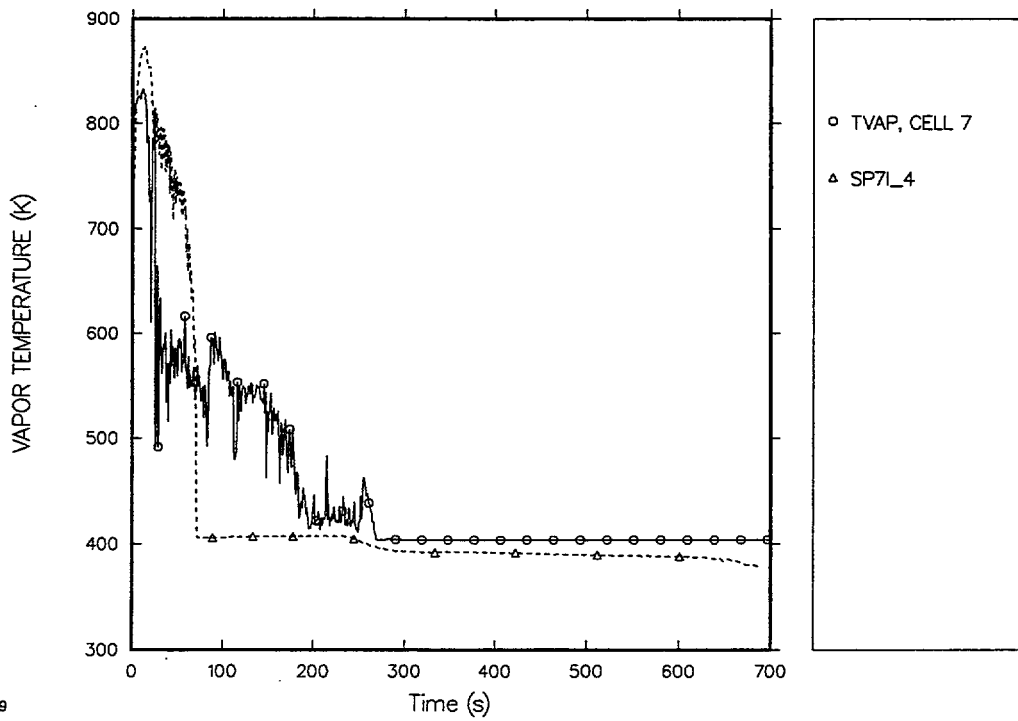


Fig. 4.8-55. Comparison of predicted and measured vapor temperatures in cell 7 (with grid-spacer model).
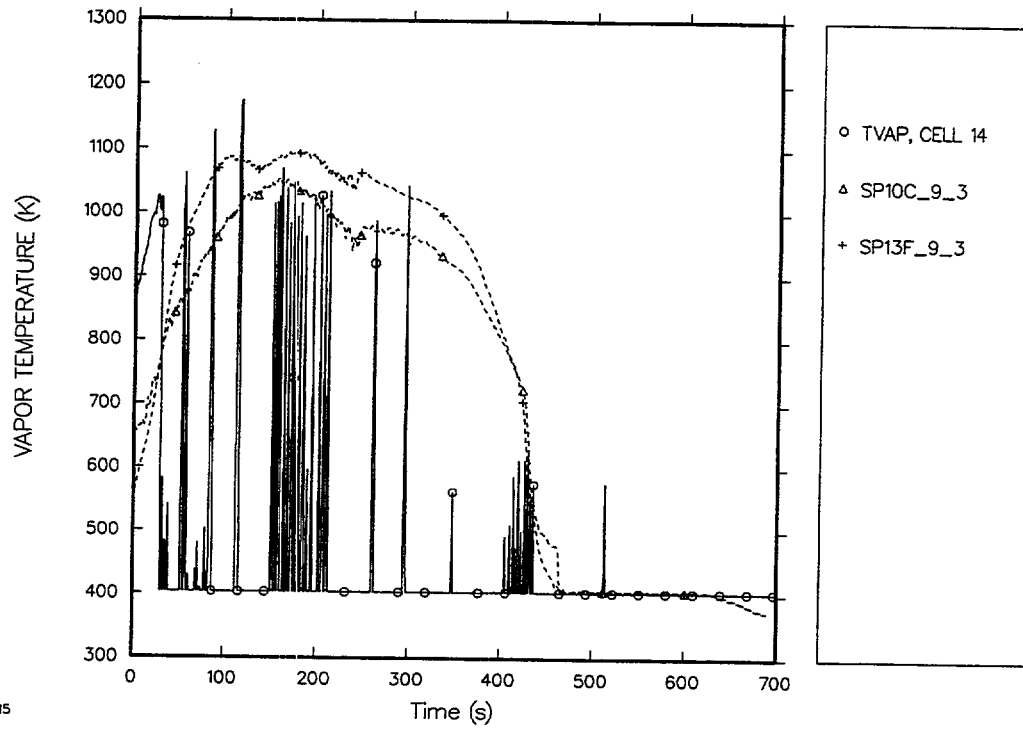
Fig. 4.8-56. Comparison of predicted and measured vapor temperatures in cell 14 (with grid-spacer model).

## 4.9. FLECHT SEASET Gravity Reflood Test 33436

The Full-Length Emergency Core Heat Transfer (FLECHT) Separate Effects and System-Effects Test (SEASET) facility was designed, built, and operated by the Westinghouse Electric Corporation. The objective of the test program was to obtain test data on reflooding heat transfer under simulated LOCA conditions for use in evaluating the heat-transfer capabilities of a PWR ECCS. The test program investigated the effects of parameters such as initial clad temperature, flooding rate, power, inlet subcooling, and system pressure on core heat transfer.

### 4.9.1. Facility Description

The FLECHT SEASET facility[4.9-1,4.9-2] was operated as a once-through system. It consisted of a low-mass-flow housing for the test bundle and upper and lower plenums, an external pipe downcomer, the test rod bundle, a coolant injection system, a coolant carryover tank, a steam boiler for back-pressure regulation, a gas supply for coolant injection, an entrainment separator, and the associated piping and valves. The low-mass-flow housing used in the test was designed to minimize the wall effects so that the rods one row or more away from the housing in the bundle are representative of any region in a PWR core. To preserve proper thermal scaling of the facility with respect to a PWR, the power-to-flow-area ratio is nearly the same as that of a PWR fuel assembly. An external downcomer (pipe) was connected to the flow housing lower plenum for the gravity reflood tests.

The rod bundle was composed of 161 heater rods (93 uninstrumented and 68 instrumented), 4 instrumented thimbles, 12 steam probes, 8 solid triangular fillers, and 8 grids. The test bundle rod geometry is typical of a Westinghouse 17 x 17 fuel-rod design and was deemed to be representative of the Westinghouse, Babcock & Wilcox, and Combustion Engineering fuel assemblies of that period (1980). Each rod has a cosine axial power profile. The fillers were welded to the grids to maintain the proper grid location; they also reduced the amount of excess flow area near the low-mass-flow housing.

The coolant injection system provided reflood water to quench the rod bundle during testing. Coolant injection water was supplied by a gas-charged accumulator, which then passed through a series of valves and flowmeters before entering the flow housing. The desired injection characteristic was accomplished by sequencing the valves to attain the specified injection flow characteristics.

Coolant injection water was supplied to the bottom elbow of the downcomer. A bidirectional turboprobe was installed in the downcomer spool piece during the gravity reflood tests to measure flow into the test section and any reverse flow from the test section to the downcomer.

The design of the upper-plenum extension prevented the entrained liquid collected in the upper plenum from falling back into the bundle. The housing for the rod bundle extended upward about 0.15 m into the upper-plenum extension. The two-phase flow exiting the bundle was forced to move radially outward, downward, and then upward into an exhaust pipe that subsequently led to the separator. Much of the liquid in the two-phase flow exiting the core was separated from the vapor as it followed the

tortuous path to the exhaust inlet. The liquid collected at the bottom of the upper-plenum extension housing where it drained through a tube to the carryover tank.

The separator, located in the exhaust line, was designed to remove any remaining water droplets exiting the test section so that a meaningful single-phase flow measurement could be obtained by an orifice section positioned downstream of the separator. The separator operated by utilizing centrifugal action to force the heavier moisture against the wall, where it drained to the bottom and through an outlet to a drain tank. A resistance orifice plate was installed before the inlet flange of the entrainment separator for the gravity reflood tests to simulate the hot-leg resistances.

The instrumentation of the FLECHT SEASET facility was extensive and included housing differential pressure cells every 0.3 m to obtain void-fraction measurements along the heated length of the bundle, steam probes in each of the 11 thimble tubes to measure steam superheat radially and axially across the bundle, and 177 heat-rod thermocouples. In addition, flow was measured at several locations as previously described. Additional instrumentation details are found in Ref. 4.9-1.

During the test program, rod distortion in the outer rows of rods was observed through the housing windows. At the end of the test program, the rod bundle was removed and examined, and the effect of the rod distortion on test data was assessed. For test 33436, it was concluded that some distortion of the center rods was possible, but that the effect was second order.[4.9-1]

### 4.9.2. Test Procedure and Description
The following general procedure was used to establish initial test conditions and perform a typical FLECHT SEASET unblocked bundle reflood test. The accumulator was filled with water and heated to the desired temperature. The carryover vessel, entrainment separator, separator drain tank, test-section upper plenum, and test-section outlet piping were heated while empty to slightly above the saturation temperature corresponding to the test-run pressure. The test section lower plenum was heated to the temperature of the coolant in the accumulator. The test section, carryover vessel, and exhaust-line components were pressurized to the desired system pressure. The coolant in the accumulator was pressurized to 2.76 MPa. Water was injected into the test-section lower plenum until it reached the beginning of the heated length of the bundle heater rods. Coolant was circulated and drained to ensure that the water in the lower plenum and injection line were at the specified temperature before the run.

Power was then applied to the test bundle, and the rods were allowed to heat up. When the temperatures in any two designated bundle thermocouples reached their preset value, coolant injection was automatically initiated, as was the power decay for the heater rods. For gravity reflood tests, the flooding rate was adjusted as necessary to ensure that the level in the downcomer did not go past the 4.88-m elevation. The injected coolant flow rate was controlled by valves. The system pressure was controlled to a preset value by releasing steam to the atmosphere through an exhaust control valve. The test was terminated when all the designated heater rods were quenched, as indicated by the rod thermocouples.

The initial conditions set for FLECHT SEASET gravity reflood test 33436 and a summary of key bundle reflood test data are given in Table 4.9-1.

### 4.9.3. TRAC Model

The FLECHT SEASET facility configured for gravity reflood tests was modeled as shown in the input model schematic (Fig. 4.9-1). The test vessel, including the lower-plenum extension, rod bundle housing, upper-plenum extension, and external downcomer, were modeled as Vessel component 3 in Cartesian geometry with 2 sectors in the x-direction, 1 sector in the y-direction and 21 axial cells. The rod bundle occupied the first (leftmost) x-direction sector, cells 3 through 17. The core axial noding is nonuniform. Cells 5 through 13 have a height of 0.183 m, cells 14 through 16 are 0.366 m (twice the height), and cell 17 is 0.457 m. The fine axial noding used in the FLECHT SEASET test 33436 input model is not consistent with the noding used in standard full-plant models. For example, core nodes in the AP600 plant model are ~0.6 m high. The lower plenum was modeled with cells 1 and 2. The upper plenum was modeled with cells 18 and 19. The downcomer, which was an external pipe in the facility, occupied the second radial sector (rightmost), cells 1 through 21. This model was produced in 1982 at the time TRAC-PD2/MOD1 was the release code. If we were to create a new model, we might elect to model the external downcomer as a Pipe component, although there is nothing technically wrong with using the Vessel representation (the hydraulics and heat transfer in the Vessel should be consistent with the Pipe component).

The separator phenomena in the upper-plenum extension is simply modeled by the Pipe component 4, which models the carryover tank and piping. As two-phase fluid passes upward through the core and into the upper plenum, it encounters a much larger flow area, which reduces the liquid and vapor velocities in upper-plenum cell 18. As the vapor slows, the liquid falls downward under the influence of gravity. This liquid passes into the entrance of Pipe component 4 and falls into the lower levels of the carryover tank modeled with Pipe component 4. There is nothing in the model to artificially induce the separation process. The vapor and any remaining liquid passes upward and exits the upper plenum through the exhaust line, modeled with Pipe component 6 and Break component 7. The exhaust pressure boundary condition is specified to be a constant 0.26890 MPa. As described in Section 4.1, Facility Description, the rod bundle housing extends upward into the upper plenum, thereby creating a tortuous path that must be followed by the two-phase flow exiting the rod bundle. The extension creates a well in which liquid can accumulate before it passes downward into the carryover tank. These features of the upper plenum are not modeled; the significance of these input model distortions is uncertain.

The top of the downcomer is vented through Pipe component 8 and Break component 9. In the facility, the downcomer vent is connected to the exhaust line. In this model, we specified the pressure for the downcomer vent as a constant pressure of 0.26884 MPa.

Coolant injection was to the downcomer through Pipe component 2. The injected coolant flow rate was specified using Fill component 1.

The 161 heater rods were modeled as a single rod component. The 8 spacer grids were modeled; the axial cell location and elevation in meters above the zero reference, i.e., the bottom of cell 1, are given in (x, y) pairs where x denotes the cell and y denotes the

elevation in meters: (2, 0.4064), (5, 0.9398), (8, 1.4478), (10, 1.9812), (13, 2.5146), (15, 3.0226), (16, 3.5560), and (17, 4.0640).

A listing of the input model used for this developmental assessment calculation is found in Appendix M. Archival storage information for this input model is provided in Section 4.9.8.

### 4.9.4. Comparison of Predicted and Measured Results

The calculation was performed with TRAC-M/F77 Version 5.5. These results are for newrfd=3, which activates the reflood model with explicit top-down reflood modeling. An identical set of graphical code-data comparisons with newrfd=1 is presented, without analysis, in Appendix N. Setting newrfd=1 activates the bottom-up reflood model of the TRAC-PF1/MOD1 code. We have run FLECHT SEASET 33436 calculations both with and without the grid-spacer model. We have determined that the grid-spacer model should not be used because it results in excessive and nonphysical heat-transfer processes in the upper portions of the core. Therefore, the base-case assessment results for FLECHT SEASET 33436 do not use the TRAC grid-spacer model (see Section 5.3-10 for details). We also report the calculation results with grid spacers to illustrate the impact of a grid-spacer model (Section 4.9-5).

FLECHT SEASET Test 33436 was one of a series of gravity reflood tests conducted in the facility. Test conditions are summarized in Table 4.9-1. All initial conditions were established via input. The mass flow at the heated-core inlet is shown in Fig. 4.9-2. The time-averaged core flooding rate, defined as the time-averaged core inlet mass flow divided by the core inlet flow area and the density of the core inlet flow, is shown in Fig. 4.9-3. The initial heater-rod axial-temperature distribution input at the start of the test is compared with the measured heater-rod axial-temperature distribution in Fig. 4.9-4. The input and measured initial cladding profiles are in reasonable agreement. However, input temperatures at both the bottom and top of the heater rod are higher than measured and may have an impact on the predicted thermal response in these two regions. The initial axial vapor temperature distribution input at the start of the test is compared with the measured axial vapor temperature in Fig. 4.9-5. The input and measured axial vapor temperature profiles are in reasonable agreement, although the input profile is shifted relative to the measured profile such that the code predicts the measured temperature at higher elevations than measured. The slight difference in initial vapor temperatures should be insignificant.

The test was initiated when power was applied to the core. The ECCS injection flow rate was ramped from 0.0 to 6.3 kg/s in 1 s, ramped down to 5.3643 kg/s over the next 14 s, decreased to 0.7847 kg/s over 1 s, and held constant thereafter. This profile was based upon data.[4.9-4]

A comparison of predicted and measured cladding quench times at various levels in the core is presented in Fig. 4.9-6. There are significant differences in the predicted and observed quenching behavior. The agreement between the predicted and measured quench times is insufficient, as neither the magnitude nor the trends of the quench behavior are predicted with sufficient accuracy. In other assessments in this report, we have shown that the code predicts too much entrainment and carryover of liquid, resulting in a deficiency of liquid ahead of the quench front. We have also shown that

the code underpredicts the amount of heat transfer ahead of the quench front. These are general deficiencies in the reflood model; however, with FLECHT SEASET 33436, we observe a second and perhaps equally important effect, at least for this test. In FLECHT SEASET 33436, the grid spacer is a key component and has a major impact on cladding thermal response.

*The following observations apply to the test.* For the first 1.25 m, the quench front advances coherently throughout the test bundle (Fig. 4.9-6) . At an elevation of 1.5 m, radial variations in quenching behavior are seen in the test data and these grow with elevation. At the 3-m level, quench times vary from 140 to 250 s. During the test, the quench front generally advances from the bottom of the core upward. For several heater rods at the top of the core, top-down cooling and quenching occur at times <25 s. Other rods at the same elevation are not quenched early.

*The following observations apply to the predicted quench behavior without grid spacers modeled.* The predicted quench front advances from the bottom of the core upward. The calculated quench front advances slower than observed in the test with ever increasing delays until an elevation of ~2.2 m. The measured quench front advances to the core midplane at a rate between ~14 and 16 mm/s. The predicted quench front advances at ~7 mm/s. At the core midplane, the predicted quench occurs ~120 s later than the latest rod to quench at that elevation in the test and ~140 s later than the earliest rod to quench at that elevation in the test. Above an elevation of 2.4 m, the cladding remains unquenched during the 400 s of calculated transient.

The predicted cladding temperature responses at a number of levels through the core are shown in Fig. 4.9-7 (lower half of core) and Fig. 4.9-8 (upper half of core). Quenching is seen to progress upward from the bottom of the core to an elevation of 2.4 m. The code does not predict quenching at elevations higher than 2.4 m during the calculated transient.

The predicted and measured cladding thermal responses at seven axial locations are compared in Figs. 4.9-9 through 4.9-15. The trends discussed previously are evident in these figures. At the 0.3048-m level above the bottom of the heated core (Fig. 4.9-9), the predicted quench time is late. Too little energy is being removed from the heater rod above the quench front. This trend is again evident at the 0.9906-m level (Fig. 4.9-10) and slightly above the core midplane at the 1.9813-m level (Fig. 4.9-11) where the undercooling is very large. This trend continues above the core midplane. At the 2.8194-m level (Fig. 4.9-12), the predicted PCT is ~350 K higher than measured. Although the predicted PCT decreases with elevation (3.048 m, 3.353 m, and 3.505 m in Figs. 4.9-13 through 4.9-15, respectively), quenching is not predicted; quenching was observed at each of these levels during the test.

The predicted and measured differential pressures across 12, 1-ft segments through the core are presented in Figs. 4.9-16 through 4.9-27. The pressure differentials are interpreted as a direct measurement of liquid present between each set of pressure taps. The predicted and measured differential pressure results are consistent with the cladding thermal discussions presented above. The predicted behavior resulting in the undercooling of the lower half of the heated core can be seen in Figs. 4.9-16 through Fig. 4.9-21. At each level, the code underpredicts the amount of coolant available for cooling

the heater rods. The differential pressure in Fig. 4.9-16 corresponds to the cladding temperature thermal response shown in Fig. 4.9-9. The predicted coolant flow into the core initially proceeds as measured but is interrupted at 3.5 s and does not regain the value of the measured differential pressure until 13 s later. The quenching behavior of the predicted and measured rods reflect this difference. The differential pressure comparison in Fig. 4.9-19 corresponds to the cladding temperature thermal response shown in Fig. 4.9-10. The same trends, both predicted and measured, continue throughout the remainder of the core.

In summary, the predicted amount of liquid in the core at any time and at any level is less than measured. The predicted and measured differential pressures over the entire length of the core (0–12 ft) are shown in Fig. 4.9-28. During the first 15 s of the test, the coolant injection rate was 5.80 kg/s, and was 0.785 kg/s thereafter. The trends associated with initial high flow rate followed by a lower flow rate for the remainder of the test are reflected in both the predicted and measured core differential pressure.

Because the injected coolant flow for the test was simulated via a boundary condition specification and, according to the predicted behavior, does not reside in the core, we looked to the inventory behavior of the downcomer (Fig. 4.9-29) and the coolant mass deposited in the carryover tank (Fig. 4.9-30). The code accurately predicts the initial rise in the downcomer liquid level, but underpredicts the level to which the downcomer fills. The downcomer level decreases as the injected coolant flow drops to the 0.785 kg/s and stays below the measured level until late in the transient. A comparison of the predicted and measured carryover tank inventory accumulation (Fig. 4.9-30) clearly indicates that the code predicts too much liquid carryover when compared with the behavior observed in the test.

### 4.9.5. Comparison of Predicted and Measured Results (with Grid Spacers)

In this section we provide a comparison of the predicted and measured results for FLECHT SEASET 33436 with the TRAC grid-spacer model activated. We present the figures in the same order as Section 4.9.4. The following tabulation is provided to facilitate the comparison of figures.

| Without Grid Spacers | With Grid Spacers |
|---|---|
| 4.9-6 | 4.9-31 |
| 4.9-7 | 4.9-32 |
| 4.9-8 | 4.9-33 |
| 4.9-9 | 4.9-34 |
| 4.9-10 | 4.9-35 |
| 4.9-11 | 4.9-36 |
| 4.9-12 | 4.9-37 |
| 4.9-13 | 4.9-38 |
| 4.9-14 | 4.9-39 |
| 4.9-15 | 4.9-40 |
| 4.9-16 | 4.9-41 |
| 4.9-17 | 4.9-42 |

| 4.9-18 | 4.9-43 |
|--------|--------|
| 4.9-19 | 4.9-44 |
| 4.9-20 | 4.9-45 |
| 4.9-21 | 4.9-46 |
| 4.9-22 | 4.9-47 |
| 4.9-23 | 4.9-48 |
| 4.9-24 | 4.9-49 |
| 4.9-25 | 4.9-50 |
| 4.9-26 | 4.9-51 |
| 4.9-27 | 4.9-52 |
| 4.9-28 | 4.9-53 |
| 4.9-29 | 4.9-54 |
| 4.9-30 | 4.9-55 |

A comparison of predicted and measured cladding quench times at various levels in the core is presented in Fig. 4.9-31. Even with the grid-spacer model activated, there are significant differences in the predicted and observed quenching behavior. The agreement between the predicted and measured quench times is minimal, as both the magnitude and the trends of the quench behavior are not well predicted. However, the increased cooling due to the TRAC grid-spacer model in the upper core is clearly evident (compare Figs. 4.9-31 and 4.9-6), leading to the conclusion that the grid spacer is a key component in FLECHT SEASET 33436 and grid-spacer model simulating the correct physical processes required to adequately predict this test.

*The following observations apply to the predicted quench behavior with grid spacers modeled.* Throughout the core, the quench front advances slower than observed in the test, with ever increasing delays until an elevation of ~2.4 m. The measured quench front advances to the core midplane at a rate between ~14 and 16 mm/s. The predicted quench front advances at ~6 mm/s. At the core midplane, the predicted quench occurs ~170 s later than the latest rod to quench at that elevation in the test, and ~190 s later than the earliest rod to quench at that elevation in the test. At core elevations above 2.6 m, the calculated quench times lie within the range of quench times observed in the test.

The predicted cladding temperature responses at a number of levels through the core are shown in Fig. 4.9-32 (lower half of core) and Fig. 4.9-33 (upper half of core). Quenching progresses upward from the bottom of the core to an elevation of 2.4 m. Beginning at 140 s, a quench front proceeds downward from the top of the core to an elevation of 2.6 m. In the test, the top-down quench is limited to elevations above 3.4 m and occurs shortly after the start of coolant injection.

The predicted and measured cladding thermal responses at 7 axial locations are compared in Figs. 4.9-34 through 4.9-40. The trends discussed previously are evident in these figures. At the 0.3048-m level above the bottom of the heated core (Fig. 4.9-34), the predicted quench time is late. Too little energy is being removed from the heater rod above the quench front. This trend is again evident at the 0.9906-m level (Fig. 4.9-35) and slightly above the core midplane at the 1.9812-m level (Fig. 4.9-36) where the undercooling is very large. Above the core midplane, the predicted cooling is greater

than observed in the test. At the 2.8194-m level (Fig. 4.9-37), the predicted cladding temperature is within the range of measured cladding behaviors. The same behavior is predicted at the 3.0480-m level (Fig. 4.9-38) where the predicted cooling is greater than for all but one of the instrumented rods in the test. The 3.3528 (Fig. 4.9-39) and 3.5052-m levels (Fig. 4.9-40) are high in the core. An early quench, i.e., <30 s, was observed in the test at each level. The predicted quenches at these level occur considerably later. This may be due, in part, to the specification of initial cladding temperatures at these levels that are as much as 30 K higher than measured. The measured quench at the 3.3528-m level occurs earlier than at the higher level of 3.5052 m.

The predicted and measured differential pressures across 12, 1-ft segments through the core are presented in Figs. 4.9-41 through 4.9-52. The pressure differentials are interpreted as a direct measurement of liquid present between each set of pressure taps. The predicted and measured differential pressure results are consistent with the cladding thermal discussions presented above. The predicted behavior resulting in the undercooling of the lower half of the heated core can be seen in Figs. 4.9-41 through Fig. 4.9-46. At each level, the code underpredicts the amount of coolant available for cooling the heater rods. The differential pressure in Fig. 4.9-41 corresponds to the cladding temperature thermal response shown in Fig. 4.9-34. The predicted coolant flow into the core initially proceeded as measured but is interrupted at 3.5 s and does not regain the value of the measured differential pressure until 13 s later. The quenching behavior of the predicted and measured rods reflect this difference. The differential pressure comparison in Fig. 4.9-44 corresponds to the cladding temperature thermal response shown in Fig. 4.9-35. Although oscillatory behavior is both predicted and measured, the coolant predicted in this level is less than the measured value after 25 s. The code predicts a continuing oscillatory behavior long after this behavior terminated during the test. A significant fraction, although not all, of the oscillatory behavior is caused by the grid-spacer model as seen by comparing Figs. 4.9-44 (with grid spacer) and 4.9-19 (without grid spacer). The same trends, both predicted and measured, continue to a level just above the core midplane, as shown by comparing Figs. 4.9-47 and 4.9-36. The amount of coolant predicted to exist at this level is again severely underpredicted.

At the 2.819-m level, 3.2 ft above the core midplane, the comparison between predicted and measured cladding thermal behavior is in reasonable agreement (Fig. 4.9-37). However, the physical processes resulting in the predicted and measured thermal responses are quite different. The predicted cladding thermal response is caused by a quench front moving downward from the top of the core while the cooling at this level in the test is by a quench front moving upward from the bottom of the core (Fig. 4.9-31). The differential pressure comparison at this level is provided in Fig. 4.9-50; again, the liquid inventory is underpredicted.

The predicted behavior at 3.0480 m (Fig. 4.9-38) is very similar to that at the 2.8194-m level. At the 3.3528-m level, all the heater rods quenched early (Fig. 4.9-39). The reason for the early quench in the test is clearly seen in Fig. 4.9-51; between 5 and 25 s, there was a large amount of liquid at this level. This behavior was not predicted by the code. A similar but less pronounced manifestation of the phenomena at the 3.3528-m level also occurs at the 3.5052-m level (Figs. 4.9-52 and 4.9-40).

In summary, the predicted amount of liquid in the core at any time and at any level is less than measured. The predicted and measured differential pressures over the entire length of the core (0–12 ft) are shown in Fig. 4.9-53. During the first 15 s of the test, the coolant injection rate was 5.80 kg/s, and 0.785 kg/s thereafter. The trends associated with initial high flow rate followed by a lower flow rate for the remainder of the test are reflected in both the predicted and measured core differential pressure.

As the injected coolant flow for the test was simulated via a boundary condition specification and, according to the predicted behavior, does not reside in the core, we looked to the inventory behavior of the downcomer (Fig. 4.9-54) and the coolant mass deposited in the carryover tank (Fig. 4.9-55). The code accurately predicts the initial rise in the downcomer liquid level. However, the downcomer level decreases as the injected coolant flow drops to the 0.785 kg/s and stays below the measured level until late in the transient. A comparison of the predicted and measured carryover tank inventory accumulation clearly indicates that the code predicts too much liquid carryover when compared with the behavior observed in the test.

### 4.9.6. Conclusions

A developmental assessment of TRAC-M, Version 5.5 has been completed using data from FLECHT SEASET test 33436. The base-case calculation was performed using an input model that contained no model of the FLECHT SEASET grid spacers. With respect to key parameters, such as cladding temperatures and coolant distribution, the agreement between code-predicted and measured values is insufficient.

We performed a parametric calculation in which the FLECHT SEASET grid spacers were modeled with the TRAC grid-spacer model. When applied to other facilities and tests, we have found that the grid-spacer model produces excessive and nonphysical cooling rates. The TRAC grid-spacer model lacks an appropriate physical basis and its use is, therefore, discouraged. However the initial assessment calculations used the TRAC grid-spacer model, and these results provide a strong indication of the significant cooling enhancement that arises from the FLECHT SEASET bundle grid spacer. It is clear that a well-founded grid-spacer model should be developed for TRAC.

We have concerns about several features of the input model used in this analysis. The model was developed in 1982 for the TRAC-PD2/MOD1 code and reflected the modeling capabilities of the code available at that time. The specific areas of concern are the modeling of the external downcomer within the vessel component, the noding of the core, and the modeling of the upper-plenum extension with respect to separation of liquid-vapor separation and liquid draining to the carryover tank. The downcomer behavior, the liquid distribution in the core, and the rate of liquid transport to the carryover tank all show minimal agreement with measurements. Although there is no definitive evidence that the present input model is inadequate, it would be prudent to revise the model for future code assessment activities. We would choose to model the downcomer with a Pipe component instead of modeling it as part of the Vessel component that is used to model the core. We would also model initial conditions, such as axial vapor temperatures in the core, more accurately.

Much of the predicted behavior for FLECHT SEASET test 33436 is consistent with that observed for the other three tests in this developmental assessment activity. These

behaviors are (1) the prediction of too little liquid inventory in the test vessel, particularly in advance of the quench front, (2) the prediction of too-little heat transfer in advance of the quench front, and (3) the prediction of a too-large liquid-transport rate through the test vessel.

### 4.9.7. Code Performance

FLECHT SEASET Test 33436 was run with code Versions 5.5; the run performance information plus other pertinent comments follow.

Code Version 5.5

| Platform | Sun Enterprise 3000 |
|---|---|
| Total CPU time (s) | 15533.0 |
| Archive location of input model | CFS    /tida/f77da_decks/infs33436 |
| Archive location of calculation | CFS    /trac-da/F77DA/1.11Rrfd3nogs/ FLECHT.tar.gz |

### REFERENCES

4.9-1.  M. J. Loftus, L. E. Hochreiter, C. E. Conway, C. E. Dodge, A. Tong, E. R. Rosal, M. M. Valkovic, and S. Wong, "PWR FLECHT SEASET Unblocked Bundle, Forced and Gravity Reflood Task Data Report," US Nuclear Regulatory Commission document NUREG/CR-1532, Electric Power Research Institute document EPRI NP-1459, Westinghouse Electric Corporation document WCAP 9699 (June 1980).

4.9-2.  "Compendium of ECCS Research for Realistic LOCA Analysis," US Nuclear Regulatory Commission document NUREG-1230 (December 1988).

4.9-3.  R. A. Nelson, Jr., D. A. Pimentel, S. Jolly-Woodruff, and J. Spore, "Reflood Completion Report, Volume I, A Phenomenological Thermal-Hydraulic Model of Hot Rod Bundles Experiencing Simultaneous Bottom and Top Quenching and an Optimization Methodology for Closure Development," Los Alamos National Laboratory document LA-UR-98-3043 (April 1998).

4.9-4.  N. Lee, S. Wong, H. C. Yeh, and L. E. Hochreiter, "PWR FLECHT SEASET Unblocked Bundle, Forced and Gravity Reflood Task Data Evaluation and Analysis Report," US Nuclear Regulatory Commission document NUREG/CR-2256, Electric Power Research Institute document EPRI NP-2013, Westinghouse Electric Corporation document WCAP 9891 (September 1981).

**TABLE 4.9-1**
**CONDITIONS AND KEY RESULTS FOR TEST 33436**

| Parameter | Test Condition Value |
|---|---|
| Upper-plenum pressure | 0.27 MPa |
| Rod initial clad temperature at 1.83-m level | 1151 K |
| Rod peak power | 2.3 kW/m |
| ECCS injection rate | 5.80 kg/s for 15 s<br>0.785 kg/s onward |
| Coolant temperature | 325 K |
| Radial power distribution | Uniform |
| Initial temperature of hot rod | 1164 K |
| Elevation of maximum temperature of hot rod | 1.78 m |
| Maximum temperature of hot rod | 1183 K |
| Temperature rise | 292 K |
| PCT time of hot rod | 4 s |
| Quench time of hot rod | 121 s |
| Bundle quench time | 174 s |

(Note: Not shown are 12 heat-structure components that model the core and downcomer vessel walls)

9  BREAK  Downcomer Back Pressure

8

8  PIPE  Downcomer Vent

7

idcu

21

20

This sector models the core section

Exhaust Line  Back Pressure

PIPE  BREAK

19

18

icru

17

3

16

15

Fuel Rods

Carryover Tank

14

VESSEL

10

4

13

3

Cartesian Geometry (x=2, y=1, z=21)

ROD

PIPE

12

11

10

9

8

This sector models the downcomer pipe

7

6

5

4

4

5

FILL

3

icrl

idcr  2

idcl

PIPE  FILL

Zero-Flow Fill Boundary

1

2  1  Coolant Injection

2  1

1  2

X

Fig. 4.9-1. FLECHT SEASET Test 33436 input model diagram.
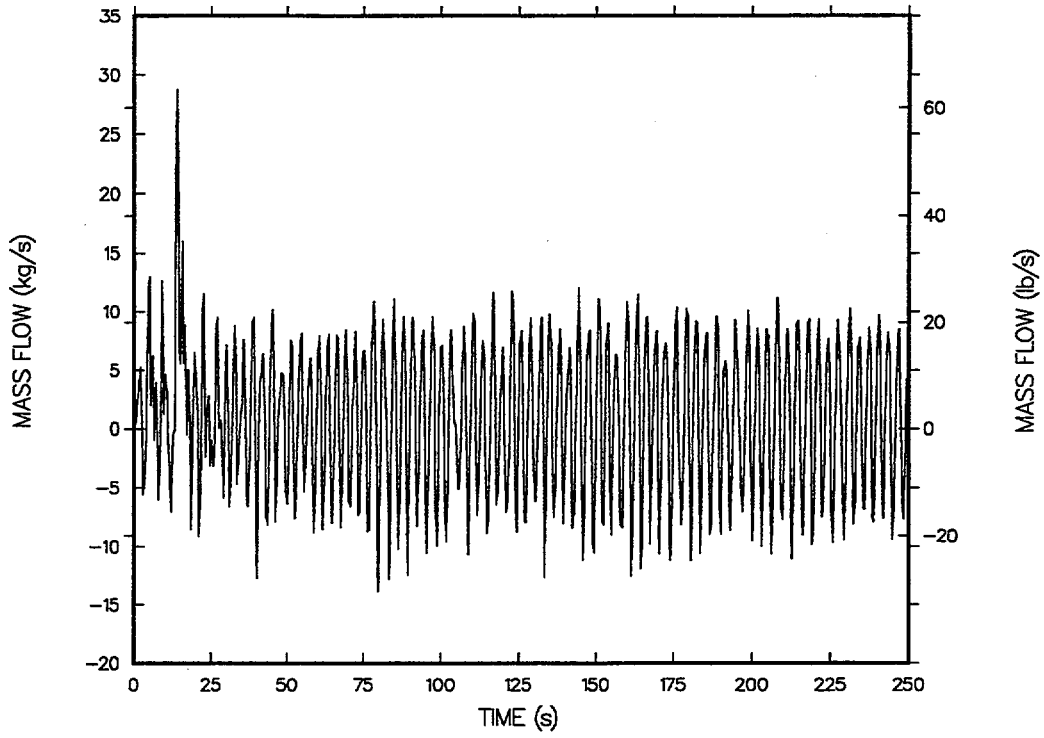
Fig. 4.9-2. Core inlet mass flow.
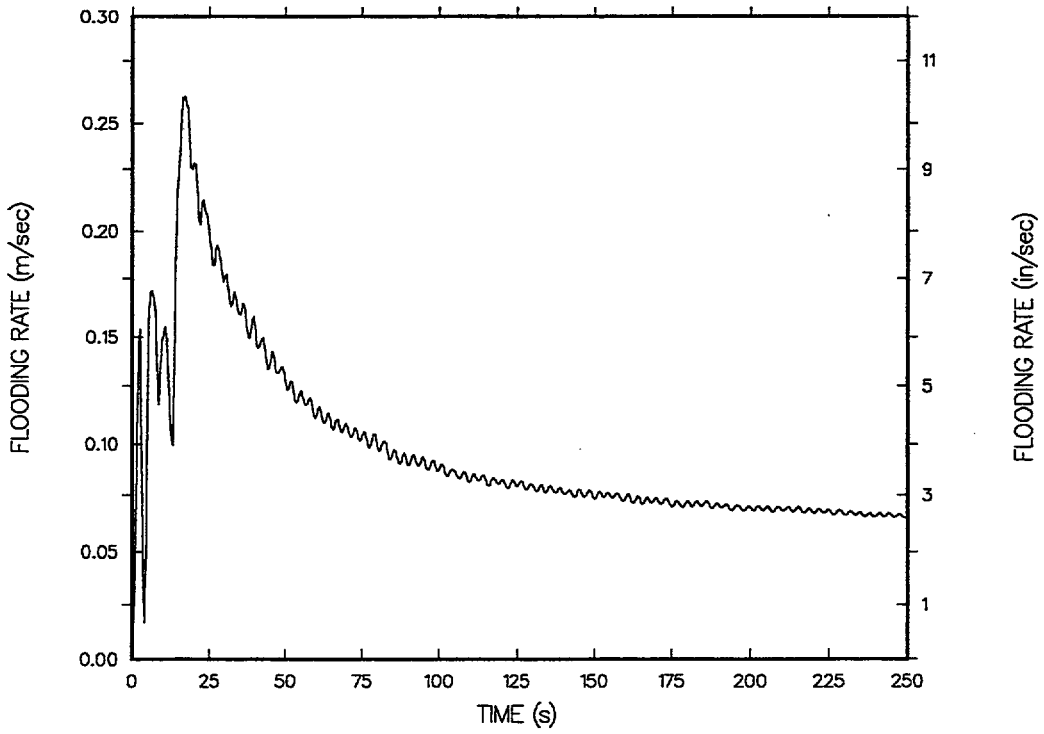


Fig. 4.9-3. Time-averaged core flooding rate.
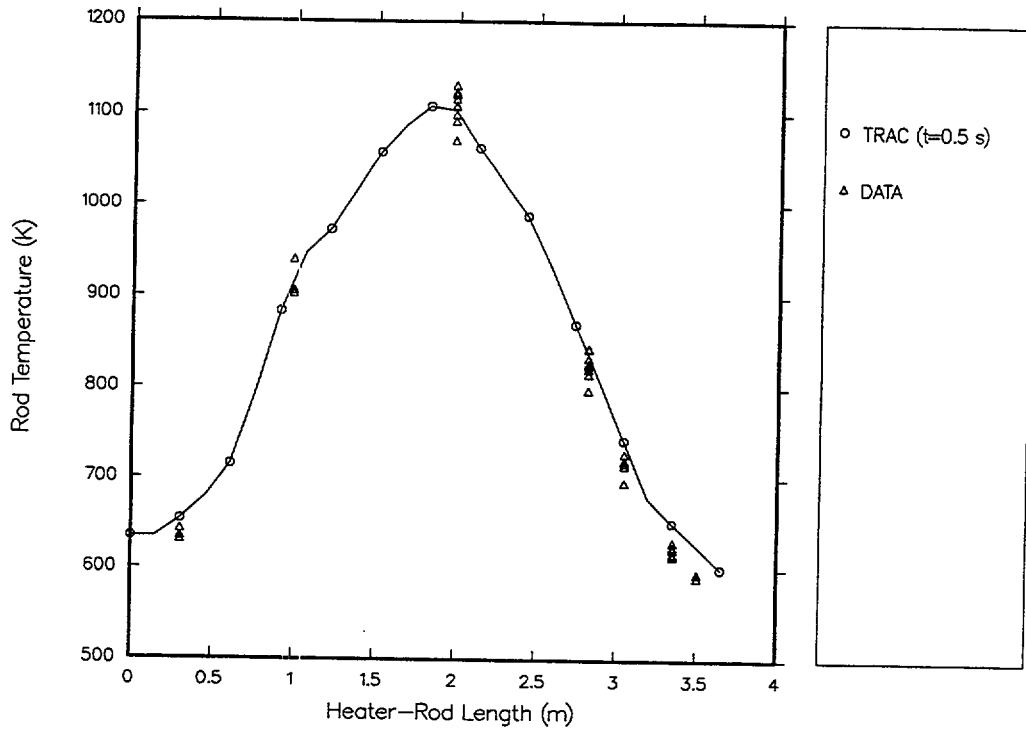
Fig. 4.9-4.   Comparison of initial predicted and measured axial heater-rod cladding temperatures (0.5 s).
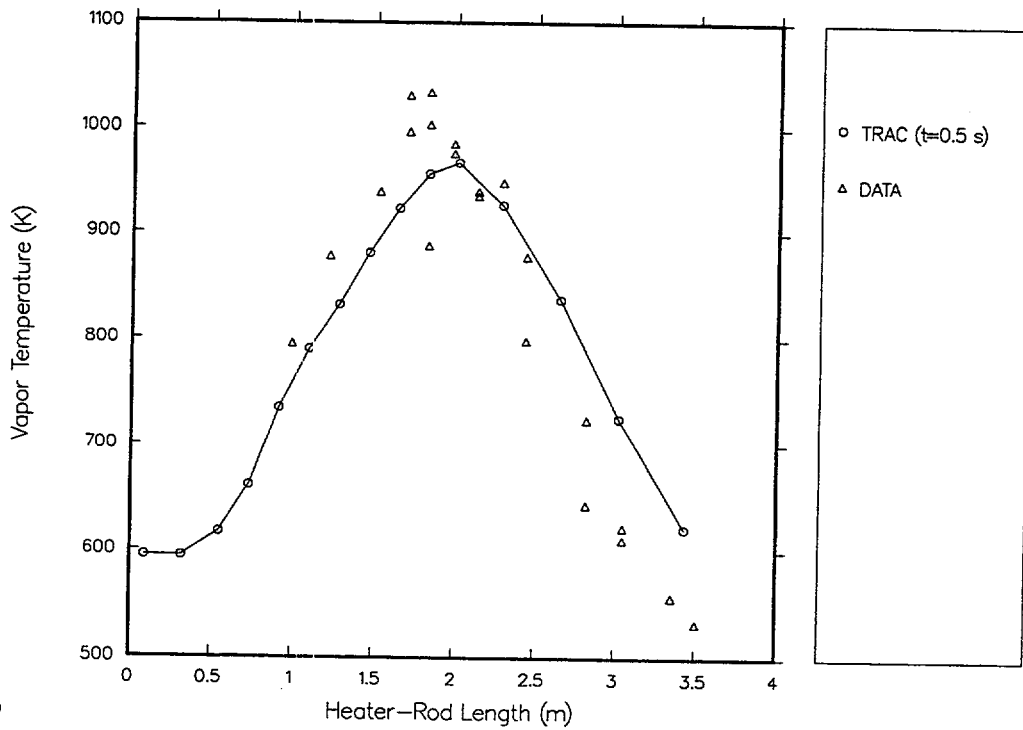


Fig. 4.9-5.   Comparison of initial predicted and measured axial vapor temperatures (0.5 s).
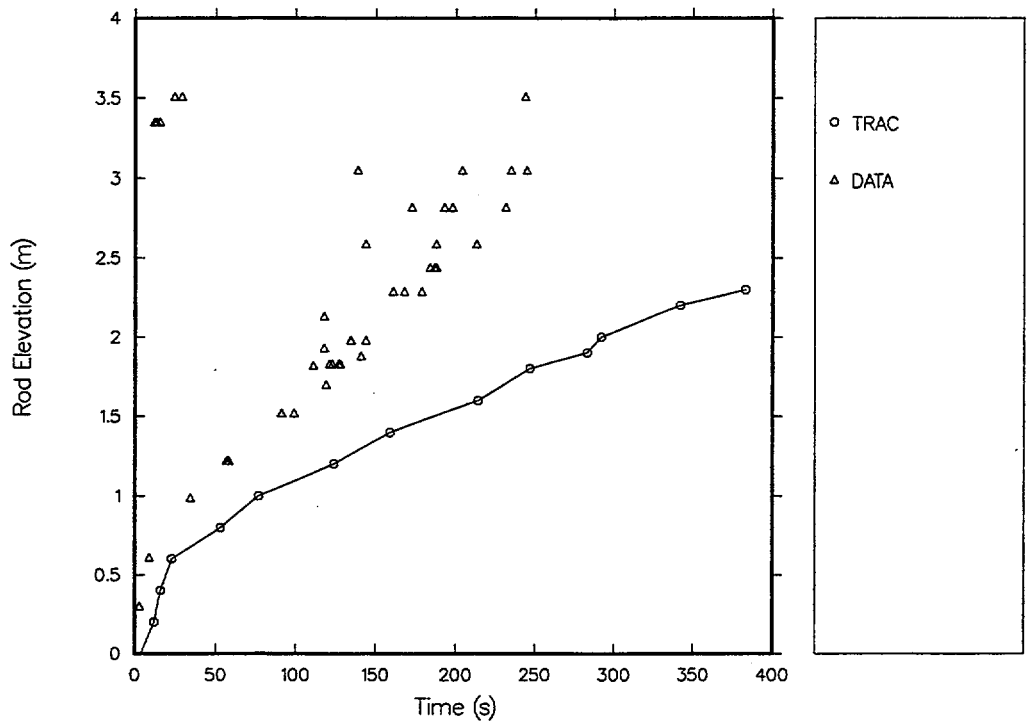
Fig. 4.9-6.    Comparison of predicted and measured cladding quench times.
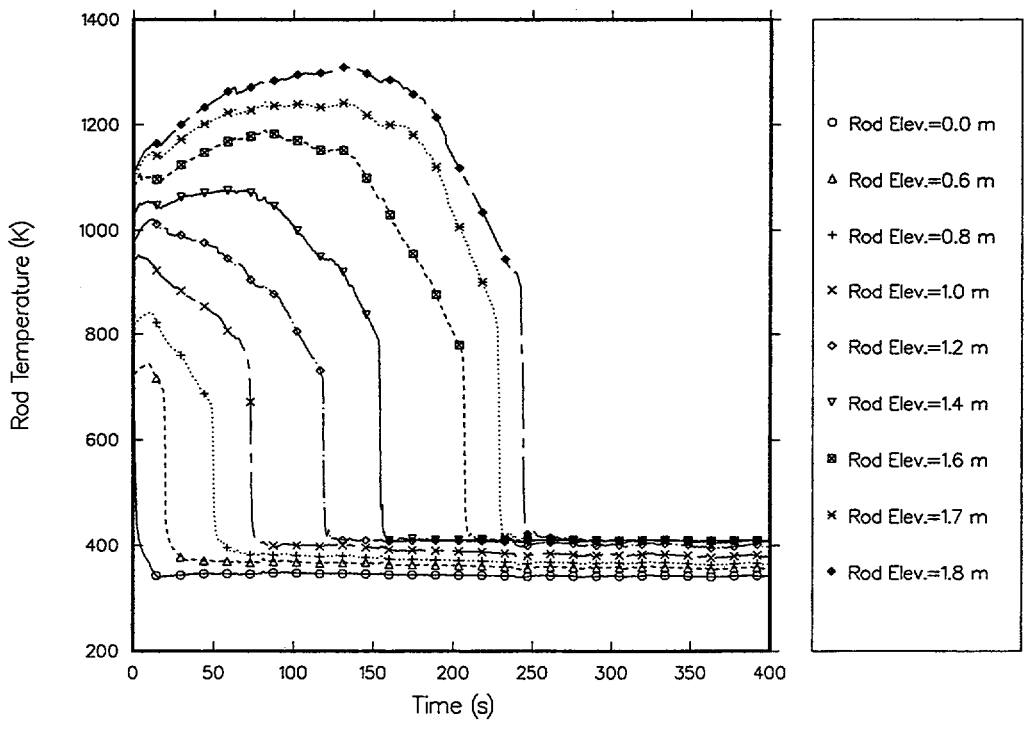


Fig. 4.9-7.    Predicted cladding temperature responses in lower half of core.
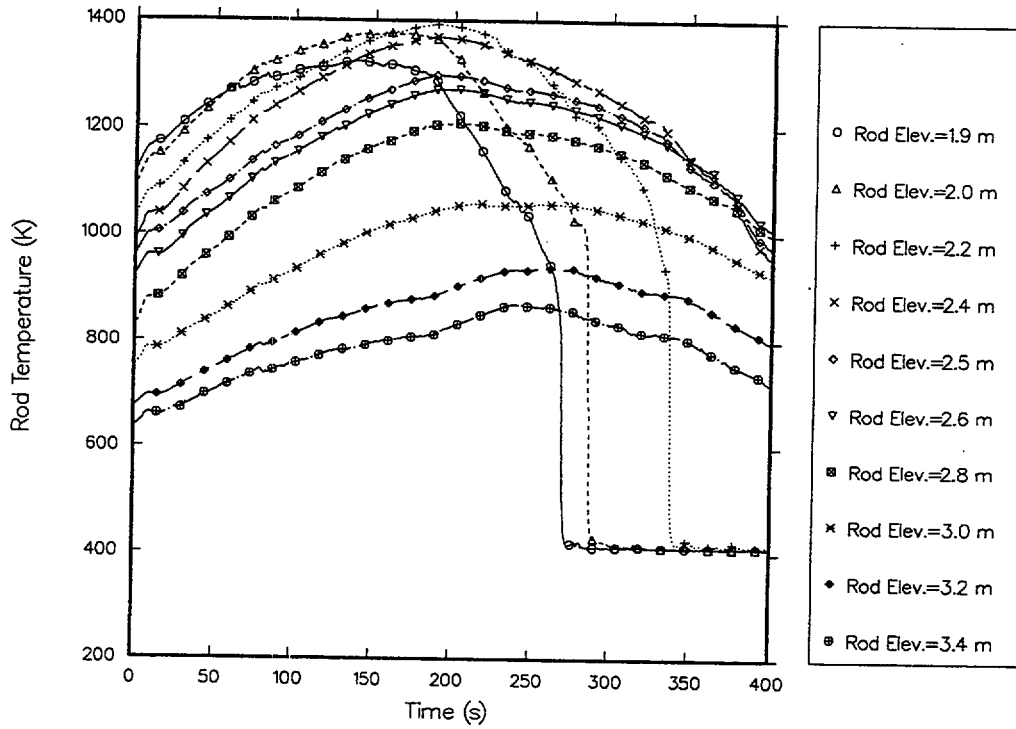
Fig. 4.9-8.    Predicted cladding temperature responses in upper half of core.
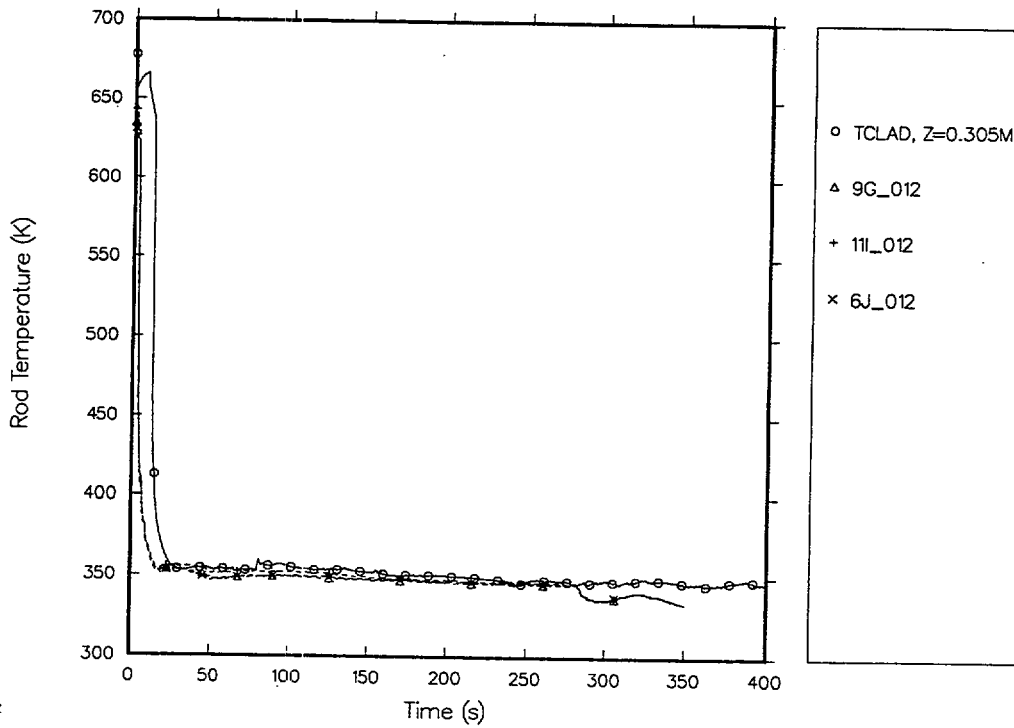


Fig. 4.9-9.    Comparison of predicted and measured heater-rod cladding temperatures at 0.3048-m elevation.
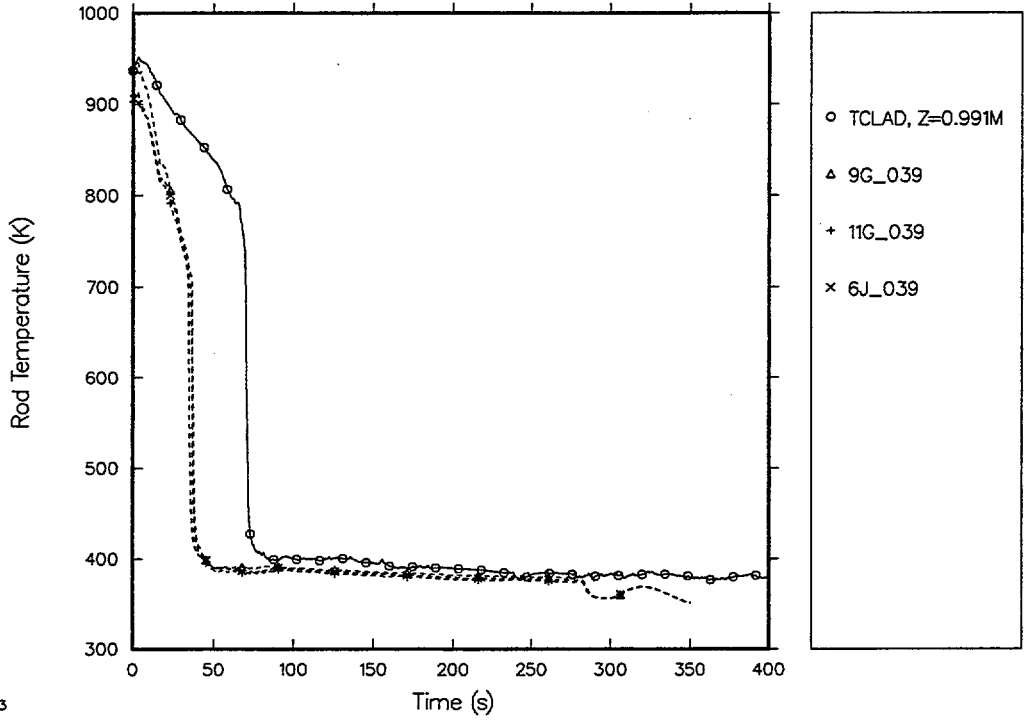
Fig. 4.9-10.   Comparison of predicted and measured heater-rod cladding temperatures at 0.9906-m elevation.
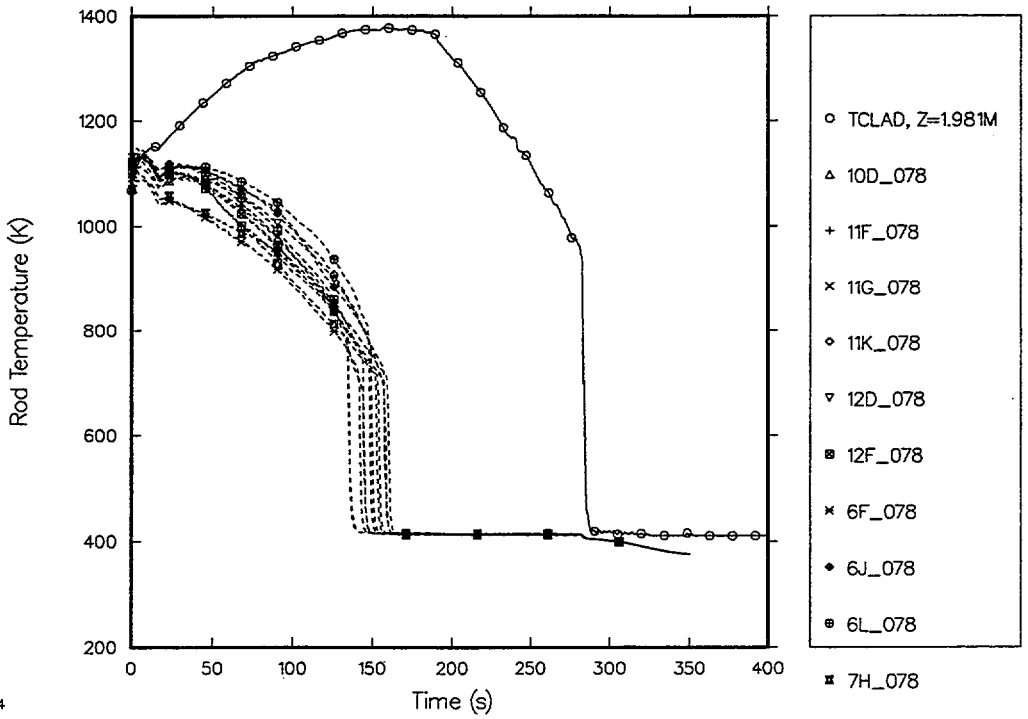


Fig. 4.9-11.   Comparison of predicted and measured heater-rod cladding temperatures at 1.9812-m elevation.
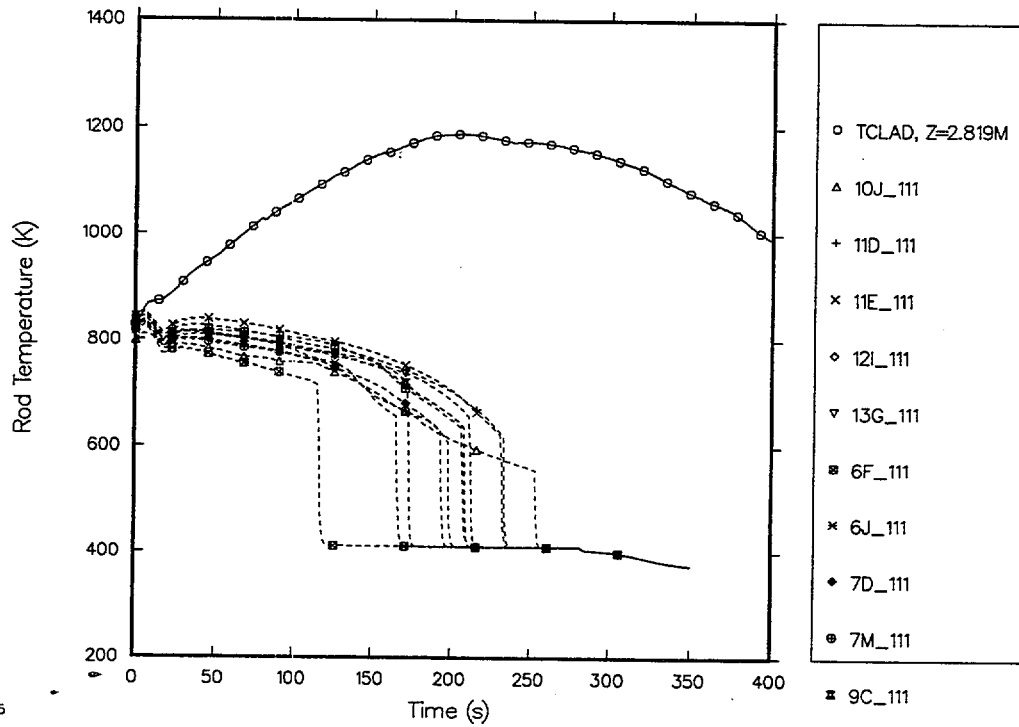
Fig. 4.9-12.  Comparison of predicted and measured heater-rod cladding temperatures at 2.8194-m elevation.
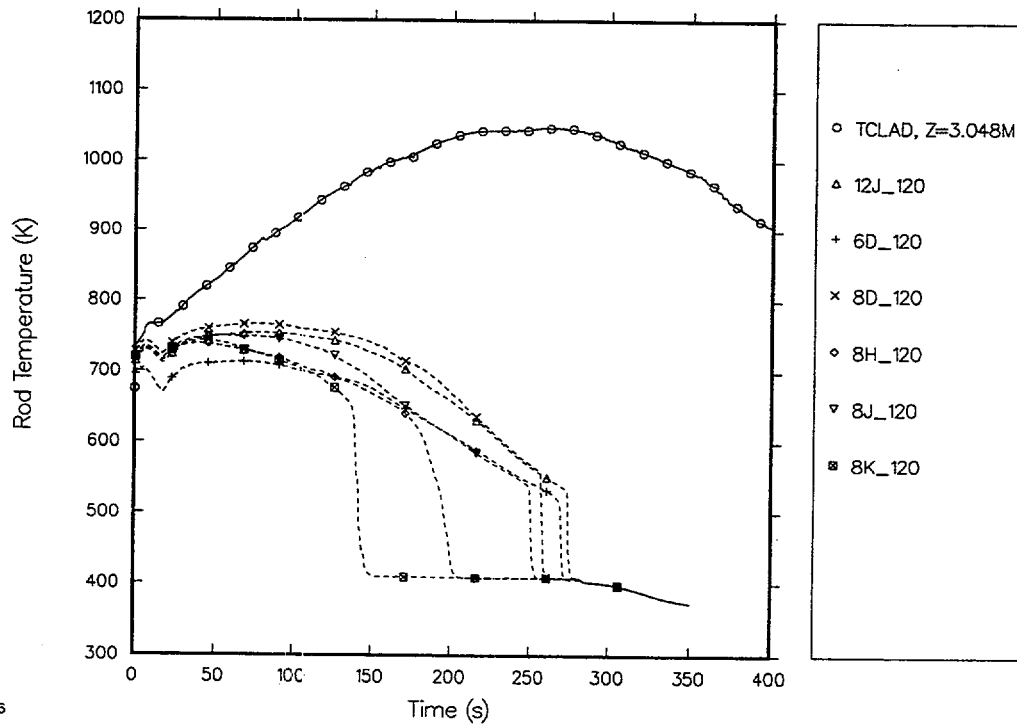


Fig. 4.9-13.  Comparison of predicted and measured heater-rod cladding temperatures at 3.0480-m elevation.
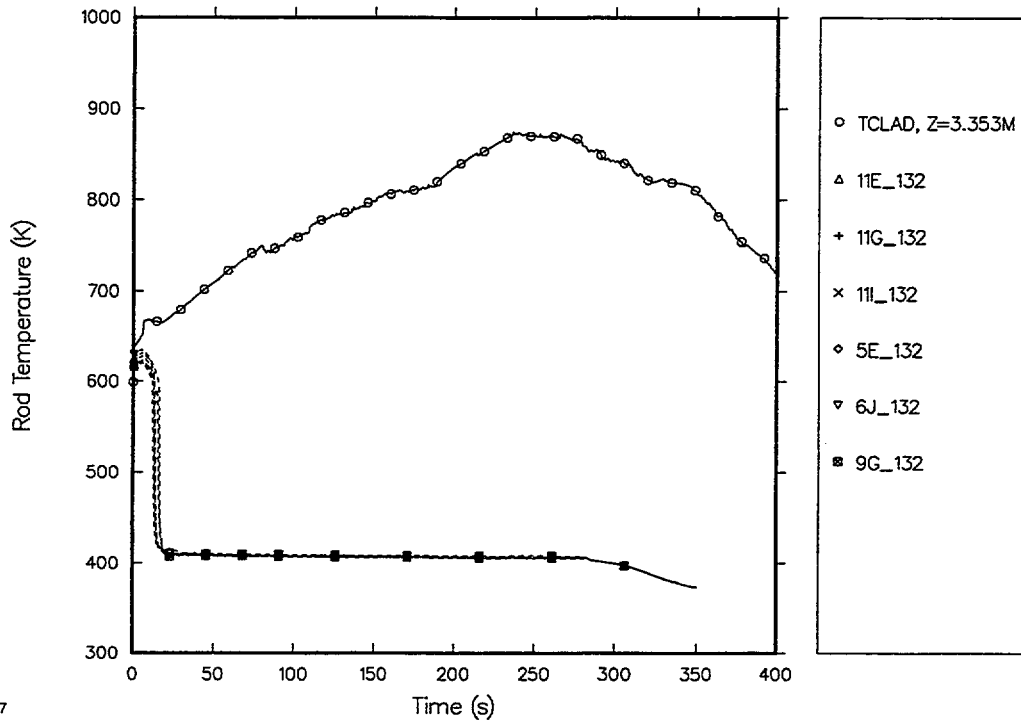
Fig. 4.9-14.   Comparison of predicted and measured heater-rod cladding temperatures at 3.3528-m elevation.
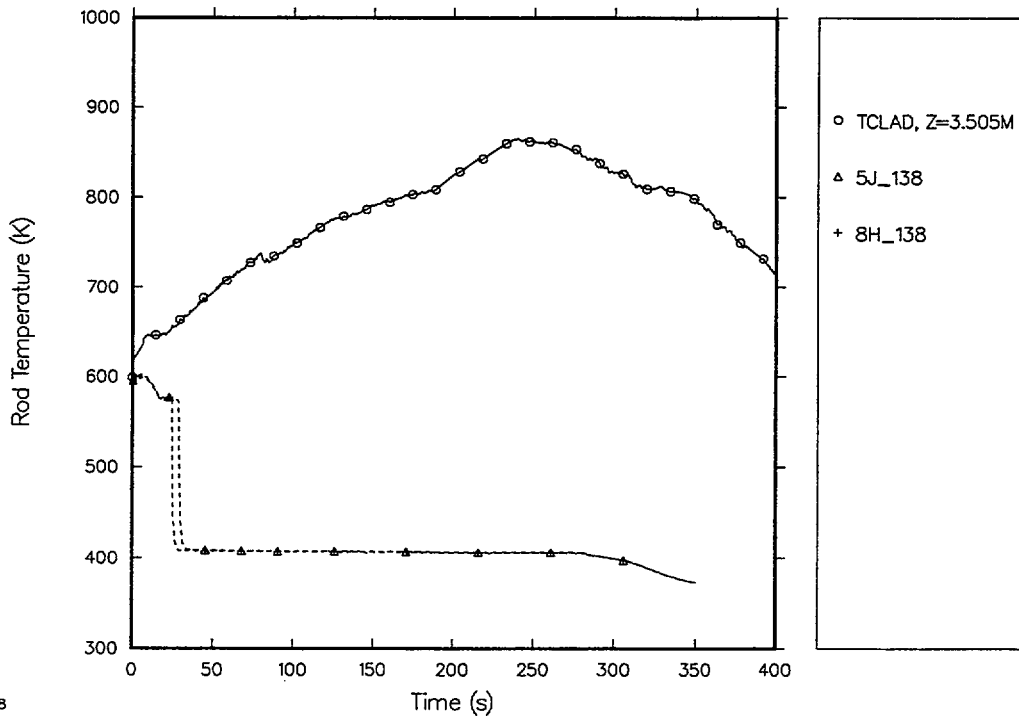


Fig. 4.9-15.   Comparison of predicted and measured heater-rod cladding temperatures at 3.5052-m elevation.
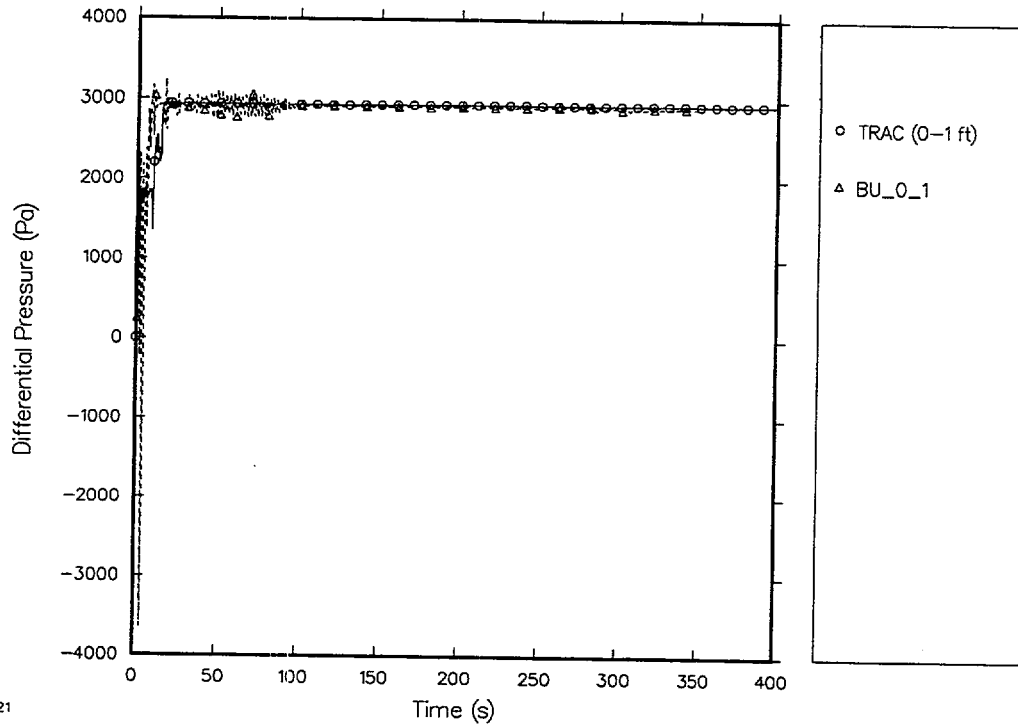
Fig. 4.9-16.   Comparison of predicted and measured differential pressures (0–1 ft).
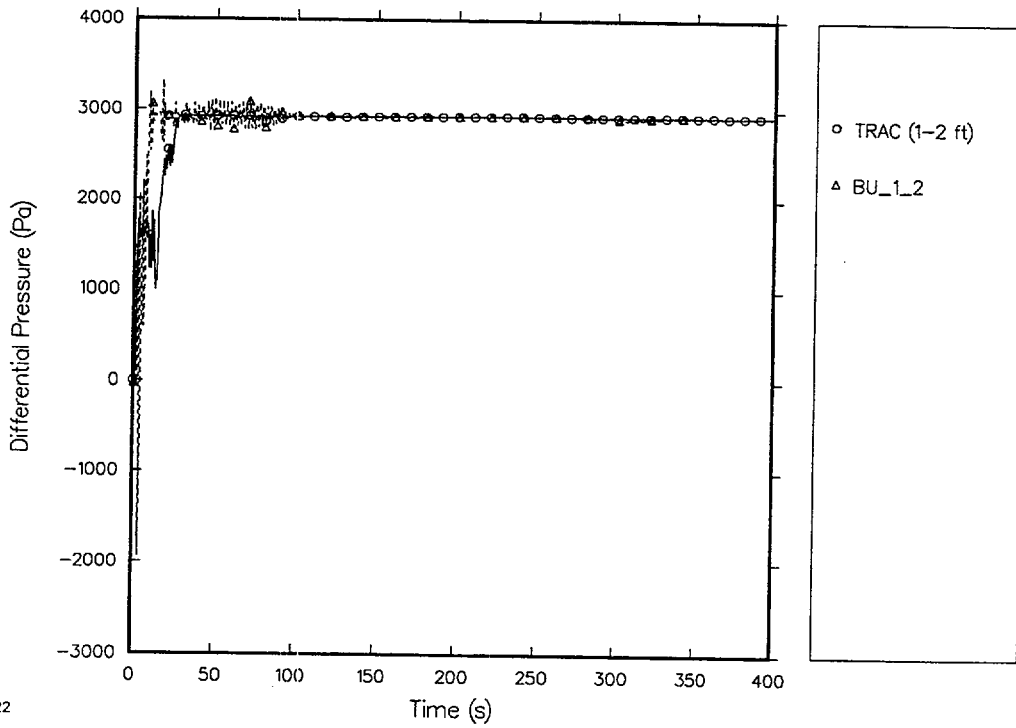


Fig. 4.9-17.   Comparison of predicted and measured differential pressures (1–2 ft).
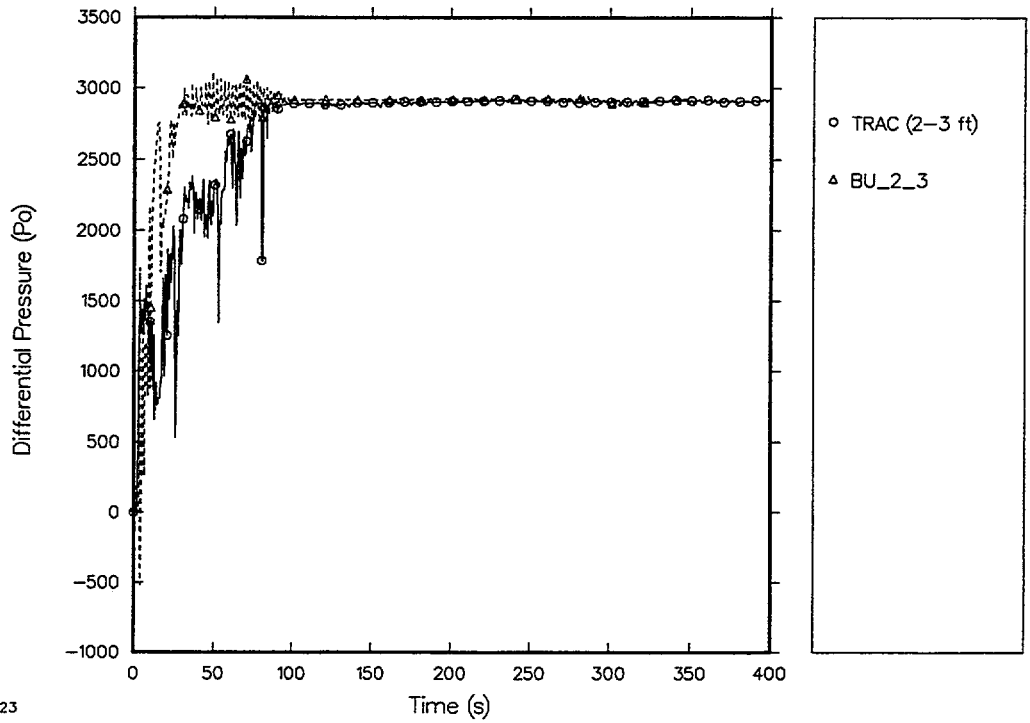
Fig. 4.9-18. Comparison of predicted and measured differential pressures (2–3 ft).
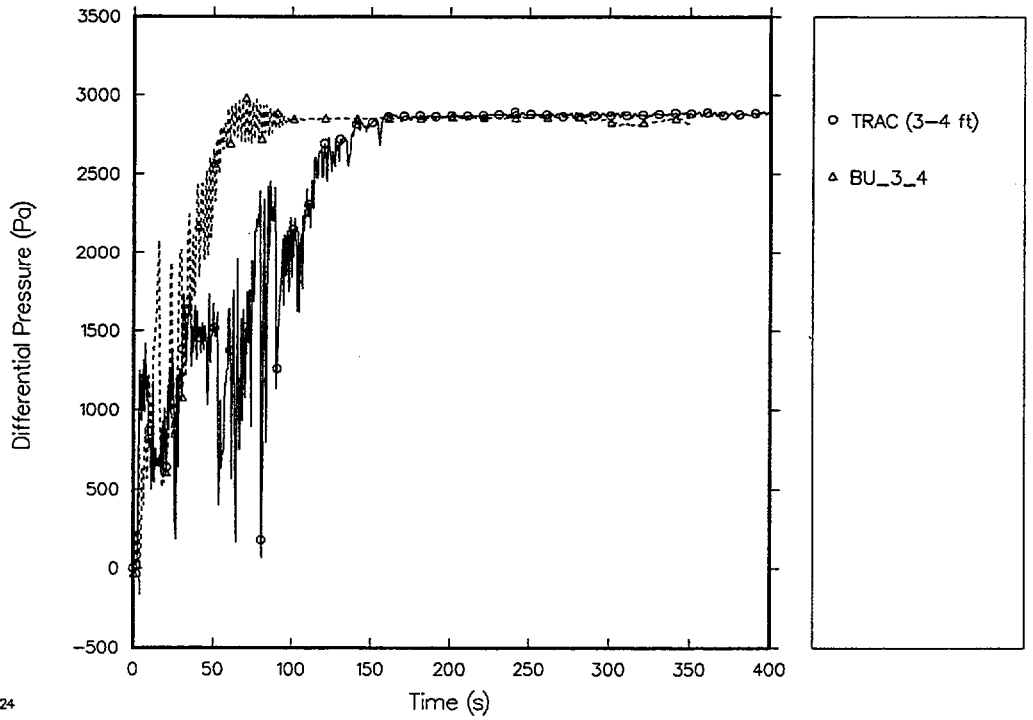


Fig. 4.9-19.   Comparison of predicted and measured differential pressures (3–4 ft).
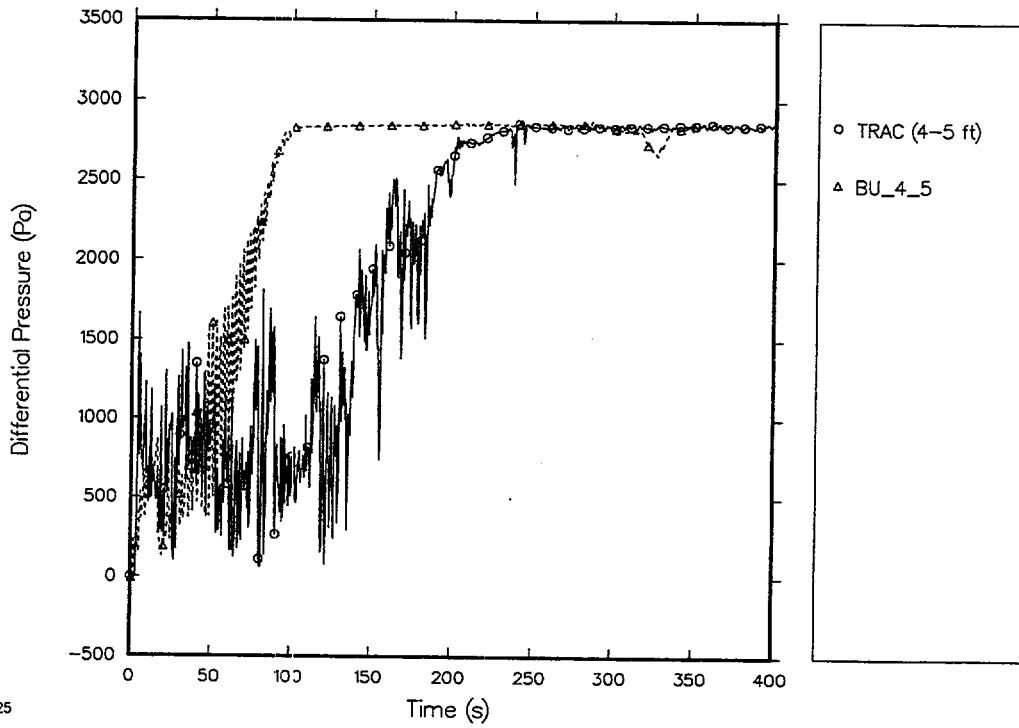
**Fig. 4.9-20.** Comparison of predicted and measured differential pressures (4–5 ft).
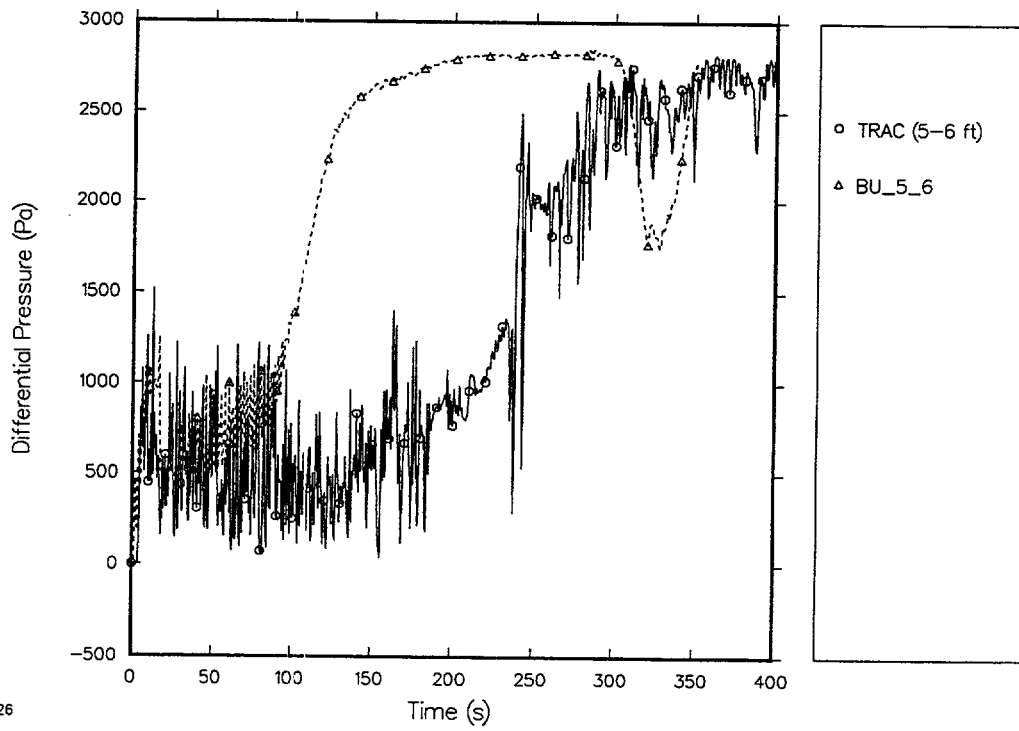


**Fig. 4.9-21.** Comparison of predicted and measured differential pressures (5–6 ft).
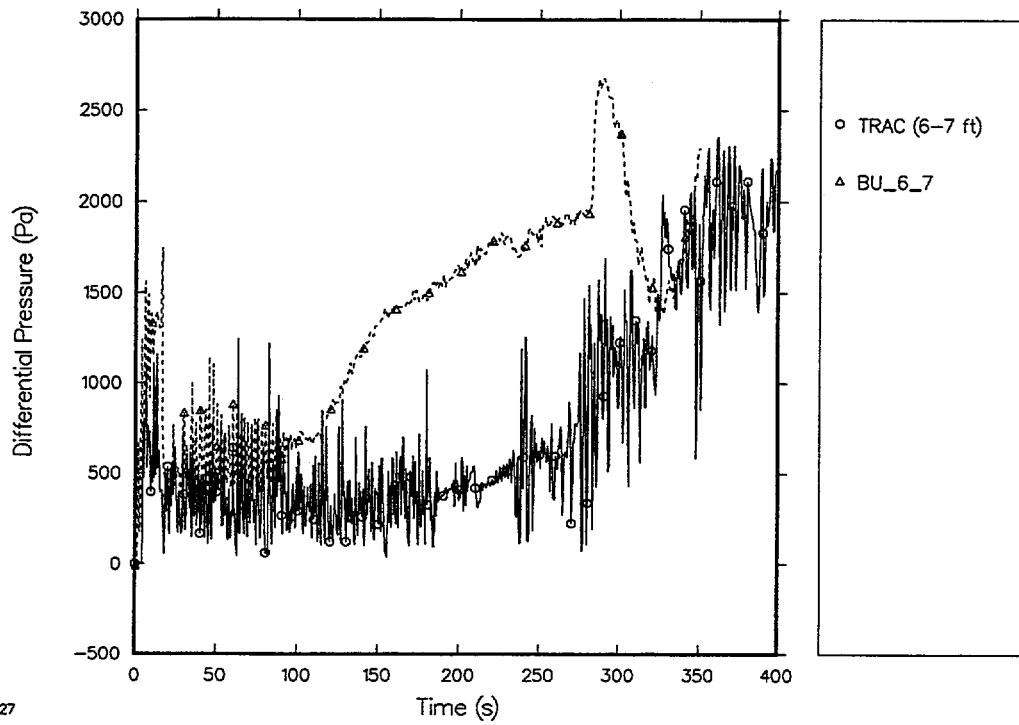
Fig. 4.9-22. Comparison of predicted and measured differential pressures (6–7 ft).
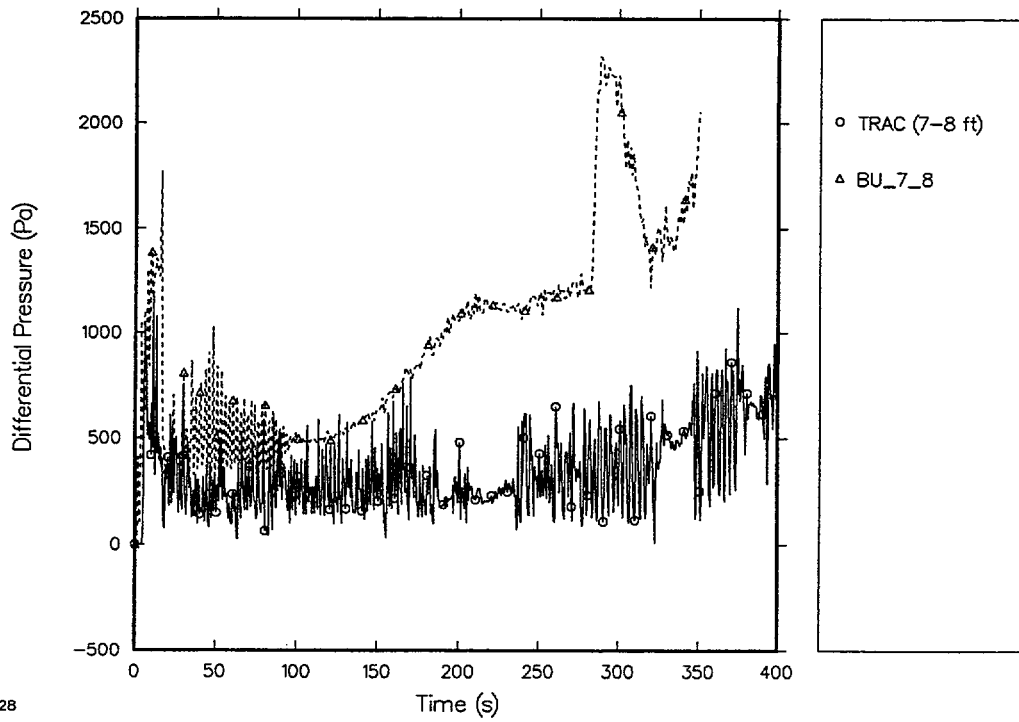


Fig. 4.9-23. Comparison of predicted and measured differential pressures (7–8 ft).
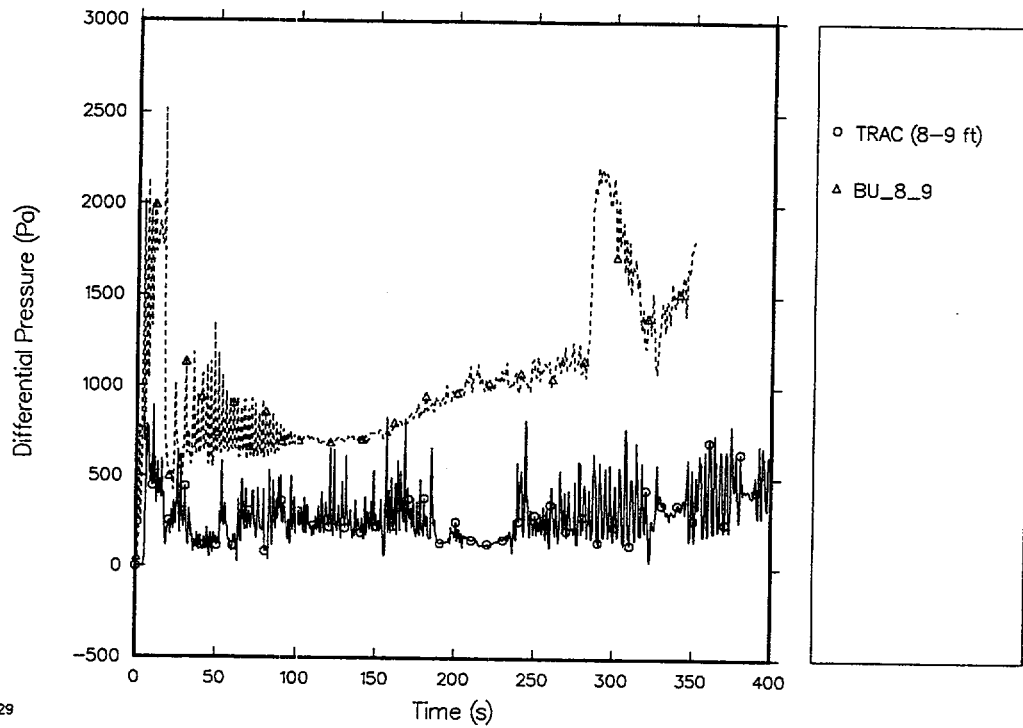
Fig. 4.9-24. Comparison of predicted and measured differential pressures (8–9ft).
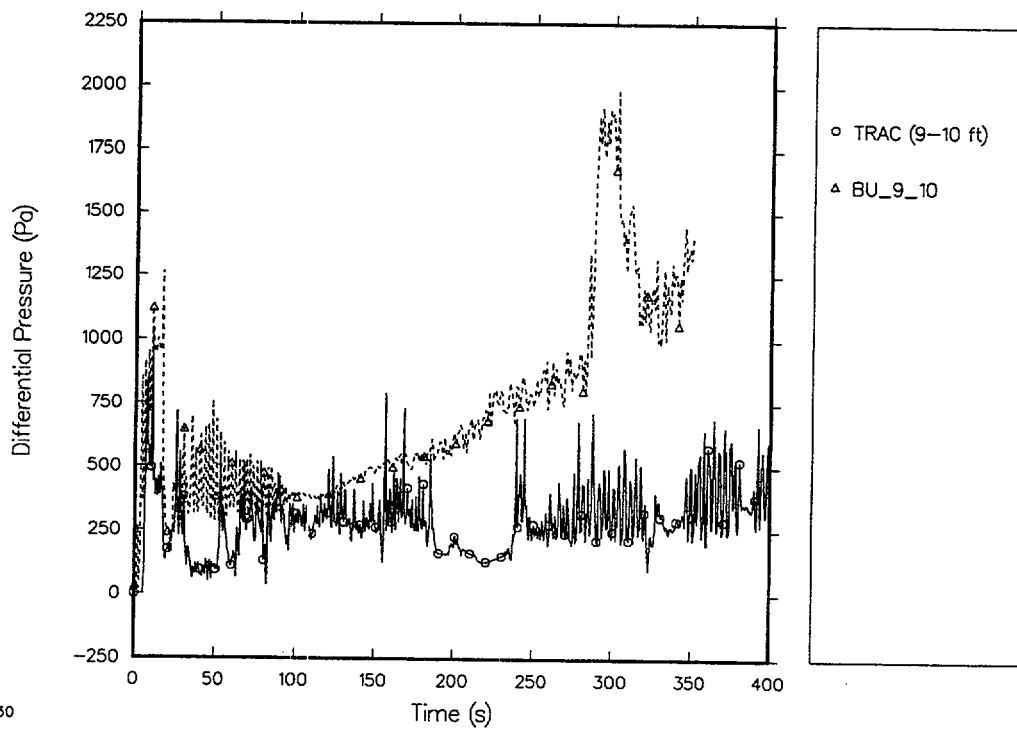


Fig. 4.9-25. Comparison of predicted and measured differential pressures (9–10 ft).
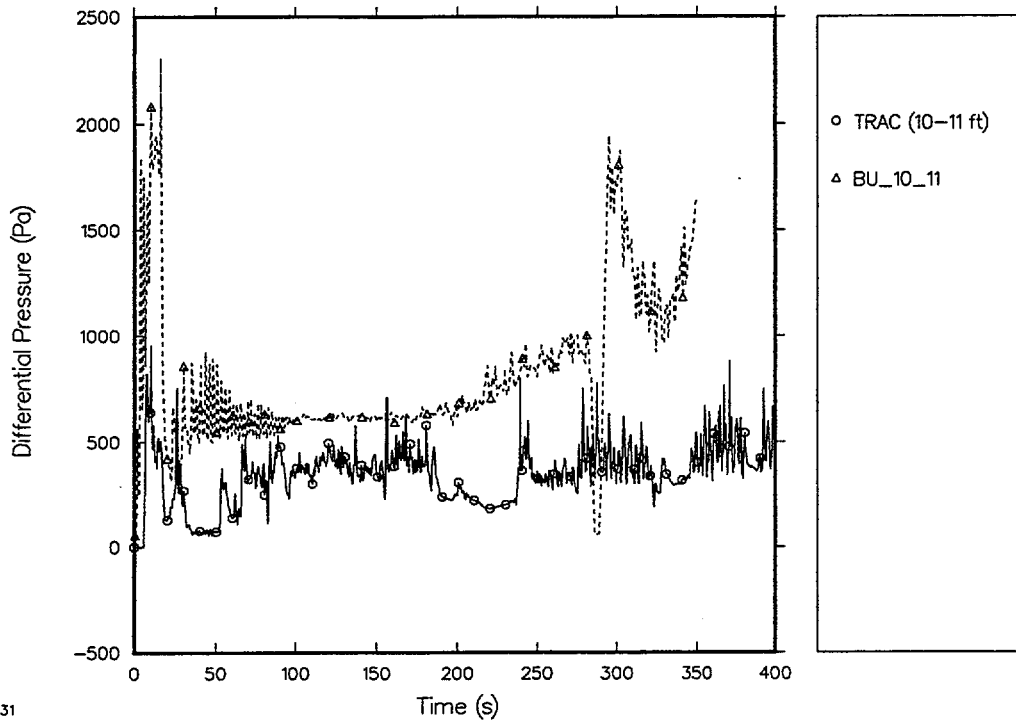
Fig. 4.9-26. Comparison of predicted and measured differential pressures (10–11 ft).
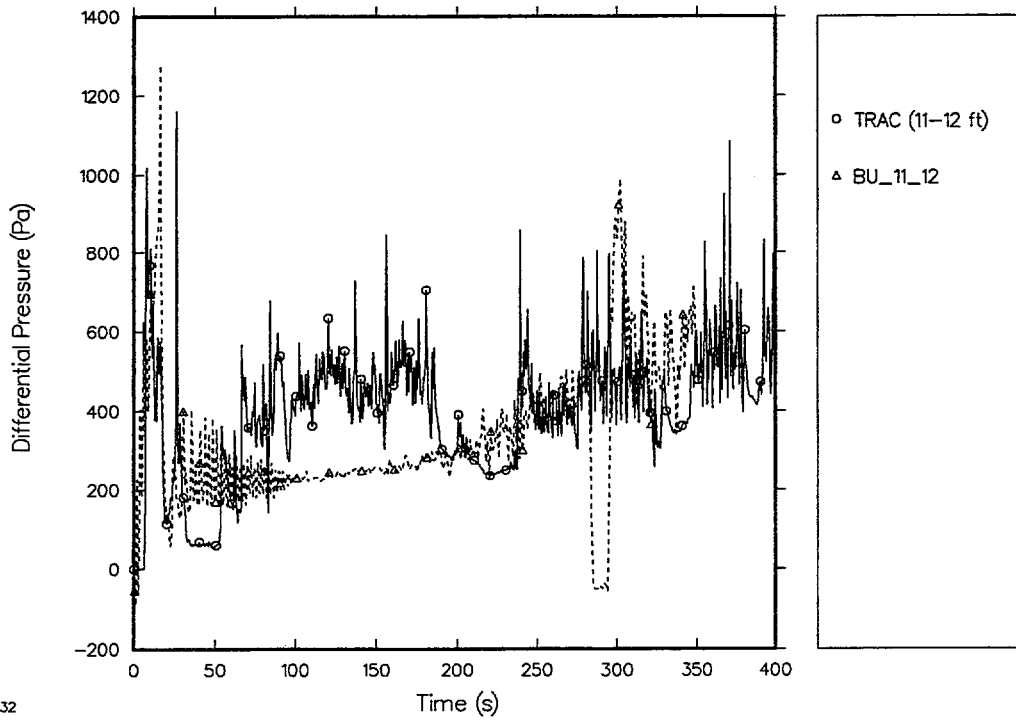


Fig. 4.9-27. Comparison of predicted and measured differential pressures (11–12 ft).
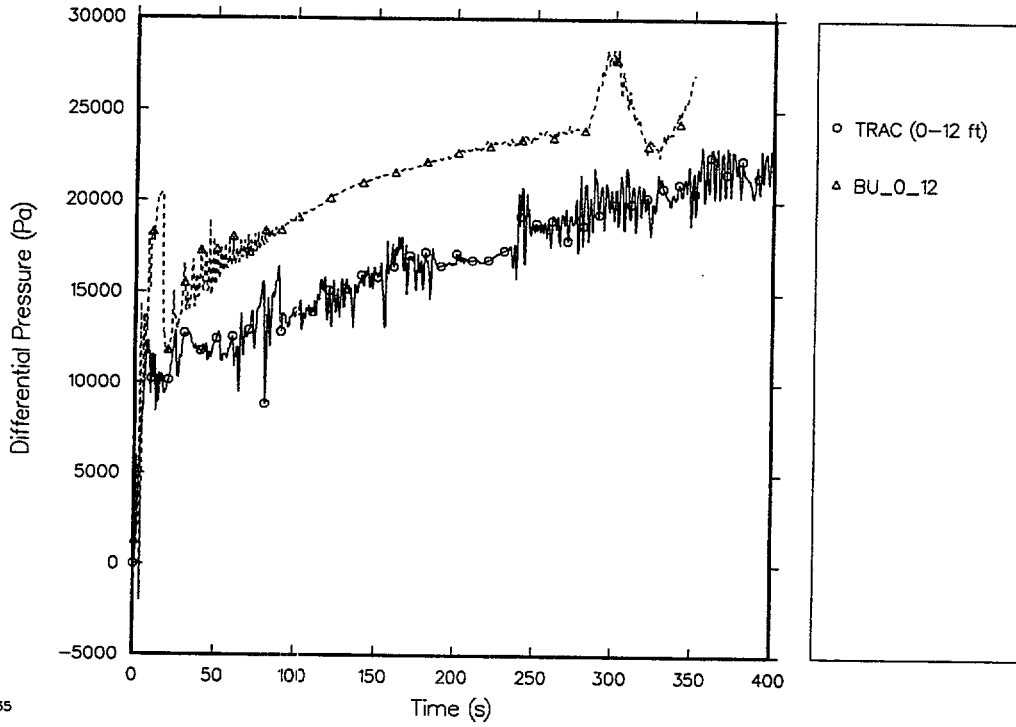
Fig. 4.9-28.    Comparison of predicted and measured total core differential pressures (0–12 ft).
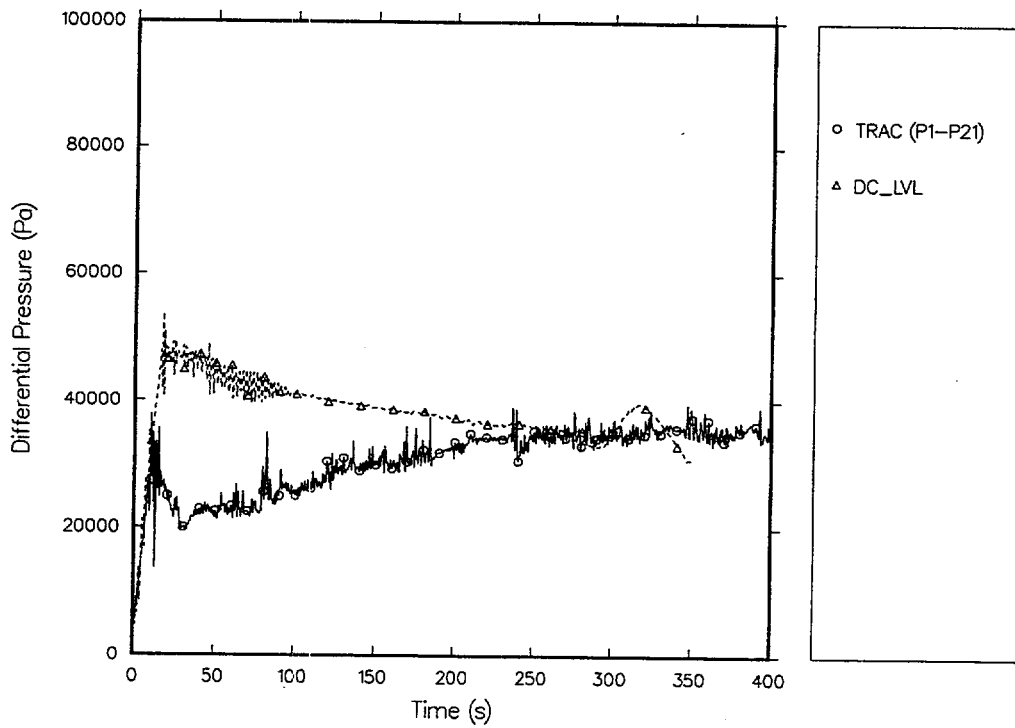


Fig. 4.9-29.    Comparison of predicted and measured downcomer differential pressures.

4.9-26
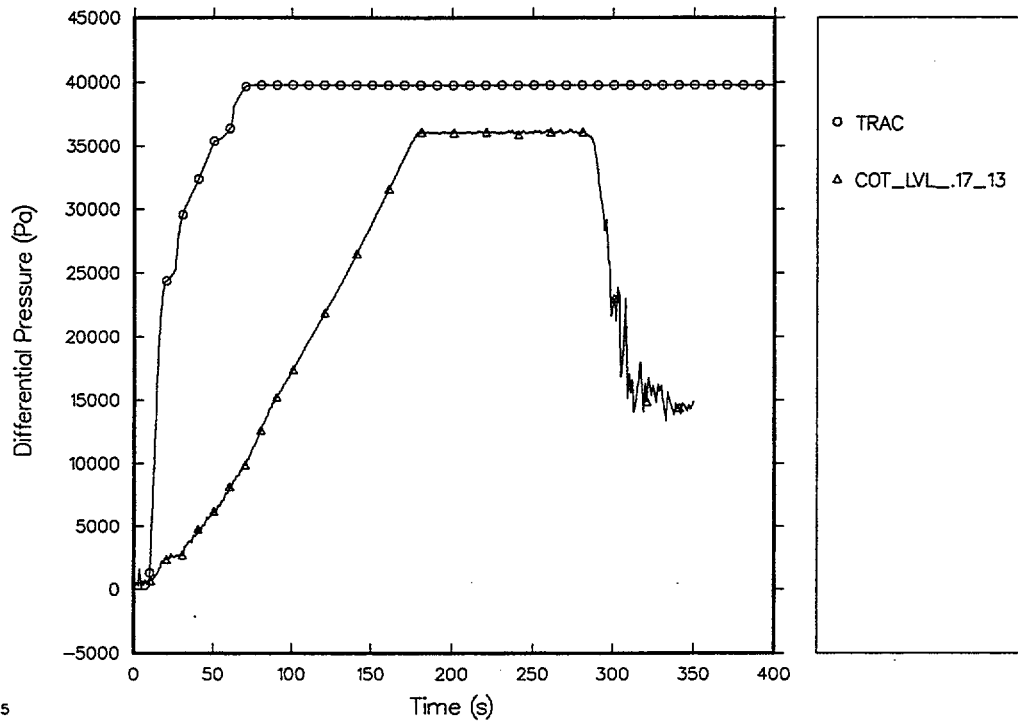
Fig. 4.9-30.  Comparison of predicted and measured carryover tank differential pressures (0–12 ft).

This space is intentionally left blank.
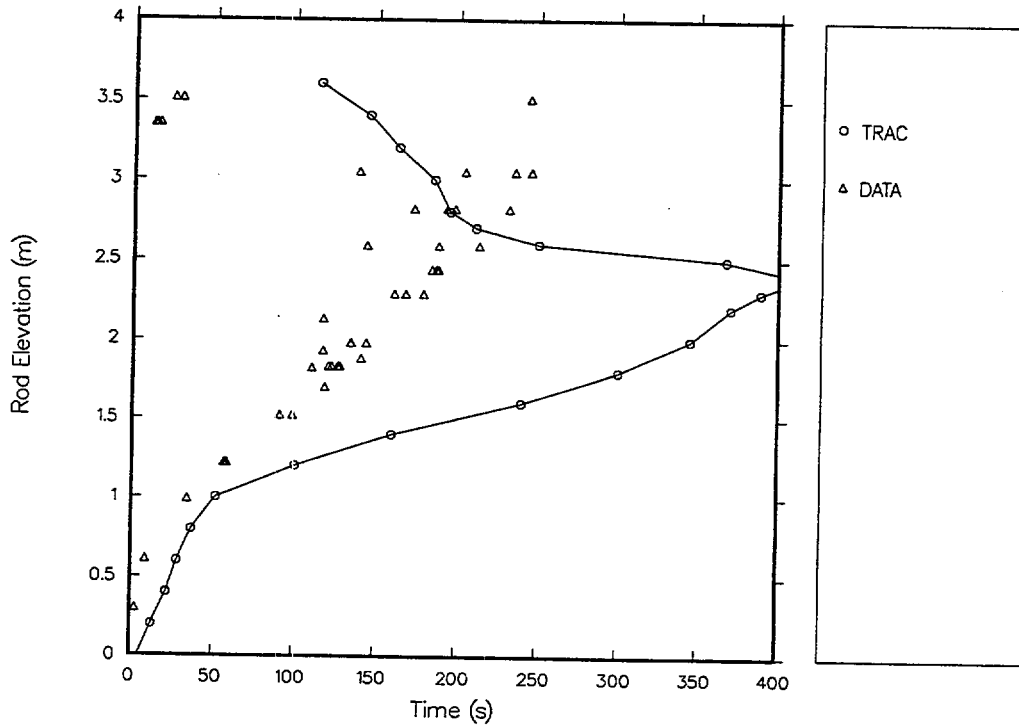
Fig. 4.9-31.    Comparison of predicted and measured cladding quench times (with grid-spacer model).
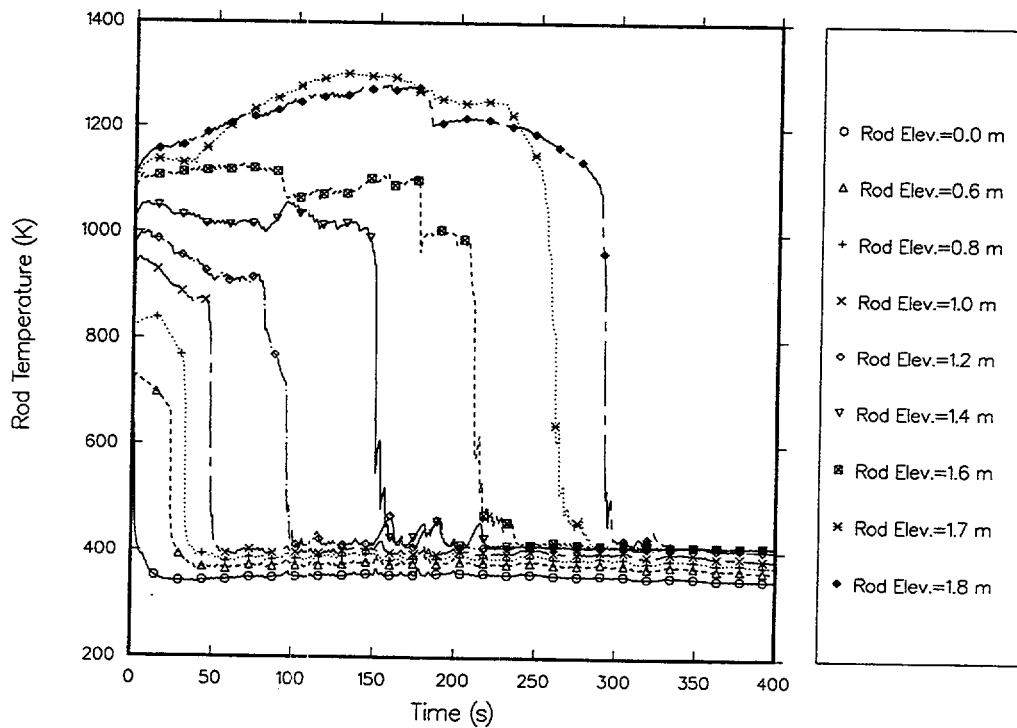


Fig. 4.9-32.    Predicted cladding temperature responses in lower half of core (with grid-spacer model).

4.9-28
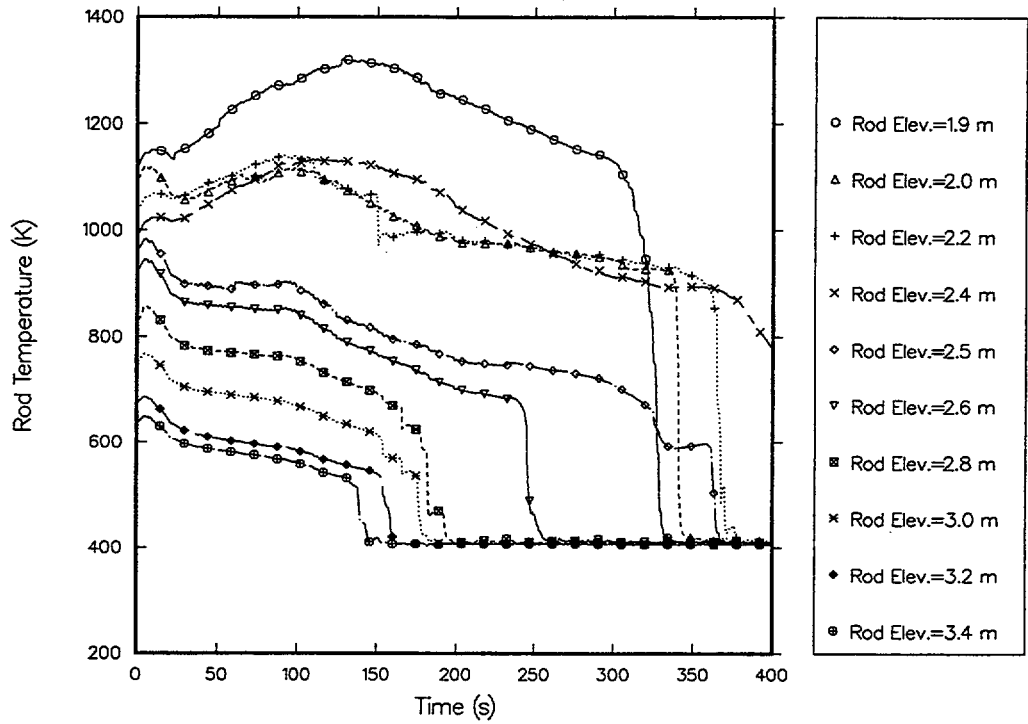
Fig. 4.9-33.   Predicted cladding temperature responses in upper half of core (with grid-spacer model).
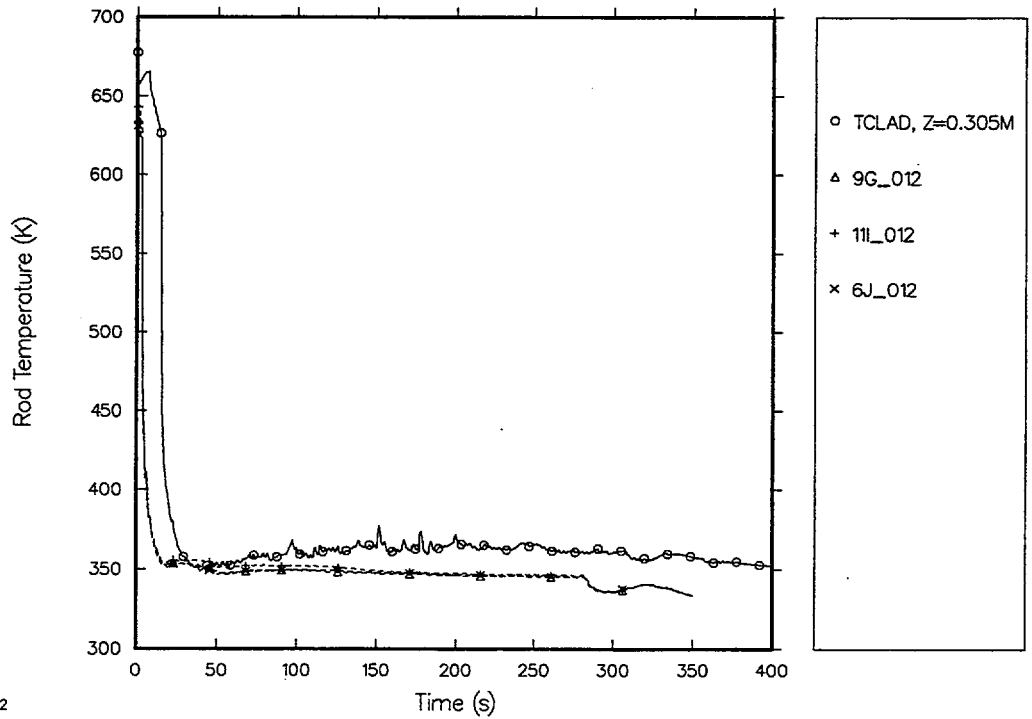


Fig. 4.9-34.   Comparison of predicted and measured heater-rod cladding temperatures at 0.3048-m elevation (with grid-spacer model).
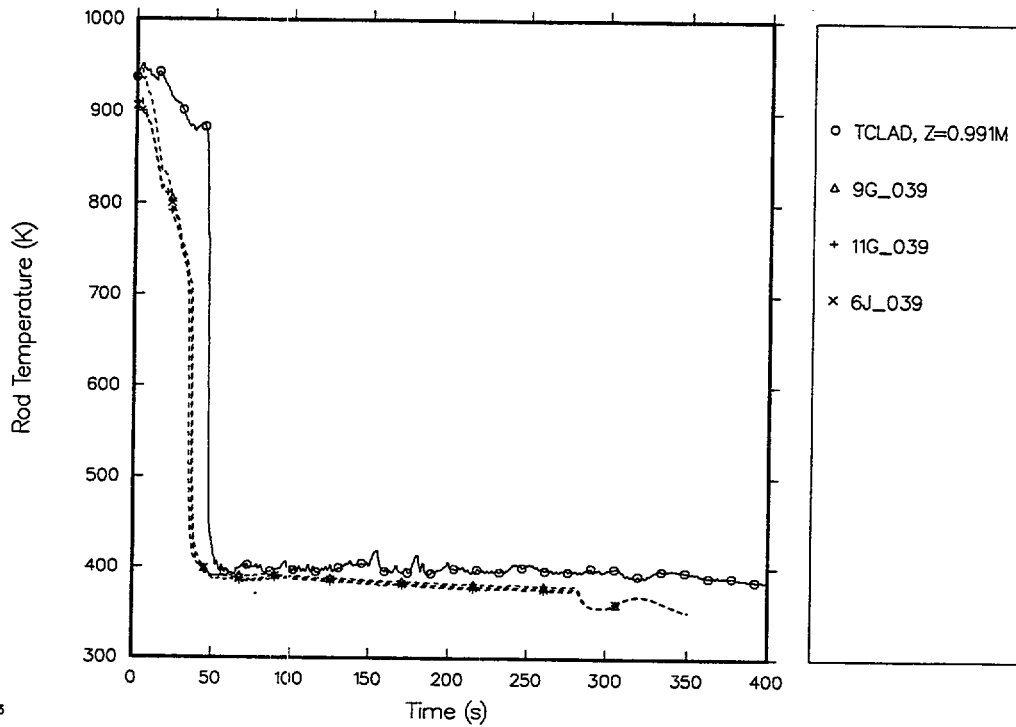
Fig. 4.9-35.   Comparison of predicted and measured heater-rod cladding temperatures at 0.9906-m elevation (with grid-spacer model).
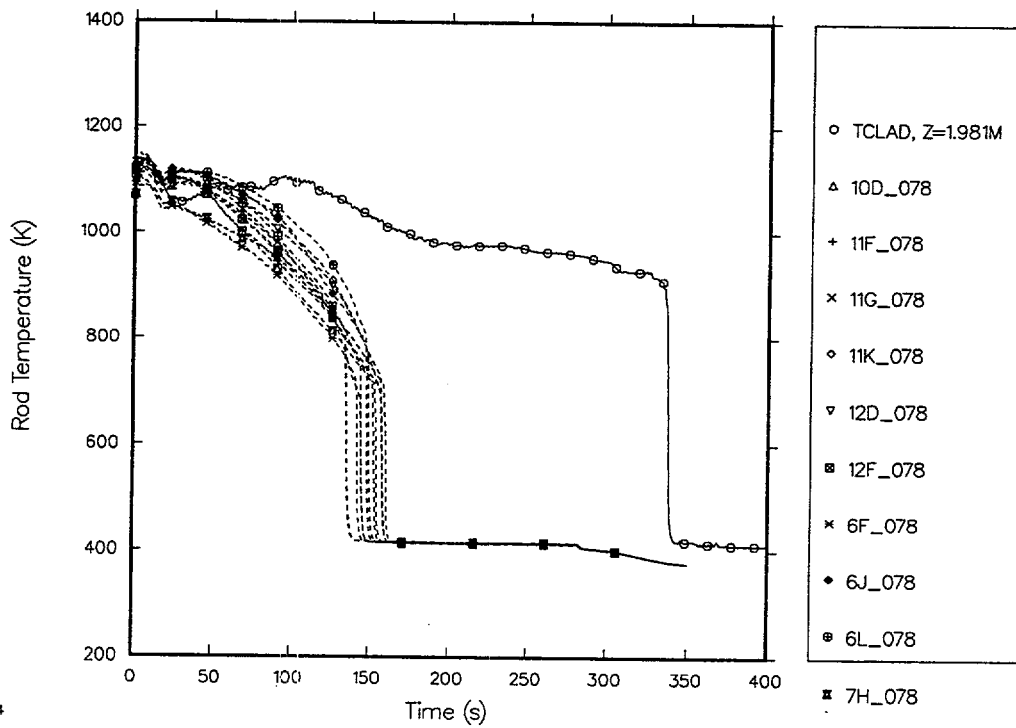


Fig. 4.9-36.   Comparison of predicted and measured heater-rod cladding temperatures at 1.9812-m elevation (with grid-spacer model).
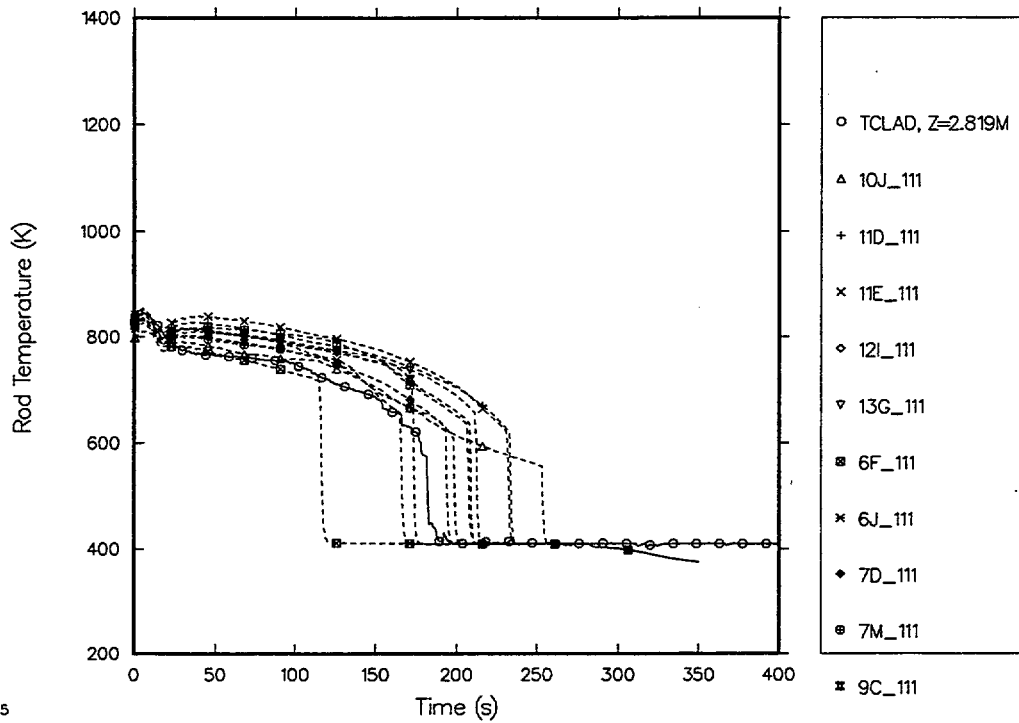
Fig. 4.9-37.  Comparison of predicted and measured heater-rod cladding temperatures at 2.8194-m elevation (with grid-spacer model).
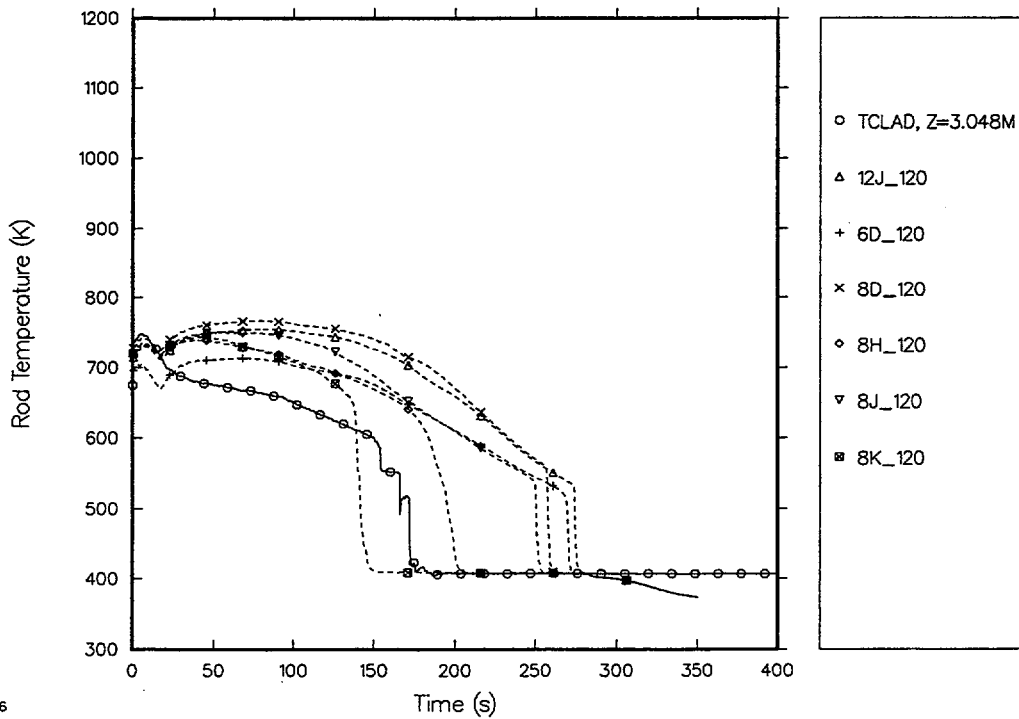


Fig. 4.9-38.  Comparison of predicted and measured heater-rod cladding temperatures at 3.0480-m elevation (with grid-spacer model).
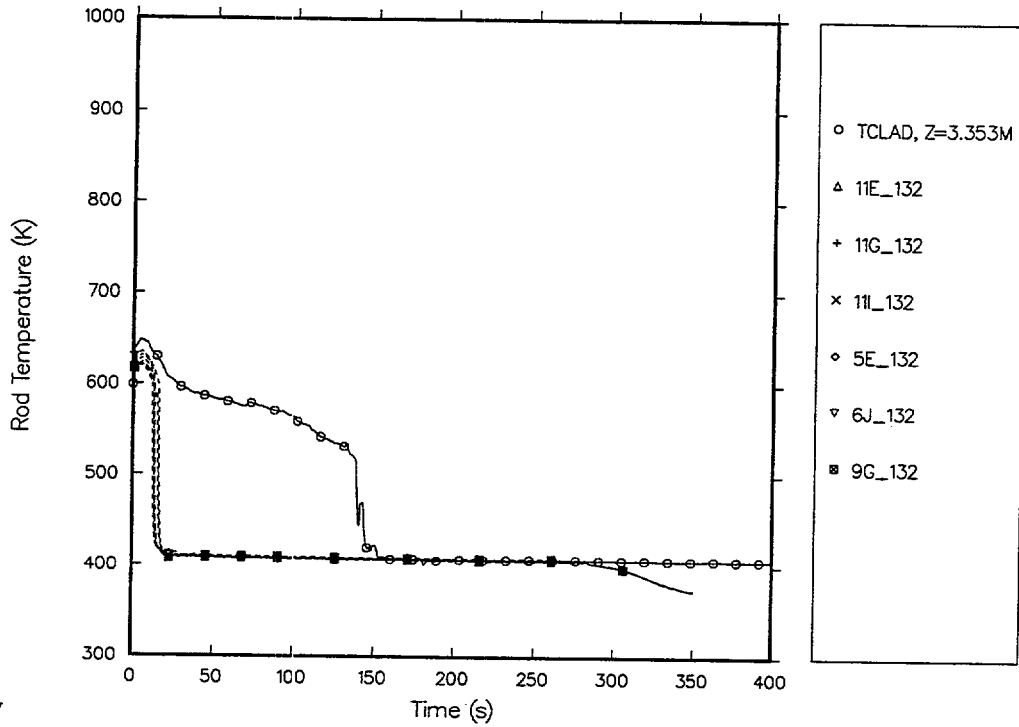
Fig. 4.9-39.   Comparison of predicted and measured heater-rod cladding temperatures at 3.3528-m elevation (with grid-spacer model).
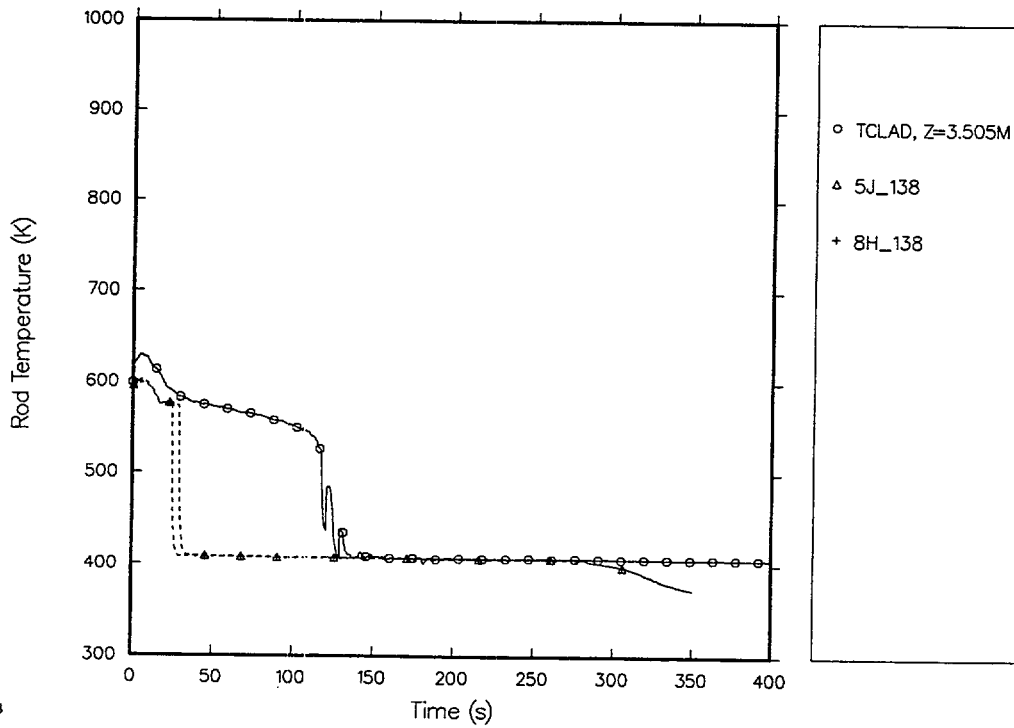


Fig. 4.9-40.   Comparison of predicted and measured heater-rod cladding temperatures at 3.5052-m elevation (with grid-spacer model).
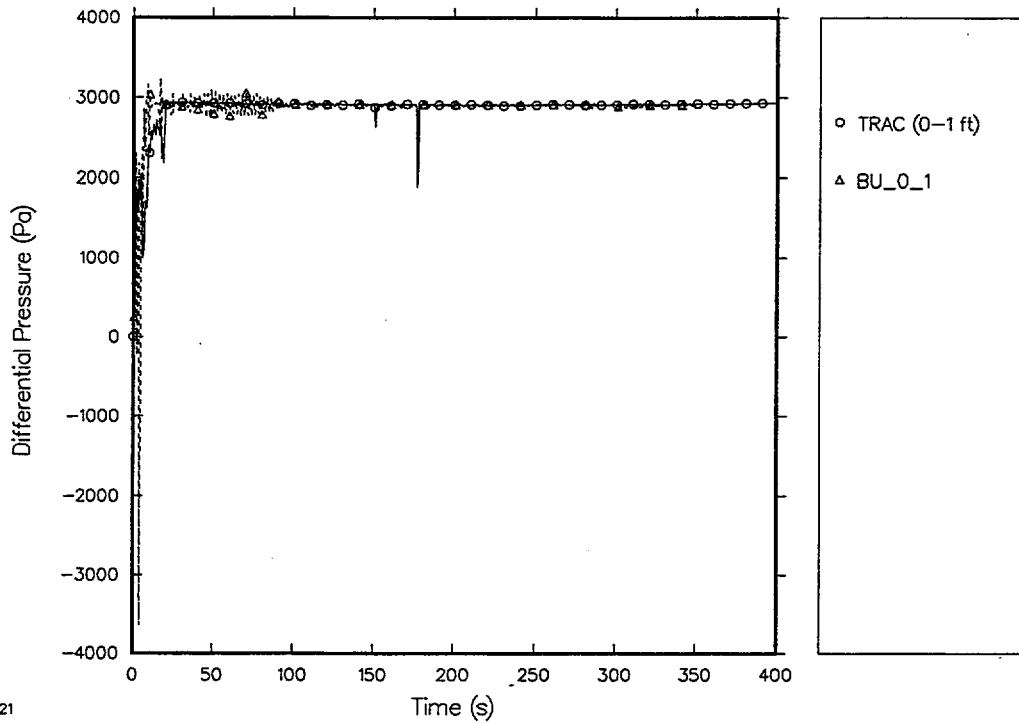
Fig. 4.9-41. Comparison of predicted and measured differential pressures (0–1 ft, with grid-spacer model).
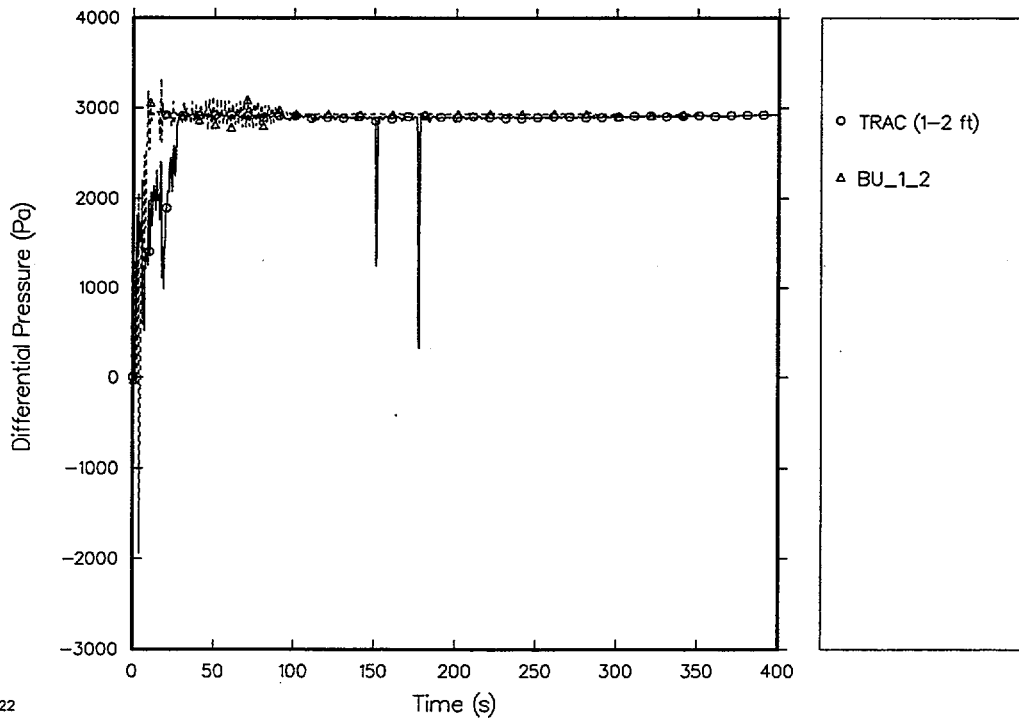


Fig. 4.9-42. Comparison of predicted and measured differential pressures (1–2 ft, with grid-spacer model).
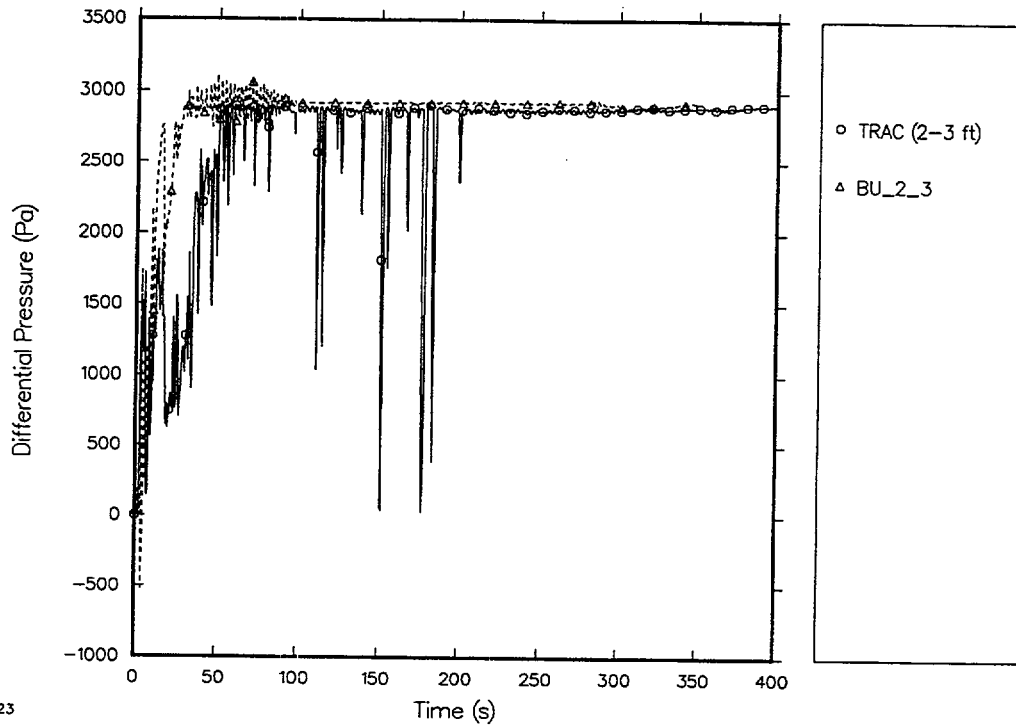
Fig. 4.9-43.  Comparison of predicted and measured differential pressures (2–3 ft, with grid-spacer model).
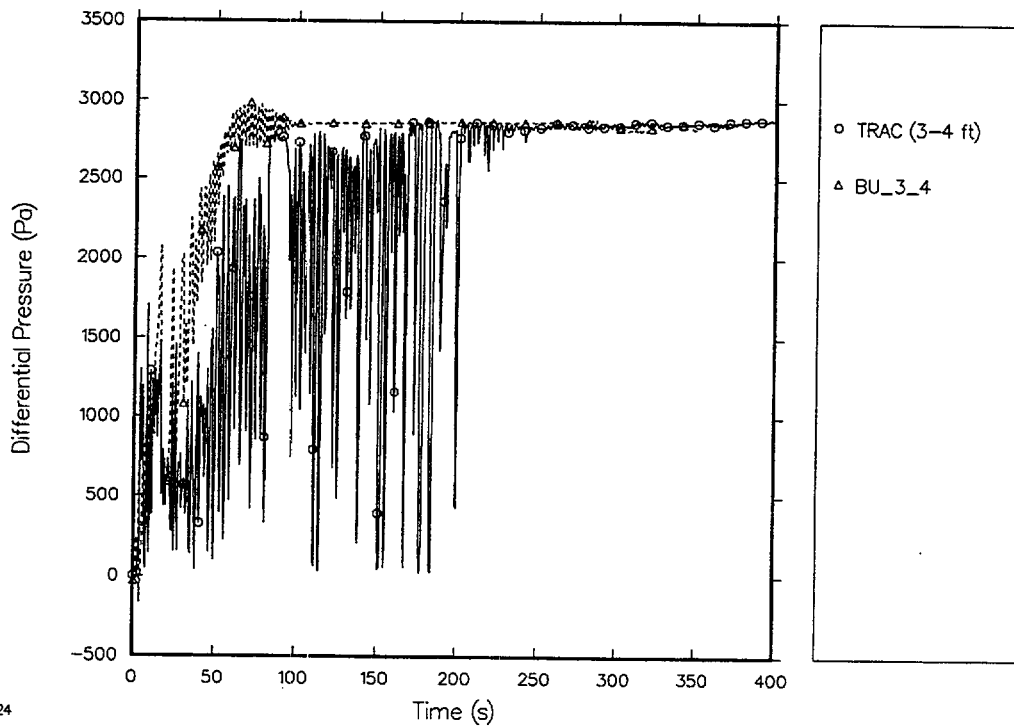


Fig. 4.9-44.  Comparison of predicted and measured differential pressures (3–4 ft, with grid-spacer model).
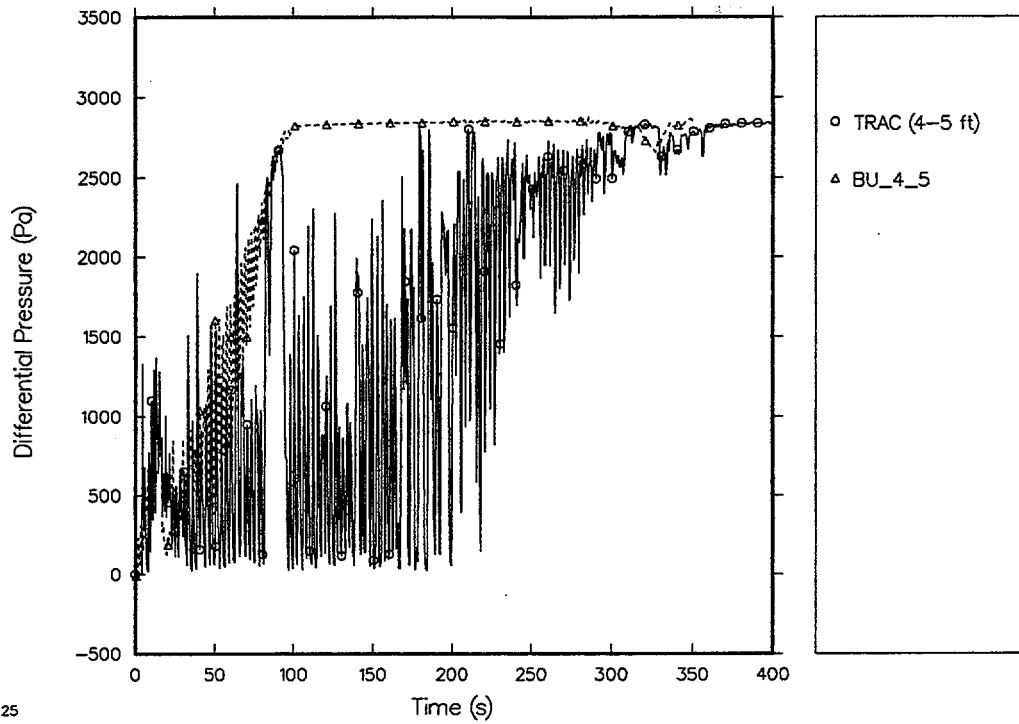
Fig. 4.9-45.   Comparison of predicted and measured differential pressures (4-5 ft, with grid-spacer model).
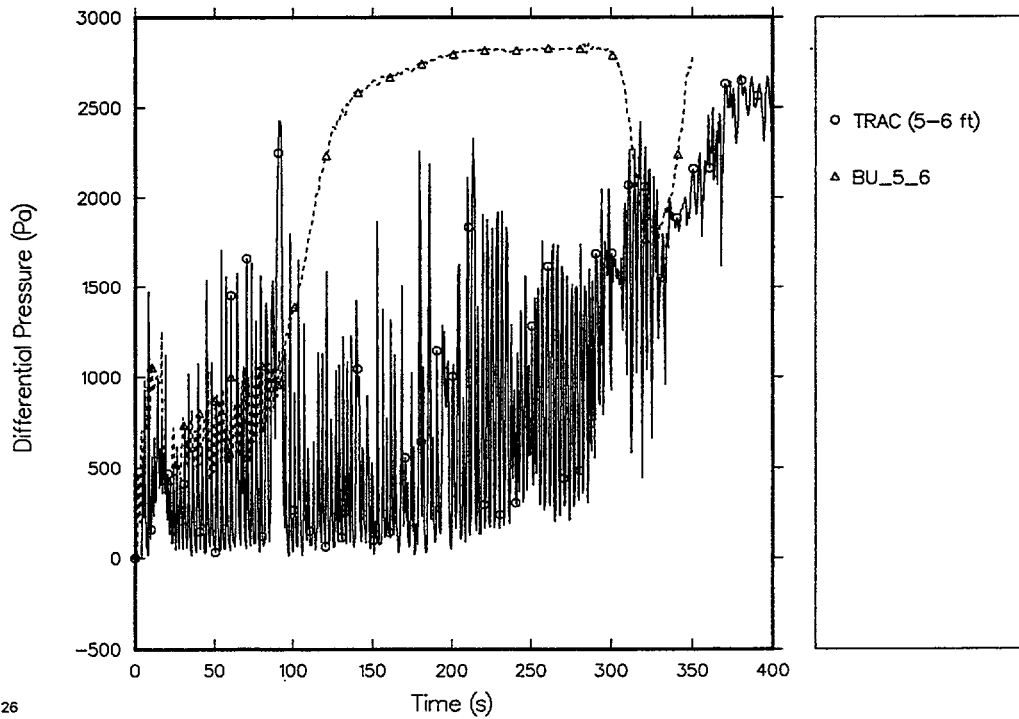


Fig. 4.9-46.   Comparison of predicted and measured differential pressures (5–6 ft, with grid-spacer model).
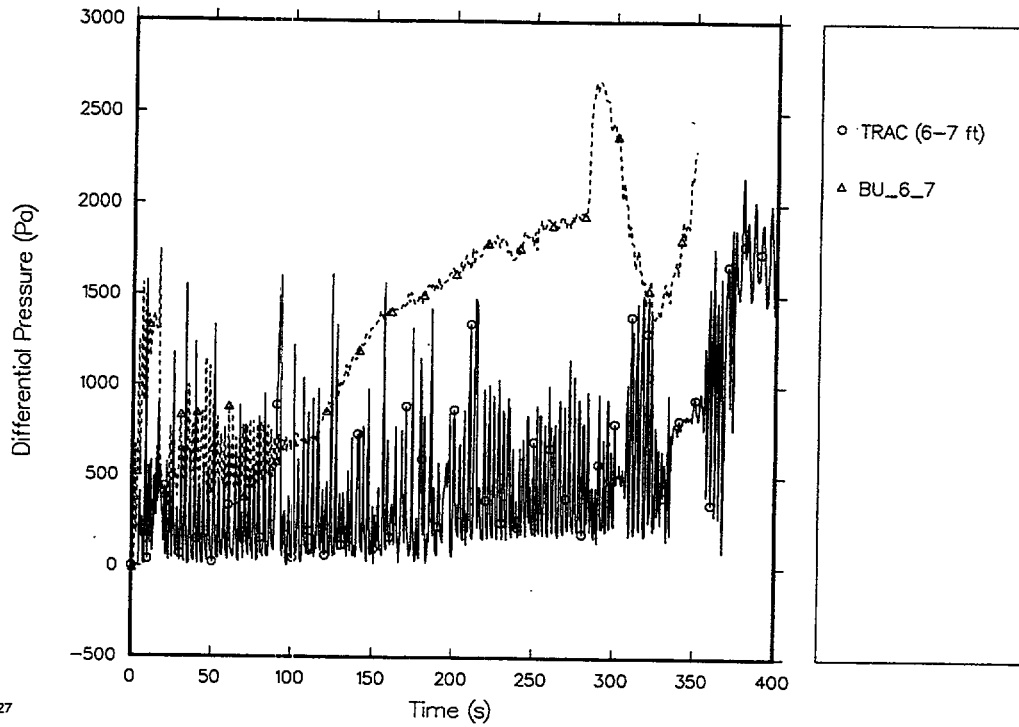
Fig. 4.9-47.   Comparison of predicted and measured differential pressures (6–7 ft, with grid-spacer model).
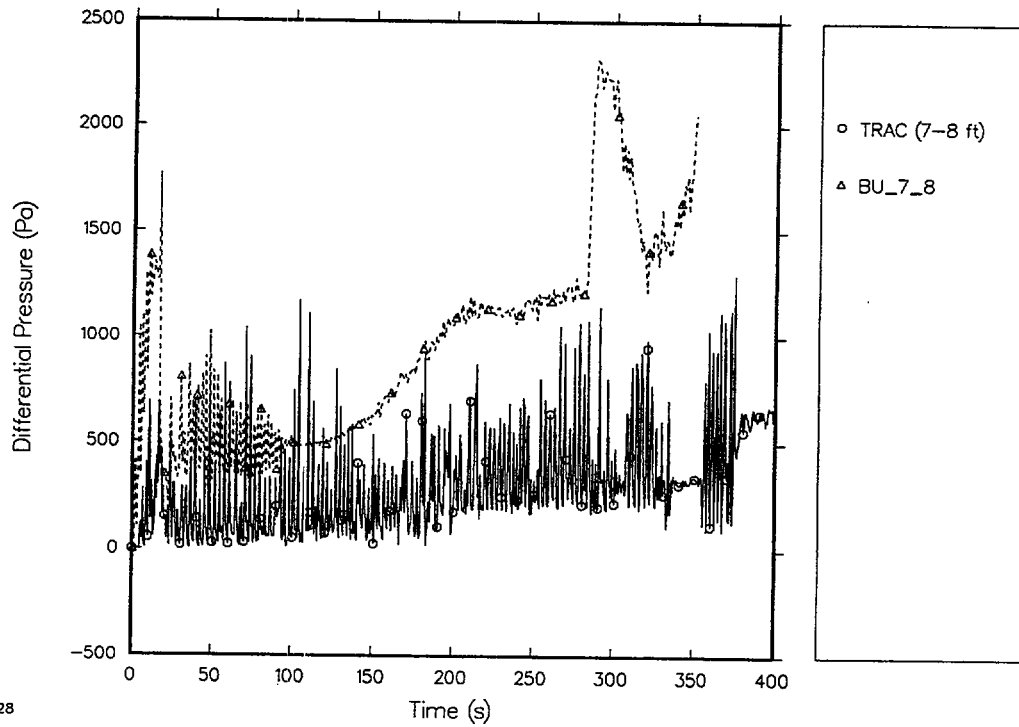


Fig. 4.9-48.   Comparison of predicted and measured differential pressures (7–8 ft, with grid-spacer model).
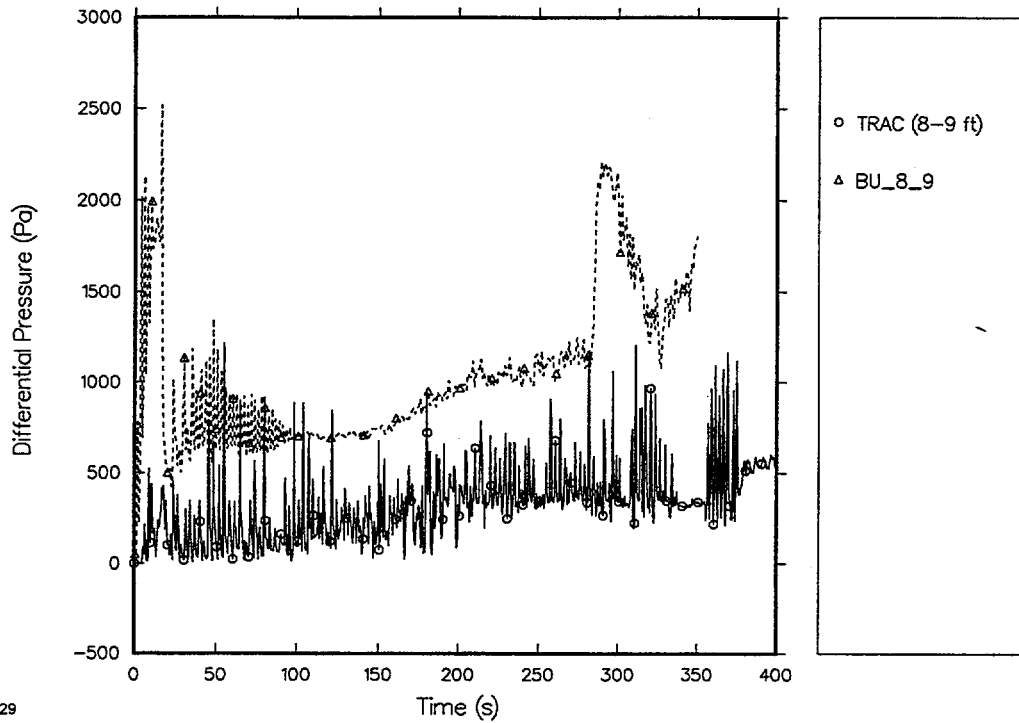
Fig. 4.9-49.  Comparison of predicted and measured differential pressures (8–9ft, with grid-spacer model).
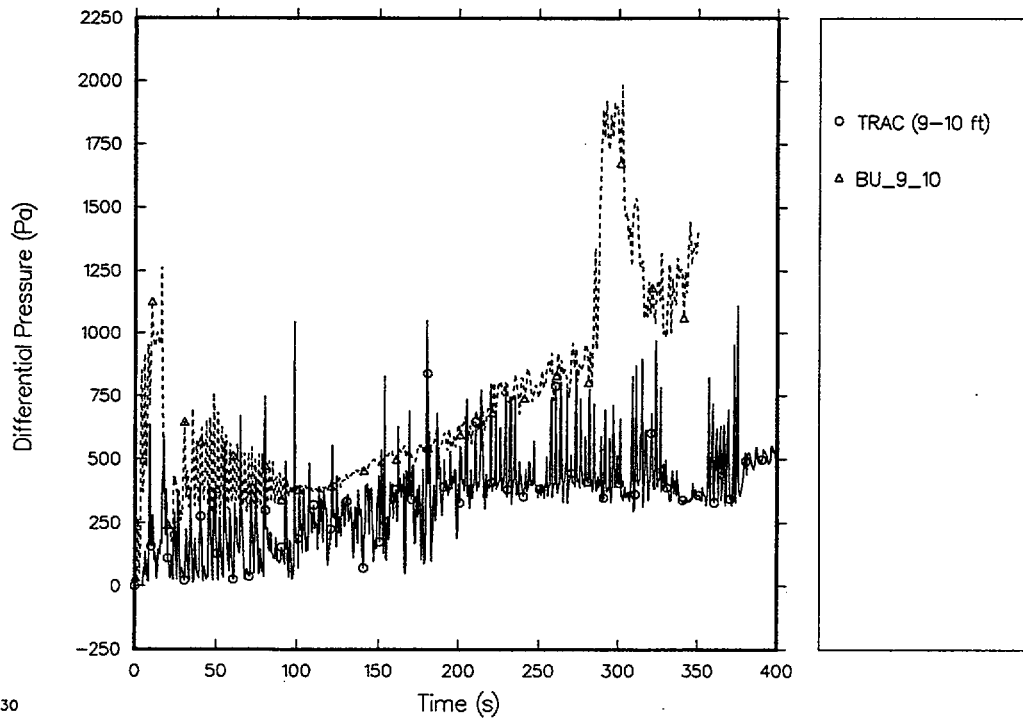


Fig. 4.9-50.  Comparison of predicted and measured differential pressures (9–10 ft, with grid-spacer model).
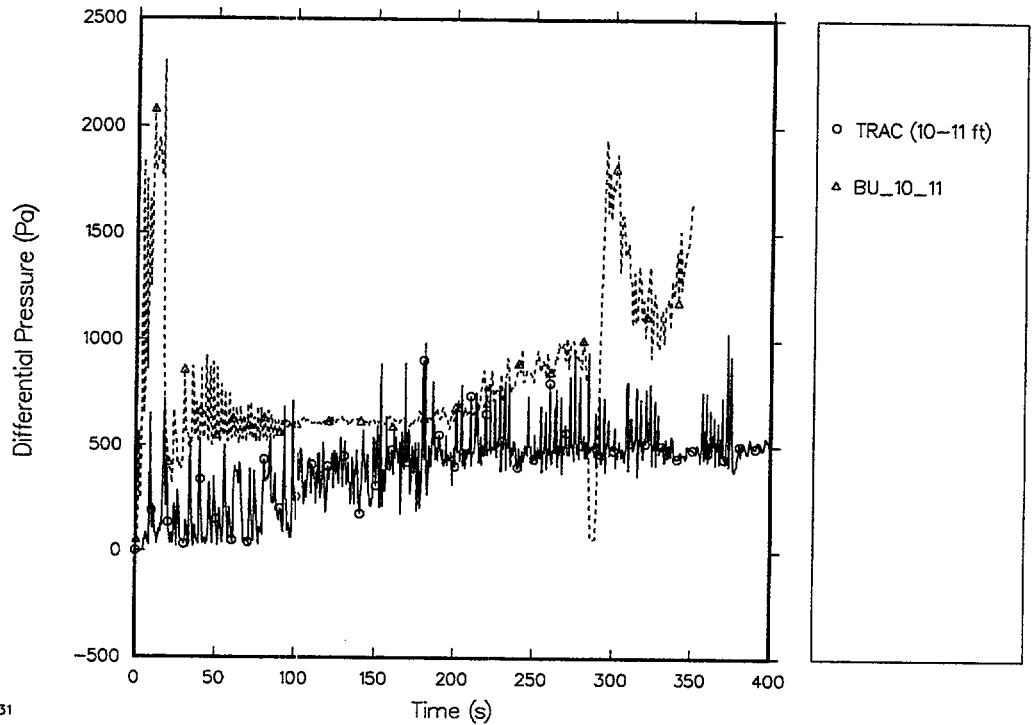
Fig. 4.9-51. Comparison of predicted and measured differential pressures (10–11 ft, with grid-spacer model).
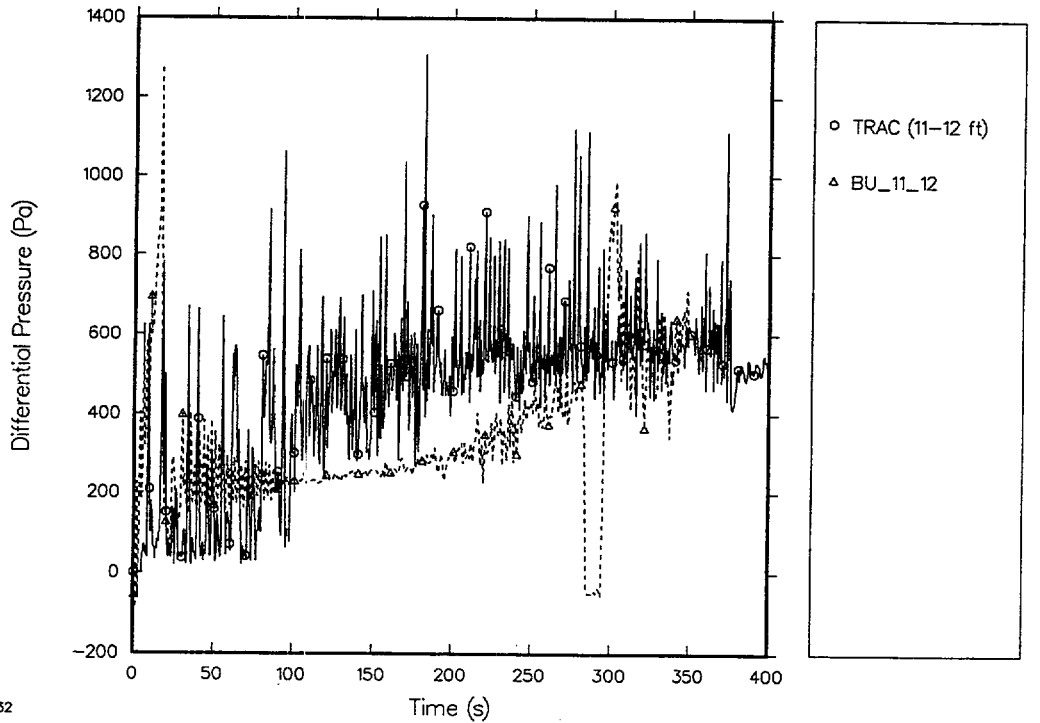


Fig. 4.9-52. Comparison of predicted and measured differential pressures (11–12 ft, with grid-spacer model).
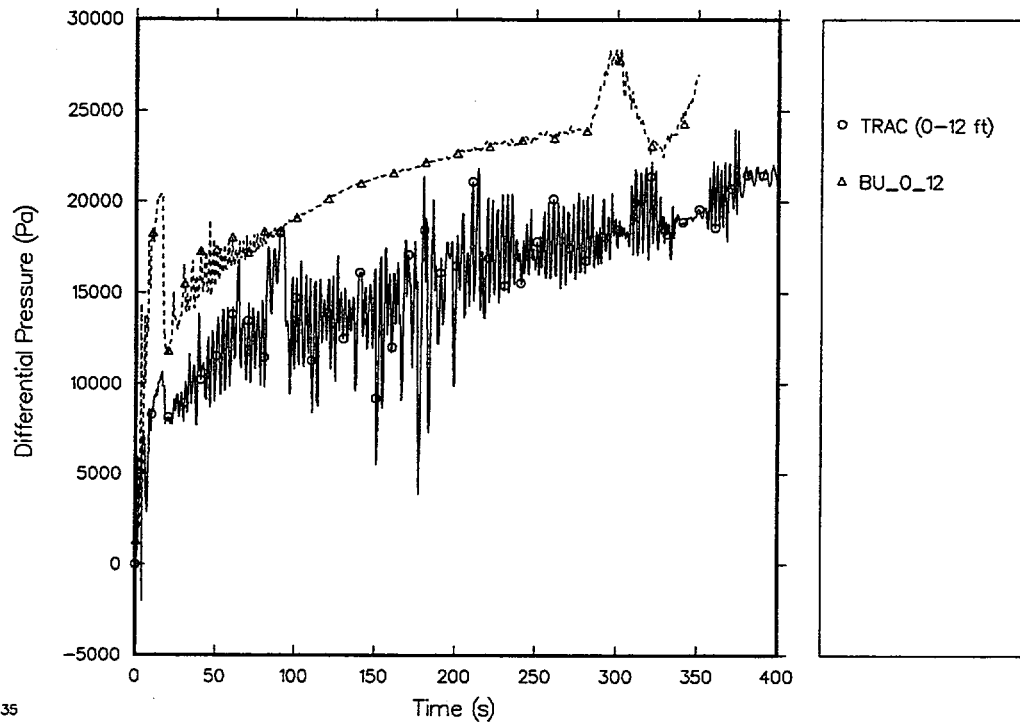
Fig. 4.9-53.  Comparison of predicted and measured total core differential pressures (0–12 ft, with grid-spacer model).
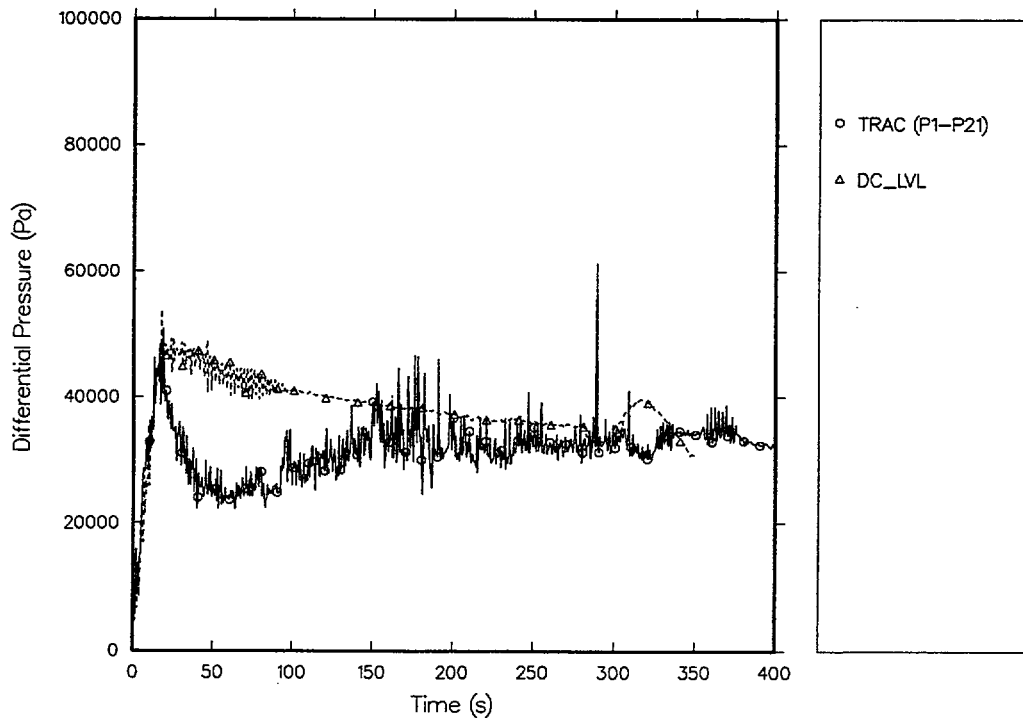


Fig. 4.9-54.  Comparison of predicted and measured downcomer differential pressures (with grid-spacer model).

4.9-39
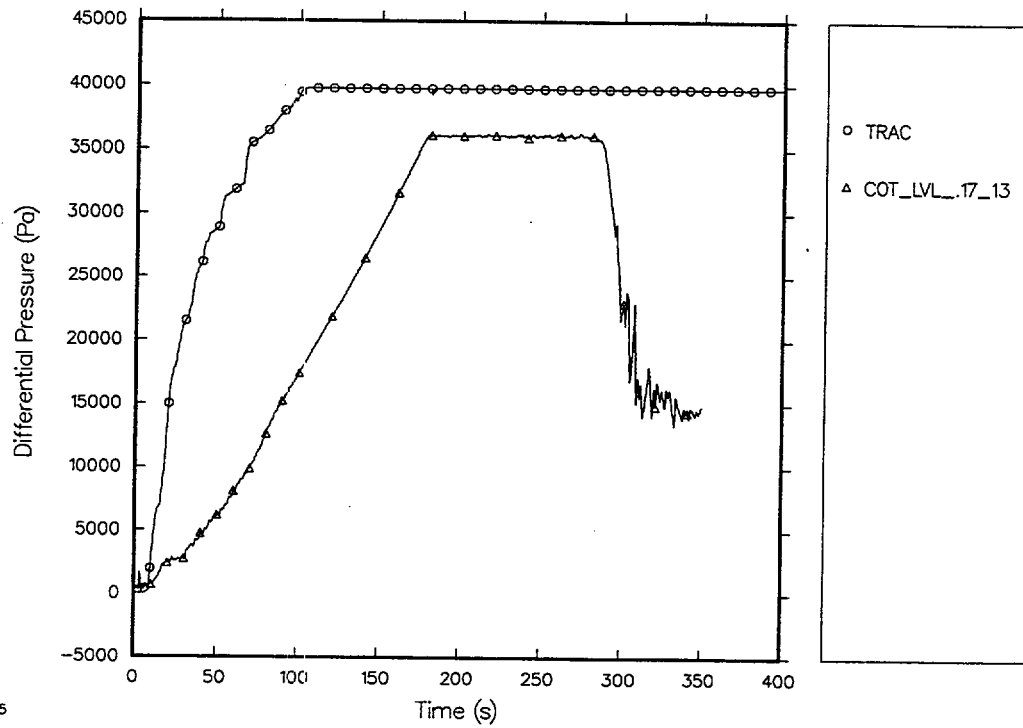
Fig. 4.9-55.  Comparison of predicted and measured carryover tank differential pressures (with grid-spacer model).

# 5. INTEGRAL EFFECT TESTS

## 5.1. LOFT Test L2-6

The Loss-of-Fluid Test (LOFT) facility was designed, constructed, and operated at the Idaho National Engineering Laboratory under the sponsorship of the Nuclear Regulatory Commission (NRC). The LOFT contained a nuclear core and was designed to simulate the major components and system responses of a commercial PWR during LOCAs and during anticipated transients caused by abnormal PWR operations. A number of experimental series were run in the LOFT, including nonnuclear LB experiments; nuclear LB, intermediate-break (IB), and SBLOCA experiments; nuclear anticipated transient experiments; and nuclear anticipated transients with multiple failures. The LOFT test used in this assessment, L2-6, simulated a 200% cold-leg break combined with a loss-of-offsite power (LOSP) at the start of the test.

### 5.1.1. Test Facility Description

The LOFT facility was a fully operational PWR with instrumentation to measure and provide data on the thermal-hydraulic conditions throughout the system. The facility was configured to represent a 1/60-scale-by-power (1/44 by volume) model of a typical 3000-MW(t) commercial four-loop PWR. An axonometric projection and a piping schematic of the LOFT facility are shown in Figs. 5.1-1 and 5.1-2, respectively. References 5.1-1, 5.1-2, and 5.1-3 provide descriptions of the LOFT facility and the primary system in particular.

The LOFT experimental system consisted of five major systems: reactor, primary coolant, blowdown suppression, emergency core cooling, and secondary coolant. These systems were heavily instrumented to provide continuous monitoring of the nuclear, thermal, hydraulic, and structural processes occurring during the LOFT experiments.

The reactor system consisted of the reactor vessel and head, core support barrel, upper- and lower-core support structures, flow skirt, reactor vessel fillers, and nuclear core. The 1.68-m LOFT core was rated at 50 MW(t) and was designed to have the same physical properties as a PWR core. The core contained two basic fuel assembly configurations, square and triangular. The square fuel assemblies contained 225 fuel rod locations, 21 of which were occupied by guide tubes. The triangular assemblies contained 78 fuel rod locations, 8 of which were occupied by guide tubes.

The primary coolant system consisted of two coolant loops connected to the reactor system. Three PWR primary-coolant loops were simulated by the single, intact loop in LOFT. This single LOFT loop was scaled to have the same volume-to-power ratio as the three PWR loops. The broken loop in LOFT simulated the fourth PWR primary-coolant loop, the loop where the break was postulated to occur. The intact loop contained a steam generator, primary coolant pumps, pressurizer, primary coolant venturi (flow measuring device), and intact-loop piping. The intact-loop active steam generator, shown in Fig. 5.1-3, has a secondary side that consists of a U-tube boiler section, a steam dome, and a downcomer. The steam-generator secondary side is connected to a main steam flow control valve (MSFCV), condenser, feedwater pump, auxiliary-feedwater pump, and a feedwater-flow control valve.

The blowdown-suppression system simulated the containment back-pressure response of commercial PWRs during LOCAs and provided containment for the blowdown effluent. The major system components were the blowdown suppression header and downcomers, blowdown suppression tank, and blowdown suppression-tank spray system.

The facility ECCS simulated a commercial-plant ECCS. There were two ECCS trains, each containing a high-pressure injection system (HPIS), the accumulator system, and the low-pressure injection system (LPIS).

LOFT was highly instrumented. A partial list of the measured parameters includes coolant temperature; coolant level; coolant velocity, momentum, and flow direction; coolant density; coolant pressure; differential pressure; pump speed; coolant flows; and metal temperatures. The available instrumentation is summarized in Ref. 5.1-2.

### 5.1.2. Test Procedure Description

Test L2-6 simulated a 200% cold-leg break combined with a LOSP at the start of the transient. The reactor was brought to a power level of 46 MW and was maintained at that level until the blowdown was initiated. The conditions in the intact loop were established to provide 247.8 kg/s flow with temperature and pressure in the hot leg at 589 K and 15.09 MPa, respectively, at the time of blowdown initiation.

ECC injection was directed to the intact-loop cold leg at a system pressure of 4.11 MPa at 17.5 s. To simulate the LOSP, the primary coolant pumps tripped at 0.8 s and coasted down under the influence of the flywheels; when the pump speed dropped below 73.54 rad/s, the flywheel uncoupled from the pump and effectively reduced the pump moment of inertia. The assumption of LOSP at the initiation of the transient resulted in a delay in the availability of the HPIS and LPIS. The HPIS injection was initiated at 21.8 s, and the LPIS injection was initiated at 34.8 s. The experiment operating specifications[5.1-4] and the quick-look report[5.1-5] document the test initial conditions and operation.

The behavior of Test L2-6 was similar to that of earlier Tests L2-2 (Ref. 5.1-6) and L2-3 (Ref. 5.1-7) in which the pumps ran at approximately constant speed throughout the test. The most significant differences occurred in the core during the first ~11 s. Because of the higher power level in Test L2-6, the PCTs were higher (i.e., 1074 K vs ~900 K in Test L2-3). Test L2-6 exhibited the same early core rewet that was observed in Tests L2-2 and L2-3. However, in Test L2-6, rapid quenches were observed from cladding temperatures as high as 1074 K. In addition, the early rewet progressed only to a core elevation of 1.113 to 1.245 m before a second temperature increase began, whereas Tests L2-2 and L2-3 exhibited complete quenching of the entire core during the early rewet.

### 5.1.3. TRAC Model

Noding diagrams of the TRAC representation of the LOFT facility are shown in Figs. 5.1-4, 5.1-5, 5.1-6, and 5.1-7. The noding scheme and input are based upon the TRAC-PD2 model, which was modified for TRAC-PF1/MOD1 by LANL, improved and modified by the United Kingdom Atomic Energy Authority, and then modified again by LANL for TRAC-PF1/MOD2.

As shown in Fig. 5.1-4, the Vessel component is used to model the reactor vessel and internals. The Vessel is divided into 12 axial levels, 4 radial rings, and 4 azimuthal sectors. The lower plenum is modeled with 2 axial levels. The core resides in the first 3 radial sectors of levels 4 through 8. The upper plenum resides in the first 3 radial sectors of level 12. The downcomer resides in radial sector 4 of levels 3 through 11. The intact and broken hot-leg and cold-leg connections to the Vessel are at axial level 11. The Vessel connections to the intact and broken loops are shown in the horizontal cross-section view in Fig. 5.1-4.

The ECCS for LOFT L2-6 was modeled by the following components: a Pipe capped by a Break to model the accumulator, a Valve to model the accumulator check valve, one pipe each for the HPIS and LPIS lines with the flow conditions specified by Fills, and a Plenum to receive the accumulator, LPIS, and HPIS flows.

The baseline input model specifies that the reflood model is tripped on at 20 s. This was elected to ensure consistency with an earlier calculation of this test with the TRAC-PF1/MOD2 code. A listing of the baseline input model is provided in Appendix O. Archival storage information for this input model is provided in Section 5.1.7.

### 5.1.4. Comparison of Calculated and Test Results
The calculation LOFT Test L2-6 was performed with TRAC-M/F77, Version 5.5. The results are for newrfd=3, which activates the reflood model with explicit top-down reflood modeling. An identical set of graphical code-data comparisons with newrfd=1 is presented, without analysis, in Appendix P. Setting newrfd=1 activates the bottom-up reflood model of the TRAC-PF1/MOD2 code. Previous developmental assessment calculations used the TRAC grid-spacer model. We have run LOFT L2-6 calculations both with and without the grid-spacer model and have determined that the grid-spacer model should not be used because it results in excessive and nonphysical heat-transfer processes in the upper portions of the core. Therefore, the base-case assessment results for LOFT L2-6 do not use the TRAC grid-spacer model (see Section 4.4.5 for details). Finally, the base-case calculation trips the reflood model on at 20 s. We have also performed a parametric calculation in which the reflood model is tripped on at 1 s. Both results are presented in Section 5.1.4.

The calculated steady-state conditions from which the transient calculation was initiated are presented in Table 5.1-1. The constrained steady-state input feature in TRAC was used to drive the solution to the specified loop flow rate, secondary-side pressure, and cold-leg temperature.

The transient core inlet mass flow is shown in Fig. 5.1-8. The time-averaged core flooding rate, defined as the time-averaged core inlet mass flow divided by the core inlet flow area and the density of the core inlet flow is shown in Fig. 5.1-9.

A comparison of the TRAC-calculated pressure and the measured pressure for the intact-loop hot leg is shown in Fig. 5.1-10. The pressure comparison is excellent through the subcooled blowdown and the initial phase of the two-phase blowdown. During the two-phase blowdown, TRAC depressurizes slightly faster than indicated by the data. The difference is not significant, and the agreement is still reasonable. During the reflood phase of the transient, the TRAC-predicted pressure is slightly larger than that

indicated by the data. The TRAC-predicted pressure for the pressurizer is compared with experimental data in Fig. 5.1-11. This data comparison supports the intact hot-leg comparison, indicating that TRAC accurately calculates the pressure transient.

The data shown in Fig. 5.1-12 compare TRAC-predicted and measured broken-loop hot-leg mass-flow rates. The TRAC predictions are within the error bands included with the mass-flow-rate data and, therefore, are in excellent agreement with the data. During the subcooled blowdown, TRAC successfully predicted the spike and surge of two-phase liquid during the two-phase blowdown. A similar data comparison for the broken cold leg is shown in Fig. 5.1-13. For the broken cold leg, the subcooled blowdown spike in mass flow and two-phase blowdown mass-flow rates are predicted very accurately by TRAC; with minor exceptions, the calculated results are in excellent agreement with the data. During the reflood, TRAC calculates significant slugs of the ECCS fluid that move down the broken cold leg, which is similar to the behavior observed in the experimental data shown in Figs. 5.1-13 and 5.1-14; the latter figure shows the broken-loop, cold-leg mixture density, which is in reasonable agreement with the data.

The intact-loop mass-flow rates for both the intact hot and cold legs are also accurately predicted, as illustrated in Figs. 5.1-15 and 5.1-16. The intact-loop hot-leg mass flow is in excellent agreement with the data. In Fig. 5.1-16, the data indicate larger spikes in mass flow in the intact cold leg than in the cold-leg plugs because of ECCS injection. Although the TRAC code does indicate spikes in the intact cold-leg mass-flow rate, their magnitude is not as large as indicated by the data. Overall, the calculated intact-loop, cold-leg mass flow is in reasonable agreement with the data.

The measured accumulator level is compared with the TRAC prediction in Fig. 5.1-17. The results indicate that TRAC accurately calculates the time required to empty the accumulator and, therefore, accurately calculates the ECCS flow rate into the intact cold leg; the agreement between the calculated and measured accumulator water level is excellent. The downcomer fluid temperature calculated by TRAC is compared with the fluid temperature measured in the downcomer in Fig. 5.1-18. The TRAC-calculated downcomer fluid temperature is in reasonable agreement with the measured temperature during the blowdown, refill, and the early phase of the reflood phase. At ~50 s, TRAC calculates an increasing downcomer fluid temperature, whereas the data indicate that the downcomer fluid temperature does not start to increase until ~60 s into the transient. This difference in downcomer fluid temperature is believed to be associated with the modeling of the downcomer heat structures. The data comparison indicates that the TRAC prediction has too much heat transfer from the downcomer walls to the ECCS water entering the downcomer.

Figures 5.1-19 and 5.1-20 indicate that TRAC predicted well the initial fuel-rod stored energy. Both fuel-centerline-temperature and pellet-surface-temperature measurements indicated that comparisons were reasonable during the first 5 s of the LOFT transient. After 5 s, less energy is removed from the fuel rods than indicated by the measured-fuel centerline temperature. This result is consistent with the failure to calculate the early quench, as will be discussed in the next paragraph. Compared with the experimental data, the TRAC quench is delayed ~10 s at the indicated elevation. Fuel-rod-centerline temperature data (Fig. 5.1-19) indicate that compared with the data, TRAC underpredicts the integrated transient cooling.

5.1-4

Pellet surface-temperature data (Fig. 5.1-20) and TRAC predictions are in reasonable agreement only during the first 5 s of the transient. Both experimental data and TRAC values indicate a cooling of the fuel surface temperature as the reactor power decreases and as the blowdown transient starts, and then a heating of the fuel surface temperature as the cladding begins to heat up rapidly. When the blowdown quench begins, both the data and TRAC values turn around and decrease. As the transient proceeds, the large difference between TRAC values and the data may be because the fuel pellet surface-temperature thermocouple reading is closer to the cladding temperature than to the actual fuel-surface temperature. For example, from 30 to 40 s, the data indicate a fuel-surface temperature of 520–600 K, whereas the fuel-centerline temperature during this same time period is 750–800 K. The centerline and pellet-surface temperatures calculated by TRAC indicate that during this time period, the decay-heat power levels are insufficient to support such a large temperature gradient across the fuel as shown by the difference in the centerline and pellet surface temperature data. Therefore, the fuel surface temperature measurement is assumed to be influenced by the cladding temperature during this time. The fuel-surface measurement, however, does indicate that compared with the data, rod quenching in TRAC is delayed by ~20 s.

Figures 5.1-21 and 5.1-22 indicate that the TRAC prediction of PCT is between minimal and reasonable. Key trends are predicted (reasonable), but the differences in magnitude are sufficiently large that the results may be considered to be in minimal agreement. TRAC predicts the start of the early quench and recovery, but less heat is removed from the heater rods. Therefore, the complete quench seen at the 0.6502-m level during the test is not calculated. The subsequent reheat, although from a much higher temperature, is calculated by TRAC. The calculated final quenching of the core at this level is delayed by slightly over 10 s. Lacking a measurement of core-inlet flow, we are unable to determine whether the underprediction of core cooling is associated with an incorrect prediction of core inlet flow during blowdown or whether the source of the under prediction lies with the heat-transfer model. An earlier study of LOFT L2-6, a similar underprediction of core cooling by RELAP5/MOD2 was observed, and the authors concluded that the core inlet flow was correctly calculated and that the problem lay with the heat-transfer model.[5.1-8]

The TRAC-calculated core-inlet flow is presented in Fig. 5.1-23. Clearly, the surge of flow into the core between 4.5 and 9.0 s is responsible for the partial TRAC-calculated quench during this interval. It appears, however, that both the magnitude and duration of the calculated insurge are too small, resulting in only the partial quench of the cladding at the 0.6502 and 0.6943-m levels shown in Figs. 5.1-21 and 5.1-22.

For completeness, comparisons of calculated and measured cladding temperature histories at the 0.2032-m level (near the bottom of the core) and 1.5409-m level (near the top of the core) are presented in Figs. 5.1-24 and 5.1-25, respectively. At the 0.2032-m level, the repeated quenching behavior of the cladding is not calculated. At the 1.5409-m level, TRAC predicts an immediate quench with only minor reheats thereafter, whereas a significant heatup of the clad at this temperature occurred in the test after an early cladding temperature decrease during the first 2 s of the test.

The calculated core-outlet mass flow is presented in Fig. 5.1-26. It appears that the reason the cladding at 1.5409 m is predicted to cool and remain quenched in the TRAC

calculation is that the liquid pulse originating at the bottom of the core during the interval 4.5–9.0 s cools that level sufficiently to prevent the subsequent reheat seen in the data. Given the pattern in the calculation that the surge of liquid entering the bottom of the core between 4.5 and 9.0 s progresses through the lower, middle, and most of the upper portion of the core (but doesn't sufficiently cool the core to produce the quenches seen in test, while overcooling the upper-most portions of the core), it appears possible that the core heat transfer associated with passage of the liquid pulse through all but the upper-most regions of the core is underpredicted. If, for example, there were greater heat transfer to the fluid lower in the core, the cladding would have quenched, and more of the coolant would have been vaporized, thereby reducing heat transfer in the upper portions of the core.

Table 5.1-2 lists the sequence of events in the LOFT L2-6 test and the TRAC calculation. The reactor scram and primary-coolant pumps were both user input for the TRAC calculation. In the TRAC calculation, the pressurizer takes longer to empty than the data indicate because a high steam flow rate out of the bottom of the pressurizer occurs as the last cell in the pressurizer component empties. We believe that the high vapor flow rate out of the bottom of the pressurizer is associated with a large interfacial-drag coefficient that TRAC calculates at the pressurizer exit. TRAC calculated the wrong flow regime at the exit of the pressurizer and calculated a large interfacial shear, which resulted in a high steam flow rate out of the bottom of the pressurizer when only liquid should have been flowing out of the bottom of the pressurizer.

The delay in emptying the pressurizer allowed TRAC to depressurize too fast during the two-phase blowdown phase of the test, which in turn caused the accumulator injection initiation to occur ~2.5 s before the data indicated initiation. HPIS and LPIS initiations were both user-input at 21.8 and 34.8 s.

Finally, we ran one parametric case in which the new reflood model was activated (tripped on) 1 s after the start the transient. This parametric result is to be contrasted with the new reflood model at 20s, as done for the base-case results previously reported. We have repeated the set of plots provided for the 20-s trip in Figs. 5.1-27 through 5.1-43. We see no significant difference between the two results, although some differences can be observed. The most observable differences relate to the PCT at each level, with the higher temperature being calculated for the 1-s trip case (see Figs. 5.1-21 and 5.1-38). A cross-reference of the figures is tabulated below.

| 20-s Trip Figures | 1-s Trip Figures | 20-s Trip Figures (continued) | 1-s Trip Figures (continued) |
|---|---|---|---|
| 5.1-10 | 5.1-27 | 5.1-19 | 5.1-36 |
| 5.1-11 | 5.1-28 | 5.1-20 | 5.1-37 |
| 5.1-12 | 5.1-29 | 5.1-21 | 5.1-38 |
| 5.1-13 | 5.1-30 | 5.1-22 | 5.1-39 |
| 5.1-14 | 5.1-31 | 5.1-23 | 5.1-40 |
| 5.1-15 | 5.1-32 | 5.1-24 | 5.1-41 |
| 5.1-16 | 5.1-33 | 5.1-25 | 5.1-42 |
| 5.1-17 | 5.1-34 | 5.1-26 | 5.1-43 |
| 5.1-18 | 5.1-35 | | |

## 5.1.5. Conclusions

The TRAC-calculated parameters for LOFT test L2-6 are in either reasonable or excellent agreement with the data, with the important exception of the predicted surface cladding temperatures. The predicted surface cladding temperatures are characterized as being in the range of minimal-to-reasonable agreement with the data. Specifically, although TRAC predicts the start of the early quench observed in the test, it does not calculate the complete quench observed in the test through the lower two-thirds of the core. Further, TRAC predicts an immediate cooldown at the top of the core and no reheat, whereas a reheat was observed in the test. During the interval 4.5 to 9.0 s, TRAC predicts a surge of coolant upward through the core. This coolant surge initiates a quench throughout the core, but the duration and magnitude of the surge do not produce the complete early quenching of the core observed in the test. Because data are not available for the core inlet flow during the test, we do not know whether the TRAC deficiency in predicting the cladding surface temperatures arises from (1) a predicted coolant pulse having a magnitude and duration that are too small, (2) inadequacies in the core heat-transfer model, or (3) a combination of the two. Given that TRAC underpredicts core cooling throughout the lower, middle, and portions of the upper core while overpredicting the cooling at the top of the core, there is cause to believe that the core hydraulic and/or heat-transfer models still retain some deficiencies relative to the prediction of core thermal-hydraulic behavior during LBLOCA transients. Using the TRAC grid spacer model, which we have deemed to be inadequate and have advised against using, the calculated cladding temperatures during reflood are lower, but the quench times are delayed.

## 5.1.6. Code Performance

LOFT Test L2-6 was run on code Versions 5.5 and 5.4.29R+. In addition to the base-case run in which the reflood model was tripped on at 20 s, a parametric run was made with the reflood model tripped on at 1 s. The run performance information plus other pertinent comments follow.

Code Version 5.5, Reflood trip at 20 s

| Platform | Sun Enterprise 3000 |
|---|---|
| Total CPU time (s) | 29321.0 |
| Archive location of input model | CFS /tida/f77da_decks/l26ss06 /tida/f77da_decks/l26tr1.20s |
| Archive location of calculation | CFS /trac-da/F77DA/1.11Rrfd3nogs/ LOFT_L2-6.tar.gz |

Code Version 5.5, Reflood trip at 1 s

| Platform | Sun Enterprise 3000 |
|---|---|
| Total CPU time (s) | 43544.0 |
| Archive location of input model | CFS /tida/f77da_decks/l26ss06 /tida/f77da_decks/l26tr1.1s |
| Archive location of calculation | CFS /trac-da/F77DA/1.11Rrfd3nogs/ LOFT_L2-6.tar.gz |

Code Version 5.4.29R9+, Reflood trip at 20 s.

| Platform | Sun Enterprise 3000 |
|---|---|
| Total CPU time (s) | 22932.0 |
| Archive location of input model | CFS /tida/f77da_decks/l26ss06 /tida/f77da_decks/l26tr1.20s |
| Archive location of calculation | CFS /trac-da/F77DA/5429R9rfd3/ LOFT_L2-6.tar.gz |

Code Version 5.4.29R9+, Reflood trip at 1 s.

| Platform | Sun Enterprise 3000 |
|---|---|
| Total CPU time (s) | 25960.0 |
| Archive location of input model | CFS /tida/f77da_decks/l26ss06 /tida/f77da_decks/l26tr1.1s |
| Archive location of calculation | CFS /trac-da/F77DA/5429R9rfd3/ LOFT_L2-6.tar.gz |

The identical input models were used for both codes.

## REFERENCES

5.1-1   D. L. Reeder, "LOFT System and Test Description (5.5-ft Nuclear Core 1 LOCES)," Idaho National Engineering Laboratory report TREE-1208, NUREG/CR-0247 (July 1978.

5.1-2   C. L. Nalezny, "Summary of Nuclear Regulatory Commission's LOFT Program Experiments," Idaho National Engineering Laboratory report Tree NUREG/CR-3214 (July 1983).

5.1-3.   H. C. Robinson, "LOFT System and Test Description Loss-of-Coolant Experiments Using a Core Simulator," Idaho National Engineering Laboratory report TREE-NUREG-1019 (November 1976).

5.1-4.   E. M. Feldman, "OECD LOFT Project Experiment Specification Document Cold Leg Large Break Experiment LP-02-6," Idaho National Engineering Laboratory report OECD LOFT-T-3402 (July 1983).

5.1-5.   J. P. Adams, K. G. Condie, and D. L. Batt, "Quick-Look Report on OECD LOFT Experiment LP-02-6," Idaho National Engineering Laboratory report OECD LOFT-T-3404 (October 1983).

5.1-6.   M. McCormick-Barger, "Experimental Data Report for LOFT Power Ascension Experiment L2-2," Idaho National Engineering Laboratory report TREE-1322, NUREG/CR-0492 (February 1979).

5.1-7. P. G. Prassinos, B. M. Galusha, and D. B. Engelman, "Experimental Data Report for LOFT Power Ascension Experiment L2-3," Idaho National Engineering Laboratory report TREE-1326, NUREG/CR-0792 (July 1979).

5.1-8. Y. Koizumi, Y. Anoda, K. Tasaka, Y. Mimura, and A. Maeda, "LOFT Experiment LP-02-6 Analysis by RELAP/MOD2 Code with Improved Minimum Film Boiling Temperature," *Journal of Nuclear Science and Technology* 25, No. 4, 395–403 (April 1988).

**TABLE 5.1-1**
**LOFT TEST L2-6 INITIAL CONDITIONS**

| Parameter | Measured | Uncertainty | TRAC |
|---|---|---|---|
| Reactor power (MW) | 46.000 | ±1.20 | 47.00 |
| Intact-loop mass flow (kg/s) | 248.700 | ±2.60 | 248.00 |
| Hot-leg pressure (MPa) | 15.090 | ±0.08 | 15.03 |
| Hot-leg temperature (K) | 589.000 | ±1.10 | 591.00 |
| Cold-leg temperature (K) | 555.900 | ±1.10 | 556.70 |
| Pressurizer steam volume (m³) | 0.390 | ±0.02 | 0.31 |
| Pressurizer liquid volume (m³) | 0.607 | ±0.02 | 0.64 |
| Steam-generator pressure (MPa) | 5.620 | ±0.10 | 5.62 |
| ECC A-system accumulator | | | |
|     Pressure (MPa) | 4.11 | ±0.06 | 4.11 |
|     Temperature (K) | 302.00 | ±6 | 322.00 |

**TABLE 5.1-2**
**LOFT TEST L2-6 SEQUENCE OF EVENTS**

| Event | Time (s) | |
|---|---|---|
| | Test | TRAC |
| Break initiated | 0.0 | 0.0[a] |
| Reactor scrammed | 0.1 | 0.1[a] |
| Primary coolant pumps tripped | 0.8 | 0.8[a] |
| Pressurizer emptied | 15.5 | 20.0 |
| Accumulator A injection initiated | 17.5 | 15.0 |
| HPIS injection initiated | 21.8 | 21.8[a] |
| LPIS injection initiated | 34.8 | 34.8[a] |

[a] User-input values.

Intact loop

Broken loop

Quick opening
valve (2)

BL-1
experimental
measurement
station

Steam
generator
simulator

PC-2
experimental
measurement
station

Pressurizer

Steam
generator

Isolation
valve
(2)

Break plane

Pump
simulator

BL-2
experimental
measurement
station

ECC injection
location

PC-3
experimental
measurement
station

Pumps

Downcomer

Core

Reactor
vessel

PC-1
experimental
measurement
station

Lower plenum

Reactor vessel

Blowdown
suppression
tank

INEL 3 0591

Fig. 5.1-1. Isometric view of the LOFT facility.

Fig. 5.1-2. Piping schematic of the LOFT facility.

Fig. 5.1-3. Intact-loop steam generator in the LOFT facility.

Broken-Loop Cold Leg
Broken-Loop Hot Leg
Intact-Loop Hot Leg
Intact-Loop Cold Leg

Hot- and Cold-leg Connections

Downcomer

Core Levels

Elev. (m)
5.900
5.130
4.846
3.400
2.924
2.467
2.010
1.781
1.553
1.248
0.727
0.627
0.0

Radius (m)
0.105
0.231
0.329
0.47

Fuel Rod Noding

Elevation (m)    Node
                 1 2 3 4 5 6 7 8 9 10
2.924
2.467
2.010
1.781
1.553
1.248

|←——Fuel——→|

Gas Gap
Cladding

| Node | Node radius (m) |
|------|-----------------|
| 1 | 0.0 |
| 2 | 7.7449e-04 |
| 3 | 1.5489e-03 |
| 4 | 2.2335e-03 |
| 5 | 3.0979e-03 |
| 6 | 3.8725e-03 |
| 7 | 4.6470e-03 |
| 8 | 4.7250e-03 |
| 9 | 5.0508e-03 |
| 10 | 5.3590e-03 |

Heat Structure Components

| 851 | Level 1 cells 1-16 |
|-----|---------------------|
| 852 | Level 2 cells 1-16 |
| 853 | Level 3 cells 1-12 |
| 854 | Level 3 cells 13-16 |
| 855 | Level 4 cells 9-12 |
| 856 | Level 4 & 5 cells 13-16 |
| 857 | Level 5 cells 9-12 |
| 858 | Level 6 cells 9-12 |
| 859 | Level 6 cells 13-16 |
| 860 | Levels 7 & 8 cells 9-12 |
| 861 | Levels 7 & 8 cells 13-16 |
| 862 | Level 9 cells 1-8 |
| 863 | Level 9 cells 9-12 |
| 864 | Level 9 cells 13-16 |
| 865 | Level 10 cells 1-8 |
| 866 | Level 10 cells 9-12 |
| 867 | Level 10 cells 13-16 |
| 868 | Level 11 cells 1-12 |
| 869 | Level 11 cells 13-16 |
| 870 | Level 12 cells 1-8 |
| 871 | Level 12 cells 9-12 |
| 991 | Fuel rod component |

Fig. 5.1-4. LOFT L2-6 reactor vessel noding diagram.

Fig. 5.1-5. LOFT L2-6 intact-loop noding diagram.

Steam Generator Simulator

Break Plane

Reflood assist
bypass pipe

31

Vessel
Connection    Broken loop hot leg    31

43

Pump Simulator

Break

32

Reflood assist
bypass pipe

Break Plane

Vessel
Connection    41

Broken loop cold leg    41

Break

42
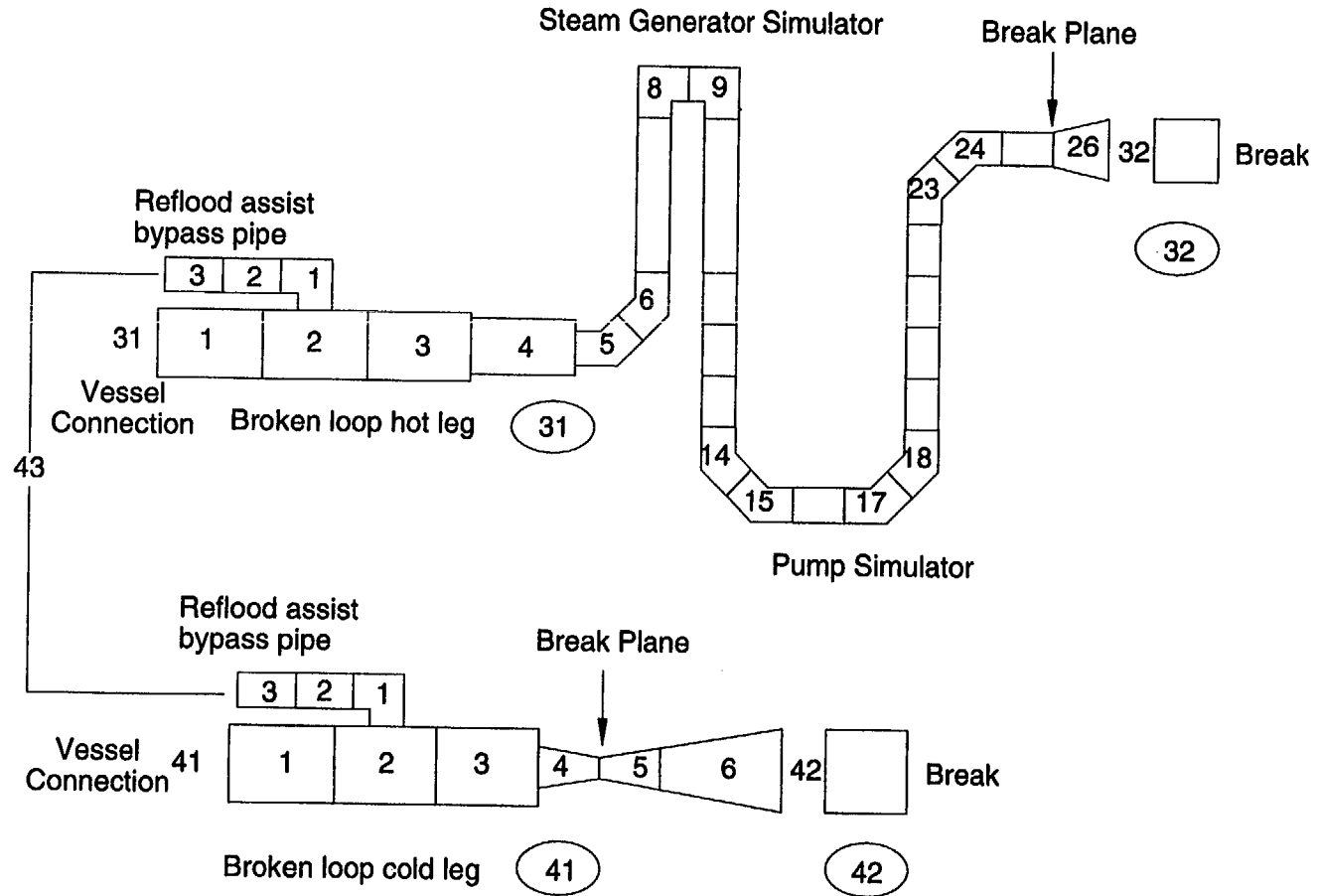
Fig. 5.1-6. LOFT L2-6 broken-loop noding diagram.
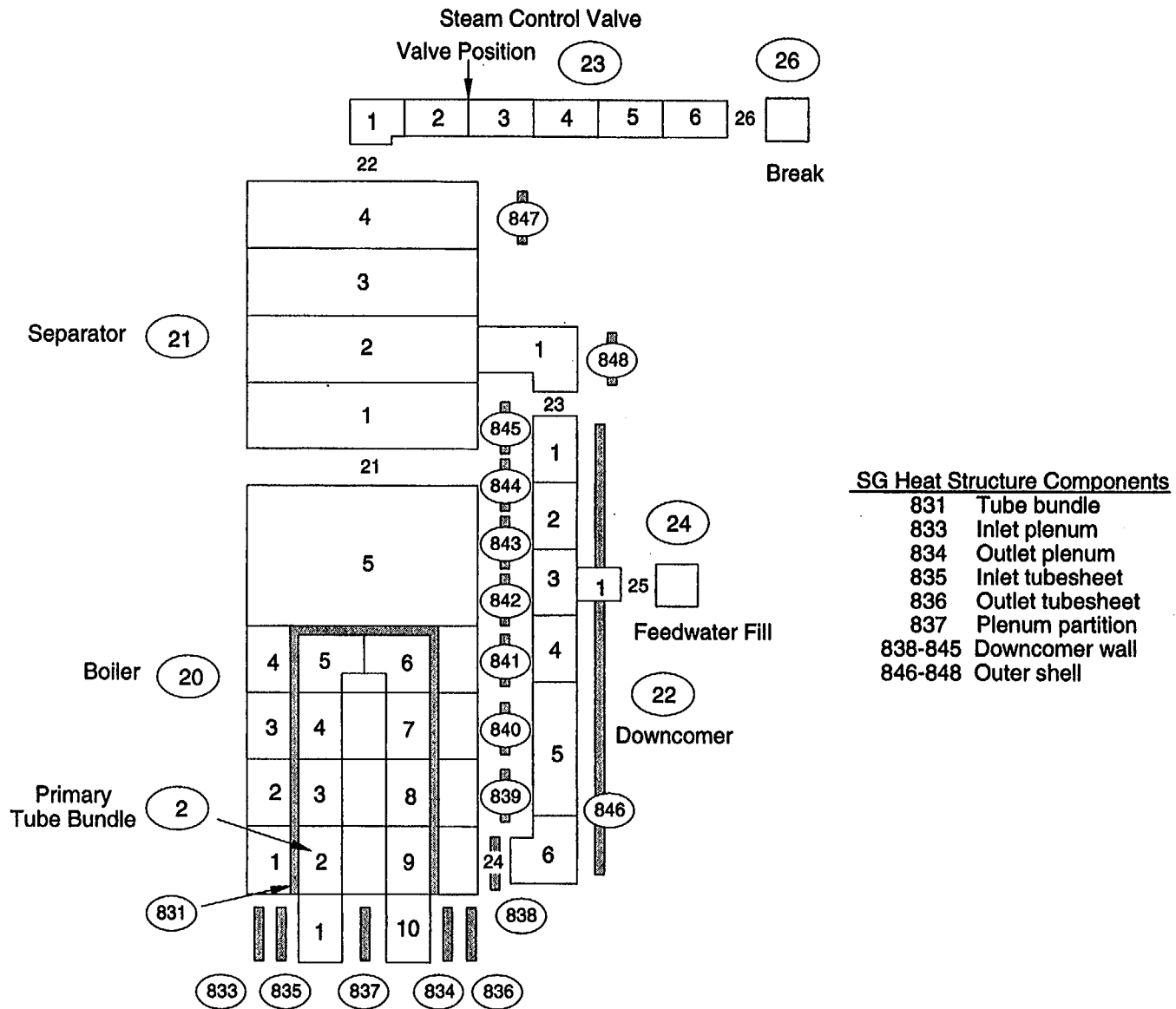
Fig. 5.1-7. LOFT L2-6 steam-generator noding diagram.
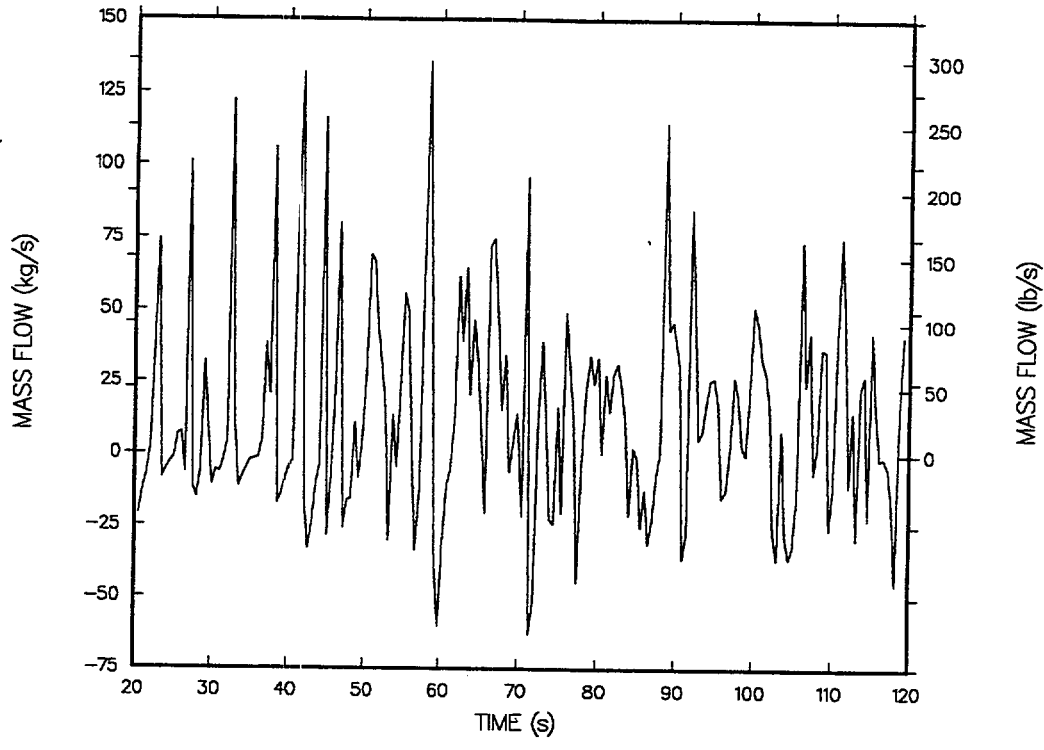
Fig. 5.1-8. Core inlet mass flow.
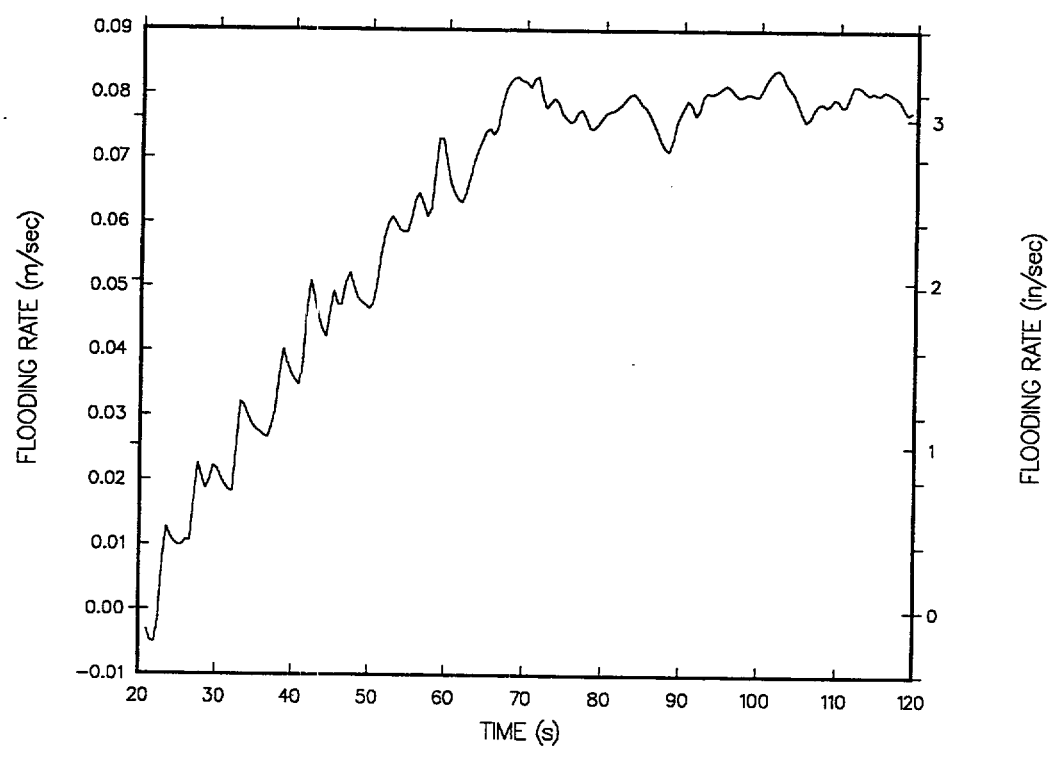


Fig. 5.1-9. Time-averaged core flooding rate.
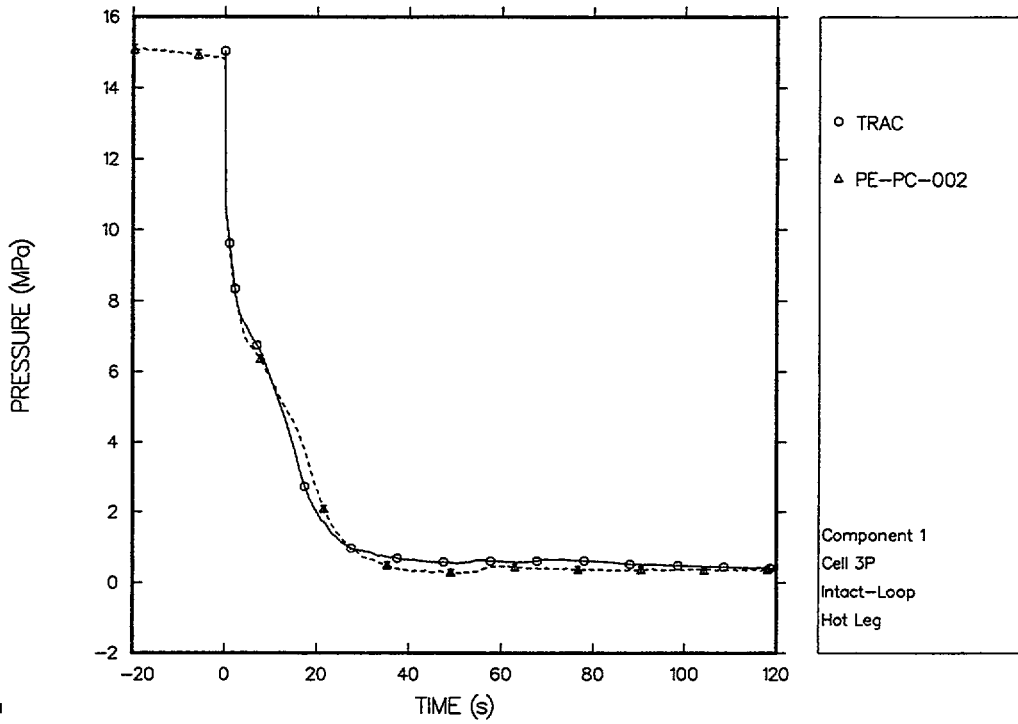
Fig. 5.1-10. Intact-loop hot-leg pressure.
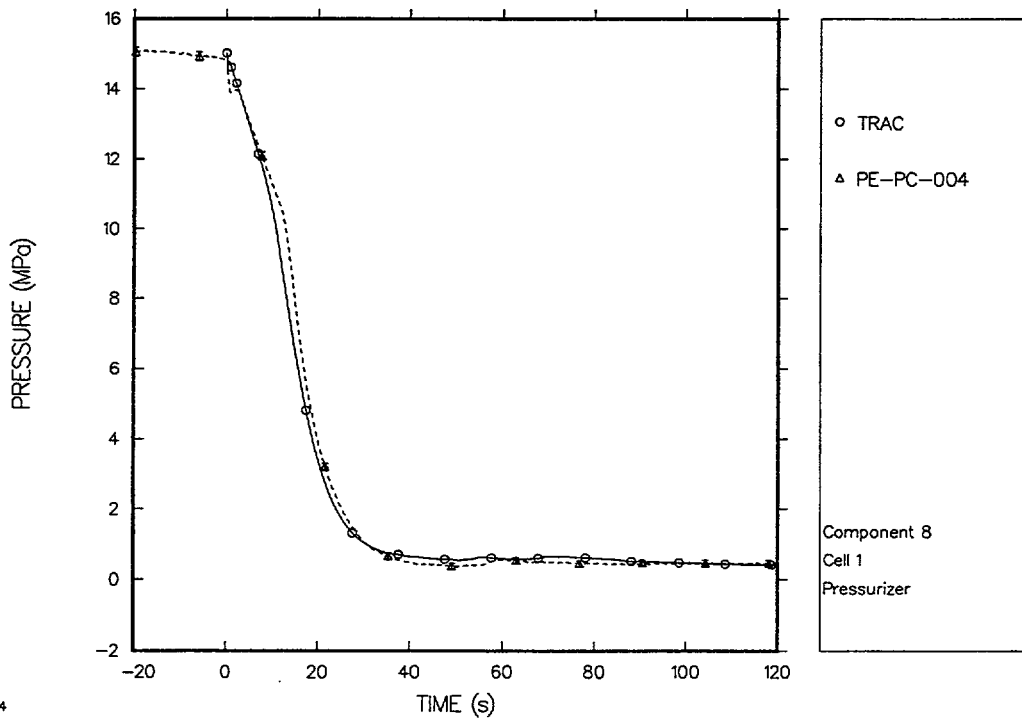


Fig. 5.1-11. Pressurizer pressure.
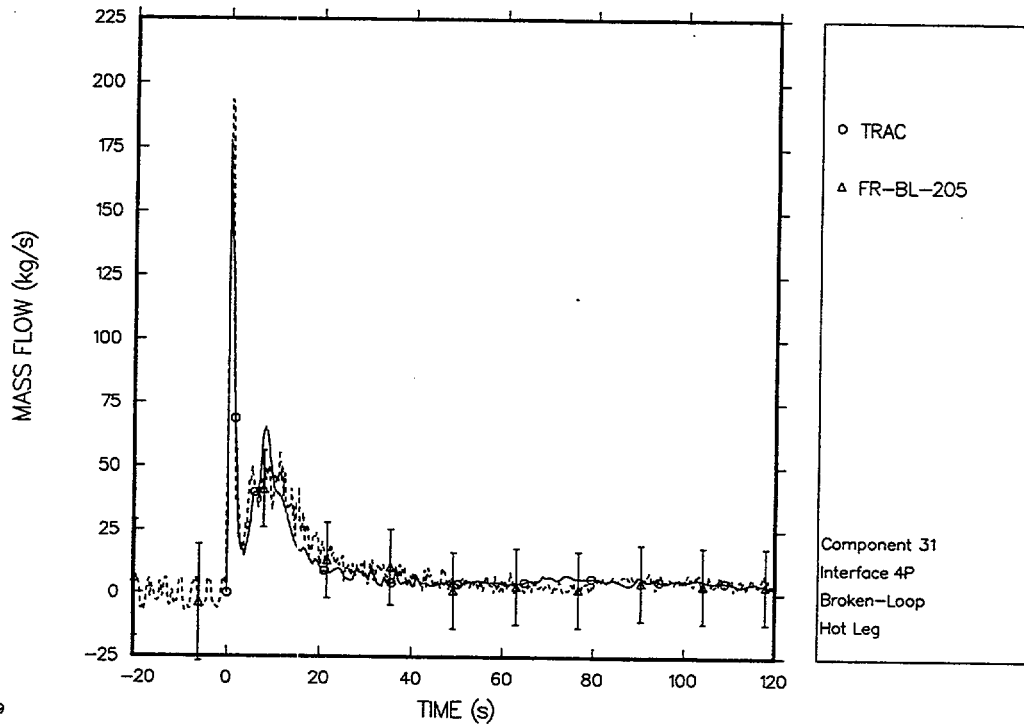
Fig. 5.1-12. Broken-loop hot-leg mass flow.
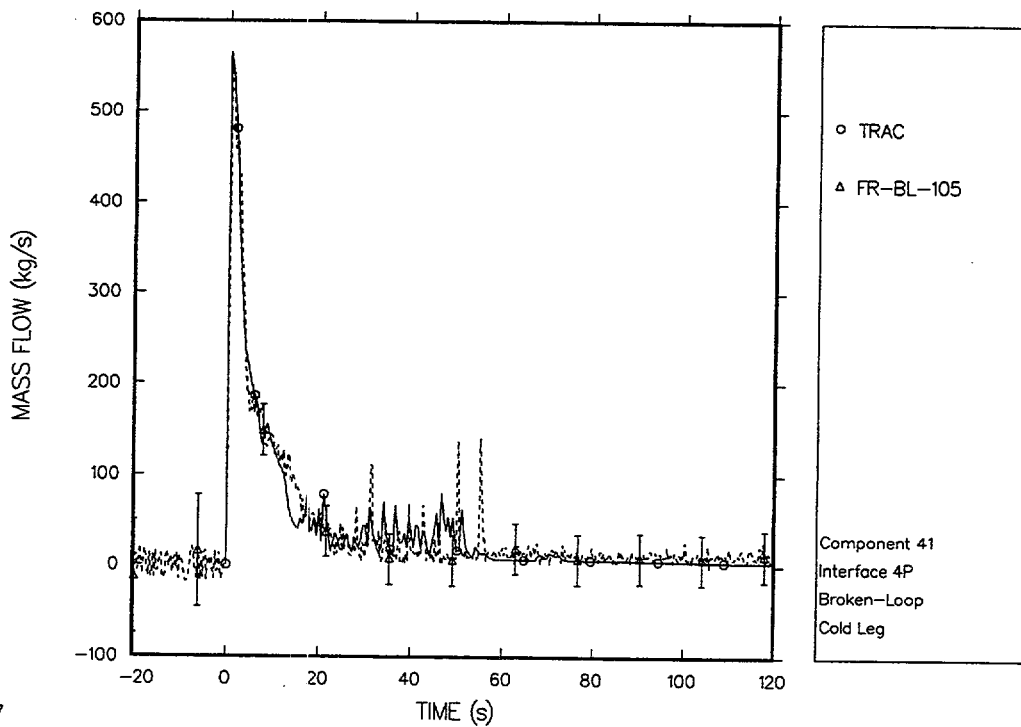


Fig. 5.1-13. Broken-loop cold-leg mass flow.

5.1-20
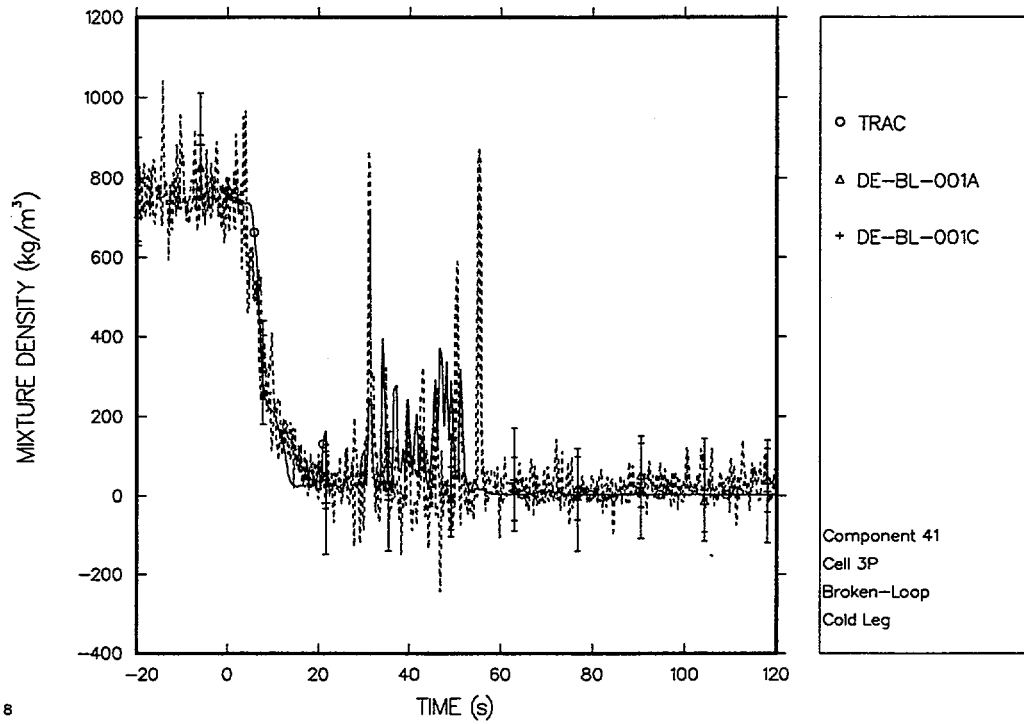
Fig. 5.1-14. Broken-loop cold-leg mixture density.
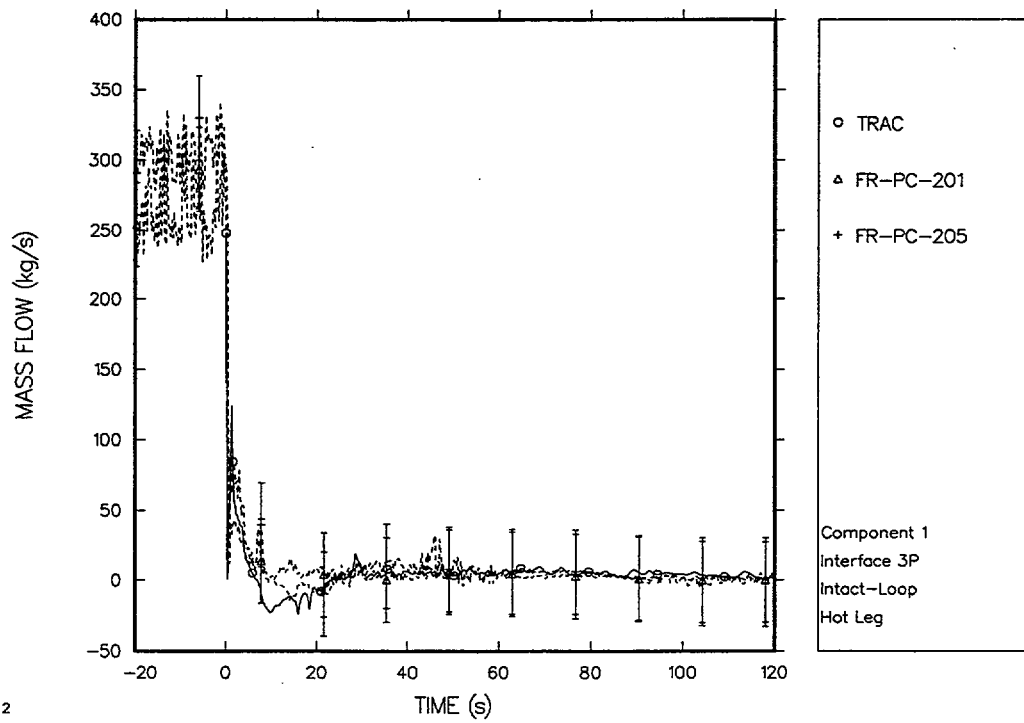


Fig. 5.1-15. Intact-loop hot-leg mass flow.

5.1-21
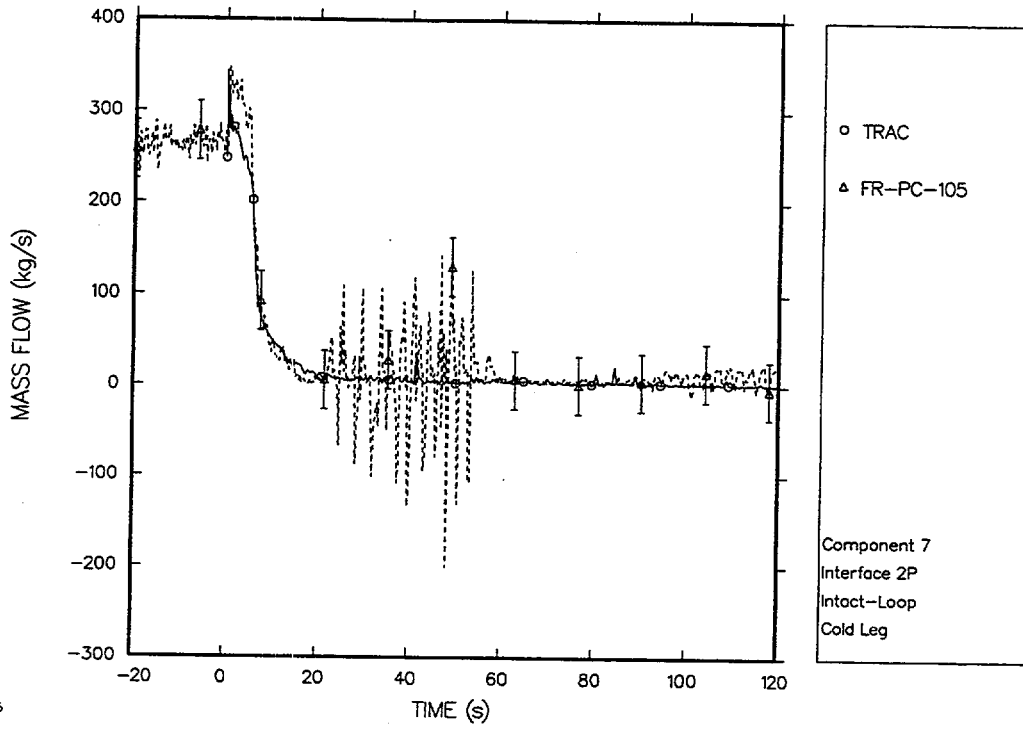
Fig. 5.1-16. Intact-loop cold-leg mass flow.
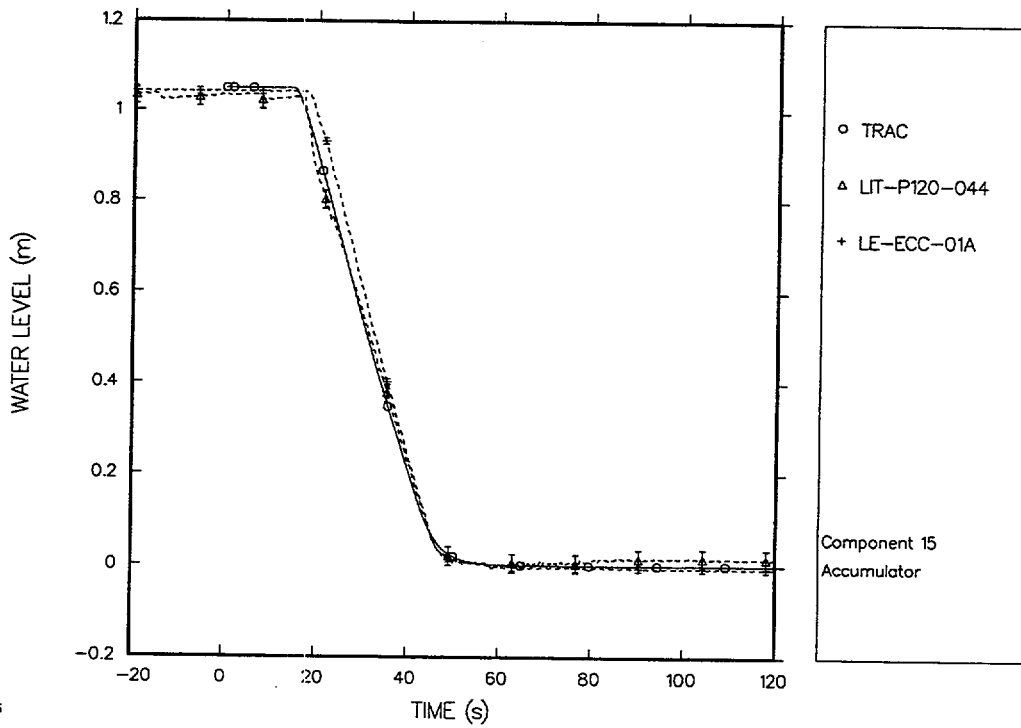


Fig. 5.1-17. Accumulator level comparison.
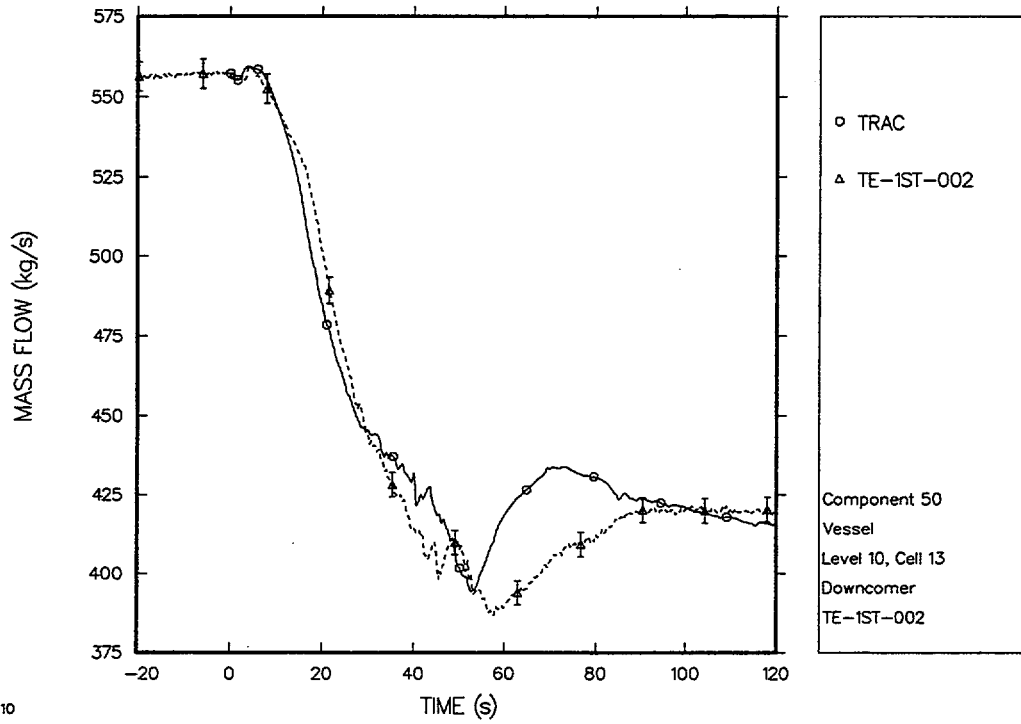
Fig. 5.1-18. Downcomer liquid-temperature comparison.
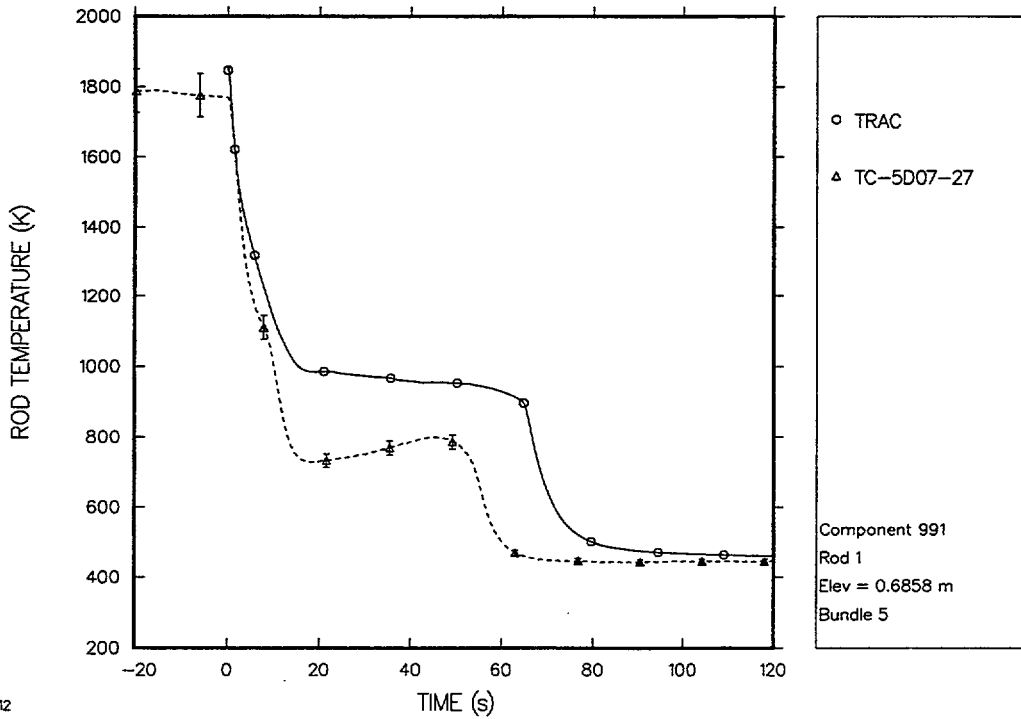


Fig. 5.1-19. Centerline fuel, temperature; Rod 1 elevation = 0.6858 m.
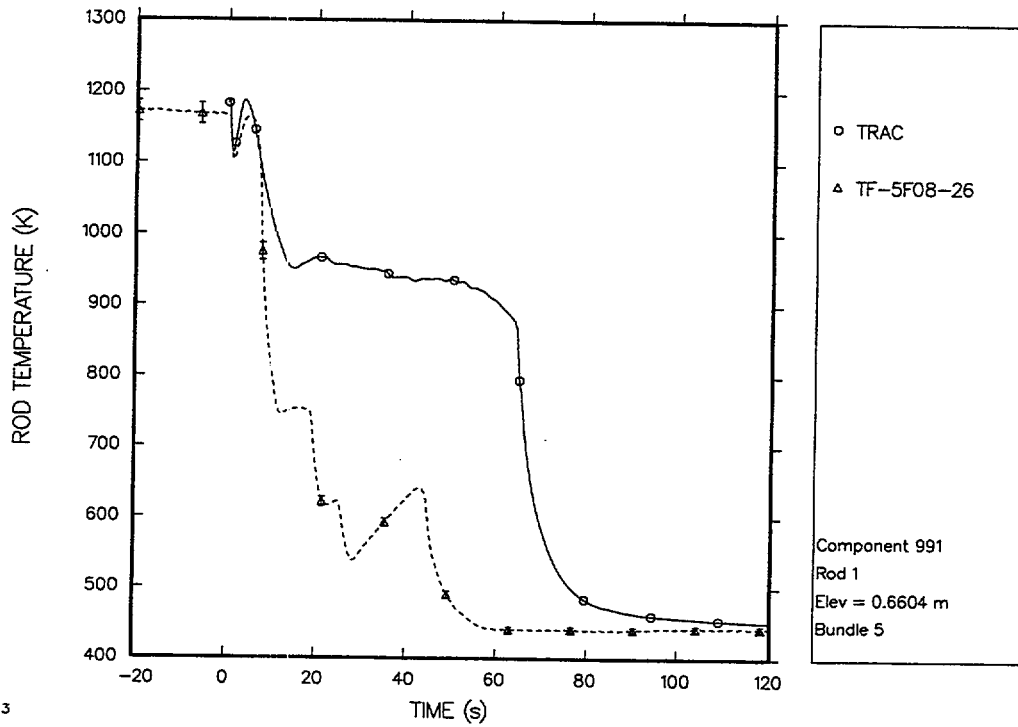
**Fig. 5.1-20. Pellet surface temperature; Rod 1 elevation = 0.6604 m.**
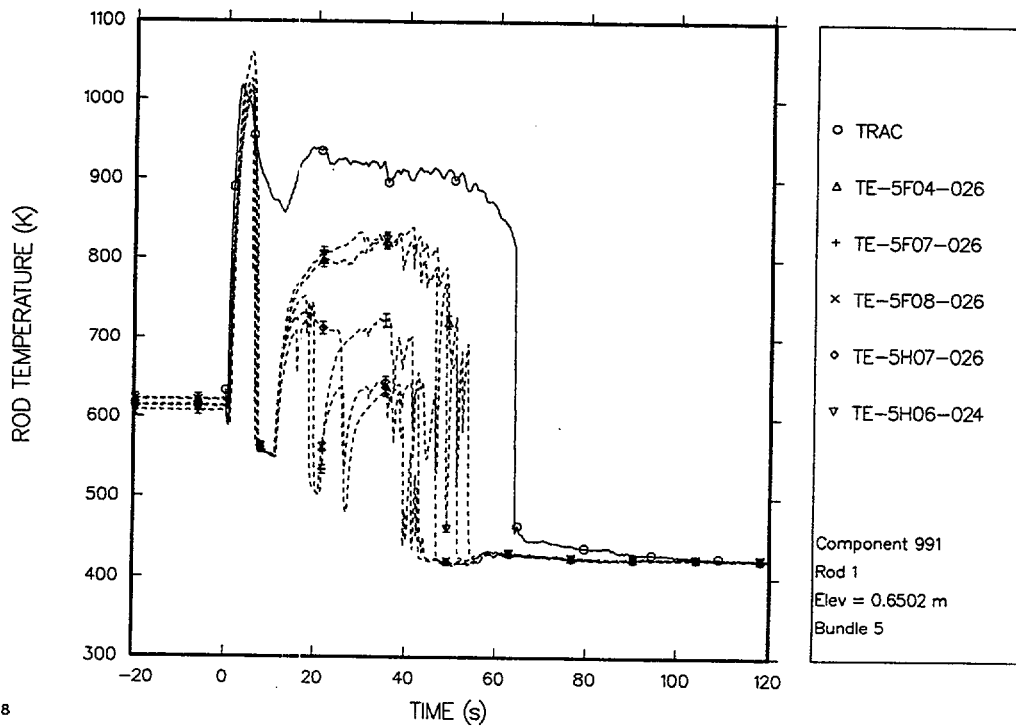


**Fig. 5.1-21. Cladding surface temperature; Rod 1 elevation = 0.6502 m.**
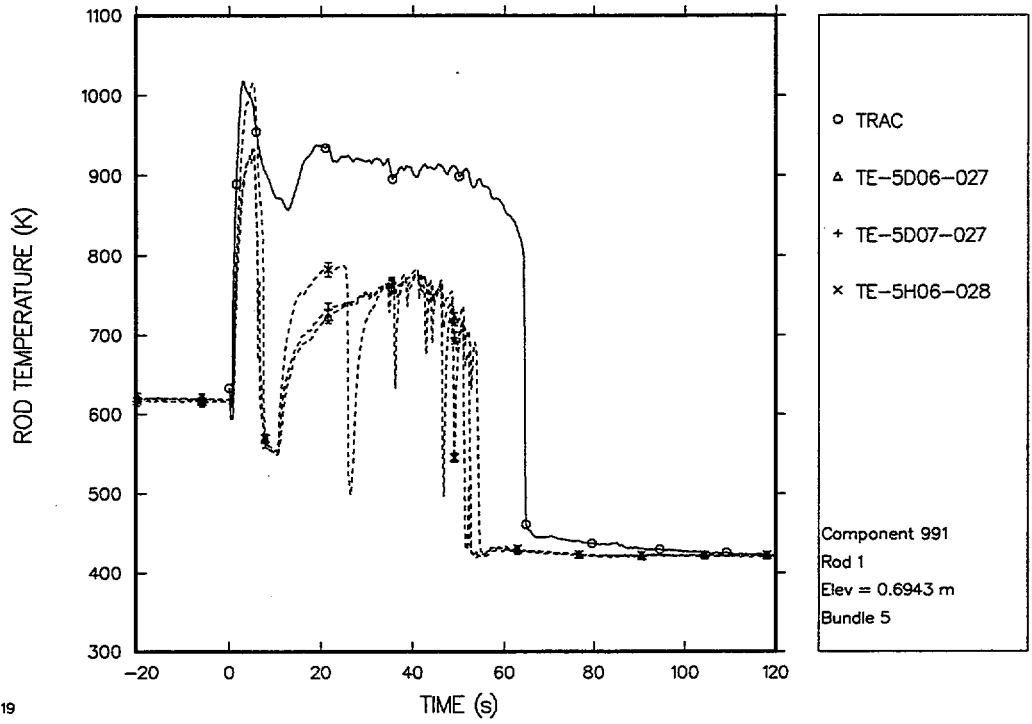
Fig. 5.1-22. Cladding surface temperature; Rod 1 elevation = 0.6943 m.
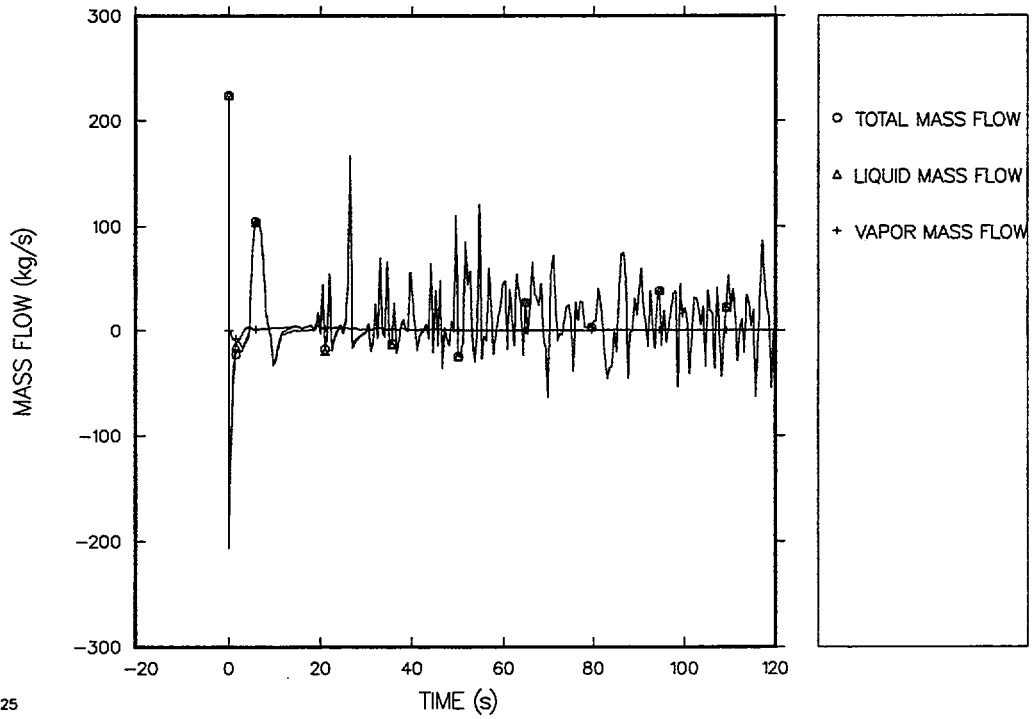


Fig. 5.1-23. Calculated core-inlet mass flow.
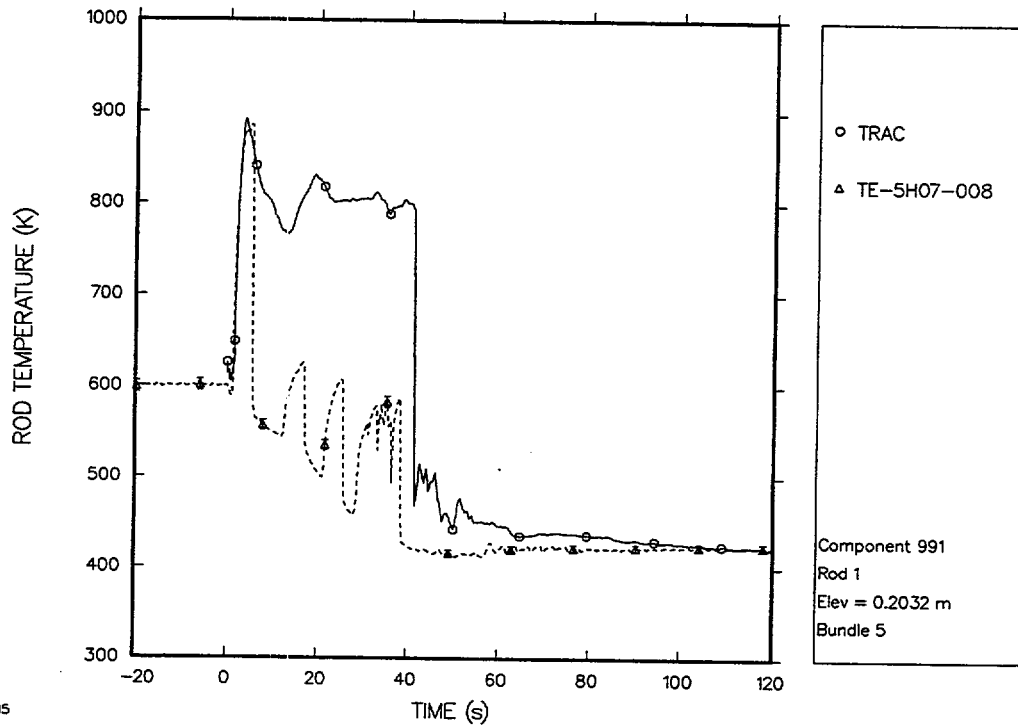
Fig. 5.1-24. Cladding surface temperature; Rod 1 elevation = 0.2032 m.
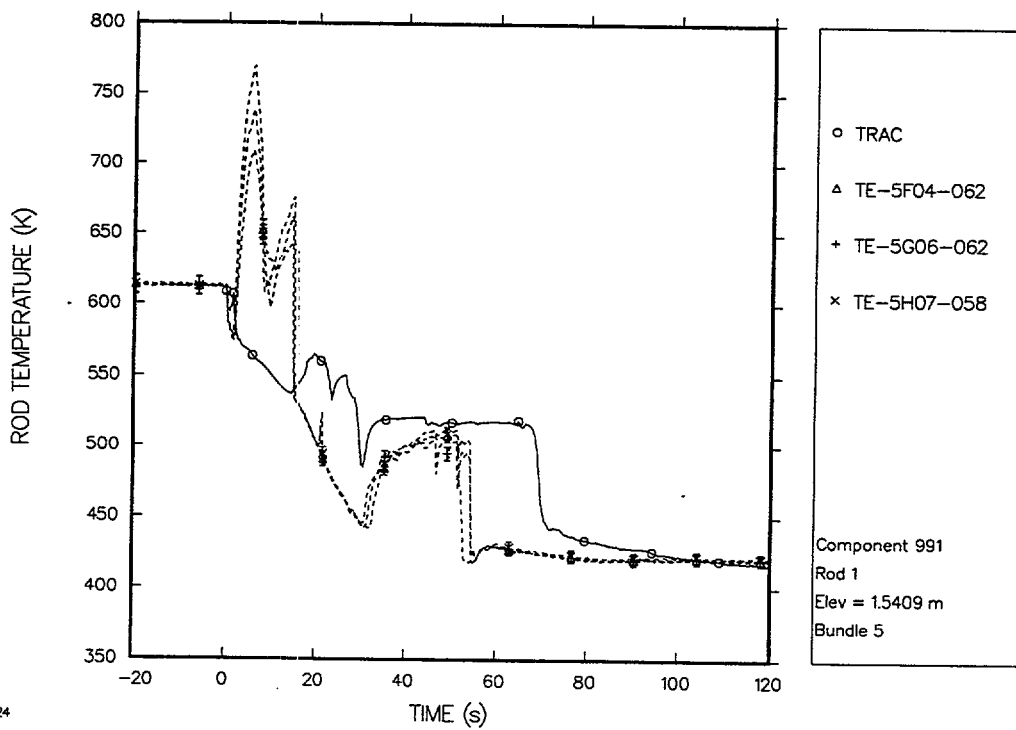


Fig. 5.1-25. Cladding surface temperature; Rod 1 elevation = 1.5409 m.
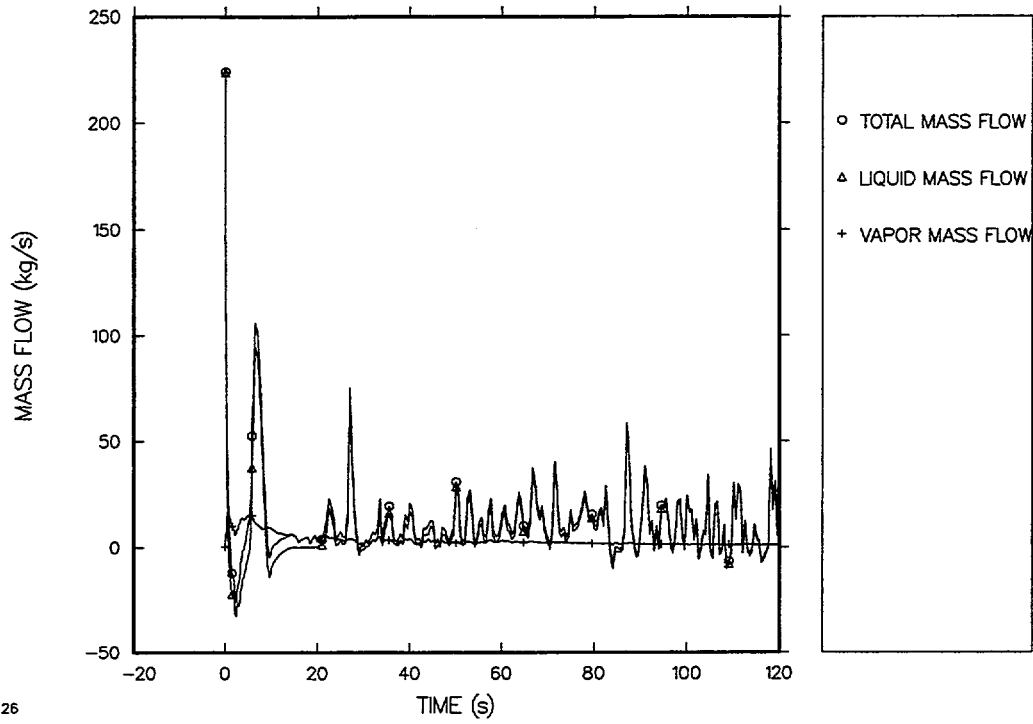
5.1-26

Fig. 5.1-26. Calculated core-outlet mass flow.

This space is intentionally left blank.
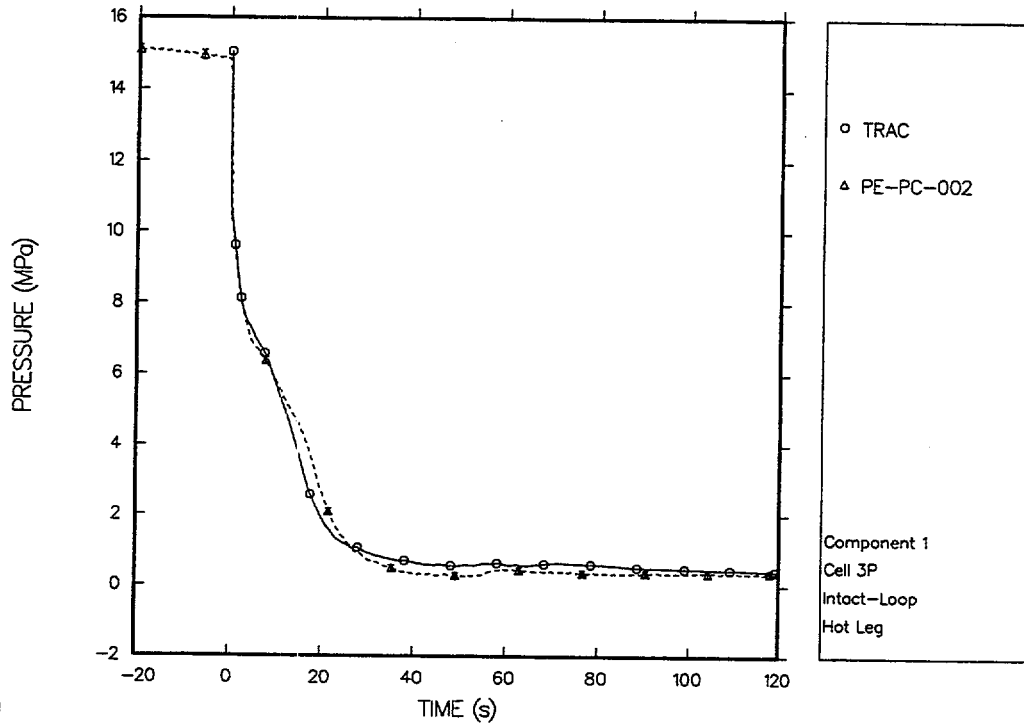
Fig. 5.1-27. Intact-loop hot-leg pressure, reflood trip at 1 s.
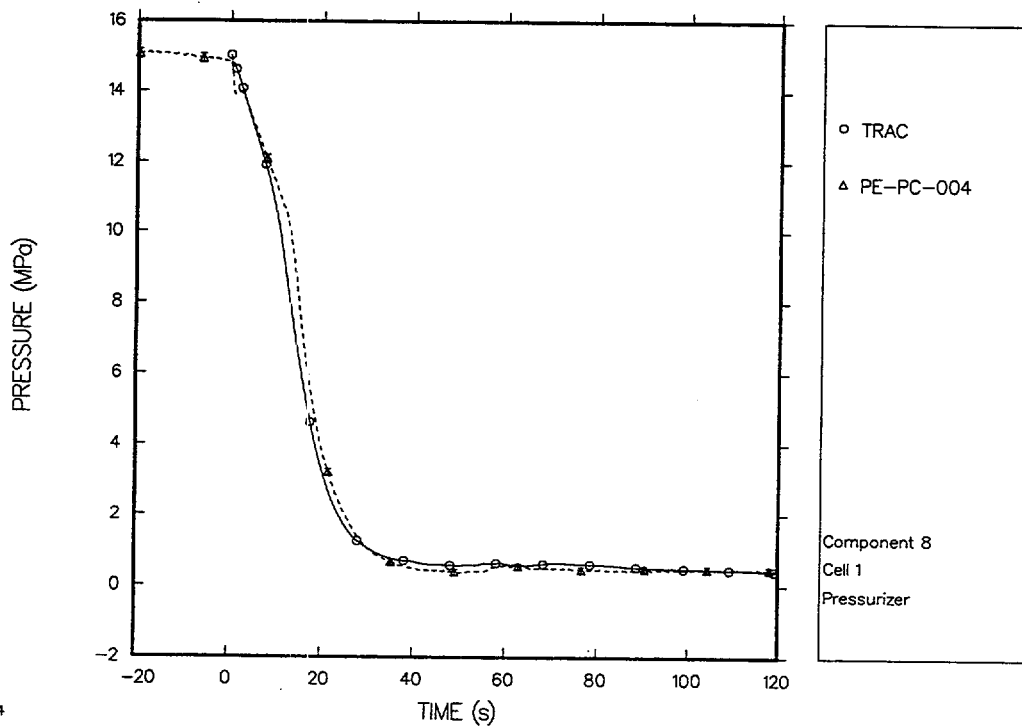


Fig. 5.1-28. Pressurizer pressure, reflood trip at 1 s.

5.1-28
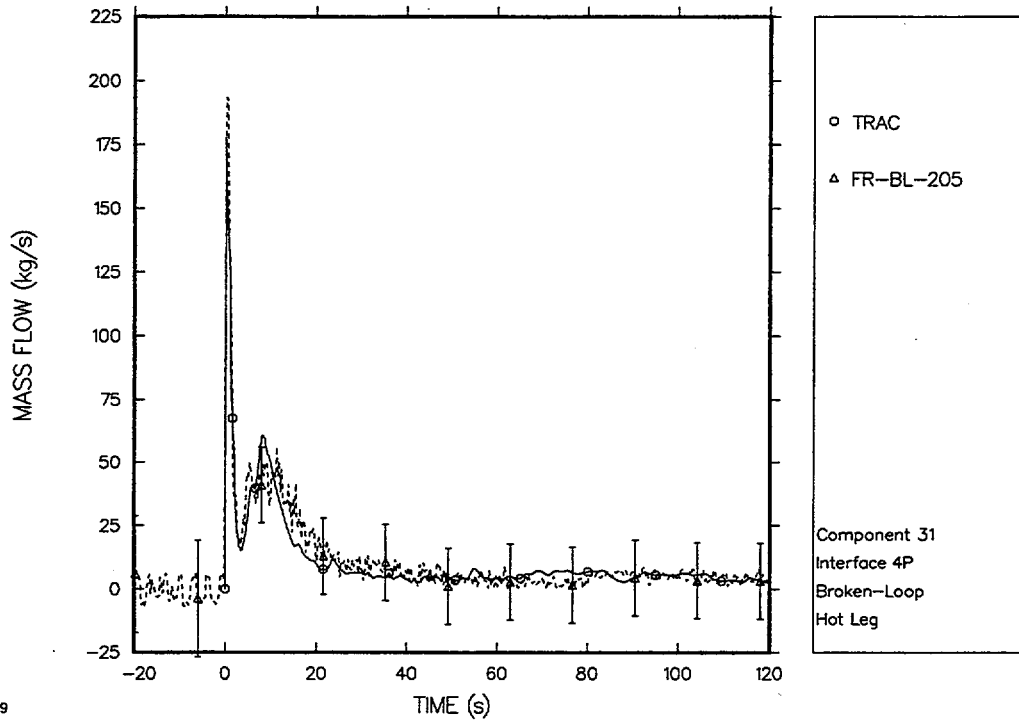
Fig. 5.1-29. Broken-loop hot-leg mass flow, reflood trip at 1 s.
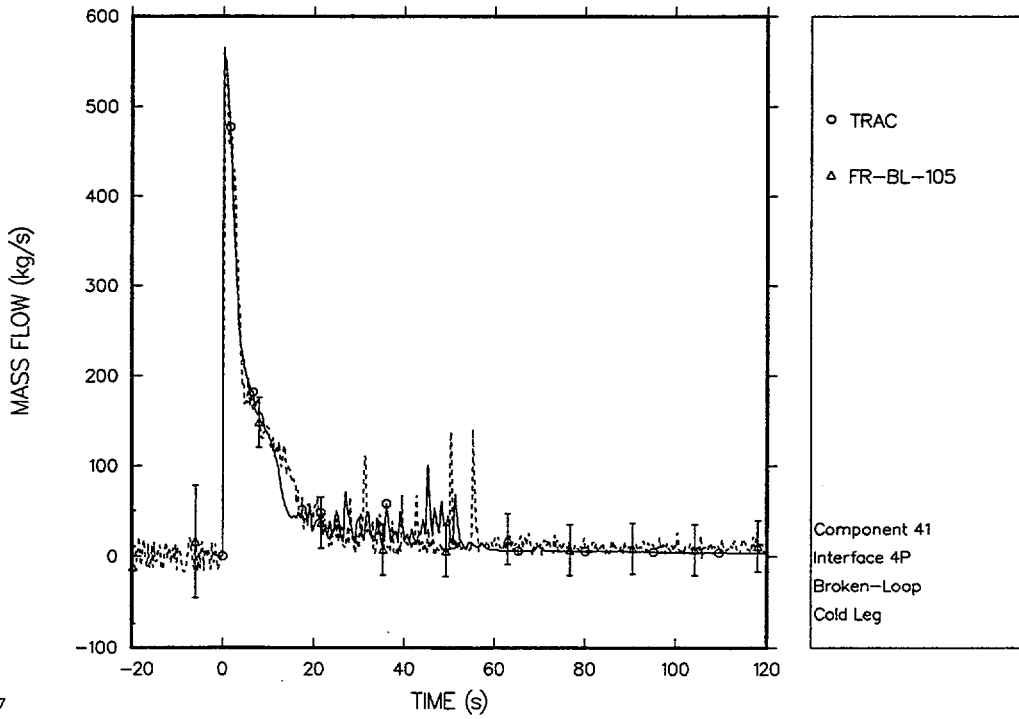


Fig. 5.1-30. Broken-loop cold-leg mass flow, reflood trip at 1 s.
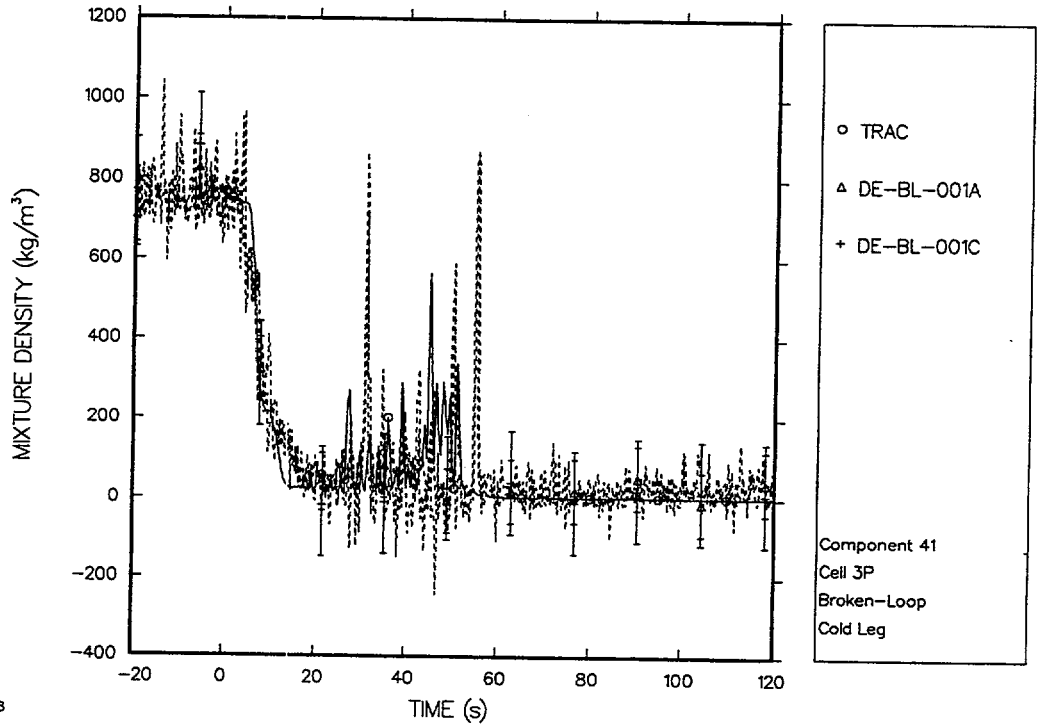
Fig. 5.1-31. Broken-loop cold-leg mixture density, reflood trip at 1 s.
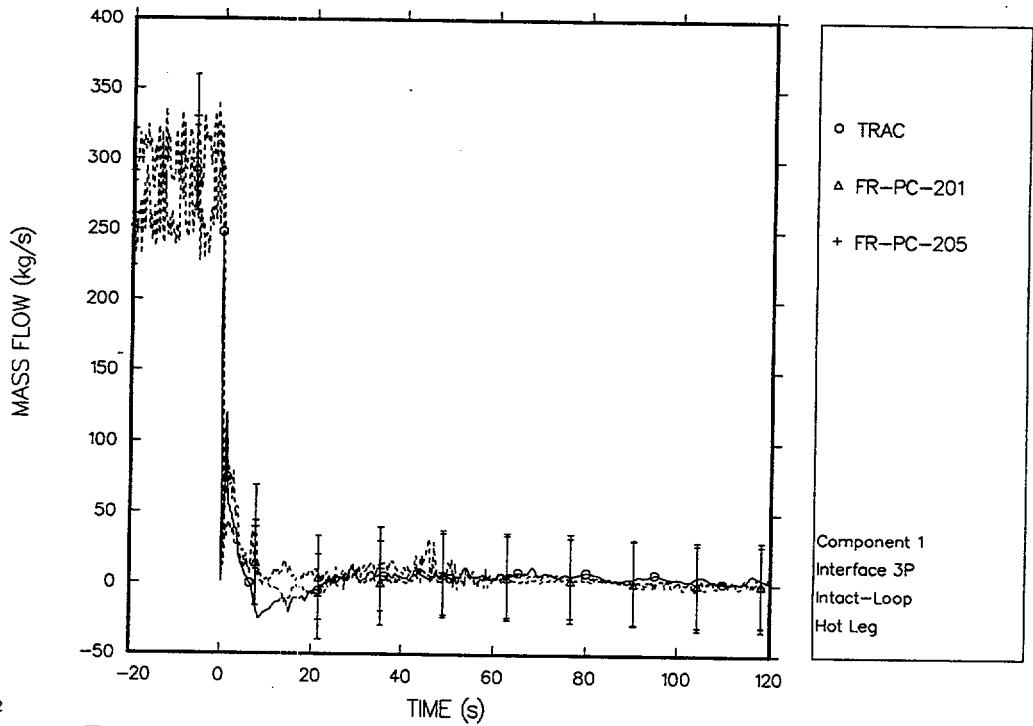


Fig. 5.1-32. Intact-loop hot-leg mass flow, reflood trip at 1 s.
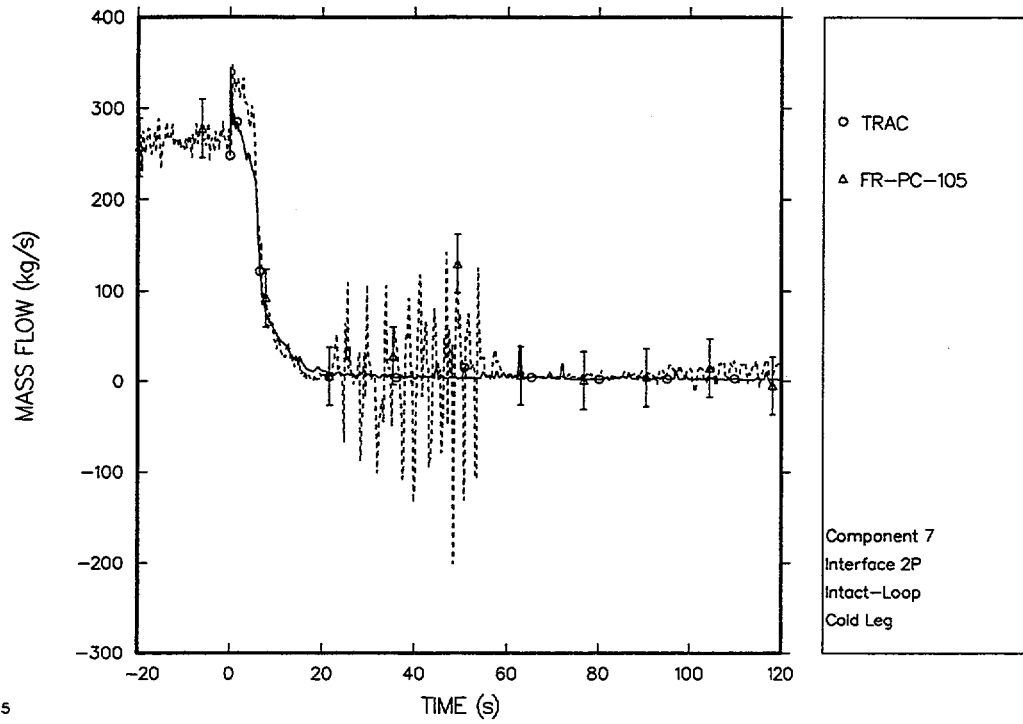
Fig. 5.1-33. Intact-loop cold-leg mass flow, reflood trip at 1 s.
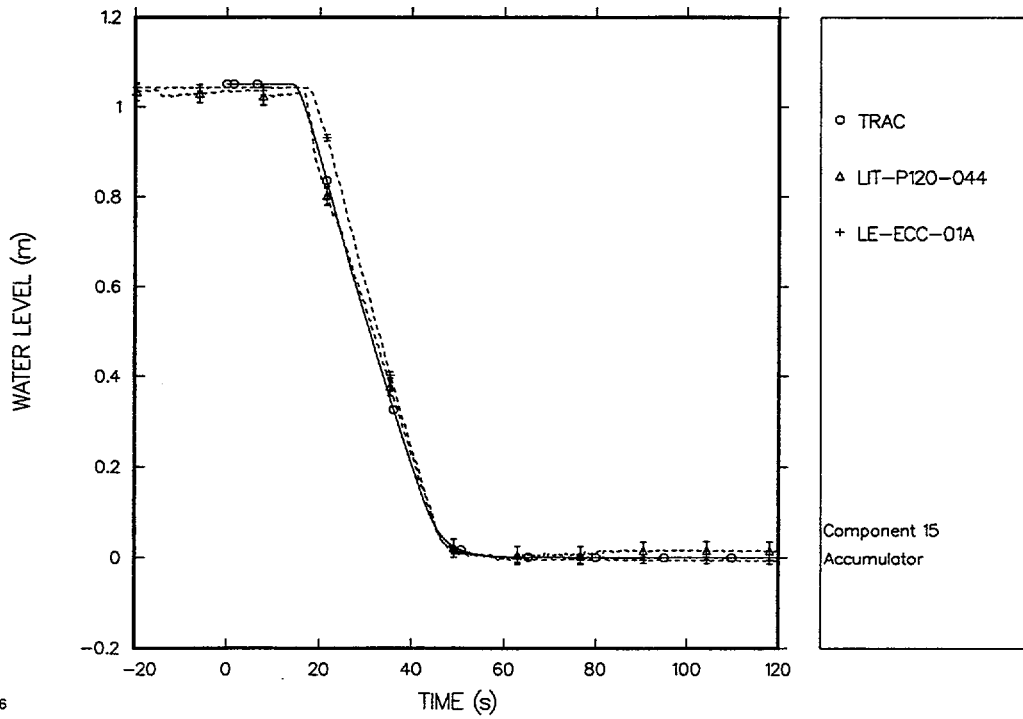


Fig. 5.1-34. Accumulator level comparison, reflood trip at 1 s.
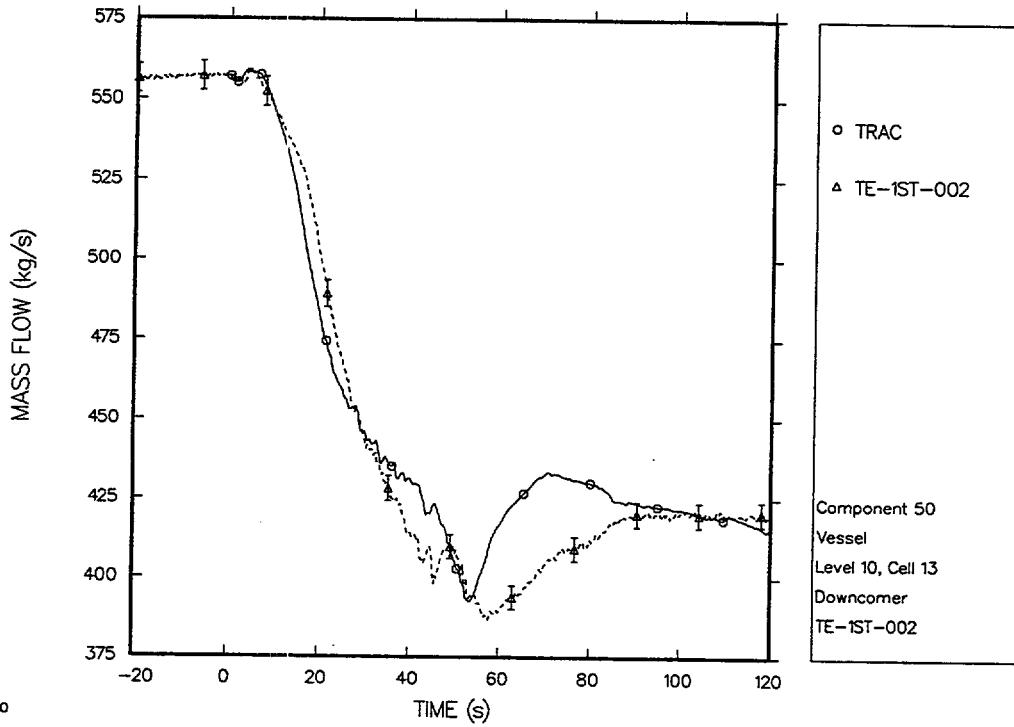
Fig. 5.1-35. Downcomer liquid-temperature comparison, reflood trip at 1 s.
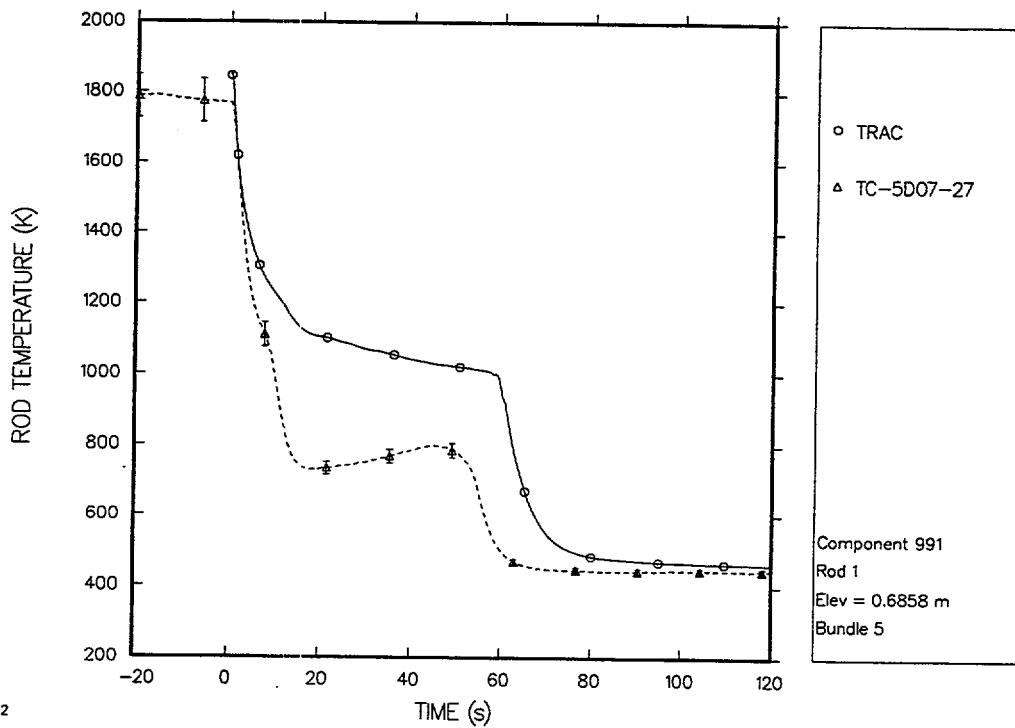


Fig. 5.1-36. Centerline fuel, temperature; Rod 1 elevation = 0.6858 m, reflood trip at 1 s.
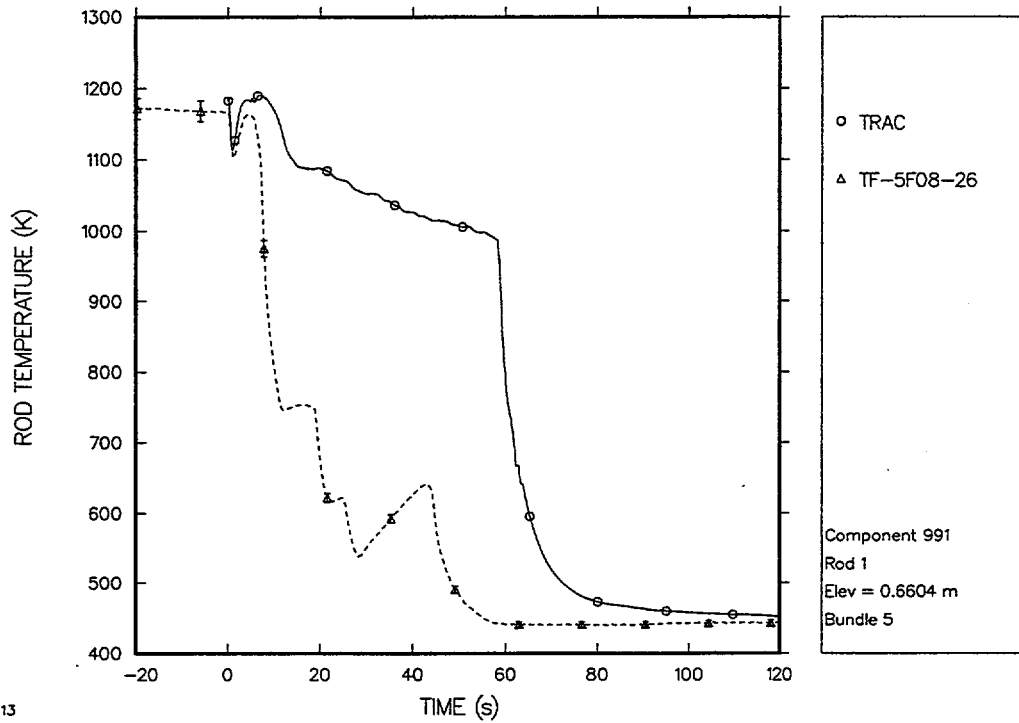
Fig. 5.1-37.    Pellet surface temperature; Rod 1 elevation = 0.6604 m, reflood trip at 1 s.
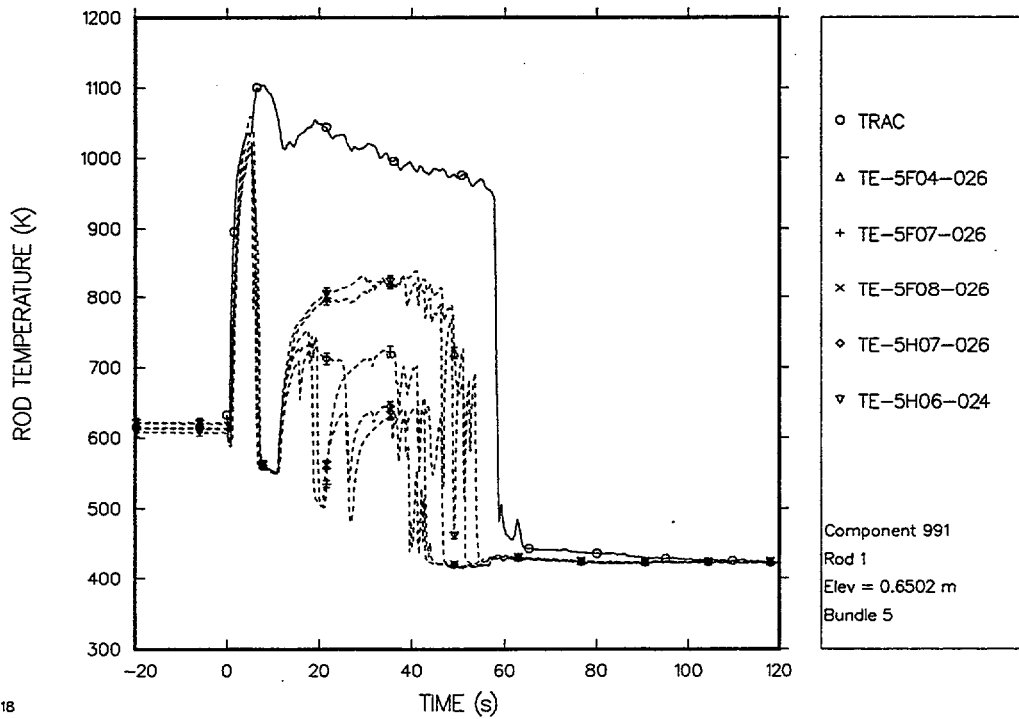


Fig. 5.1-38.    Cladding surface temperature; Rod 1 elevation = 0.6502 m, reflood trip at 1 s.

5.1-33
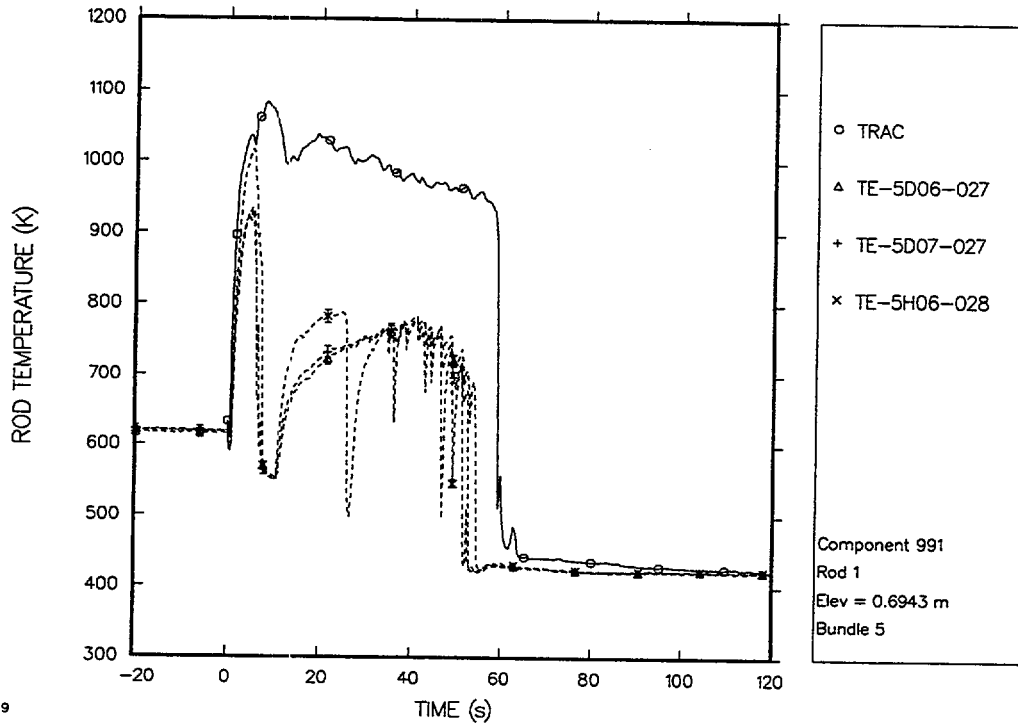
**Fig. 5.1-39.** Cladding surface temperature; Rod 1 elevation = 0.6943 m, reflood trip at 1 s.
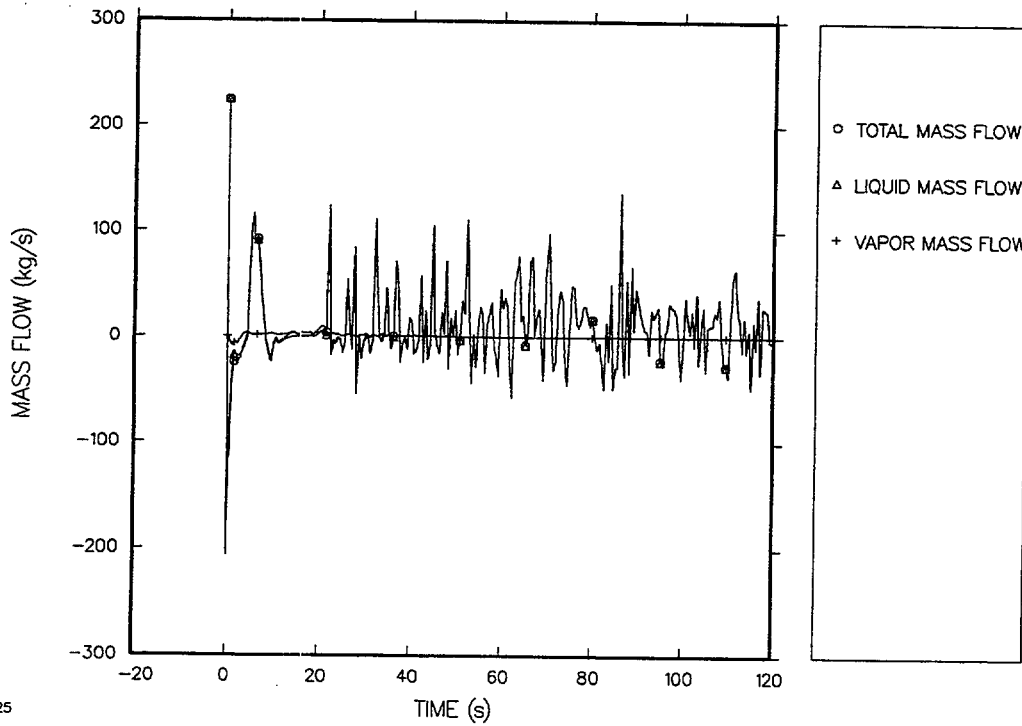


**Fig. 5.1-40.** Calculated core-inlet mass flow, reflood trip at 1 s.
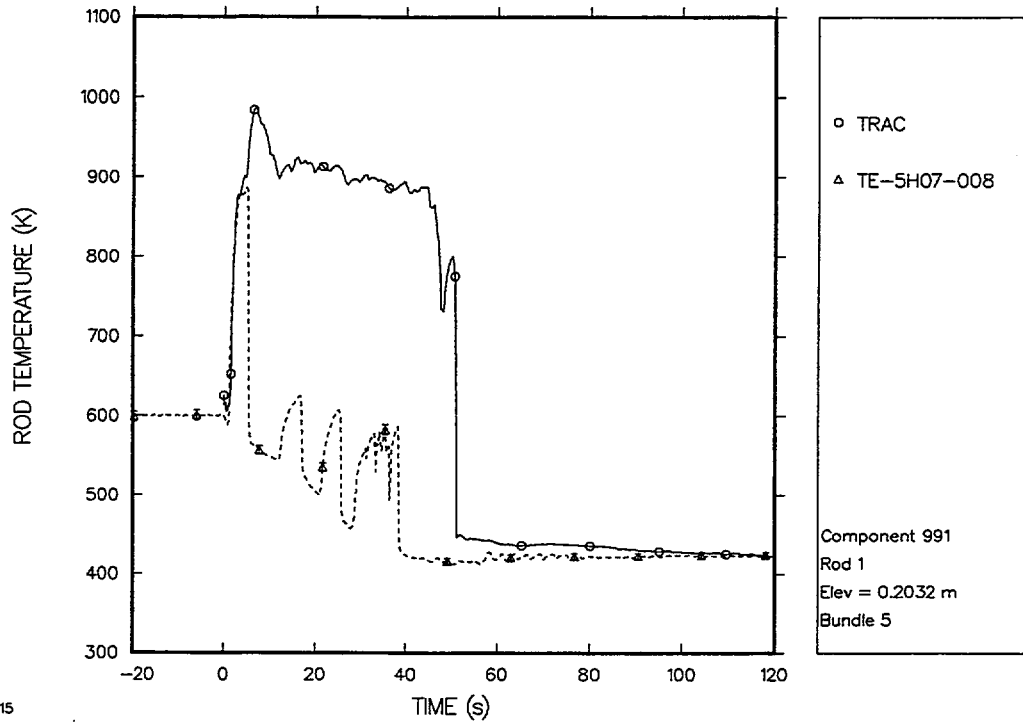
Fig. 5.1-41. Cladding surface temperature; Rod 1 elevation = 0.2032 m, reflood trip at 1 s.
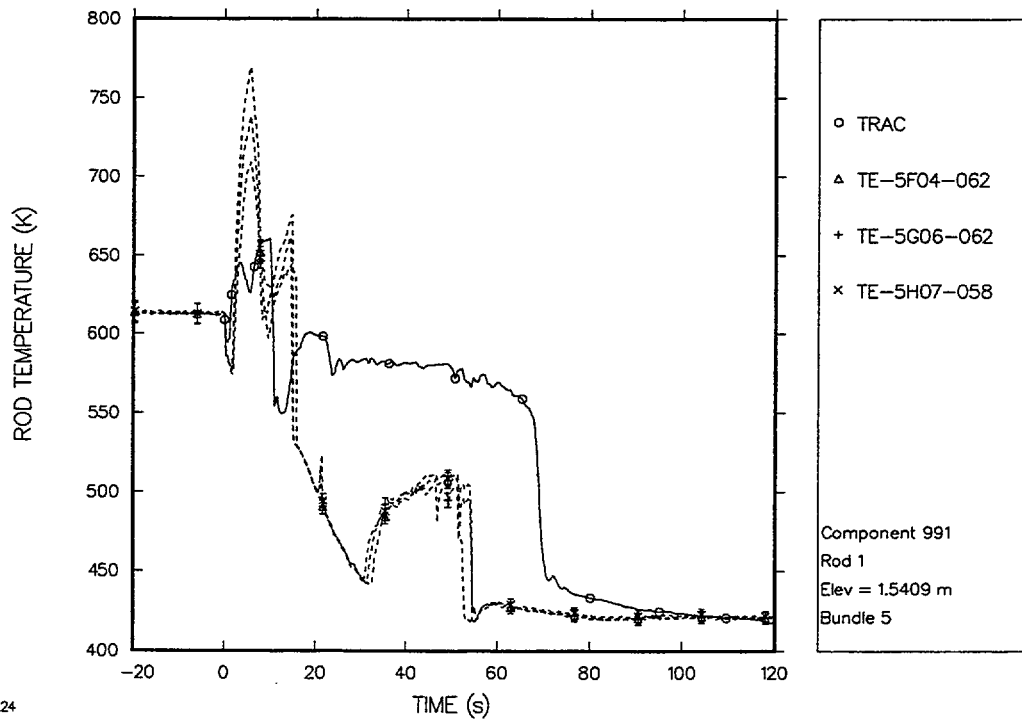


Fig. 5.1-42. Cladding surface temperature; Rod 1 elevation = 1.5409 m, reflood trip at 1 s.

5.1-35
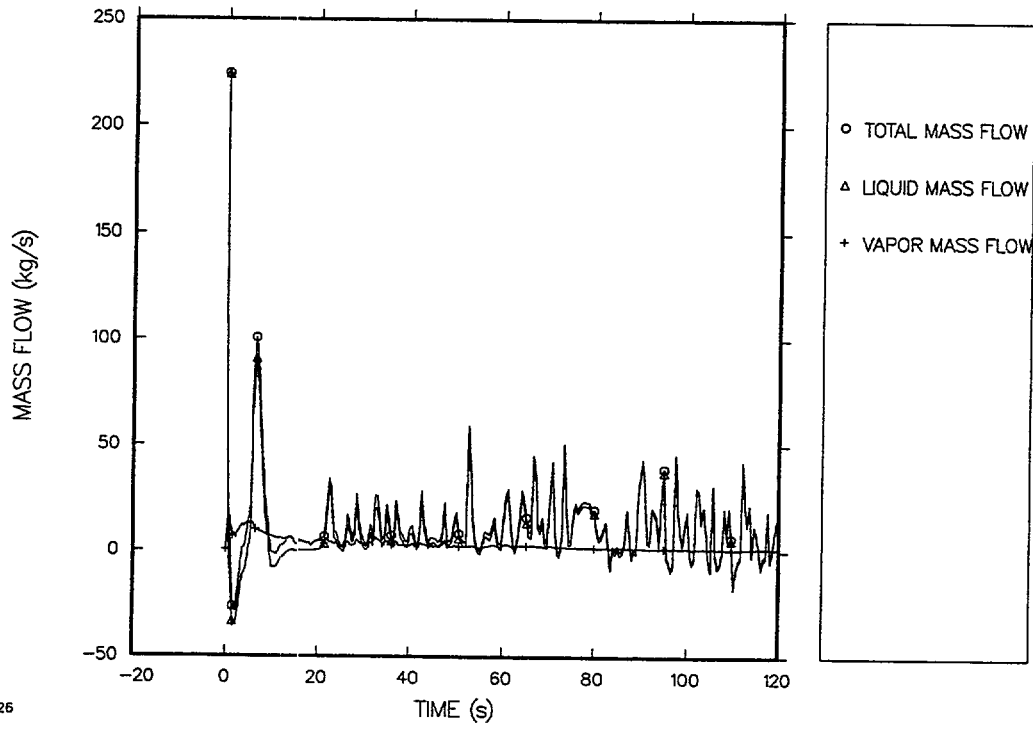
Fig. 5.1-43. Calculated core-outlet mass flow, reflood trip at 1 s.

## 5.2. LOFT Anticipated Transient Experiment L6-1 Simulating the Loss of Steam Load

### 5.2.1. Test Facility Description

The LOFT facility was a fully operational PWR with instrumentation to measure and provide data on the thermal-hydraulic conditions throughout the system. The facility was configured to represent a 1/60-scale-by-power (1/44 by volume) model of a typical 3000-MW(t) commercial four-loop PWR. An axonometric projection and a piping schematic of the LOFT facility are shown in Figs. 5.1-1 and 5.1-2, respectively. References 5.1-1, 5.1-2, and 5.1-3 provide descriptions of the LOFT facility and of the primary system in particular.

The LOFT experimental system consisted of five major systems: reactor, primary coolant, blowdown suppression, emergency core cooling, and secondary coolant. These systems were heavily instrumented to provide continuous monitoring of the nuclear, thermal, hydraulic, and structural processes occurring during the LOFT experiments.

The reactor system consisted of the reactor vessel and head, core support barrel, upper- and lower-core support structures, flow skirt, reactor vessel fillers, and nuclear core. The 1.68-m LOFT core was rated at 50 MW(t) and was designed to have the same physical properties as a PWR core. The core contained two basic fuel assembly configurations, square and triangular. The square fuel assemblies contained 225 fuel rod locations, 21 of which were occupied by guide tubes. The triangular assemblies contained 78 fuel rod locations, 8 of which were occupied by guide tubes.

The primary coolant system consisted of two coolant loops connected to the reactor system. Three PWR primary-coolant loops were simulated by the single, intact loop in LOFT. This single LOFT loop was scaled to have the same volume-to-power ratio as the three PWR loops. The broken loop in LOFT simulated the fourth PWR primary-coolant loop, the loop where the break was postulated to occur. The intact loop contained a steam generator, primary coolant pumps, pressurizer, primary coolant venturi (flow measuring device), and intact-loop piping. The intact-loop active steam generator, shown in Fig. 5.1-3, has a secondary side that consists of a U-tube boiler section, a steam dome, and a downcomer. The steam-generator secondary side is connected to an MSFCV, condenser, feedwater pump, auxiliary-feedwater pump, and a feedwater-flow control valve.

The blowdown-suppression system simulated the containment back-pressure response of commercial PWRs during LOCAs and provided containment for the blowdown effluent. The major system components were the blowdown suppression header and downcomers, blowdown suppression tank, and blowdown suppression-tank spray system.

The facility ECCS simulated a commercial-plant ECCS. There were two ECCS trains, each containing an HPIS, the accumulator system, and the LPIS.

LOFT was highly instrumented. A partial list of the measured parameters includes coolant temperature; coolant level; coolant velocity, momentum, and flow direction;

coolant density; coolant pressure; differential pressure; pump speed; coolant flows; and metal temperatures. The available instrumentation is summarized in Ref. 5.1-2.

## 5.2.2. Test Procedure Description

Test L6-1 simulated a loss-of-steam load in a large PWR. The transient was initiated by closing the MSFCV, which increased the steam-generator secondary-side pressure and the two-phase coolant temperature (at the saturation temperature based on the secondary-side pressure). The resulting decreased temperature difference between the primary- and secondary-side coolants then reduced the primary- to secondary-side heat removal, which increased the primary-side temperature and pressure as well. The pressurizer cycling heater, which was turned on at the beginning of the experiment, was shut off automatically at 6.1 s as the primary-side pressure increased above its cycling-heater high-pressure set point. The pressurizer sprayer was initiated at 9.1 s as the primary-side pressure continued to rise above the sprayer low-pressure set point. As the primary-side pressure rose, the high primary-side pressure reactor-core scram set point was reached, causing the reactor-core control-rod system to scram at 21.8 s. Immediately after the control-system scram, the primary-side began to depressurize because of the rapid reduction in reactor-core power. The depressurizing resulted from the primary-side cooldown that was caused by the loss of the reactor-core heat source while the steam generator provided a heat sink. The rising secondary-side pressure (with the MSFCV closed) crossed the MSFCV high-pressure set point, which caused the MSFCV to automatically begin opening at 22.2 s. The secondary-side pressure then began to fall until at 31.4 s, the MSFCV low-pressure set point was crossed. Then the MSFCV stopped opening, began closing, and reached its closed state at 40.6 s. The falling primary-side pressure caused the pressurizer sprayer to be turned off at 30.4 s, the pressurizer cycling heater to be turned on at 31.4 s, and the pressurizer back-up heater to be turned on at 32.5 s. With the MSFCV closed, the secondary-side pressure began to rise again because of the primary-side heat source that resulted from decay-heat power. Based on the MSFCV's high-pressure set point, we again opened it automatically starting at 91.2 s. Based on its low-pressure set point, we closed it automatically starting at 97.8 s, reaching its closed state at 104.4 s. A similar opening and closing of the MSFCV was performed manually (rather than automatically) starting at 312.6 s and ending at 339.4 s with the MSFCV closed. The pressurizer back-up heater was turned off at 415.4 s when the primary-side pressure rose above the back-up heater high-pressure set point. The experiment was terminated at 700 s. No coolant-line break was initiated in this experiment, and the blowdown suppression system was not used. The broken loop was connected to the intact loop through 1-in. warm-up lines during the transient to prevent broken-loop coolant stagnation and its potential effect on the vessel thermal-hydraulic state.

## 5.2.3. TRAC Model

The calculations of two L6-1 plant models are presented, one with the vessel modeled with 1D hydro components and the other with the vessel modeled with a 3D Vessel component. Figures 5.2-4 and 5.2-5 show the respective TRAC-model plant-system loops and the intact-loop steam generator modeled by 1D hydro components. The steam generator used to be modeled with the Stgen component; however, since the Stgen component in TRAC is no longer supported, it is now modeled with separate Pipe, Tee, and heat-structure components. The primary and secondary loops in both plant models are the same. Figure 5.2-6 shows the vessel region that is modeled by 13

1D hydro components and a fuel-rod heat-structure component. Figure 5.2-7 shows the 3D VESSEL hydro component and 11 heat-structure components, 1 heat-structure component to model the fuel rods, and the remaining 10 to model the vessel structural components.

The 1D-vessel TRAC model used for the L6-1 calculation consisted of 40 hydro and 12 heat-structure components. The heat-structure components model the fuel-rod component and the steam-generator structural components. The 3D-vessel TRAC model consisted of 28 hydro and 22 heat-structure components. One of the heat-structure components models the fuel rod, 11 model the steam-generator components, and the remaining heat-structure components model the vessel wall and other structural components. In the 1D plant model, the vessel walls and other internal structure are modeled using the wall-modeling capability in each 1D hydro component. These TRAC models correspond to the LOFT hardware configuration with the following exceptions.

1. The broken-loop quick-opening blowdown values and blowdown suppression tank were not modeled because they were not used in the L6-1 experiment.

2. The LPIS and accumulator of the ECC injection system were not modeled because they were not used in the L6 series of experiments (the HPIS was modeled by Fill component 17 but did not operate during the L6-1 experiment).

3. The pressurizer pressure-operated relief valve (PORV) was not modeled because it did not operate during the L6-1 experiment.

In Fig. 5.2-4, rather than modeling the pressurizer with a single Prizer component, we modeled the pressurizer with two Prizer components, with a Pipe component above and between and a Tee component below the Prizer components. Pipe component 12 was located between the Prizer components to model accurately the pressurizer cycling and back-up heaters using the option for direct power deposited in the coolant. The following difficulties would have been encountered using the heater option available in the Prizer component.

1. The Prizer-component heater option does not control the heaters in the manner that they were operated in the L6-1 experiment.

2. The LOFT pressurizer has both cycling and back-up heaters that could not be simulated using the Prizer-component heater option.

3. The Prizer-component heater option would have uniformly distributed the deposited energy everywhere in the liquid, whereas the actual energy is deposited only in the liquid near the bottom of the pressurizer where the heaters are located. More discussion on how the heaters were simulated using trip-controlled direct power deposited in the coolant is provided later in this section.

The pressurizer sprayer inlet line is connected to Pipe component 9 at the top of the pressurizer. The Prizer-component sprayer option cannot simulate the actual LOFT sprayer system because it is a means only for controlling the system pressure, not for

modeling the behavior of an actual sprayer. Therefore, the LOFT sprayer was modeled with Valve component 10 to simulate the sprayer fluid-control hardware. The sprayer droplet/mist-generating hardware could not be modeled directly, and as the discussion on calculated results will point out later, this hardware may be the most limiting TRAC-modeling area for this experiment. Reference 5.2-4 reports that when closed, the LOFT sprayer valve has a leakage flow-area-fraction of ~0.025. The TRAC-PF1/MOD1 valve model calculated a steady-state mass flow of 0.01 kg/s using this flow area. Because the primary-side pressure was accurately predicted with this leakage mass flow during the transient in the MOD1 manual sample problem,[5.2-5] we decided to adjust the modified TRAC-PF1/MOD2 valve model to give the same leakage mass flow. The leakage-flow-area fraction was determined to be 0.00686. The LOFT pressurizer never reaches an actual steady-state condition because the heater energy source and sprayer energy sink are not in balance. To ensure a steady-state solution that is consistent with experimental conditions at the start of the transient, a trip-controlled direct power of 5 kW was deposited in the coolant of Pipe component 9 during the steady-state calculation to bring the leaking sprayer liquid to saturation. This small energy addition is terminated at the start of the transient when its controlling trip goes off, hence this heater does not affect the anticipated transient portion of the simulation.

The external surface heat losses in the LOFT facility were reported by Ollikkala[5.2-6] to be a 6-kW heat loss from the pressurizer, a 10-kW heat loss from the steam-generator secondary side, and a total 174-kW heat loss from the primary system (excluding the pressurizer). These heat losses have been included in the TRAC model. By assuming that the surrounding air temperature was 305 K, we calculated the average heat-transfer coefficients to the air in the room based on the outside surface areas of the pressurizer, steam-generator secondary side, and primary system piping.

Evaluating reactor power is based on a point-kinetics model with fuel- and coolant-temperature reactivity feedback. The TRAC default reactor-kinetics parameters were used for 6 delayed-neutron groups and 11 American Nuclear Society (ANS)-72 decay-heat groups. The delayed-neutron and decay-heat-group concentrations were determined from the L6-1 experiment core-power history before the transient.

All control procedures employed in the L6-1 experiment were modeled using the signal-variable, control-block, and trip control-system modeling capability that is available in TRAC-PF1/MOD2. The TRAC model used 21 signal variables, 13 control blocks, and 20 trips. Five signal variables define trip signals and the trip set status. A second control-parameter evaluation pass is required to determine the trip set status and to evaluate six control blocks that use those signal variables after the trips are evaluated on the first control-parameter evaluation pass. The trip set points that trigger control-procedure actions are listed in Table 5.2-1. The sources of information for these set-point values include the best-estimate prediction,[5.2-7] the experimental data report,[5.2-4] the quick-look report,[5.2-8] and the post-test analysis report.[5.2-9] Some discrepancies among the set points in these reports were resolved by determining the actual test conditions from the experimental data report plots at the times when the events took place. Trips are defined and evaluated by TRAC for all these set points. Trip 11, which is defined to control the pressurizer PORV, triggers no action if set ON because the PORV hardware is not modeled. The modeling of the control procedures employed in the L6-1 experiment is described in the following subsections.

A listing of the 1D-vessel steady-state and transient input models is provided in Appendix Q. A listing of the 3D-vessel steady-state and transient input models is provided in Appendix R. Archival storage information for the input models and calculations is provided in Section 5.2.9.

## 5.2.4. Control Procedures

**5.2.4.1. Pressurizer Heaters.** As discussed before in this section, the cycling and back-up heaters are simulated by adding direct power into the coolant in Pipe component 12. The heaters are controlled by four trips, with the pressurizer pressure as a signal variable defining the trip signal for two trips. No control blocks are used. The LOFT pressurizer has two kinds of heaters: a 36-kW cycling heater that is first to come on at a low-pressure set point and last to go off at a high-pressure set point, and a 12-kW back-up heater that supplements the cycling heater if its power is insufficient to maintain the pressurizer pressure. The low-pressure set point and the high-pressure set point of the back-up heater are lower than those of the cycling heater, as shown in Table 5.2-1. The cycling and back-up heaters are controlled by trips 13 and 14, respectively. The trips, which have positive identification (ID) numbers, are not evaluated during the steady-state calculation where trip 13 has an input-specified set status (ISET) of 1, defining it to be ON$_{forward}$, and trip 14 has an input-specified set status of 0, defining it to be OFF. Hence, the cycling heater is on and the back-up heater is off during the steady-state calculation.

A Pipe component allows the input of only one power-deposited in-the-coolant table. Splitting Pipe component 12 into two separate Pipe components would be one approach to modeling two different heaters. However, because the heaters are at the same locations, we decided to model both banks of heaters using only one Pipe-component power table, as follows:

1.  A trip-controlled trip with ID -24 was defined to have a trip-signal value that is the sum of the ISET values of trips 7, 7, 13, and 14. The trip signal of trip -24 is also used to define the power-table independent variable by signal variable 21. Trip 7 has an input-specified ISET = -1, which is not reevaluated during the steady-state calculation because the trip ID is positive. The negative-valued ID for trip -24, however, results in it being evaluated each steady-state calculation time step.

2.  During the steady-state calculation, the ISET values of trips 7, 13, and 14 are -1, 1, and 0, respectively, which results in the trip -24 trip signal and signal variable 21 having a value of (-1 -1 +1 +0 = -1). The power-deposited in-the-coolant table of Pipe component 12 (shown in Fig. 5.2-8) for an abscissa-coordinate value of -1 defines a power of 398 W during the steady-state calculation. This is equal to the Pipe component 12 outer-surface heat loss to the air and is done to achieve a steady-state solution in this component.

3.  At the start of the transient, trip 7 is set OFF (ISET = 0). Hence, during the transient calculation, the trip -24 trip signal and signal variable 21 have the value 0 if both trips 13 and 14 are OFF, 1 if trip 13 is ON and trip 14 is OFF, and 2 if both trips 13 and 14 are ON. Therefore, the power table defines a power

level of 0 if both heaters are off, 36 kW if only the cycling heater is on, and 48 kW (36 kW + 12 kW) if both heaters are on. Thus, the trip-controlled trip signal sums the set status of trips 7, 7, 13, and 14, which defines four different power states for the pressurizer cycling and back-up heaters as shown in Table 5.2-2. In this way, the control procedure simulates the actual dual-heater control system during the transient calculation.

**5.2.4.2. Pressurizer Liquid Level.** The pressurizer liquid level is not a control-procedure parameter. The level is calculated for plotting purposes only, using control blocks -1 and -2 (control blocks are designated by negative ID numbers to distinguish them from signal variables having positive ID numbers). Control block -1 sums the liquid levels in Prizer and Pipe components 13, 12, and 8 (which are determined by signal variables 6, 7, and 8, respectively). Adding the liquid level was not necessary in Pipe component 9 because it has only saturated vapor with a small number of liquid droplets from the pressurizer sprayer. The calculated liquid level in the pressurizer is offset by having control block -1 add -0.11 m to the control block -1 liquid level. This was done to account for the slight difference between the actual pressurizer geometry and the right-circular cylinder geometry of the TRAC model. The −0.11 m offset value was determined from the steady-state solution where defining the same liquid volume in the pressurizer resulted in the TRAC model having a control block -1 liquid level that is 0.11 m too high.

**5.2.4.3. Pump-Speed Controller.** During the steady-state calculation, two CSS controllers were used to adjust the pump-impeller rotational speed of the intact-loop pumps to achieve the desired mass flow through the intact loop. The measured mass flow through the intact loop in the L6-1 experiment was 478.5 kg/s in the hot leg between the pressurizer connection and the warm-up line connection to the broken-loop cold leg. Because of the warm-up lines to the broken loop, the coolant mass flow at the hot-leg location is different from the sum of the mass flows through the two pumps connected in parallel. The necessity to input the desired mass flow at the pumps for the CSS controllers was complicated further by the requirement that the desired mass flow through each pump had to be specified.

This requirement was resolved by manually adjusting the input-specified, desired coolant mass flow through each pump by performing two iterations of the steady-state calculation. After each iteration, the desired mass flow through each pump was renormalized to adjust the coolant mass flow in the hot leg to the measured coolant mass flow. Then the renormalized mass flow of each pump was adjusted further so that the same pump-impeller rotational speed would be determined for both pumps in the next steady-state calculation. A linear relationship between mass flow and pump-impeller rotational speed was assumed when making this later adjustment. We started with the desired mass flow through each pump at half the measured mass flow through the intact-loop hot leg, and then made the above adjustments after each of two steady-state calculations. The third steady-state calculation then gave the same pump-impeller rotational speeds, and the measured coolant mass flow in the intact-loop hot leg was significantly accurate to almost four digits. The converged pump-impeller rotation speed was then held constant throughout the transient calculation.

**5.2.4.4. Steam-Generator Secondary-Side Feedwater Controller.** Feedwater control maintains the liquid inventory on the steam-generator secondary side during the steady-state calculation through a correlation to the desired steam-generator downcomer liquid level. The void fraction of vapor on the steam-generator secondary side is determined in Pipe component 20 and Tee components 21 and 22 by signal variables 11 through 15. Their summed vapor volume on the steam-generator secondary side is determined by control blocks -3 through -6 and then converted to a steam-generator downcomer liquid level by the tabular-data correlation of control block -7.

The tabular data in control block -7 are derived from a plot of the collapsed liquid level vs liquid volume given in Ref. 5.2-1. We had to convert the data from dependence on a collapsed liquid level at a no-flow condition to an uncollapsed liquid level during an at-power flow condition because TRAC must convert the calculated liquid volume to an uncollapsed liquid level for comparison with the measured steam-generator downcomer liquid level. Hence, the feedwater liquid mass flow is adjusted during the steady-state calculation to have the uncollapsed liquid level determined by control block -7 equal the measured steam-generator downcomer liquid level, which should provide the same steam-generator liquid inventory as in the experiment. This was done by noting in Ref. 5.2-1 that the steam-generator secondary-side liquid volume at full power (50 MW) is 2.52 m$^3$ with an uncollapsed liquid level of 3.2004 m. From the plot in Ref. 5.2-1, the liquid volume is 3.8166 m$^3$ for a collapsed liquid level of 3.2004 m. To generate tabular data for the uncollapsed liquid level vs liquid volume, the liquid volumes in the collapsed liquid-level plot have been multiplied by the ratio 2.52/3.8166.

Fill component 24 defines the steam-generator secondary-side feedwater mass flow by control block -10 During the steady-state calculation, this is based on a proportional and integral (PI) controller evaluated by control block -8 that drives the TRAC-calculated liquid level of the steam-generator downcomer. This level was determined by control block -7 to equal the measured level of 3.183 m above the top of the boiler tube sheet. During the transient calculation, control block -10 defines the output signal of control block -9, which ramps the feedwater mass from its steady-state value of 20.1 kg/s to zero from 1 to 12 s during the transient, as defined in the experiment specifications.

**5.2.4.5. Steam-Generator Secondary-Side Main Steam-Flow Control Valve Controller.** An automatic-control procedure was applied to the Valve component 23 MSFCV to adjust (during the steady-state calculation) and constrain (during the transient calculation) the steam-generator secondary-side pressure. A constrained steady-state (CSS) controller was used to adjust the valve flow-area fraction to achieve the desired steady-state secondary-side pressure of 5.37 MPa measured in the steam dome. The mesh-cell pressure a half mesh-cell length upstream of the valve interface (five mesh cells downstream of the steam dome) was monitored by the controller and had to be adjusted to a desired value of 5.3411 MPa to achieve the desired pressure of 5.37 MPa in the steam-generator steam dome. The pressure change between those locations was determined by performing one iteration of the steady-state calculation.

For the transient calculation, different control procedures before and after the reactor-core power scram were applied to the MSFCV. At the start of the transient, the MSFCV was ramped-closed at a valve-stem rate of 5% s$^{-1}$ Starting from a 63.8% valve-stem

opening at steady state, the MSFCV was ramped closed in 12.76 s. Reference 5.2-4 states that the MSFCV closure was initiated at the start of the transient, but the timing of the measured pressures in its plots indicates that the closure was initiated at 2.0 s into the transient. Hence, the MSFCV was ramped-closed by TRAC from 2 to 14.76 s during the transient. After the reactor-core power scram, a second control procedure specified opening the MSFCV at a valve-stem rate of 5% $s^{-1}$ when triggered by the steam-generator steam-dome pressure exceeding a high-pressure set point. This control procedure also specified closing the MSFCV at the same rate when triggered by the steam-generator steam-dome pressure falling below a low-pressure set point. The effect from this control procedure was that the MSFCV was closed most of the time, with periodic short time intervals of opening and closing the MSFCV to relieve a steam-generator secondary-side pressure buildup.

Both control procedures were implemented during the transient by control blocks -11, -12, and -13. Control block -11 outputs the trip set status (ISET) of either trip 20, which implements the ramped closure before the reactor-core power scram, or trip 22, which constrains the steam-generator secondary-side pressure from exceeding the high- and low-pressure set points after the reactor-core power scram. The input to control block -11 is -1 or 0 from trip 20 and -1, 0, or 1 from trip 22. The respective values of -1, 0, or 1 correspond to the valve closing, remaining stationary, or opening. A gain factor of 0.05 in control block -11 results in a valve-stem movement rate of 5% $s^{-1}$. Thus, control block -11 outputs -0.05, 0.0, or 0.05, which directs the valve to close at a 0.05 valve-stem movement per second rate, to remain stationary, or to open at a 0.05 valve-stem movement per second rate, respectively. Control block -12 is an integrator that determines the new valve-stem position from its previous position by adding the control block -11 rate integrated over the time step. Control block -13 converts the valve-stem position to its equivalent flow-area fraction from tabular data to define the valve flow-area fraction applied to Valve component 23.

Trip 22 constrains the steam-generator secondary-side pressure after the reactor-core power scram. Trip 22 has trip-set-point-factor tables applied to both its upper and lower pressure set points because the pressure set points where MSFCV movement was initiated were observed to vary slightly during the experiment, as shown in Table 5.2-1.

Trip 22 also implements special time-step data for 3.0 s after the trip is set ON. The reason is not the need for special time-step data but rather for having TRAC estimate by linear extrapolation the time that the trip is expected to cross a set point and change set status. Before evaluating the time step where a change in the trip set status is expected to occur, TRAC reduces the time-step size so that the set point is crossed at the end of the time step. Therefore, the trip action is implemented at the correct time when the set point is crossed rather than at some fraction of the time step later. Trips that implement special time-step data also implement this more precise timing of their set-status change and the action they initiate. The precise opening and closing of the MSFCV, based on the timing of pressure set points being crossed, subsequently was very important for accurately predicting the behavior of the L6-1 experiment.

During the L6-1 experiment, the trip 22-implemented automatic control procedure activated valve movement twice. Then the operator manually opened and closed the MSFCV, starting at 312.6 s and ending at 339.4 s (with the valve closed). A third control

procedure is needed to override the second procedure and to implement the manual opening and closing, but it was not modeled. The 26.8-s time interval of that valve movement would open the MSFCV to a valve-stem position of 0.67 and release more than three times the steam than the behavior of the measured pressure after 320 s would indicate. Either one or both measured times for manual control on the valve movement is incorrect, or the rate of valve-stem movement is less than 5%/s when under manual control. Rather than implement such an uncertain third control procedure, we decided to leave control of the MSFCV with the second procedure. Consequently, under automatic control, the MSFCV was opened and closed between 353.2 to 366.1 s and 415.2 to 428.9 s for the respective 1D- and 3D-vessel-model TRAC-PF1/MOD2 calculations, so that the simulation out to 700 s was not too different from the measurements.

### 5.2.5. Comparison of Predicted and Measured Results.

The L6-1 calculations presented herein were performed with an earlier version of the TRAC-M/F77 code, Version 5.4.29R9+. It was subsequently discovered that the 3D-model calculations performed with the release version of the TRAC-M/F77 code, Version 5.5, were incorrect because of a code bug. The code bug was fixed in the TRAC-M/Fortran 90 code; the 3D-model calculations performed with the TRAC-M/Fortran 90 code gave nearly identical results as the results of the 5.4.29R9+ code. This code bug did not affect the 1D-model calculations. The 1D-model calculations performed with the 5.4.29R9+ code were identical to the 1D-model calculations performed with Version 5.5.

### 5.2.5.1. Steady-State Calculations. 

Table 5.2-3 shows the LOFT experiment-L6-1-measured initial conditions and the TRAC steady-state calculation results after 200 s of problem-time evaluation. Fortunately, for most of the steam-generator secondary-side parameters, the results from both TRAC codes were at the midrange of their oscillations at 200 s, so agreement with the measured values of all parameters is very good.

Time plots of calculated results from the 1D and 3D steady-state calculations and the measured initial conditions are shown in Figs. 5.2-9 through 5.2-20. Figure 5.2-9 shows the pump-impeller rotational speeds that are controller adjusted to achieve the desired 478.5.2 kg/s mass flow through the intact-loop hot leg shown in Fig. 5.2-10. The TRAC results are in excellent agreement with the measured pump-impeller rotational speed, which indicates that the reversible and irreversible form losses around the intact loop are accurately modeled. Figures 5.2-11 and 5.2-12 show the intact-loop steam-generator primary-side inlet and outlet liquid-coolant temperatures to be in good agreement with the measured temperatures. Figures 5.2-13 and 5.2-14 show the primary-side pressure in the vessel upper plenum and the secondary-side pressure in the steam-generator steam dome. Figures 5.2-15 and 5.2-16 show the steam-generator secondary-side feedwater-liquid and MSFCV-vapor mass flows. TRAC tends to slightly underpredict the measured MSFCV-vapor mass flows. Figure 5.2-17 shows the steam-generator downcomer level, which is monitored to control the feedwater mass flow. The MSFCV flow area is shown in Fig. 5.2-18. Figures 5.2-19 and 5.2-20 show the time-step size and CPU time of the 1D and 3D TRAC calculations. Both steady-state calculations were able to proceed at its maximum specified time-step size. The 3D calculation took slightly less CPU time to complete its calculation.

**5.2.5.2. Transient Calculations.** The transient calculations were initiated from the last restart-data dump of the steady-state calculations at 200 s. All parameter information defining the initial conditions for the transient came from the dump-restart file. The experimentally measured and TRAC-calculated times of the events that occurred during the LOFT L6-1 experiment transient are shown in Table 5.2-4. A small difference in the calculated pressure resulted in a large difference in the time that a set point was crossed in the TRAC calculations.

The time plots of the experimental data and TRAC calculated results are shown in Figs. 5.2-21 through 5.2-37. The experimental data were processed from a LOFT L6-1 experimental data tape for the TRAC-PF1/MOD1 developmental assessment for the initial 250 s of the transient. For developmental assessment, the first 250 s of the transient were plotted because most of the interesting events of the transient occurred then. Figure 5.2-21 shows that the reactor-core neutronic power was scrammed at 21.8 ± 0.2 s because the intact-loop hot-leg pressure exceeded its 15.77-MPa high-pressure set point (Table 5.2-1). The TRAC-PF1/MOD2 calculations predicted the power scram to occur at 18.3 ± 0.1 s, whereas the TRAC-PF1/MOD1 calculations predicted 16.8 ± 0.2 s. Before the scram, reactivity feedback from a rise in the core-averaged fuel and coolant temperatures reduced the reactor-core power by about 10%. Underpredicting the reactivity-feedback effect by 5% to 10% because of its reactor-core point-kinetics model probably causes TRAC's early prediction of the scram time. The better prediction by TRAC-PF1/MOD2 is due to having corrected the MOD1 evaluation of the core-averaged reactivity-feedback parameters in MOD2 by eliminating the donor-cell effect.

The pressure in the vessel upper plenum is shown in Fig. 5.2-22. The initial closing and periodic opening and closing of the MSFCV during the transient varies the heat sink provided by the steam-generator secondary side, resulting in these primary-side pressure oscillations in the vessel. The pressurizer cycling and back-up heaters and sprayer react to constrain these pressure oscillations based on a similar pressure variation in the pressurizer steam dome shown in Fig. 5.2-34. These effects and the differences in the calculated results will be discussed later.

The liquid mass flow in the intact-loop hot leg, shown in Figs. 5.2-23 and 5.2-24, varies only a small amount during the transient because the intact-loop pump-impeller rotational speed continues to operate at its 334-rad/s initial condition, and the primary side remains single-phase liquid. The only difference between the two plots is in the measured data from two different flow-transmitter detectors, which bound the magnitude and time variation of the results from all four TRAC calculations.

Figures 5.2-25 and 5.2-26 show the liquid temperature at the intact-loop steam-generator primary-side inlet and outlet. All TRAC results lie within the measurement uncertainty of the data. The observed time delay in the measured temperature-difference reduction is longer than expected because of the loss of the steam-generator heat sink (caused by the initial closing of the MSFCV) and the loss of the reactor-core heat source (caused by the power scram). The timing of the measurements is suspect because we see a consistent behavior with the timing of those events in the TRAC temperature variations during the first 50 s.

After the power scram, to constrain the steam-generator secondary-side steam-dome pressure between the 6.75.2-MPa low-pressure and 6.99-MPa high-pressure set points, respectively (which are somewhat lower after 75 s), the MSFCV is opened and closed three different times for short time intervals as shown in Fig. 5.2-27. The timing of the first two MSFCV movements is accurately predicted by the TRAC calculations. The timing of the third MSFCV movement at 312.6 s (data not shown) was done manually and said to be open two-to-three times longer than what would have resulted in the measured secondary-side pressures for the remainder of the transient. Because of this uncertainty in the manual adjustment, the TRAC-calculation control procedures were left under automatic control that was based on pressure set points rather than on the stated manual control. Because the manual adjustment probably was done before the automatic control procedure high-pressure set point was reached, only the MOD1/3D MSFCV movement at 239.4 s is suspected of being too early. We observed that for all four TRAC calculations, initiating the opening of the MSFCV had to be delayed by the same 2.0 s as when initiating the initial closing of the MSFCV to realize the observed timing of the steam-generator secondary-side pressure variation. A 2.0-s delay in initiating the closing of the valve, however, caused the pressure to fall too far. Because of the slightly different rates of steam-generator secondary-side pressure variation among the four calculations during the MSFCV movement, delay times of 0.0 s (MOD1/1D), 1.6 s (MOD1/3D), 0.35 s (MOD2/1D), and 1.0 s (MOD2/3D) were applied to achieve the same vapor loss during the first opening of the MSFCV and during the pressure recovery afterwards.

Vapor (steam) mass flow through the MSFCV and feedwater liquid mass flow is shown in Figs. 5.2-28 and 5.2-29. The apparent discrepancy between the observed and calculated vapor mass flows when the MSFCV is fully closed is felt to be due to the measured flow within the dead-band range of the instrument. The LOFT documentation does not give a leakage rate for this valve when it is closed. Although most closed valves leak a small amount, no leakage through the closed MSFCV was modeled by TRAC. The accuracy of the evaluated timing of the MSFCV second opening adjustment appears to indicate that this assumption is valid. The feedwater control valve (Fill component 24) was ramped closed from 1 to 12 s with no leakage modeled after closure. The steam-generator steam-dome pressure that was monitored and constrained between the above pressure set points by periodic openings of the MSFCV is shown in Fig. 5.2-30. One can see that the timings of the second and third openings of the MSFCV are very sensitive to small errors in the calculated steam-generator steam-dome pressure because of its asymptotic approach to a pressure level slightly above the high-pressure set point. The steam-generator downcomer liquid level, shown in Figure 5.2-31, indicates that the TRAC-calculated levels and the measured levels do not agree. The measured level is based on a differential-pressure transducer measurement of the hydraulic head in the steam-generator downcomer, which includes both static and dynamic effects. The TRAC level is based on the steam-generator secondary-side liquid volume being converted to an uncollapsed liquid level in the steam-generator downcomer (described in Section 5.2.4.4). We feel that these two different approaches for defining the steam-generator downcomer liquid level are inconsistent and that the difference in measured and calculated levels in Fig. 5.2-31 is not real. Comparing the calculated pressure difference in the steam-generator downcomer would have been a more appropriate means for inferring steam-generator downcomer behavior.

Figures 5.2-32 through 5.2-33 show the thermal-hydraulic behavior of the pressurizer. Whereas the periodic adjustment of the MSFCV drives the dynamics of the experiment by constraining the steam-generator secondary-side pressure (which affects the primary-side to secondary-side heat transfer), the pressurizer sprayer and cycling and back-up heaters are reacting by constraining the pressurizer primary-side pressure (which is affected by the imbalance between the reactor-core decay-heat-after-scram heat source and steam-generator secondary-side heat sink). Figure 5.2-32 shows that the pressurizer sprayer was on from 9.1 to 30.4 s during the initial pressure rise of the entire system after the MSFCV was initially ramped closed. When turned off, the sprayer did not get turned on again during the remainder of the transient by its high-pressure set point. While closed, the sprayer did have a 0.01 kg/s leakage mass flow because of its minimum closure state. The combined power of the 36-kW cycling heater and 12-kW back-up heater, which was deposited in the liquid of Pipe component 12, is shown in Fig. 5.2-33.

### 5.2.6. Lessons Learned and User Guidelines

After converting the input-data file, we combined similar geometry Heat-Structure components (derived from the TRAC-PF1/ MOD1 Core and Vessel components) for calculation efficiency. We specified a few undefined input-data parameters for the HEAT-STRUCTURE components, and enhanced the generalized steady-state calculation to a constrained steady-state calculation to provide a more accurate initial condition for the transient calculation. We also modified the NFF and FRIC array values to model the actual form losses at flow-area changes and defined trip-controlled time-step data to accurately evaluate set-status changes for the trip controlling the MSFCV. Using a GOCVRT-converted input-data file does require such additional modifications to correctly apply the many enhanced features of TRAC-PF1/MOD2.

We also found a few questionable input-data values in several sensitive modeling areas of experiment L6-1 that we modified using referenced data.[5.2-3,5.2-7] Performing an appropriate level of input-data checkout, especially in sensitive modeling areas, is always a good practice. Having detailed documentation notes on the development of the input-data file from which one starts is especially helpful during the data checkout. Any changes made to the data should also be incorporated into that documentation. Such documentation on the TRAC-PF1/MOD1 input-data file was minimal, which makes performing the checkout process more difficult. Knowledge of the assumptions made and the calculations performed in determining parameters, such as the large K factor at the bottom of the steam-generator downcomer and boiler section, is necessary to assess the appropriateness of the parameter for modeling the equipment and transient.

Converting an input-data model from a different experiment requires that the user also consider the appropriateness of the accuracy level of different aspects of the model for the experiment of interest. For example, a 1D component model for the vessel may be appropriate in another experiment but not in the experiment of interest for which the user has converted the input-data file. Such was not the case here, even though we did obtain a coarse-mesh 3D Vessel component from a LOFT L2-6 experiment input-data file for analyzing the LOFT L6-1 experiment. The 1D component model for the vessel is acceptable for the LOFT L6-1 experiment because its results were about the same as the results from the 3D Vessel component model. This may not be so in a vessel region

where the coolant becomes two phase or where internal circulating flows are important. One reason for analyzing both vessel models was to show that the calculation times were similar. It is recommended that the Vessel component be used to model a vessel even if the vessel is intended to be modeled in 1D flow.

## 5.2.7. Conclusions

The input-data model for LOFT experiment L6-1 was checked out in an appropriate manner for this developmental assessment problem. The steam-generator, pressurizer, and intact loop received more attention because they were the more sensitive modeling areas that affect the transient of the LOFT L6-1 experiment. Other system modeling areas were not checked out as thoroughly because they have less effect on the behavior of the LOFT L6-1 experiment. The calculated results show that TRAC accurately predicted the pressure-sensitive behavior of the LOFT L6-1 experiment. TRAC results agreed with almost all experimental measurements within their range of uncertainty. The situations of disagreement have in most cases been attributed to suspect data measurements.

The two modeling situations recognized as potentially deficient were TRAC's evaluation of heat transfer between vapor and the sprayer liquid droplets falling in the pressurizer steam dome and evaluation of the modeling inconsistency in how the steam-generator downcomer liquid level was experimentally measured and defined by the TRAC input-data model. It was observed that the slow rise in primary-side pressure while the MSFCV was closed was very sensitive to a small amount of vapor quenching in the pressurizer steam dome caused by a very small mass-flow leakage through the closed pressurizer-sprayer valve. It is felt that TRAC evaluates a sprayer-liquid droplet size that is too large as a result of underestimating the liquid-vapor interfacial drag based on the flow regime. Hence, the heat transfer between the vapor and liquid droplets is too low, which in turn results in less vapor quenching in the pressurizer steam dome and a higher rate of pressure rise. Another cause might be not having enough leakage mass flow through the closed sprayer valve. We chose to model the same leakage mass flow that we used in an earlier TRAC-PF1/MOD1 calculation of this experiment.

The steam-generator downcomer liquid-level differences are probably due to the measured liquid level being derived from differential-pressure measurements. The TRAC-defined liquid level, however, is based on converting the steam-generator secondary-side liquid volume to an uncollapsed liquid level in the downcomer that is based on collapsed liquid level data. Such a relationship is defined in Ref. 5.2-1 and converted to an uncollapsed liquid level as described in Section 5.2.3.4. A somewhat better indicator of steam-generator downcomer liquid level might be possible if we compare the calculated and measured differential pressures. This would compare a composite of the downcomer liquid-level hydraulic head and pressure loss caused by flow. Agreement between the calculated and measured differential pressures would require that both the downcomer liquid level and mass-flow fraction recirculated through the downcomer be accurately modeled.

## 5.2.8. Code Performance

LOFT Test L6-1 was run on code Versions 5.5 and 5.4.29R9+. The calculation results presented herein are from code Version 5.4.29R9+. The run performance information plus other pertinent comments follow.

1D model steady state

| Platform | Sun Enterprise 3000 |
|---|---|
| Total CPU time (s) | 97.6 |
| Archive location of input model | CFS    /tida/f77da_decks/inl61ss1d |
| Archive location of calculation | CFS    /trac-da/F77DA/nonreflood/ l61-5429r9+targz |

1D model transient

| Platform | Sun Enterprise 3000 |
|---|---|
| Total CPU time (s) | 270.5 |
| Archive location of input model | CFS    /tida/f77da_decks/inl61tr1d |
| Archive location of calculation | CFS    /trac-da/F77DA/nonreflood/ l61-5429r9+targz |

3D model steady state

| Platform | Sun Enterprise 3000 |
|---|---|
| Total CPU time (s) | 94.9 |
| Archive location of input model | CFS    /tida/f77da_decks/inl61ss3d |
| Archive location of calculation | CFS    /trac-da/F77DA/nonreflood/ l61-5429r9+targz |

3D model transient

| Platform | Sun Enterprise 3000 |
|---|---|
| Total CPU time (s) | 306.7 |
| Archive location of input model | CFS    /tida/f77da_decks/inl61tr3d |
| Archive location of calculation | CFS    /trac-da/F77DA/nonreflood/ l61-5429r9+targz |

# REFERENCES

5.2-1  D. L. Reeder, "LOFT System and Test Description (5.5-ft Nuclear Core 1 LOCES)," Idaho National Engineering Laboratory report TREE-1208, NUREG/CR-0247 (July 1978).

5.2-2. C. L. Nalezny, "Summary of Nuclear Regulatory Commission's LOFT Program Experiments," Idaho National Engineering Laboratory report EGG-2248, NUREG/CR-3214 (July 1983).

5.2-3. H. C. Robinson, "LOFT System and Test Description (Loss-of-Coolant Experiments Using a Core Simulator)," Idaho National Engineering Laboratory report TREE-NUREG-1019 (November 1976).

5.2-4. D. L. Batt and J. M. Carpenter, "Experiment Data Report for LOFT Anticipated Transient Experiments L6-1, L6-2, and L6-3," Idaho National Engineering Laboratory report EGG-2067, NUREG/CR-1797 (December 1980).

5.2-5. "TRAC-PF1/MOD1: An Advanced Best-Estimate Computer Program for Pressurized Water Reactor Thermal-Hydraulic Analysis," Los Alamos National Laboratory report LA-10157/MS, NUREG/CR-3858 (July 1986).

5.2-6. H. Ollikkala, "Best-Estimate Prediction for LOFT Anticipated Transient Slow and Fast Rod Withdrawal Experimental L6-8B," Idaho National Engineering Laboratory report EGG-LOFT-5983 (August 1982).

5.2-7. C. D. Keeler, "Best-Estimate Prediction for LOFT Nuclear Experiments L6-1, L6-2, L6-3, and L6-5," Idaho National Engineering Laboratory report EGG-LOFT-5161 (October 1980).

5.2-8. D. L. Reeder, "Quick-Look Report on LOFT Nuclear Experiments L6-1, L6-2, and L6-3," Idaho National Engineering Laboratory report EGG-LOFT-5270 (October 1980).

5.2-9  H. Ollikkala and S. R. Behling, "Posttest Analysis of LOFT Anticipated Transient Experiments L6-1, L6-2, L6-3, and L6-5," Idaho National Engineering Laboratory report EGG-LOFT-6159 (January 1983).

## TABLE 5.2-1

## TRIP SET POINTS FOR EXPERIMENT L6-1

| Parameter | Set Point |
|---|---|
| System low-pressure scram (MPa) | 14.36 |
| System high-pressure scram (MPa) | 15.77 |
| Intact-loop hot-leg high-temperature scram (K) | 583.3 |
| Low primary-coolant mass flow ($kg \cdot s^{-1}$) | 433.5 |
| High core-averaged power scram (MW) | 51.5 |
| Steam-generator secondary-side low liquid-level scram (m) | 2.0 |
| PORV opening set point (MPa) | 16.70 |
| PORV closing set point (MPa) | 16.56 |
| Pressurizer spray on | 15.24 |
| Pressurizer spray off | 14.90 |
| Pressurizer cycling heater on (MPa) | 14.75 |
| Pressurizer cycling heater off (MPa) | 14.93 |
| Pressurizer back-up heater on (MPa) | 14.62 |
| Pressurizer back-up heater off (MPa) | 14.80 |
| HPIS on (MPa) | 13.297 |
| HPIS off (MPa) | 15.500 |
| MSFCV opening set point before reactor scram (MPa) | 5.425 |
| MSFCV opening set point after reactor scram (MPa): | |
| between 0 and 75 s | 6.99 |
| between 75 and 200 s | 6.9764 |
| between 200 s and end of transient | 6.9464 |
| MSFCV closing set point before reactor scram (MPa) | 5.315 |
| MSFCV closing set point after reactor scram (MPa): | |
| between 0 and 75 s | 6.7500 |
| between 75 and 200 s | 6.6500 |
| between 200 s and end of transient | 6.6000 |

## TABLE 5.2-2

## DEFINING THE FOUR POWER STATES OF THE
## PRESSURIZER CYCLING AND BACK-UP HEATERS

| Calculation | Trip 7 ISET | Trip 13 ISET | Trip 14 ISET | Trips 7+7+13+14 ISET Sum | Heater Power (kW) |
|---|---|---|---|---|---|
| Steady-state | −1 | 1 | 0 | −1 | 0.398 |
| Transient | 0 | 0 | 0 | 0 | 0.0 |
| Transient | 0 | 1 | 0 | 1 | 36.0 |
| Transient | 0 | 1 | 1 | 2 | 48.0 |

## TABLE 5.2-3

## LOFT EXPERIMENT L6-1 INITIAL CONDITIONS AND
## TRAC-EVALUATED STEADY-STATE CALCULATION RESULTS

| Parameter | Measured | 1D-Vessel plant model | 3D-Vessel plant model |
|---|---|---|---|
| Reactor-core neutronic power (MW)[a] | 36.9±0.9 | 36.9 | 36.9 |
| Pressurizer pressure (MPa)[a] | 14.78±0.20 | 14.78 | 14.78 |
| liquid level (m) | 1.18±0.07 | 1.182 | 1.182 |
| Intact loop | | | |
| hot-leg mass flow $(kg \cdot s^{-1})$ | 478.5±6.3 | 479.5 | 479.7 |
| hot-leg temperature (K) | 567.5±1.8 | 567.6 | 567.6 |
| cold-leg temperature (K) | 552.8±1.2 | 552.8 | 552.8 |
| Pump impeller rotational speed (rad/s)[b] | 334.0±1.5 | 332.2 | 333.5 |
| Steam-generator secondary-side | | | |
| steam-dome pressure (MPa) | 5.37±0.06 | 5.374 | 5.3 |
| downcomer liquid level (m)[d] | 3.183±0.034 | 3.220 | 3.213 |
| steam mass flow $(kg \cdot s^{-1})$ | 20.1±0.6 | 19.62 | 19.57 |

[a] Specified steady-state condition.

[b] Adjusted to achieve the desired intact-loop hot-leg mass flow.

[c] Constrained within 5.425-MPa maximum value and 5.315-MPa minimum value (Table 5.2-4).

[d] Constrained to 3.183 m [a downcomer liquid level of 2.9464 + 0.00508 x (core power in MW) = 3.134 m at a 36.9-MW reactor-core power was the specified liquid level for the L6-1 experiment].

# TABLE 5.2-4

## LOFT EXPERIMENT L6-1 SEQUENCE OF EVENTS

| Events | Measured Times (s) | 1D Model Predicted Times | 3D Model Predicted Times |
|---|---|---|---|
| MSFCV started to close | 2.0±0.1[a] | 2.08 | 2.08 |
| Pressurizer cycling heater off | 6.1±0.1 | 8.37 | 8.37 |
| Pressurizer spray on | 9.1±0.1 | 11.13 | 10.96 |
| Reactor-core power scrammed | 21.8±0.2 | 18.47 | 18.29 |
| MSFCV started to open | 22.2±0.2 | 22.50 | 22.49 |
| Pressurizer spray off | 30.4±0.1 | 29.48 | 30.08 |
| Pressurizer cycling heater on | 31.4±0.1 | 30.77 | 31.11 |
| Pressurizer back-up heater on | 32.5±0.1 | 32.98 | 33.23 |
| MSFCV started to close | 33.2±0.2[b] | 30.98 | 31.04 |
| MSFCV started to open | 91.2±0.2 | 181.57 | 81.77 |
| MSFCV started to close | 99.2±0.2[b] | 186.84 | 87.90 |
| Pressurizer back-up heater off | —[c] | 128.13 | 168.00 |
| Pressurizer cycling heater off | —[c] | 165.13 | 197.00 |
| MSFCV started to open | 312.6±0.2 | 550.74 | 307.05 |
| MSFCV started to close | 326.0±0.4[b,d] | 557.00 | 312.72 |
| Pressurizer cycling heater on | —[c] | 187.10 | 313.08 |
| Pressurizer back-up heater on | —[c] | 188.75 | 314.15 |
| Pressurizer back-up heater off | 415.4±0.1 | 248.55 | 381.68 |
| Pressurizer cycling heater off | —[c] | 280.55 | 412.00 |
| Pressurizer cycling heater on | —[c] | 556.72 | 662.27 |
| Pressurizer back-up heater on | —[c] | 558.05 | 663.27 |
| Pressurizer back-up heater off | —[c] | 630.10 | — |
| Transient terminated | 700.0±10.0 | 700.01 | 700.64 |

[a] The valve closing was reported to have been initiated at 0.0 s. Pressure data show, however, an ~2-s time delay before any effect of movement in the valve position was observed.

[b] Only the time that the valve was fully closed was reported in Ref. V.B-3. The time when the value started to close was estimated to be midway through the valve-adjustment time interval.

[c] Not observed in LOFT experiment L6-1.

[d] Questionable because having the valve open during such a large time span would thereafter cause the steam mass to discharge more than three times the steam mass consistent with the measured pressure behavior.

Fig. 5.2-1. Isometric view of the LOFT facility.

INEL 3 0587

▲ ECC Rake 1
△ ECC Rake 2
—4— Pipe size in inches
Ɗ Reducer
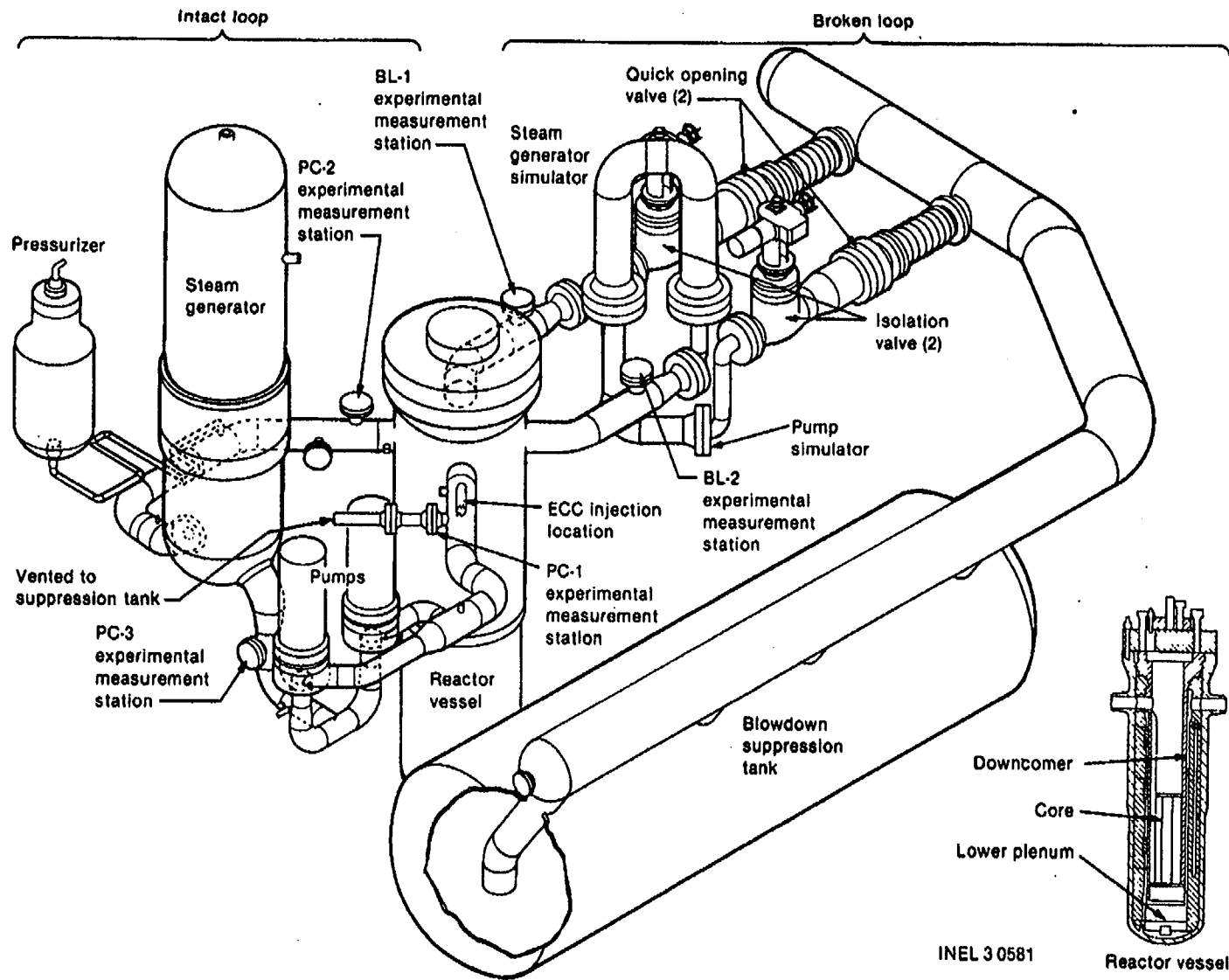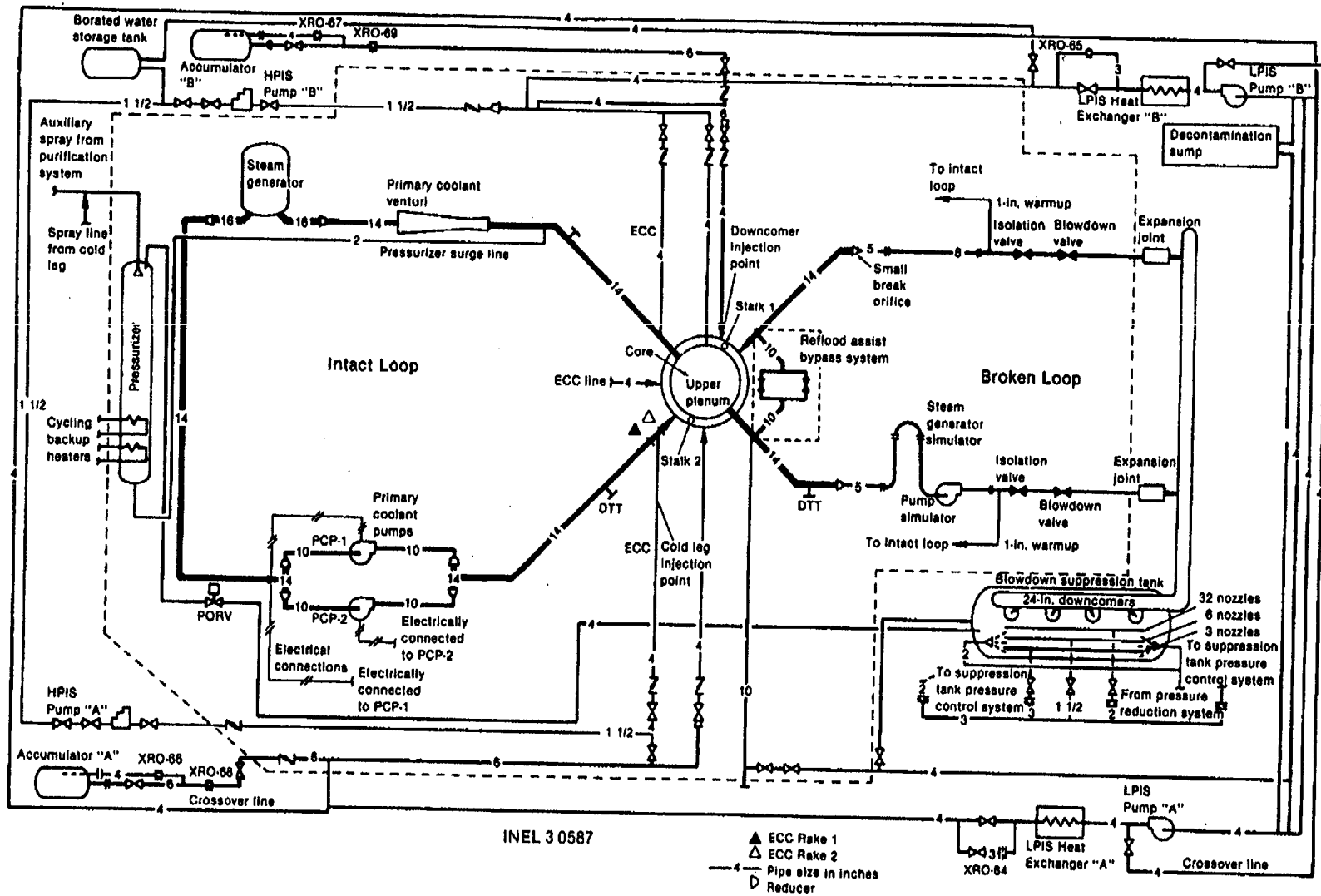
Fig. 5.2-2. Piping schematic of the LOFT facility.
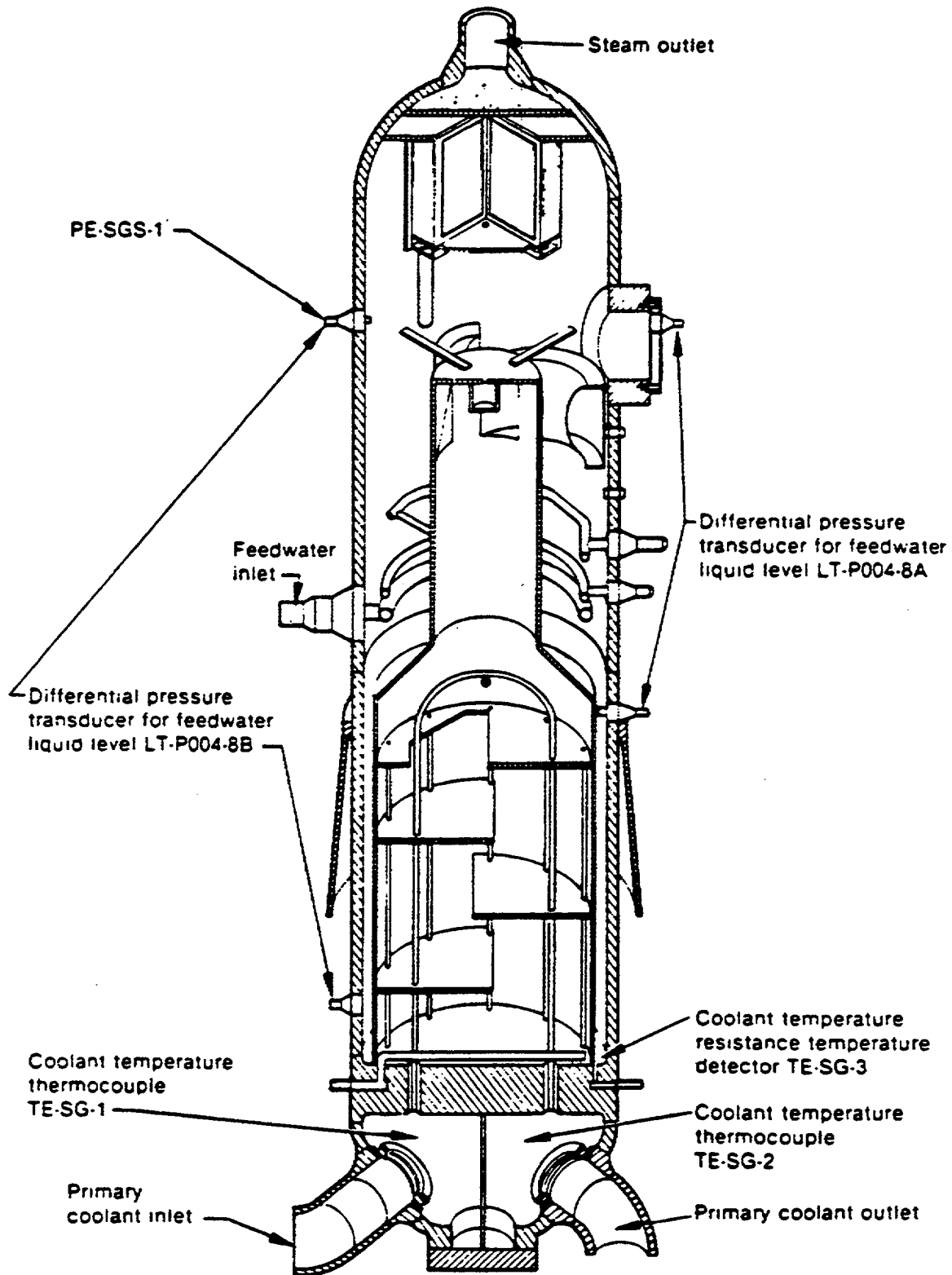
Fig. 5.2-3. Intact-loop steam generator in the LOFT facility.
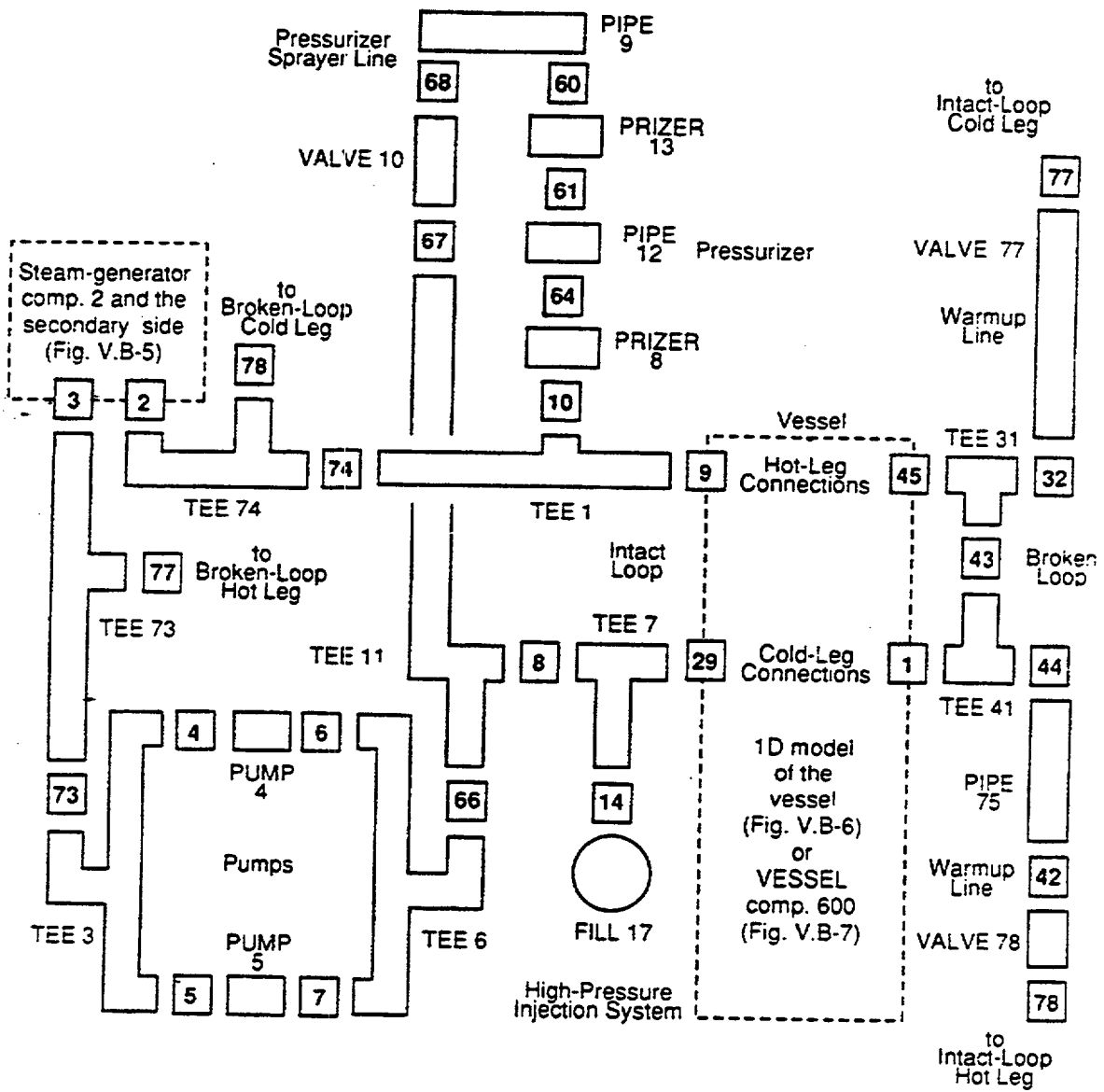
Fig. 5.2-4. TRAC model of the LOFT facility.
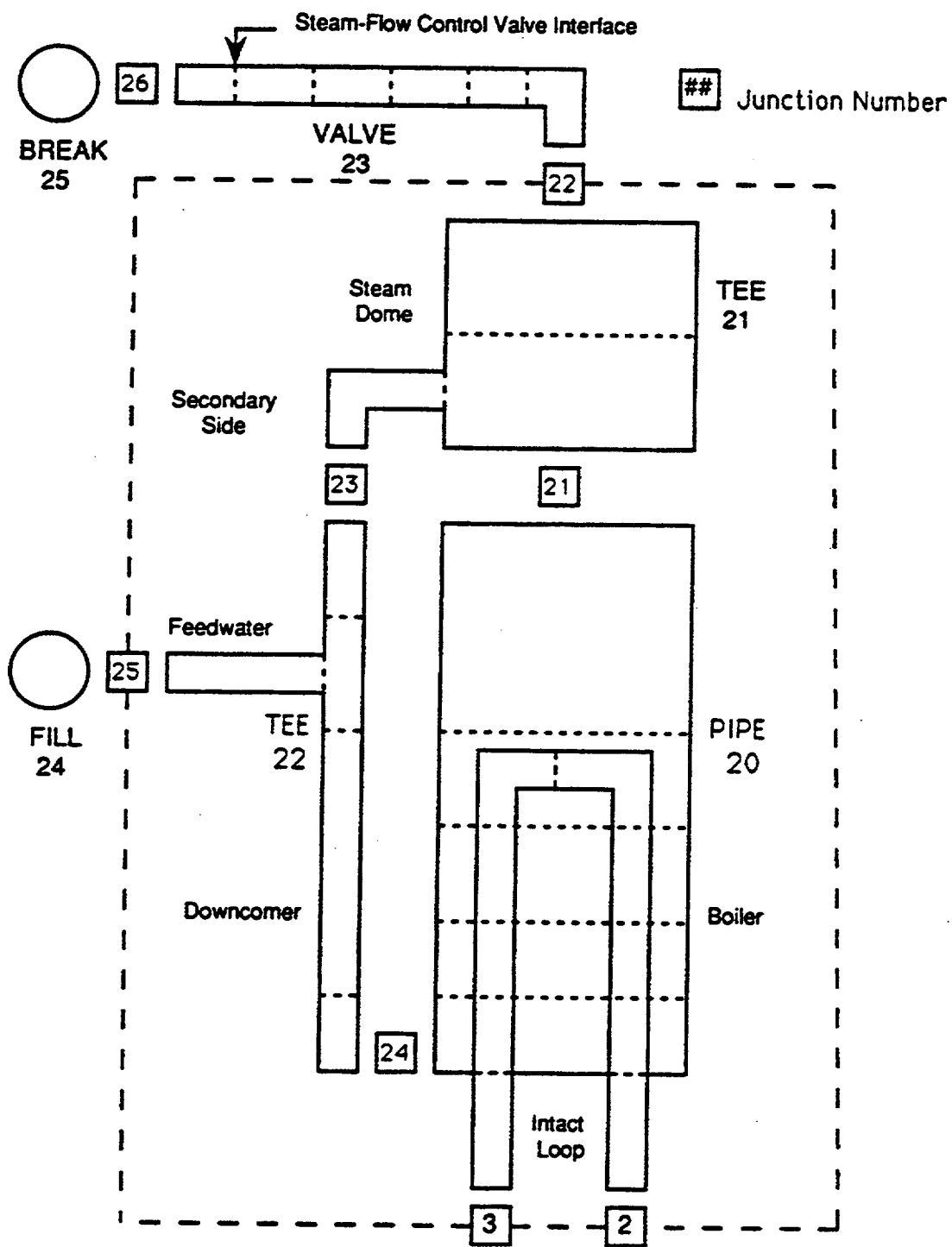
Fig. 5.2-5. TRAC model for the LOFT facility intact-loop steam generator.
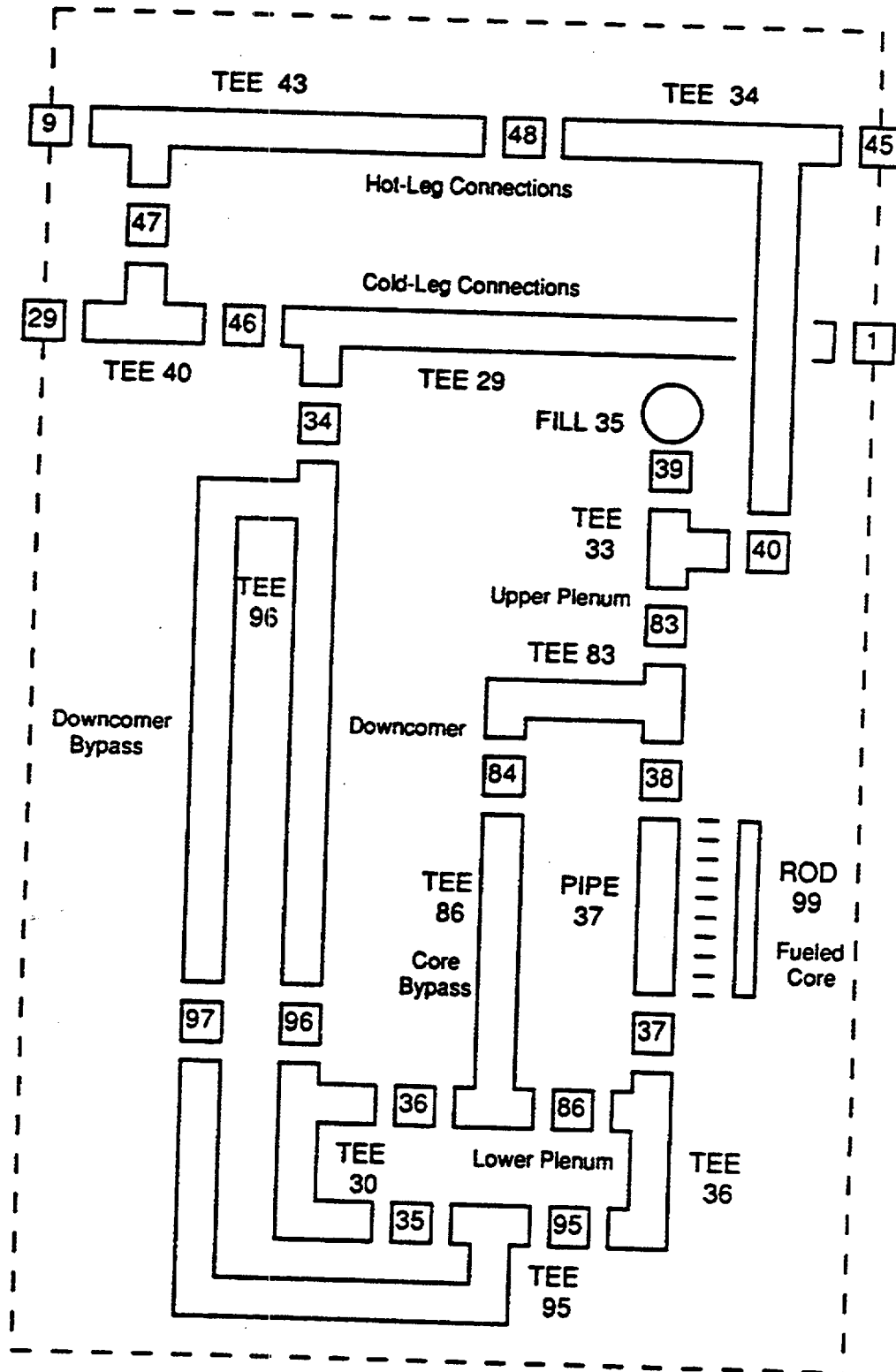
Fig. 5.2-6. 1D hydro components that model the LOFT facility vessel.

VESSEL component 600
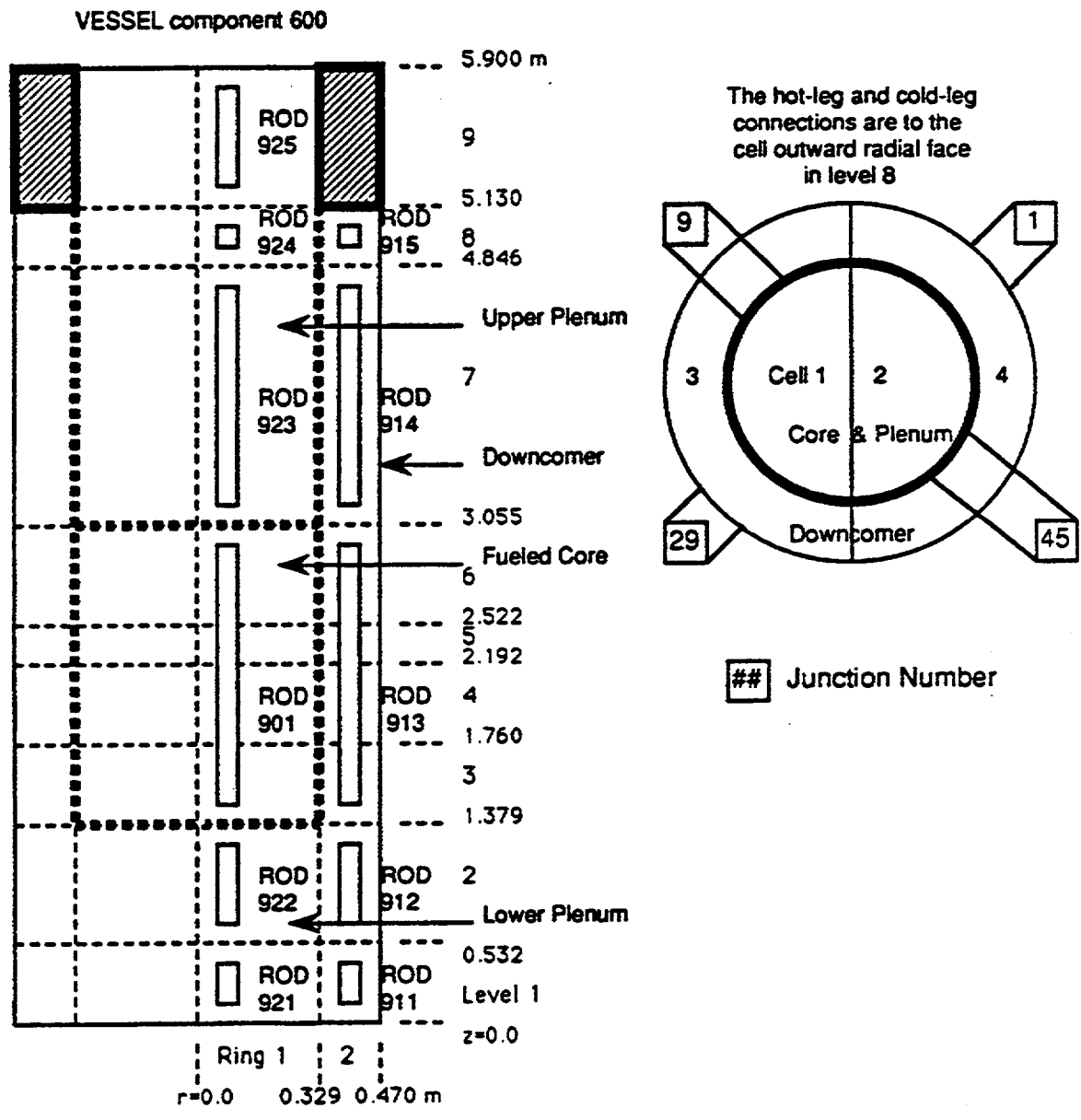


Fig. 5.2-7.  3D Vessel, fueled-core Rod, and structure Rod components modeling the LOFT facility vessel.
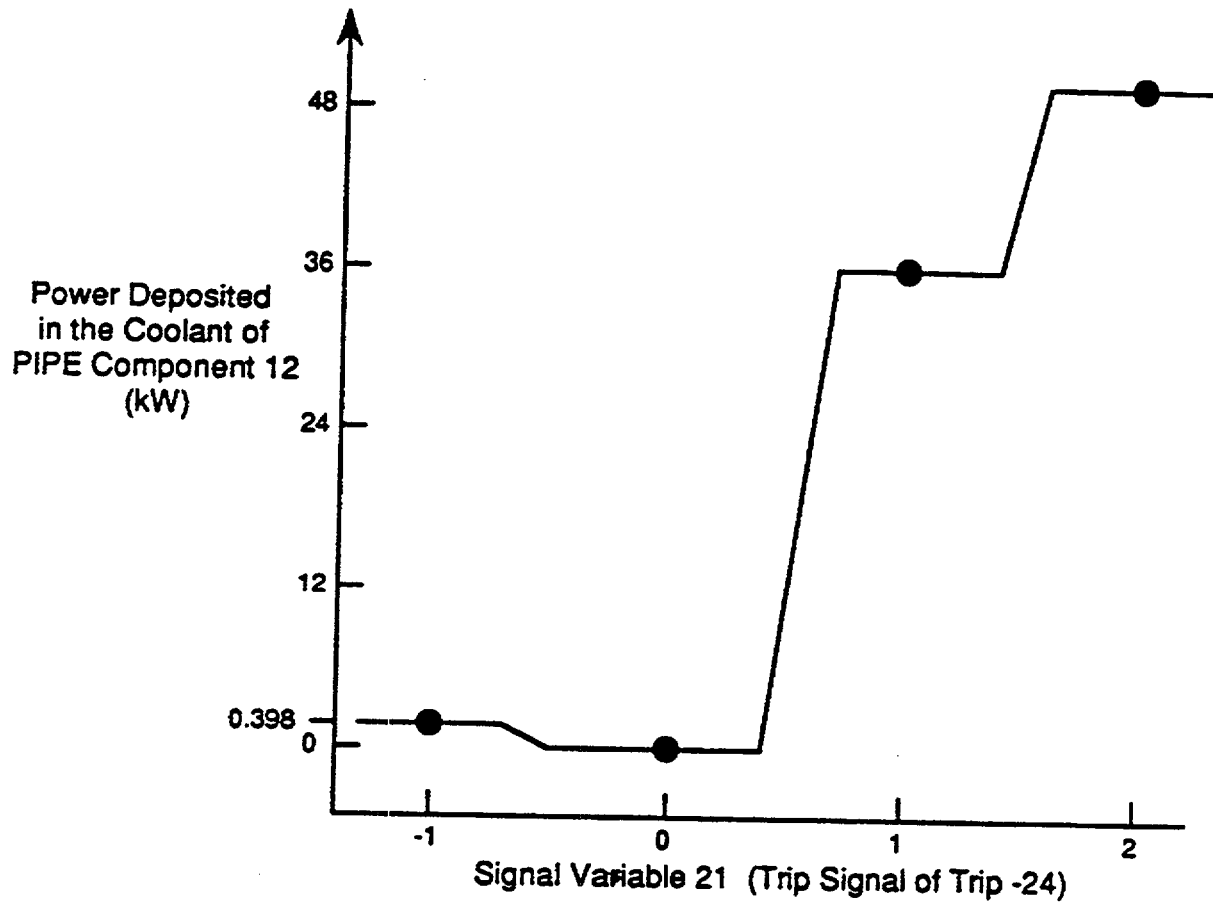
Fig. 5.2-8. PIPE component 12 power-deposited-in-the-coolant table used to define the power generated by the pressurizer cycling and back-up heaters
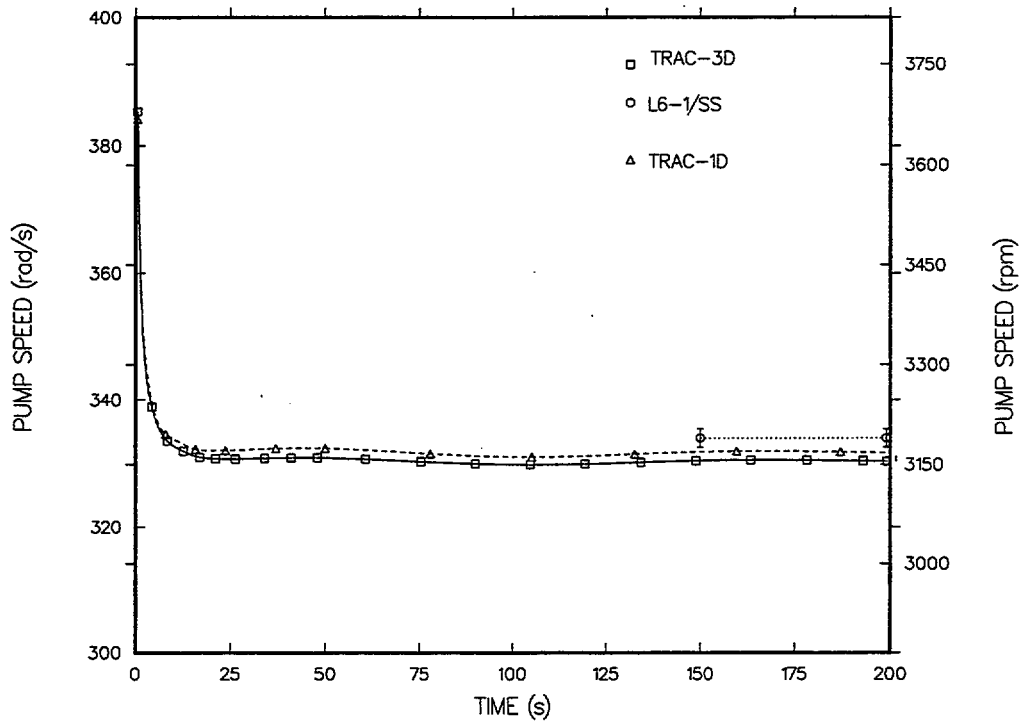
Fig. 5.2-9.    Intact-loop pump-impeller rotational speed, steady-state calculation.
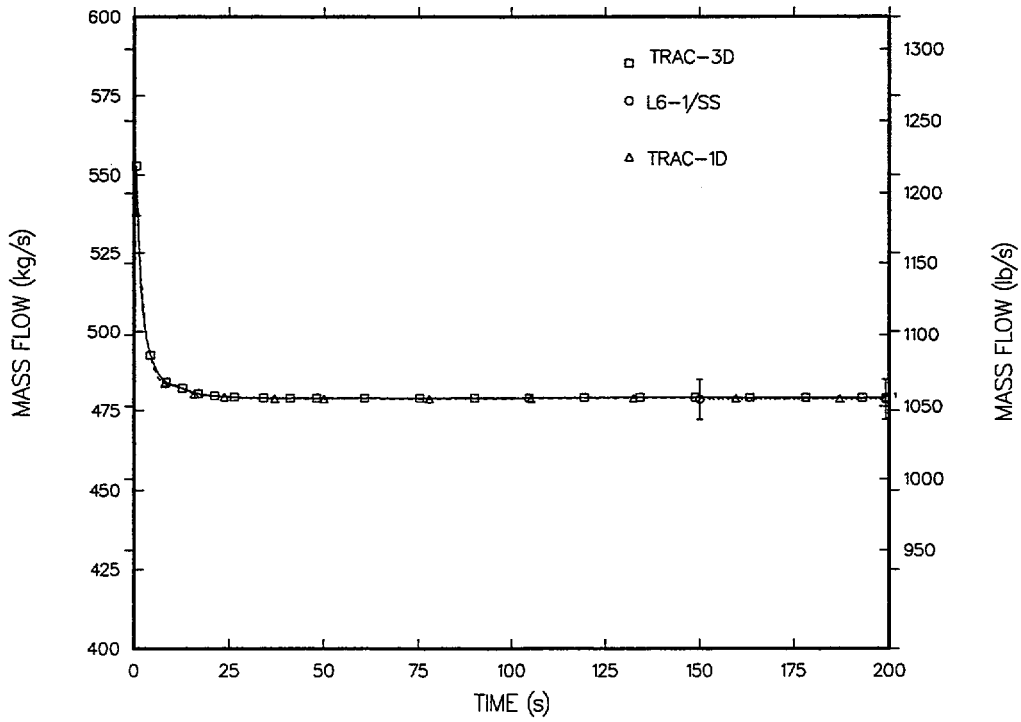


Fig. 5.2-10.    Intact-loop hot-leg coolant mass flow, steady-state calculation.
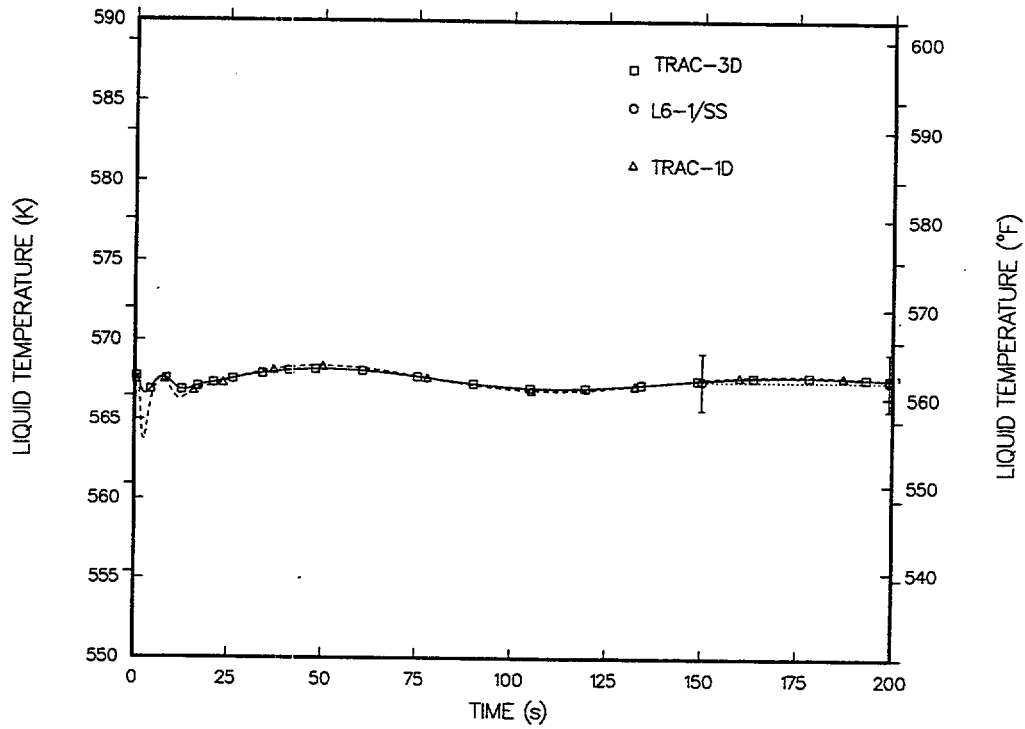
Fig. 5.2-11. Steam-generator primary-side inlet liquid temperature, steady-state calculation.
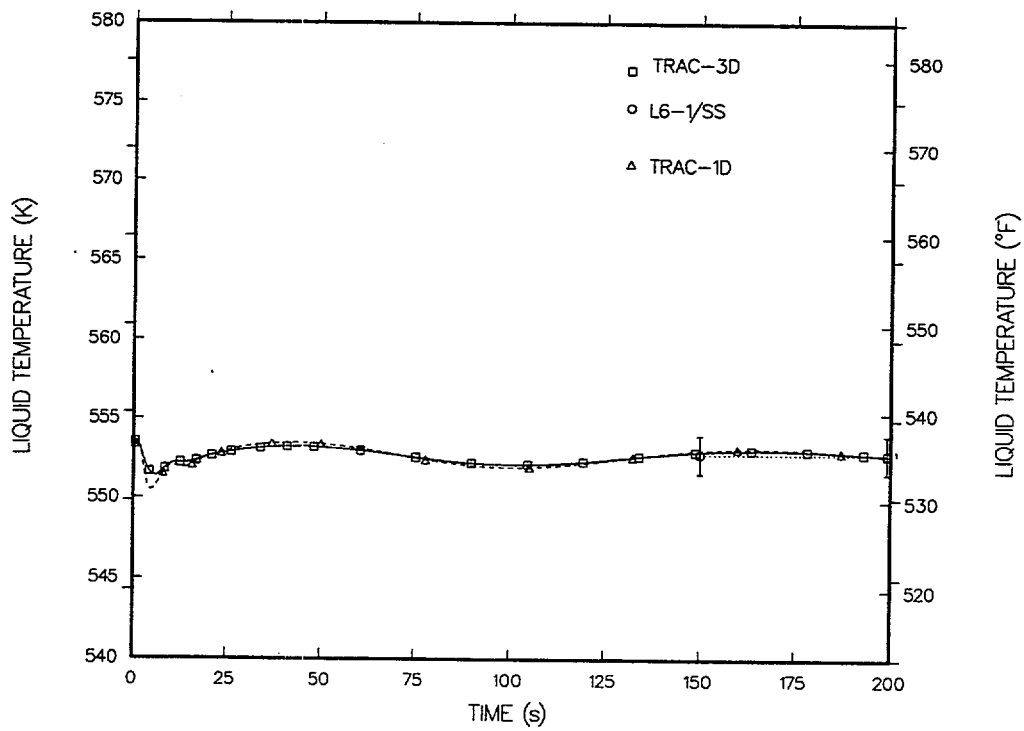


Fig. 5.2-12. Steam-generator primary-side outlet liquid temperature, steady-state calculation.
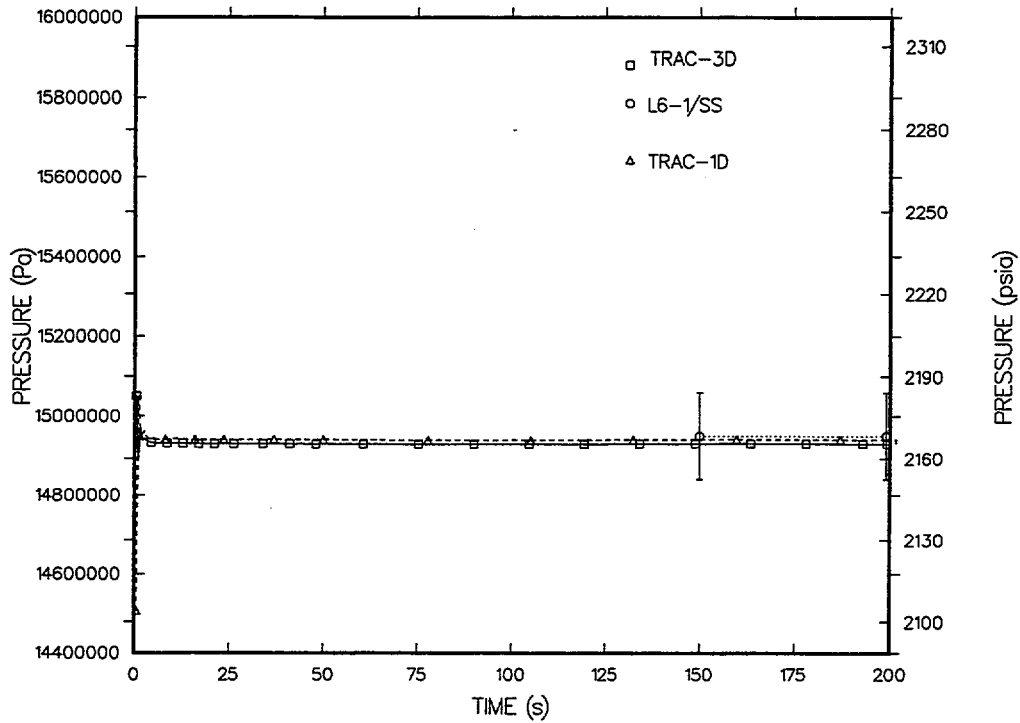
Fig. 5.2-13. Vessel upper-plenum pressure, steady-state calculation.
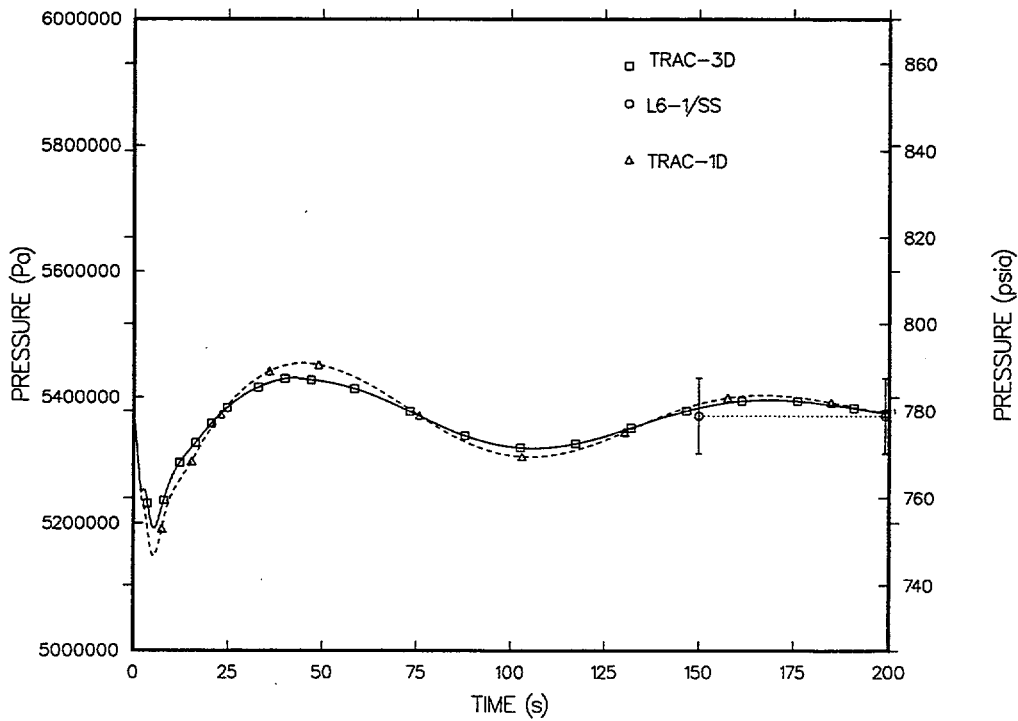


Fig. 5.2-14. Steam-generator secondary-side steam-dome pressure, steady-state calculation.
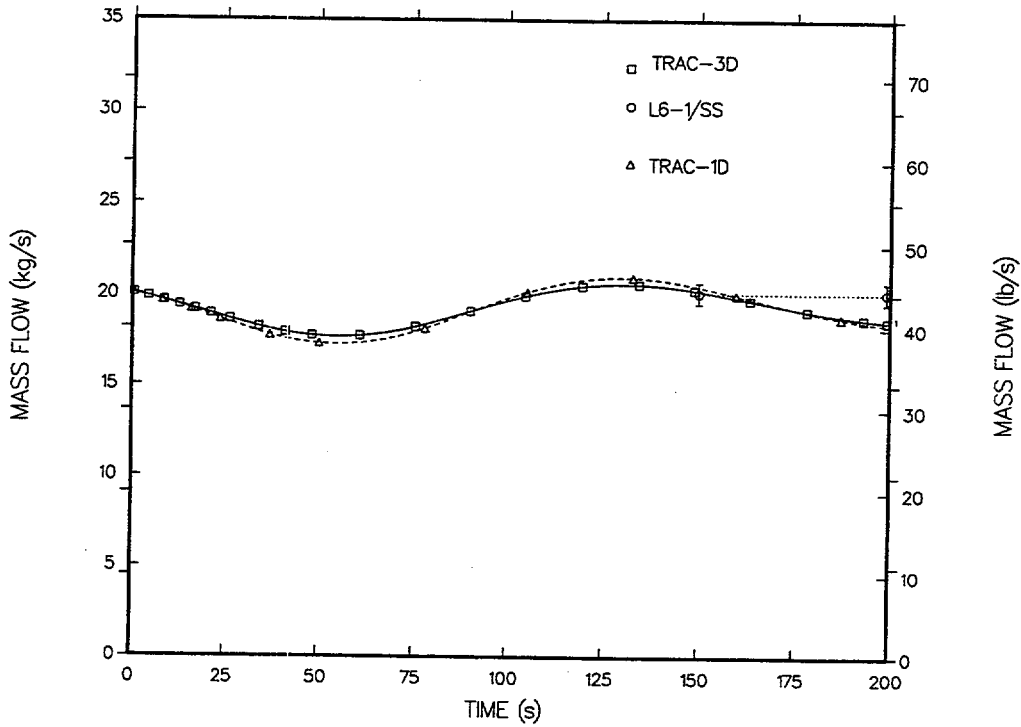
**Fig. 5.2-15.** Steam-generator secondary-side feedwater-liquid mass flow, steady-state calculation.
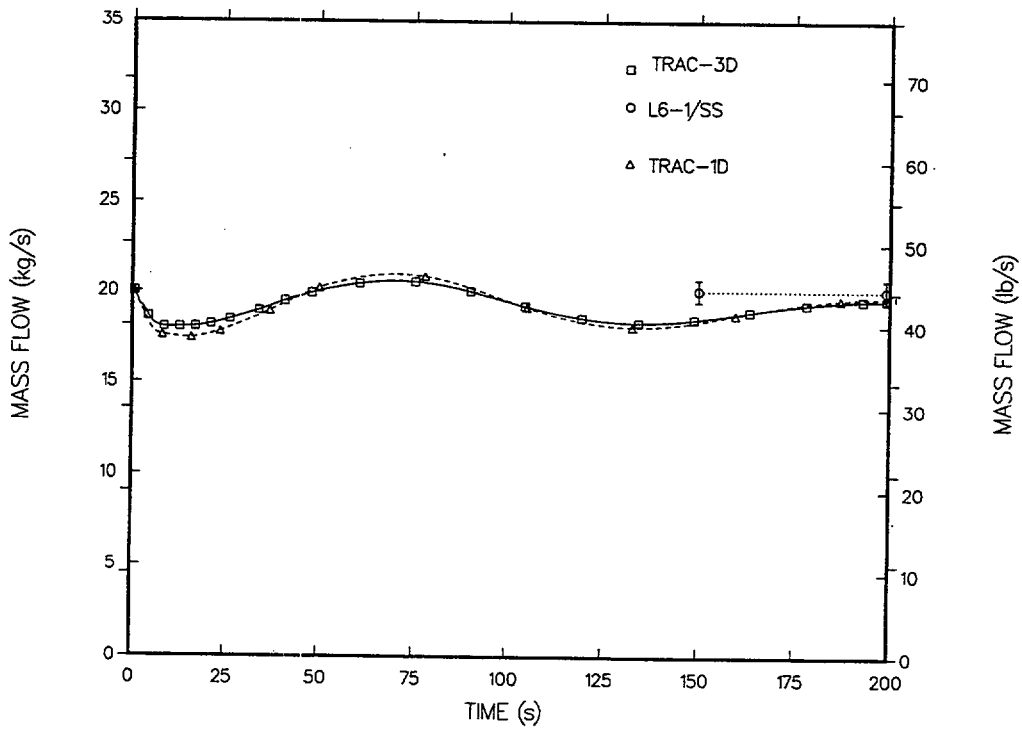


**Fig. 5.2.-16.** Steam-generator secondary-side steam-flow control valvevapor mass flow, steady-state calculation.
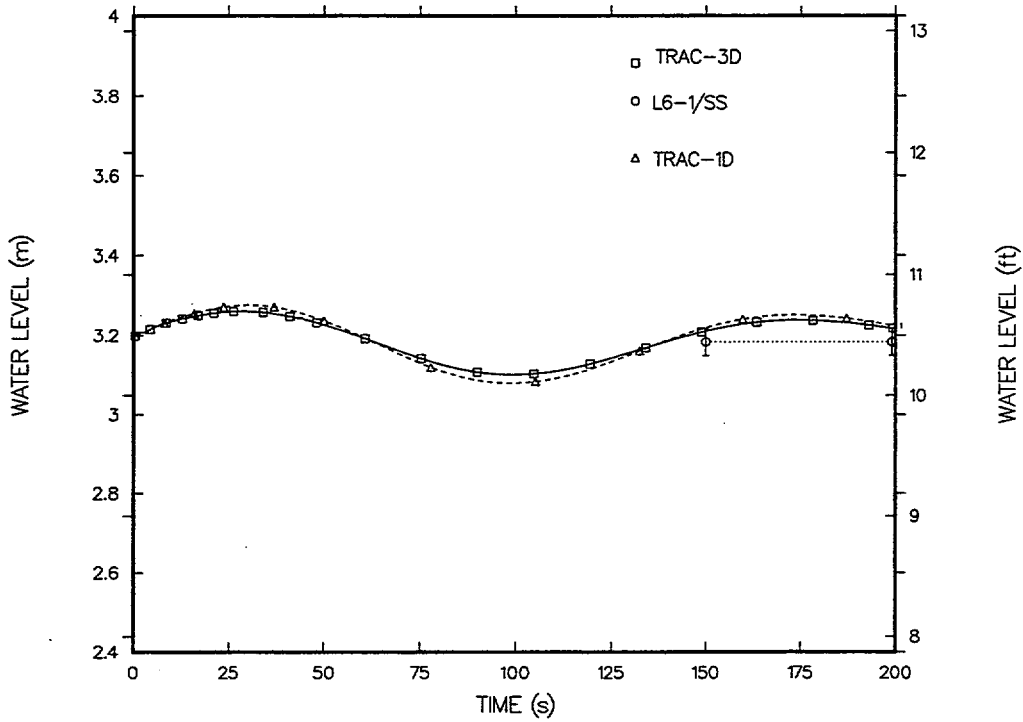
Fig. 5.2-17.    Steam-generator secondary-side downcomer level, steady-state calculation.
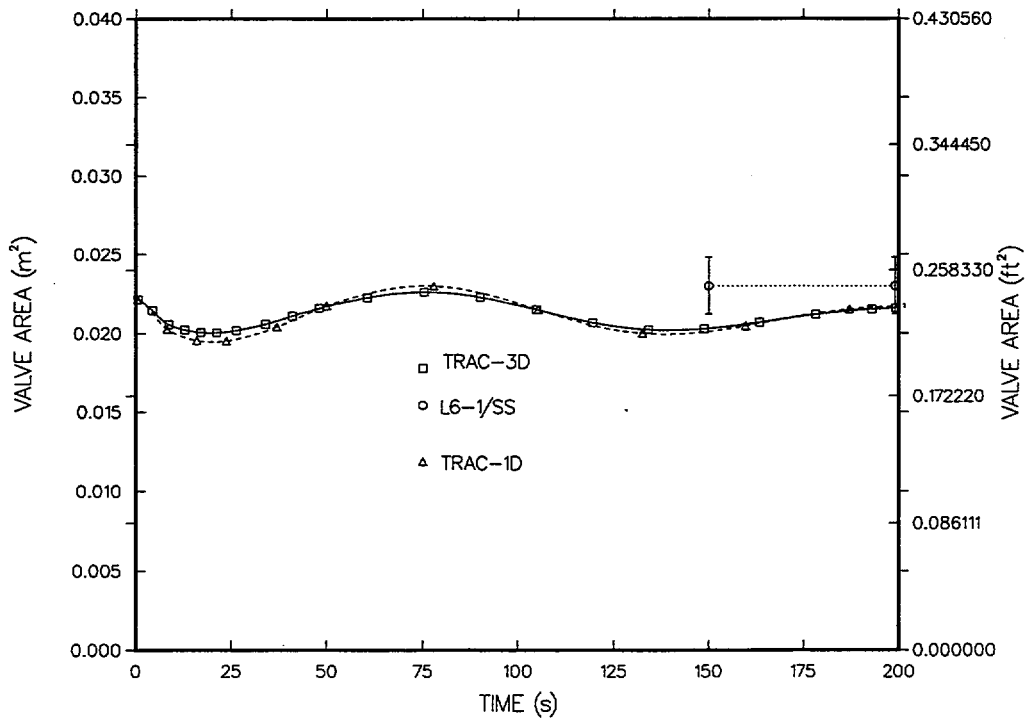


Fig. 5.2-18.  Steam-generator secondary-side steam-flow control valve flow-area fraction, steady-state calculation.
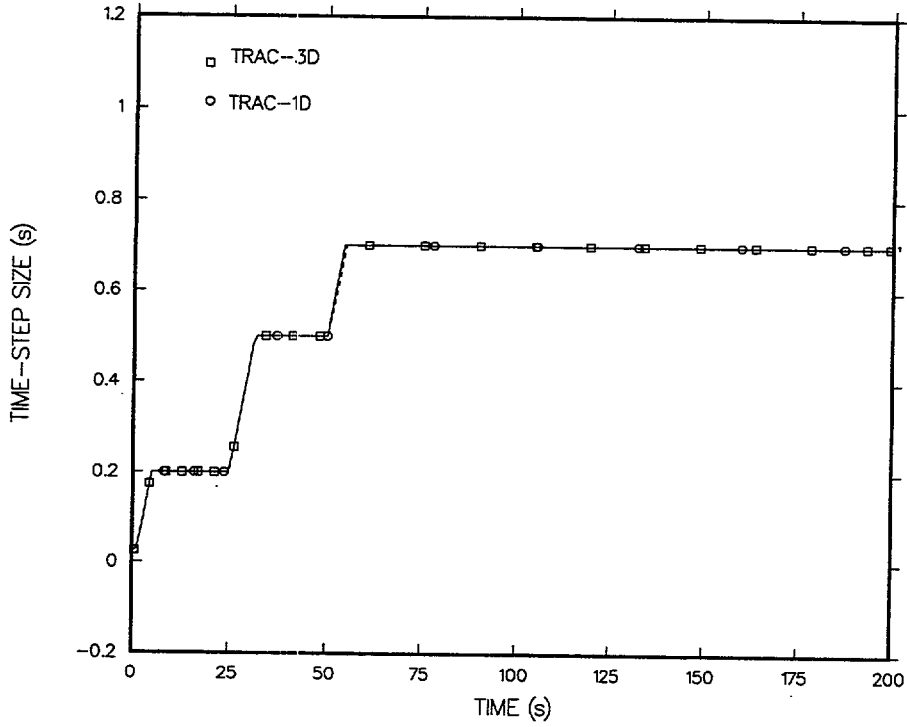
Fig. 5.2-19.    Steady-state calculation time-step size.
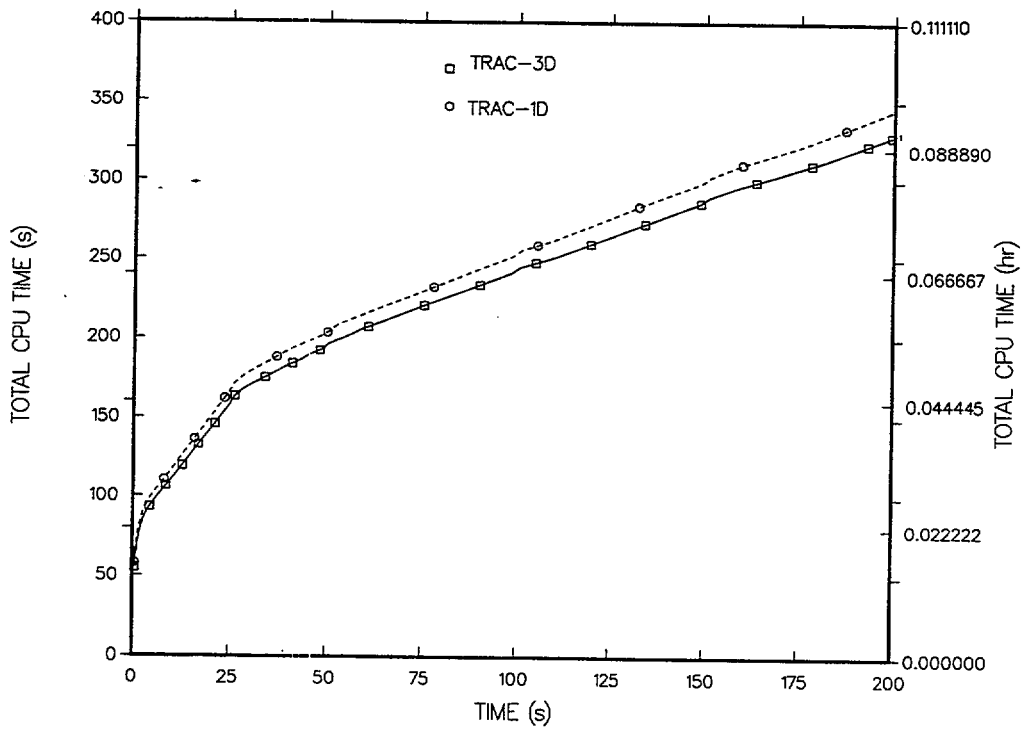


Fig. 5.2-20.    Steady-state calculation CPU time (Sun Enterprise 3000 platform).
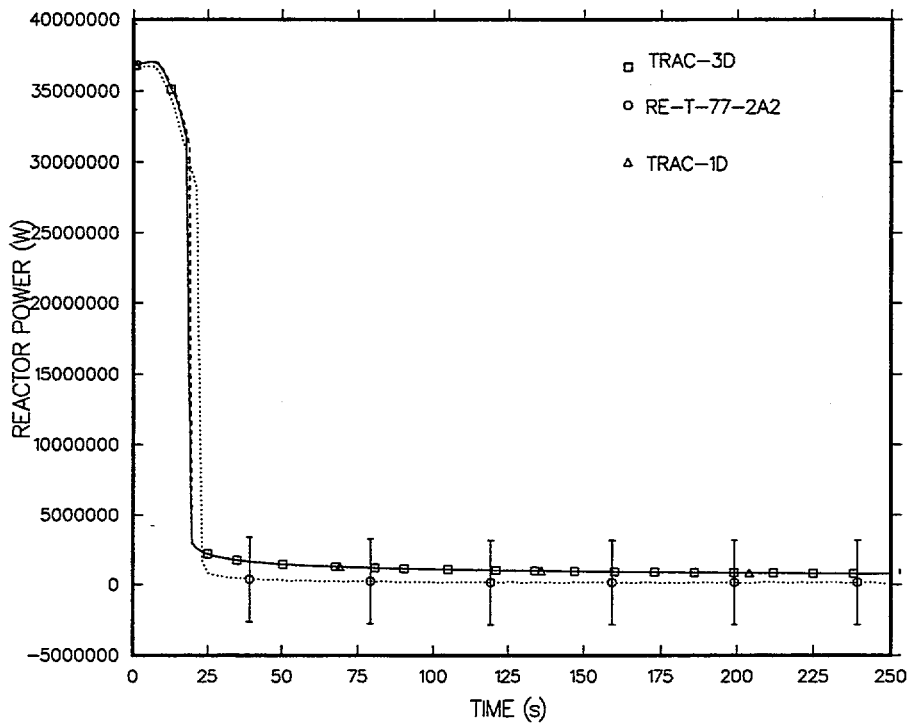
Fig. 5.2-21.    Reactor-core neutronic power, transient calculation.
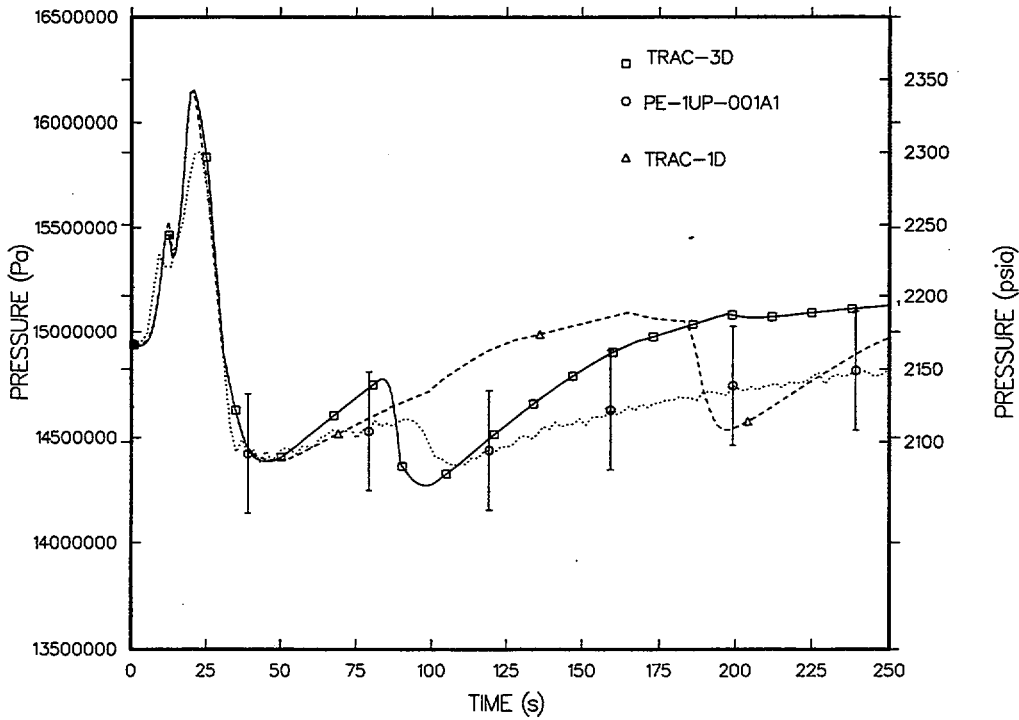


Fig. 5.2.22.    Vessel upper-plenum pressure.
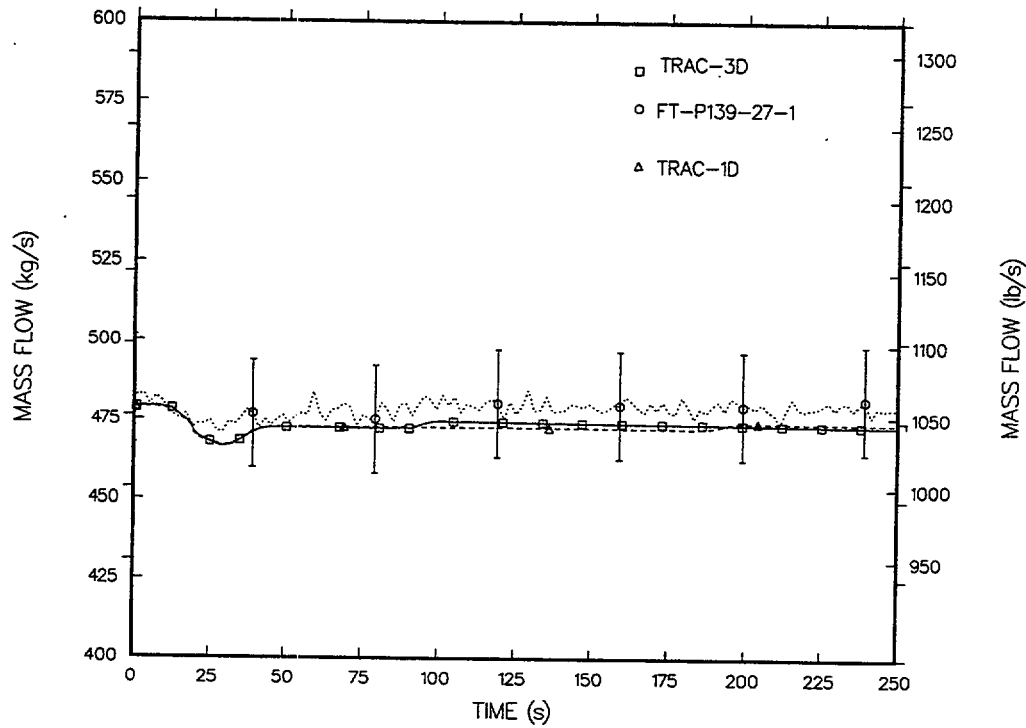
Fig. 5.2-23.   Intact-loop hot-leg liquid mass flow (detector 1), transient calculation.
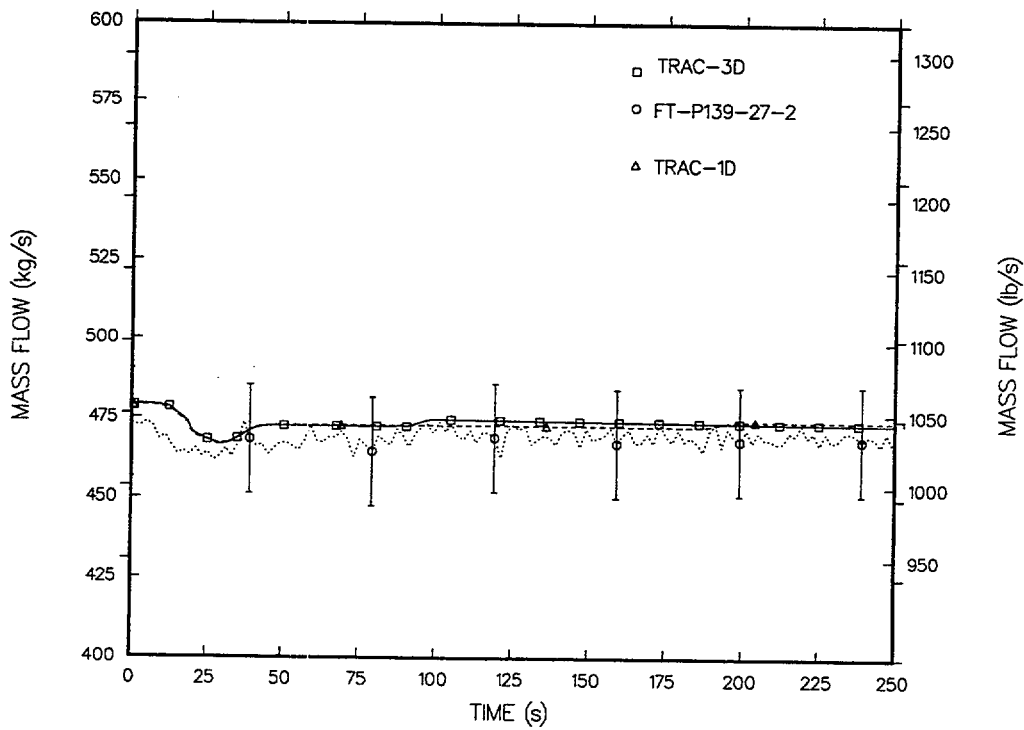


Fig. 5.2-24.   Intact-loop hot-leg liquid mass flow (detector 2), transient calculation.
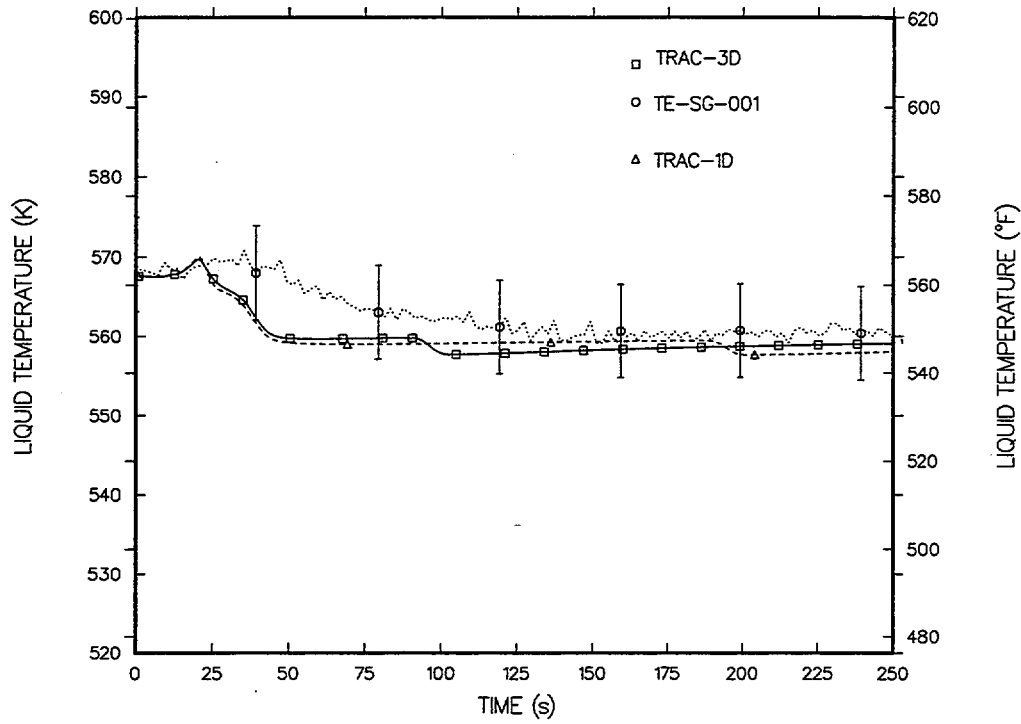
Fig. 5.2-25.  Steam-generator primary-side inlet liquid temperature, transient calculation.
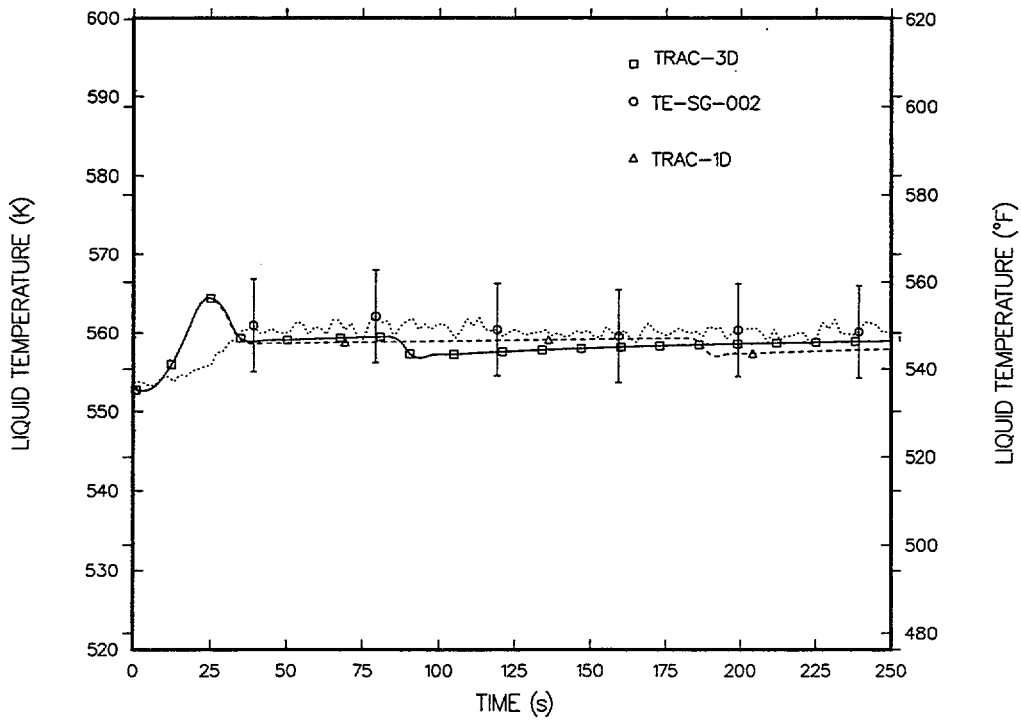


Fig. 5.2-26.  Steam-generator primary-side outlet liquid temperature, transient calculation.
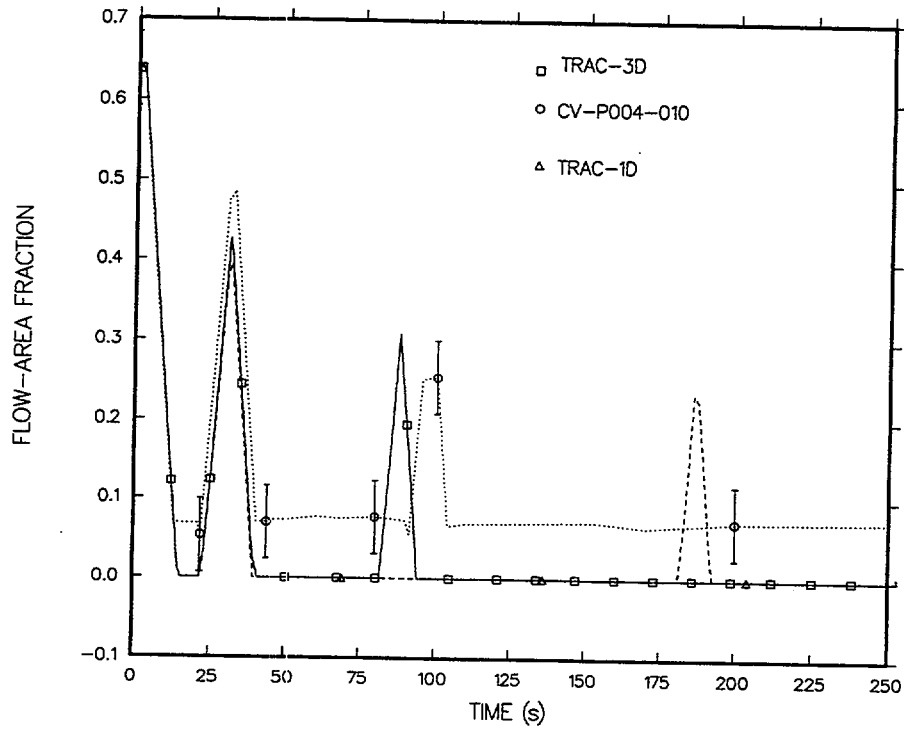
Fig. 5.2-27.    Steam-flow control valve valve-stem position, transient calculation.
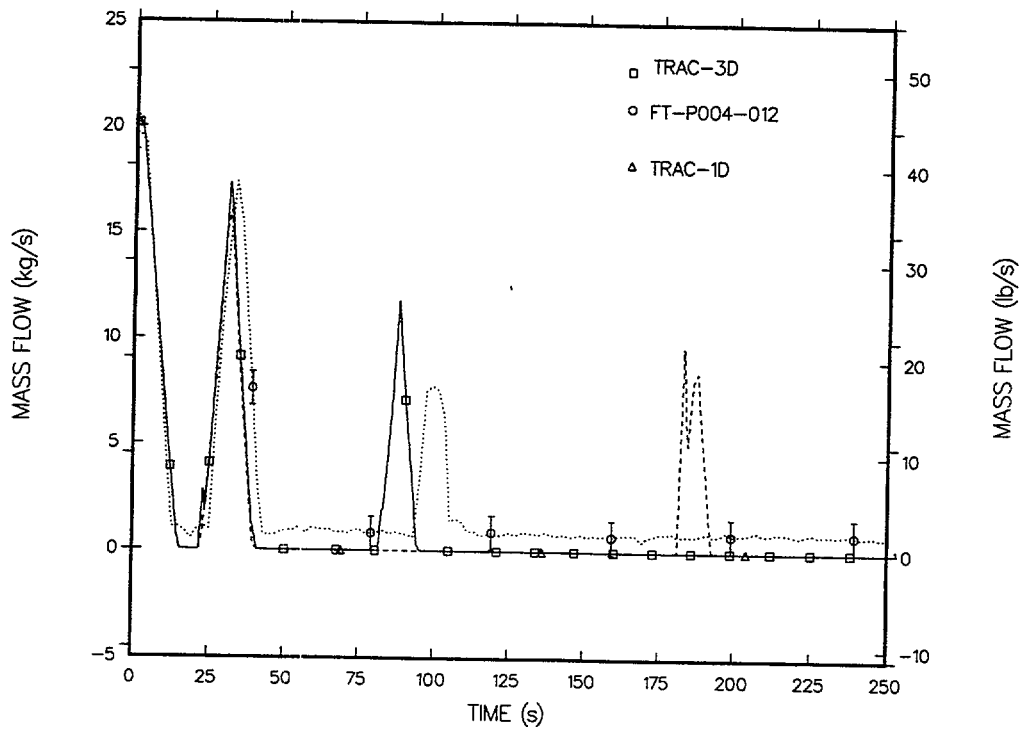


Fig. 5.2-28.    Steam-flow control-valve vapor mass flow, transient calculation.
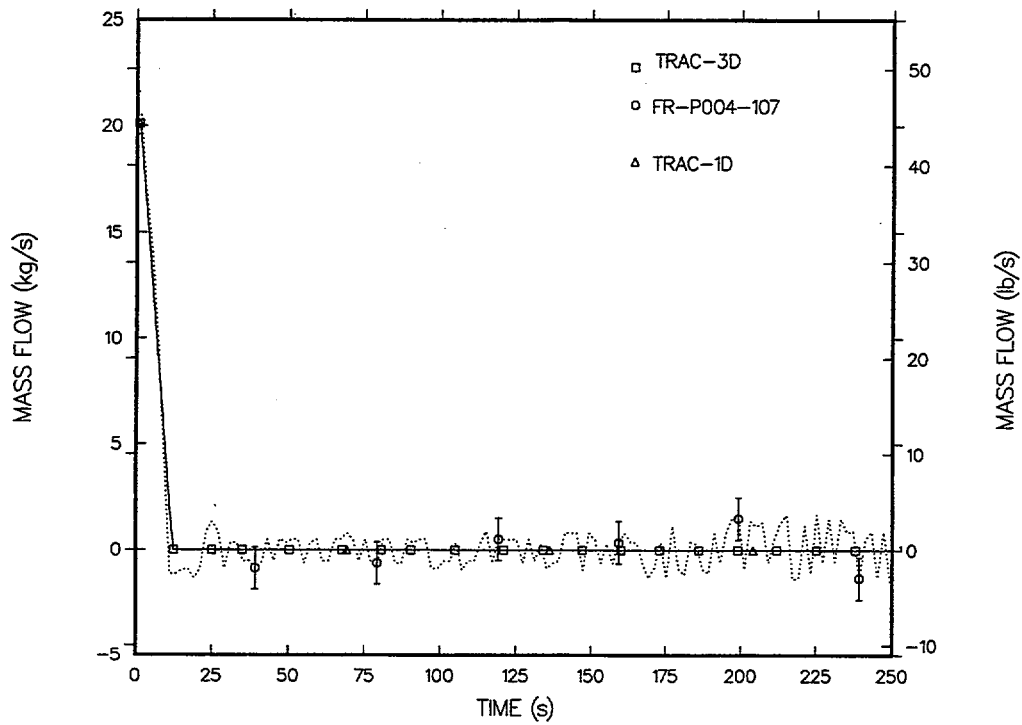
Fig. 5.2-29.    Steam-generator feedwater liquid mass flow, transient calculation.
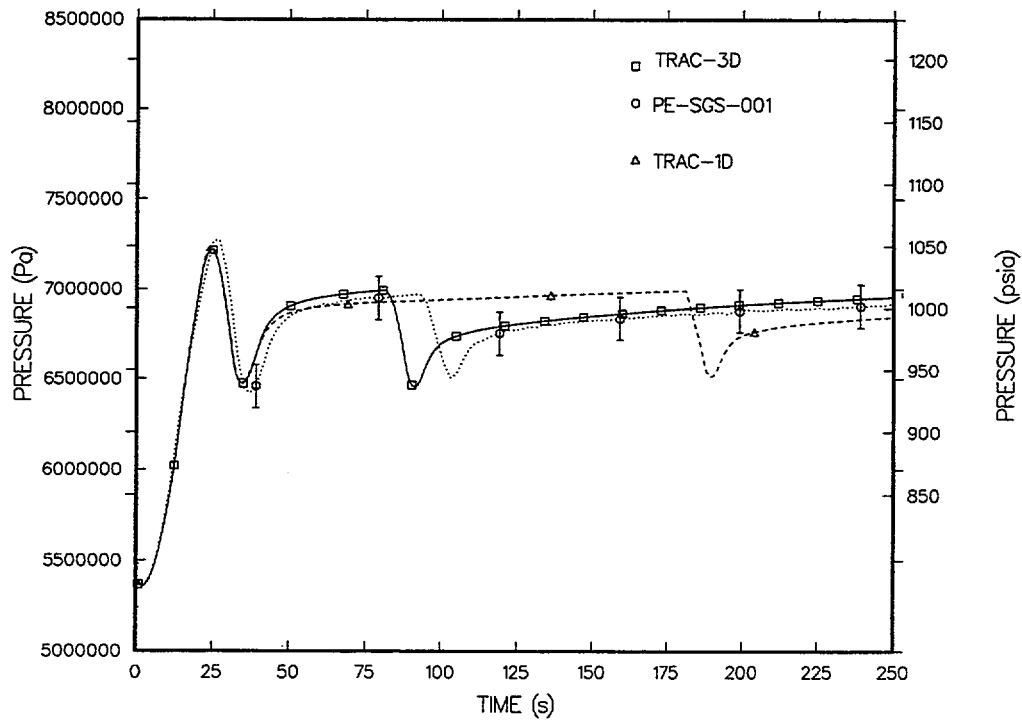


Fig. 5.2-30.    Steam-generator steam-dome pressure, transient calculation.
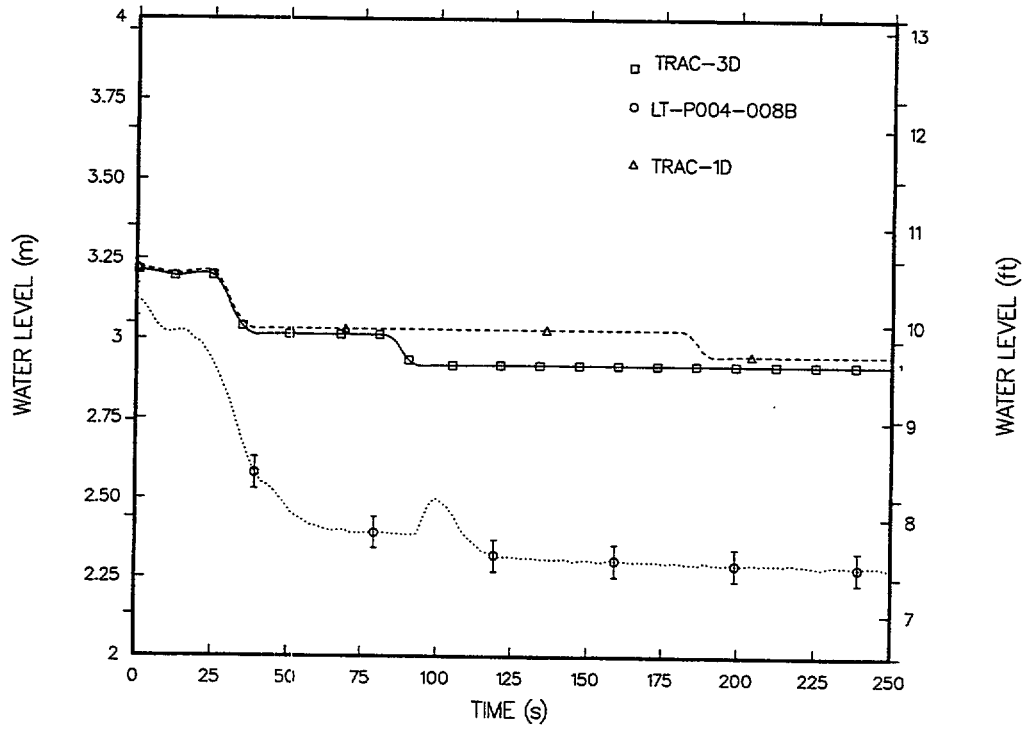
Fig. 5.2-31.    Steam-generator downcomer liquid level, transient calculation.
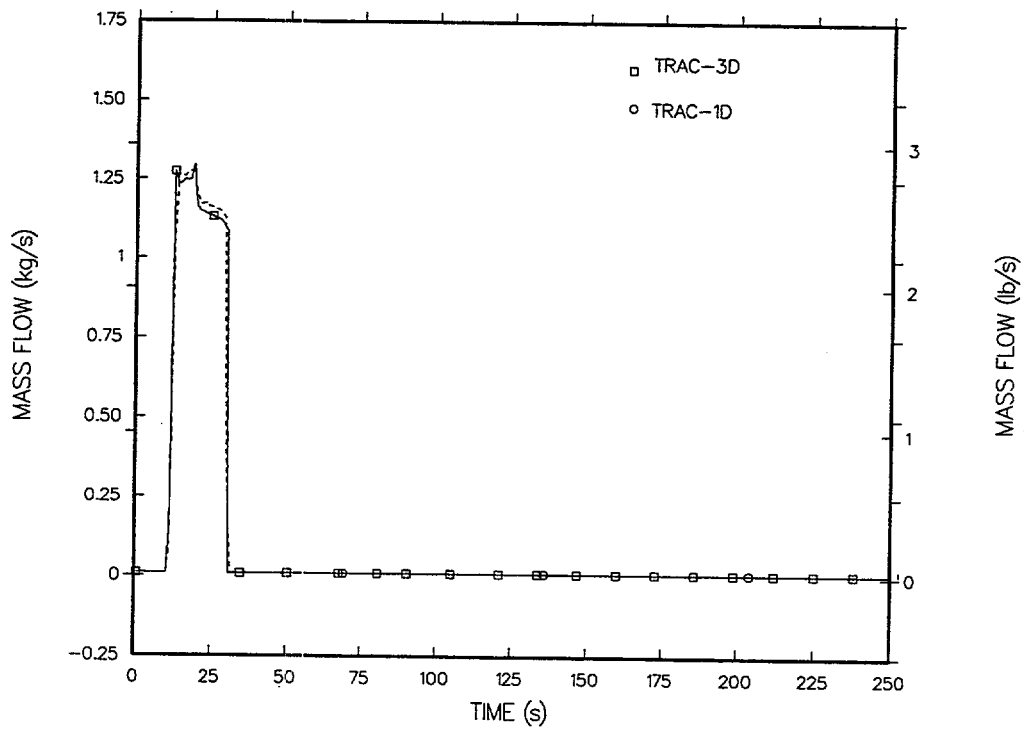


Fig. 5.2-32.    Liquid mass flow through the pressurizer sprayer valve, transient calculation.
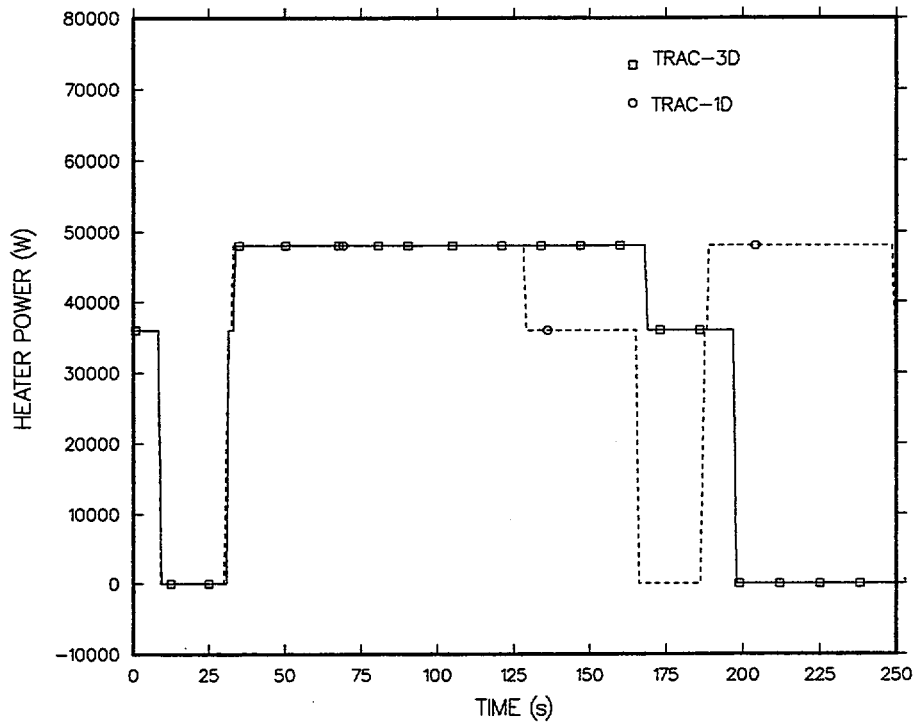
Fig. 5.2-33. Power generated by the pressurizer cycling and back-up heaters, transient calculation.
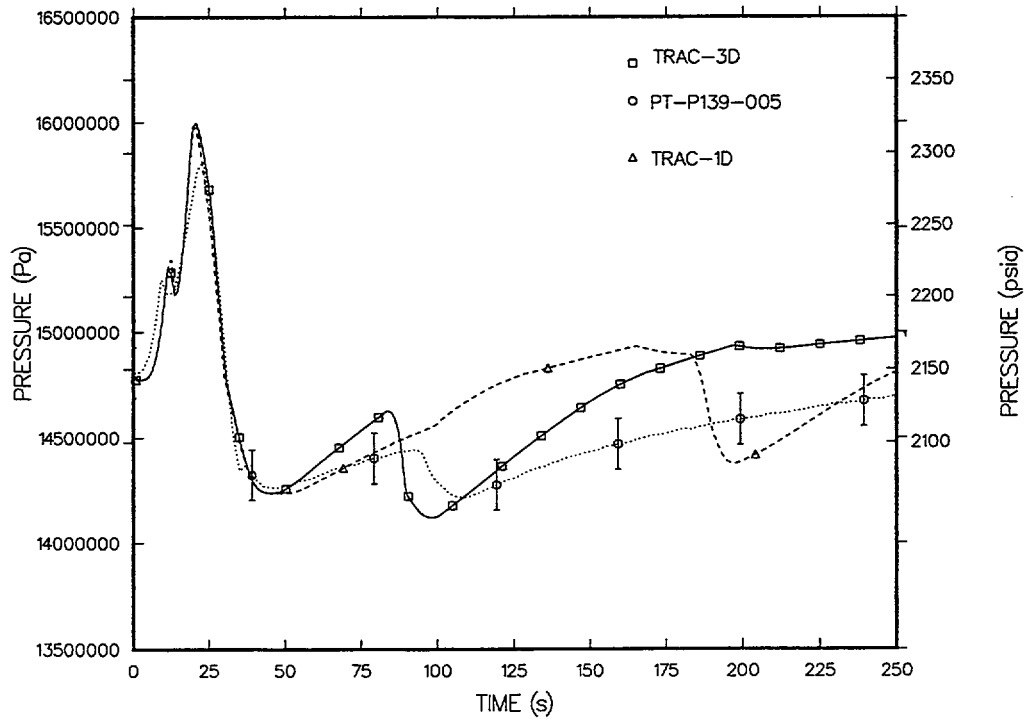


Fig. 5.2-34. Pressurizer steam-dome pressure, transient calculation.
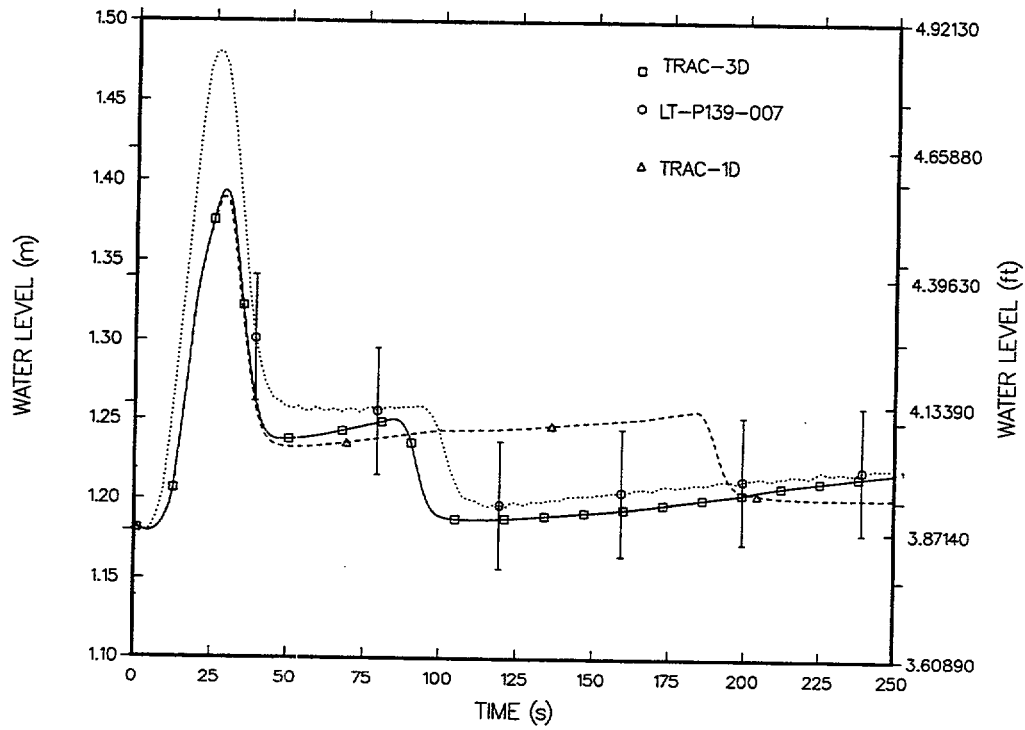
Fig. 5.2-35.    Pressurizer liquid level, transient calculation.

## 5.3. CCTF Core-II Run 54

### 5.3.1. Facility Description

The CCTF is an experimental test facility designed to model a full-height core section and four primary loops with components of a PWR.[5.3-1] Figure 5.3-1 shows an isometric view of the facility. The facility was designed and operated by JAERI and is used to provide information on fluid behavior in the core, downcomer, and upper plenum, including steam and water carryover (steam binding) and integral system (steam-generator and pump simulator) effects during the refill and reflood phases of a hypothetical LOCA in a PWR. The central part of the test facility is a nonnuclear core that consists of 1824 electrically heated rods and 224 nonheated rods arranged in a cylindrical array. The core is housed in a test vessel that includes a downcomer, lower plenum, upper plenum, and core region. The core design is based on 8 x 8 rod assemblies that model a typical 15 x 15 fuel assembly of a PWR. Volumetric scaling is based on core-flow-area scaling. The objectives of the CCTF tests are to

1. demonstrate ECC behavior during refill and reflood period;

2. verify reflood analysis codes; and

3. collect information to improve the thermal-hydraulic models in such analysis codes as (a) multidimensional core thermal hydrodynamics, including the radial power distribution effect, fallback effect, and spatial oscillatory behavior; (b) flow behavior in the upper plenum and hot legs; (c) behavior of accumulated water at the bottom of the upper plenum, including possible countercurrent flow and sputtering effects; (d) hydrodynamic behavior of the injected ECC water and the water passing through the steam generator; (e) multidimensional thermal-hydrodynamic behavior in the hot annular downcomer; and (f) overall oscillatory behavior in the system.

The facility was completed on March 10, 1979. By April 1981, 22 tests had been performed with CCTF Core-I.[5.3-2] The first core was replaced by the new second core on November 1981 for the CCTF Core-II test series. By April 1982, six tests, including two acceptance tests and two shakedown tests, had been performed with CCTF Core-II. The test discussed in Ref. 5.3-1 was a second shakedown test, which is called by several names, including Test C2-SH2, Test-43, and Run 54. (In this report, it will be called Run 54.) Run 54 was conducted successfully on March 30, 1982. The objectives of the test were to check the functions of the modified CCTF Core-II facility, confirm the similarities between Core-I and Core-II, and study the effect of the power supplied into the core. The test was conducted under the same initial and boundary conditions as in the base case of the CCTF Core-II test series, except for the supplied power. The ECC flow conditions were the same as those of the evaluation model tests[5.3-3,5.3-4] in CCTF Core-I.

The CCTF Core-II was designed according to the following objectives and criteria.

### 5.3.1.1. Design Objectives

- The facility should provide the capability to simulate reasonably the flow conditions in the primary system of a PWR during the refill and reflood phases of a LOCA.

- The downcomer design should provide ECC flow behavior throughout the test, which reasonably represents that of the PWR downcomer.

### 5.3.1.2. Design Criteria

- The Trojan reactor in the United States (US) and certain aspects of the Ohi reactor in Japan are the reference reactors.

- The vertical dimensions and locations of system components are kept as close as possible to those of the reference reactors.

- The flow areas of the system components are scaled down in proportion to the scaling factor of the core flow area.

- The facility is equipped with four loops, which are composed of three intact loops and a broken loop.

- A cold-leg break is simulated.

- The ECC system consists of an accumulator and an LPCI system, and the injection locations are the upper plenum and the downcomer, as well as the lower plenum and cold legs.

- The maximum allowable pressure of the facility is 588 kPa.

- The maximum allowable temperature of the simulated fuel rods is 1173 K (900°C).

- The maximum allowable temperature of the components in the primary system except the simulated fuel rod assembly is 623 K (350°C).

- The design of upper-plenum internals is based on that of a new 17 x 17 type of fuel assembly.

- The flow resistance of each loop is adjusted by an orifice in the pump simulator.

- The containment system consists of two tanks.

The scaled dimensions of the components are given in Tables 5.3-1 and 5.3-2.

### 5.3.2. Pressure Vessel and Internals

The pressure vessel is a cylindrical type, as shown in Fig. 5.3-2. The height is the same as the reference reactor pressure vessel. The radial direction is scaled down in

proportion to the core flow area scaling, i.e., 1/21.44. The upper ring was newly installed in the Core-II facility for the upper-plenum ECC water-injection nozzles (called core-flooding nozzles). Core-flooding nozzles were not used in the Run 54 test. The vent valves and core flooding nozzles are for the simulation of a Babcock & Wilcox (B&W)-type PWR. Below are some of the features of this facility.

- The cross section of the pressure vessel is shown in Fig. 5.3-3. The core, which consists of thirty-two 8 x 8 electrically heated rod bundles, is arranged in a cylindrical configuration and simulates Westinghouse 15 x 15 fuel assemblies.

- The downcomer is an annulus of a 61.5-mm gap. In determining the gap size, the flow area of the core-baffle-flow area is included in the downcomer region. Thus, the core-baffle-flow area is included in the downcomer simulation and is not simulated separately in this vessel.

- The vessel wall is constructed of carbon steel that is clad with stainless-steel lining. The wall is 90 mm thick to simulate the stored energy as reasonably as possible during ECC water injection.

- The design of upper-plenum internals is based on that of the Westinghouse 17 x 17 fuel assemblies. The internals consist of 10 control-rod guide tubes, 10 support columns, and 12 open holes. The radius of each internal is scaled down by a factor of 8/15 from that of an actual reactor. Flow-resistance baffles are inserted into the guide tubes.

- The end box tie plate and the upper-core support plate (UCSP) are installed between the core and upper plenum. The end box tie plate is 10 mm thick and perforated with round holes. Plugging devices are installed in the Core-II facility to simulate the flow resistance. The UCSP is a 60-mm-thick perforated plate. The geometry of the perforation is analogous to that of an actual reactor.

### 5.3.3. Heater-Rod Assembly
The heater-rod assembly that simulates the fuel assembly consists of thirty-two 8 x 8 array rod bundles. Each bundle consists of 57 electrically heated rods and 7 nonheated rods. The core is usually subdivided into three regions to achieve a desired radial power distribution. The local peaking factor of heated rods in a bundle is unity; that is, all heated rods in a bundle have the same density in the Core-II facility.

A heater rod consists of a nichrome heating element, magnesium oxide (MgO) and boron nitrite (BN) insulators, and an Inconel-600 sheath. BN is used only for the central part of the heated region, and MgO is used for the other part. The respective heated length and outer diameter of the heater rods, 3.66 m and 10.7 mm, respectively, are identical to the corresponding dimensions of actual PWR fuel rods. The sheath-wall thickness is 1.0 mm, which is thicker than the actual fuel cladding because of the requirements for thermocouple installation. The heating element is a helical coil with a varying pitch to generate a 17-step chopped-cosine axial-power profile, as shown in Fig. 5.3-4. Nonheated rods are either stainless-steel pipes or solid bars having an outer diameter of 13.8 mm. All the pipes are used for the installation of such instruments as steam superheat probes and thermocouples and are used for carrying the assembly

loads.

The heater rods and nonheated rods are held in a radial position by grid spacers that are located at six elevations along the axial length, as shown in Fig. 5.3-4. A grid spacer is a lattice structure composed of 0.4-mm-diam, 0.8-mm-thick, 40-mm-high stainless-steel plates. The top and the bottom edges of the stainless-steel plates are sharpened in CCTF Core-II. The rod pitch is 14.3 mm, which is same as that of the reference PWR.

The heater rods penetrate through the bottom plate of the vessel to facilitate lead out of the power cables from the bottom of the vessel. The outer diameter of the rods in the lower plenum is reduced to 8.6 mm. Three-phase electric current is used for heating the heater rods, and the electrical neutral point is at the top of the rods, where they are interconnected to each other.

### 5.3.4. Primary Loops and the Emergency Core Cooling System (ECCS)

The primary loop consists of three intact loops and a broken loop. Each loop consists of hot- and cold-leg piping, a steam-generator simulator, and a pump simulator. The cold-leg break is simulated for the broken loop. The broken cold leg is connected to two containment tanks through blowdown valves. The primary-loop arrangement is shown in Fig. 5.3-5.

The inner diameter of the piping is scaled down in proportion to the core flow area scaling. The length of each piping section is almost the same as the corresponding sections of the reference PWR.

The steam-generator simulators are the U-tube and shell type. The tube length is ~5 m shorter than the reference PWR. The vertical height of the steam-generator simulators is also ~5 m lower than the reference PWR. The primary coolant passes through the tube side, and the secondary coolant is stagnant in the shell side. The steam-generator simulators of two loops are housed in a single-shell assembly that has two sets of separated inlet and outlet headers for two loops. The wall thickness of the U-tube is 2.9 mm instead of 1.27 mm for the reference PWR because of a higher pressure difference between the primary and secondary sides in the steam-generator simulator. The pump simulator consists of the casing and vane simulators and an orifice plate.

Each loop resistance is simulated with the orifice plate and has a hole with a diameter and thickness of 95 and 10 mm, respectively.

The ECCS consists of an accumulator and LPCI. The injection points are at each cold leg and at the lower plenum. The upper plenum and downcomer injection system are available for further alternative ECCS tests.

### 5.3.5. Instrumentation

The instrumentation is divided into two groups. One group consists of JAERI-supplied instruments that measure the temperatures, absolute pressure, differential pressures, water levels, and flow rates. Thermocouples measure the temperatures of the rod surface, fluid, and structure. The absolute pressures are measured in the upper and lower plena, steam-generator plena, and containment tanks. The differential pressure measurements are carried out at many locations that cover the entire system almost

completely. The liquid levels are measured in the ECC water supply tanks and containment tank 1. The flow meters measure the ECC water flow rates. Furthermore, flow rates in the downcomer and loop-seal-piping vent line from containment tank 2 to the atmosphere are measured with the drag disk flow meter, Pitot tubes, and venturi tube, respectively. The JAERI-supplied instruments total 1316 channels; the signals from these instruments are recorded on a magnetic tape.

The other group of instrumentation consists of the US Nuclear Regulatory Commission (NRC)-supplied advanced instrumentation for the two-phase flow measurement, which totals 536 channels.

### 5.3.6. Description of CCTF Run 54
The test conduct and test conditions are described in the following subsections.

**5.3.6.1. Preparatory Operations.** In preparation for the test, the accumulator tank, LPCI tank, saturated water tank, and secondary sides of the steam-generator simulators were filled with water purified with ion exchange resin. The instruments were checked for their zero points and sensitivity after all of he components and instruments were inspected for mechanical and electrical leakage.

After the preparatory operations, the primary system was heated to its specified temperatures (downcomer wall, 468 K; core internals, 423 K; and primary loop piping wall, 406 K) with the preheaters and pressurized to a specified pressure (0.2 MPa) by substituting steam for nitrogen gas in the system. The water in the accumulator tank was electrically heated to its specified temperature (310 K) and pressurized with nitrogen gas to provide sufficient head to drive the injection flow required. The water in the LPCI tank was also heated to its specified temperature (310 K) and was circulated through the circulation line, including the LPCI line, to preheat the line to the same temperature as the water. The water in the saturated water tank was heated close to the saturation temperature (394 K) of the expected primary system pressure (0.2 MPa). The water in the secondary side of each steam-generator simulator was also heated and pressurized to the specified temperature (539 K) and pressure (5.3 Mpa).

After the initial conditions of the test were established, the electric power for preheating was turned off and the lower plenum was filled to 0.86 m directly from the saturated water tank. Electric power was applied to the heater rods in the core, and the data recording was started when the water level in the lower plenum reached the specified level and other initial conditions of the test stabilized at the allowable tolerance. A computer was used to monitored the temperature rises of the rods. When a specified initial clad temperature (1003 K) was reached, direct injection (0.104 m$^3$/s) of the accumulator water into the lower plenum was initiated. The system pressure was maintained at the specified initial pressure (0.2 MPa) throughout the test by controlling the outlet valve of containment tank 2. Decay of power input to the rods was programmed to begin when the water reached the bottom of the heated region of the core. The specified initial clad temperature (995 K) of the heater rods for initiation of coolant injection was predetermined by interpolation between the clad temperature (394 K) after preheating and the clad temperature (1073 K) assumed for the time of core bottom recovery. The specified power decay was obtained by normalizing the 1.0 X ANS standard + U$^{238}$ capture decay curve at 30 s after shutdown.

When the assumed water level reached the specified level (0.5 m) from the bottom of the heated region of the core, the injection port was changed from the lower plenum to the three intact cold-leg ECC ports. This water level was assumed to be the level at which considerable steam generation occurs in the core to minimize oscillatory behavior caused by the condensation at the ECC ports. The accumulator injection flow rate was then reduced to 0.088 m³/s in the cold-leg injection period. At a specified time (16.5 s) after the time of core bottom recovery, the valves in the accumulator lines and LPCI circulation lines were closed, and the valves in LPCI injection lines were opened. These actions transferred the ECC injection from accumulator injection mode to LPCI mode. A specified LPCI flow rate (0.0116 m³/s) was maintained constantly until the ECC injection was turned off.

The generated steam and the entrained water flowed via broken and intact loops to the containment tanks. The steam was then vented to the atmosphere to maintain a constant pressure in the containment tanks. After all thermocouples on the surface of the heater rods indicated quenching of the rods, the power supply to the heater rods decreased linearly. The linear power decay was performed to study any particular reflood phenomena under very low power supply. The linear power decay was initiated at 690.5 s, and the power was turned off at 898 s. After the ECC injection was turned off, the recording system was stopped, thus terminating the test.

**5.3.6.2. Planned Test Conditions.** The specified initial test conditions were similar to those of the evaluation model test in CCTF Core-I [Run 38 (Ref. 5.3-2)] and the base-case test in CCTF Core-II [Run 53 (Ref. 5.3-4)], except for the power supply to the heater rods. The measured test conditions are shown in Table 5.3-3. In this test, the system was pressurized to 0.4 MPa with saturated steam before test initiation to establish the desired initial wall temperature of vessel internals and the wall temperature of the primary piping.

**5.3.6.3. Chronology of Events.** The sequence of events that occurred during the test is listed in Table 5.3-4. Data recording was initiated at the same time as the initiation of power supply to the heater rods in the core. The accumulator injection into the lower plenum was initiated at 81.0 s, the power decay was initiated at 90.5 s, which was the bottom of core recovery time, and the ECC injection mode was changed from accumulator injection to LPCI at 107 s. All heater rods were quenched at 552.5 s. The linear power decay was initiated at 690.5 s. The power was turned off at 898 s, LPCI was terminated at 979 s, and the data recording was ended at 1032 s.

### 5.3.7. Description of TRAC Input Model

**5.3.7.1. Reactor Vessel Modeling.** The input model was a straightforward conversion of an earlier TRAC-PF1 model that was used for the analysis of CCTF Run 54 that was done as part of the 2D/3D program.[5.3-3,5.3-4] The input model used the intermediate-node model of the CCTF reactor vessel, as shown in Fig. 5.3-6. The vessel nodalization includes 2 azimuthal zones, 4 radial rings, and 16 axial levels.

**5.3.7.2. Loop Modeling.** The three CCTF intact loops are combined and modeled as a single loop. The intact-loop components are shown in Fig. 5.3-7. Figure 5.3-8 shows the noding for the broken-loop components.

**5.3.7.3. Initial and Boundary Conditions.** Initial thermal and hydraulic parameter values are generally consistent with the initial values listed in Table 5.3-3. In most instances, initial pressures and temperatures are at the nominal values given in the table. For instances such as the steam-generator secondary, the variation in liquid temperature with height was taken into account based upon the thermocouple data recorded in the experiment. The axial and radial distribution of the power input to the core in the various power zones agrees with the distribution given in the Run 54 data report (Ref. 5.3-1).

Seven time-dependent boundary conditions were used for these calculations, including total core power, lower-plenum injection velocity and ECC temperature, cold-leg injection velocity and ECC temperature, and both containment tank pressures. The inputs were tabulated from instrument records. The ECCS flows are shown in Fig. 5.3–9.

**5.3.7.4. Generation of the TRAC Input Model.** The model was generated by running the old TRAC-PF1 model through the GOCVRT program. The following changes were made to the resulting model.

- Several junction flow areas were adjusted so that the cell volume/lengths on either side of the junction would not be greater than the junction flow areas.

- Several hydraulic diameters were adjusted as required by the revised code input requirements. This should have no effect on the calculated results because this was done only for junctions having zero flow areas on the steam-generator secondary.

- TRAC input parameter NFF flags for all 1D components were set to -1 to cause an automatic calculation of abrupt expansion/contraction additive form losses.

- The new reflood model was turned on (NAMELIST variable newrfd=1 was added), and the required array data were added. A new trip identification number (IRFTR2, card # 9) was added to the rod component to turn on the reflood model after a specified trip is turned on. This trip describes the end of the blowdown period of a LOCA accident.

- The time-step sizes were increased.

- The rod power history was expanded from 10 points to over 1200 points (based on experimental data) to match the input power better.

- The temperatures everywhere except the lower plenum and fills were changed from 393.0 to 414.2 (the average of the te30yxx thermocouple data from the test) to match the initial fluid and wall temperatures better.

- The cold-leg ECC FILL liquid temperature table was adjusted to match the experimental data better.

- The NAMELIST variable nosets = 2 was added to cause the code to calculate

the sets3d equation every time step.

- The vessel CFCL-Zs were all set to negative numbers to get an automatic calculation of abrupt expansion/contraction form losses.

- All roughness numbers were changed from 0.0 to 4.5720e-05 so that Fanning frictional losses would be computed.

- The heat-conductor temperatures in the reactor vessel ring 4 were changed from 4.142e+02 to 4.680e+02 for levels 2 and above. The heat-conductor temperatures in the inner rings were changed from 4.142e+02 to 4.230e+02. This is consistent with the initial conditions listed in the data report.

- The location of the ring-3/ring-4 boundary was moved from inside the core barrel to outside of the core barrel, and the vessel VOL, FA-T, FA-Z, HD-T, and HD-Z arrays were recomputed. This was done to eliminate VOL and FA values >1.0.

- The radial CFZL-Rs at the level of the nozzles and in the lower plenum was set to small negative values to get an automatic calculation of abrupt expansion/contraction form losses.

In addition, the maximum number of axial fine-mesh heat conduction rows was raised from 100 to 250, and the criterion for inserting fine-mesh heat conduction rows was changed to cause more fine-mesh rows to be inserted so that a more accurate reflood calculation could be obtained.

Two corrections were made to the CCTF-54 input model used in the previous developmental assessment. The first correction was to change the two azimuthal noding sectors from 180°/180° to 90°/270°, which is what the azimuthal noding should be when the three intact loops are modeled as one combined loop. The second correction was to model the actual axial power shape of the heater-rod assembly. The previous input model modeled the axial power shape with seven axial levels. The corrected axial power shape models the 17-level axial power shape of Fig. 5.3-4. Figure 5.3-10 shows a comparison of the previous and corrected axial power shapes.

### 5.3.8. Description of Input Model Assumptions and Approximations
The measured pressure from containment 2 has been used as input in both containment 1 and 2 tanks; therefore, the input pressure for the containment 1 tank in the TRAC model is slightly greater than the measured pressure for this boundary condition. It is not clear what influence this zero-pressure-drop boundary condition has on the calculated results.

A listing of the input model used for this developmental assessment calculation is found in Appendix S. Archival storage information for this input model is provided in Section 5.3.13.

### 5.3.9. Comparison of Calculated and Test Results
These results are for newrfd=3, which activates the reflood model with explicit top-

down reflood modeling. An identical set of graphical code-data comparisons with newrfd=1 is presented, without analysis, in Appendix T. Setting newrfd=1 activates the bottom-up reflood model of the TRAC-PF1/MOD2 code. We have run CCTF Run 54 calculations both with and without the grid-spacer model. We have determined that the grid-spacer model should not be used because it results in excessive and nonphysical heat-transfer processes in the upper portions of the core. Therefore, the base-case assessment results for CCTF Run 54 do not use the TRAC grid-spacer model (see Section 5.3-10 for details).

Figure 5.3-11 shows the heated-core inlet mass flow and Fig. 5.3-12 shows the time-averaged core flooding rate, defined as the time-averaged core inlet mass flow divided by the core inlet flow area and the density of the core inlet flow.

Figures 5.3-13 through 5.3-27 show the rod-temperature comparisons between the 2-theta model and the experimental results (Ref. 5.3-1) for the high-powered rods (Figs. 5.3-13 through 5.3.17), intermediate-powered rods (Figs. 5.3-18 through 5.3-22), and low-powered rods (Figs. 5.3-23 through 5.3-27) at different axial elevations. Code data comparisons for the remainder of the system are shown in Figs. 5.3-28 through 5.3-40. In general, the calculated results of the corrected model were not as good as the previous model. Table 5.3-5 gives a qualitative evaluation of the effect of the modeling corrections on rod peak cladding temperatures and quench times relative to the previous model, first for the correction in azimuthal noding only and then for the correction of both the azimuthal noding and axial-power profile. Based on this comparison, it appears the axial-power profile correction had a stronger effect on the calculated results than did the azimuthal-noding correction.

The differences between predicted and observed rod thermal response of the high-powered rods are considered for four periods. The duration of each period varies with elevation; near the bottom of the core, the rod passes through several of the periods so quickly that it cannot be distinguished. Period 1 is the interval during which the rod experiences heat up under adiabatic conditions in pure steam. This period lasts until the coolant reaches the bottom of the heated core. Period 2 is an interval in which the rod continues to heat but at a slower rate. Even though the power supplied to the rod simulates decay heat, less heat is removed by the two-phase coolant than is supplied to the rod to simulate decay heat. The transition to period 3 occurs when the power supplied to the rod equals the two-phase heat-transfer removal rate. The temperature rise of the cladding stops, and the cladding begins to cool. Period 4 occurs when the rod has cooled sufficiently to quench.

At the axial elevation of 2.480 m (all elevations are referenced to the 0.0 elevation in Fig. 5.3-6), the predicted and measured PCTs for the high-powered rod are in reasonable agreement (Fig. 5.3-13). There is excellent agreement between the predicted and measured adiabatic heatup rate. The predicted PCT is ~10 K higher than measured, and the predicted quench time is ~20 s earlier than measured.

Figure 5.3-14 shows the predicted and measured wall temperatures for the high-powered rod at the elevation of 3.115 m. The predicted PCT and PCT time are about the same as measured, but the quench time is 65 s earlier than measured. Overall, the code-data comparison at this level is judged to be reasonable.

The rod heat-transfer characteristics, both predicted and observed, are more pronounced at the midplane and upper elevations, as illustrated in Figs. 5.3-15 to 5.3-17. At the core midplane (Fig. 5.3-13), the location of highest measured temperature, the predicted wall temperature follows the observed trace through the PCT time and through a period of ~35 s where the cladding temperature slowly increases and then begins to decrease slowly. However, at ~140 s, the predicted cooling degrades and the cladding temperature increases by 75 K over a period of 130 s, whereas the measured cladding temperature decreases by 255 K during the same interval. At 280 s, rapid cooling is calculated, and quenching of the rod occurs at 290 s, which is 70 s earlier than measured. At the 4.540- and 5.150-m levels (Figs. 5.3-16 and 5.3-17, respectively), the calculated trends more closely follow the observed cladding behavior. At both levels, the heatup rate is slowed shortly after coolant enters the bottom of the heated core. The same trend is predicted. At the 4.540-m level, more cooling occurs in the test than is predicted. Thus, the predicted PCT is 55 K higher than measured and the PCT time occurs 35 s later. Once again, rapid cooling is predicted, which causes this level to quench 35 s earlier than measured. At the 5.150-m level, the code predicts both the rapid and slower heating rates until 265 s. At this time, the cladding began to cool in the test at a faster rate than predicted. At 500 s, the rapid cooling is predicted, which causes this level to quench 10 s earlier than measured. Overall, the code-data comparisons at these two levels are judged to be reasonable.

The code captures the major trends in each of the four periods just described. However, there are deficiencies that are best observed in the code-data comparisons presented in Figs. 5.3-15 through 5.3-17. At each of these three levels (3.930 m, which is the core midplane; 4.540 m; and 5.150 m), the adiabatic heatup is accurately modeled. The code-data comparisons for the interval of slow heatup, period 2, are also in reasonable agreement. However, the code does not accurately predict the precursory cooling that occurs in period 3. At the core midplane (Fig. 5.3-15), continued heating is predicted while the rod is cooling in the experiment. At the 4.540- (Fig. 5.3-16) and 5.150-m levels (Fig. 5.3-17), cooling is predicted but at a rate less than observed in the test. In each case, however, TRAC predicts an earlier quench. The data clearly indicate that precursory cooling occurs over a large portion of the core in advance of the quench front. The TRAC heat-transfer model confines the precursory cooling to a much smaller interval near the quench front so that rod elevations away from the quench front continue to heat until the time the quench front advances to an elevation where the higher calculated heat-transfer rates rapidly quench the rod at that elevation.

The cladding-temperature trends for the intermediate-powered rods (Figs. 5.3-18 through 5.3-22) and the low-powered rods (Figs. 5.3-23 through 5.3-27) are very similar to those reported for the high-powered rods. In each case, the code data comparisons are judged to be reasonable.

The differences between the predicted and measured rod thermal responses can best be understood in the context of core ΔP comparisons. The ΔP traces are a direct indication of the liquid residing in the core at any time. The predicted and measured lower-plenum ΔPs are shown in Fig. 5.3-28. These show that the predicted and measured filling of the lower plenum are in reasonable agreement. The predicted and measured ΔPs for the lower and upper halves of the core are shown in Figs. 5.3-29 and 5.3-30, respectively. For the lower half of the core and until 160 s, the predicted and measured

ΔPs are in reasonable agreement, with slightly more liquid predicted to reside in the lower half of the core than measured. However, from 160 to ~265 s, the core liquid content is underpredicted. Similarly, the core heat transfer is underpredicted during this period (Figs. 5.3-13 through 5.3-15), until such time as the quench front reaches a given level, either predicted or in the test. The core liquid content is also underpredicted for the interval 165 s to 200 s in the upper region of the core. The impact of the liquid deficiency on predicted core cooling in the upper half of the core can be observed at the 4.540-m level in Fig. 5.3-16.

The predicted and measured cold-leg vapor fraction, pressure, temperature, vapor mass flow, and liquid mass flow are presented in Figs. 5.3-31 through 5.3-35, respectively. The predicted and measured hot-leg vapor fraction, pressure, temperature, vapor mass flow, and liquid mass flow are presented in Figs. 5.3-36 through 5.3-40. There is a clear indication that early in the transient there is too much vapor generation in the core, which carries too much two-phase mixture from the core and into the hot leg. This can be seen in the hot-leg vapor fraction, vapor mass flow, and liquid mass flow (Figs. 5.3-36, 5.3-39, and 5.3-40), respectively. It appears that this behavior causes the underprediction of core liquid content and the subsequent overprediction of rod temperatures.

The predicted core liquid mass is shown in Fig. 5.3-41. The calculated core mass displays a long-interval (50 to 100 s) oscillatory behavior from the time coolant enters the core until ~360 s. The first long-interval decline appears to be induced by the reduction in injected flow as the flow simulating the accumulator injection transitions to the lower flow simulation of the low-pressure injection system. With the associated core-flow reduction, steam generation increases and carries two-phase liquid through the upper plenum and into the hot leg at a much higher rate than measured (Figs. 5.3-39 and 5.3-40). Throughout the test, the predicted vapor generation rate is too high (Fig. 5.3-41). The cause of the remaining oscillations is unknown; however, both the undercooling and rapid quenching behavior at all but the highest levels of the core appear to be directly related.

### 5.3.10. Lessons Learned and User Guidelines

As a result of this and other assessments reported in this document, we determined that the TRAC grid-spacer model is seriously flawed. To illustrate, we performed a CCTF Run 54 calculation with the identical code and input model, the only exception being that the grid spacers in the test facility were modeled with the TRAC grid-spacer model. The predicted and measured high-powered rod temperatures at the 3.930- (core midplane), 4.540-, and 5.150-m levels are shown in Figs. 5.3-42, 5.3-43, and 5.3-44, respectively. These figures are to be compared with the baseline calculations for CCTF Run 54, which do not use the TRAC grid-spacer model. The corresponding figures are 5.3-15, 5.3-16, and 5.3-17. The grid-spacer model produces excessive overcooling, which is particularly evident at the 4.540- and 5.150-m levels. We observed this result in other assessment calculations using the TRAC grid-spacer model.

The grid-spacer model for interfacial heat transfer comes on when the code finds that a grid spacer is located within a hydro cell, the hydro cell is above the transition boiling regime for bottom up reflood or below the transition boiling regime for top-down

reflood, and the vapor temperature in this hydro cell is above the saturation temperature. The TRAC grid-spacer model for interfacial heat transfer is

$$h_{ig}A_i = C_sH_D/(vol(T_v-T_{sat}))$$

where

$h_{ig}$ = interfacial heat-transfer coefficient from the vapor phase to the interface,

$A_i$ = interfacial area,

$C_s$ = correlation constant = $10^6$,

$H_D$ = hydraulic diameter,

vol = volume of the hydro cell,

$T_v$ = vapor temperature, and

$T_{sat}$ = saturation temperature.

When a grid spacer has been modeled and the conditions governing its initiation are satisfied, the grid-spacer model for interfacial heat transfer is actuated.

A constant interfacial heat-transfer rate from the vapor phase to the interface continues until the vapor temperature reaches approximately the saturation temperature. The TRAC grid-spacer model for interfacial heat transfer in the TRAC reflood model is ad hoc; it was developed based on the Lehigh test rod surface temperatures that showed significant levels of cooling in the vicinity of the grid spacer.

We strongly recommend that the current TRAC grid spacer **not** be used in any assessment or plant calculation. However, it is clear that without an appropriate grid-spacer model, key heat-transfer processes occurring in the core for many applications will not be modeled. Therefore, we strongly recommend that a physically realistic grid-spacer model be developed and implemented.

### 5.3.11. Core Renoding Sensitivity Study

A core renoding sensitivity study was performed in which the 7-level core was renoded into 17 levels, where the levels matched the 17-level axial power profile of Fig. 5.3-4. The renoded vessel model is shown in Fig. 5.3-45; the renoded model input listing is presented in Appendix Z. A comparison of the 17- and 7-level, core-model calculated rod cladding temperatures to measured data is presented in Figs. 5.3-46 through 5.3-60. These figures correspond to the same set of plots presented in Figs. 5.3-13 through 5.3-27 but with the 17-level, core-model calculated results added. The comparison is for the calculation where newrfd=3 and grid spacers are not modeled.

For the high-power heater rods shown in Figs. 5.3-46 through 5.3-50, the 17-level core model predicts later quench times and higher PCTs than the 7-level core. For the intermediate-power heater rods, later quench times are predicted with the 17-level core for all measured rod elevations except at the 5.150-m elevation, where the 17-level, core-

model, predicted quench time is earlier than the 7-level core. The 17-level, core-model, predicted PCT, which is about the same as for the 7-level core at the below-midplane elevations, is lower at the midplane elevation and is higher at the above-midplane elevations. For the low-power heater rods, the 17-level, core-model, predicted PCTs and quench times are about the same as for the 7-level core at the midplane and below-midplane elevations. The 17-level, core-model, predicted PCTs are about the same as the 7-level, core-model, predicted PCTs at the above-midplane elevations. The 17-level, core-model quench time at the 4.54-m elevation is much later than the 7-level, core-model quench time but is much earlier at the 5.150-m elevation.

A full set of calculations was performed for the renoded model, which is the same set as those calculations performed for the 7-level core model: (1) newrfd=3 without grid spacers, (2) newrfd=3 with grid spacers, (3) newrfd=1 without grid spacers, and (4) newrfd=1 with grid spacers. A full set of calculation plots for the renoded model, corresponding to Figs. 4.7-13 through 4.7-44 for the 7-level core model, is presented in Appendix AA for the newrfd=3 calculations (with and without grid spacers) and in Appendix BB for the newrfd=1 calculations (with and without grid spacers).

In general, for the CCTF Run 54 assessment problem, there seems to be no improvement in calculated results with a finer core noding. This is different from the CCTF Run 14 assessment problem, where coarser code noding resulted in poorer calculated results. This difference may be due to the 3D modeling of the CCTF Run 54 vessel vs the 1D modeling of the CCTF Run 14 vessel.

### 5.3.12. Conclusions
From the assessment, we conclude the following.

- The present TRAC grid-spacer model is seriously flawed and should not be used. For CCTF Run 54, use of the model caused a severe underprediction of cladding temperatures in the upper half of the core. The current grid-spacer model assumes that all heat-transfer enhancement associated with the presence of a grid spacer is reflected in an increased interfacial heat transfer.

- Overall, the predicted core thermal-hydraulic behavior, without the grid-spacer model, is in reasonable agreement with the data.

- Predictions of cladding thermal response in the lower half of the core are in better agreement with data than predictions of cladding thermal response in the upper half of the core. At each level in the core, the cladding thermal response passes through four periods: (1) adiabatic heatup, (2) slow heatup, (3) slow cooldown, and (4) quench. TRAC failed to predict the third period accurately, frequently showing either a continued heatup or a cooldown that was too slow. This behavior is linked to a deficiency of liquid in the core during this period. The root cause has not yet been determined.

- A finer renoding of the CCTF Run 54 core did not improve the calculated results.

### 5.3.13. Code Performance

CCTF Run 54 was run on code Version 5.5. The run performance information plus other pertinent comments follow.

**Coarsely noded 7-level core input model**

| Platform | Sun Enterprise 3000 |
|---|---|
| Total CPU time (s) | 38718 |
| Archive location of input model | CFS /tida/f77da/task4.4bdecks/incctf54.corr |
| Archive location of calculation | CFS /trac-da/F77DA/task4.4b/cctf54.corr.tar.gz |

**Finely noded 17-level core input model**

| Platform | Sun Enterprise 3000 |
|---|---|
| Total CPU time (s) | 48133 |
| Archive location of input model | CFS /tida/f77da/task4.4bdecks/incctf54.renode |
| Archive location of calculation | CFS /trac-da/F77DA/task4.4b/cctf54.corr.tar.gz |

## REFERENCES

5.3-1.  Y. Murao, "Data Report on Large Scale Reflood Test-43—CCTF Core-II Shakedown Test C2-SH2 (Run 054)," Japan Atomic Energy Research Institute document JAERI-memo 58-155 (1983).

5.3-2.  Y. Murao, "Analysis Report on CCTF Core-I Reflood Tests," Japan Atomic Energy Research Institute document JAERI-memo 57-057 (1982).

5.3-3.  K. Hirano, "Quick-Look Report on Large Scale Reflood Test-23, CCTF TEST C1-19 (RUN 038)," Japan Atomic Energy Research Institute document JAERI-memo 9767 (1981).

5.3-4.  Y. Murao, "Evaluation Report on CCTF Core-II Reflood Tests for the Safety Analysis on the Reflood Phase of a PWR-LOCA," Japan Atomic Energy Research Institute document JAERI-memo 57-053 (1982).

## TABLE 5.3-1

## CCTF COMPONENT SCALED DIMENSIONS

| Component | PWR | JAERI | Ratio |
|---|---|---|---|
| **Pressure Vessel** | | | |
| Vessel inside diameter (mm) | 4394 | 1084 | |
| | (173 in.) | | |
| Vessel thickness (mm) | 216 | 90 | |
| | (8.5 in.) | | |
| Core barrel outside diameter (mm) | 3874 | 961 | |
| Core barrel inside diameter (mm) | 3760 | 929 | |
| Thermal shield outside diameter (mm) | 4170 | | |
| Thermal shield inside diameter (mm) | 4030 | | |
| Downcomer length (mm) | 4849 | 4849 | 1/1 |
| Downcomer gap (mm) | 114.3 | 61.5 | |
| Downcomer flow area (m²) | 4.23 | 0.197 | 1/21.44 |
| Lower-plenum volume (m³) | 29.6 | 1.38 | 1/21.44 |
| Upper-plenum volume (m³) | 43.6 | 2.04 | 1/21.44 |
| | | | |
| **Fuel (Heater-Rod) Assembly** | | | |
| Number of bundles | 193 | 32 | |
| Rod array | 15x15 | 8x8 | |
| Rod heated length (mm) | 3660 | 3660 | 1/1 |
| Rod pitch (mm) | 14.3 | 14.3 | 1/1 |
| Fuel rod outside diameter (mm) | 10.72 | 10.7 | 1/1 |
| Thimble tube diameter (mm) | 13.87 | 13.8 | 1/1 |
| Instrument tube diameter (mm) | 13.87 | 13.8 | 1/1 |
| Number of heater rods | 39372 | 1824 | 1/21.58 |
| Number of nonheated rods | 4053 | 244 | 1/18.09 |
| Core flow area (m²) | 5.29 | 0.25 | 1/21.2 |
| Core fluid volume (m³) | 17.95 | 0.915 | 1/19.6 |
| | | | |
| **Primary Loop** | | | |
| Hot-leg inside diameter (mm) | 736.6 (29 in.) | 155.2 | 1/4.75 |
| Hot-leg flow area (m²) | 0.426 | 0.019 | 1/22.54 |
| Hot-leg length (mm) | 3940 | 3940 | 1/1 |
| Pump-suction inside diameter (mm) | 787.4 (31 in.) | 155.2 | 1/5.07 |
| Pump-suction flow area (m²) | 0.487 | 0.019 | 1/25.77 |
| Pump-suction length (mm) | 9750 | 7950 | 1/1 |
| Cold-leg inside diameter (mm) | 698.5 (27.5 in.) | 155.2 | 1/4.50 |
| Cold-leg flow area (m²) | 0.383 | 0.019 | 1/20.26 |
| Cold-leg length (mm) | 5600 | 5600 | 1/1 |

TABLE 5.3-1 (cont)

## CCTF COMPONENT SCALED DIMENSIONS

| Component | PWR | JAERI | Ratio |
|---|---|---|---|
| Containment tank 1 (m³) | | 30 | |
| Containment tank 2 (m³) | | 50 | |
| Storage tank (m³) | | 25 | |
| Accumulator tank (m³) | | 5 | |
| Saturated water tank (m³) | | 3.5 | |
| **Steam-Generator Simulator** | | | |
| Number of tubes | 3388 | 158 | 1/21.44 |
| Tube length (average) (m) | 20.5 | 15.2 | 1/1.35 |
| Tube outside diameter (mm) | 22.225 (0.875 in.) | 25.4 | |
| Tube inside diameter (mm) | 19.7 (0.05 in.) | 19.6 | 1/1 |
| Tube wall thickness (mm) | 1.27 | 2.9 | |
| Heat-transfer area (m²) | 4784 (51 500 ft²) | 192 | 1/24.92 |
| | 1.03 | 0.048 | 1/21.44 |
| Inlet-plenum volume (m³) | 4.25 | 0.198 | 1/21.44 |
| Outlet-plenum volume (m³) | 4.25 | 0.198 | 1/21.44 |
| Primary-side volume (m³) | 30.50 (1077 ft³) | 2.4 | 1/15.25 |
| Secondary-side volume (m³) | 157.33 (5556 ft³) | 4.9 | 1/26.22 |

## TABLE 5.3-2

## COMPONENT ELEVATIONS OF THE CCTF

| Component | PWR | CCTF | Discrepancy |
|---|---|---|---|
| Bottom of heated region in core (mm) | 0 | 0 | 0 |
| Top of heated region in core (mm) | 660 | 3660 | 0 |
| Top of downcomer (mm) | 4849 | 4849 | 0 |
| Bottom of downcomer (mm) | 0 | 0 | 0 |
| Centerline of cold leg (mm) | 5198 | 4927 | -271 |
| Bottom of cold leg (inside) (mm) | 4849 | 4849 | 0 |
| Centerline of loop-seal lower end (mm) | 2056 | 2047 | -9 |
| Bottom of loop-seal lower end (mm) | 1662 | 1959 | +297 |
| Center of hot leg (mm) | 5198 | 4927 | -271 |
| Bottom of hot leg (inside) (mm) | 4830 | 4849 | +19 |
| Bottom of upper core plate (mm) | 3957 | 3957 | 0 |
| Top of lower core plate (mm) | -108 | -50 | +58 |
| Bottom of tube sheet of steam-generator simulator (mm) | 7308 | 7307 | -1 |
| Lower end of steam-generator simulator plenum (mm) | 5713 | 5712 | -1 |
| Top of tubes of steam-generator simulator (avg.) (mm) | 17952.7 | 14820 | |

## TABLE 5.3-3

## SUMMARY OF MEASURED TEST CONDITIONS

1. Test type: Low-power test
2. Test No. : Shakedown test 2 (Run 54)
3. Test Data: March 30, 1982
4. Power : Total; 7.87 MW, Linear; 1.18 kW/m
5. Radial power distribution:

   A    B    C

   1.37 : 1.20 : 0.76

6. Pressure (MPa):

   Containment; 0.2

   Steam-generator secondary; 5.3

7. Temperature (K):

   Downcomer wall; 468 K vessel internals; 423 K

   Primary piping; 406 K lower-plenum liquid; 394 K

   ECC liquid; 310 K

8. ECC injection type: Lower-plenum and cold-leg injection
9. Pump K-factor: 15
10. ECC injection rates, durations, and injection locations:

    ACC ; 0.104 m$^3$/s from 81.0 to 94.0 s into lower plenum[a]

    0.088 m$^3$/s from 94.0 to 107.0 s into cold legs[a]

    LPCI; 0.0116 m$^3$/s from 107.0 to 979.0 s into cold legs[a]

11. Initial water level:

    In lower plenum; 0.86 m

    In steam-generator secondary side; 7.4 m

12. Power decay:

    Constant; from 0 to 90.5 s[a]

    ANS 1.0 + actinide (30 s after scram); from 90.5 to 690.5 s[a]

    Linear decay; from 690.5 to 898.0 s[a]

13. Reflood initiation time: 90.5 s[a]
14. PCT at reflood initiation: 1074 K at TE31Y17

---

[a]Time in this table is defined as time after test initiation.

# TABLE 5.3-4

## CHRONOLOGY OF EVENTS FOR CCTF RUN 54

| Event | Time After Test Initiation (s) | Time Relative to Reflood Initiation (s) |
|---|---|---|
| Test initiated (Heater rods power on) (Data recording initiated) | 0(15.15.39) | -90.5 |
| Accumulator injection initiated | 81.0 | -9.5 |
| Power decay initiated (Bottom of core recovery) (Reflood initiated) | 90.5 | 0.0 |
| Accumulator injection switched from lower plenum to cold leg | 94.0 | 3.5 |
| Accumulator injection ended and LPCI injection initiated | 107.0 | 16.5 |
| Maximum PCT time | 123.0 | 32.5 |
| All heater rods quenched | 552.5 | 462.0 |
| Linear power decay initiated | 690.5 | 600.0 |
| Power off | 898.0 | 807.5 |
| LPCI injection ended | 979.0 | 888.5 |
| Test ended (data recording ended) | 1032.0 | 941.5 |

## TABLE 5.3-5

## EFFECT OF MODELING CORRECTIONS ON CALCULATED PEAK CLADDING TEMPERATURES AND QUENCH TIMES

| Rod Type | Rod Elevation (m) | Corrected Azimuthal-Noding Model Compared to Previous Model | | Corrected Azimuthal-Noding and Axial Power Model Compared to Previous Model | |
|---|---|---|---|---|---|
| | | Effect on PCT | Effect on QT | Effect on PCT | Effect on QT |
| High power | 2.48 | ~Same | Later | Higher | Earlier |
| | 3.115 | ~Same | Earlier | ~Same | ~Same |
| | 3.93 | Lower | ~Same | ~Same | ~Same |
| | 4.54 | ~Same | Later | ~Same | Later |
| | 5.15 | ~Same | Later | Lower | Later |
| Intermediate power | 2.48 | ~Same | Earlier | Higher | Earlier |
| | 3.115 | ~Same | Earlier | Higher | Earlier |
| | 3.93 | ~Same | Later | ~Same | ~Same |
| | 4.54 | ~Same | Later | ~Same | ~Same |
| | 5.15 | ~Same | Later | ~Same | Later |
| Low power | 2.48 | ~Same | Later | Higher | Later |
| | 3.115 | ~Same | ~Same | Higher | ~Same |
| | 3.93 | ~Same | ~Same | Lower | ~Same |
| | 4.54 | ~Same | Later | Lower | ~Same |
| | 5.15 | Higher | Earlier | Lower | Earlier |
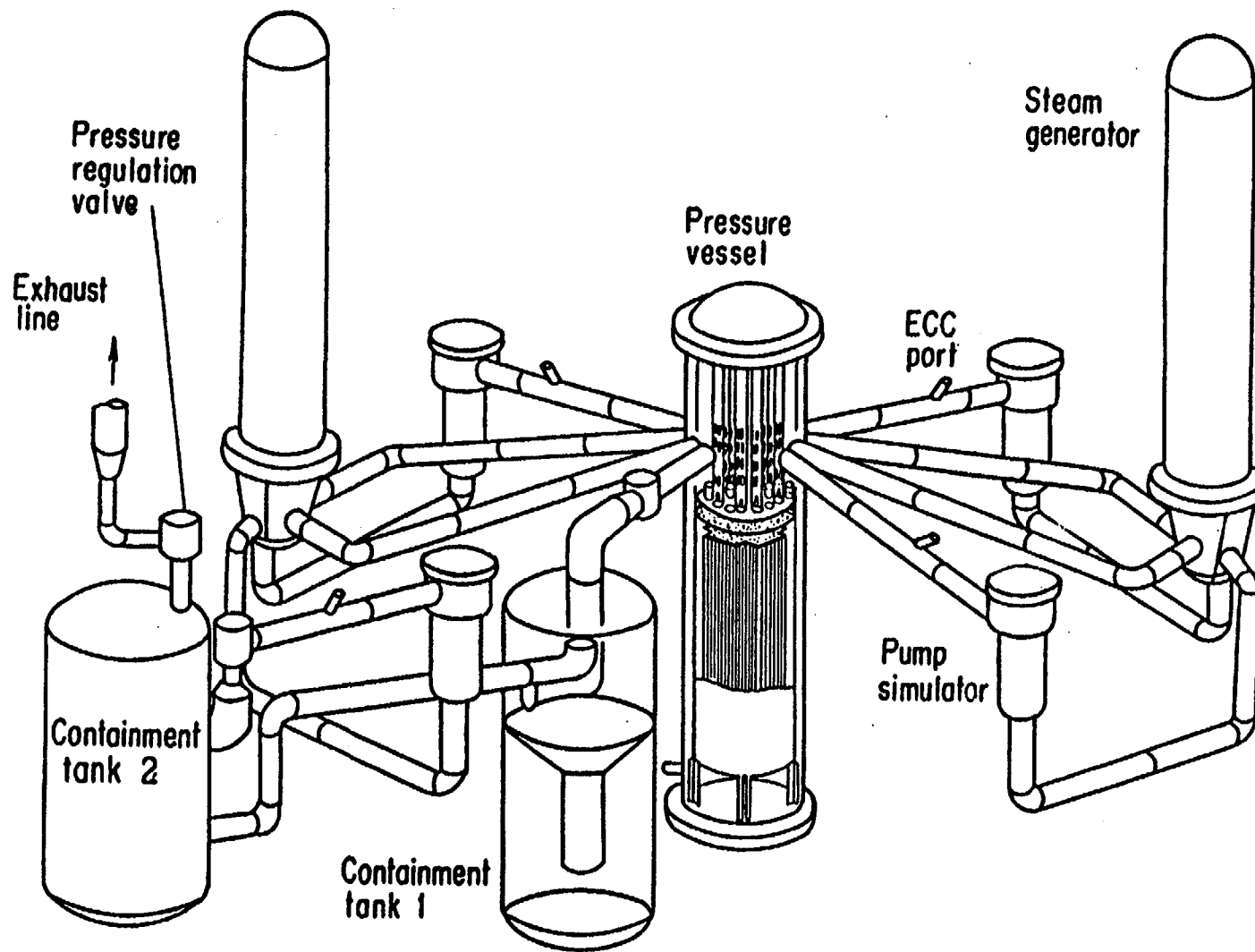
Fig. 5.3-1. Isometric view of the CCTF.
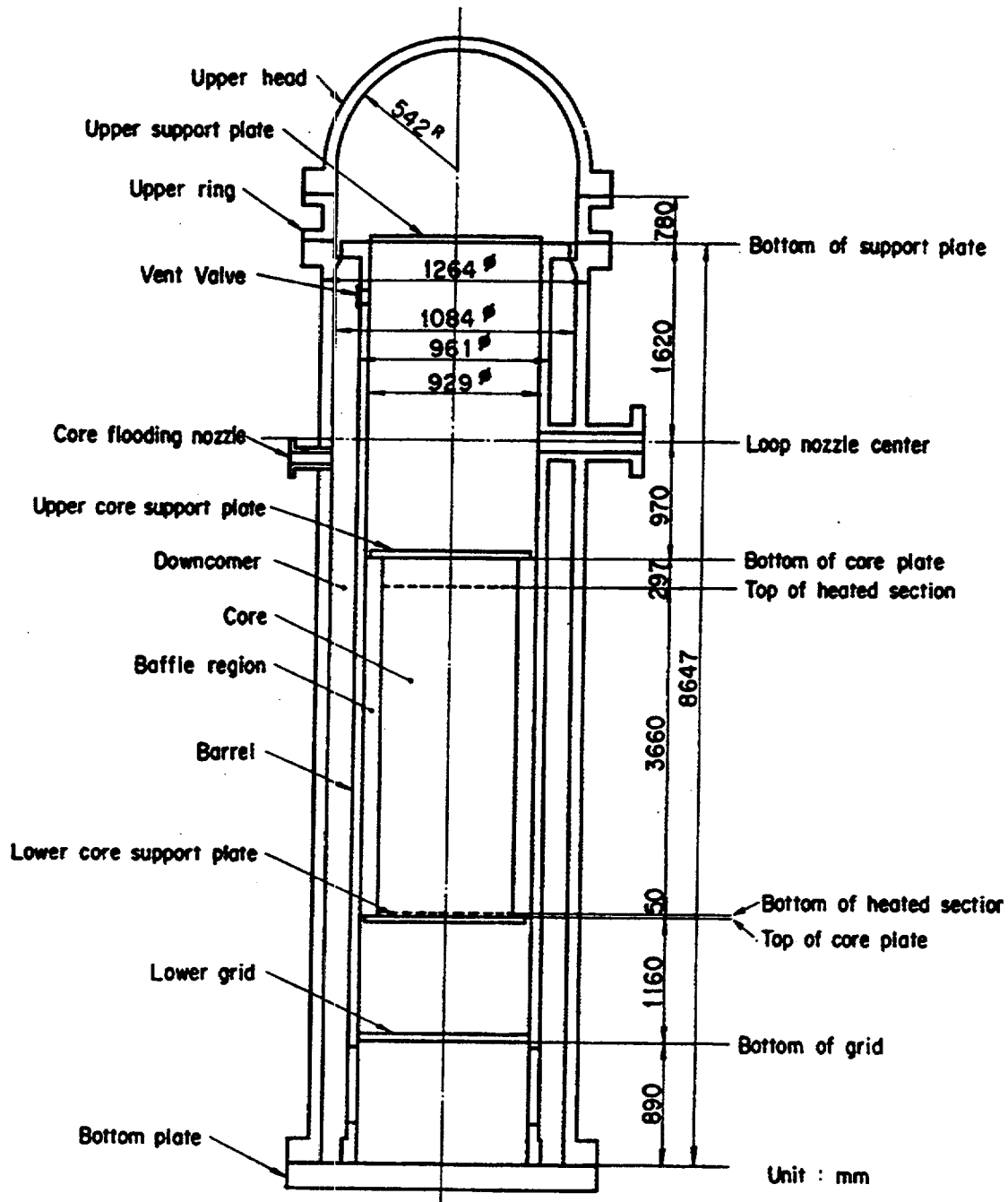
Fig. 5.3-2. CCTF pressure vessel.

PN

Hot leg

Downcomer
injection
nozzle

Hot leg

High power zone
(4 Assemblies)

Medium power zone
(12 Assemblies)

Cold leg

Low power zone
(16 Assemblies)

vv

vv

Cold leg

A   B   C

Cold leg

vv

vv

Broken cold leg

Cold leg

Hot leg

Broken hot leg

Downcomer
injection
nozzle

vv : Vent valve

90

1084

615

961

16

929

686

458

Vessel wall

Downcomer

Barrel

Baffle region

Core

Pipes for
pressure
measurement

Core
· 32 Bundles
· Bundle size   113.4
Bundle pitch  114.4

Unit : mm

Fig. 5.3-3. Cross-sections of the CCTF pressure vessel.
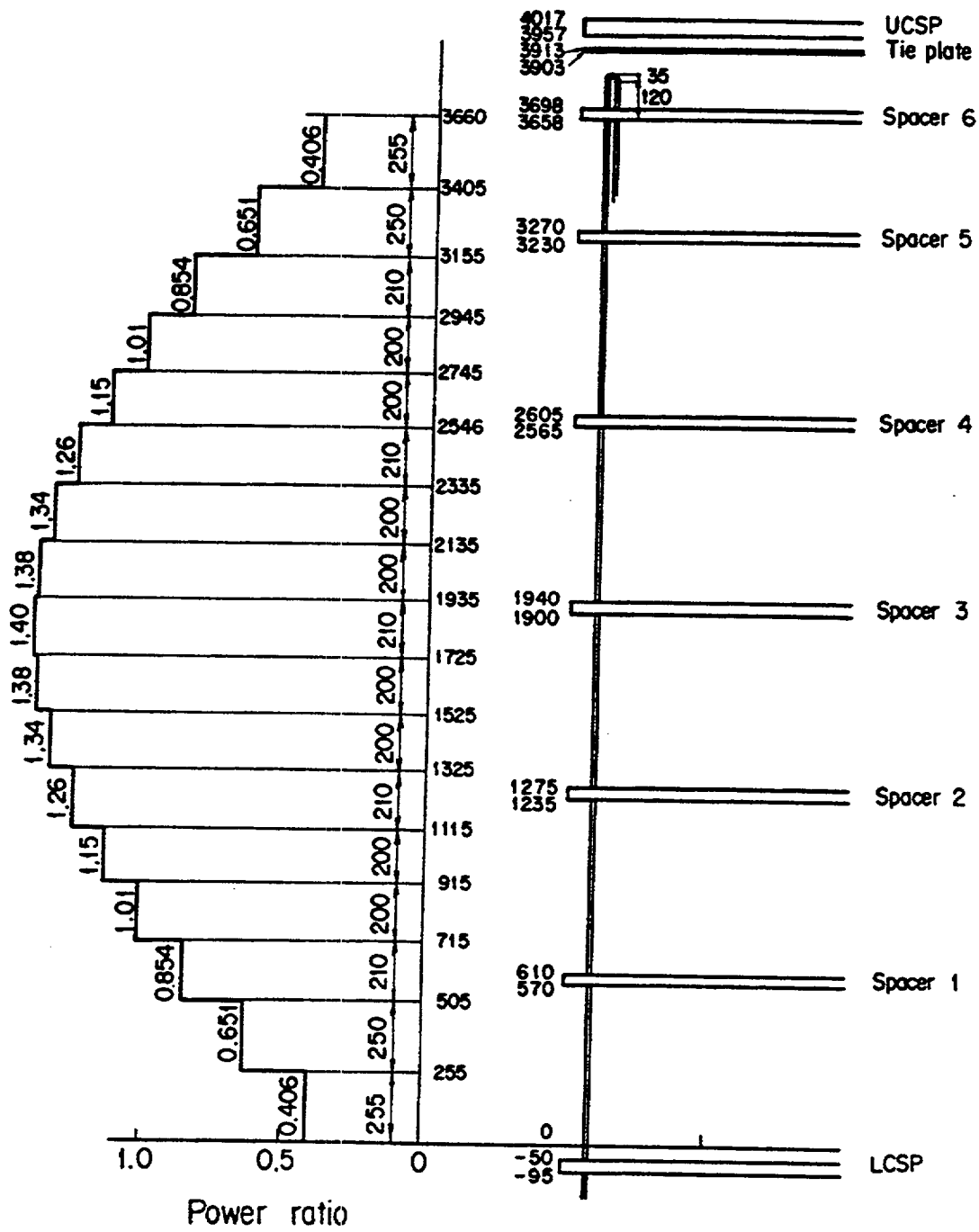
Fig. 5.3-4. CCTF heater-rod axial power profile.
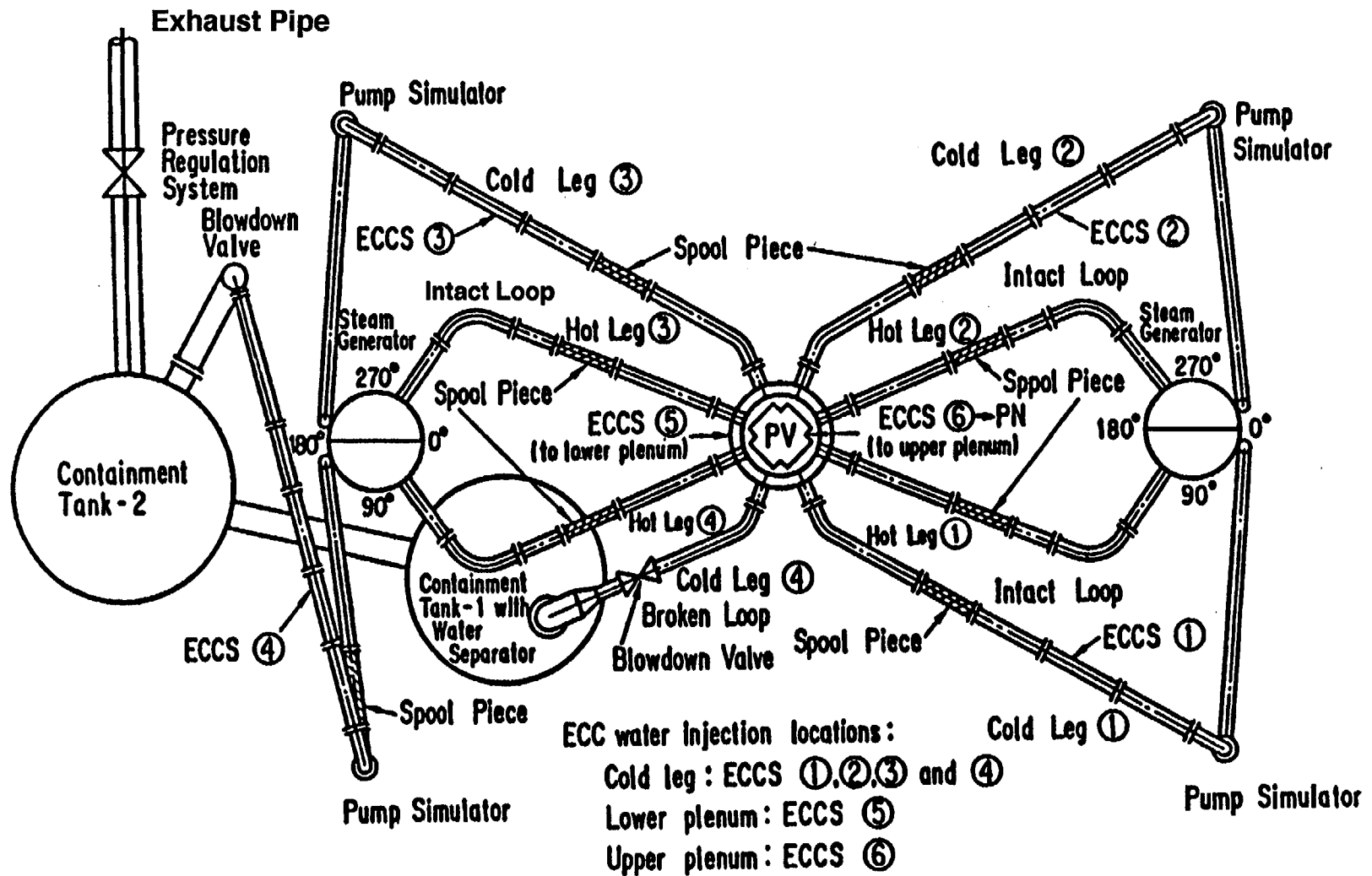
Fig. 5.3-5. Top view of the primary-loop piping layout.

Fig. 5.3-6. CCTF pressure vessel noding diagram: 2-theta model.
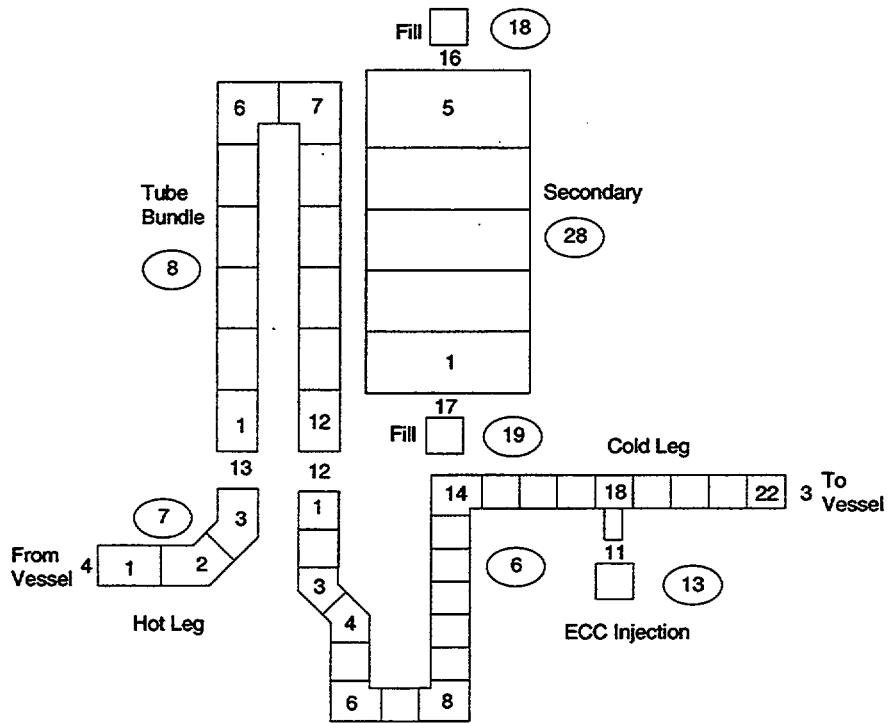
Fig. 5.3-7. CCTF intact-loop noding diagram.
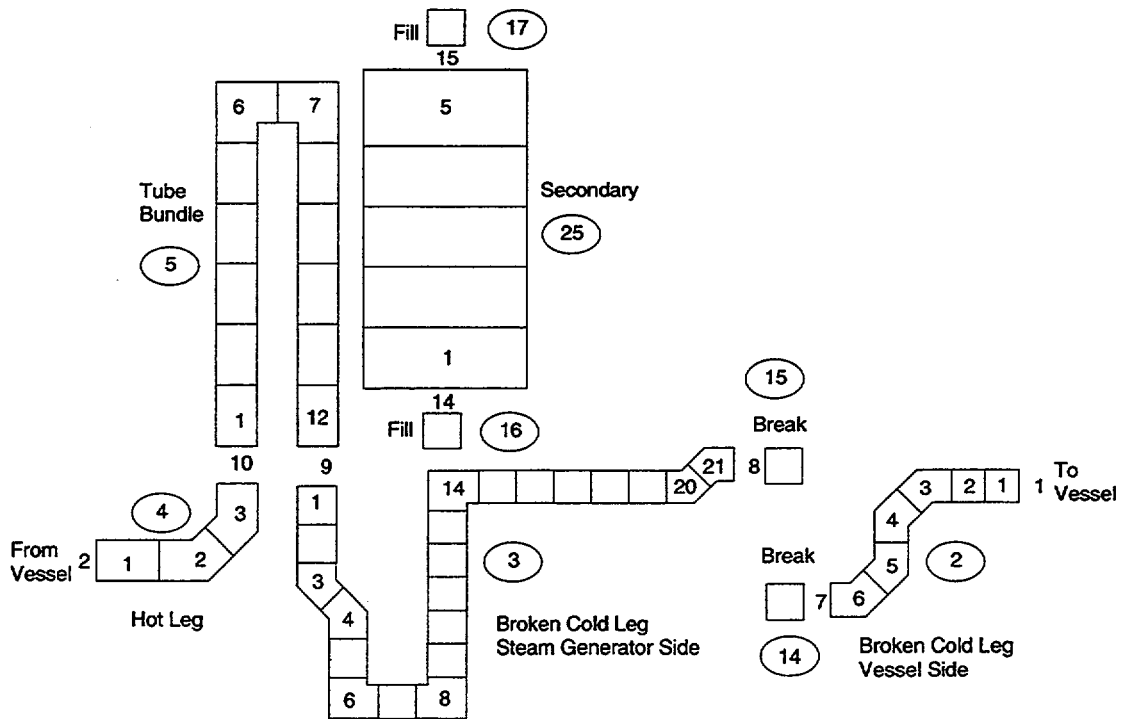


Fig. 5.3-8. CCTF broken-loop noding diagram.
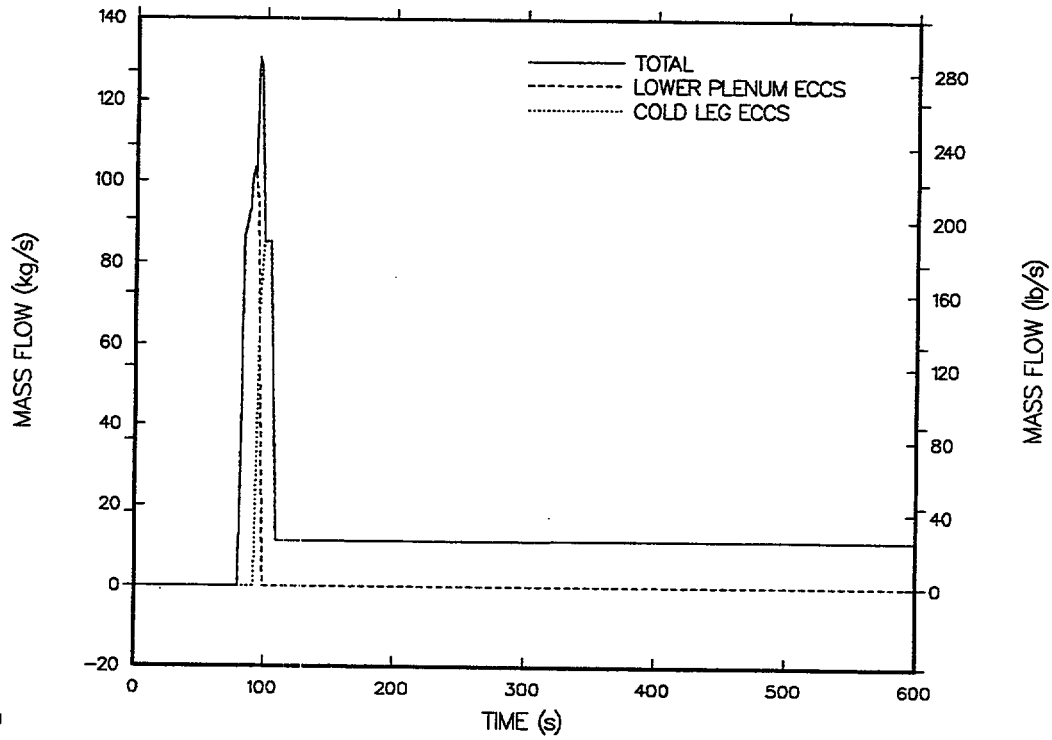
Fig. 5.3-9. ECCS flow injection in CCTF Run 54.
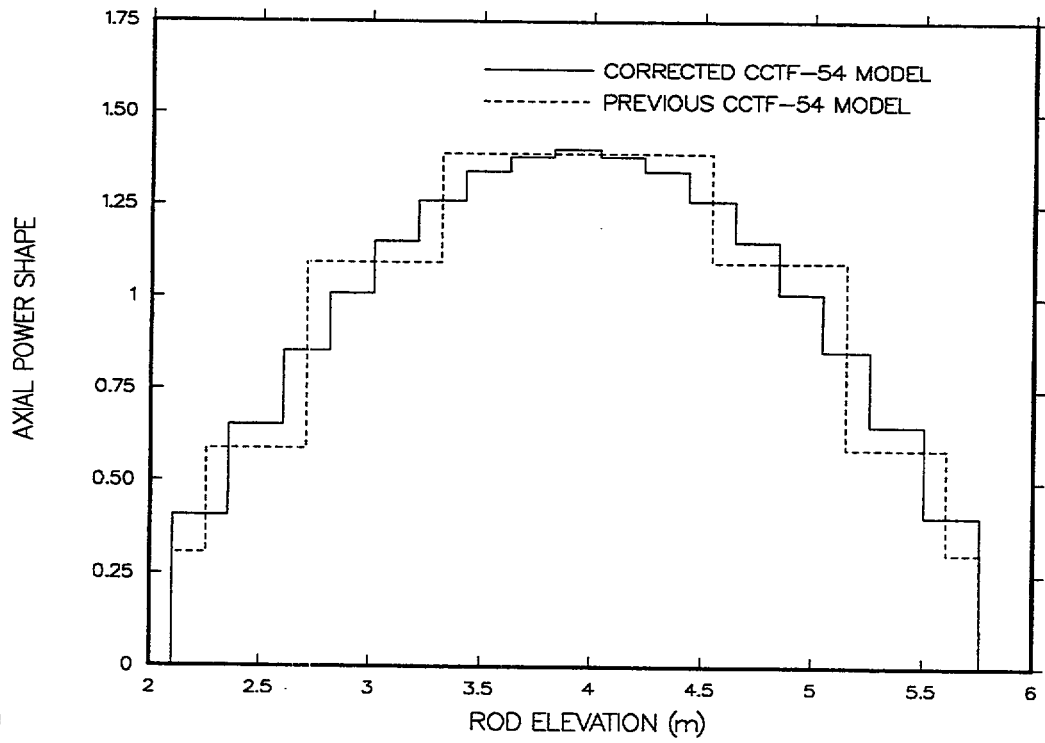


Fig. 5.3-10. Axial power profiles modeled in the corrected and previous CCTF Run 54 input models.
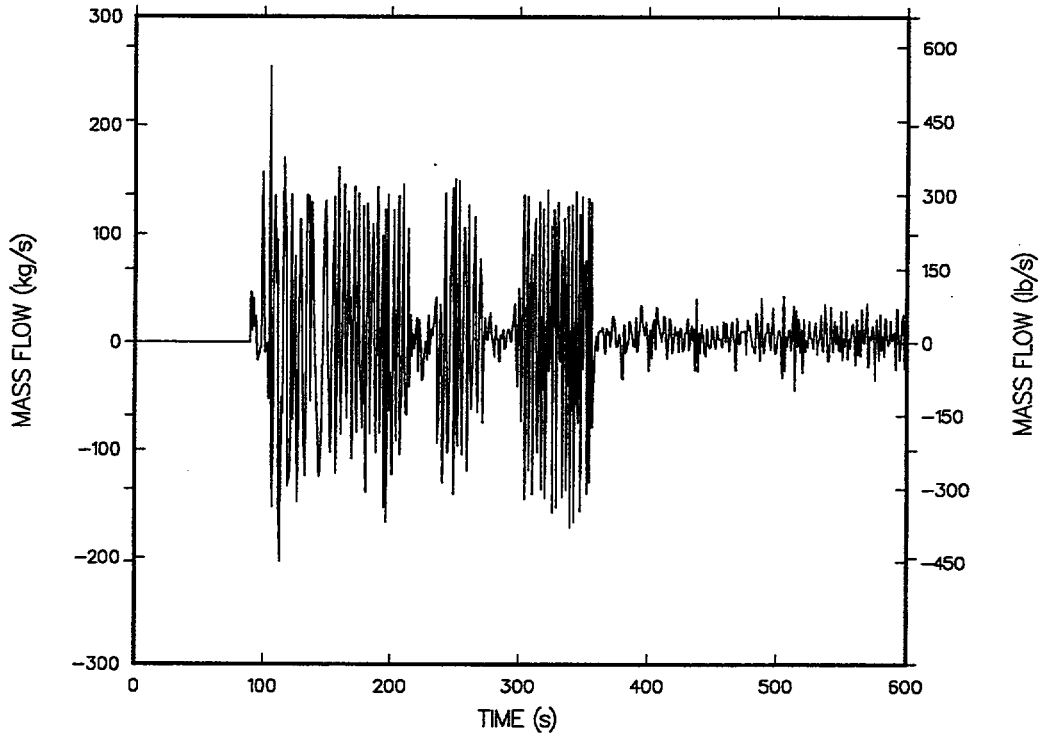
Fig. 5.3-11. Core inlet mass flow.
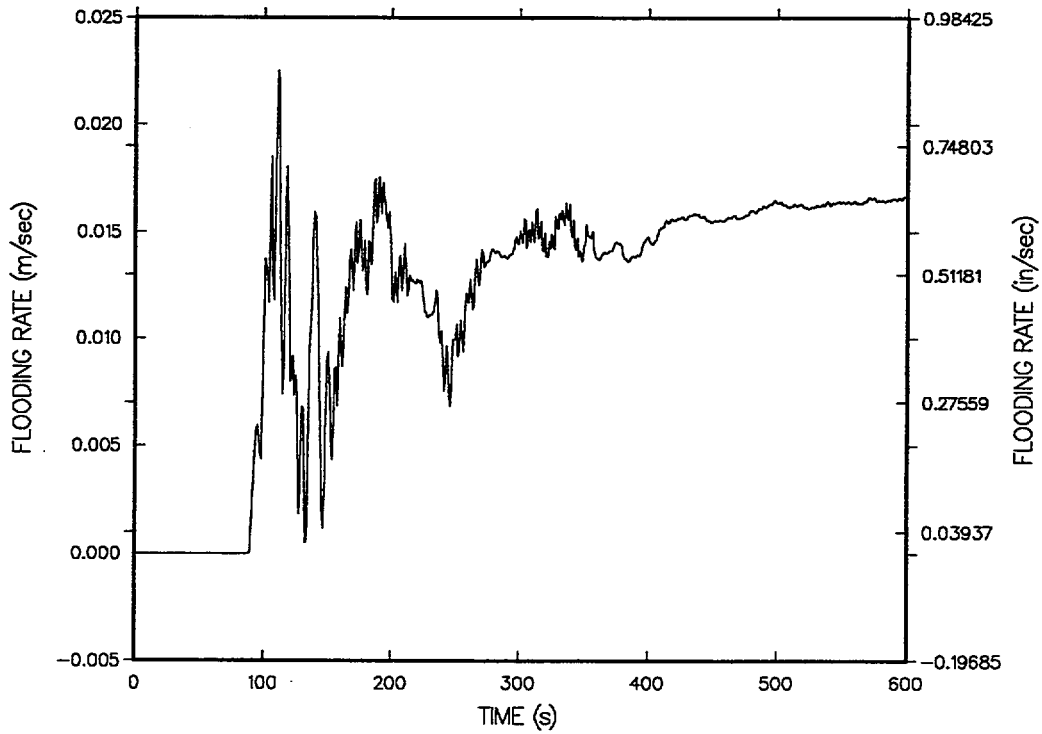


Fig. 5.3-12. Time-averaged core flooding rate.
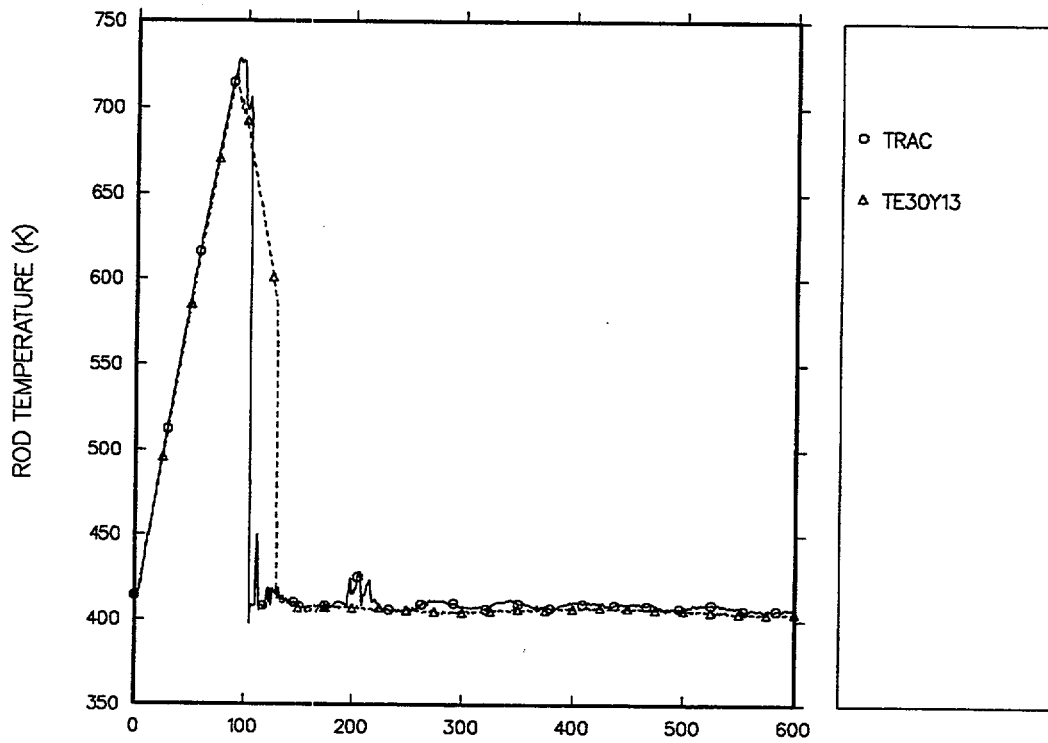
Fig. 5.3-13. Calculated and measured cladding temperatures for the hot rod at the 2.480-m elevation.
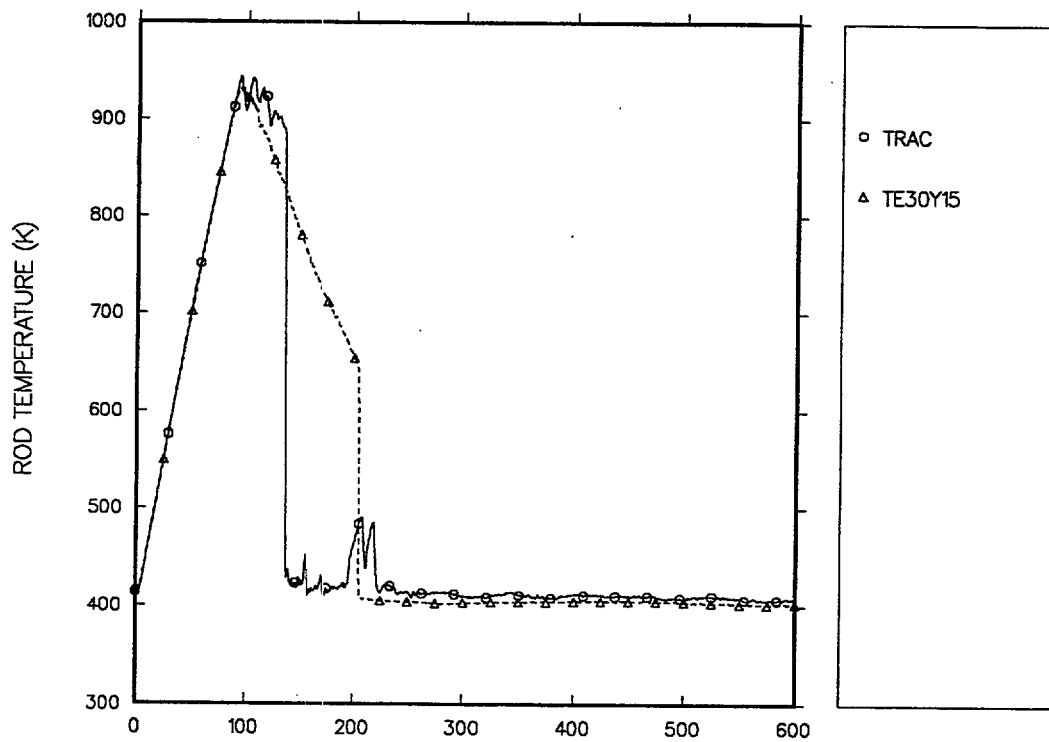


Fig. 5.3-14. Calculated and measured cladding temperatures for the hot rod at the 3.115-m elevation.
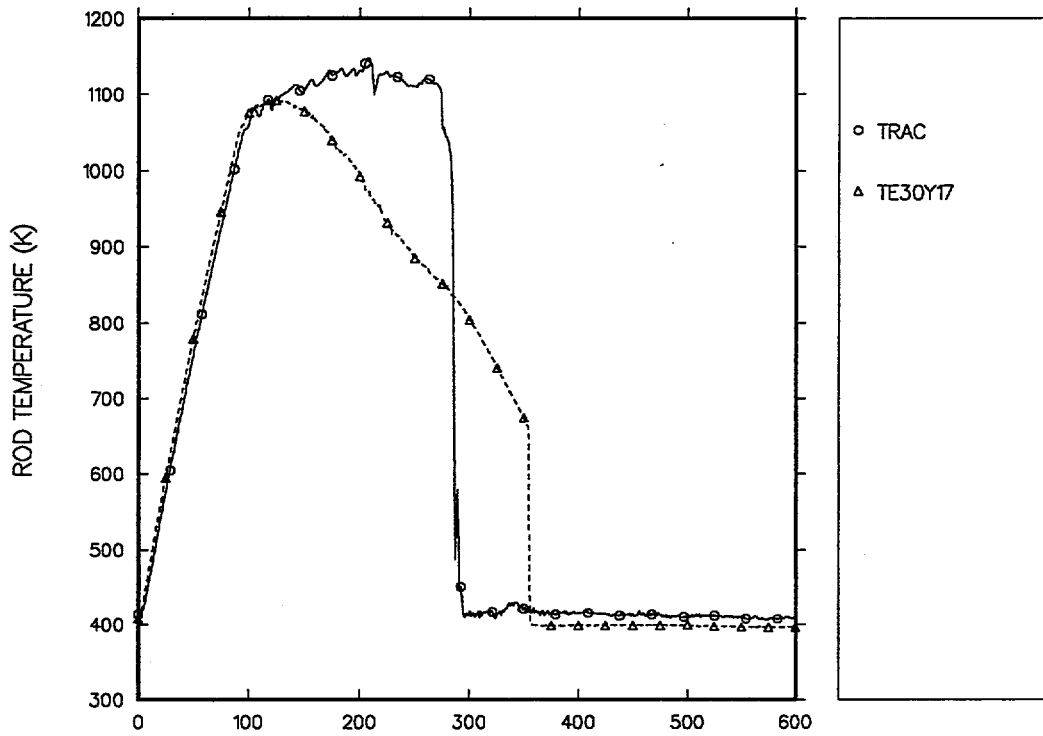
Fig. 5.3-15. Calculated and measured cladding temperatures for the hot rod at the 3.930-m (core midplane) elevation.
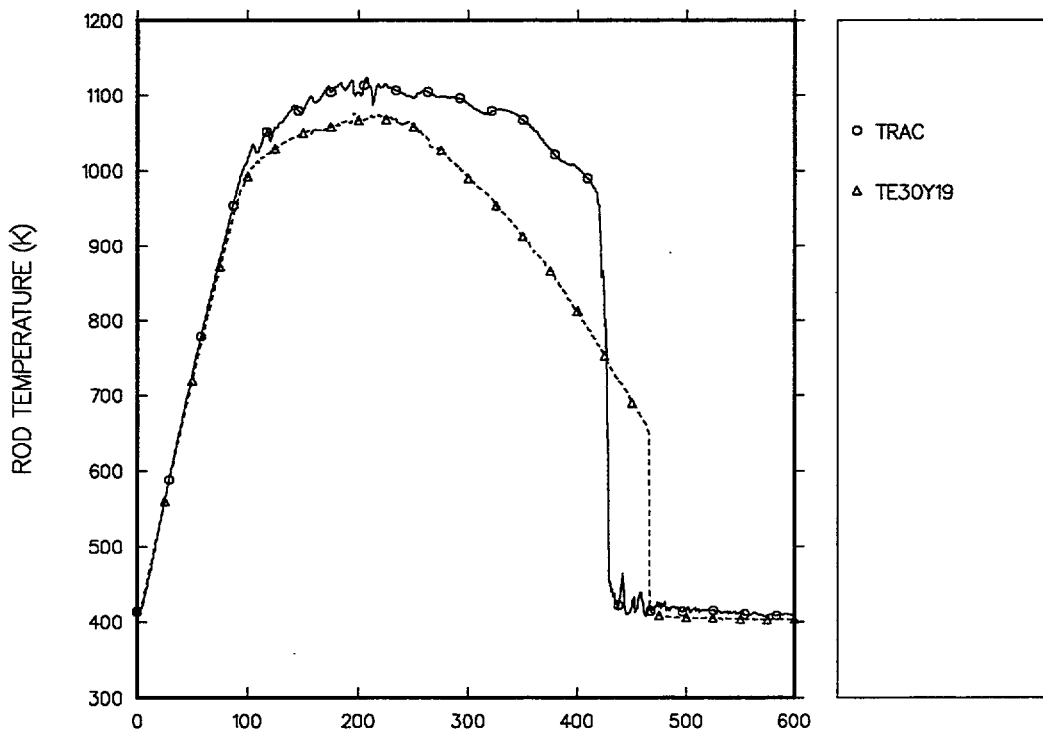


Fig. 5.3-16. Calculated and measured cladding temperatures for the hot rod at the 4.540-m elevation.
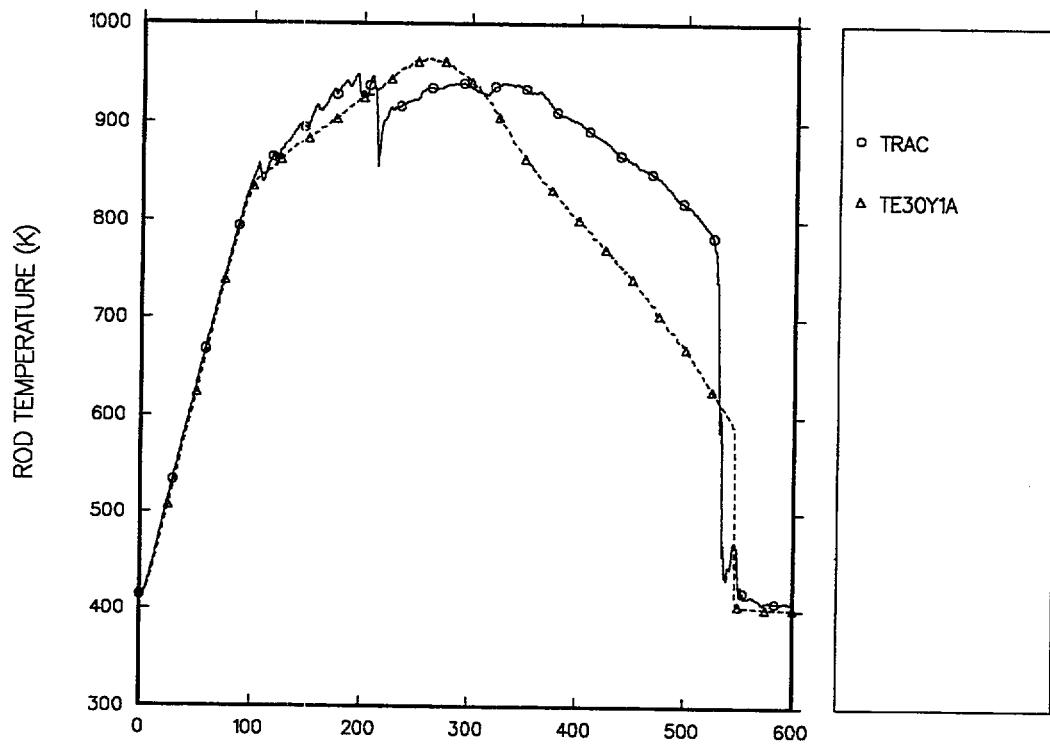
Fig. 5.3-17. Calculated and measured cladding temperatures for the hot rod at the 5.150-m elevation.
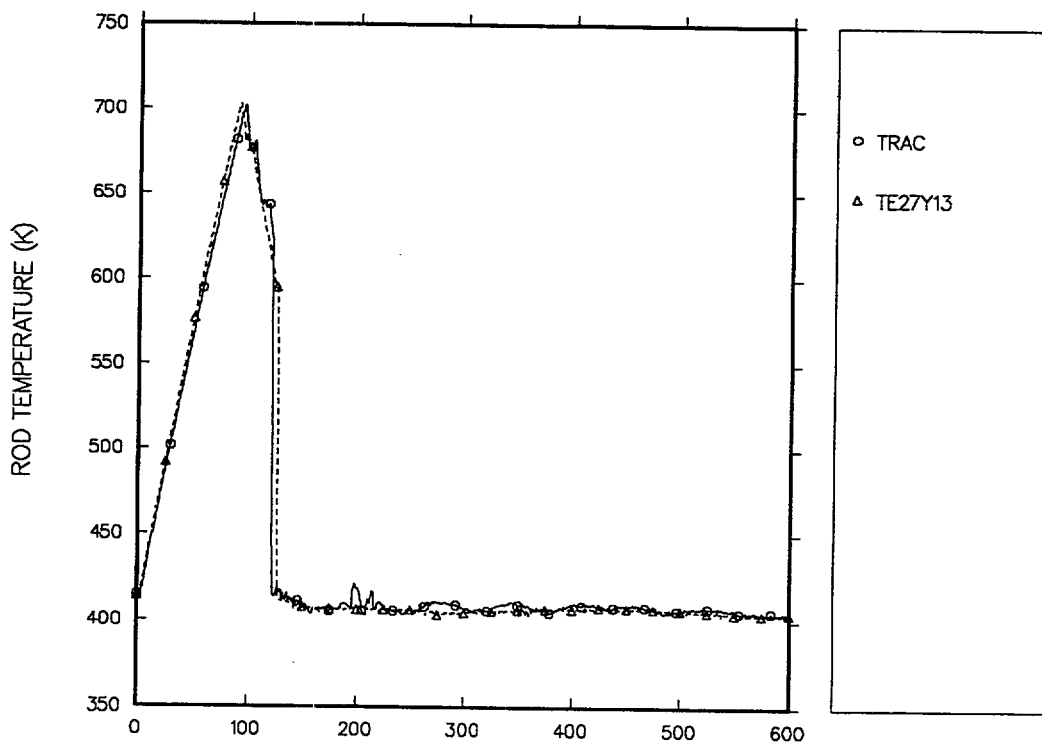


Fig. 5.3-18. Calculated and measured cladding temperatures for the intermediate-powered rod at the 2.480-m elevation.
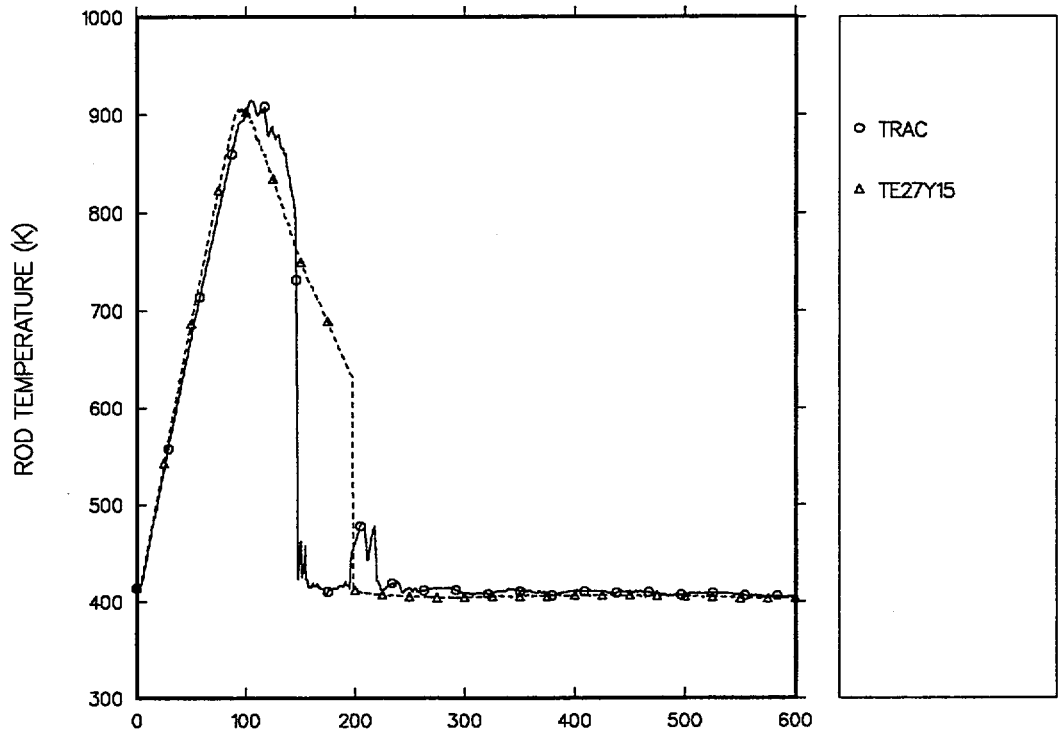
Fig. 5.3-19. Calculated and measured cladding temperatures for the intermediate-powered rod at the 3.115-m elevation.
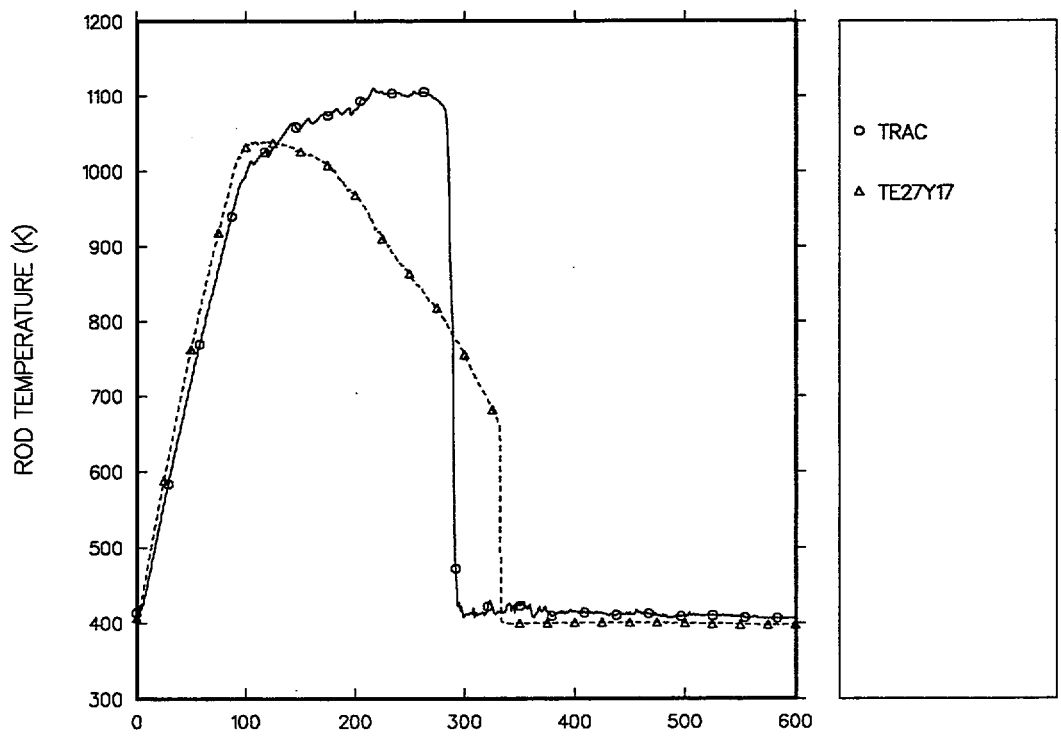


Fig. 5.3-20. Calculated and measured cladding temperatures for the intermediate-powered rod at the core midplane.
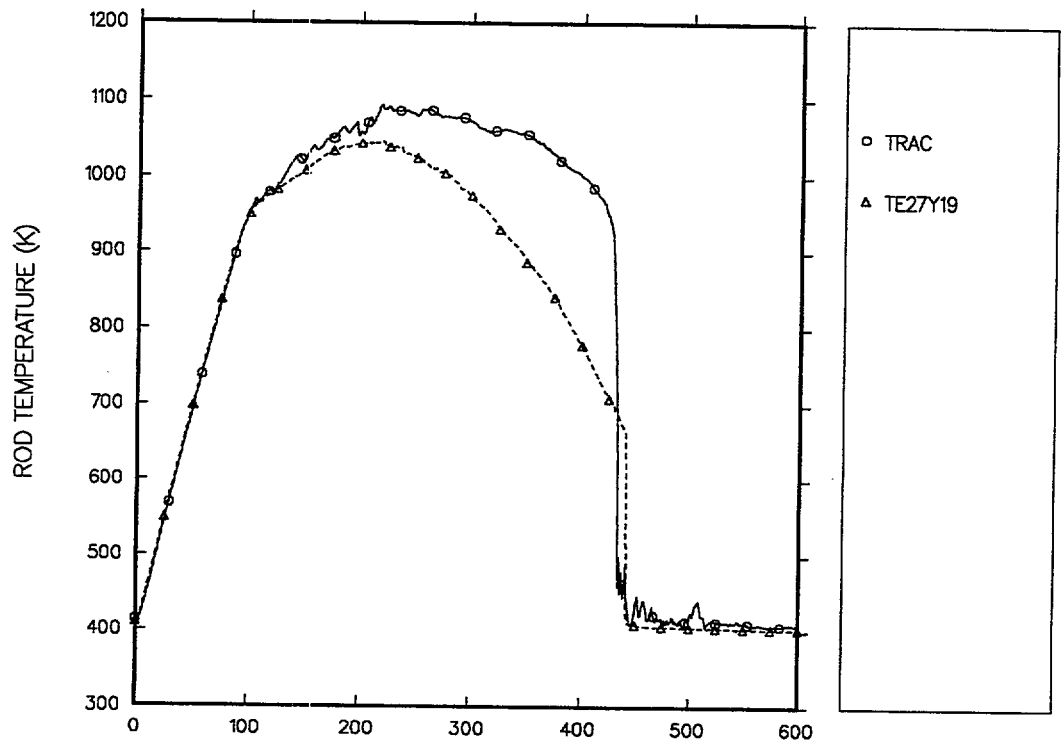
Fig. 5.3-21. Calculated and measured cladding temperatures for the intermediate-powered rod at the 4.540-m elevation.
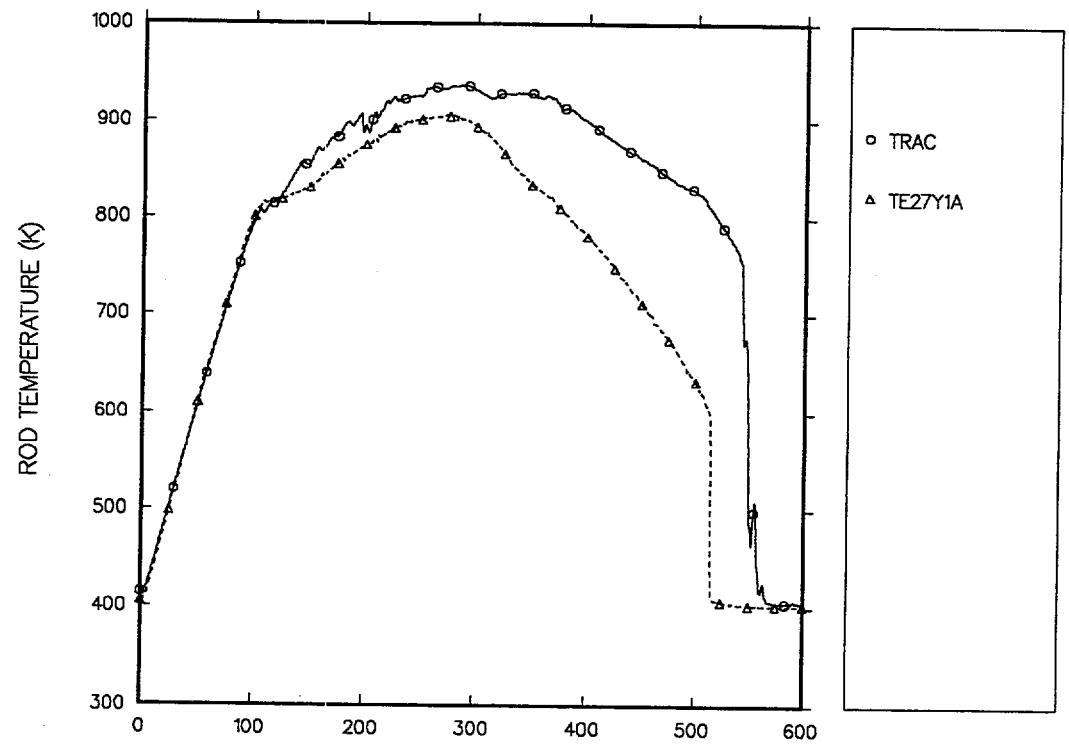


Fig. 5.3-22. Calculated and measured cladding temperatures for the intermediate-powered rod at the 5.150-m elevation.
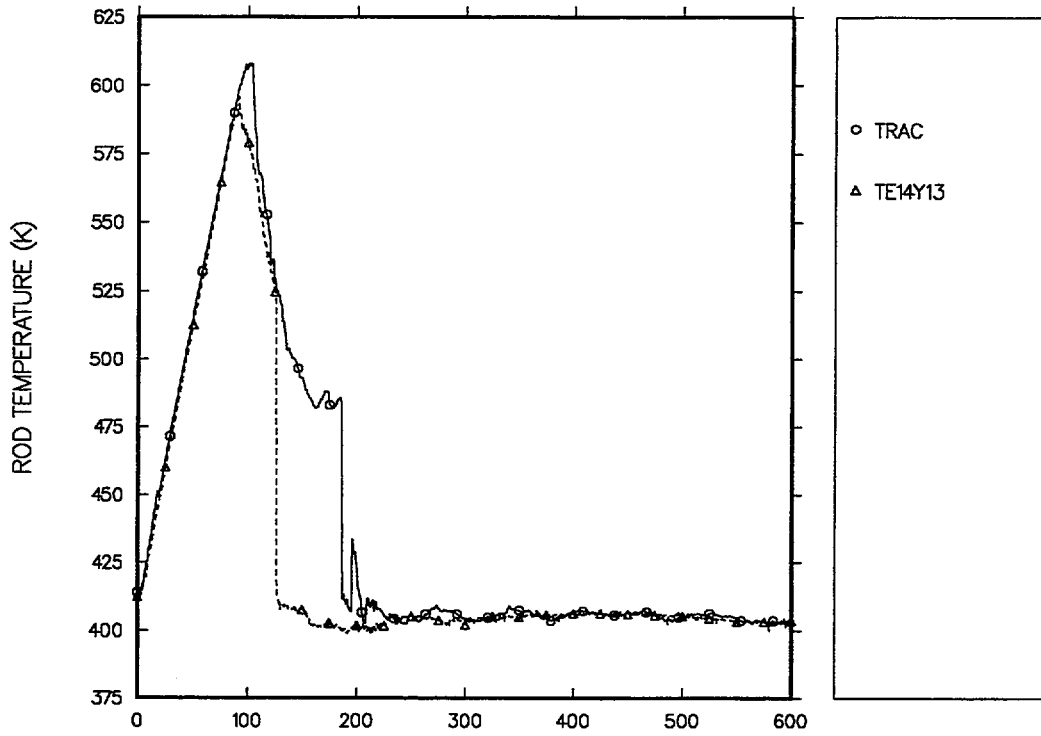
Fig. 5.3-23. Calculated and measured cladding temperatures for the low-powered rod at the 2.480-m elevation.
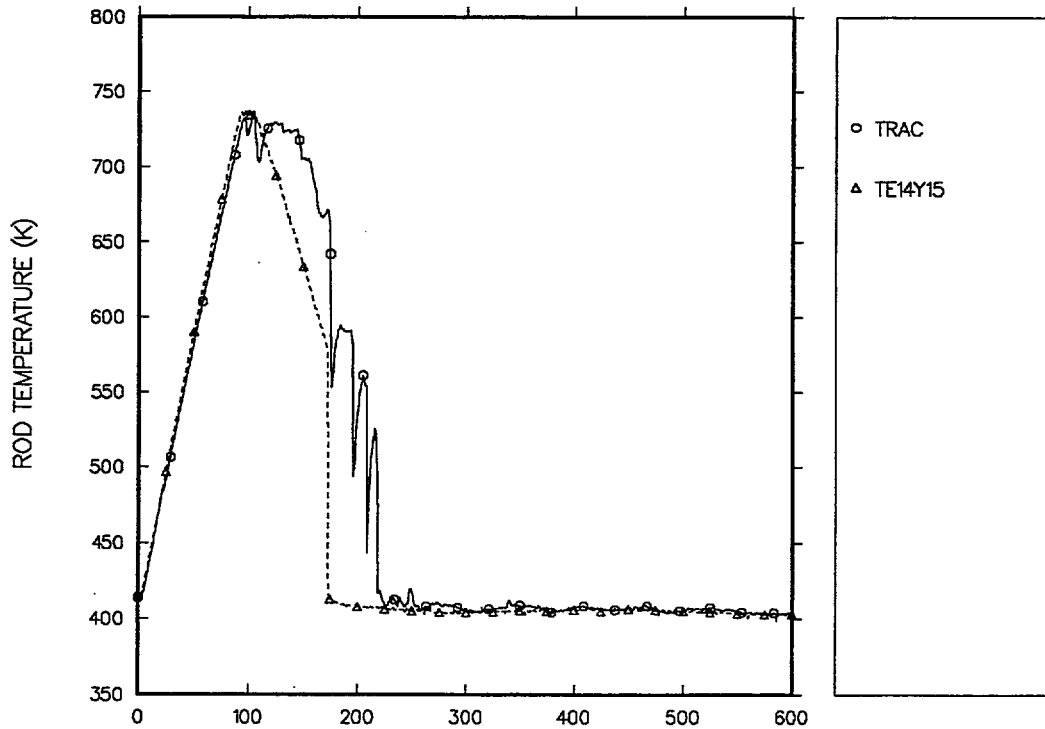


Fig. 5.3-24. Calculated and measured cladding temperatures for the low-powered rod at the 3.115-m elevation.
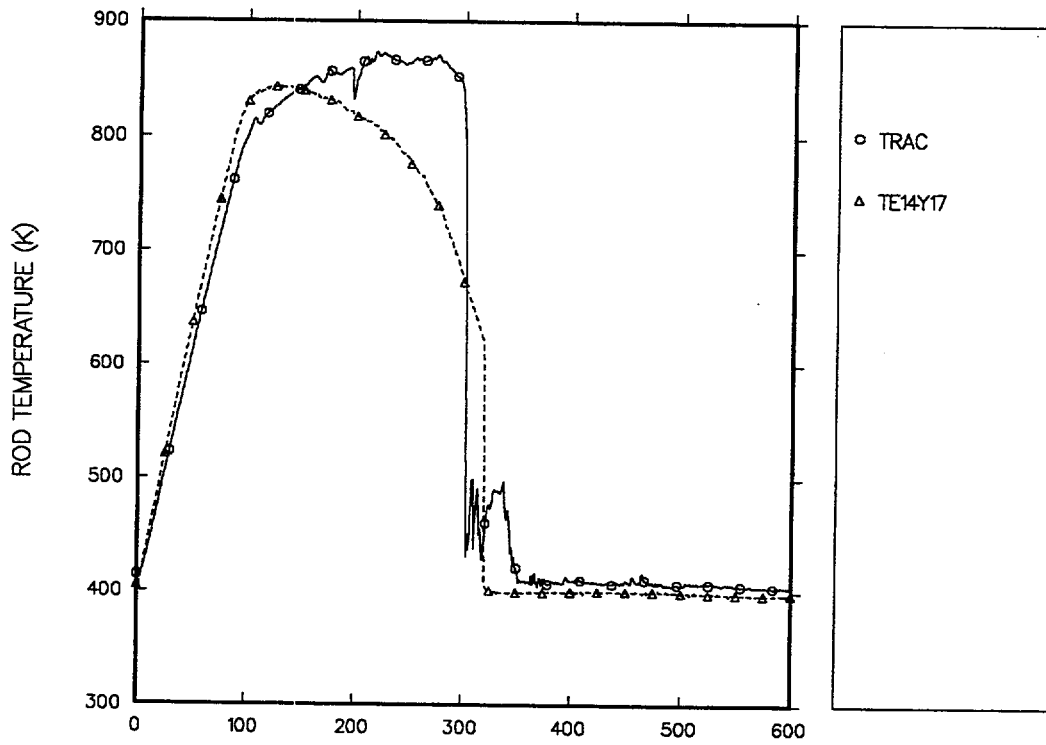
Fig. 5.3-25.  Calculated and measured cladding temperatures for the low-powered rod
at the core midplane.
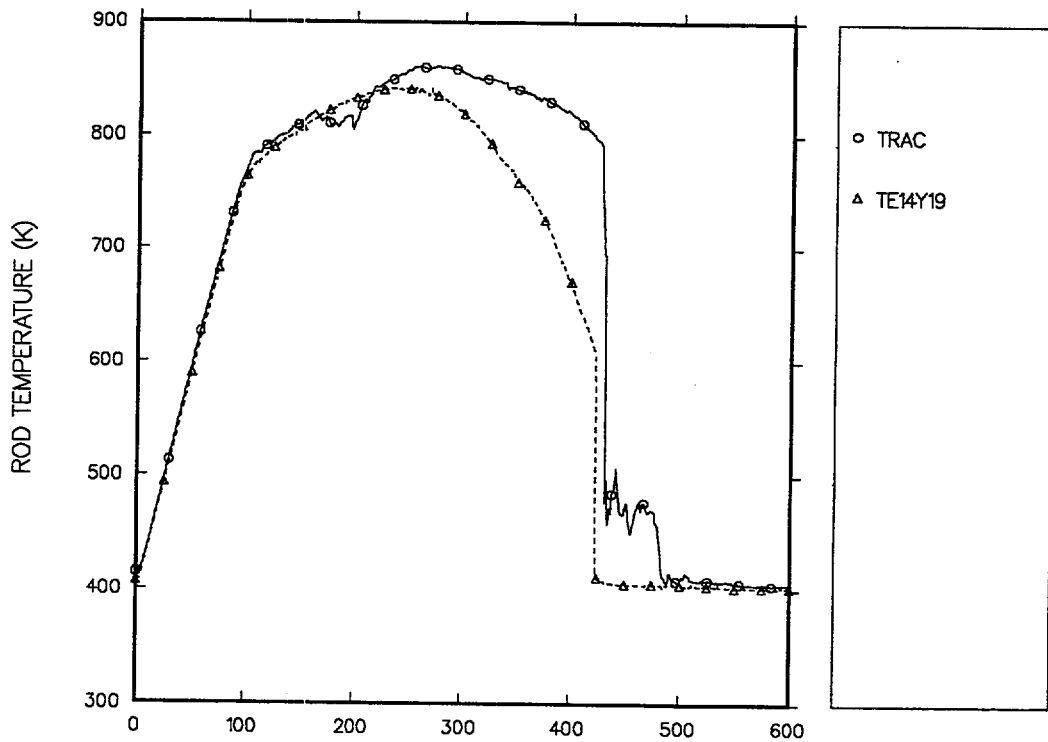


Fig. 5.3-26.  Calculated and measured cladding temperatures for the low-powered rod
at the 4.540-m elevation.
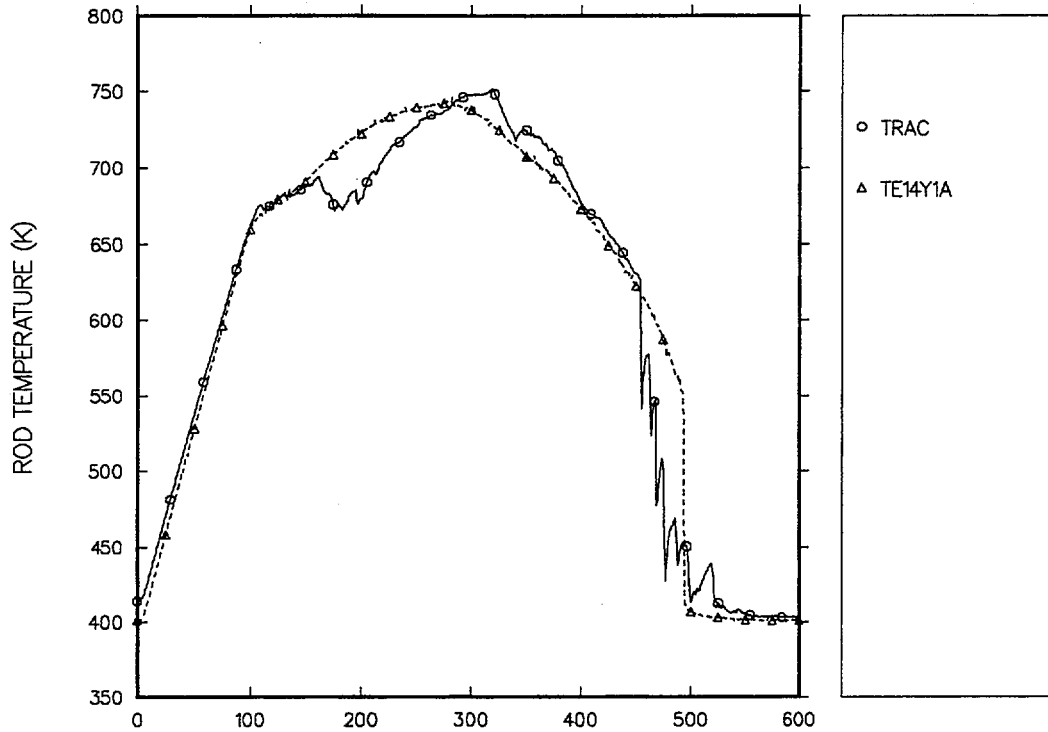
Fig. 5.3-27. Calculated and measured cladding temperatures for the low-powered rod at the 5.150-m elevation.
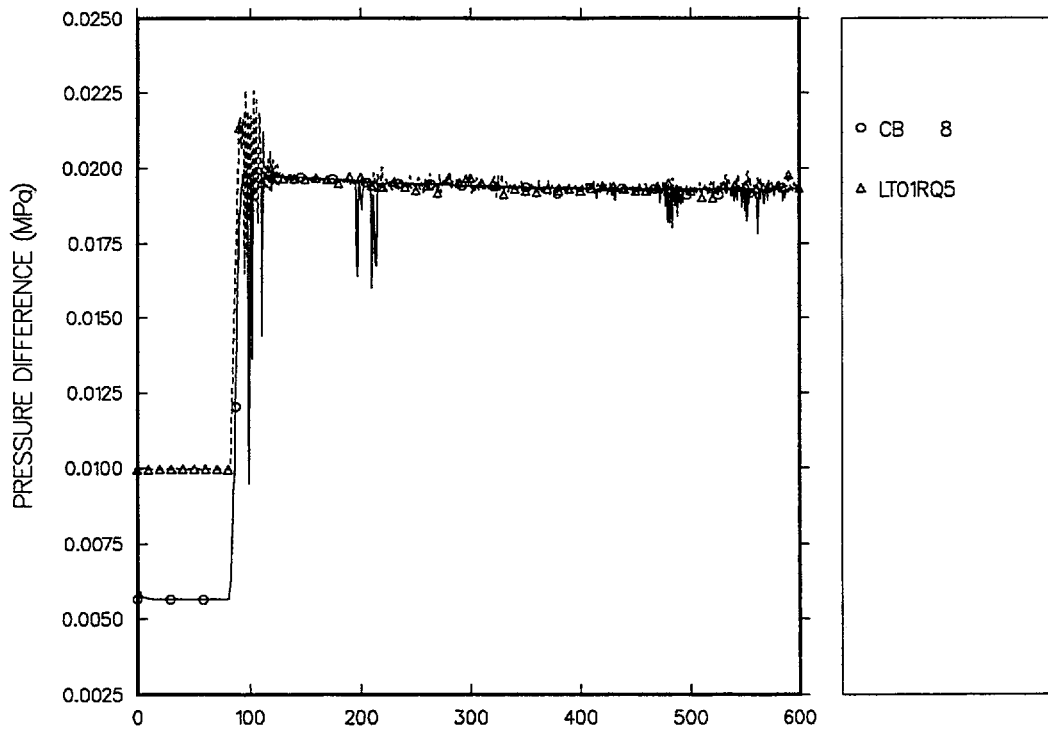


Fig. 5.3-28. Calculated and measured pressure vessel differential pressure: lower plenum.
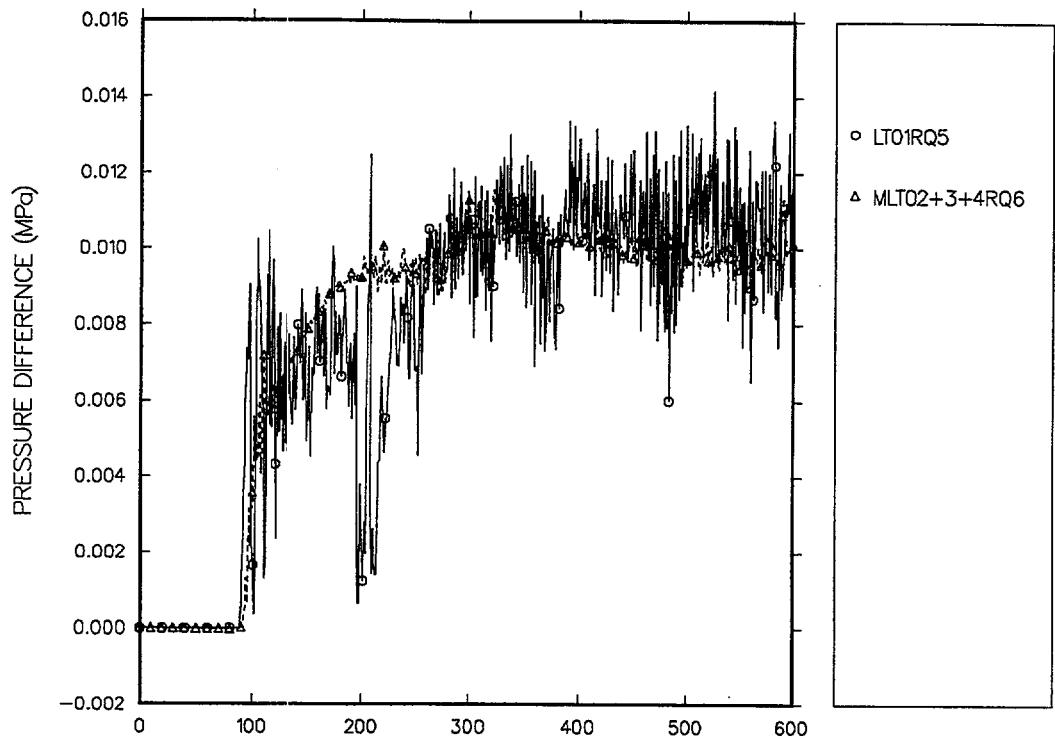
Fig. 5.3-29. Calculated and measured pressure vessel differential pressure: lower half of the core.
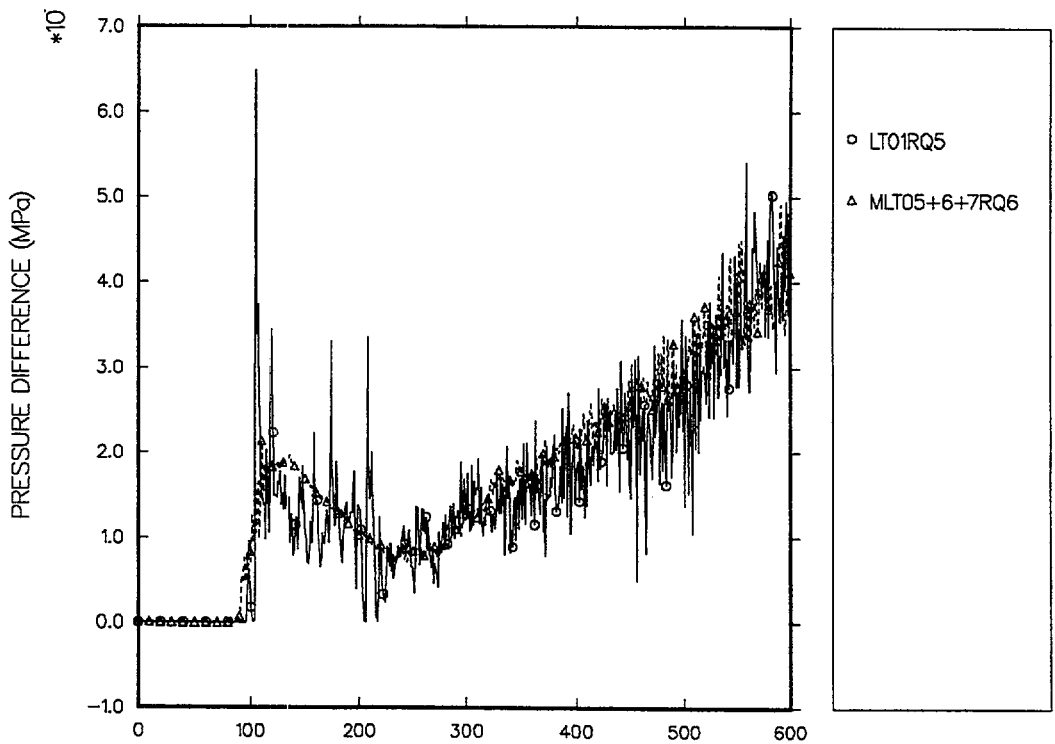


Fig. 5.3-30. Calculated and measured pressure vessel differential pressure: upper half of the core.
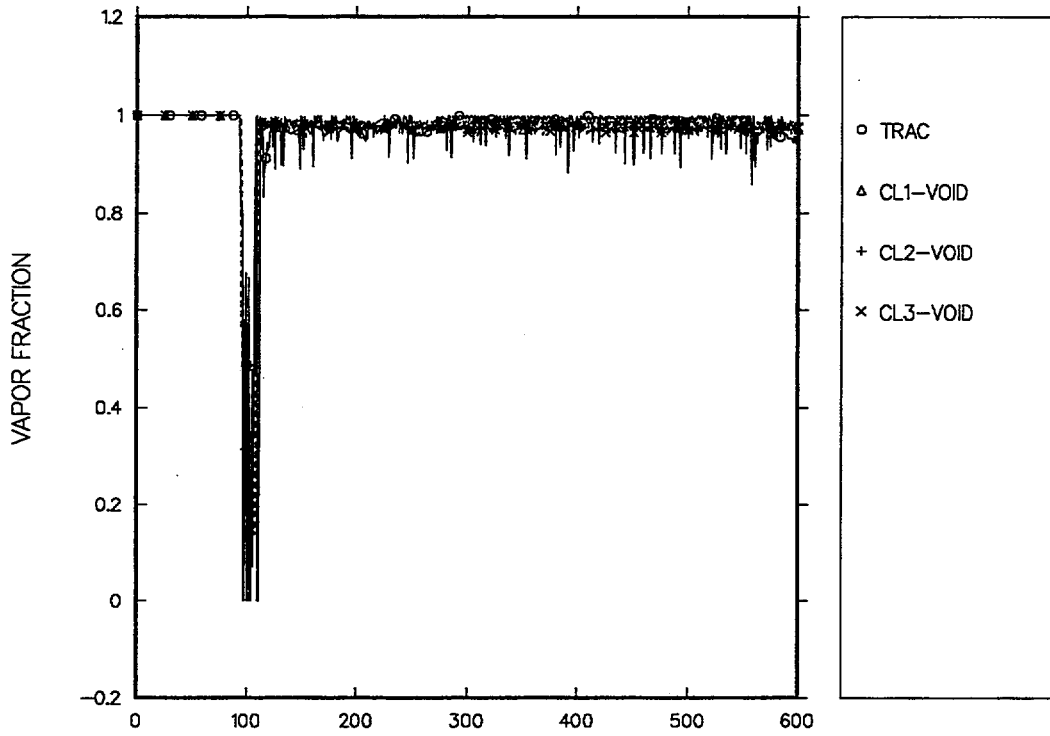
Fig. 5.3-31. Calculated and measured cold-leg spool-piece void fraction.
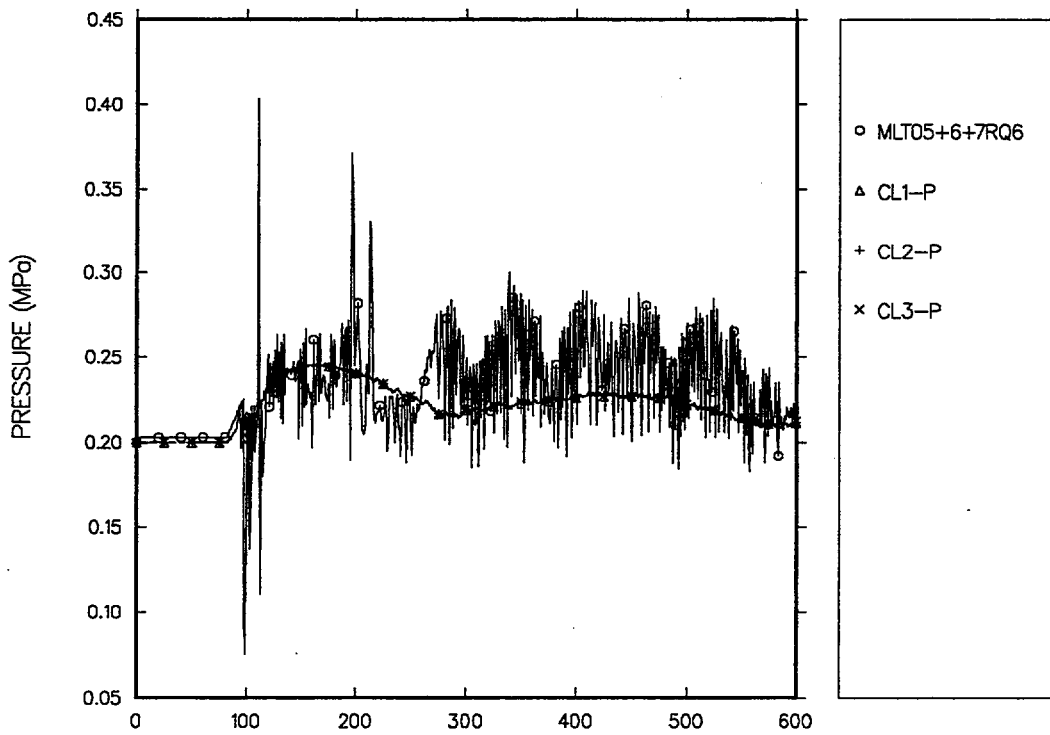


Fig. 5.3-32. Calculated and measured cold-leg spool-piece pressure.
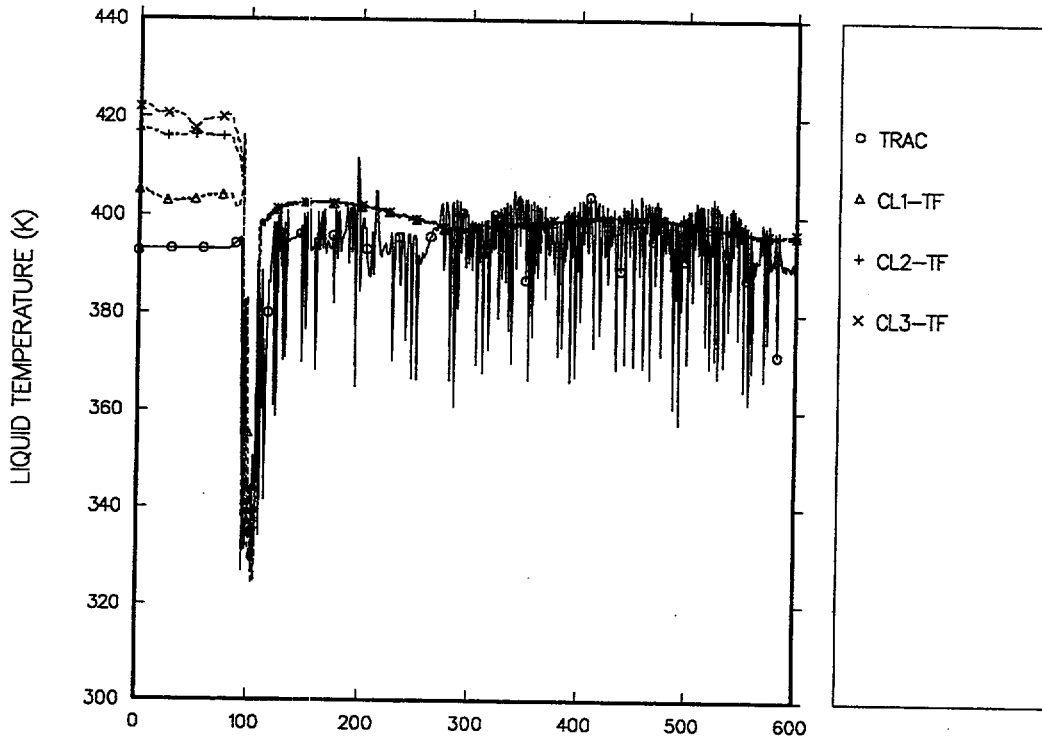
Fig. 5.3-33. Calculated and measured cold-leg spool-piece fluid temperature.
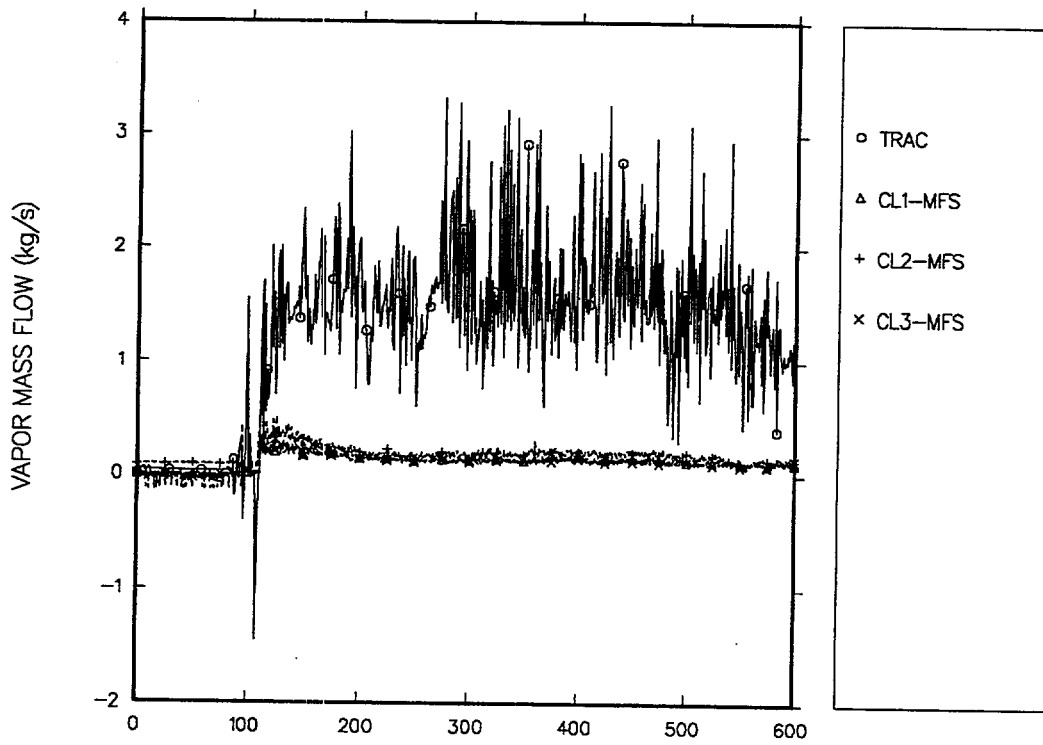


Fig. 5.3-34. Calculated and measured cold-leg spool-piece steam mass flow.
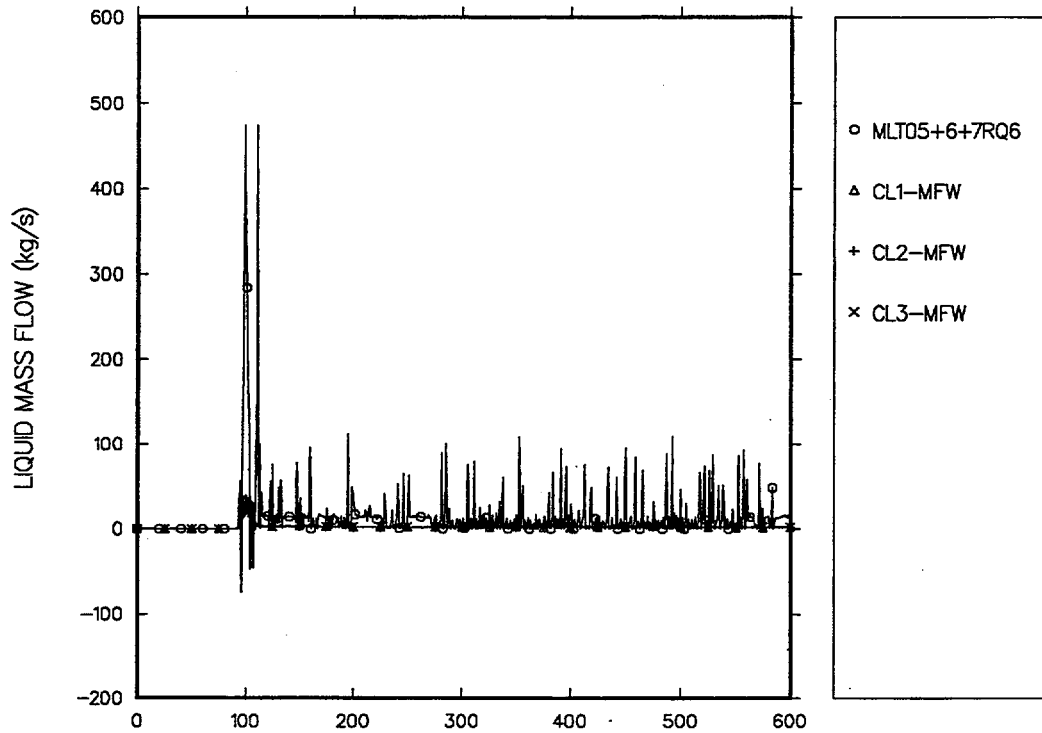
Fig. 5.3-35. Calculated and measured cold-leg spool-piece liquid mass flow.
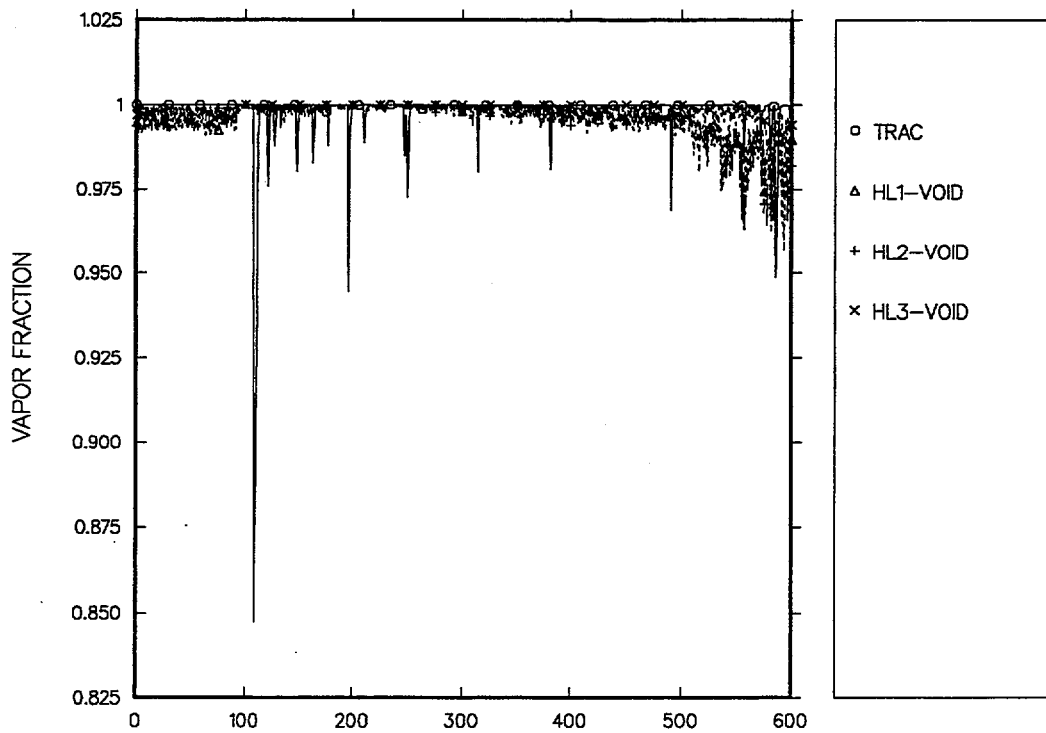


Fig. 5.3-36. Calculated and measured hot-leg spool-piece void fraction.
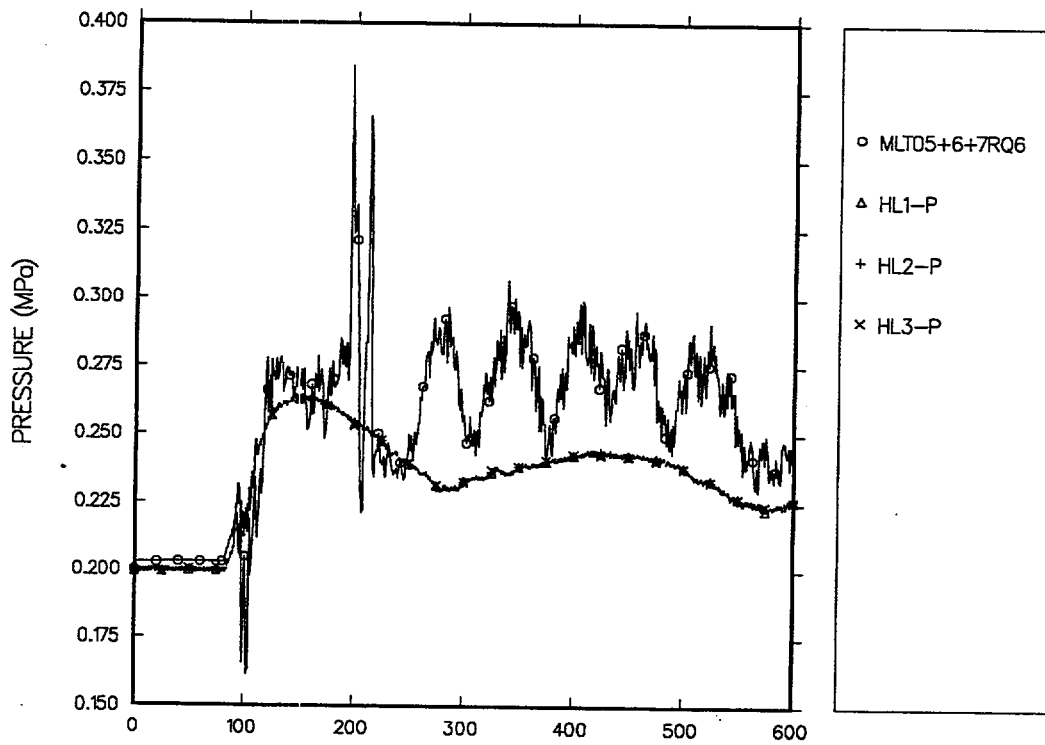
Fig. 5.3-37. Calculated and measured hot-leg spool-piece pressure.
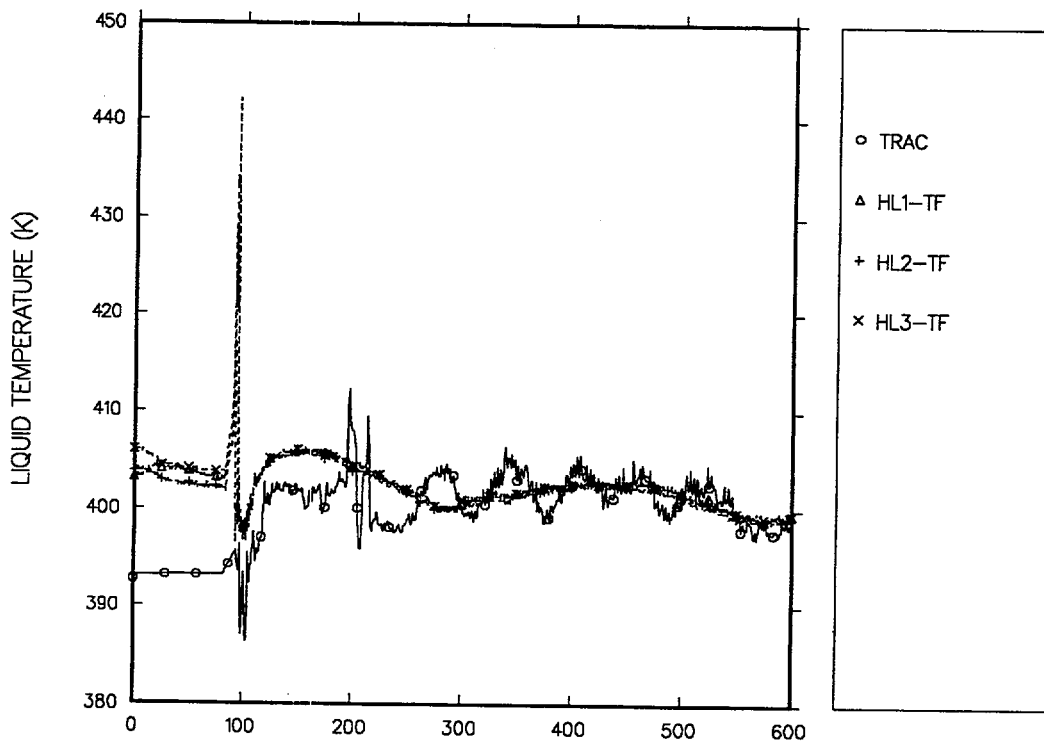


Fig. 5.3-38. Calculated and measured hot-leg spool-piece fluid temperature.
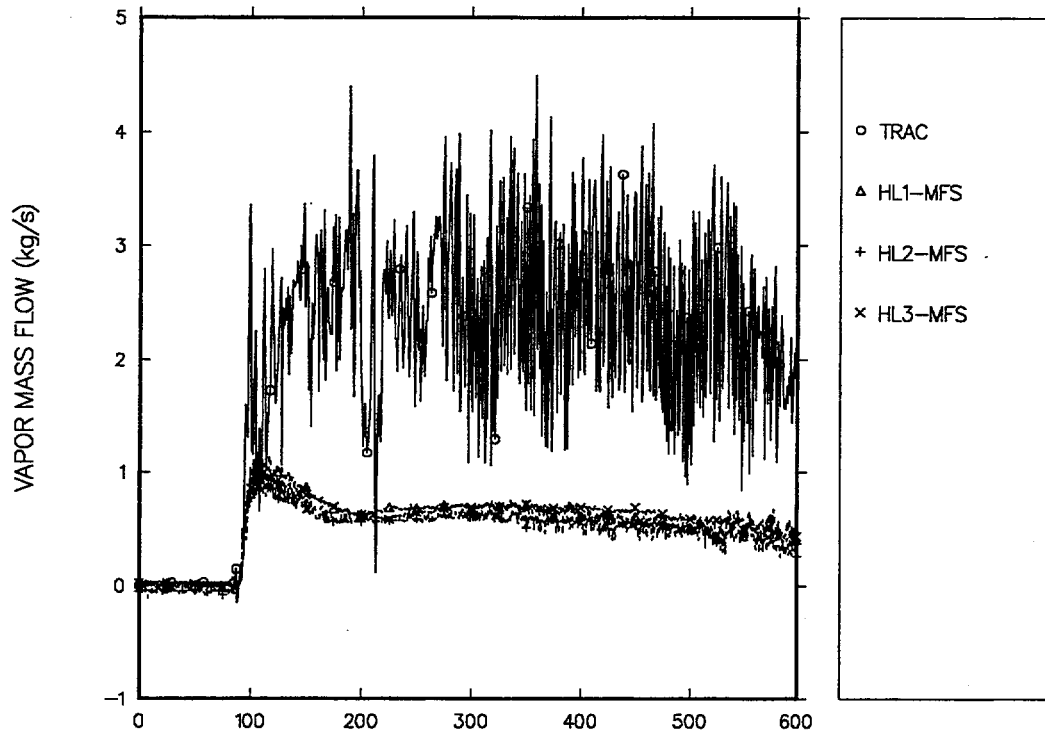
Fig. 5.3-39. Calculated and measured hot-leg spool-piece steam mass flow.
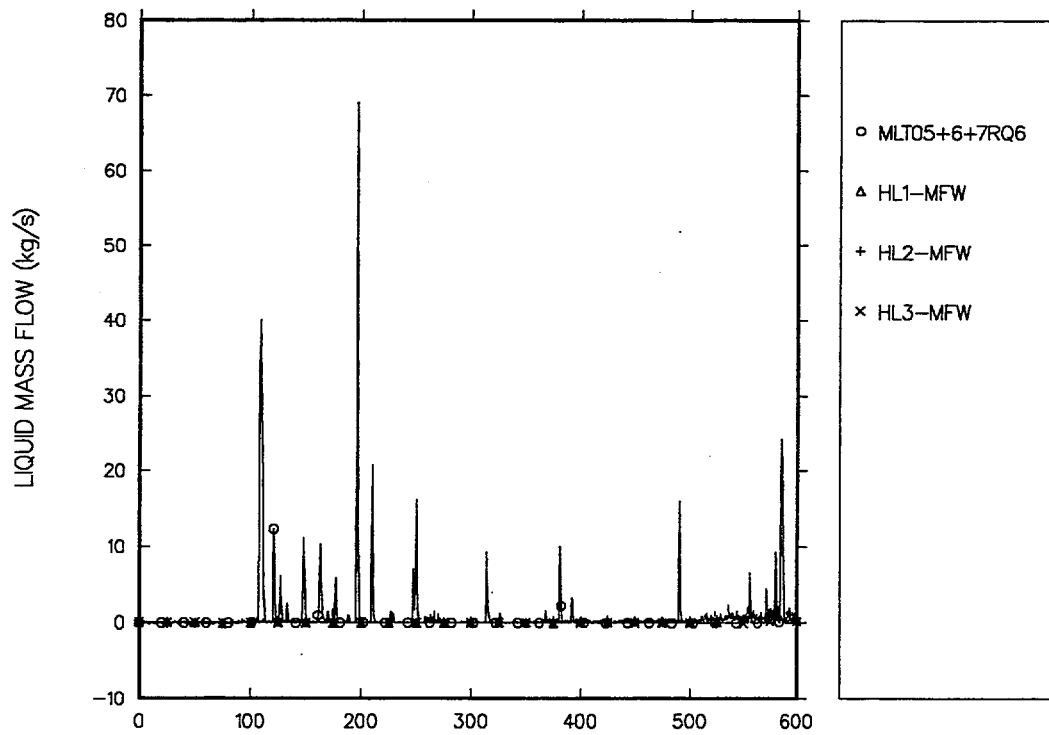


Fig. 5.3-40. Calculated and measured hot-leg spool-piece liquid mass flow.
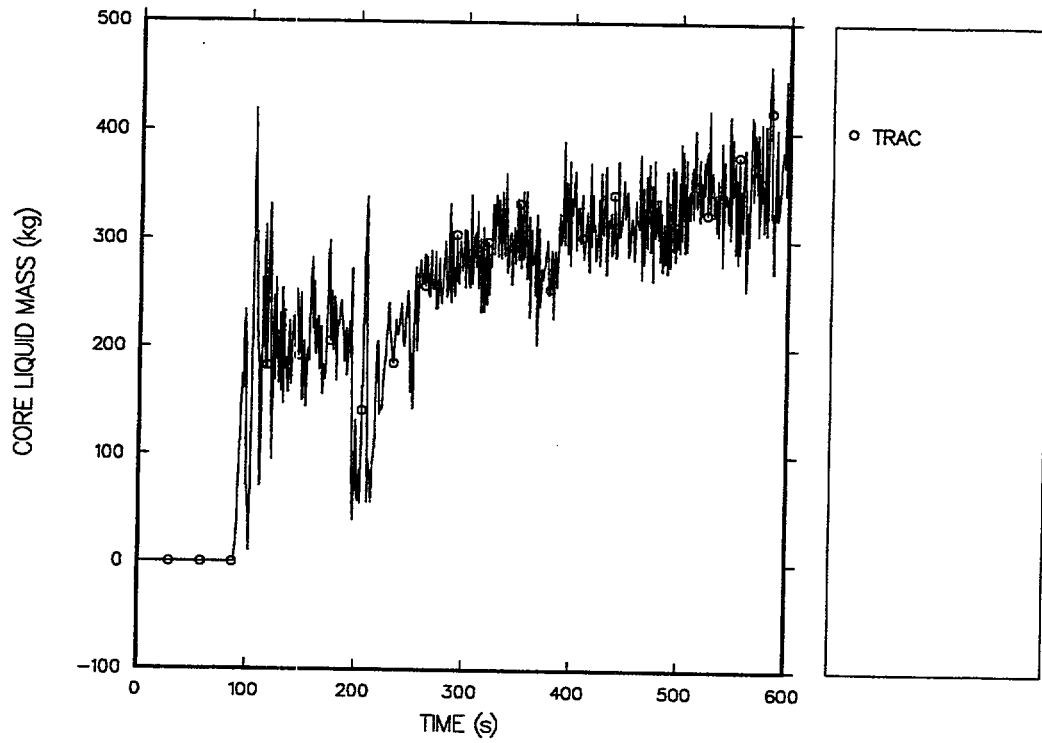
Fig. 5.3-41. Calculated core liquid mass.
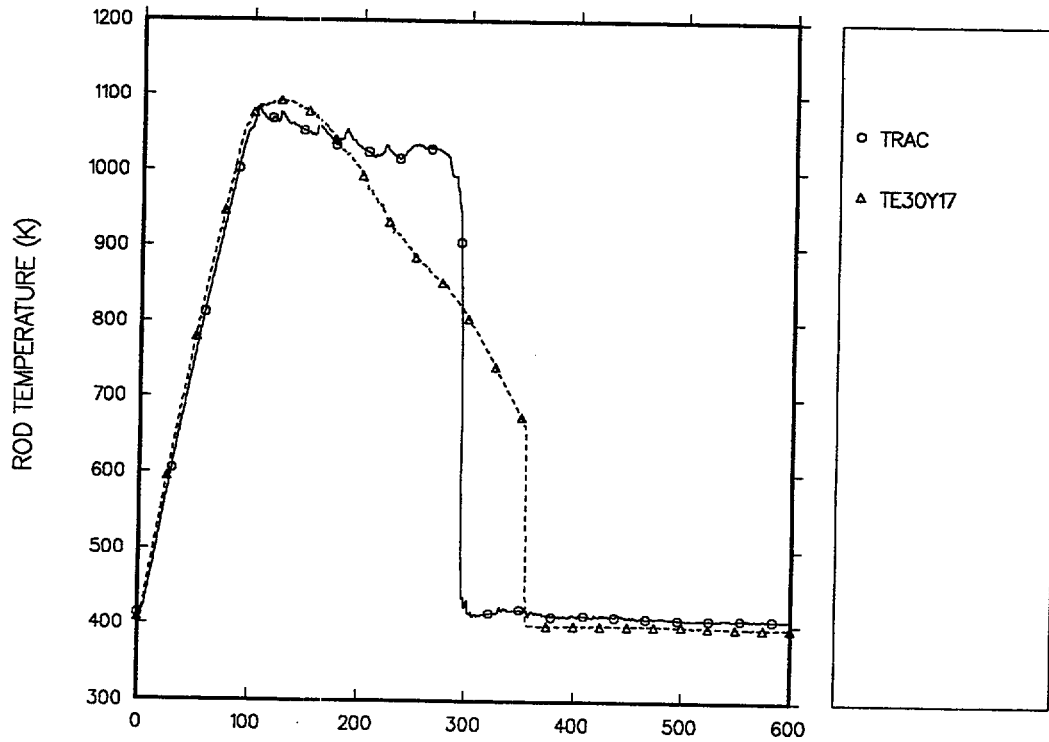


Fig. 5.3-42. Calculated and measured cladding temperatures for the hot rod at the 3.930-m (core midplane) elevation (with grid-spacer model).
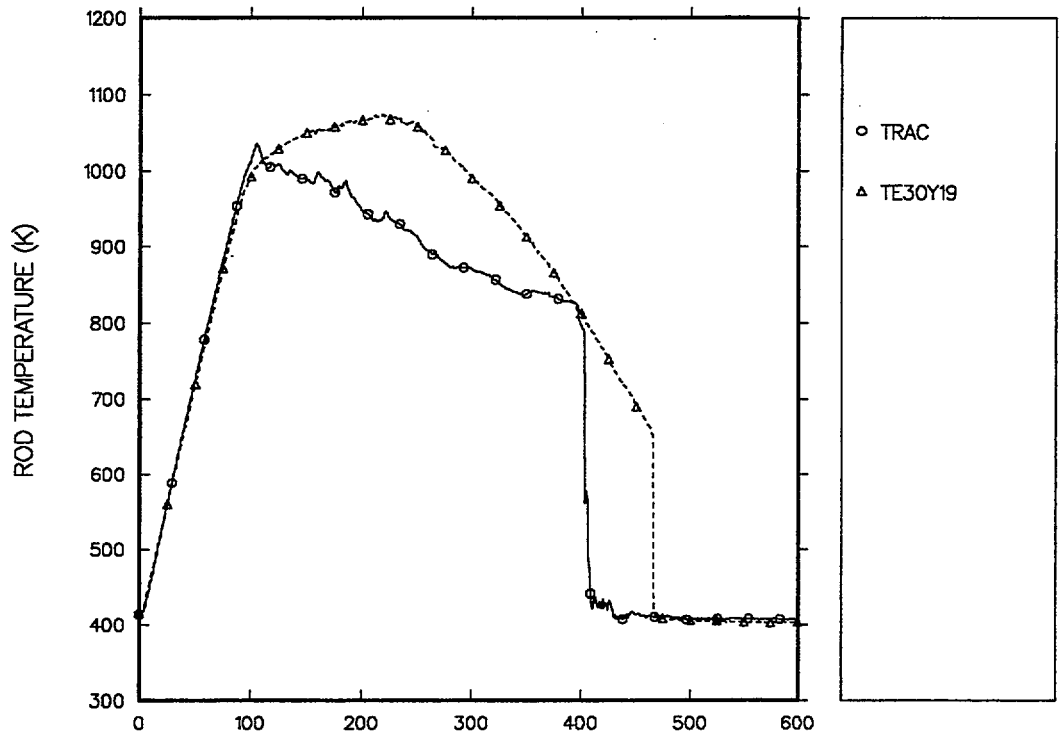
Fig. 5.3-43. Cladding temperatures for the hot rod at the 4.540-m elevation (with grid-spacer model).
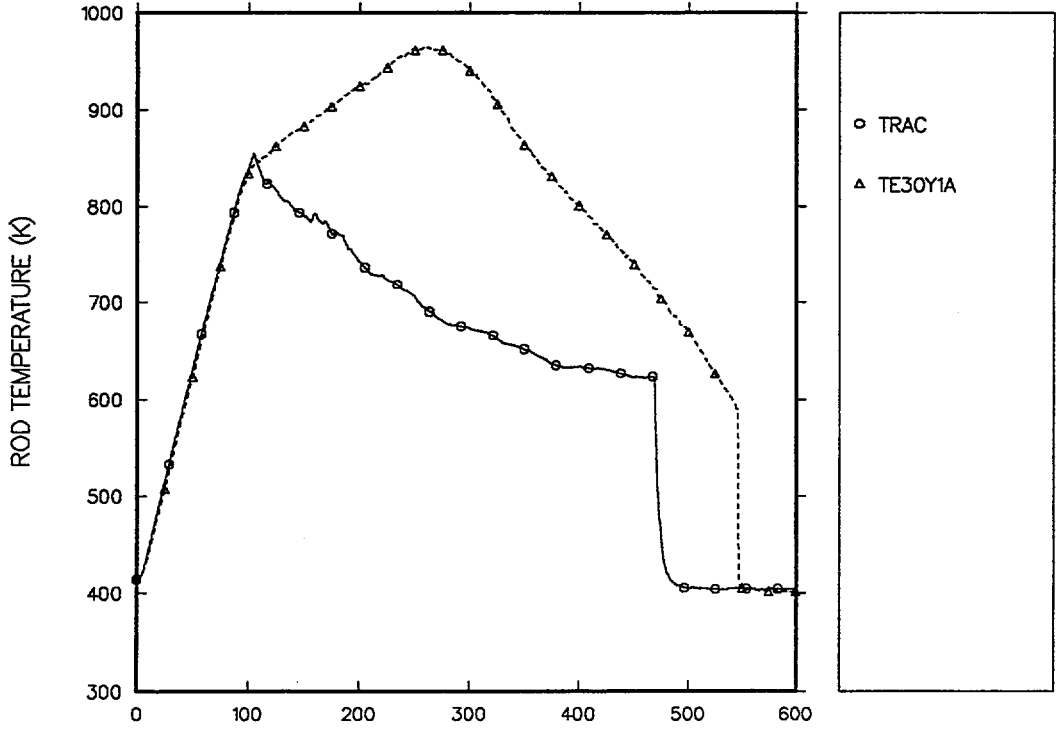


Fig. 5.3-44. Cladding temperatures for the hot rod at the 5.150-m elevation (with grid-spacer model).

5.3-45

Fig. 5.3-45. Renoded CCTF-54 vessel noding diagram.
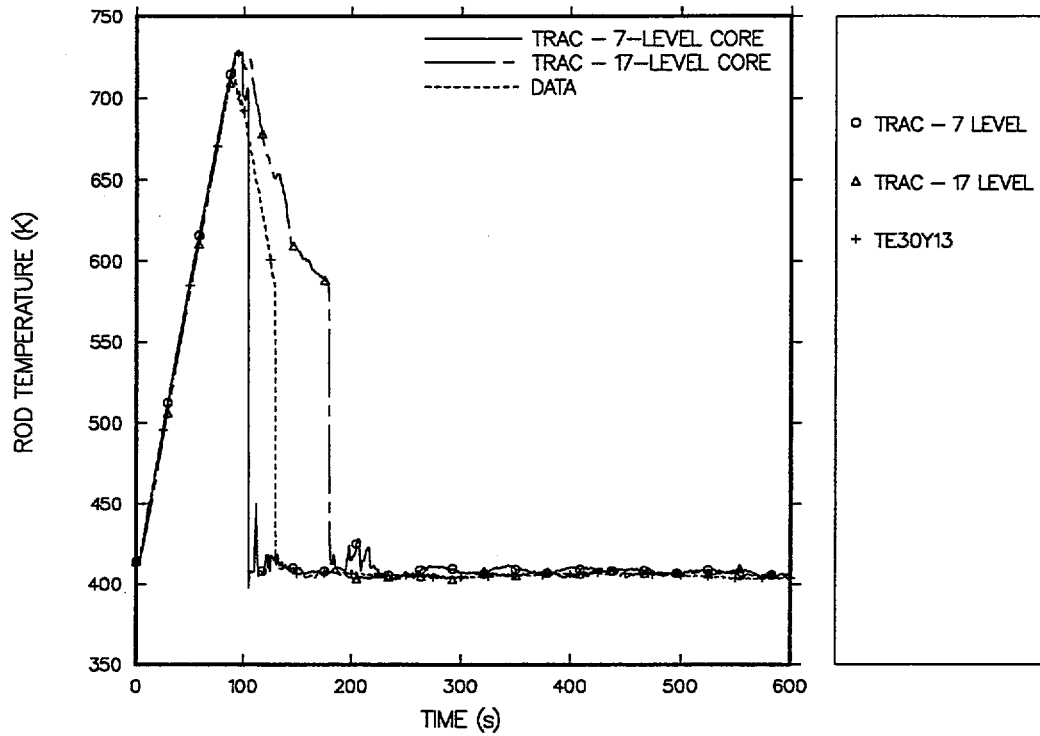
Fig. 5.3-46. Calculated 7- and 17-level, core-model cladding temperatures for the hot rod at the 2.480-m elevation compared to data.
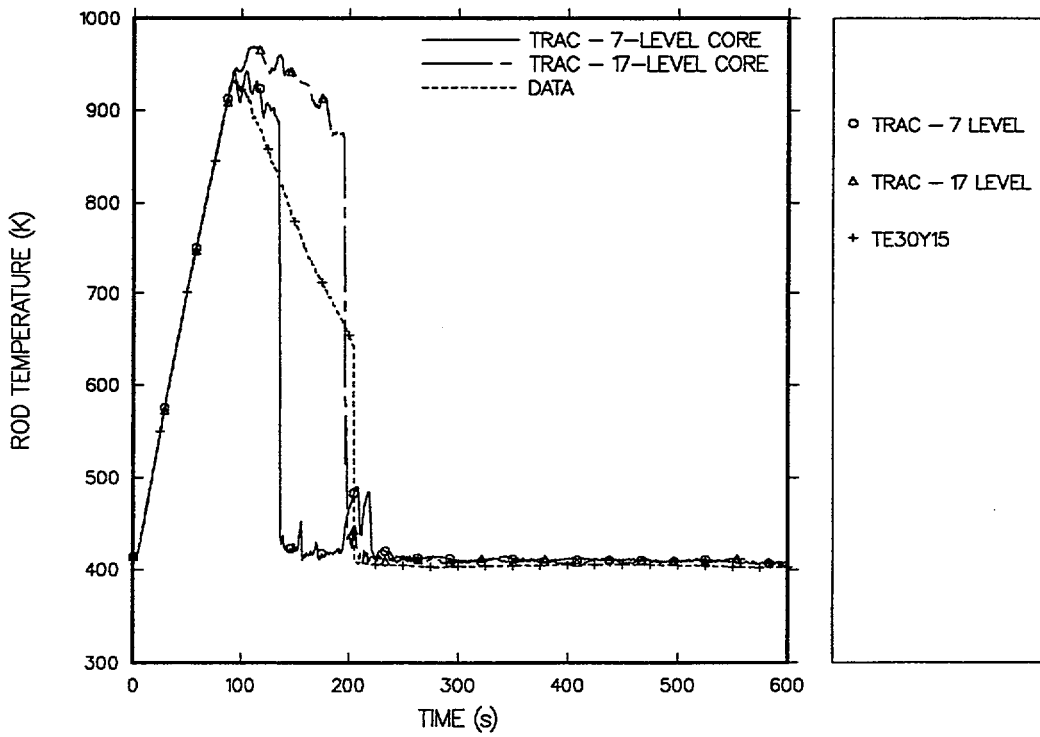


Fig. 5.3-47. Calculated 7- and 17-level, core-model cladding temperatures for the hot rod at the 3.115-m elevation compared to data.
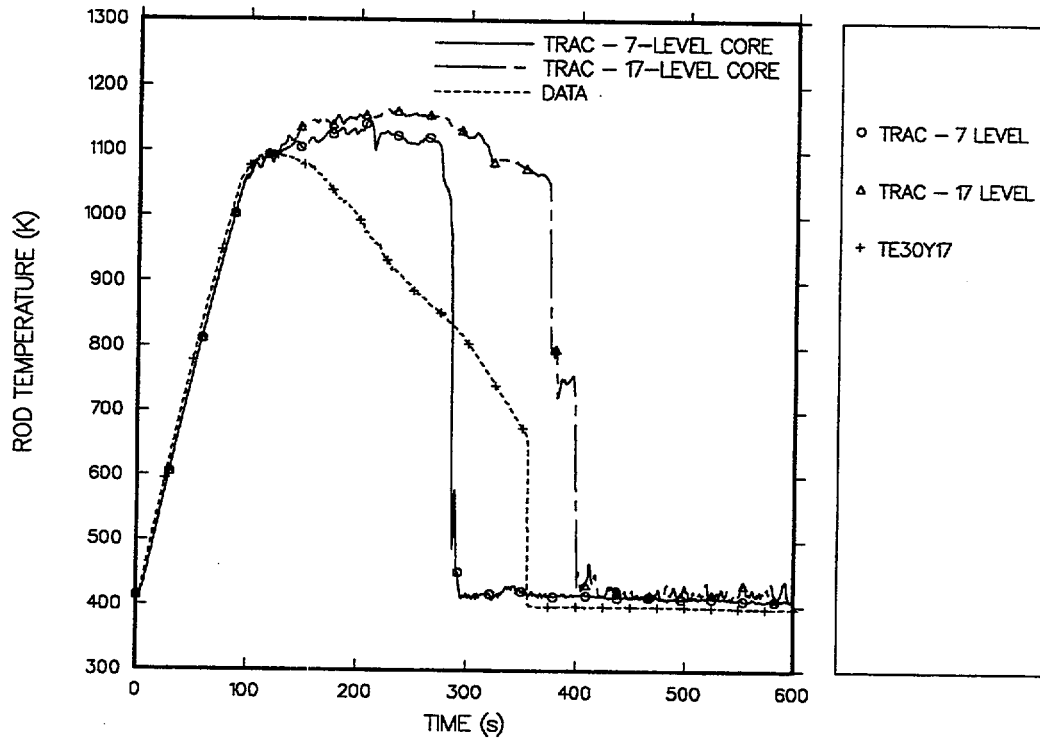
Fig. 5.3-48. Calculated 7- and 17-level, core-model cladding temperatures for the hot rod at the 3.930-m elevation compared to data.
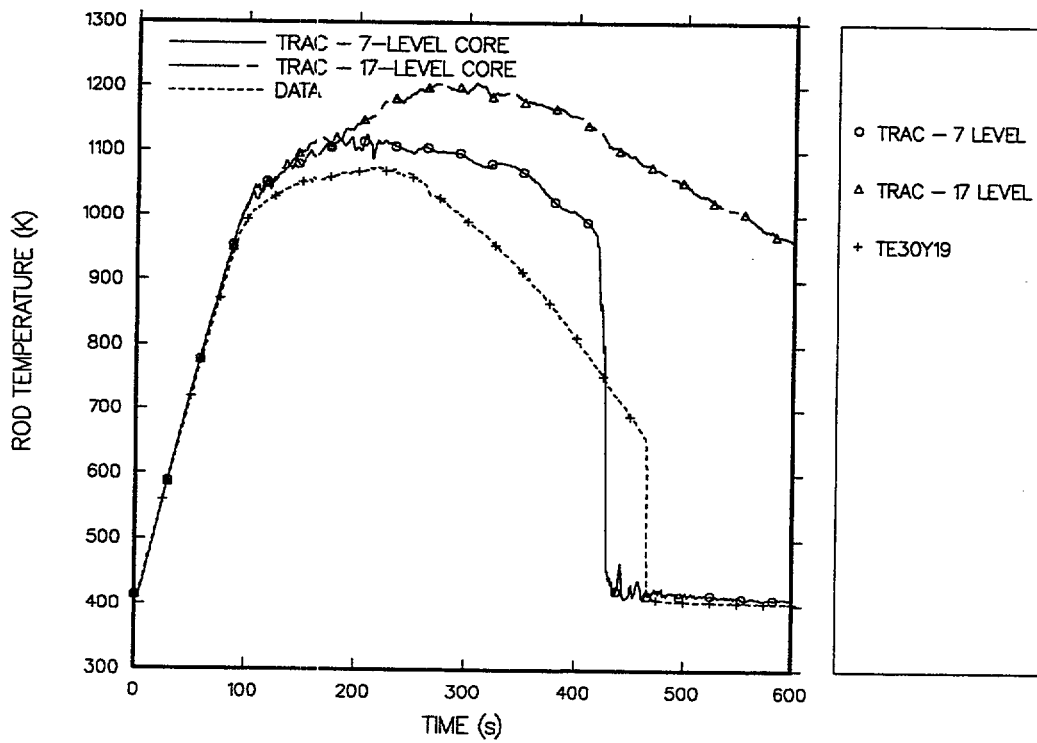


Fig. 5.3-49. Calculated 7- and 17-level, core-model cladding temperatures for the hot rod at the 4.540-m elevation compared to data.
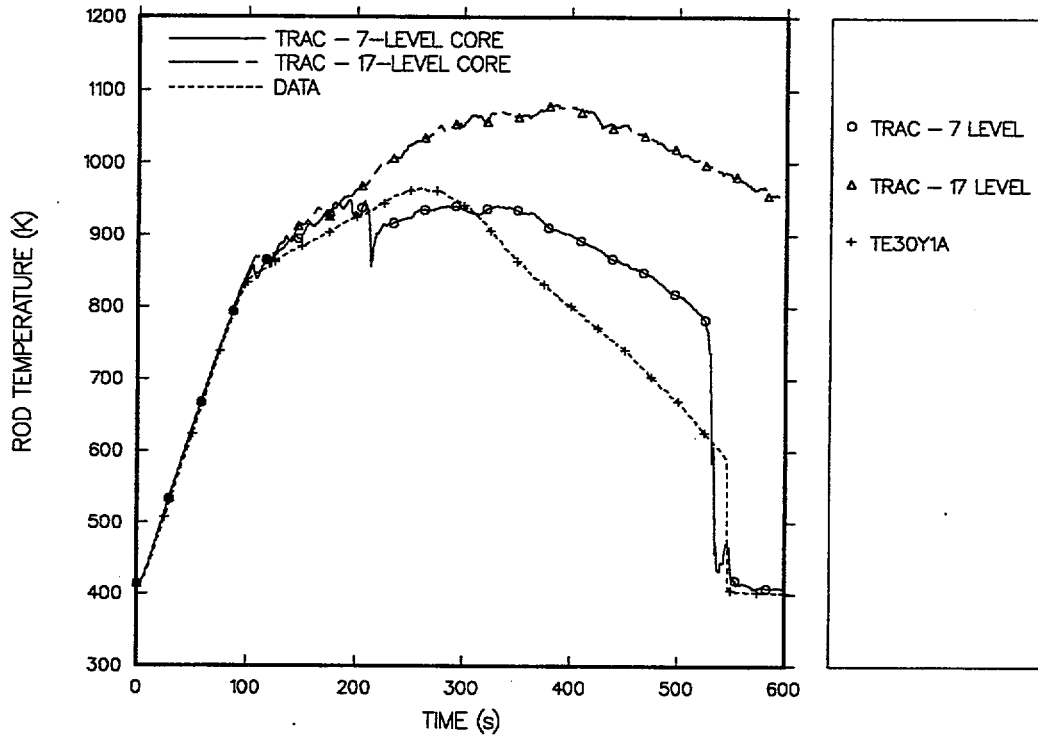
Fig. 5.3-50. Calculated 7- and 17-level, core-model cladding temperatures for the hot rod at the 5.150-m elevation compared to data.
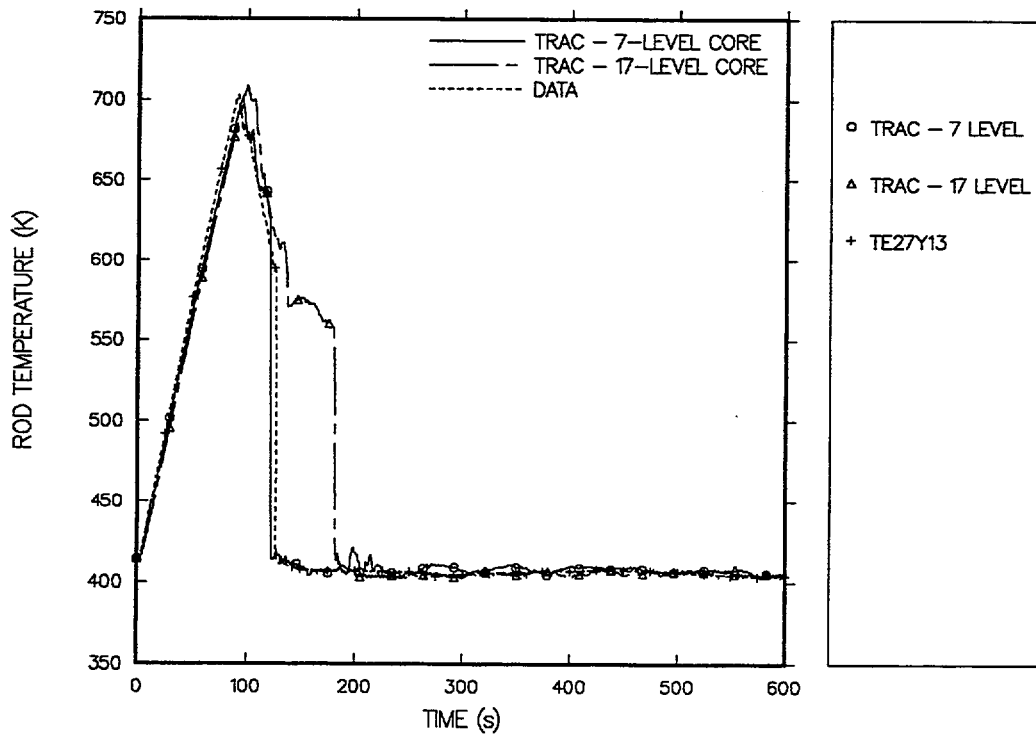


Fig. 5.3-51. Calculated 7- and 17-level, core-model cladding temperatures for the intermediate-powered rod at the 2.480-m elevation compared to data.
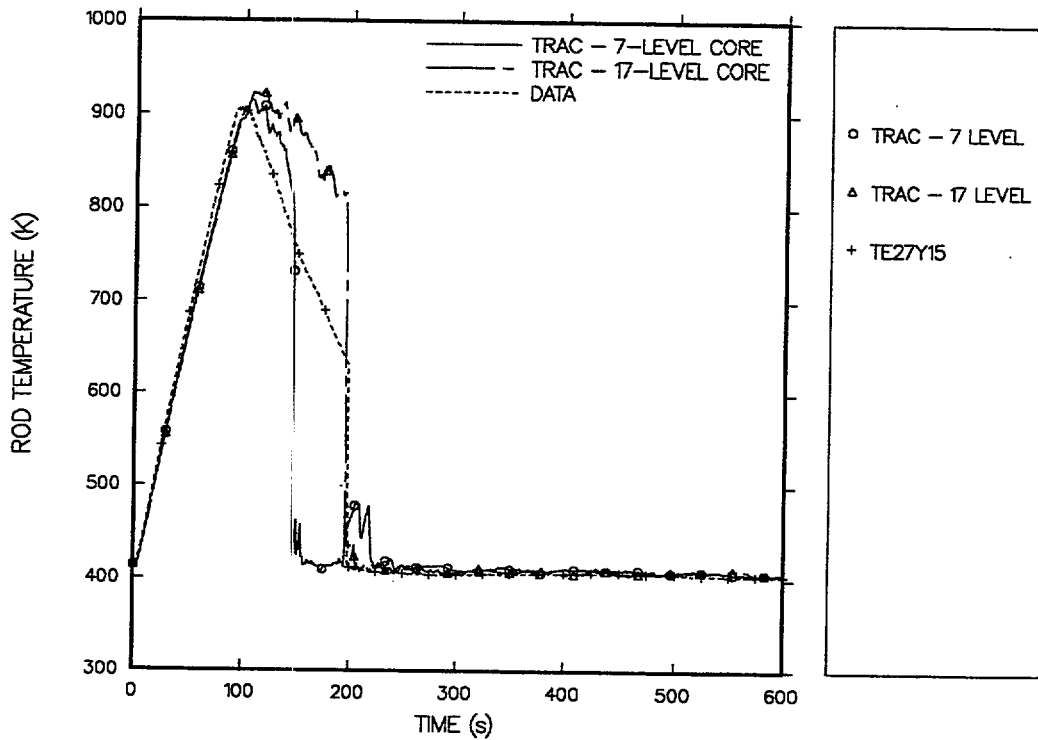
Fig. 5.3-52. Calculated 7- and 17-level, core-model cladding temperatures for the intermediate-powered rod at the 3.115-m elevation compared to data.
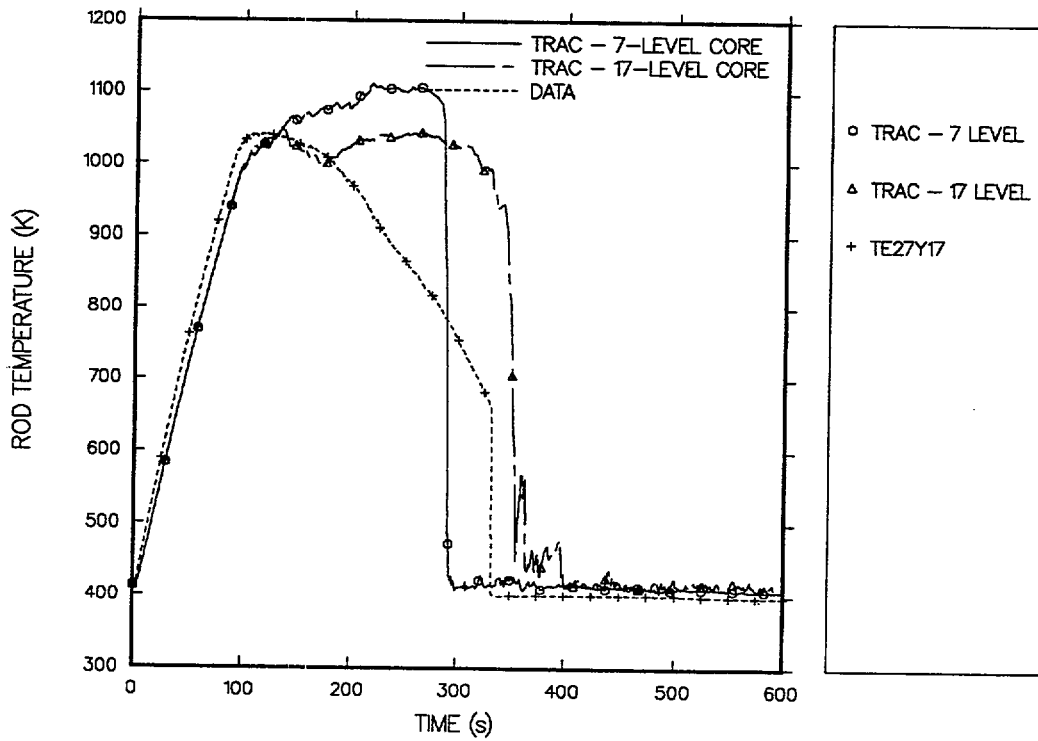


Fig. 5.3-53. Calculated 7- and 17-level, core-model cladding temperatures for the intermediate-powered rod at the core midplane compared to data.
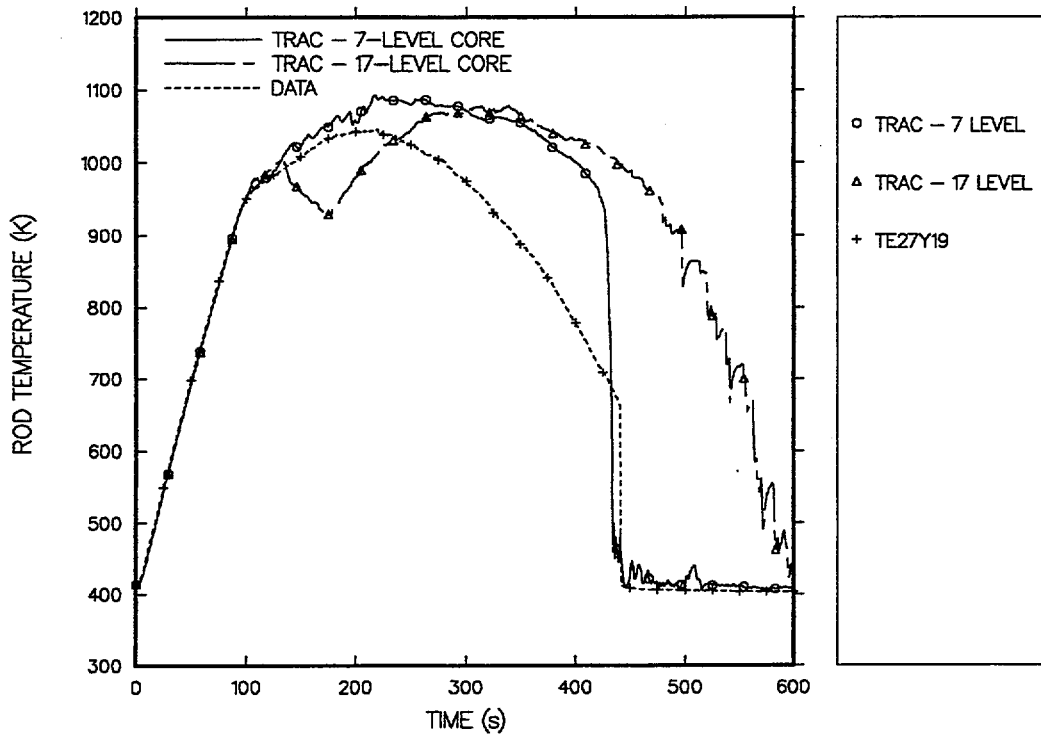
Fig. 5.3-54. Calculated 7- and 17-level, core-model cladding temperatures for the intermediate-powered rod at the 4.540-m elevation compared to data.
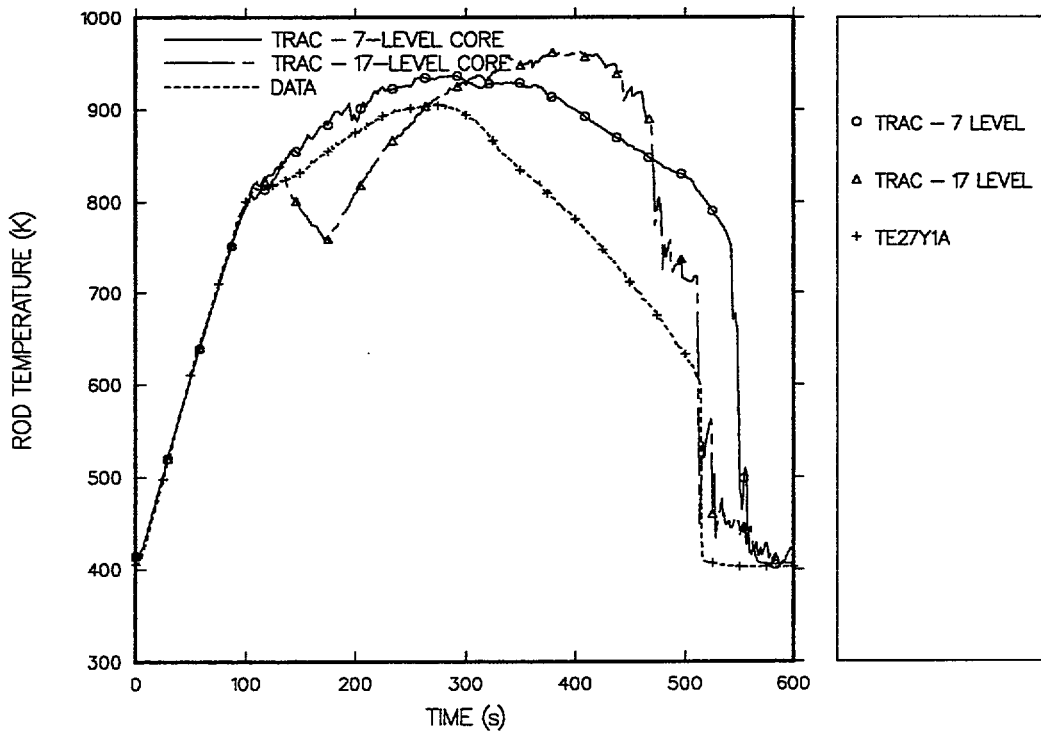


Fig. 5.3-55. Calculated 7- and 17-level, core-model cladding temperatures for the intermediate-powered rod at the 5.150-m elevation compared to data.
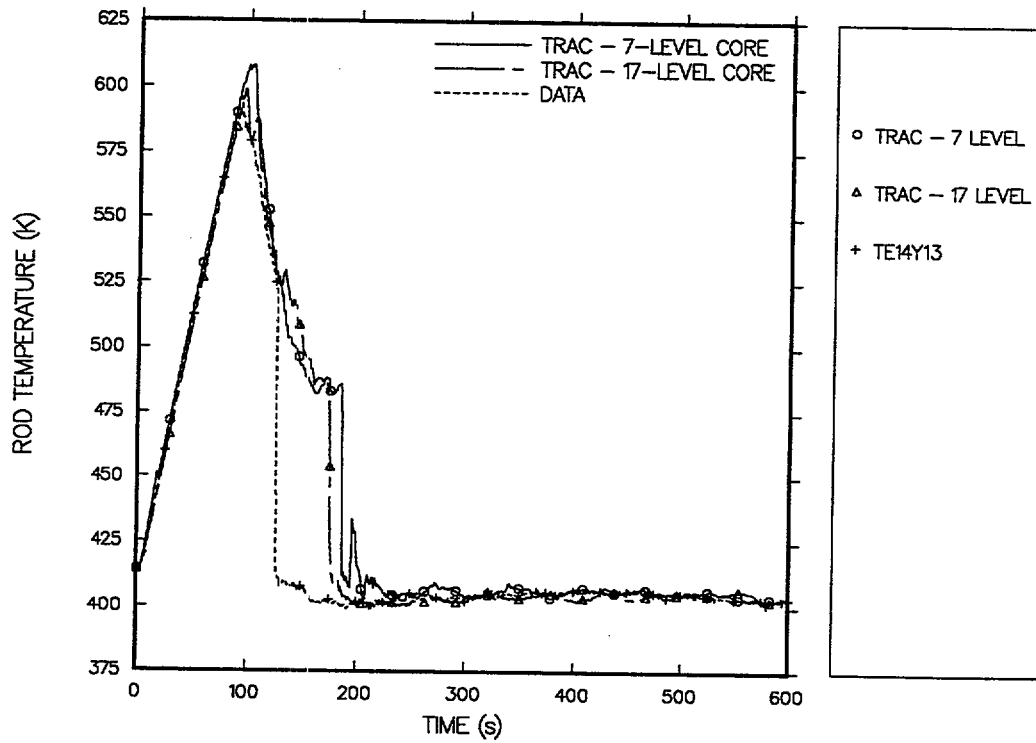
Fig. 5.3-56. Calculated 7- and 17-level, core-model cladding temperatures for the low-powered rod at the 2.480-m elevation compared to data.
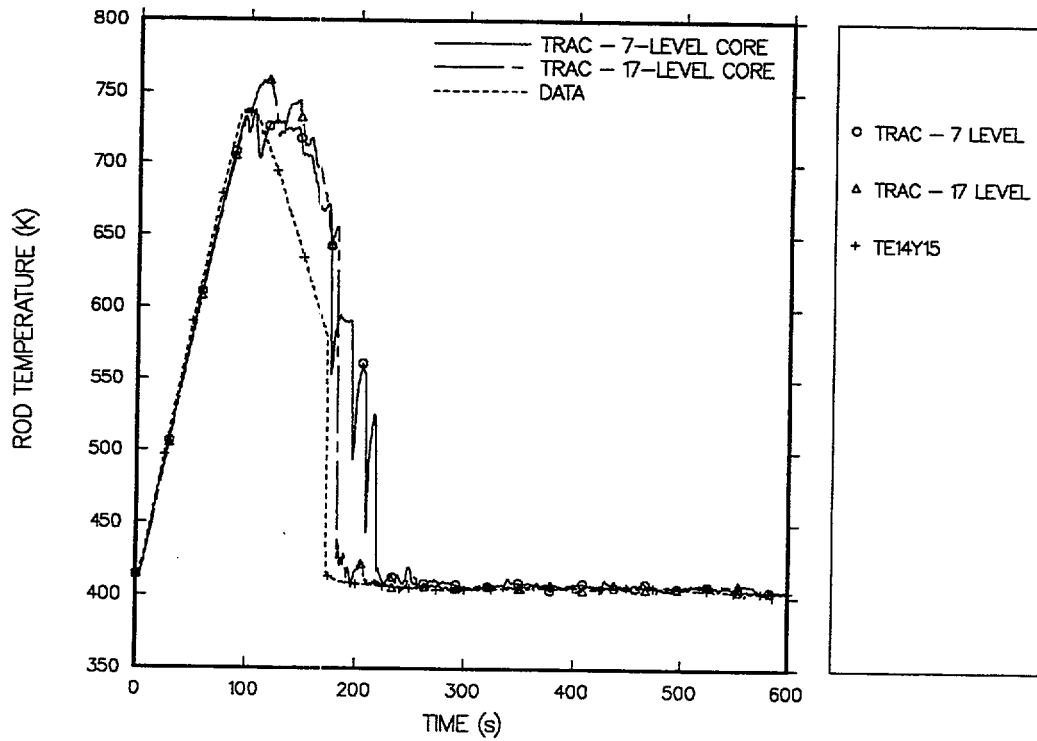


Fig. 5.3-57. Calculated 7- and 17-level, core-model cladding temperatures for the low-powered rod at the 3.115-m elevation compared to data.
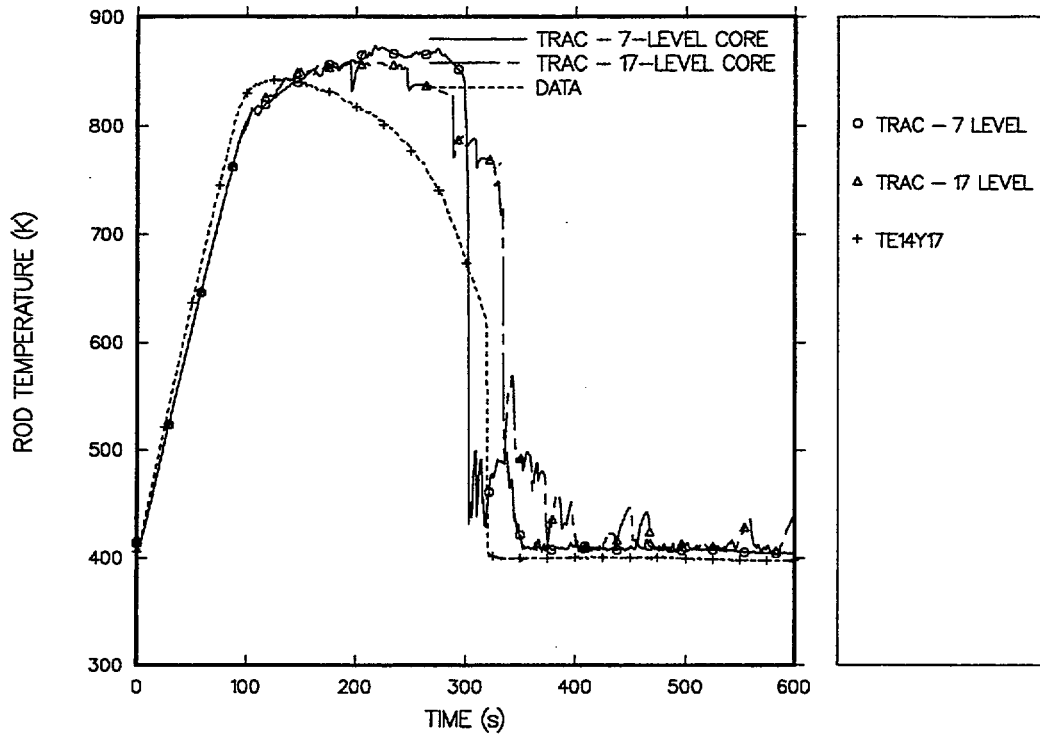
Fig. 5.3-58. Calculated 7- and 17-level, core-model cladding temperatures for the low-powered rod at the core midplane compared to data.
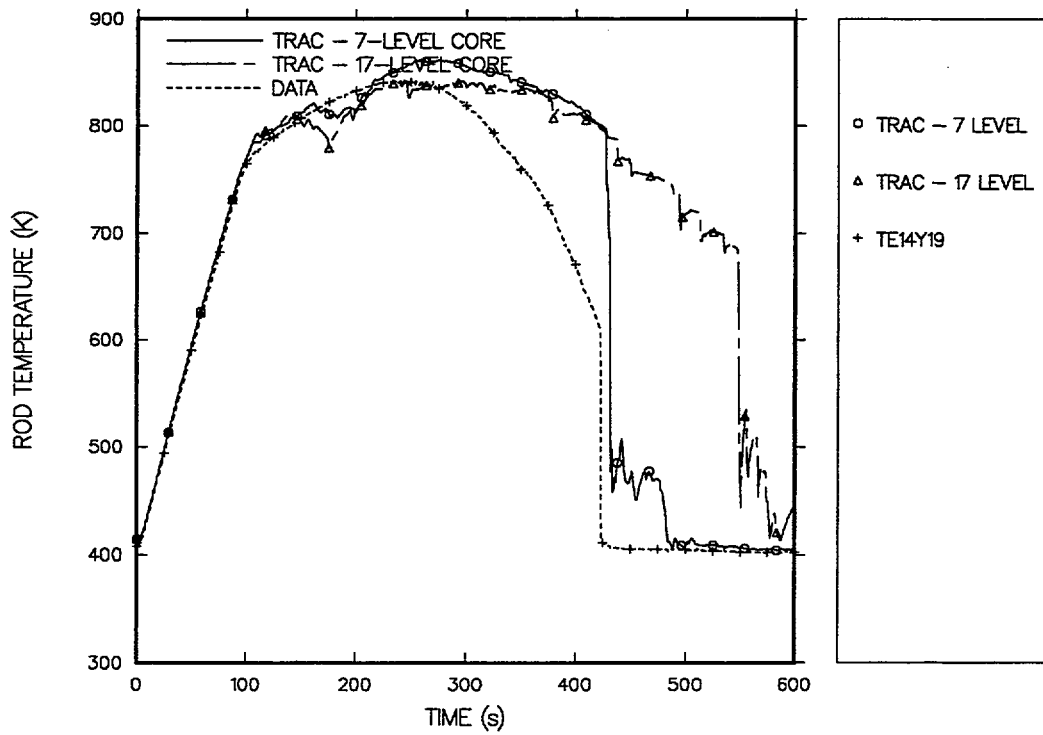


Fig. 5.3-59. Calculated 7- and 17-level, core-model cladding temperatures for the low-powered rod at the 4.540-m elevation compared to data.
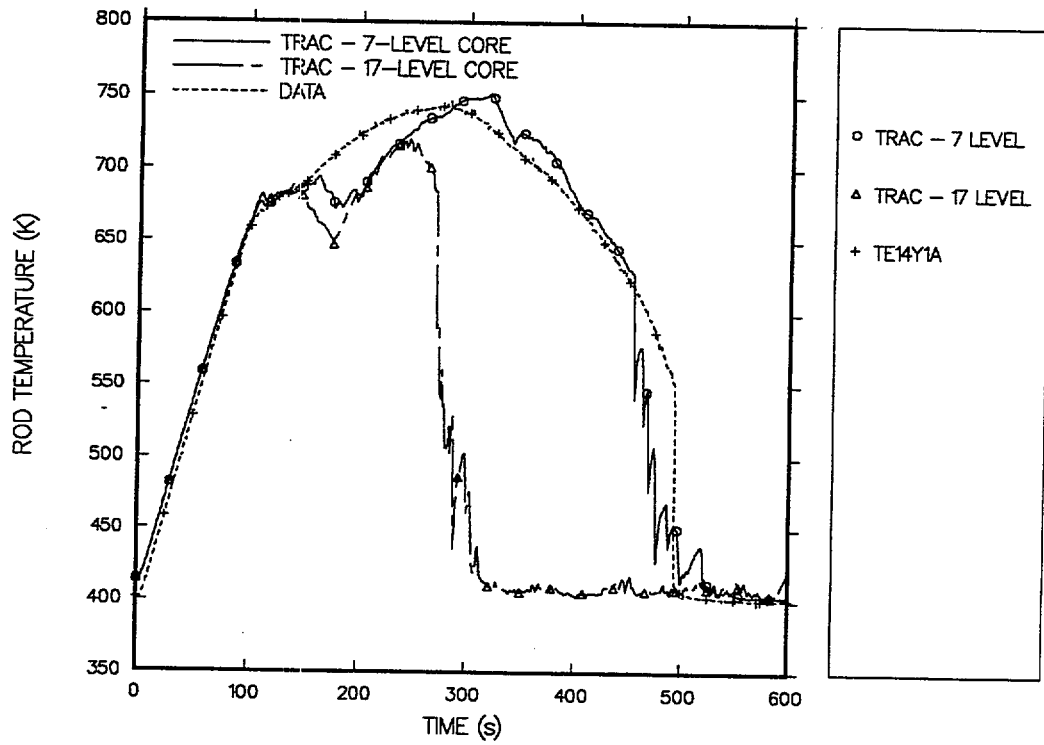
Fig. 5.3-60. Calculated 7- and 17-level, core-model cladding temperatures for the low-powered rod at the 5.150-m elevation compared to data.

## 5.4. Slab Core Test Facility Run 719

### 5.4.1. Test Facility

The Slab Core Test Facility (SCTF) is designed to investigate the 2D thermal-hydraulic phenomena occurring in a PWR during the end of blowdown, refill, and reflood phases of a postulated LBLOCA in a PWR. The SCTF is a full-height facility; most major vessel and primary-loop dimensions are volume-scaled in a ratio near 1/21 relative to a four-loop PWR with lower-plenum and cold-leg ECC injection. A complete description of the SCTF Core-III facility is provided in Ref. 5.4-1. Figure 5.4-1 shows an overview of the SCTF Core-III system. A major feature of the SCTF is that it contains a full-height and full-radius heated core with a width of one tube bundle. The current configuration of the core is designated as Core-III, with the upper plenum and upper head representative of a German PWR. The facility is operated by JAERI.

Figure 5.4-2 shows a vertical cross-sectional view of the SCTF pressure vessel. A special emphasis is placed on the modeling of the components in the pressure vessel; the vessel contains a downcomer, lower plenum, electrically heated core simulator, core baffle region, upper plenum, and upper head. The core simulator models a sector of the core from the centerline to the outer wall of the vessel. The name of the facility, "slab core," is descriptive of the core simulator arrangement. A slab-like sector of the vessel from core centerline to vessel outer wall contains eight heater rod bundles arranged in a row, the core baffle region, and the downcomer. Whereas the design of the Core-II upper plenum was based on that for a Westinghouse plant with 17 x 17 array fuel assemblies, the design of the Core-III upper plenum is based on that of a German PWR.

Each heater-rod bundle contains 236 electrically heated rods and 20 nonheated rods. A heater rod, shown in Fig. 5.4-3, consists of a Nichrome heater element wound in a helix about a ceramic core rod (magnesium oxide), and a Nichrofer 7216 (equivalent to Inconel 600) sheath, with boron nitride (central region) or magnesium oxide (upper and lower regions) packed between the heater element and the sheath. The pitch of the heater element winding is varied to produce a 17-step chopped cosine axial power profile, as shown in Fig. 5.4-4.

Simplified models of the primary coolant loops are provided in the facility. The facility is equipped with a hot leg that is equivalent to four hot legs in a PWR. The hot-leg cross-sectional shape is not typical of a PWR. It is tall and narrow rather than circular in shape. The hot leg connects the vessel upper plenum to a steam/water (S/W) separator. The S/W separator simulates single-phase steam flow downstream of a steam generator in a PWR and also facilitates the measurement of liquid carryover from the upper plenum, through the hot-leg simulator, and into the S/W separator. The S/W-separator inlet plenum models a steam generator inlet plenum to correctly simulate the flow characteristics of carryover water into the U-tubes. The intact cold leg in the SCTF is equivalent to three intact loops in a PWR. A pump simulator and a loop seal are provided in the intact cold-leg simulator. Two broken-loop components are provided; each of these is connected to a separate containment tank through a break valve. The loop resistance is adjusted with orifice plates that can be placed in the intact cold leg, the S/W-separator-side and pressure-vessel-side broken cold legs, and the pump simulator in the intact loop.

The coolant flows delivered by the ECCS are also modeled. These simulate flows from the accumulator, an LPCI system, and a combined-injection system. ECC water injection ports are at the cold leg, the hot leg, through the upper head into the top of the upper plenum, into the upper plenum at the UCSP, into the downcomer, and into the lower plenum. The specific injection ports are selected according to the objectives of the given test.

### 5.4.2. Test Description

SCTF Run 719 (Test S3-15), Ref. 5.4-2, was an integral test that simulated the condition of a US/Japan-type PWR during the reflood phase of a 200% cold-leg LBLOCA. SCTF Run 719 was a lower-plenum-injection test. The test objective of Run 719 was to investigate the effect of radial power distribution shape and radial power ratio on 2D heat-transfer behavior. The radial power distribution was inclined; the peak-to-average power ratios were 1.36, 1.20, 1.20, 1.00, 0.91, 0.86, 0.81, and 0.76 for bundles 1 through 8, respectively. Before test initiation, the facility was filled with saturated steam at 0.2 MPa. The lower plenum was filled with saturated water (393 K) to a height of 1.2 m. The core then began to heat in near-adiabatic conditions. The core power was tripped and ECC initiated when a preselected number of rod cladding temperatures exceeded 1134 K. The maximum cladding temperature reached was 1183 K; this temperature was measured at the midplane of bundle 1, the bundle receiving the highest power. The entire core was quenched at 574.5 s. The core thermal-hydraulic behavior was strongly two-dimensional (2D) in Run 719. A single recirculating flow was established with upflow through the high-power bundles and downflow through the low-power bundles. A summary of the planned conditions for this test is presented in Table 5.4-1.

### 5.4.3. TRAC Input Model of SCTF Core-III Facility

The SCTF Core-III facility is modeled in TRAC with 32 hydrodynamic components, two of which are Vessel components, and 47 heat-structure components. The primary features of each element in the TRAC input model are discussed in the following sections. A listing of the input model used for this developmental assessment calculation is found in Appendix U. Archival storage information for this input model is provided in Section 5.4.7.

#### 5.4.3.1 Pressure Vessel. 
The pressure vessel is modeled with the TRAC Vessel component in two-dimensional Cartesian coordinates with 12 sectors in the horizontal direction and 15 levels in the vertical direction, as shown in Fig. 5.4-4. All the major elements in the experimental facility are modeled in the input. The lower plenum is modeled in sectors 1 through 9 and levels 1 through 3. The lower-core support plate is modeled at the top of level 3. The lower plenum is noded into 3 axial levels to capture the geometry below the tube bundles and to model the opening between the lower plenum and downcomer. The electrically heated core is modeled in sectors 1 through 8 and axial levels 4 through 9. Each of the 8 sectors represents a heater-rod bundle. The core baffle occupies sectors 9 and 10 and the same axial levels as the core. The upper plenum is modeled in sectors 1 through 9 and axial levels 10 through 14; the upper tie plate, which contains the minimum flow area between the core and upper plenum, is located in level 10, and the upper-core support plate is located in level 11. The support columns connecting the upper head and the upper plenum are modeled with PIPE components in sectors 1, 3, 5, 6, and 7 to provide a flow path between the upper plenum and the upper head. The upper head is modeled in sectors 1 through 12 at level 15. The

downcomer is modeled in sectors 11 through 12 and axial levels 2 through 14. The intact cold-leg and broken cold-leg connections to the pressure vessel are in level 12 of sectors 11 and 12, respectively. The hot-leg connections to the upper plenum are at the outer interface of sector 10 in level 13. The lower-plenum ECC injection point is located in sector 10 at level 1.

Two model corrections were made to the pressure vessel modeling. First, counter-current flow limitation (CCFL) was added to the pressure vessel. In previous SCTF assessments with the TRAC-PF1/MOD1 code, counter-current flow limitation (CCFL) was modeled in the pressure vessel at axial level 10. When the SCTF model was converted over from TRAC-PF1/MOD1 to TRAC-PF1/MOD2, early code versions of TRAC-PF1/MOD2 could not model CCFL in the Vessel component, so the CCFL input in the SCTF model was commented out. When later versions of the TRAC-PF1/MOD2 code were able to model CCFL in the Vessel component, the CCFL input in the SCTF model was never reactivated.

The second pressure-vessel model correction was to set the liquid additive friction loss coefficients in the axial direction (CFZLZ in the TRAC Vessel input) back to the same value as the vapor additive friction loss coefficients (CFZVZ in the TRAC Vessel input). The liquid additive friction loss coefficient values were two magnitudes larger than the vapor additive friction loss coefficient values. In previous SCTF assessments, the liquid additive loss coefficient had been increased in an attempt to account for liquid retention in the core region caused by cold vessel walls. The cold vessel wall effect is now accounted for by using the Vessel component input parameters FUNH and NHSCA.

### 5.4.3.2  Heater Rods.

Figure 5.4-6 shows the heater-rod noding. The TRAC fuel-rod model has six axial sectors to match the pressure vessel noding. The horizontally inclined power distribution is shown in Fig. 5.4-7. Figure 5.4-8 shows the axial power shape assumed in previous SCTF models and the axial power shape corrected to model the actual 17-step axial power shape of Fig. 5.4-4. In the TRAC-PF1/MOD1 code assessments, the number of axial levels used to model the axial power profile had to match the heater-rod axial noding. This modeling limitation presented several challenges in modeling the electrically heated core as described in earlier SCTF Run 179 assessments calculations.[5.4-3] To model the axial power distribution, the areas under the power distribution of the heater rods in the test facility and that of the TRAC model were set equal to preserve the total power. Also, the TRAC six-level axial-power shape had to be adjusted to match the pre-ECC injection axial cladding temperatures of the test. These adjustments resulted in a axial power shape quite different from the actual power shape.

The TRAC code allows an independent specification of the axial levels for the axial power shape to provide a more accurate modeling of the axial power shape. The axial power shape was corrected to model the 17-step axial power shape.

A second problem encountered with the earlier SCTF assessment calculations was with specifying the correct heater-rod material properties. SCTF Core-I studies showed that the heater-rod material properties had a large effect on cladding temperature. In the SCTF Core-I assessments, a brief parametric study was conducted by varying the density and specific heat of magnesium oxide. To verify the input, the cladding

temperature was calculated for the adiabatic heatup conditions of Run 719 and then compared with the initial and boundary condition data provided by JAERI. For case one, the values for density and specific heat provided by the heater-rod manufacturer were used (density = 2500 kg/m$^3$, specific heat is a temperature-dependent table). For case two, the values for density and specific heat selected for use in the TRAC Core-I and Core-II models were used (density = 2800 kg/m$^3$, specific heat is a temperature-dependent table increased by 2800/2500 from the manufacturer's recommended values). For case three, intermediate values were used (density = 2625 kg/m$^3$). Considering the results of this brief study, a magnesium oxide density of 2650 kg/m$^3$ and corresponding specific heat were used for the Run 719 analysis. The material properties for nichrome, magnesium oxide, and inconel 600 are specified as part of the SCTF input model.

In the current assessment, a sensitivity study was performed to determine the effect of different insulation material properties on the heater-rod cladding temperatures. The reason for this study is that the SCTF heater rods has two different insulation materials between the nichrome heating element and the outer cladding as shown in Fig. 5.4-3. Boron nitrate (BN) is used in the center region of the rod while magnesium oxide (MgO) is used in the upper and lower regions of the rod. TRAC can only model one insulation material for the entire length of the heater rod as shown in Fig. 5.4-7. To determine the effect of the insulation material properties on cladding temperature, we performed three sensitivity calculations. Case 1 assumed magnesium oxide for the entire heater rod length. Case 2 assumed boron nitride for the entire heater rod length. Both Cases 1 and 2 used the previous six-step axial power shape. Case 3 assumed magnesium oxide but with the 17-step axial power shape. We calculated the cladding temperatures for the first 120 s of the test, the heatup period of the test. The calculated temperatures are compared to the measured temperature at each of the 10 thermocouple locations along the heater rod as shown in Fig. 5.4.-6. These results are presented in Appendix V. Based on this study it was decided that the insulation material had a minor effect on the calculated temperatures and the axial power shape had a greater effect. Magnesium oxide is retained as the insulation material for the entire length of the heater rod.

### 5.4.3.3 Loop Components and S/W Separator.

The loop compoents and S/W-separator noding are shown in Fig. 5.4-9. The hot leg is modeled with a Pipe component containing four cells. The outer surface of the hot leg is assumed to be insulated. The S/W separator is modeled with a 3D Vessel component with four axial levels, one radial sector, and two azimuthal sectors. The hot-leg connection to the S/W separator is in the outer radial face of cell 1 at level 3. The respective intact and broken cold-leg connections to the S/W separator are made at level 2 to the outer radial faces of cells 1 and 2.

The intact cold leg is modeled with a Tee component consisting of seven cells in the primary side and one cell in the secondary side. The secondary of the TEE component is connected to the primary at cell 7. The primary includes the loop seal and the pump simulator. The intact cold-leg orifice and pump-simulator orifice are located at cell faces 2 and 6. The secondary models the ECC injection port.

The broken cold-leg noding between the pressure vessel and containment tank 1 is modeled with a Valve component containing six cells. The break valve is at the interface

between cells 3 and 4. The opening and closing actions of the valve are modeled with the trip and control logic in TRAC. For Run 719, the valve was set fully open and not actuated. The containment tank 1 is modeled as a Break component using the measured containment pressure as the boundary condition.

The broken cold-leg noding between the S/W separator and containment tank 2 is modeled with a Valve component containing eight cells. The break valve for this segment of the broken cold leg is at the interface between cells 3 and 4. The opening and closing actions of the valve are modeled with the trip and control logic in TRAC. For Run 719, the valve was set fully open and not actuated. The containment tank 2 is modeled as a Break component using the measured containment pressure as the boundary condition.

**5.4.3.4 Pressure Vessel Injection Components.** Figures 5.4-10 and 5.4-11 show the upper-head and upper-core-support-plate injection modeling. The upper-head injection is modeled with a series of Pipe and Fill components that are connected to the axial level 13 interface at sectors 2, 4, 6, and 8. The upper-core-support-plate injection is modeled with a series of Tee and Fill components. The Fill components connect to the side cell of each Tee component and the main pipe of each Tee component connect to the Y-direction interface of sectors 1 through 8 at axial level 10.

**5.4.3.5 Pressure Vessel and S/W Heat-Structure Components.** Figure 5.4-12 show the heat-structure component modeling for the pressure vessel and the S/W separator. A total of 46 Slab heat-structure components are used to model the vessel and S/W separator walls and partitions.

**5.4.4. Comparison of Calculated and Test Results**
In this section, TRAC results are compared with data from JAERI instrumentation and with selected data from US instrumentation. In the comparison figures, the dotted lines represent the data and the solid lines the TRAC results. These results are for newrfd=3, which activates the reflood model with explicit top-down reflood modeling. An identical set of graphical code-data comparisons for Version 5.5 with newrfd=1 is presented, without analysis, in Appendix CC. Setting newrfd=1 activates the bottom-up reflood model as it existed in previous TRAC-PF1/MOD2 developmental assessment calculations. We have run SCTF Test 719 calculations both with and without the grid spacer model. We have determined that the grid spacer model should not be used because it results in excessive and nonphysical heat-transfer processes in the upper portions of the core. Therefore, the base-case assessment results for SCTF Test 719 do not use the TRAC grid spacer model. However, for completeness of the assessment, the calculation results with grid spacers modeled are presented in Appendix DD for newrfd=3 and in Appendix EE for newrfd=1.

**5.4.4.1. Thermal-Hydraulic Behavior in the Vessel.** Figure 5.4-13 shows the calculated heated-core inlet mass flow and Fig. 5.4-14 shows the time-averaged core flooding rate, defined as the time-averaged core inlet mass flow divided by the core inlet flow area and the density of the core inlet flow. Figure 5.4-15 compares the TRAC-calculated and measured lower-plenum liquid levels. The TRAC prediction shows that the lower plenum fills rapidly when ECC injection starts, and a maximum 14,900-Pa level is reached at 122 s when bottom of core recovery (BOCREC) occurs. The lower plenum

remains full after 124 s. The TRAC-calculated results and the data are in reasonable agreement.

Figure 5.4-16 compares the TRAC-calculated and measured upper-plenum liquid levels above bundles 5 through 8. The predicted and measured results are judged to be in minimal agreement. TRAC overpredicts the liquid level in the upper plenum until 300 s because too much liquid and vapor passes into the upper plenum as the code overpredicts the cooling of the core early in the transient.

A comparison of the calculated and measured liquid levels for bundles 2 and 8 is shown in Figs. 5.4-17 and 5.4-18. The TRAC-calculated liquid levels for the total bundle height are noticeably lower than those in the test. A review of the core-lower-half and core-upper-half liquid levels (data not shown) shows the same trends. The same condition is illustrated further in Fig. 5.4-19, which shows the void fraction at the midplane of the heated core in bundles 2, 4, 6, and 8. The TRAC-calculated void fraction or deficiency of liquid is higher than that of the data after 200 s.

The US NRC has supplied tie-plate instrumentation for the SCTF Core-III facility. A comparison of the calculated and measured bundle-4 vapor velocity is presented in Fig. 5.4-20. TRAC overpredicts the data by a factor between 2 and 6.

A comparison of calculated and measured liquid levels in the downcomer is shown in Fig. 5.4-21. TRAC underpredicts the data by 15,000 Pa, largely as the result of underpredicting the pressure in the core (Fig. 5.4.22). The pressure response within the core is most directly related to the amount of steam generated within the core as the core is first cooled and then quenched. In the test, the core pressure increased until about 155 s, decreased at a moderate rate until 240 s, and then decreased at a slower rate until the test was terminated. The pressure break points observed in the test are directly related to the coolant injection profile, which simulated the accumulator injection from 122 to 135 s, and then transitioned to the LPCI flow rate until 230 s, and continued at the LPCI flow rate thereafter. The initial TRAC-calculated core pressurization following BOCREC is in reasonable agreement with the data. However, within 20 s following BOCREC, the TRAC-calculated pressure increase is terminated, which occurred ~15 s before the pressure rise in the test was terminated and while the high-flow-rate accumulator-injection phase was still under way.

The differences between the predicted and observed rod thermal response of the heater rods are considered for four periods. The duration of each period varies with elevation; near the bottom of the core, the rod passes through several of the periods so quickly that they cannot be distinguished. Period 1 is the interval during which the rod experiences heatup under adiabatic conditions in pure steam. This period lasts until the coolant reaches the bottom of the heated core, which occurs at ~120 s in the test. Period 2 is an interval in which the rod continues to heat but at a slower rate. Even though the power supplied to the rod simulates decay heat, less heat is removed by the two-phase coolant than is supplied to the rod to simulate decay heat. The transition to period 3 occurs when the power is supplied to the rod and the two-phase heat-transfer balance. The temperature rise of the cladding stops and the cladding begins to cool. Period 4 occurs when the rod has cooled sufficiently to quench.

A comparison of the calculated and measured core-lower-half cladding temperatures for bundles 2 and 8 are presented in Figs. 5.4-23 and 5.4-24. For both bundles, the adiabatic heatup rate ending at 124 s is well simulated at all levels. This is an improvement over the previous assessment and is due largely to the more accurate 17-step axial-power shape modeling.

Once coolant enters the core, both the predicted and measured cladding temperatures peak and begin to decline. For the first three levels of the core, period 2, an interval of slow heating is nonexistent. The cooling rate during period 3 is underpredicted as is clearly seen by comparing the predicted and measured cooling rates prior to quenching. For bundle 2, the quenching times for levels 1 through 3 are late by as much as 40 s but at levels 4 and 5, they are within 10 s of the measured quench times. For bundle 8, except at level 1, there is virtually no agreement between the predicted and measured quench times.

We observe that there are clear multidimensional effects in the test that are not modeled in the TRAC calculation. The peak cladding temperature in the lower half of bundle 2, a high-power bundle, is ~150 K higher than the lower bundle. Accordingly, the lower half of high-power bundle 2 quenches 50 s later than bundle 8. The predicted thermal behavior of bundle 2 is in reasonable agreement with data, but the predicted thermal behavior of bundle 8 is in minimal to reasonable agreement with data. TRAC correctly predicts the higher peak cladding temperature in bundle 2 but underpredicts the level-5 peak cladding temperature and also predicts that bundle 8 quenches later than bundle 2.

A comparison of the calculated and measured core-upper-half cladding temperatures for bundles 2 and 8 is shown in Figs. 5.4-25 and 5.4-26. In both bundles the period of adiabatic heatup is well predicted. At the highest elevation, level 10, the rod quenched early in the test, but TRAC predicts a continuing heatup. Otherwise, TRAC correctly predicts the general trends of slow heatup, slow cooling, and quench. However, during period 3, the period of slow cooling, TRAC underpredicts the cooling rate. For bundle 2, the predicted and measured quench times at levels 6 and 7 agree very well. The predicted thermal response for the upper half of bundle 2 is judged to be from minimal to reasonable. The predicted thermal response for the upper half of bundle 8 is in minimal agreement with the data. In the test, the cladding at level 10 continued to heat, although an early quench is predicted by TRAC. At level 10 the predicted thermal behaviors for bundles 2 and 8 are reversed. For bundle 2, TRAC predicts a continuing heatup at level 10, which quenches early in the test. For bundle 8, TRAC predicts an early quench at level 10, which continues to heat up. For the remaining levels of bundle, TRAC predicts essentially no period of slow heating, whereas this period is clearly evident at all levels in bundle 8. Further, the cooling rate during the period of slow cooling is underpredicted. Finally, TRAC predicts the upper half of bundle 8 to quench early. As with the lower part of the core, TRAC correctly predicts the higher peak cladding temperature in bundle 2 but incorrectly predicts that bundle 8 quenches later than bundle 2. Overall, the predicted thermal response in the upper half of the core is in minimal agreement with the data.

**5.4.4.2. Loop Behavior.** A comparison of the calculated and measured pressure-vessel-side, broken cold-leg mass-flow rate is shown in Fig. 5.4-27. TRAC underpredicts the data, but the trend is similar and thus the agreement is between minimal and reasonable. A comparison of the calculated and measured broken cold-leg (pressure vessel side) total (integrated) mass flow is shown in Fig. 5.4-28. TRAC underpredicts the flow by ~40% at 500 s. This underprediction appears to be directly related to the underprediction of the downcomer liquid level, i.e., a higher downcomer liquid level would lessen the distance between the top of the downcomer liquid and the inlet to the pressure-vessel-side broken cold leg.

A comparison of the calculated and measured hot-leg mass flow rate is presented in Fig. 5.4-29. The agreement lies in the range between minimal and reasonable. The predicted flow into the hot leg for the first 100 s following BOCREC exceeds the measured value. A comparison of the calculated and measured hot-leg total (integral) mass flow is presented in Fig. 5.4-30, where the agreement also is between minimal and reasonable.

A comparison of the calculated and measured S/W-separator-side, broken cold-leg mass-flow rate is presented in Fig. 5.4-31. Although TRAC overpredicts the mass flow rate between BOCREC and 500 s, the trend is similar. The agreement is minimal.

A comparison of the calculated and measured intact cold-leg mass flow rate is presented in Fig. 5.4-32. TRAC overpredicts the flow by as much as 100% during the first 125 s after the start of coolant injection and underpredicts the mass flow rate for the remainder of the transient. The agreement is minimal.

### 5.4.5. Conclusions
From the assessment, we conclude the following.

- Overall, the predicted core thermal-hydraulic behavior is in minimal agreement with the data.

- Cladding temperatures calculated by TRAC-M in the lower half of the core are in reasonable agreement with the data. Cladding temperatures calculated by TRAC-M in the upper half of the core are in minimal agreement with the data.

- TRAC-M predicts some significant dimensional trends. For example, TRAC-M predicts the multidimensional effects induced by the radially skewed power profile. The highest-powered bundles attain the highest temperatures, and the lowest-powered bundles are cooled by a recirculating flow from the top of the core. TRAC does not predict the multidimensional trends associated with quenching.

5.4-8

### 5.4.6. Code Performance

The updated SCTF Run 719 assessment was calculated with code Version 5.5.2. The run performance information plus other pertinent comments follow.

Code Version 5.5.2

| Platform | Sun Enterprise 3000 |
|---|---|
| Total CPU time (s) | 8686 |
| Archive location of input model | CFS   /tida/f77da_decks/task4.4b/insctf719 |
| Archive location of calculation | CFS   /trac-da/task4.4b/5.5.2nrfd3ngs/ SCTF-719.tar.gz |

## REFERENCES

5.4-1. H. Adachi, T. Iguchi, A. Kamoshida, T. Oyama, K. Komori, Y. Niitsuma, T. Iwqmura, A Ohnuki, Y. Abe, H. Akimoto, and Y. Murao, "Design of the Slab Core Test Facility (SCTF) in Large Scale Reflood Test Program, Part III: Core-III," JAERI-memo 62-110 (March 1987).

5.4-2. T. Iwamura, T. Iguchi, T. Oyama, A. Kamoshida, Y. Niitsuma, H. Akimoto, T. Okubo, A. Ohnuki, I. Sakaki, K. Nakajima, T. Chiba, H. Watanabe, K. Komori, H. Sonobe, A. Owada, H. Adachi, and Y. Murao, "Data Report on Large Scale Reflood Test-121, SCTF Test S3-15 (Run 719)," JAERI-memo 63-330 (September 1987).

5.4-3. B. E. Boyack, "Posttest Assessment of TRAC-PF1/MOD1 and TRAC-PF1/MOD2 Using SCTF Core-III Run 719 (Test S3-15)," Los Alamos National Laboratory report LA-CP-90-27 (January 1990).

## TABLE 5.4-1

## SUMMARY OF TEST CONDITIONS FOR SCTF RUN 719 (S3-15)

| PARAMETER | TEST CONDITION |
|---|---|
| System pressure | 0.2 MPa |
| Initial total core power | 7.12 MW |
| Radial power distribution (bundle 1,2/3,4/5,6/7,8) | 1.36/1.2/1.1./1.0 0.91/0.86/0.81/0.76 "inclined" |
| Decay power | $1.02 \times ANS + 1.02 \times actinides$ |
| Initial peak cladding temperature (at initiation ECC injection) | 1134 K |
| ECC injection mode | Lower-plenum injection |
| Upper-head injection | None |
| UCSP injection | None |
| Lower-plenum injection flow rate | 37 $kg \cdot s^{-1}$ for 13 s 37 to 13 $kg \cdot s^{-1}$ over 15 s 13 to 4.1 $kg \cdot s^{-1}$ over 70 s 4.1 to 3.75 $kg \cdot s^{-1}$ over 10 s 3.75 $kg \cdot s^{-1}$ for 500 s |
| Water temperature | 353 K for 36 s 393 K for remainder of test |
| Injection period | 608 s |
| Cold-leg injection | None |
| Lower-plenum liquid level | 1.2 m, saturated at 393 K |

5.4-10
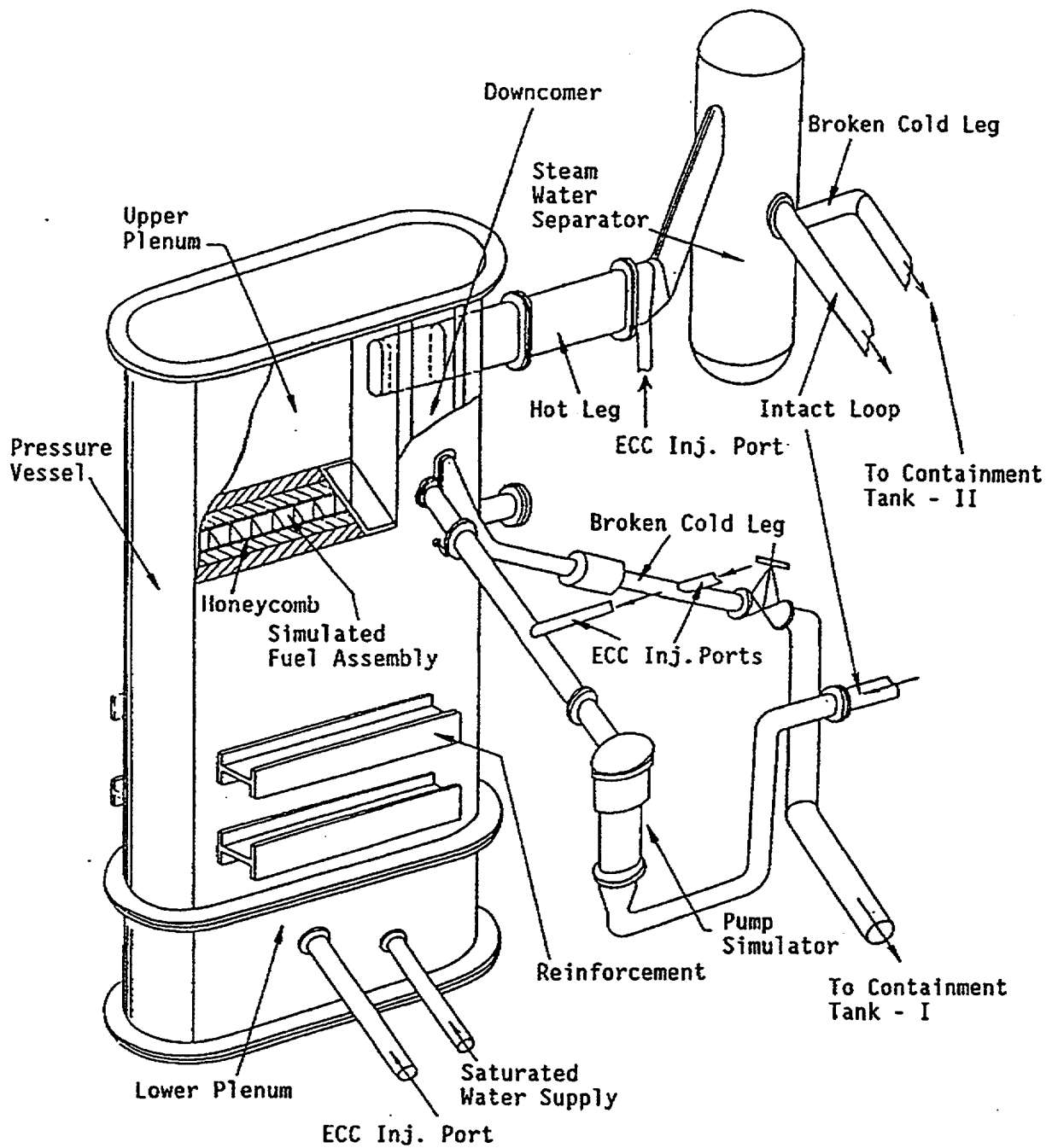
Fig. 5.4-1. Overview of the Slab Core Test Facility.
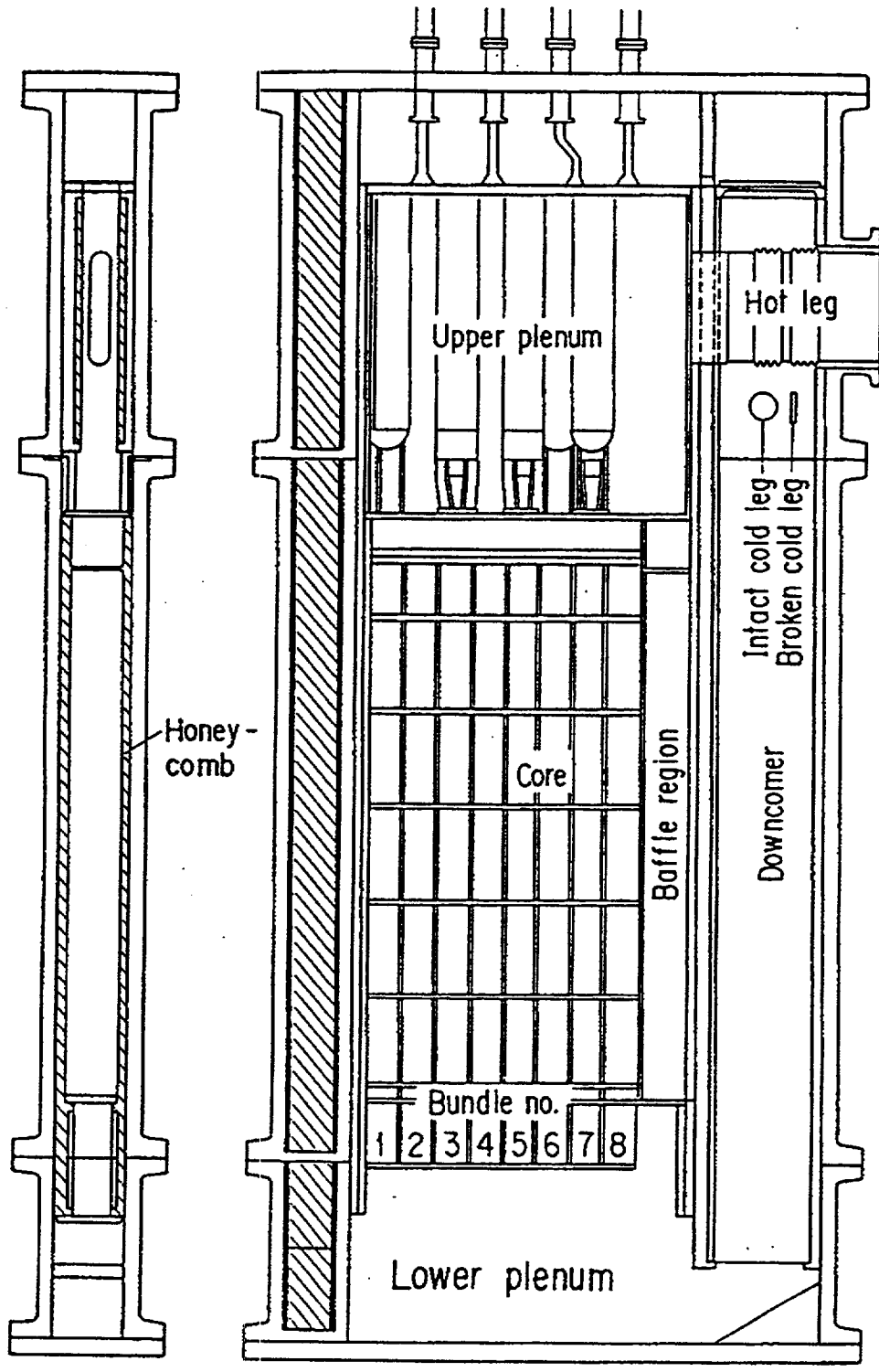
Fig. 5.4-2. Vertical cross-section view of SCTF pressure vessel.

Upper Region

Lower Region | Center Region

Cladding

BN (Center Region)
/ MgO (Upper & Lower Region)

MgO

Heater Element

SECTION A-A
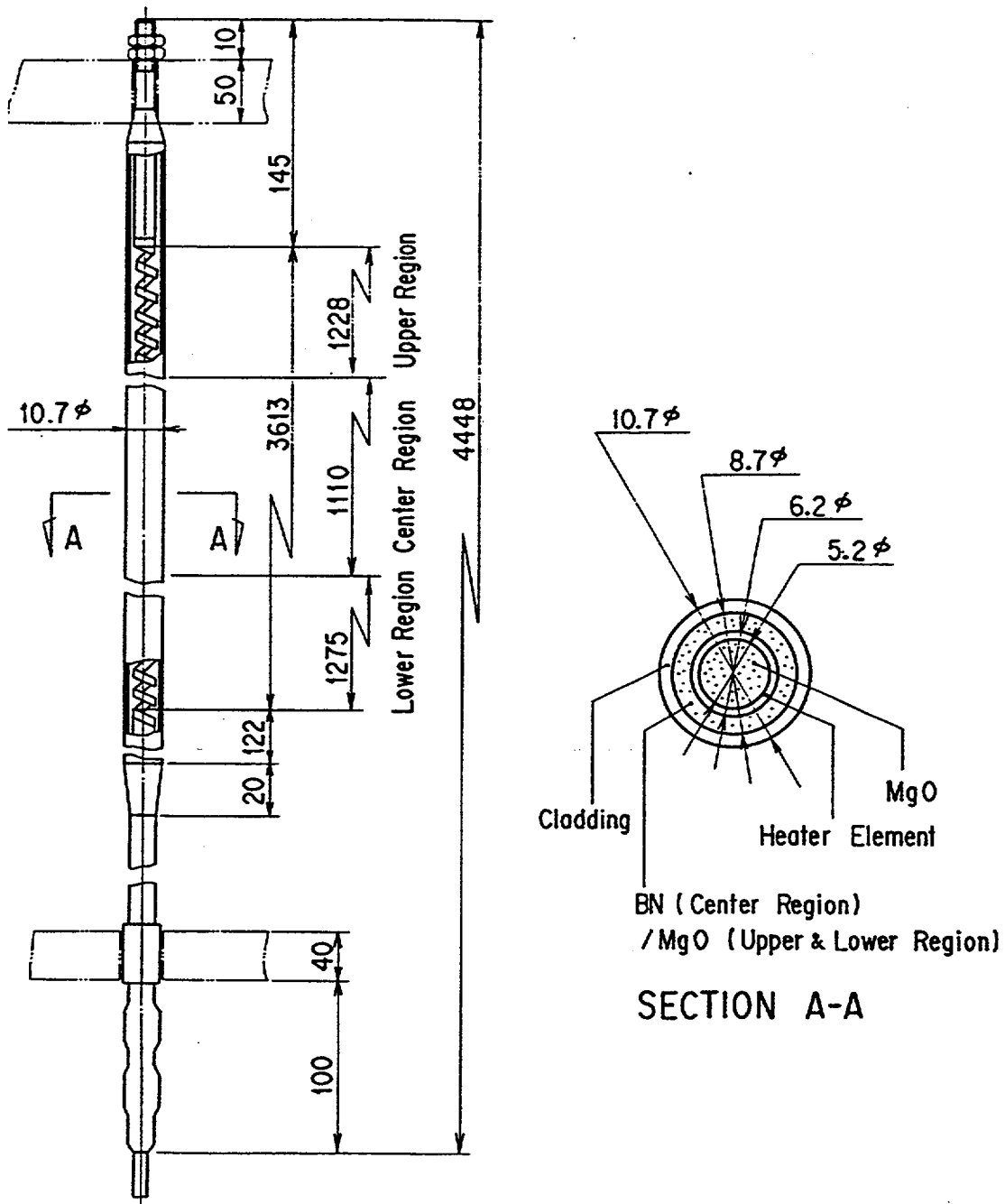
Heater Rod

Fig. 5.4-3. Dimensions and configuration of heater rods.
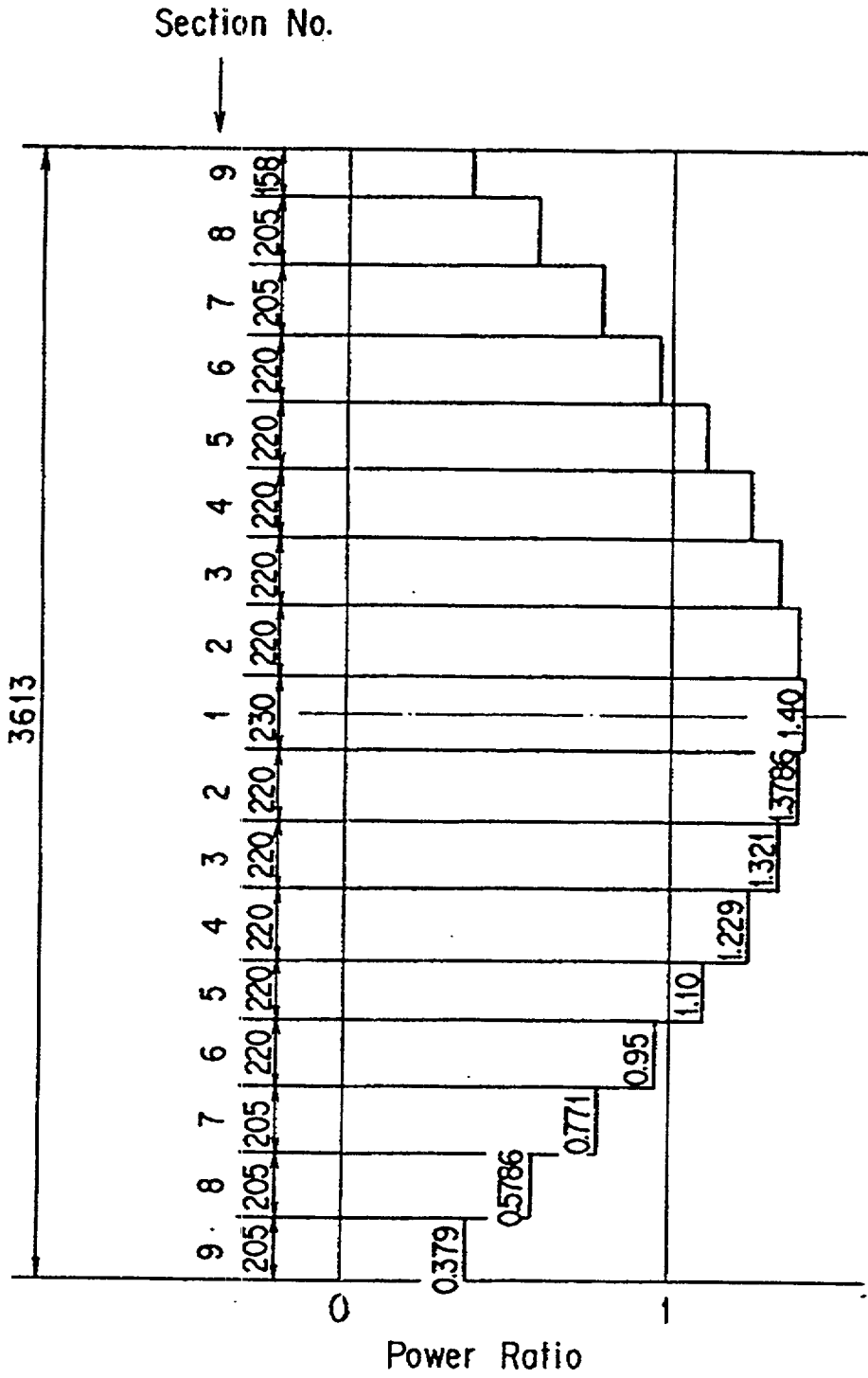
Fig. 5.4-4. Axial power distribution of heater rods.

5.4-14
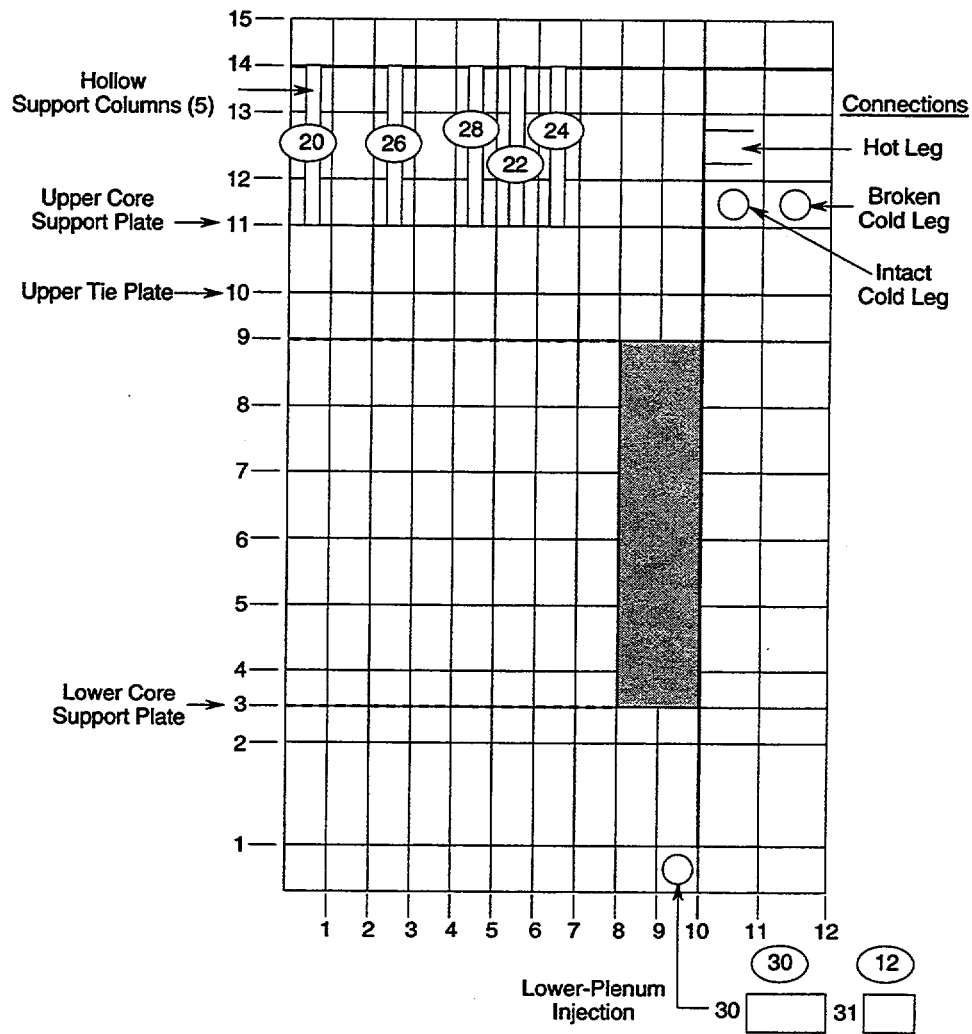
| Axial Level | Elevation (m) | Horizontal Sector | Distance (m) |
|---|---|---|---|
| 1 | 0.502 | 1 | 0.23 |
| 2 | 1.432 | 2 | 0.46 |
| 3 | 1.719 | 3 | 0.69 |
| 4 | 1.9595 | 4 | 0.92 |
| 5 | 2.6245 | 5 | 1.15 |
| 6 | 3.2895 | 6 | 1.38 |
| 7 | 3.9545 | 7 | 1.61 |
| 8 | 4.6195 | 8 | 1.84 |
| 9 | 5.332 | 9 | 2.017 |
| 10 | 5.748 | 10 | 2.334 |
| 11 | 6.337 | 11 | 2.667 |
| 12 | 6.822 | 12 | 3.020 |
| 13 | 7.559 | | |
| 14 | 7.996 | | |
| 15 | 8.657 | | |

Fig. 5.4-5. Pressure vessel noding diagram.
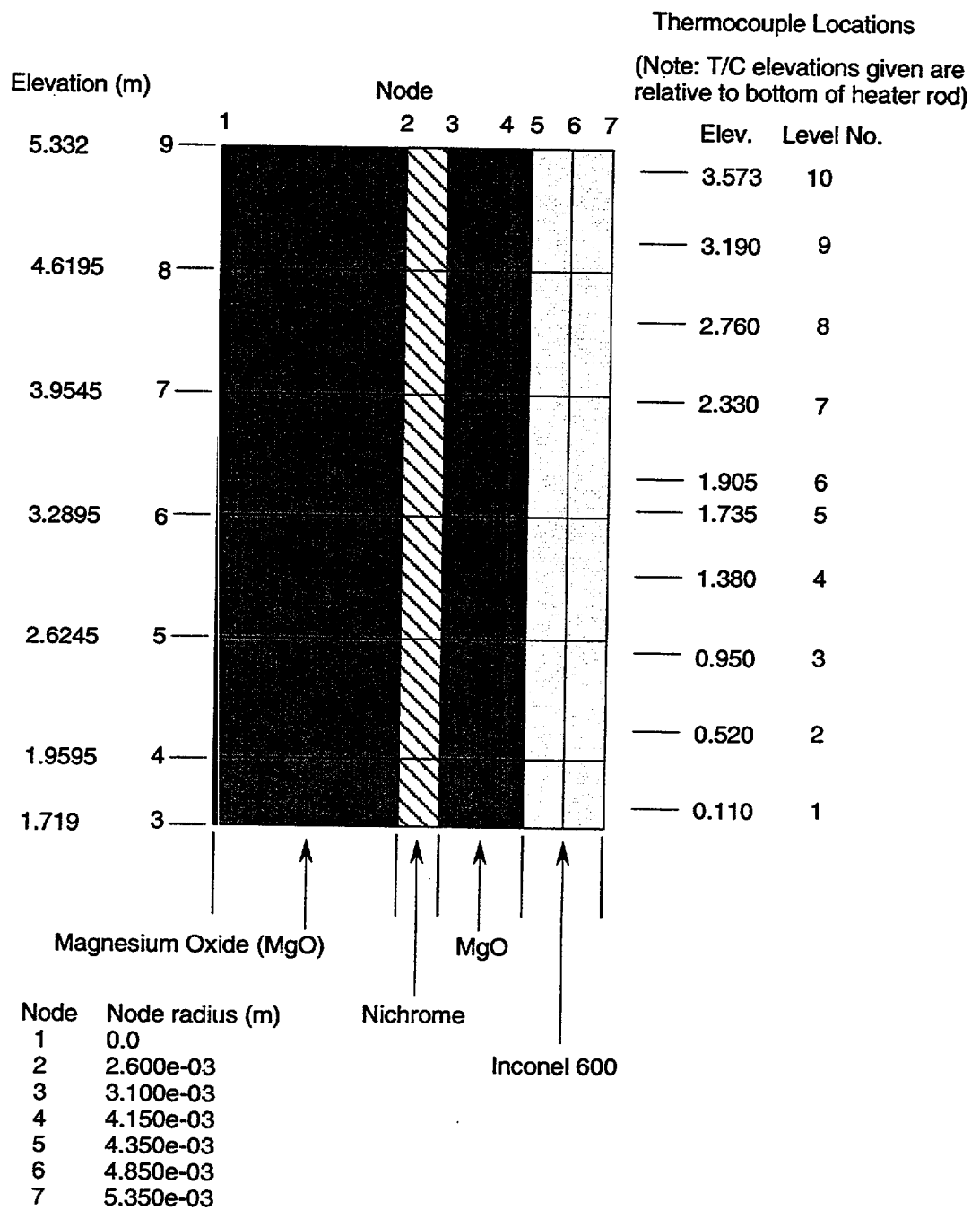
Fig. 5.4-6.  Heater-rod noding and thermocouple locations.

Elevation (m)

| Elevation (m) | Node |
|---|---|
| 5.332 | 9 |
| 4.6195 | 8 |
| 3.9545 | 7 |
| 3.2895 | 6 |
| 2.6245 | 5 |
| 1.9595 | 4 |
| 1.719 | 3 |

Node  1  2  3  4 5 6 7

Thermocouple Locations

(Note: T/C elevations given are relative to bottom of heater rod)

| Elev. | Level No. |
|---|---|
| 3.573 | 10 |
| 3.190 | 9 |
| 2.760 | 8 |
| 2.330 | 7 |
| 1.905 | 6 |
| 1.735 | 5 |
| 1.380 | 4 |
| 0.950 | 3 |
| 0.520 | 2 |
| 0.110 | 1 |

Magnesium Oxide (MgO)

MgO

Nichrome

Inconel 600

| Node | Node radius (m) |
|---|---|
| 1 | 0.0 |
| 2 | 2.600e-03 |
| 3 | 3.100e-03 |
| 4 | 4.150e-03 |
| 5 | 4.350e-03 |
| 6 | 4.850e-03 |
| 7 | 5.350e-03 |

Fig. 5.4-7. Rod bundle horizontal relative power distribution.
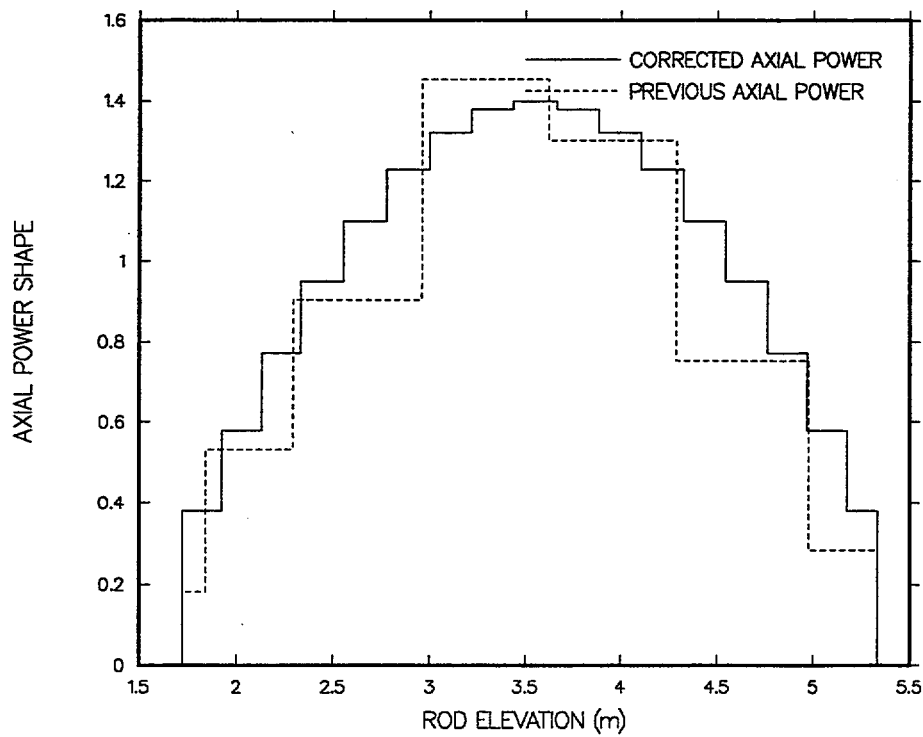


Fig. 5.4-8. Heater-rod axial-power shape.
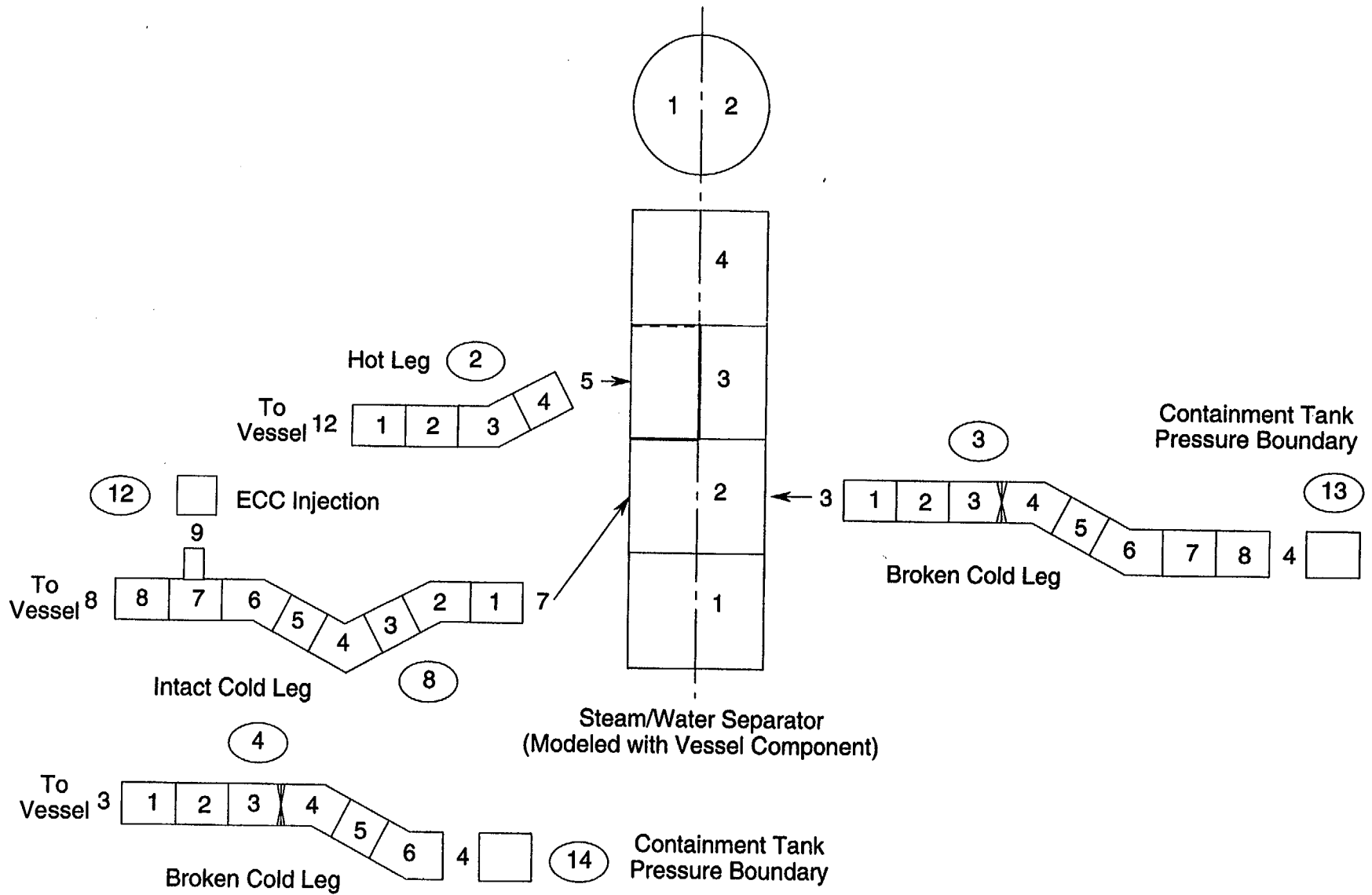
Fig. 5.4-9. Loop and Steam/Water component modeling
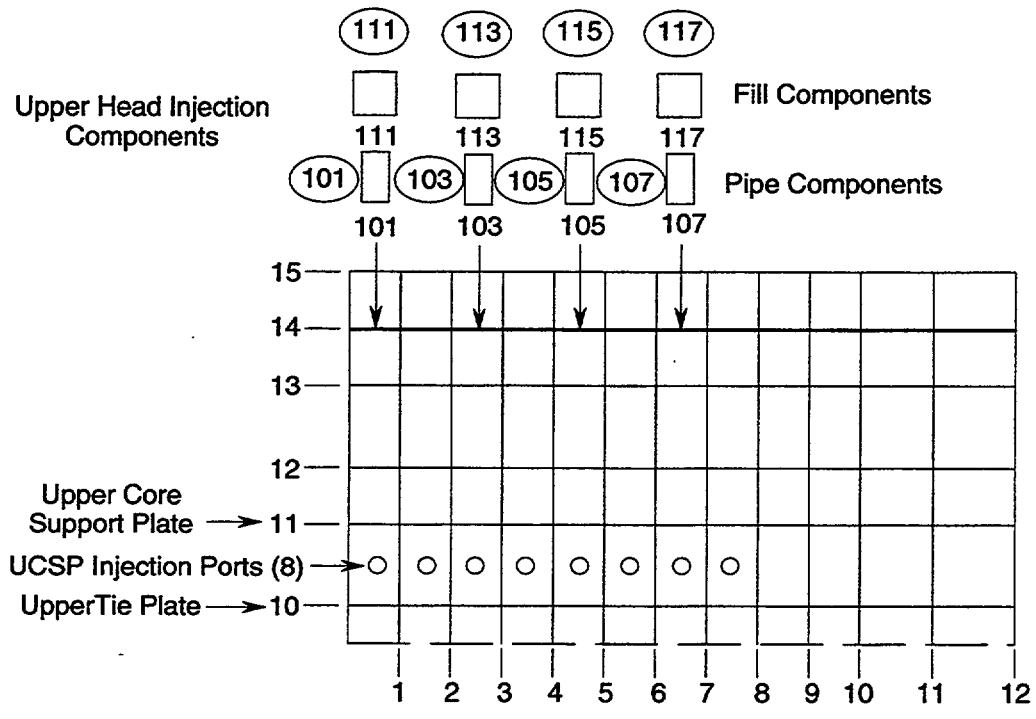
(Elevation View of Pressure Vessel at Levels 10 -15)

Fig. 5.4-10. Upper-head injection modeling.

(Plan View of Pressure Vessel at Level 11)
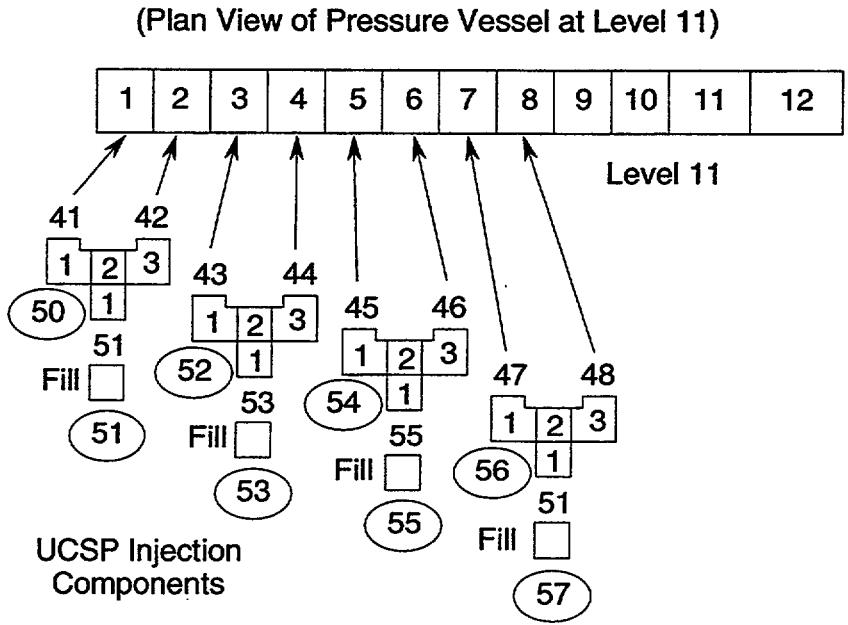


Fig. 5.4-11. Upper-core-support-plate injection modeling.
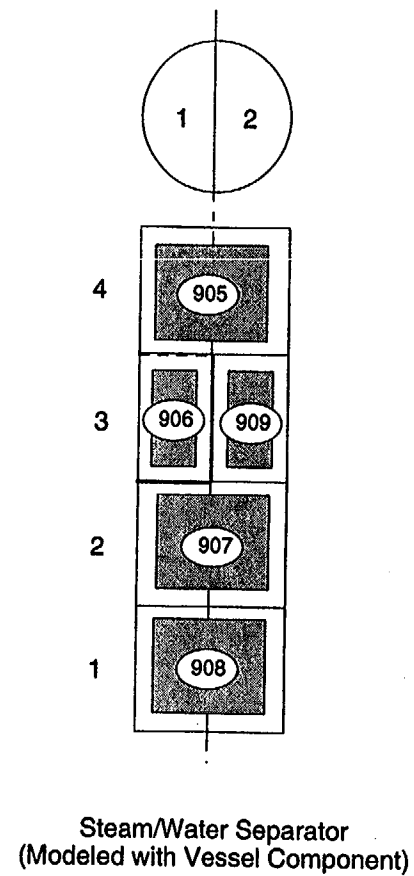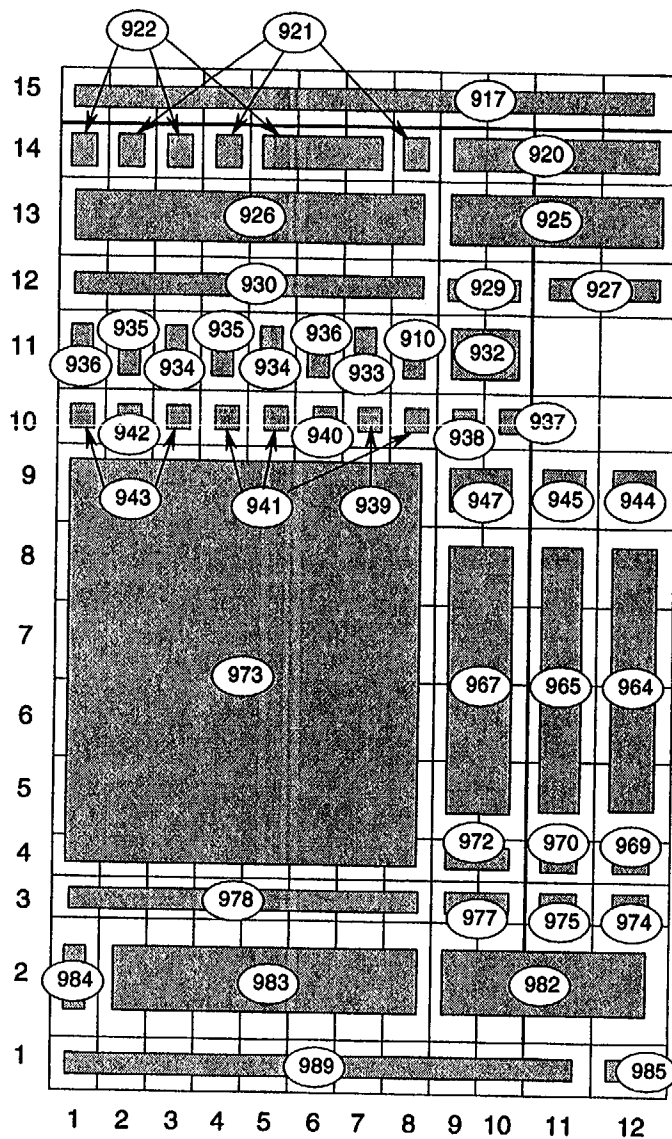
Fig. 5.4-12. Vessel and S/W heat-structure components.
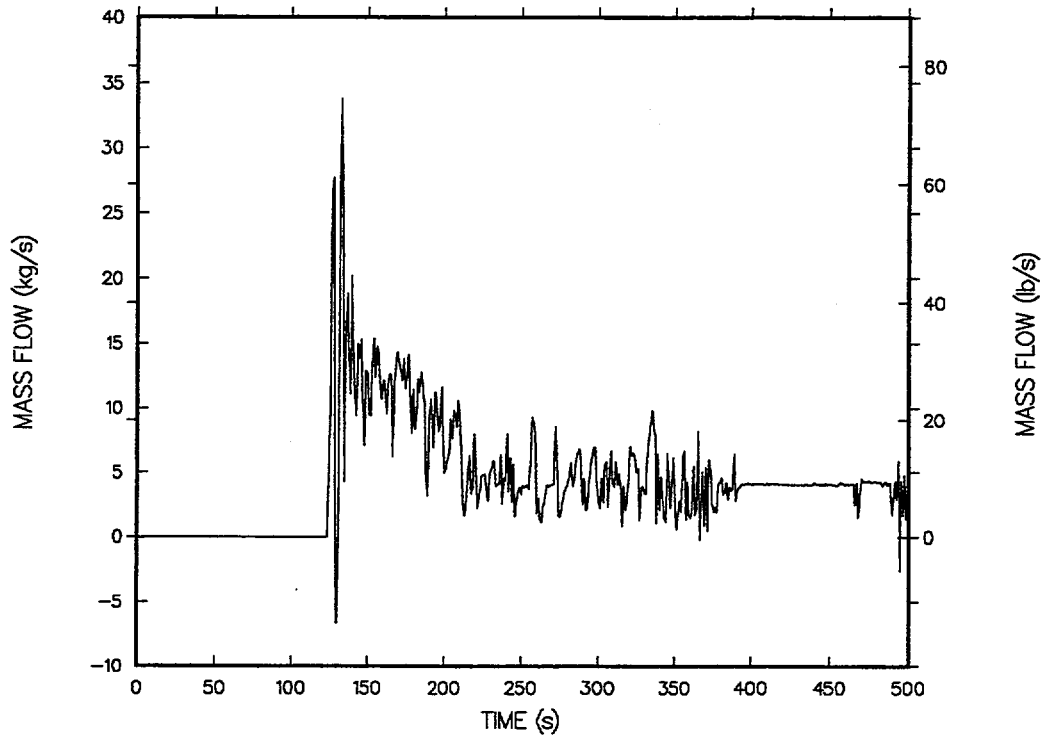
Fig. 5.3-13.  Core inlet mass flow.
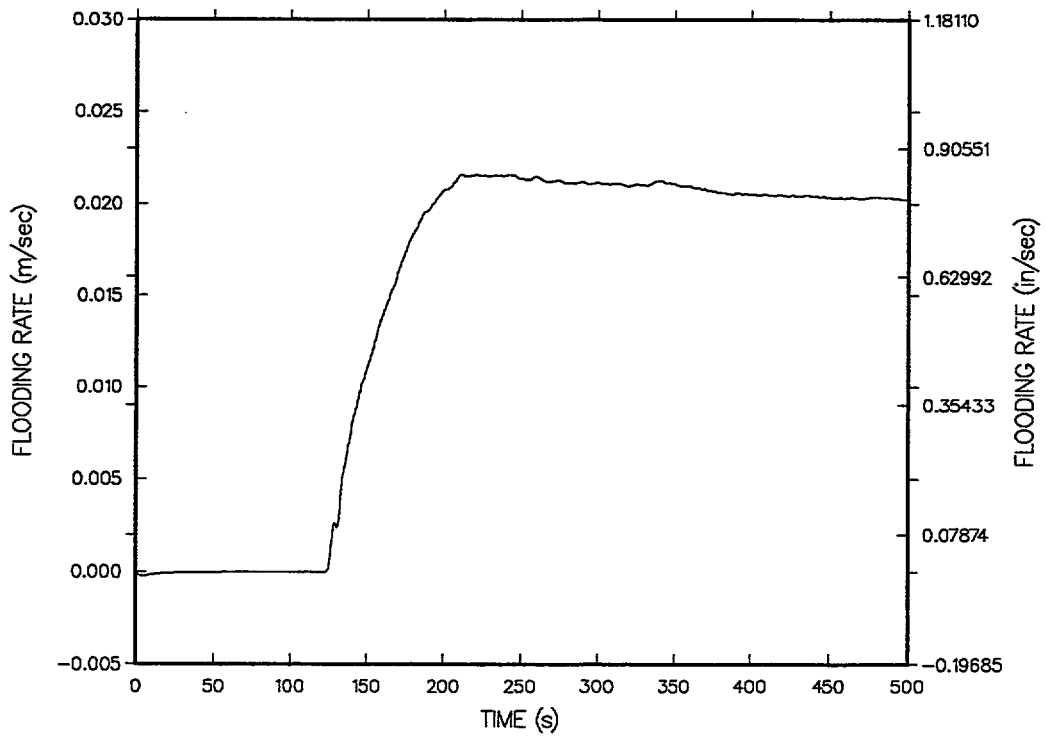


Fig. 5.3-14.  Time-averaged core flooding rate.
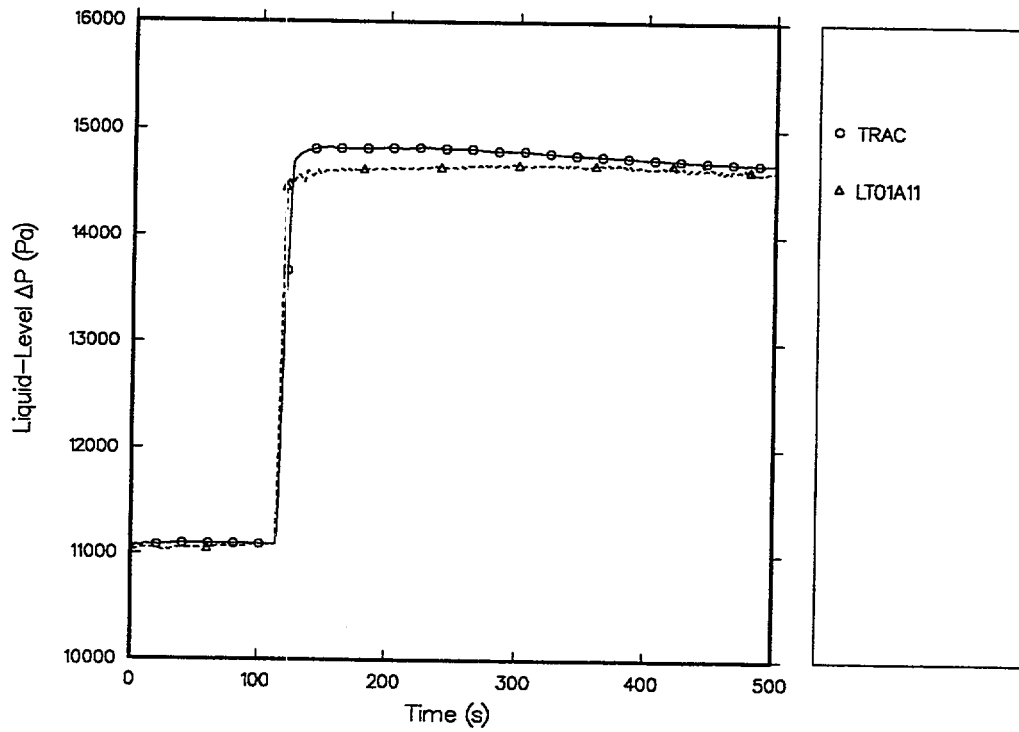
Fig. 5.4-15. Lower-plenum liquid level.
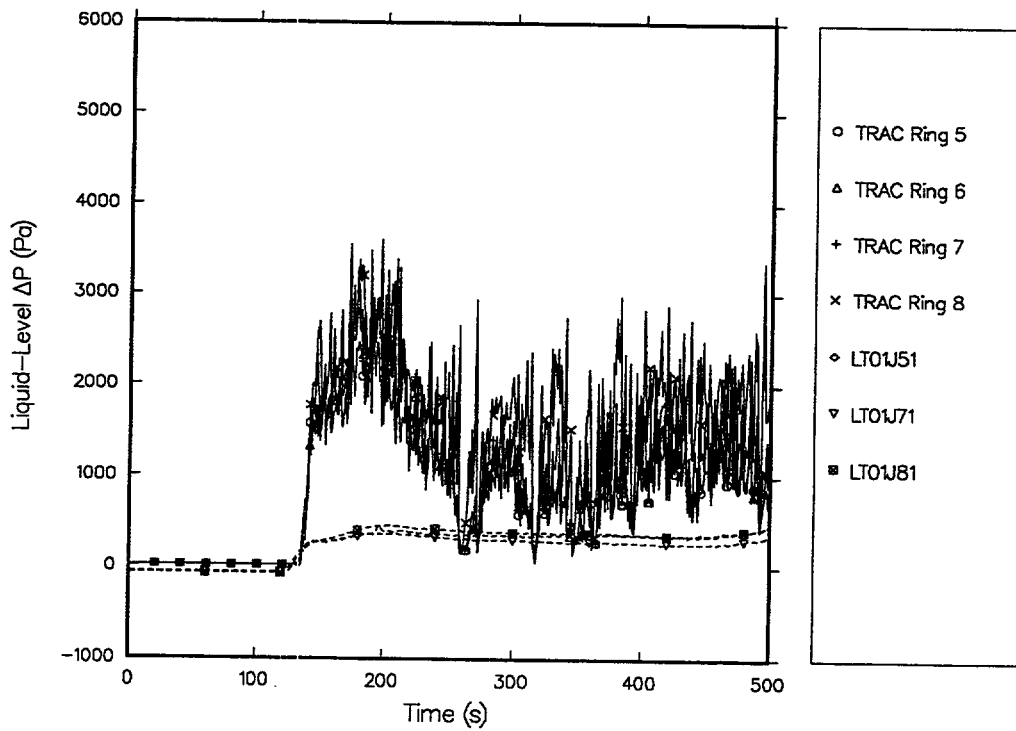


Fig. 5.4-16. Calculated and measured upper-plenum liquid levels above bundles 5 through 8.
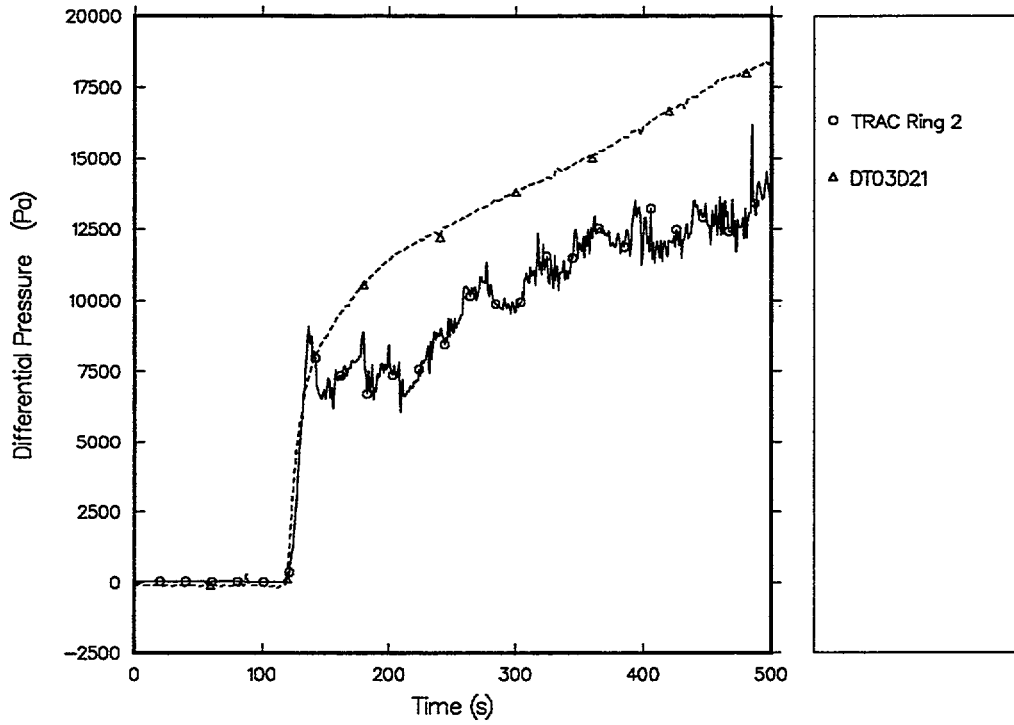
Fig. 5.4-17. Calculated and measured core full-height level in bundle 2.
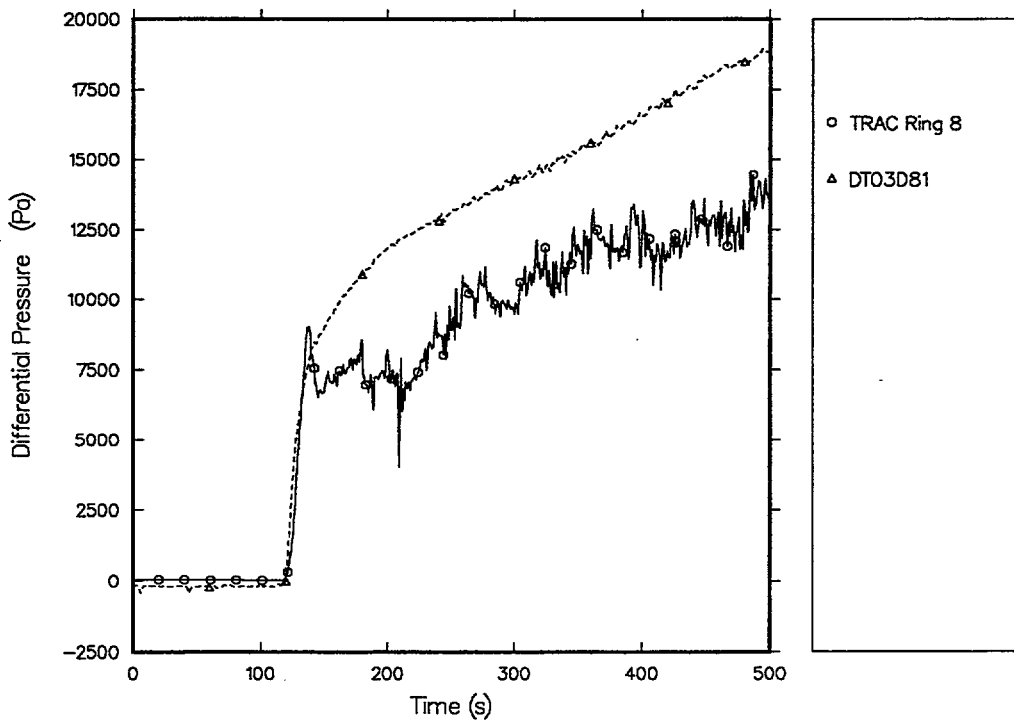


Fig. 5.4-18. Calculated and measured core full-height level in bundle 8.
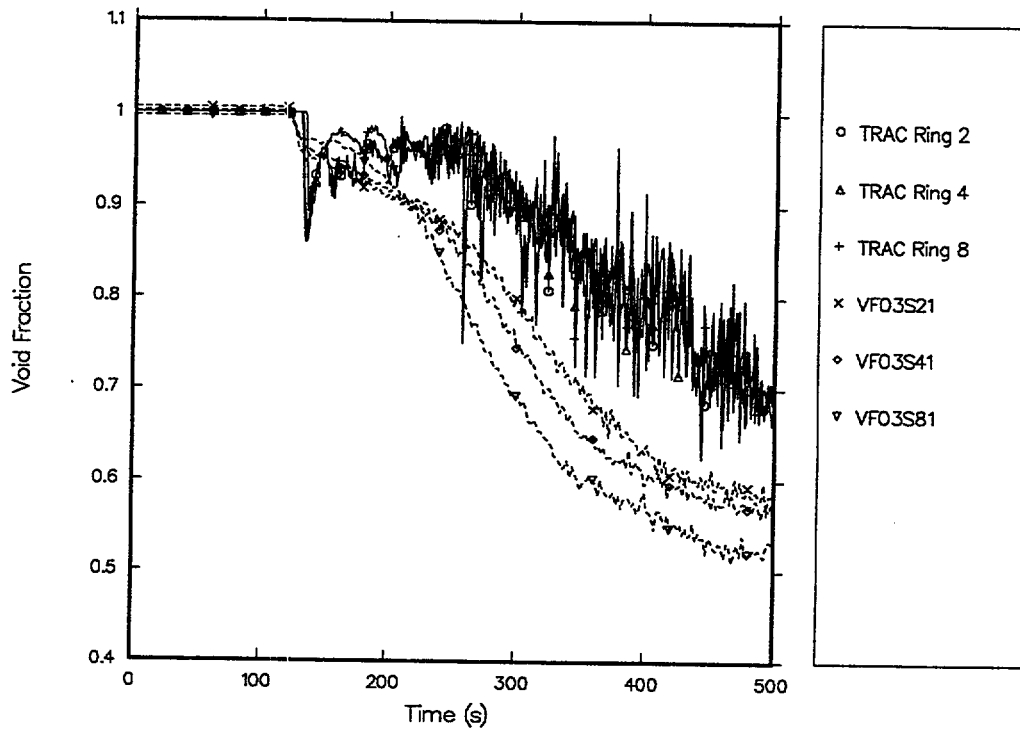
Fig. 5.4-19. Void fractions in bundles 2, 4, 6, and 8 at the 1.905-m level.
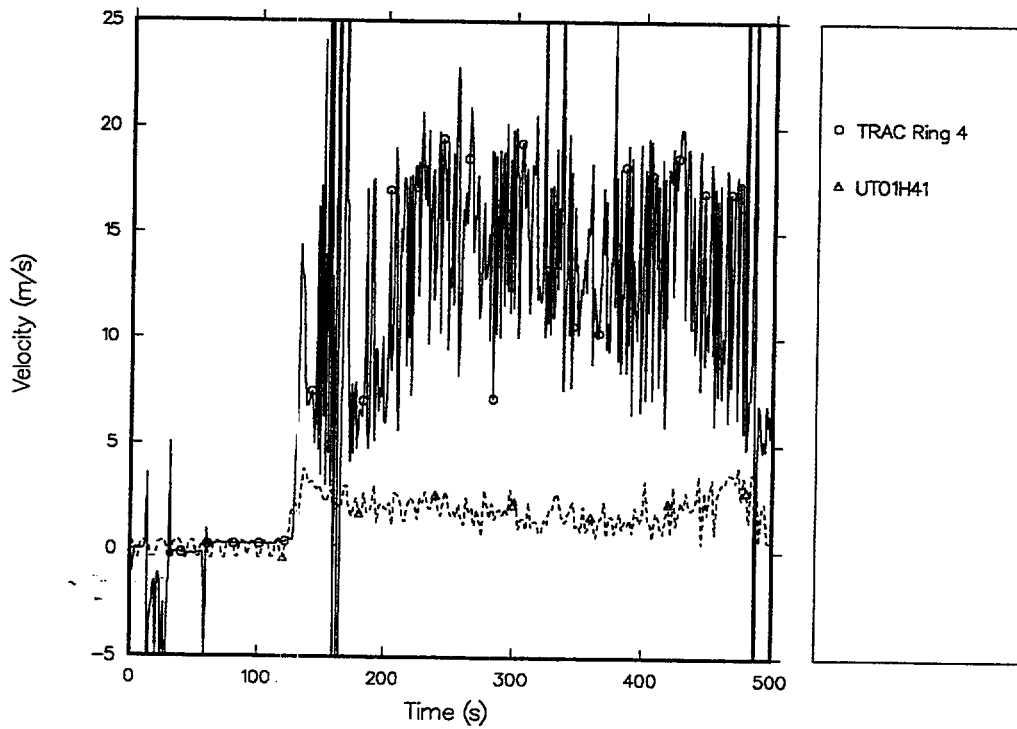


Fig. 5.4-20. Calculated and measured bundle 4 tie-plate vapor flows.
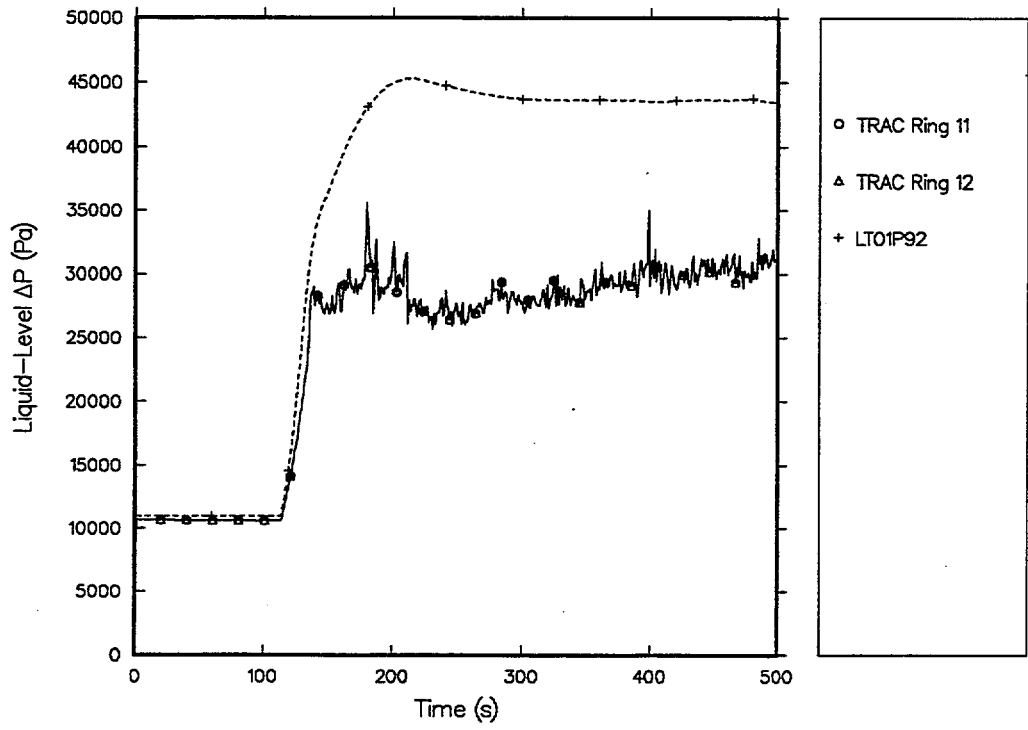
Fig. 5.4-21. Calculated and measured downcomer liquid level.
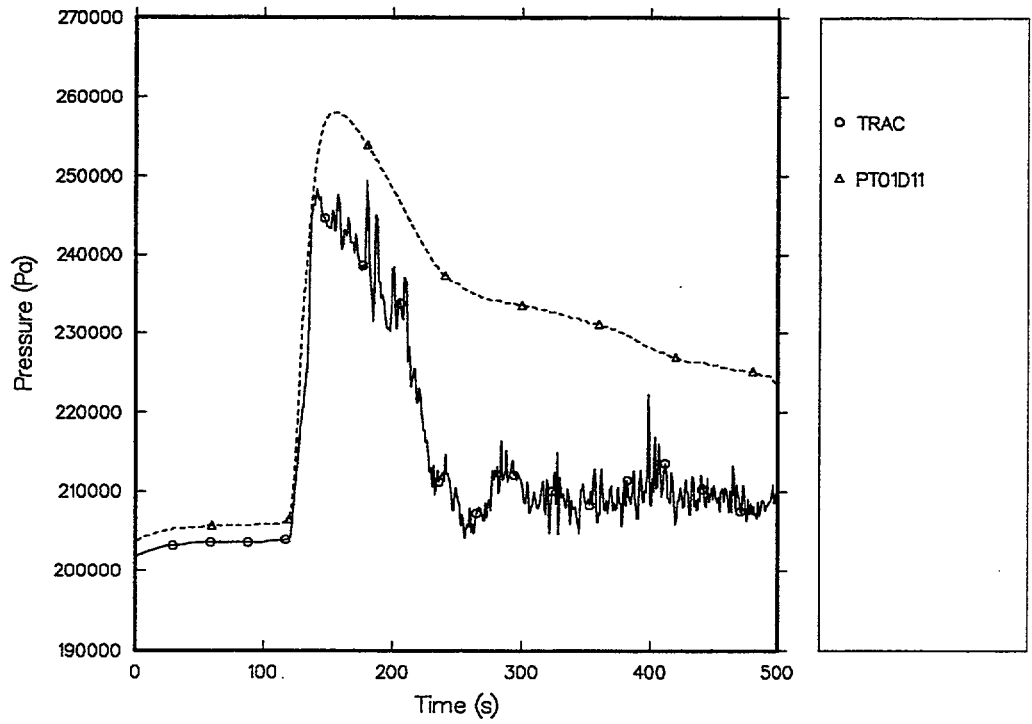


Fig. 5.4-22. Calculated and measured core average pressure.
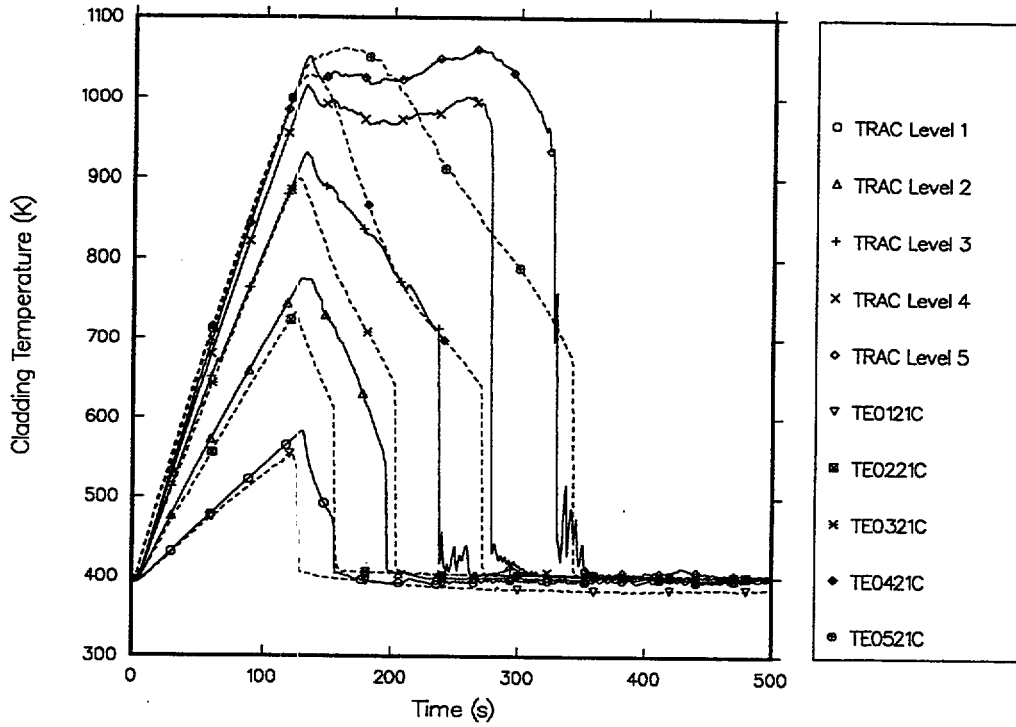
5.4-25

Fig. 5.4-23. Calculated and measured core-lower-half cladding temperature of bundle 2.
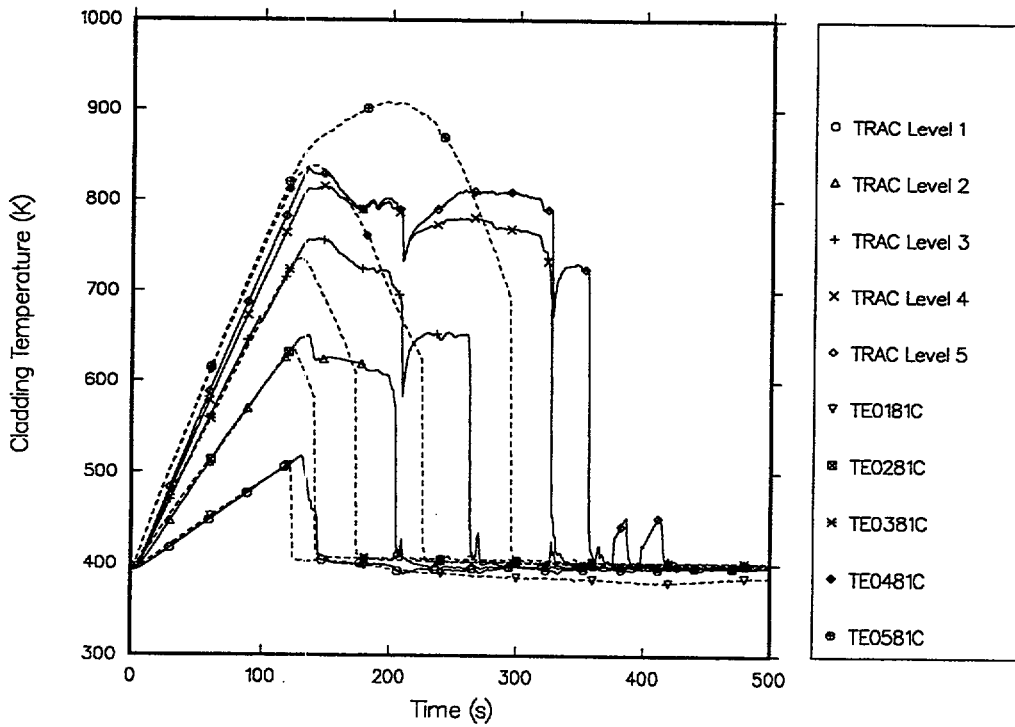


Fig. 5.4-24.   Calculated and measured core-lower-half cladding temperature of bundle 8.
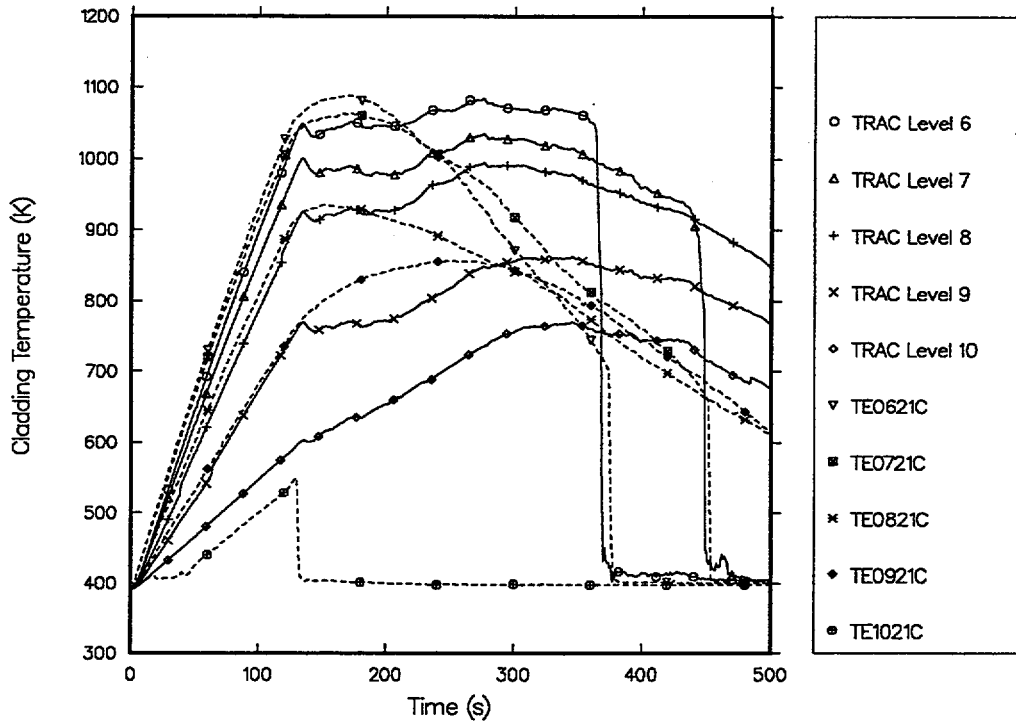
Fig. 5.4-25. Calculated and measured core-upper-half cladding temperature of bundle 2.
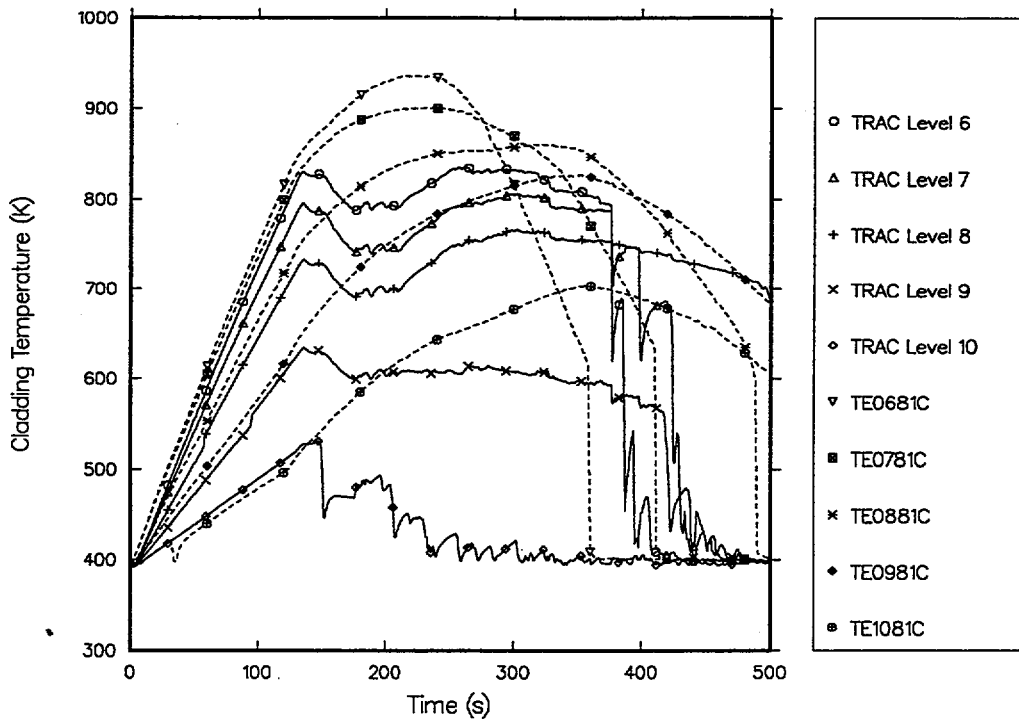


Fig. 5.4-26. Calculated and measured core-upper-half cladding temperature of bundle 8.
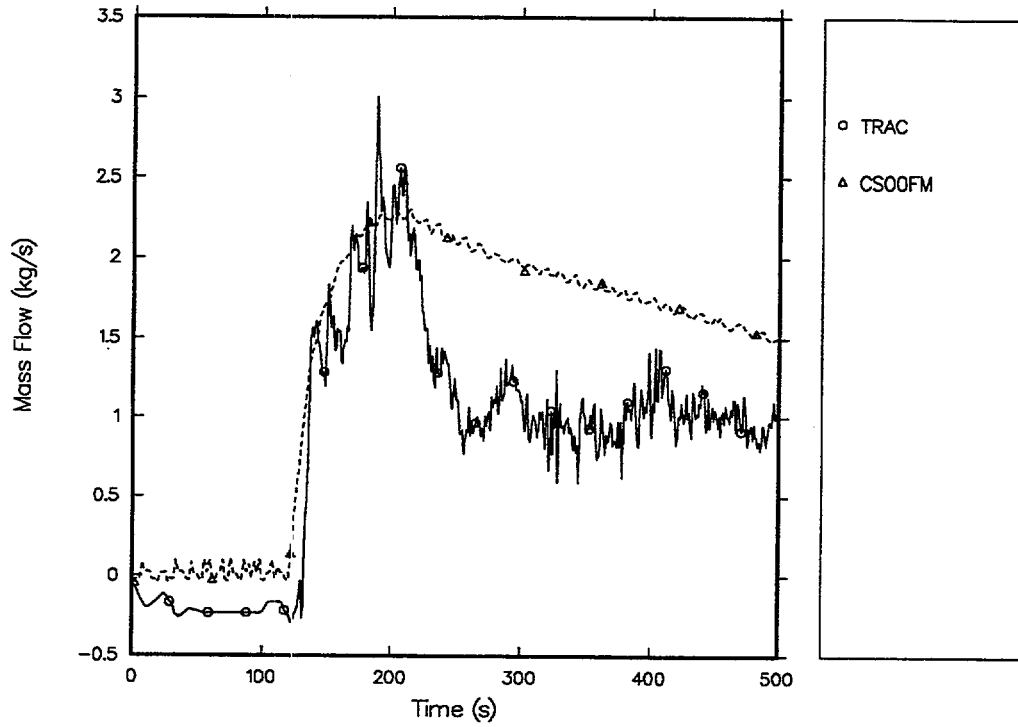
Fig. 5.4-27.   Calculated and measured pressure-vessel-side, broken cold-leg mass-flow rate.
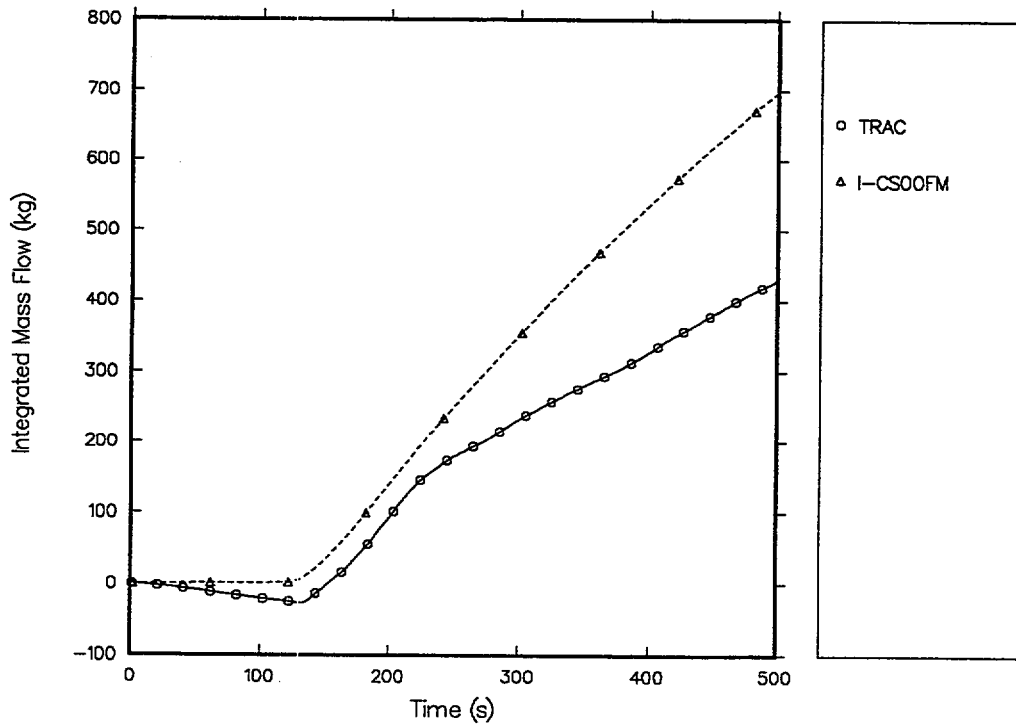


Fig. 5.4-28.   Calculated and measured pressure-vessel-side, broken cold-leg integrated mass flow.
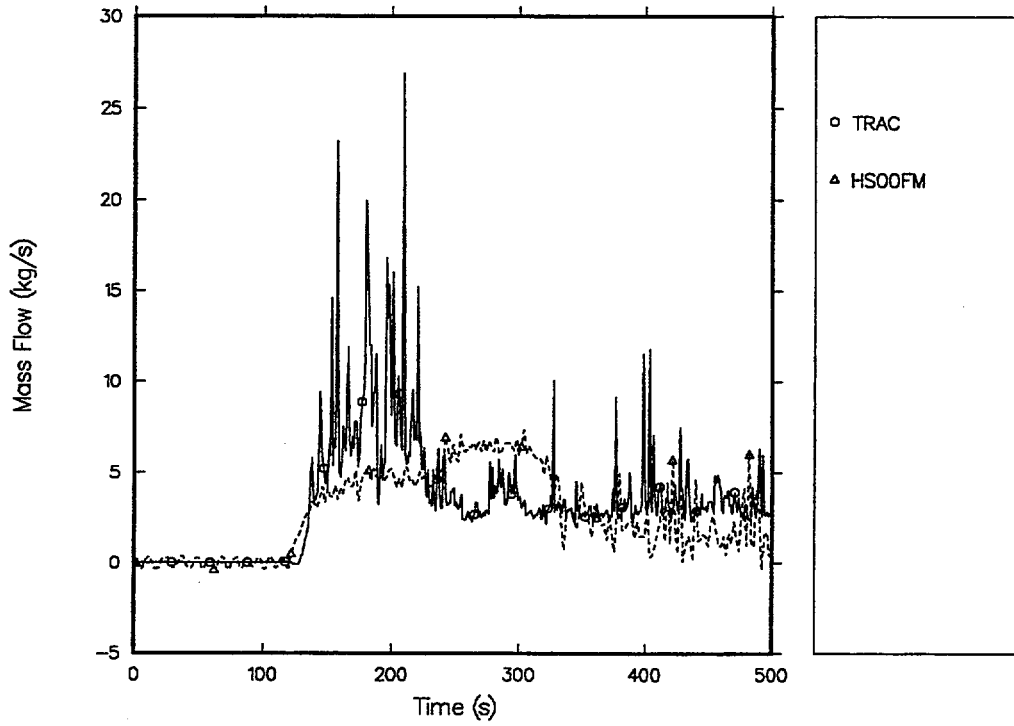
Fig. 5.4-29. Calculated and measured hot-leg mass-flow rate.
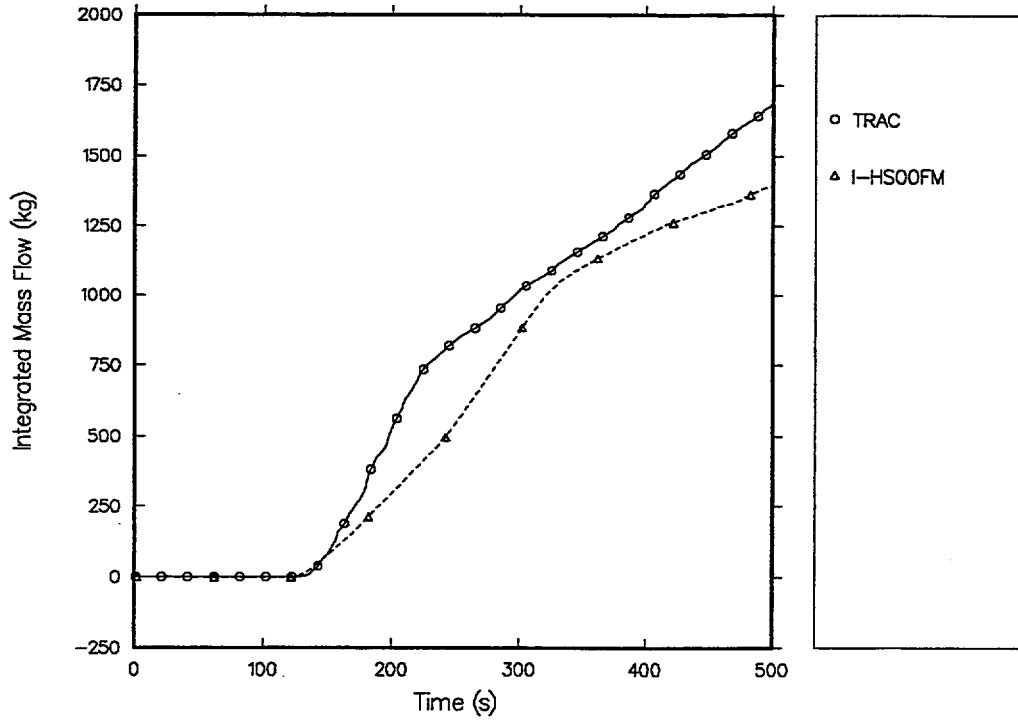


Fig. 5.4-30. Calculated and measured hot-leg integrated mass flow.
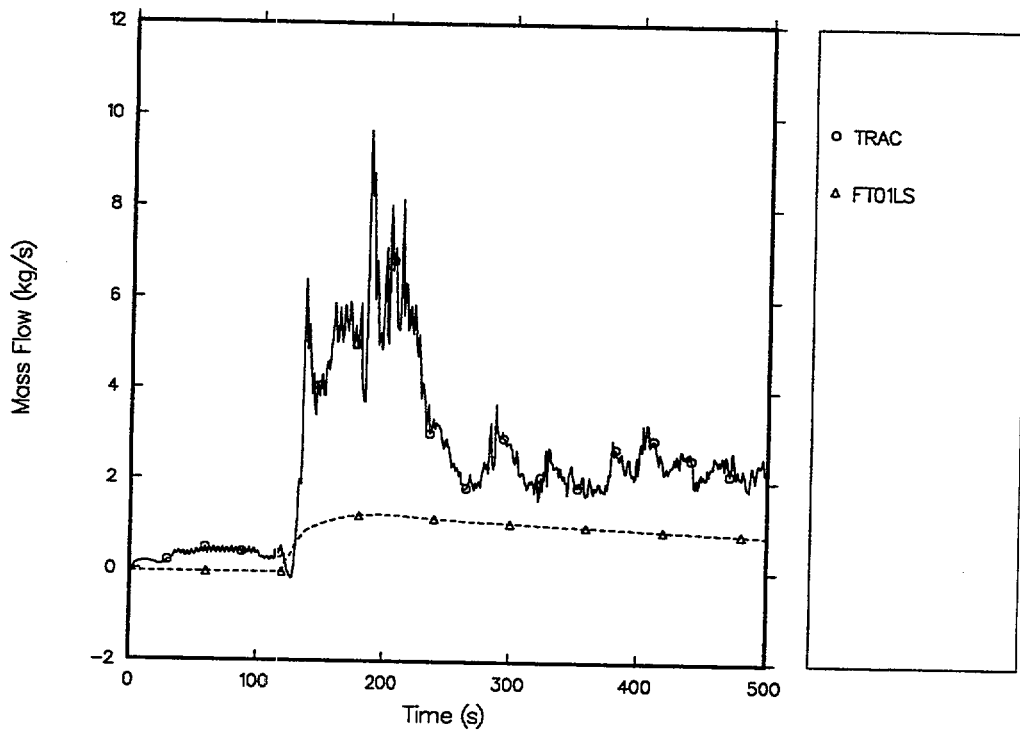
Fig. 5.4-31. Calculated and measured S/W-separator-side, broken cold-leg mass-flow rate.
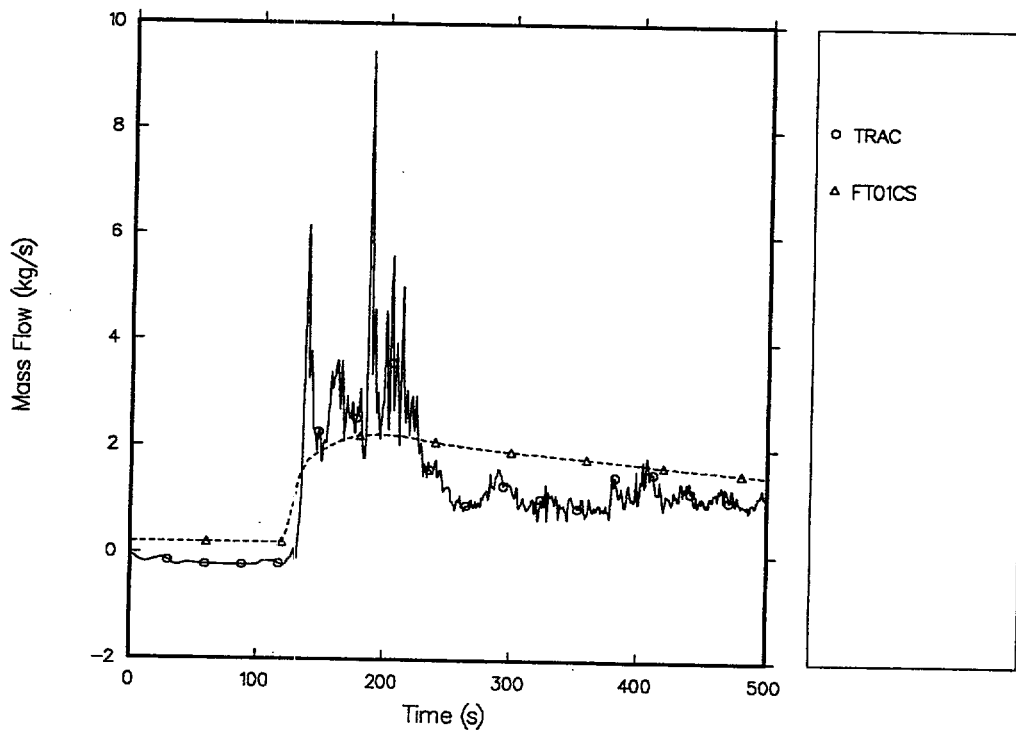


Fig. 5.4-32. Calculated and measured intact cold-leg mass-flow rate.

2. TITLE AND SUBTITLE

TRAC-M/F77, Version 5.5
Developmental Assessment Manual

Assessments

5. AUTHOR(S)

B.E. Boyack, J.F. Lime, D.A. Pimentel, J.W. Spore, J.L. Steiner

8. PERFORMING ORGANIZATION - NAME AND ADDRESS *(If NRC, provide Division, Office or Region, U.S. Nuclear Regulatory Commission, and mailing address; if contractor, provide name and mailing address.)*

Los Alamos National Laboratory
Los Alamos, NM 87545

10. SUPPLEMENTARY NOTES
F. Odar, NRC Project Manager

11. ABSTRACT *(200 words or less)*

Los Alamos National Laboratory has developed the Transient Reactor Analysis Code (TRAC) to provide advanced, best-estimate simulations of real and postulated transients in pressurized water reactors (PWRs). The modernized TRAC-M/F77, Version 5.5, is the latest release version. TRAC-M/F77 (1) is more portable and maintainable than Version 5.4; (2) retains TRAC's essential features, a one- and/or three-dimensional, two-fluid treatment for the thermal hydraulics; (3) has other necessary modeling capabilities to model a reactor system, and (4) has a newly enhanced reflood model. The Developmental Assessment Manual describes the assessment calculations that were compared with analytical calculations and experimental data. The comparisons were performed to determine the accuracy and the applicability of TRAC-M/F77. Based on these assessments against analytical solutions, separate-effects tests, and integral tests, we believe that TRAC-M/F77 is suitable for analyzing PWRs during a loss-of-coolant accident and operational transients. The developmental assessment calculations demonstrate that TRAC-M/F77 is applicable to a wide range of test facilities and is accurate in terms of predicting major trends.

12. KEY WORDS/DESCRIPTORS *(List words or phrases that will assist researchers in locating the report.)*

TRAC
developmental assessment
thermal hydraulics
pressurized water reactor